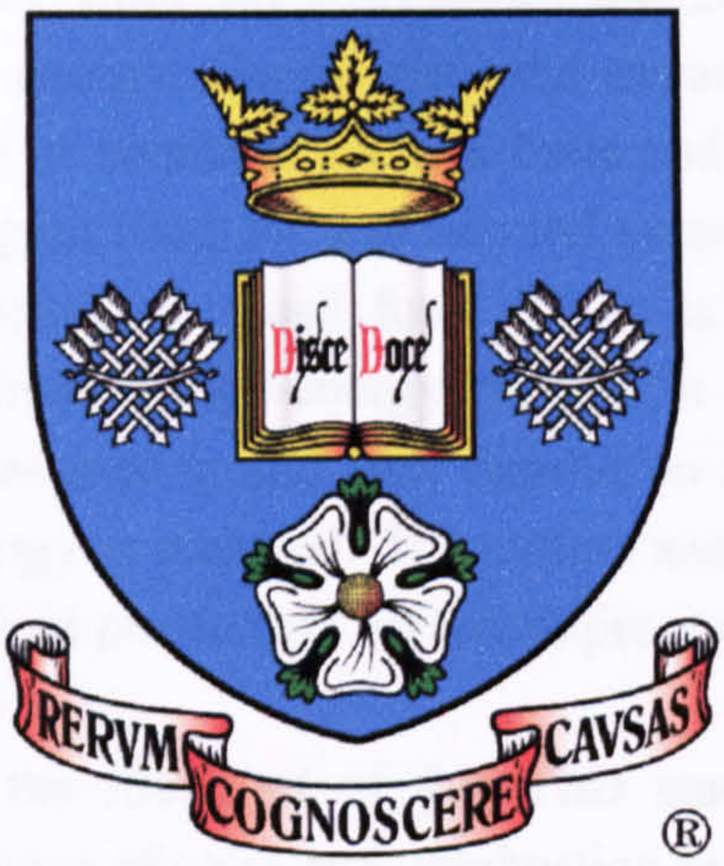

ENERGY FROM BIOFUEL

Thesis submitted to the Department of Chemical and Process Engineering, University of Sheffield, for the Degree of Doctor of Philosophy (PhD)

by

Adela KHOR I Ling, BEng (Hons)

Department of Chemical and Process Engineering

University of Sheffield

August 2006

SUMMARY

Coal energized the 19th century while oil worked for the 20th century. The question that remains pending is the future energy source. With the expanding population and growing demands from industrialization of countries such as India and China, total reliance on fossil fuel is not sustainable. The urgent need for a green and sustainable fuel prompted research into energy crops as an alternative to fossil fuels. There is a need to identify a suitable biomass species, which can provide high-energy outputs in order to replace conventional fossil fuel. The type of biomass used would then depend on the energy conversion process and the form in which the energy is required. Theoretical and experimental studies are also required to investigate the relevant parameters for future process optimisation.

In response to this demand, the first part of this PhD study focuses on examining the parameters affecting the behaviour of solid bed combustion in a fixed bed reactor. Extensive experimental investigation aimed at studying the behaviour of various biomass materials in fixed bed combustion was successfully completed. The parameters investigated in this experimental programme were the influence of primary air flow rates and particle sizes. Complementary conversion technology studied in this PhD is the solid bed gasification in a counter-current fixed bed reactor. The proposed gasifier is part of a two-stage integrated unit that ultimately aims to utilise biomass fuel such as wood chips and fuel pellets derived from agricultural waste. Experimental work was carried out to increase the understanding of the underlying principle of the gasification process. Parameters studied were the steam/air ratio, reactor temperature and particle size.

The results obtained from the combustion tests showed that the burning rate, ignition velocity and flue gas composition were governed by the primary air flow. Single stage combustion occurred at higher air flow rates. It was also observed that the ignition front speed was inversely proportional to the bulk density. Larger particles have a lower ignition front speed and burning rate. The average burning rates of herbaceous fuels were 3-4 times slower compared to other biomass materials such as willow wood, miscanthus pellets and RDF waste. Channelling occurred around the side wall of the reactor for small miscanthus pellets and at several locations in the bed for larger particles (35mm cube). However, the observed channelling effect is severe in the test cases for uncut straw. The study of the gasification process showed that the hydrogen yield is influenced by the steam/air ratio, total flow rate of reactants, reactor temperature and particle size. The production of methane was negligible and no higher hydrocarbons were detected.

A computational code known as the Fluid Dynamics of Incinerator Combustion code (FLIC) was used to interpret the experimental data. In this model, the initial solid waste undergoes step changes in the volume of its components consisting of moisture, volatile, fixed carbon, ash and internal pore space. The code was adapted to incorporate the steam-char reactions and gas phase reactions for the modelling of the gasification process. Comparison between the experimental results and model predictions showed good agreement. The combustion and gasification characteristics such as the burning rate, ignition rate, temperature profiles and gaseous emissions showed similar trends.

ACKNOWLEDGEMENTS

I would like to express my gratitude to my supervisors Professor Vida Nasserzadeh Sharifi and Professor Jim Swithenbank for their help, guidance and support throughout the duration of this research

I am also very grateful to Dr Changkook Ryu and Dr Yao Bin Yang for their invaluable help and suggestions on the research project.

I would also like to thank CPS Civic Ltd for the supplies of biomass material that made the experimental work possible. I am also thankful to Nicola Yates from Plant and Invertebrate Ecology Division (JACR Romthamsted) for the supply of Miscanthus. I would also like to acknowledge the financial support from EPSRC Supergen who funded this project.

I would like to thank the technical and secretarial staff at the Chemical and Process Engineering Department, University of Sheffield: Mike O'Meara, Mr Oz McFarlane, Mr Mike Wilde for the technical assistance with the experimental work and analytical assistance, and Ms Maria Soto for her secretarial support. Special thanks to Chris Wright who helped in the construction of the test rig and helped me run the experiments, worked with me from the very early stages of the research. I am also very appreciative to Mr Graham Glossop from the Department of Materials Engineering and Miss Jane Stanbra from the Department of Chemistry for their laboratory help.

I would like to offer my deepest gratitude to my family and friends for their constant support, guidance, inspiration and encouragement that have helped me through times of difficulty.

"At times our own light goes out and is rekindled by a spark from another person. Each of us has cause to think with deep gratitude of those who have lighted the flame within us." [Albert Schweitzer]

TABLE OF CONTENTS

LIST OF FIGURES

LIST OF TABLES

NOMENCLATURE

Upper Case Symbols

A	Pre-exponential factor	[s^{-1}]
C	Discharge coefficient, Concentration	[-], [kg/m^3]
CC	Carbon conversion	[kg/m^2hr]
C_p	Specific heat capacity	[$Jkg^{-1}K^{-1}$]
D	Bed diameter, Pipe Diameter, Molecular diffusivity	[m], [m], [m^2/s]
D_{ig}	Fluid dispersion coefficient of species ig	[m^2/s]
E	Activation energy	[J/mol]
E^0	Effective diffusion coefficient	[m^2s^{-1}]
E_b	Blackbody radiation intensity	[$Wm^{-2}\mu m^{-1}$]
F	Fractional increase of internal pore space	[-]
h	Enthalpy	[J/kg]
H^0_{298}	Standard enthalpy of reaction	[kJ/mol]
I, I^+, I^-	Radiation intensity	[$Wm^{-2}\mu m^{-1}$]
M_w	Molecular weight	[kg/mol]
P	Mean Pressure	[Pa]
Q_{cr}	Heat adsorbed by the solids	[W/m^3]
Q_{sh}	Thermal source term for solid phase	[W/m^3]
R_o	Process rate, Universal gas constant (8.314 $Jmol^{-1}K^{-1}$)	[$kgm^{-3}s^{-1}$], [$Jmol^{-1}K^{-1}$]
S	Stoichiometric coefficient, Source term	[-], [-]
S_a	Surface area of solid particles	m^2
T	Temperature	[K]
V	Volume, Velocity	[m^3], [m/s]
Y	Mass fraction	[-]

Lower Case Symbols

a_1	Area of pipe	[m^2]
a_2	Orifice area	[m^2]

d	Particle diameter, Diameter orifice bore,	[m], [m]
g	Gravitational acceleration (9.81ms^{-2}), Gibbs energy	[ms^{-2}], [kJ/kg]
h	Enthalpy	[kJ/kmol]
h_s	Convective mass transfer coefficient between solid and gas	[m/s]
h_s'	Convective heat transfer coefficient between solid and gas	[Wm^{-2}K^{-1}]
k	Rate constant	[s^{-1}]
k_a	Radiation absorption coefficient	[m^{-1}]
k_s	Radiation scattering coefficient	[m^{-1}]
m	Mass flow rate, mass combusted	[kg/s], [kg/m^{2}hr]
n	Number of moles	[kmol]
q_r	Radiative heat flux	[Wm^{-2}]
t	Time	[s]
u	Flow velocity	[m/s]
v	Remaining yield of volatile	[-]
v_∞	Ultimate yield of volatile	[-]
w	Volume fraction	[-]

Greek Symbols

β	Ratio of orifice bore to pipe diameter (β=d/D)	[-]
ε	Emissivity, void fraction	[-]
ε_{sys}	System emissivity	[-]
λ	Thermal dispersion coefficient, Equivalence Ratio	[W/mK], [-]
μ	Viscosity, chemical potential	[Ns/m^2], [kJ/kmol]
ρ	Density	[kg/m^3]
σ_b	Boltzmann radiation constant, 5.86 x 10^{-8}	[W/m^{2}K^4]
χ	Mole fraction	[kmol/kmol]
Φ	Parameter to be solved	[-]
Φ	Bed Porosity	[-]

Dimensionless Numbers

Nu
(Nusselt)

$$Nu = \frac{hL}{k_f}$$

(L = characteristic length, k_f= thermal conductivity of the "fluid" and h = convection heat transfer coefficient)

Pr
(Prandtl)

$$\Pr = \frac{\nu}{k}$$

(v = kinematic viscosity and k = thermal diffusivity)

Re
(Reynolds)

$$\mathrm{Re} = \frac{\rho u L}{\mu}$$

(ρ = fluid density, u = fluid velocity, d = characteristic length, μ = fluid viscosity)

Sc
(Schmidt)

$$Sc = \frac{\nu}{D}$$

(v = kinematic viscosity, D = mass diffusivity)

Sh
(Sherwood)

$$Sh = \frac{K_c L}{D}$$

(K_c = overall mass transfer coefficient, L = characteristic length and D= diffusion coefficient)

Subscripts

2	Moisture
3	Volatile Matter
4	Ash
5	Fixed Carbon
A	Dried, pyrolsed and gasified fuel
B	Initial fuel
C	Dried fuel
C	Char
D	Dried and pyrolysed waste
d	Diffusion

env	environment
evp	evaporation
g	Gas
ig	Component identifier in the gas phase
mix	mixing
p	particle
r	Chemical kinetics
s	Solid
sg	Conversion from solid to gas phase
v	devolatilisation
w	Moisture

ACRONYMS

Aebiom	European Biomass Association
ASTM	American Society of Testing Material
BFB	Bubbling Fluidised Bed
CAP	Common Agricultural Policy
CCGT	Gas Turbine Combined Cycle
CCT	Clean Coal Technology
CEA	Chemical Equilibrium with Application
CFB	Circulating Fluidised Bed
CFD	Computational Fluid Dynamics
CFM	Cubic Feet per Minute
CGCU	Cold Gas Clean-Up
CHP	Combined Heat and Power
CV	Calorific Value
DEFRA	Department of Environment, Food and Rural Affair
DPM	Discrete Particle Model
DTI	Department of Trade and Industry
ECS	Energy Crop Scheme
EECI	European Energy Crops Internetwork
EECO	European Energy Crops Overview
EIA	European Information Administration
EU	European Union
EUR	European Currency Unit
FB	Fixed Bed
FC	Fixed Carbon
FLIC	Fluid Dynamics Incineration Code
FSD	Full Scale Deflection
FSR	Full Scale Reading
GCV	Gross Calorific Value
GHG	Greenhouse Gases
HGCU	Hot Gas Clean-Up
HHV	Higher Heating Value
HMSO	Her Majesty's Stationery Office
HTT	Heat Treatment Temperatures
IC	Internal Combustion
ID	Induced Draft

IEC	International Electrotechnical Commission
IGCC	Integrated Gasification Combined Cycle
IGFC	Integrated Gasification Fuel Cell
LCV	Low Calorific Value
MAFF	Ministry of Agriculture Fisheries and Food
MGA	Multi-Gas Analyser
MSW	Municipal Solid Waste
NASA	National Aeronautics and Space Administration
NCV	Nett Calorific Value
NFFO	Non Fossil Fuel Obligation
NTDF	New Technologies Demonstrator Programme
PAH	Polyaromatic Hydrocarbons
PCDD/F	Polychlorinated Dibenzodioxin and Dibenzofuran
PE	Polyethylene
PGC	Process Gas Chromatograph
PID	Proportional Integral-Derivative
PRG	Perennial Rhizomatous Grasses
PSIG	Pound(s) per Square Inch Gauge
RCEP	Royal Commission on Environmental Pollution
RCG	Reed Canary Grass
RDF	Refused Derived-Fuel
RIGES	Renewable Intensive Global Energy Scenario
RO	Renewables Obligation
SEE	Standard Estimate of Error
SRC	Short Rotation Crop
SUWIC	Sheffield University Waste Incineration Centre
TCD	Thermal Conductivity Detector
TPS/ARBRE	Termiska Processor Arable Biomass Renewable Energy System
VM	Volatile Matter

CHAPTER 1

INTRODUCTION

The interest in energy from biomass has expanded dramatically over the last few years. In this chapter, an overview of the main biomass sources, current energy crop application and the potential of energy crops as an alternative to fossil fuel are presented.

1.1 BACKGROUND

1.1.1 Energy crops

Worldwide, biomass is the fourth largest energy resources after coal, oil and natural gas, estimated to be about 14% of the global primary energy. Biomass is a potential source of renewable energy as the conversion of plant material into a suitable form of energy can be achieved using different routes.

Biomass energy comes from both primary and secondary sources. The primary sources are energy crops that have the sole purpose of energy production. Such crops include woody plants, sugar beet and rape-seed oil. Secondary sources include sugar cane fibre, rice husks and wood waste from forestry, waste liquors from the pulp and paper industry, and manure from animal farming. More than 30 potential energy crop species have been investigated in Europe but only a few have achieved commercial status. The introduction of energy crops in agriculture is relatively easy for well-known agricultural crops such as rape and grain crops. However, new crops are hampered by technical and non-technical barriers (Venendaal *et al*, 1997).

An example of a large-scale commercial energy crop in European agriculture is the production of willow for heat and power in Sweden. The crops investigated are suited to different climatic conditions throughout Europe. Crops like Cynara, sorghum and Eucalyptus are grown in most southern parts of Europe. Reed canary grass is adapted to the cold climate of Finland and northern Sweden while willow and rape are grown in northern Europe. Miscanthus is grown in the more central parts of Europe covering regions as far apart as Denmark and Sicily.

1.1.2 Waste

Waste is another source of biomass that provides a potential form of renewable energy. Municipal solid waste (MSW) produced worldwide is increasing every year. The safe disposal of waste has now become an urgent environmental problem. *Table 1.1* shows the estimated MSW produced in 2002 in some European countries.

Country	Typical MSW production per annum (Million tones)	Landfill (%)	Incineration with energy recovery (%)	Incineration without energy recovery (%)
Austria	4.63	32.37	10.57	0
Belgium	4.76	12.48	31.36	2.81
Denmark	3.59	5.99	55.98	0
France	33.02	39.34	30.99	2.65
Germany	52.77	21.35	0.29	22.12
Greece	4.64	91.23	0	0
Ireland	2.46	79.72	0	0
Italy	29.93	61.81	8.64	0.37
Netherlands	9.88	8.20	31.62	0
Spain	26.60	55.36	5.89	0
Sweden	4.17	19.77	40.15	0
UK	35.54	77.52	7.52	0.02

Table 1.1: Amount of municipal solid waste in some selected countries (Eurostat, 2002).

1.1.3 Current Situation

The use of energy crops in the combustion industry is fairly novel in the UK compared to other European countries. Willow chips are used for co-firing, district heating stations and CHP plants in Denmark. Willow and reed canary grass (RCG/Phalaris) are also considered to be the most promising energy crops in Sweden. Straw combustion is popular in Denmark as proven by the numerous straw burning plants; Haslev (Combined Heat and Power, (CHP), Slagelse (CHP), Rudkoebing (CHP), Hvidebaek (District Heating). Ely is one of the UK's first straw burning power stations and also one of the worlds' largest straw burning plants.

While large demonstration plots exist in Sweden and Denmark, smaller demonstration plots are in operation for energy purposes in Finland. Scandinavian countries and Austria are

successful in developing the energy crop industry. Miscanthus, RCG and willow/poplar coppice are novel crops and thus there are barriers of agriculture acceptance. Other crops such as Triticale, sorghum, rape seed oil and hemp do not have the same problem as they are currently grown for non-energy purposes. Nevertheless, policy support from the government is crucial for the successful application of the energy crops. The most advanced countries in the use of solid biofuels based on energy crops are Sweden and Denmark because of the heavy taxation on fossil fuels. The countries that use liquid biofuels are France, Germany and Austria. However, work on the combustion of dedicated energy crops are still at a premature stage compared to wood, coal and waste.

1.1.4 Key benefits of energy from biofuels

Greenhouse gas (GHG) emissions are soaring towards a crucial level leading to serious calls both nationally and locally for the highest possible reduction. The Kyoto Protocol imposes emission targets under which the UK agreed to keep annual greenhouse emission during the period of 2008-2012 to 12.5% below 1990 levels (DEFRA, 2005). The UK government set a higher target of 20%. Biomass is an ideal source of sustainable energy as it reduces greenhouse emissions. The carbon given off in combustion is compensated for by that sequestered in growing the biomass.

Other benefits include job-creation as the production and harvesting and transportation of biomass require labour. Biomass is estimated to take up 4 to 5 times more labour compared to fossil fuels. In the German state of Bavaria alone, the use of biomass as a major source of energy has resulted in creation of about 18 000 jobs (Fujita, 1999). A change in emphasis from food production to energy producing crops will provide a more varied agricultural landscape and increase the biodiversity of farmland.

Development of the conversion technologies promises the application of biomass at lower cost and higher conversion efficiency. When low cost biomass residues are used for fuel, the cost of electricity is often competitive with fossil-fuel powered generation.

Thermal treatment of energy crops yielding biofuel provides for indigenous energy production and security of a sustainable national supply of fuel. Energy crops are easier to predict and control compared to wind or solar power. There is a greater flexibility of supply as the production can be adapted to the national requirements. The EU considers biomass energy as the most important renewable resource. In the Rio United Nations Conference

(RIGES), 1992, half of the worlds' current primary energy consumption, 400EJ/yr is set to be met by biomass while 60% of the worlds' electricity market will be supplied by renewable sources (McKendry, 2002). There is further support from the Non-Fossil Fuel Obligation (NFFO) scheme obliging companies to purchase a fixed amount of power from non-fossil power production (Aebiom, 1999). Biomass is available on a renewable basis, either through natural processes, or it can be made available as a by-product of human activities i.e organic waste. The potential of biomass energy derived from forest and agricultural residues world-wide is estimated at 30EJ/yr, compared to an annual world-wide energy demand of over 400EJ. If biomass is to contribute to a larger extend to the worlds' energy supply, then the cultivation of dedicated crops for energy purposes will be required. When energy crops are considered as a source of biomass, the total energy potential of biomass for energy production may be considerably larger than the energy potential of biomass residues.

1.1.5 Gasification background

Gasification technology dates back to the late 19th and early 20th centuries. In the 1850 period, gas was initially used for cooking, power generation, city and home lighting as referred to in Dickens novels as "gaslight". Coke for steel making was a useful by-product. Gasifiers were then successfully used with engines for power generation in 1878 making the gasifier-engine systems very popular in the period of 1901-1920. During World War II, Germany converted existing vehicles to producer gas due to national security and independence. Gasification technology remained dormant after that as plentiful gasoline and diesel were available. The rise in natural gas prices in the 1970s, revived gasification technology as Shell, Texaco and Dow Chemicals initiated research projects and built coal gasification plants.

Recently, the addition of ten Accession Countries in the EU in May 2004 boosted the EU coal reserves by over 40%. Of the 25 states that now comprise the enlarged EU, 24 rely on coal to meet their primary energy requirement despite competition from other fuels. Coal's major market lies in power generation although national industrial sectors will continue to consume a significant amount. The integrated gasification combined cycles (IGCC), IGCC-fuel cells and hybrid gasification/combustion systems are some of the technologies highlighted for the clean coal technologies (CCT) and near-zero emissions technologies.

The demand for conversion of renewable to hydrogen may increase due to the amount of hydrogen needed in refineries and its possible utilization as a fuel. The shift towards a low CO_2 emission regime has stimulated research into the methods of hydrogen and synthesis gas

production from common catalytic reforming of natural gas towards the production of hydrogen from water electrolysis or thermal conversion processes. The current energy and environmental situation has led to many major companies such as Toyota, Daimler-Benz and General Motors investing in hydrogen-powered vehicle technology.

1.2 OBJECTIVE OF RESEARCH

This PhD research aimed at investigating and comparing two thermal conversion processes; combustion and gasification. The combustion characteristics of a broad spectrum of biomass; Salix (i.e willow), pine wood, Miscanthus and RDF (Refused Derived Fuel) was studied. The use of wood and biomass resources in electricity generation had grown in the recent years. However, improvements in efficiency and burning profile needed establishing before the biomass could be exploited for future development. As the combustion and gasification of biomass is a relatively new field, there is limited data available.

The PhD work was divided into two phases. The first stage involved the combustion of different biomass materials in a fixed bed reactor. The influences of parameters such as the particle size and primary air flow rate on the combustion behaviour were examined. Manipulation of the combustion parameters is important in achieving good combustion efficiency and reduction of pollutant emission. The second stage of this PhD focussed on the design and manufacture of a high temperature steam/air gasifier as part of a novel integrated two-stage unit. Extensive experimental work is needed to increase the understanding of the underlying principle of the gasification process that will hopefully lead to the application of these new technologies, overcoming present barriers. In support of this, a mathematical model was developed and applied to the fixed bed combustion and gasification to further understand the process behaviour thus enabling optimisation of future design work and operation.

1.3 LAYOUT OF THESIS

This PhD thesis presents the research work carried over a period of three years. It consists of eight chapters. These are as follows:

Chapter one introduces the purpose of this research by giving the background of the current biomass applications and the benefit of biomass as an ideal source of sustainable energy. A brief background to gasification is also presented. This section outlines the aim of this PhD research.

Chapter two gives an overview of the biomass energy crops focussing on the origins, availability and properties of the different sources of energy. Discussion includes the legislation covering the agricultural policy, environmental policy and energy policy. This chapter also presents the technological development of two processes; combustion and gasification.

Chapter three presents the fundaments of solid fuel combustion and gasification in a fixed bed reactor. The aim was to show the current progress of research in this field. This section reviews the experimental and numerical research work previously carried out.

Chapter four gives a description of the experimental setup, results and some discussion of the fixed bed combustion. This includes temperature measurement along the bed height, flue gas composition and key results such as the burning rate.

Chapter five concentrates on the experimental setup, results and some discussion of the high temperature steam/air gasification process. The experimental work investigates the carbon conversion of char under varying reactor and reactant conditions.

Chapter six covers the theoretical foundation used in the comprehensive mathematical model. This section presents the conditions and sub-models applied in the mathematical model that was used to simulate the fixed bed combustion and gasification. The discussion of the computational modelling results includes comparison with experimental values.

Chapter seven compares the energy production from biofuel through two thermal conversion processes; fixed-bed combustion and gasification. The limitations of these two processes, affecting the subsequent energy recovery systems and application in 'real' plants are discussed.

Chapter eight lists the conclusion derived from this study as well as suggestions for future work in the next stage of this research programme.

CHAPTER 2

LITERATURE REVIEW

In the last few years, interest in energy from biofuel has expanded dramatically as the urgent need for a sustainable, renewable green energy deepens. The energy recovery techniques divide crudely into thermal processes and low temperature processes. The latter are generally based on bioreactors. This chapter reviews the thermal conversion technologies, focussing in detail on the combustion and gasification process. It begins with an overview of the main biomass sources, the current energy situation in the UK and proceeds to discuss the technological development in these two fields. The chapter concludes with the suitability of biofuel as a high-energy output fuel to replace or supplement conventional fossil fuel.

2.1 BIOMASS, BIOFUEL & ENERGY CROPS

2.1.1 Background

The term *biomass* refers to organic matter available on a renewable basis. Biomass can be obtained from residues or purpose grown crops. Biomass can be divided into four primary classes:

1) wood and woody materials,
2) herbaceous and other annual growth materials such as straw, grasses, leaves
3) agricultural by-products and residues
4) refuse-derived fuels (RDF) and waste or non-recyclable papers often mixed with plastics.

According to the Wikipedia dictionary, 'biofuel' comprises of any fuel derived from biomass. On the other hand, energy crops are a form of biomass grown specifically for their fuel value. Energy crops can be classified in three groups according to the raw materials from which energy is obtained as shown in *Figure 2.1*. The main energy chains are: biodiesel, based on oilseed crops through oil extraction and esterification; ethanol, derived by fermentation from

crops rich in cellulose, sugar and starch; biomass, from species yielding high dry matter production treated with processes such as combustion, pyrolysis and gasification.

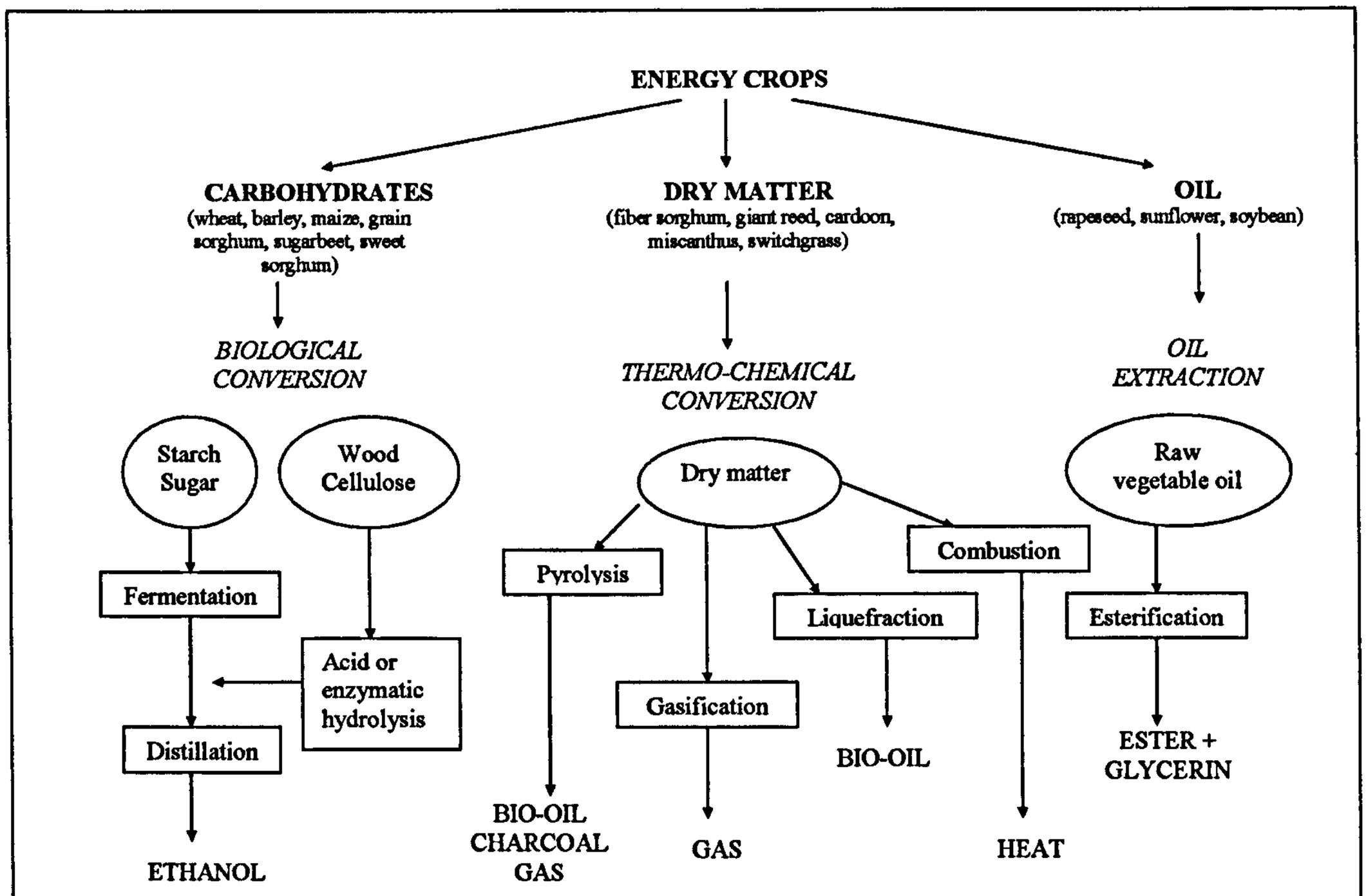

Figure 2.1: Main energy crops, conversion processes and available products for energy uses (Venturi and Venturi, 2003).

The biomass properties determine the choice of conversion process; combustion, gasification, pyrolysis or fermentation (Jenkins *et al*, 1998). The main material properties that affect the subsequent biomass processing as energy sources are the moisture content, calorific value, proportions of fixed carbon and volatile matter, ash/residue content, alkali metal content and bulk density. Thermal conversion processes require biomass with low moisture content as moisture reduces the available energy.

The calorific value (CV) of a fuel can be expressed in two forms, the gross CV (GCV), or higher heating value (HHV) and the nett CV (NCV) or lower heating value (LHV). The significance of the O:C and H:C ratios on the CV of solid fuels was illustrated using a Van Krevelen diagram by McKendry (2002) in which a higher proportion of oxygen and hydrogen, compared with carbon, reduces the energy value of a fuel, due to the lower energy contained in carbon–oxygen and carbon–hydrogen bonds, than in carbon–carbon bonds. The ash content affects the handling and processing cost and presents a significant operational problem particularly if 'slag' is formed at elevated temperatures. Herbaceous fuels are known to

contain silicon and potassium as their principle ash-forming constituents making them difficult for application as they cause severe ash deposition problems.

The low bulk density of herbaceous fuels impacts the transport, storage and thermo-chemical processing cost causing a concomitant increase in cost for it to be competitive on the same energy density basis. Biomass implementation in agriculture requires time because decisions have to be made regarding innovation of biomass. Conventional crops are easier to develop compared to new crops. The high risk and investment puts a limit to biomass implementation as farmers are not keen to undertake this.

In Europe, 20 perennial grasses have been tested and four perennial rhizomatous grasses (PRG); miscanthus, reed canary grass (RCG), giant reed and switchgrass were chosen for extensive research. Some of the grasses and woody materials investigated in this research work are the miscathus, switchgrass, reed canary grass, straw and willow wood. The following part briefly discusses the yield potential, characteristics and limitation of these four grasses and the willow wood as the feasiblity of new crops will depend largely on production costs, cost of conversion of biomass to usable energy and cost of competing fuels.

2.1.1.1 Miscanthus & Switchgrass

Miscanthus and switchgrass are C-4 perennial plants that reduce the atmospheric CO_2 by using a supplementary method of CO_2 uptake which forms 4-carbon molecule instead of 3-carbon molecules. As these C-4 grasses require temperate and warm regions, the productivity is limited to central and southern Europe where the temperature is higher. Miscanthus provides a high dry-matter yield of 8-15t/ha (Scurlock, 1998) while the second year yield of switchgrass is about 8-10tdm.ha (Wageningen, 2003). The annual cropping cycle provides biomass supply throughout the year. The chemical composition of miscanthus and switchgrass is largely similar and is favourable for combustion. The composition of miscanthus on the average comprises of 50% carbon, 43% oxygen and 6% hydrogen with 1% ash (Lewandowski *et al*, 2000) on a dry mass basis. The characteristics vary considerably from year to year between different locations. The mineral content is low compared to wheat straw but higher compared to willow/poplar coppice. The main problem of combustion of these two perennial plants are the low ash melting point showing clear sintering tendensies at temperatures as low as 600°C. Miscanthus has an equivalent CV to SRC willow but a greater crop yield. This reduces the necessary land-take requirement as shown in *Table 2.1*.

Biomass	Crop yield (dmt/ha/a)	HHV (MJ/kg, dry)	Energy Yield (GJ/ha)
SRC willow	10-15	18.7	187-280
Switchgrass	8	17.4	139
Miscanthus	12-30	18.5	222-555

Table 2.1: Energy yield from selected biomass (McKendry, 2002).

Miscanthus production costs are comparable to other annual and perennial energy crops, about 70Euro/t (US $82/t) (Scurlock, 1998). The crops are marginally viable if agricultural set-aside payments are included. The market price of straw is about 80Euro/t in Denmark; in contrast the price of wood chips in Sweden is as low as 32Euro/t. As with new crops, there is a steep 'learning curve' as costs are expected to drop and uncertainties reduce as first demonstration trials and commercial plantings become more widespread. The cost of switchgrass production compares favourably with miscanthus as the cost and associated risk of establishment is lower.

2.1.1.2 Willow wood

Willow is grown mainly in the northern parts of the EU. It is considered the most promising short rotation crop in the UK. An annual yield of between 8 and 20odt/ha.yr (odt=oven dry condition) is expected under commercial conditions. The moisture content of willow wood is fairly low, 25-30% by weight if the wood is stored in a stack and allowed to dry out. The calorific heating value of the willow wood is about 19MJ/kg. Willow consists of low ash and sulphur content, 1.0-1.2% and 0.03% respectively. The content of micronutrients Zn, Mn, Cu and heavy metals Cd, Ni and Pb is higher in willow wood compared to conventional forest wood and straw due to the good ability to take up nutrient (Ledin, 1996).

A willow plantation can be used for 20-30 years before it is necessary to establish a new one or change to another crop. The growing of willow on farmland improves the soil structure due to accumulation of root and leaf litter and on-going natural soil aggregating processes. In the production of willow wood, no insecticides or fungicides are used and only a few herbicide treatments are necessary during the whole crop cycle making it environmentally friendly. However, the harvesting, packaging and transport of coppice wood that takes place in winter causes compaction and permanent soil damage.

2.1.1.3 Straw

The UK produces an estimated 14 million tonnes of straw annually from Eastern England and parts of Central and Southern England (DTI, 1999). Half of the produced straw is used for animal feed and bedding while the rest was previously disposed of by in-field burning but this is now forbidden. The alternative method of straw removal leads to increase transportation and baling costs as well as a penalty in reduction of subsequent crop yield due to the removal of nutrients.

Straw has a low gross calorific value (15GJ/tonne) approximately the same as seasoned wood, one half that of coal, and one-third that of oil (Martindale, 1985). Loose straw has a bulk density of 30kg/m^3, which can be increased to 100-150kg/m^3 by baling. However, this would incur an additional cost of £18/tonne to the farmer for the baling, handling, storage and transportation if straw was to be used in power stations. Delivery cost over 10km would increase the cost to £22/tonne (DTI, 1999). Further fuel processing such as compression to briquettes or pellets increases the bulk density 5-10 fold to 450-650 kg/m^3 (Wilen, 1987).

2.1.2 Current Situation

In the European Energy Crops Overview (EECO), it was found that both liquid and solid biofuel can be economically feasible only with financial incentives, like tax exemptions (as in France and Austria for liquid biofuels), heavier taxes on fossil fuels (like in Denmark and Sweden in the order of magnitude of 5-6EUR/GJ for non-industrial users) and grants for farmers who cultivate energy crops grown on set-aside land. Although the crop has become highly technically developed, farmers' perception of the crop is still a major barrier to increasing the cropped area. The lack of long-term legislation and risk of increase in pest problems are among the barriers. The technical barriers and institutional barriers for liquid biofuels are much smaller than for solid biofuels since the liquid biofuels use traditional and well-known crops. In Austria renewable energy sources supply 27% of the country's total energy consumption and biomass provides half of this. Waste and by-product of the forest industry represent the major biomass input in Sweden and Finland. District heating systems are based on forest and agricultural residues, wastes and peat (Coombs, 1996).

The use of energy crops in the combustion industry is fairly novel in the UK compared to other European countries. Willow chips are used for co-firing, district heating stations and CHP plants in Denmark. Willow and reed canary grass (RCG/Phalaris) are considered the two

most promising energy crops in Sweden. Straw combustion is popular in Denmark as proven by the numerous straw burning plants; Haslev (CHP), Slagelse (CHP), Rudkoebing (CHP) and Hvidebaek (District Heating). Ely is the UK's first straw burning power station and also one of the worlds' largest straw burning plants. However, work on the combustion of energy crops are still at a premature stage compared to wood, coal and waste.

2.1.3 Waste

Waste represents a source of biomass that could be utilized to produce energy to reduce reliance on fossil fuel. Previously, landfill was the major waste disposal method. However, landfill contributes to greenhouse gas emissions and squanders energy equivalent to 25% of the current coal consumption. The total amount of UK municipal waste material is 30 million tones per year, which could provide 10 000MW of power. An electricity generation efficiency of 20% provides 2000MW plus about 6000MW of district heating representing 10% of power and heat consumption (Swithenbank *et al*, 2003).

The Waste Hierarchy is a framework that provides a guide in considering the assessment of waste management. The generation of waste should be first reduced and when it is not practicable, reuse of waste is the next option. If none of the above provides the appropriate solution, incineration would be the choice of disposal.

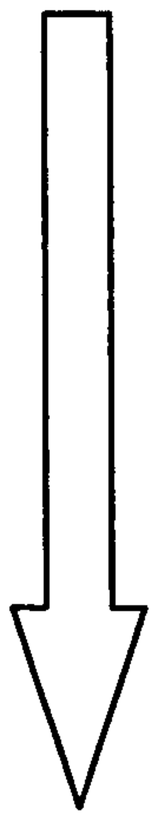

1) Waste Prevention
2) Waste Reduction
3) Re-use/ Re-Manufacturing
4) Recycling
5) Energy from Waste
6) Incineration Without Energy Recovery
7) Landfill

The UK government policy on waste in England is based on 'Less Waste More Value' (Coggins, 1999). Although recycling would be the preferred solution, it was proposed that there should be a substantial increase in the options.

The recovery of energy from waste is important to achieve sustainable waste management especially for the fraction of waste that cannot be economically reused or recycled. The UK has a maximum electricity capacity from waste processing of 3%. Therefore, part of this research sets out to investigate the combustion characteristics of processed waste (refused-derived waste) which focuses on both the emissions and ash composition.

RDF is processed municipal waste that is largely cellulosic in nature. Household and commercial waste are mixed and processed through various screening and conditioning to extract recyclable material. Metallic compounds are removed. The stages involved in RDF processing are shown in *Figure 2.2*. In comparison with MSW, RDF has more homogenous feed material with considerably consistent particle size and shape.

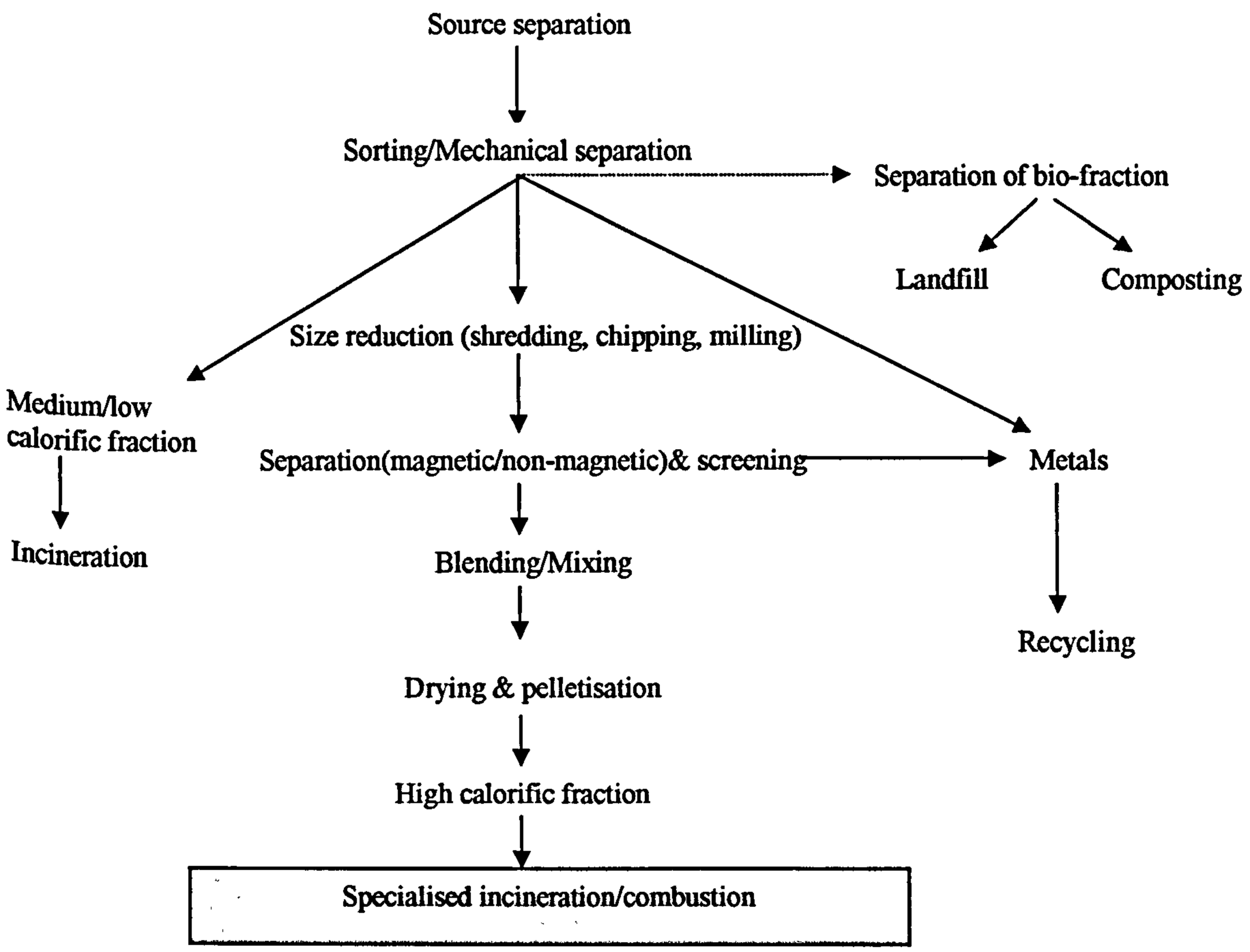

Figure 2.2: Stages of RDF processing (Eduljee, 2003).

The household and commercial waste content varies widely with lifestyle, location, season and local authority collection point. *Table 2.2* shows the calorific value of each dry component and the contribution of each component to the calorific value of the waste.

Polystyrene and fried fats give the highest calorific value compared to the vegetable fats due to the negligible amount of moisture content in these two components compared to 78% in vegetable fats. The ash content and low volatile content reduces the calorific value of PVC as compared to polystyrene.

Component	Moisture, %	Volatiles, %	Fixed carbon, %	Ash, %	Calorific Value, kJ/g
Paper and card	5-10	76-81	8-12	2-5	15.7-18.6
Waxed cartons	3.4	90.9	4.5	1.2	26.4
Vegetable (food)	78.3	17.1	3.5	1.1	4.2
Fried fats	0.0	97.6	2.4	0.	38.3
Grass	75.2	18.7	4.5	1.6	4.8
Plants & shrubs	50-69	25-42	5-8	1-2	4.8-8.6
Wood	20	67.9	11.3	0.8	19.6
Rubber	1.2	84.0	4.9	9.9	25.9
Upholstery	6.9	76.0	14.5	2.6	16.1
Polystyrene	0.2	98.7	0.7	0.4	38.0
PVC	0.2	86.9	10.8	2.1	22.6
Vacuum dirt	5.5	55.7	8.5	30.3	14.8

Table 2.2: Household and commercial waste content (Eduljee, 2003).

The potential of incineration is affected by technical, economic and social factors. Implementation of incineration depends on the technical feasibility of the conversion process, efficiency, reliability and availability. Economic factors such as feedstock production, conversion, storage, transport, utilization and the current prices of conventional fuel are determining factors. The social factors involve the ease of integration with other related activities and reactions to technologies or social acceptance attitudes towards the implementation of incineration. Limited landfill site availability and rising cost provides an incentive for alternative routes. From the Green Alliance Report in the Netherlands, the maximum recycling rate is 45% leaving 55% for incineration (Coggins, 2003). In the waste management hierarchy, the next option after recycling would be energy recovery.

Socially, the public misperception that incinerators emit high levels of dioxin limits the development of biomass incineration. While most people recognize the need to reduce reliance on landfills for waste disposal, they are reluctant to allow incineration operations in or near their communities. Public acceptance rather than technological development limits the use of incineration for waste treatment. Incineration of waste had been successful in Sweden and Scandinavia (Clift, 1999). The legal dioxin emission from an incinerator is 10^{-13}, ten

thousand times less contaminant allowed compared to the manufacturing of microchips. The emission of dioxins from incinerators contributes only 3% of the total UK dioxin emission (Swithenbank et al, 2003). More `appealing` architecture of incinerator plants and public accessible information sources could improve the situation (Schmidt, 1999).

2.1.4 Legislations

Government policy and legislation plays a vital role in the implementation of the new technology as a tax system on energy and new regulation on the power market help to make biofuel competitive with other conventional energy resources. However, the production of energy crops depends just as much on agricultural policy as on the planning of future land use otherwise they cannot present as high a return compared to subsidised arable or livestock production. This section reviews the agricultural, environmental and energy policy that push towards the application of renewable resource or biomass in the energy industry.

2.1.4.1 Agricultural Policy

The attractiveness of new energy crops to farmers depends on the profitability of the land in the alternative uses, which in turn depends on the terms of agricultural support schemes.

- Set-Aside Rules: Set-aside land in Ireland may be used for growing crops for manufacture of products not intended for human or animal consumption (EECI, 1999).
- Finance Bill: Tax relief is introduced for corporate equity investment in wind energy or biomass projects which are approved by the Minister for Public Enterprise (EECI, 1999).
- Woodland Grant Scheme: Provides grant aid for the establishment of short rotation coppice (EECI, 1999).
- Regulation 1257/99 ("the Rural Development Regulation"): Provides establishment grants for approved energy crops such as willow, poplar and miscanthus, if the crops are used for heat, combined heat and power and power generation (Defra, 2003).
- Government strategy for alternative crops: The Ministry of Agriculture Fisheries and Food (MAFF), is working to encourage new developments of industrial and energy crops. MAFF will allocate £30 million to support the growing of energy crops (RCEP).

- Energy Crop Scheme (ESC): Offers establishment grants covering 40-50% of the cost of establishing energy crops. The EU Objective areas are Cornwall (including the Isles of Scilly), Merseyside and South Yorkshire (Defra, 2003).
- Energy Crop Regulation 2000: Financial aid will be given to projects involving the establishment of miscanthus and short rotation coppice that will be used in equipment or a plant that produces energy through the use of such crops (HMSO).
- Common Agricultural Policy (CAP): Energy crops are allowed to grow on land for which they receive set-aside payment to keep it out of food production. It is estimated that there is a global area of 800 million hectares available for growing of energy crops (RCEP).

2.1.4.2 Environmental Policy

Greenhouse gas (GHG) emission is heading towards a critical level, leading to a serious call nationally and locally for the highest possible reduction. 'Dangerous' climate change with increasing damage is projected if global temperature increases about 1 to 3°C above current levels. Probability analysis estimated that concentration of CO_2 levels below 400ppm is required to avoid warming of 2°C (International Scientific Committee, 2005). The UK accounts for 2.5% of the total world energy consumption and is responsible for 2.3% of the total world carbon emissions. The Kyoto Protocol to the United Nations Framework Convention on Climate Change imposes emission targets under which the UK has agreed to the reduction of carbon emission by 12.5% of the 1990 level, by 2010 (EIA, 2003). The commitment of the government to the development of a bioenergy industry is seen in the increasing investment in the renewable energy sources. Under the New Technologies Demonstrator Programme (NTDP) a total of over £30 million funding was allocated to the innovation of new technologies with gasification and pyrolysis being two technologies supported under the development scheme (Defra, 2004).

The Climate Change Levy that came into effect in 2001 imposes a tax on industrial and commercial energy used. This causes industries to look towards alternative energy as a 'clean' source of energy. Most combined heat and power (CHP), as well as solar and wind-powered plants are exempted under the Climate Change Levy (EIA, 2003).

2.1.4.3 Energy Policy

The EU considers biomass energy as the most important renewable source. Energy targets were set at doubling the share of renewable in the overall energy production, rising from 6% in 1997 to 12% in 2010, and renewable electricity from the current 14.5% to 23.5% in 2010 overall in the EU. The UK targets 10% electricity from renewables by 2010 with the current level less than 3% (DTI, 1999). Below is some of the energy policies set out to encourage commercial electricity generation from biomass technologies:

- Non Fossil Fuel Obligation (NFFO): Electricity supply companies have an obligation to secure specified amounts of new generating capacity from non-fossil sources using renewable generators at premium rates. The difference between the premium price paid to "green" electricity suppliers and the market prices is finance by the Fossil Fuel Levy (DTI, 2001).
- Renewables Obligation (RO): Aims to supply 10% of the total energy from renewables by 2010. From 2006, 25% of co-fired biomass must come from energy crops making energy crops an important source of energy for the UK (RCEP).
- White Paper Energy: The White Paper sets to double the share of renewable energy in the total energy demand of the European Union from 6% to 12% (Aebiom, 1999). The White Paper Goals for renewables are as summarise in *Table 2.3*.

Type of RES	Contribution in 1995 (Mtoe)	Contribution in 2010 (Mtoe)	Additional contribution
Biomass	44.80	135.00	+ 90.20 (+201 %)
Hydropower	26.40	30.55	+ 4.15 (+15.7 %)
Wind energy	0.35	6.90	+ 6.55 (1871 %)
Solar collectors	0.26	4.00	+ 3.74 (+1438 %)
Photovoltaics	0.002	0.26	+ 0.26 (+3 000 %)
Geothermal	2.5	5.20	+ 2.70 (+108 %)
Total :	74.31	181.91	**107.60**

Table 2.3: Renewable energies, white paper goal for 2010 (Mtoe) (Aebiom, 1999)

The biomass sector is clearly important to the UK's environmental and energy commitments in the coming decade.

2.2 THERMO-CHEMICAL CONVERSION OF BIOMASS

The conversion of biomass or waste into a suitable form of energy, usually electricity or fuel for an internal combustion engine, can be achieved using a number of different routes. Wood and other biomass can be treated in different ways to provide solid, liquid and gaseous fuel.

In general, the conversion methods are divided into thermal and biological (anaerobic digestion and fermentation). Biomass can be converted into three main products: two related to energy, power/heat generation and transportation fuels and one as a chemical feedstock. The four thermo-chemical conversion options available are combustion, pyrolysis, gasification and liquefaction as illustrated in *Figure 2.3*.

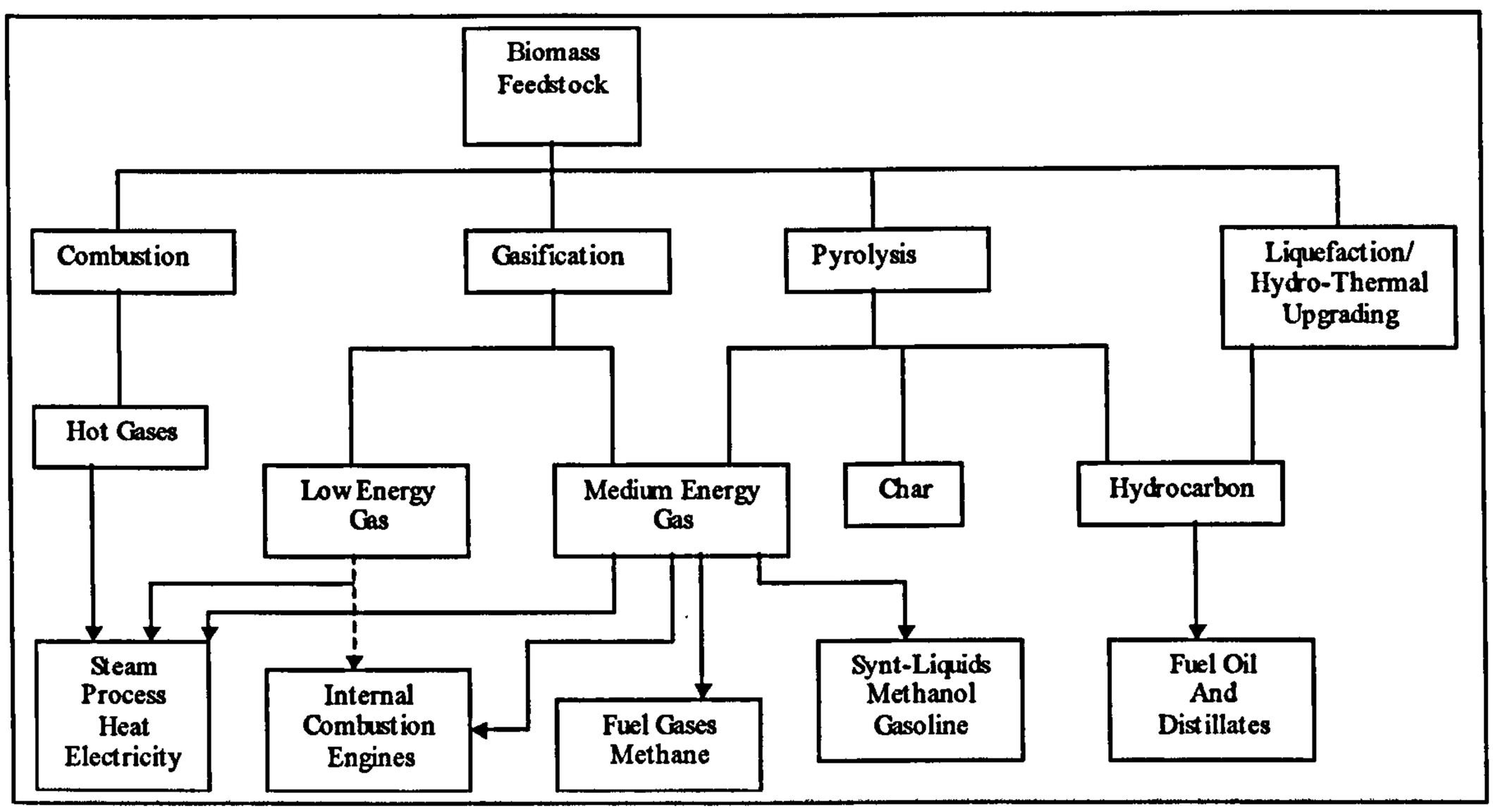

Figure 2.3: Main processes, intermediate energy carriers and final energy products from the thermo-chemical conversion of biomass (McKendry, 2002).

2.2.1 Combustion

Combustion, gasification and pyrolysis are high temperature chemical reaction processes that convert organic materials to energy or a useful chemical using different amounts of oxygen. Combustion is a process that utilizes the full calorific value of the fuel to generate heat for direct use. Combustion or incineration is a more proven and simpler process compared to pyrolysis and gasification and is widely applied. However, the technological development is limited due to the lack of public acceptance. The types of incinerator can be classified into

four groups: *moving grate, incinerator chamber, fluidized bed and rotary-kiln*, depending on the way in which the fuel and oxidant flow are supplied.

2.2.1.1 Moving Grate

Moving grate furnaces have been a popular system for municipal waste incineration to allow mixing of waste with an appropriate excess of air. There are a few types of moving grate furnaces: travelling grate, ARR Widmer, Ernst System Double Motion Overthrust grate, reciprocating grate, reverse acting reciprocating grate, rocking grate and the roller grate.

Travelling Grate

The travelling grate has two or more continuous metal-belt conveyors. The first grate receives waste from the hopper. The waste is dried, devolatilised and burned. It is then dropped onto the second grate known as the burning grate. The bottom ash is collected in an ash hopper at the end of the burning grate. The system is reliable and relatively cheap. However, there is poor waste mixing during combustion. It requires a large amount of air to improve combustion and consequently emits a large volume of flue gas. This causes an overload to the particulate removal system (Zakaria, 2000).

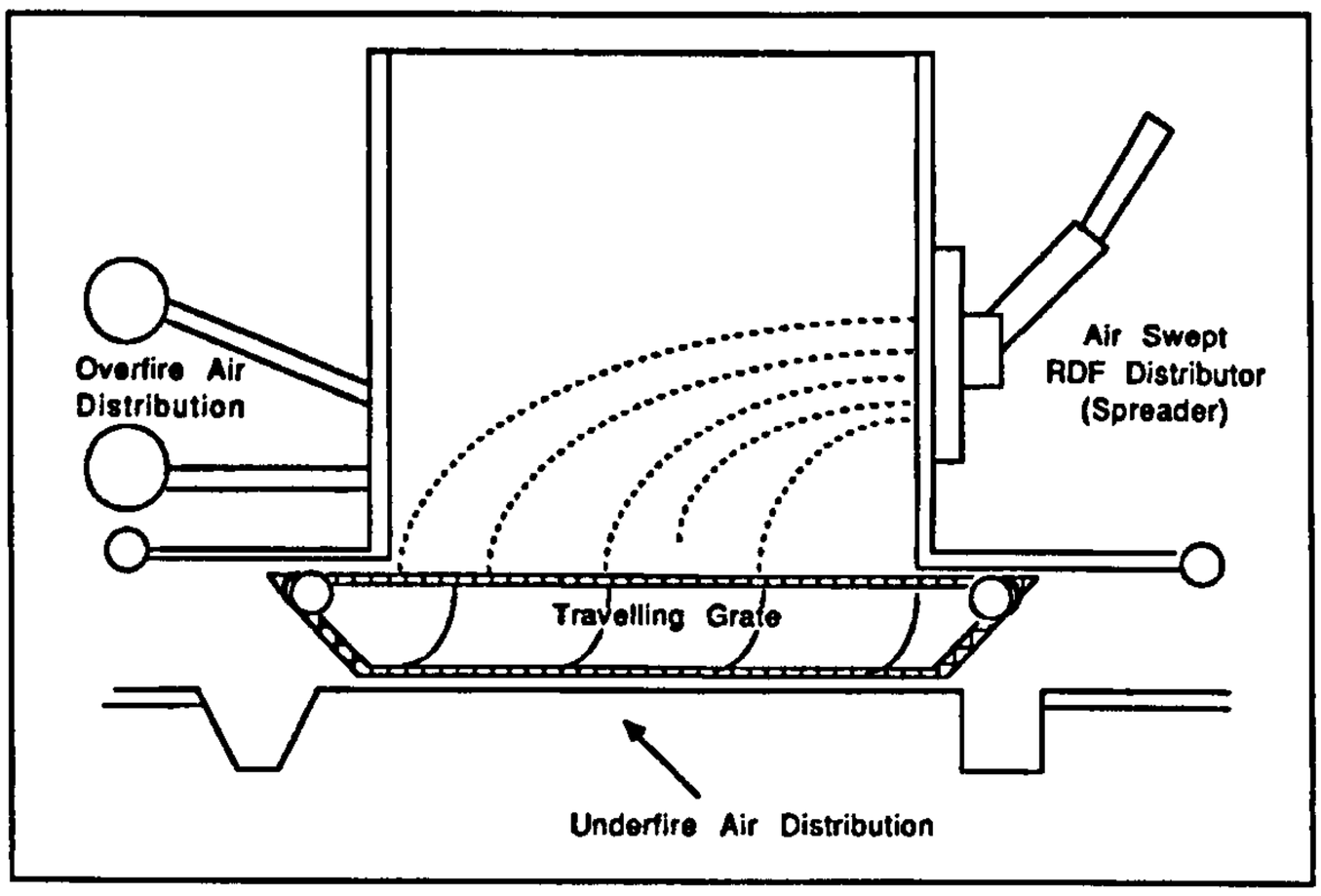

Figure 2.4: Travelling Grate ((Tillman, 1991).

ARR Widmer and Enst System Double Motion Overthrust Grate

The double-motion overthrust grate consists of stationary bars and a superimposed arrangement of grate bar rows moving in opposite directions. As the grate bars adjacent to a stationary bar move away from each other, the grate bars immediately adjacent to the next stationary bar move towards each other. The continuous movement of the rows and the horizontal construction of the grate allow the waste to be advanced in a controlled manner and prevent the waste from sliding. When the grate bars move away from each other, the waste layer is loosened and transported to the next section of the grate, falling into the space created by the grate bars moving towards each other.

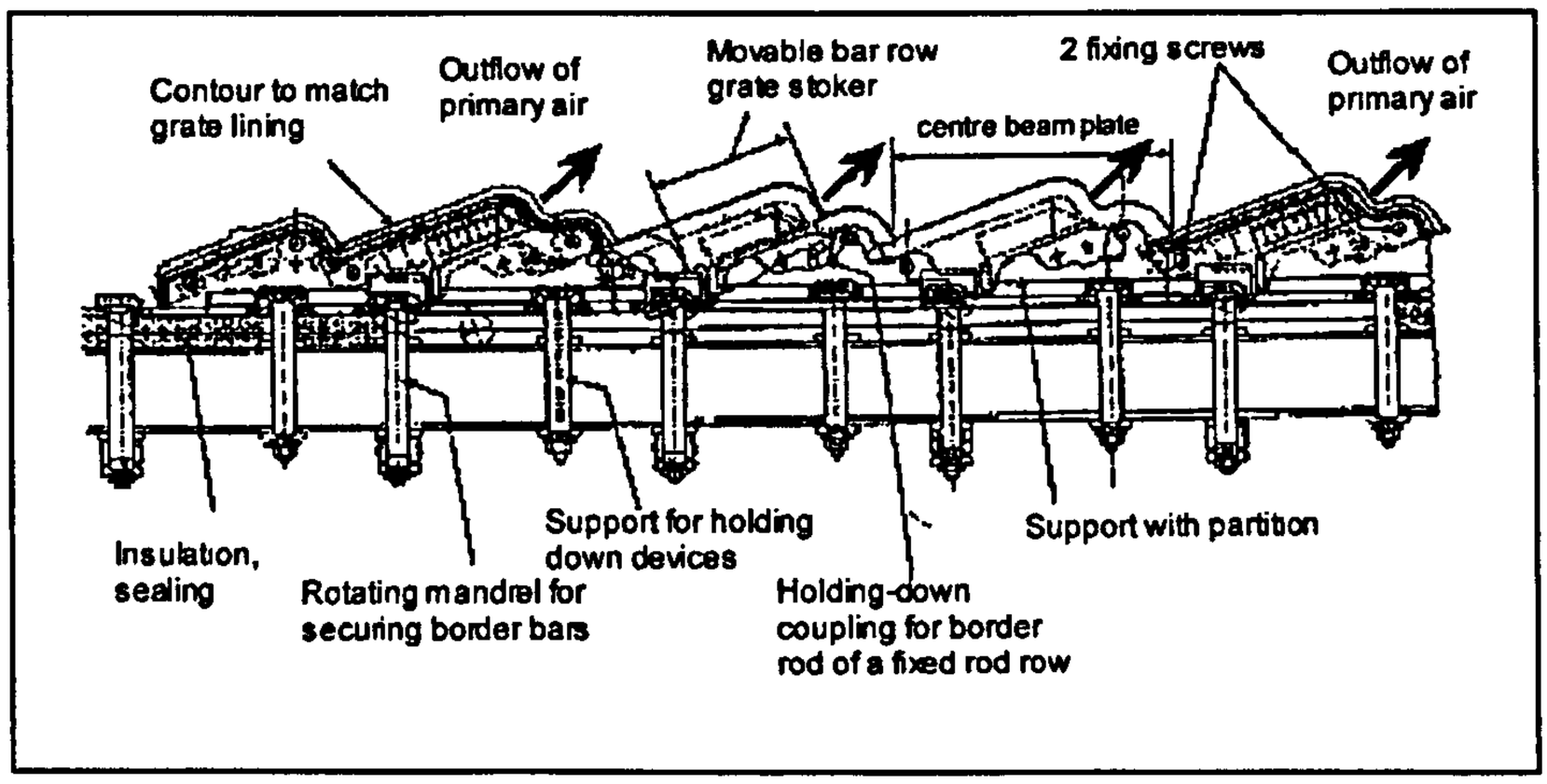

Figure 2.5: ARR Widmer and Enst System Double Motion Overthrust Grate(Umwelttechnick, 1995).

Reciprocating Grate

A reciprocating grate consists of a stack of steps configured with moving and fixed grate sections inclined downward toward the ash discharge pit. The moving grates slide back and forth in between the fixed grates, agitating the waste and transporting it to the ash hopper. The reciprocating grate provides additional agitation and is arranged in a multiple-level series. This grate works well for burning wet refuse as it has very good primary air distribution producing good burnout. However, this grate has poor mixing of waste.

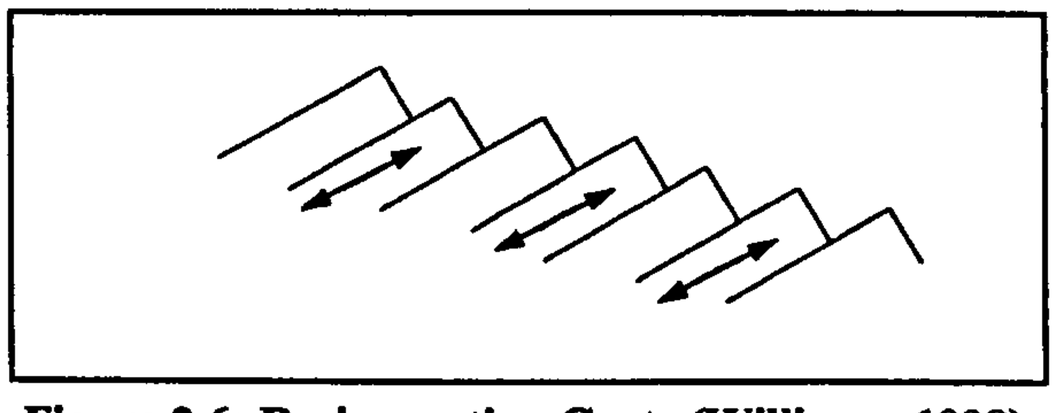

Figure 2.6: Reciprocating Grate (Williams, 1998).

Reverse Acting Reciprocating Grate

The reverse acting-reciprocating grate consists of moving and fixed grate sections, inclined downwards, with a steeper angle toward the discharged end. The grate elements reciprocate uphill against the downward movement of waste, causing a rolling motion of burning material as a result of the upward reverse trust. Additional mixing is obtained when the waste tumbles from one level to the next in a step-like configuration of the grate. This system is very reliable and produces good burnout and is able to withstand long operation hours. However, it is an expensive grate that requires high maintenance cost. Systems with a reciprocating grate include the Martin reverse-acting reciprocating grate, the Ansaldo Volund forward acting grate and the Von Roll reciprocating grate.

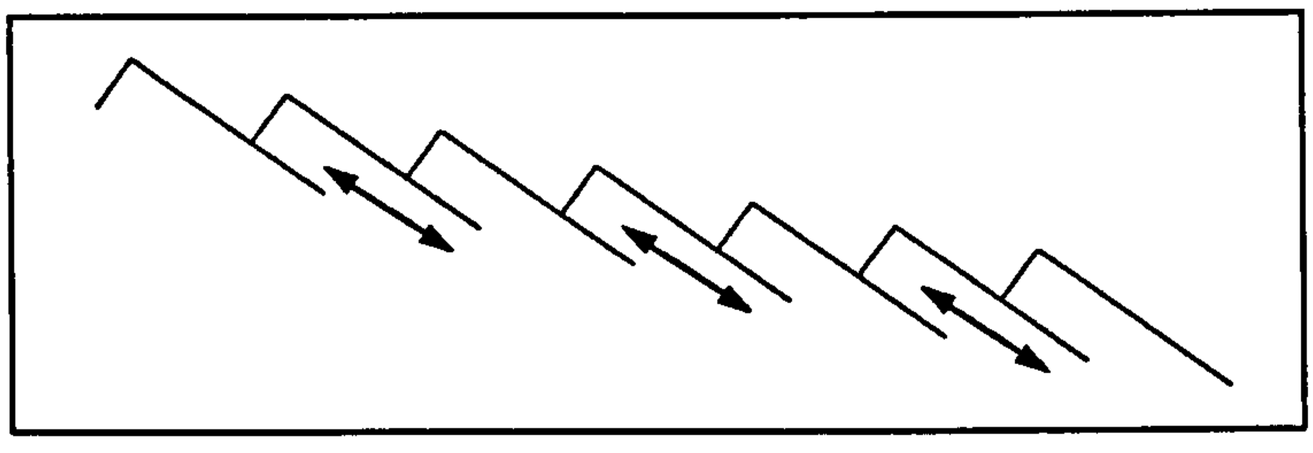

Figure 2.7: Reverse Acting Reciprocating Grate (Williams, 1998).

Rocking Grate

The rocking grate is configured so that it slopes downward toward the ash discharge end as shown in *Figure 2.8*. It comprises of two or more grate sections, having the same width as the furnace. Alternate grate rows are rotated 90° forward about the axis to produce an upward and forward motion to agitate the waste and move it forward. The grates then rotate back to the initial resting positions while the alternate grate rows rotate forward. This continuous motion of back and forth rotation of alternate grates, agitates and pushed the waste forward. This grate is known to produce good burnout. However, small objects can be trapped between the grates causing a need for frequent operational maintenance and in severe cases weekly maintenance is required. The Esslingen system and Nichols system are typical rocking grate systems (Zakaria, 2000).

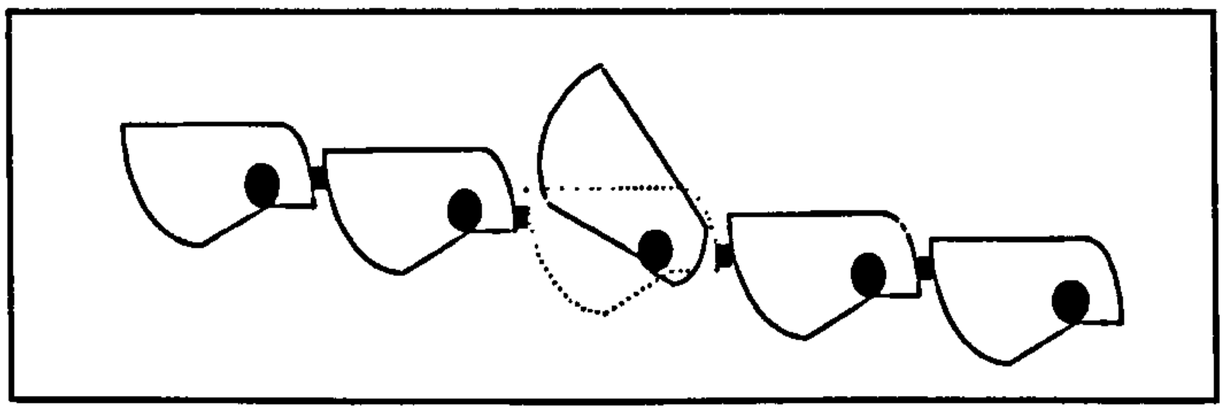

Figure 2.8: Rocking Grate (Williams, 1998).

Roller (Dusseldorf) Grate

This system consists of a series of slotted rotating drums. The drums rotate forward, agitating the waste and transporting it onto the next drum. The drum rotation mixes the waste between them. Each drum extends across the whole furnace width and has its own variable speed control to provide better grate control during combustion than other types of grate. The main disadvantage of this system is that small objects can get trapped between the drums and stop their rotation. The VKW system and Bruun and Sorensen system are examples of the roller grate (Zakaria, 2000; Whiting, 2001).

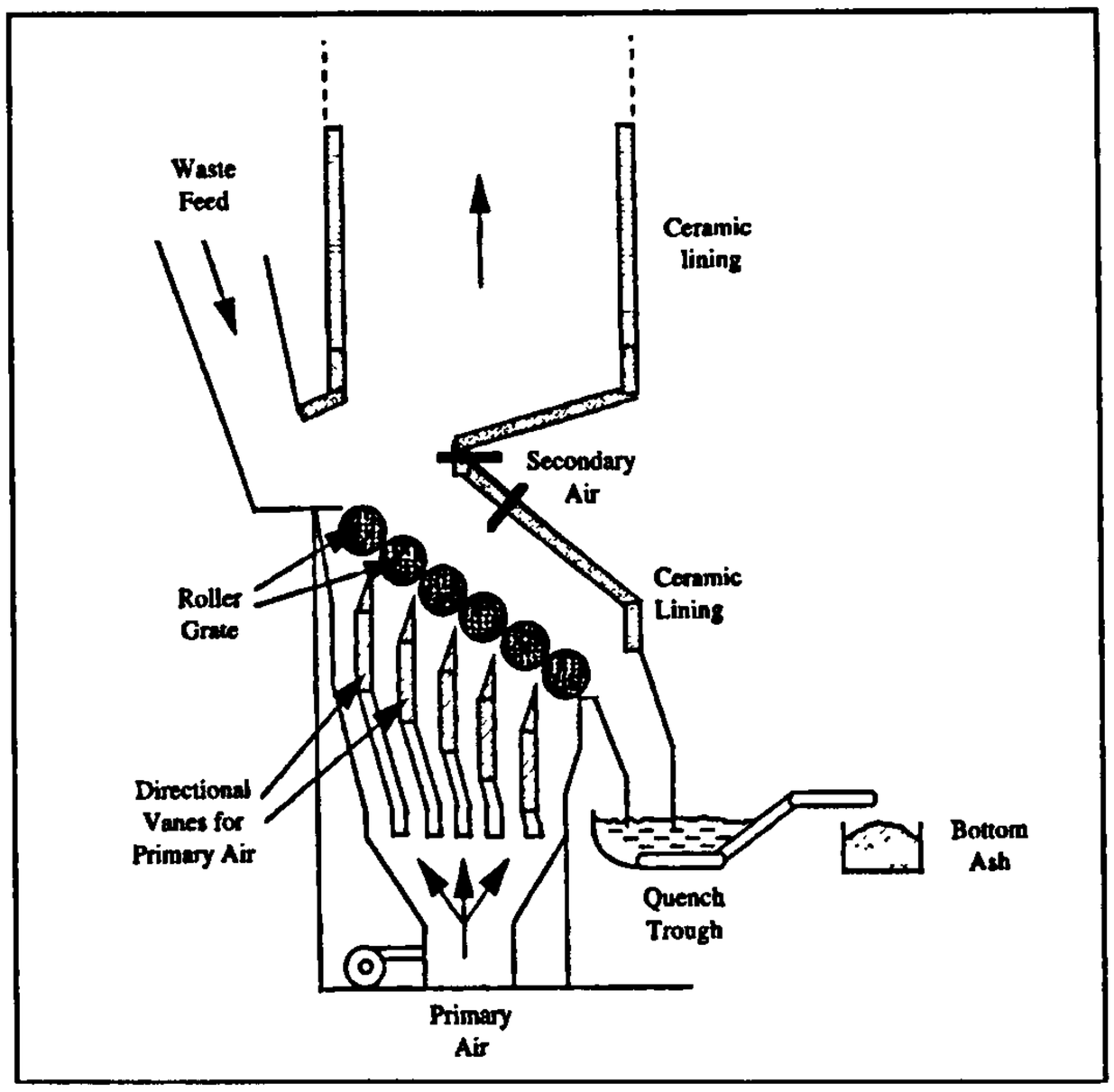

Figure 2.9: Roller (Dusseldorf) Grate (Williams, 1998).

2.2.1.2 Incinerator Chamber

The combustion chamber is located above the grate, where volatile compounds from the waste are burned. The chamber size determines the gaseous volatiles` mean residence time while its shape affects the waste heat pattern. Heat received from the hot flue gases and furnace wall affects the gaseous flow pattern, recirculation and mixing. Common types of combustion chambers are *vertical shaft type*, *box type* and *cone profile*.

A vertical shaft combustion chamber is used with reverse reciprocating or roller grates. The design provides good gas mixing and long gas residence time. The performance is dependent on the combustion air distribution. Currently, there are three types of vertical shaft combustion chamber: parallel gas flow designs, contra gas flow types and centre gas flow design as shown in *Figure 2.10(a)*. Contra gas flow is used for high moisture content or low volatility waste. The parallel flow design favours dry and easily ignited waste while centre gas flow combines features of the first two designs.

The box type combustion chamber is used with the rocker and W-grate plants. It has a variation of rectangular box, slightly longer and lower as shown in *Figure 2.10(b)*. However, the gas turbulence in this type of combustion chamber is not as good compared to the vertical shaft type because of the poor combustion air distribution. A cone profile type is usually used with an L-stoker grate as shown in *Figure 2.10(c)*. This design does not allow a long residence time.

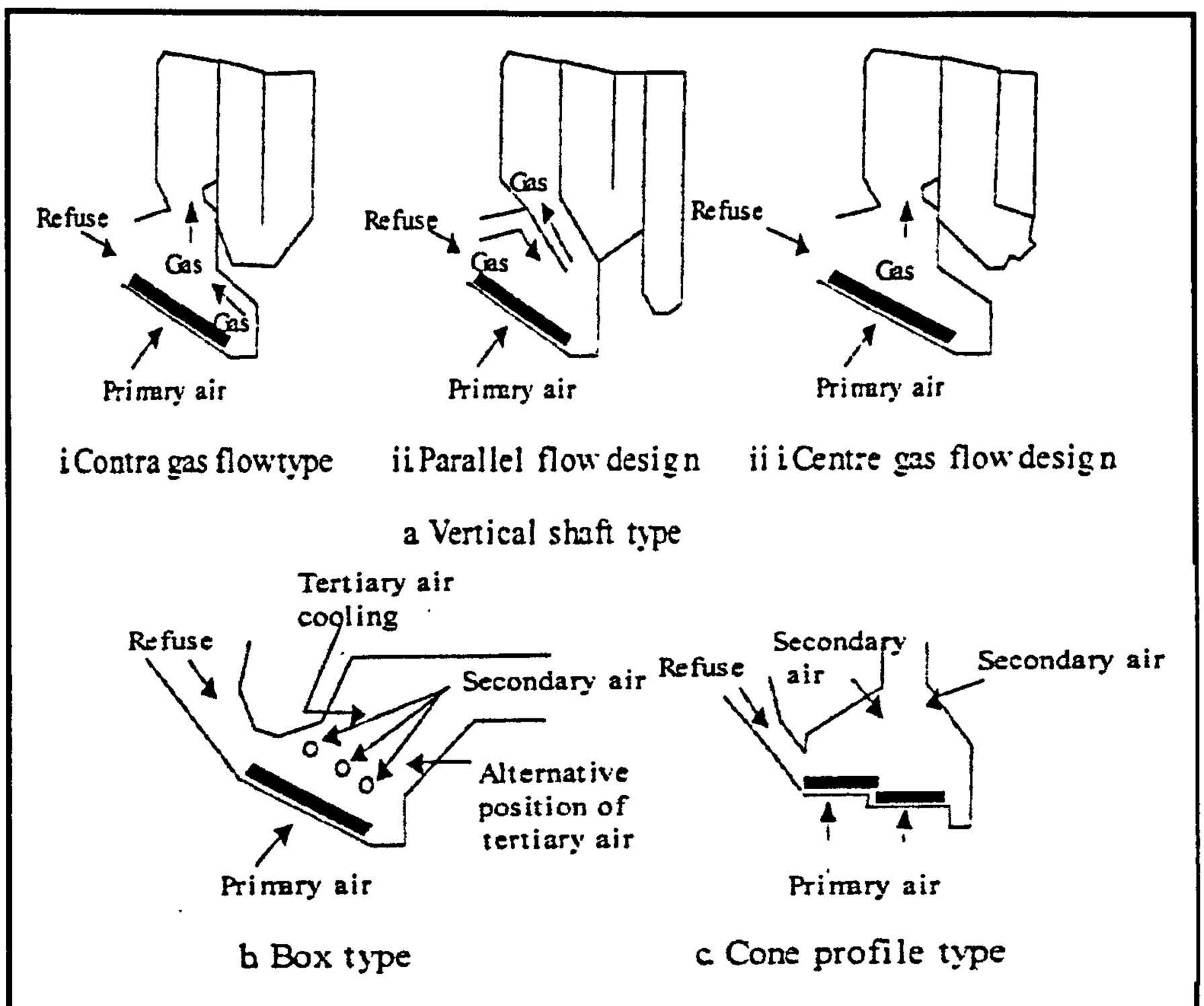

Figure 2.10 Types of incineration chamber (Clayton, 1991; Hisaki, 2003).

2.2.1.3 Fluid Bed Incinerator

The fluid-bed furnace is a cylindrical, refractory-lined shell with a supporting structure above its bottom surface to hold a series of tuyeres, which allow the passage of air upward into the bed and tend to prevent the passage of sand. The *tuyere plate*, can be either refractory or constructed of steel alloy. Air is introduced through the fluidizing-air inlet at pressures in the range of 3.5 to 5 psig creating a high degree of turbulence in the sand bed. The top of the bed undulates and has the appearance of a fluid. Air can be introduced into the windbox either cold or preheated by the exiting flue gas. The simple system illustrated in *Figure 2.11* includes an air preheater. The bed material is most commonly silica sand but may be limestone, alumina or ceramic material. The drying process is practically instantaneous; moisture flashes into steam upon entering the hot bed. Fluidization provides maximum contact with air, maximizing the burning efficiency. Ash and some sand become airborne and exit the furnace with the flue-gas stream. Some waste materials, particularly those containing metal salts, may cause the bed particles to grow in size and combine and agglomerate. Clinkers may be formed and these clinkers will reduce the fluidization of the bed leading to bed seizures (Brunner, 1993).

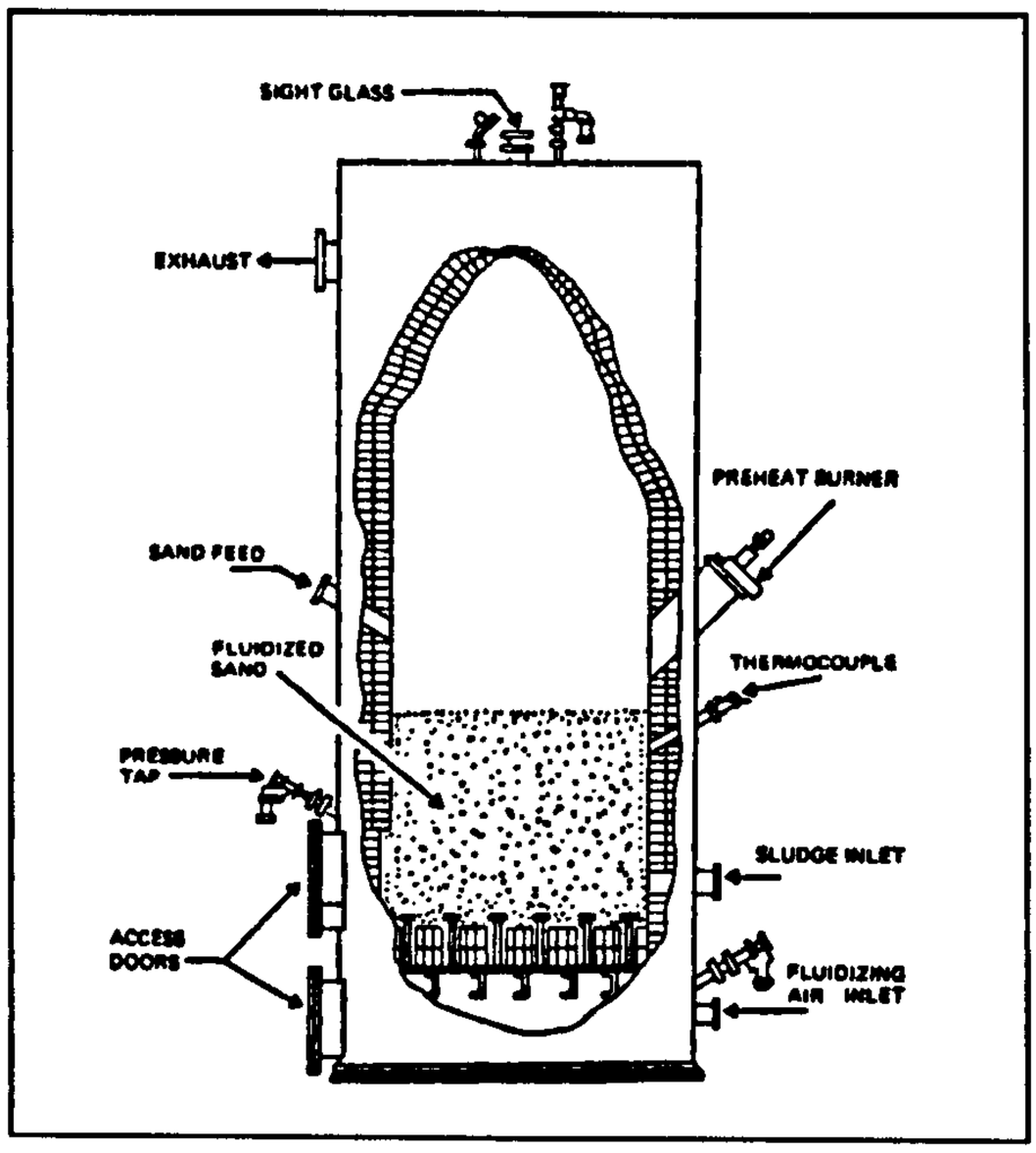

Figure 2.11: Fluidized Bed (Brunner, 1993).

2.2.1.4 Rotary-Kiln Incineration Systems

The rotary-kiln incinerator can handle solid, liquid, gaseous and sludge wastes. It has provisions for waste feed, air injection, the kiln itself, an afterburner and ash collection. The gas discharge from the afterburner is directed to an air emissions control system. An induced draft (ID) fan is provided within the control system to draw gases from the kiln through the equipment line and discharge them through a stack to the atmosphere. The conventional rotary kiln is a horizontal cylinder, lined with refractory, which turns about its longitudinal axis. Waste is deposited in the kiln at one end and waste burns out to an ash by the time it reaches the other end. Kiln rotation speed varies in the range of ¾ to 4 revolutions per minute. A source of heat is required to bring the kiln up to operating temperature and to maintain its temperature during incineration of the waste feed.

2.2.2 Gasification

The work on gasification processes can be dated back to as early as the 16th century. Some of the first generation gasifiers developed are the Winkler Fluidised Bed Process (1926), the Lurgi Moving Bed Pressurised Gasification Process (1931), the Koppers-Totzek Entrained Flow Process (1940) and the Wellman Fixed Bed.

Gasification provides an option for inertisation and reduction of waste weight and volume, offering considerable potential for highly efficient destruction of hazardous waste. It prevents corrosion and emissions by retaining alkali and heavy metals (except mercury and cadmium), sulphur and chlorine within the process residues preventing PCDD/F formation and reducing thermal NO_X formation due to the lower temperature and reducing condition (Phillips *et al*, 2001). Additional merit of gasification would be the production of large volumes of valuable hydrogen, carbon monoxide and methane compared to the production of carbon dioxide and water from the conventional incineration processes.

2.2.2.1 Gasification System

Gasification involves the thermochemical conversion of solid carbon-based material (biomass) to combustible gaseous products by the supply of oxygen. The major gasification outputs are the gases; CO_2, CO, H_2, CH_4, H_2O, liquid fraction; tars and oils and chars, which consist of pure carbon plus inert material originally present in the feedstock. There are three

alternative gasification processes with different main reactants resulting in product gases with different calorific values and composition:

- *Direct Gasification:* An oxidant gasification agent is used to partially oxidize the feedstock. The oxidation reactions supply the energy required to sustain the process.
- *Indirect Gasification*: No oxidizing agent is required. Steam is used as it increases the hydrogen content of the combustible gas.
- *Oxygen gasification*: Produces `synthesis gas`

The calorific values of the product gas are low for air gasification, about 4-7MJ/Nm^3, and medium, about 10-12MJ/Nm^3 for oxygen gasification. Steam gasification produces a fuel gas with calorific value of 15-20MJ/Nm^3 (Belgiorno *et a*l, 2003).

A wide variety of gasifier designs have been developed depending on the end-use of the gasification products and the type of feedstock. The gasification processes can be characterised in terms of the four main design parameters; temperature, pressure, reactant gases and the method of contacting (Merrick, 1984).

The gasification operating temperatures are higher compared to pyrolysis, being about 800-1100°C with air gasification and 1000-1400°C with oxygen. In general, a higher temperature increases the rate of the gasification reaction. However, operation at very high temperatures could risk the possibility of ash forming molten slag.

Gasification operation at high pressure discourages the decomposition of carbon dioxide and steam, reducing the formation of carbon monoxide and hydrogen. However, operation at elevated pressure is useful for a gas turbine power generation cycle that operates at high pressure as it reduces the need for additional compression energy needed for the large volume of product gas.

The three basic reactants for the gasification processes are oxygen, steam and hydrogen. The choice of reactants depends on the applications and properties of the required product gas as pure reactant or a mixture of reactants could be used in the gasification reactions. The use of air instead of oxygen in the system is usually accompanied by a lower volume of steam as sensible heat is required to heat the air. Steam gasification produces a nitrogen-free gas at the expense of the requirement for an external source of heat. Gasification systems with hydrogen as a reactant are commonly used when methane is the required product.

A gasification system is made up of the three major fundamental elements (Belgiorno *et al*, 2003): gasifier, gas cleanup system and energy recovery system.

2.2.2.2 Types of Gasifier

Gasifiers fall into four groups: *fixed bed gasifier, fluidised bed gasifier, entrained-flow* and *indirect gasifier.* Two types of gasification systems are available, the single-stage processes and the two-stage processes. Single-stage processes employ a single carbonisation/gasification bed. In the two-stage processes the carbonisation and gasification zones are separated. Air and steam are supplied to the bottom of the lower stage in which the gasification reactions take place. At the top of this stage part of the gas is removed to provide a tar-free product gas. The remaining gas passes into the upper carbonisation stage to which it supplies sensible heat. A product gas containing tar is obtained from a second gas off-take at the top of this stage. This result in an extended, low-temperature carbonisation zone and minimises the soot and pitch in the product gas (Merrick, 1984).

Fixed-Bed Gasifier

This system is employed in the commercial Lurgi gasifier. Fixed bed gasifiers can be classified as updraft, downdraft or cross-flow depending on the airflow.

Updraft Gasifier

The updraft gasifier is a counter-current flow reactor where fuel is introduced from the top by a lockhopper/rotary valve and flows downward through the reactor to a grate where ash is removed. The gasifying medium is supplied at the bottom of the unit via a grate and flows upwards through the reactor. The gasification process could be divided to four different stages taking place along the height of the gasifier as shown in *Figure 2.12.*

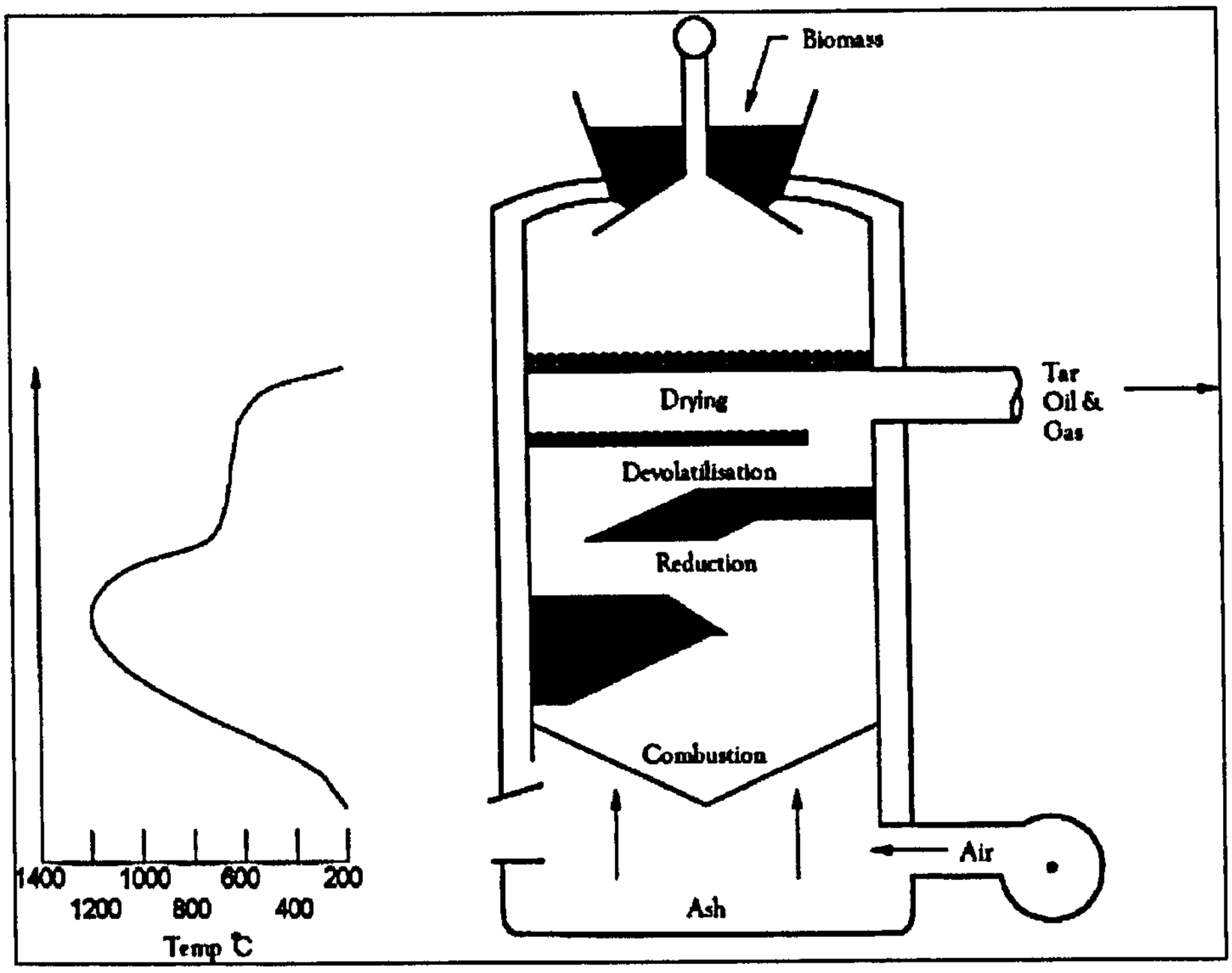

Figure 2.12: Schematic of updraft gasifier (McKendry, 2002)

The combustion zone occurs at the bottom of the reactor whereby char burns to form carbon dioxide (CO_2) and steam (H_2O) which flows upward counter-currently to the down flowing solid. The exothermic process drives the gasification, pyrolysis and drying. The maximum temperature in this zone is higher than 1200°C. CO_2 and H_2O are then partially reduced to carbon monoxide (CO) and hydrogen (H_2) through reaction with carbon in the char at temperatures of 800-1200°C. The gases contact the dry biomass (400-800°C) and devolatilize the biomass to produce pyrolysis products and residual char. The gases and pyrolytic vapours dry the wet biomass and the product exit temperatures are 80-100°C. The product gas from an updraft gasifier contains a considerable quantity of tars and oil that is produced initially in the pyrolysis zone. This is compensated by the higher overall efficiency of the process due to the low temperature of gases leaving the gasifier (Bain, 2004).

Downdraft Gasifier

In the downdraft gasification process, the air and product flow in the same direction of the solid fuel (*Figure 2.13*). The downdraft gasifiers are designed to minimised tar and oil production. The fuel and pyrolytic gases move co-currently downward through the bed. Pyrolysis products pass the char combustion zone where they are contacted with air and tars and are thermally cracked and partially oxidized. The tar conversion is greater than 99%, and

is a function of temperature, combustion efficiency and channelling. The combustion zone temperature is about 800-1200°C. The hot char in the reduction zone reduces CO_2 and H_2O to CO and H_2. The exit gas temperature is about 700°C resulting in a lower efficiency (Bain, 2004). The updraft and downdraft gasifier are limited by similar constraints whereby fairly uniform feed with few-fines is required to maintain the bed physical properties and minimize channelling effects. A low ash with high fusion temperature is required in the feed to prevent slagging.

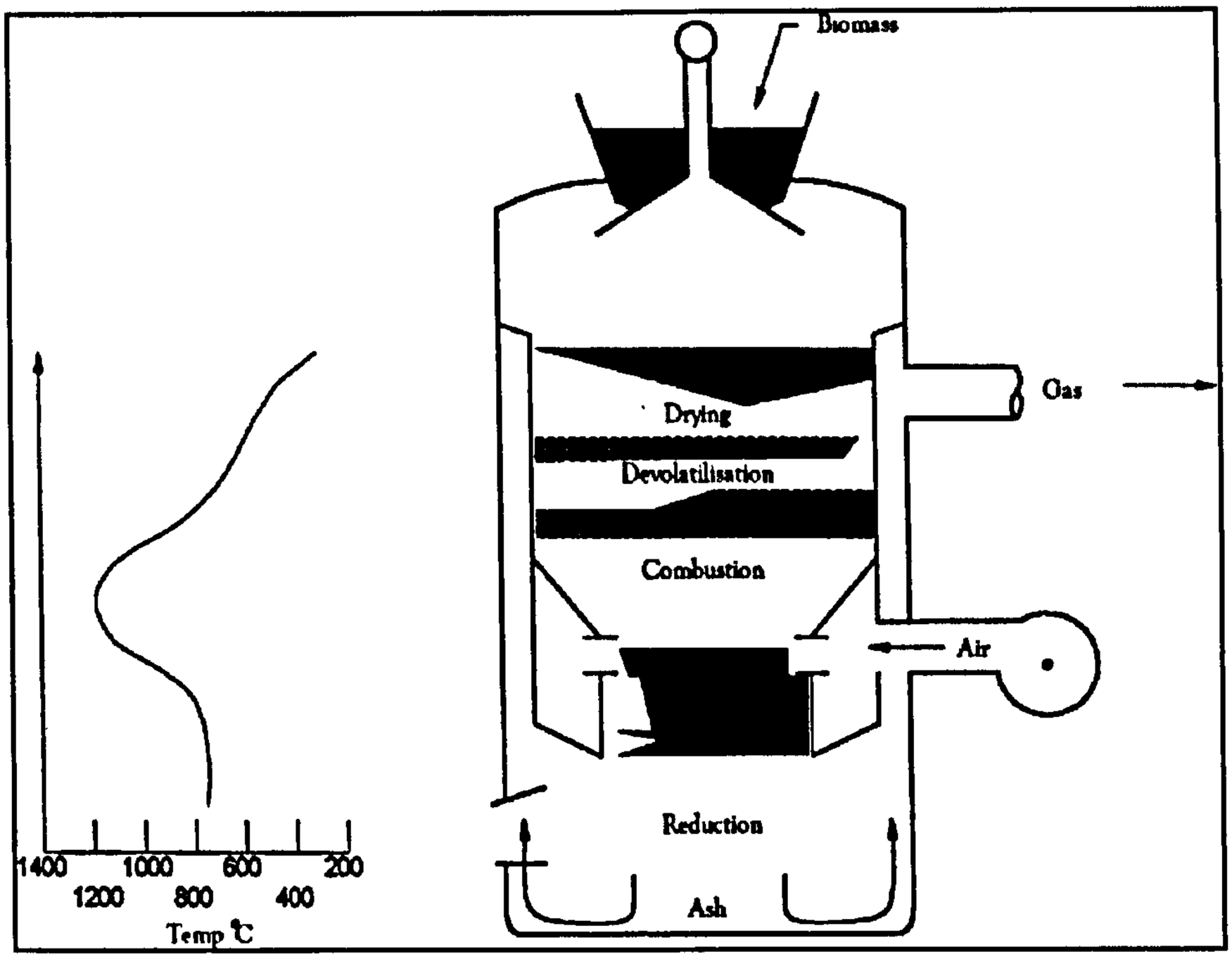

Figure 2.13: Schematic of downdraft gasifier (McKendry, 2002).

Cross Flow Gasifier

The feed moves downwards while air is introduced from the side, with the gases withdrawn from the opposite side of the unit at the same level. A hot combustion/gasification zone is formed around the entrance of the air, with the pyrolysis and drying zones being formed higher up in the vessel. Ash is removed at the bottom and the temperature of the gas leaving the unit is about 800-900°C; as a consequence this gives a low overall energy efficiency for the process and a gas with high tar content (McKendry, 2002).

Fluidised Bed Gasifier

The fluidised bed gasifier is essentially a fixed bed of fine solids in which silica sand is transformed into a liquid-state by contact with an upward flowing gas. The heat transfer efficiency is five times that of the fixed bed and there is only a single reaction zone. The

isothermal bed operates at a lower temperature compared to a fixed bed gasifier, 700-900°C (Belgiorno, 2003). There are two different fluidized beds as shown in *Figure 2.14* below:

- Bubbling Fluidised Bed (BFB)
- Circulating Fluidised Bed (CFB)

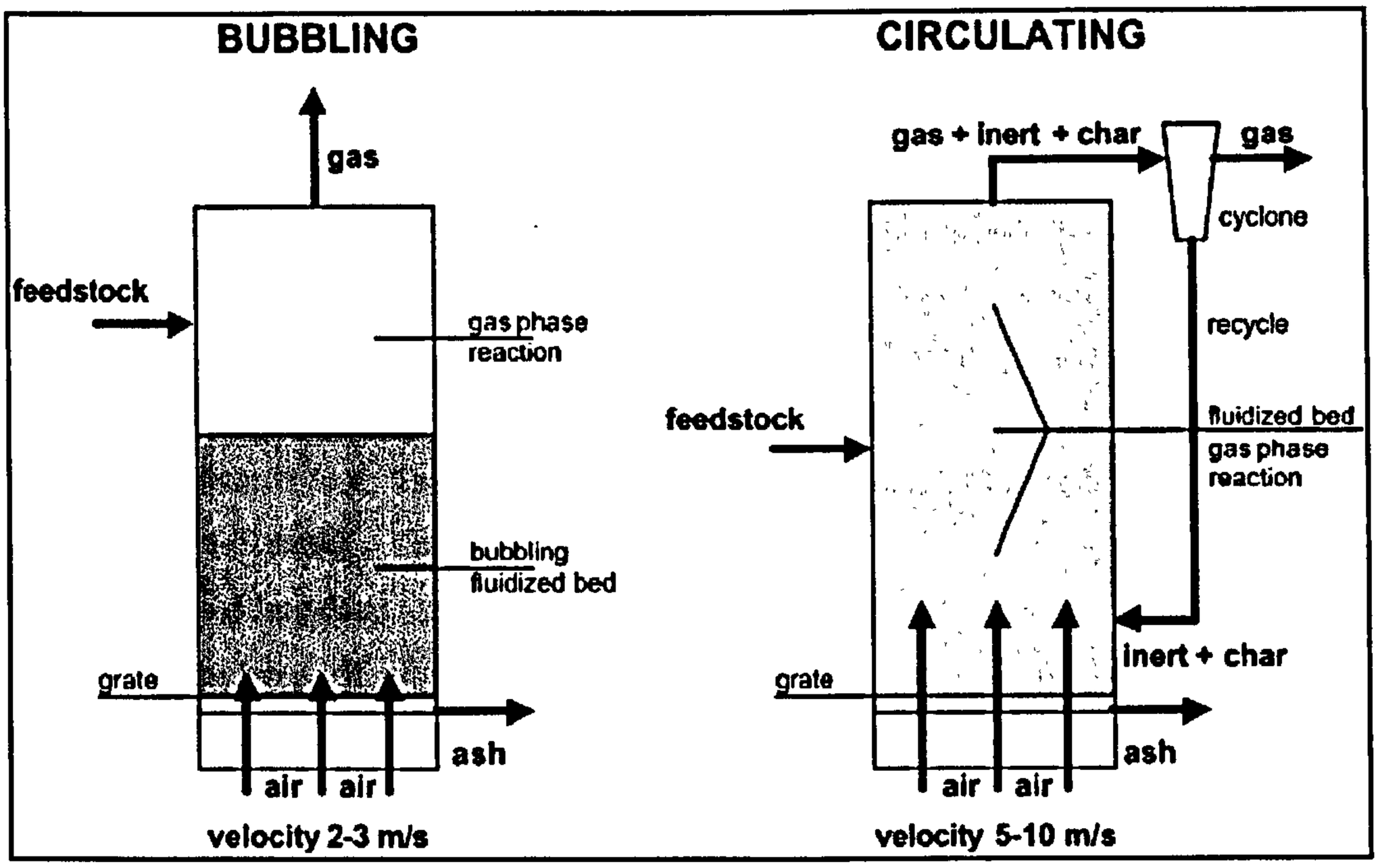

Figure 2.14: Fluidised bed gasifiers (Belgiorno *et al*, 2003).

In a bubbling bed gasifier, air or oxygen is introduced at the bottom of the bed acting both as a fluidising medium and oxidant. The gas passes upward through the bed of free-flowing granular materials (sand, limestone, dolomite or alumina) separating and circulating the solid particles. The bed is usually designed with a larger cross section area in the freeboard to lower the superficial gas velocity below the fluidization velocity to maintain the bed inventory and act as a disengaging zone. The larger cross sectional area is extended to obtain the total desired gas-phase residence time for complete devolatilisation. The bed is usually preheated to the fuel ignition temperature using the hot flue gas from an external heater. For biomass, this temperature is around 540°C. At this point, biomass is slowly introduced into the bed to raise the bed temperature to the desired operating range, normally 790-870°C. Fluidised bed gasifiers have the advantage of extremely good mixing and high heat transfer, resulting in uniform bed conditions giving about 95-99% carbon conversion (Bain, 2004). The product gas has a low tar content, typically <1-3mg/Nm^3 (McKendry, 2002).

In a circulating bed, the gas flow is increased and the gas bubbles become larger, forming large voids in the bed and entraining substantial amounts of solids. The turbulent bed solids are collected, separated from the gas, and return through a solid circulation loop. The difference from a bubbling fluid bed is that there is no distinct separation between the dense solid zones. Circulating fluid bed densities are about 560kg/m³ compared to a bubbling bed density of 720kg/m³. The gas velocity of a circulating bed is about 9.1m/s compared to the gas velocity of a bubbling fluid bed of 1.5-3.7m/s (Bain, 2004).

Entrained flow

Entrainment is the region of pneumatic transport attained when the flow velocity of the gasifying medium is increased so much that the tractive force exerted on the solid particles exceeds their weight (Schilling, 1979). In an entrained flow gasifier, pulverised coal or atomised oil flows co-currently with the gasifying medium and the flow within this gasifer can be downwards (e.g. Texaco), upwards (e.g Shell and Prenflo) or horizontal (e.g Destiec and Koppers-Totzek). The most important inherent characteristic of fully entrained suspension or dilute-phase gasification processes is their ability to utilise any grade or class of coal (von Fredersdorff, 1963). The high oxidation temperature (typically 1,300-1,400°C) means that the ash is generally removed as a liquid slag. There is limited experience with biomass in such a system due to the high cost of feed preparation to reduce its moisture content to low levels and reduce the particle size, along with low heat content. Refractory life is also a concern for biomass feeds with high potassium content (Bain, 2004).

2.2.2.3 Pre-Treatment of Gas

Gas pre-treatment is required to avoid environmental pollution and dangerous components such as tar and particulates.

The atmospheric emission depends on the air pollution control equipment and energy recovery system. Gas combustion provides a better pollution control compared to solid combustion, leading to a more effective reduction in emission of CO, NO_x, dioxins and unburned compounds. The gasifier residues, char and ash can be used to fertilize the ground, or disposed in sanitary landfill, or used for industrial processes. Wastewater from the gas cooler and wet scrubber contains a high amount of pollutants such as acid, sulphur, phenols and oxygenated organic compounds and tar. The low pH and high salt content can be controlled by neutralization but chemical precipitation for effluent tar removal requires

expensive treatment. The fuel gas contaminants and the associated problems and clean-up methods are summarized in *Table 2.4*.

Contaminant	Range (g/Nm^3)	Examples	Problems	Cleanup Method
Particulate	3-70	Ash, char, fluid bed material	Erosion, emission	Filtration, Scrubbing
Alkali Metals		Sodium and potassium compounds	Hot corrosion	Condensation and filtration
Fuel Nitrogen	1.5-3.0	Mainly NH_3 and HCN	NO_x formation	Scrubbing, SCR
Tar	10-100	Refractory aromatics	Clog filters, deposit internally	Tar cracking, scrubbing
Sulphur, Chlorine	2.5-3.5	H_2S, HCL	Corrosion, emission	Lime Scrubbing

Table 2.4: Fuel gas contaminants: problems and clean-up processes (Belgiorno *et al*, 2003).

2.2.2.4 Energy Recovery System

Three of the main energy recovery systems are the *steam cycle*, *internal combustion engine* and *gas turbine*. The steam cycle could handle contaminant and tar content as the fuel is burned in a combustor to provide heat for the steam boiler. However, the practical steam temperature is limited due to the cost of special alloys to endure the high temperature. Gas turbine systems show the opposite characteristic to the steam cycle. They has a much higher efficiency at the expense of a higher sensitivity to the quality of gas and only extremely low levels of contaminant, principally tar, alkali metals, sulphur and chlorine compounds can be tolerated. Internal combustion engines have a more robust and higher tolerance to contaminants than a gas turbine but a low increase in efficiency using the combined-cycle mode and poor economy of scale. *Table 2.5* gives the gas quality requirements for power generators:

		IC engine	Gas turbine
Particles	mg/Nm^3	<50	<30
Particle size	µm	<10	<5
Tar	mg/Nm^3	<100	
Alkali metals	mg/Nm^3		0.24

Table 2.5: Gas quality requirements for power generators (Hasler and Nussbaumer, 1999).

Below are examples of three types of process cycle; *gasification/steam cycle (stand-alone configuration), gasification/steam-cycle (co-firing gasification)* and *integrated gasification combined cycle (IGCC)*, reviewed by Belgiorno *et al* (2003) for energy recovery from gasification systems. *Figure 2.15* shows the synthesis scheme of the TPS installation in Greve in Chianti (Italy). The gases are directly burned without gas-pre-treatment to give heat for onsite heating and electricity production. Therefore, the superheater tubes temperatures are limited to 450°C to avoid excessive corrosion of the tube by HCL in the flue gas giving a maximum net electrical efficiency of only 23%.

In the co-firing configuration (Figure 2.16), gas is used to provide some of the energy for a steam cycle power generation plant. The gas can be used in the same fuel boiler or in a second one that produces steam, which is subsequently superheated in the first boiler. In the first system, the acid gases are diluted and in the second configuration, the temperature of the steam tubes is maintained below 180°C. A higher efficiency, 30% can be obtained as the system utilizes a higher temperature.

Figure 2.17 shows an integrated gasification combined cycle with catalytic tar cracking in the Termiska Processer Arable Biomass Renewable Energy System. A conventional power plant based on combined cycle gas turbine has an efficiency of 60%. However, the effective electrical output with biomass gasification is lower than 40% because of the energy consumption for gas pre-treatment. The limitation of this system is the need for a cleanup system for control of corrosive gas phase compounds such as tar, acid gas and alkali metals. Therefore, catalytic tar cracking or a wet scrubber is implemented for tar control.

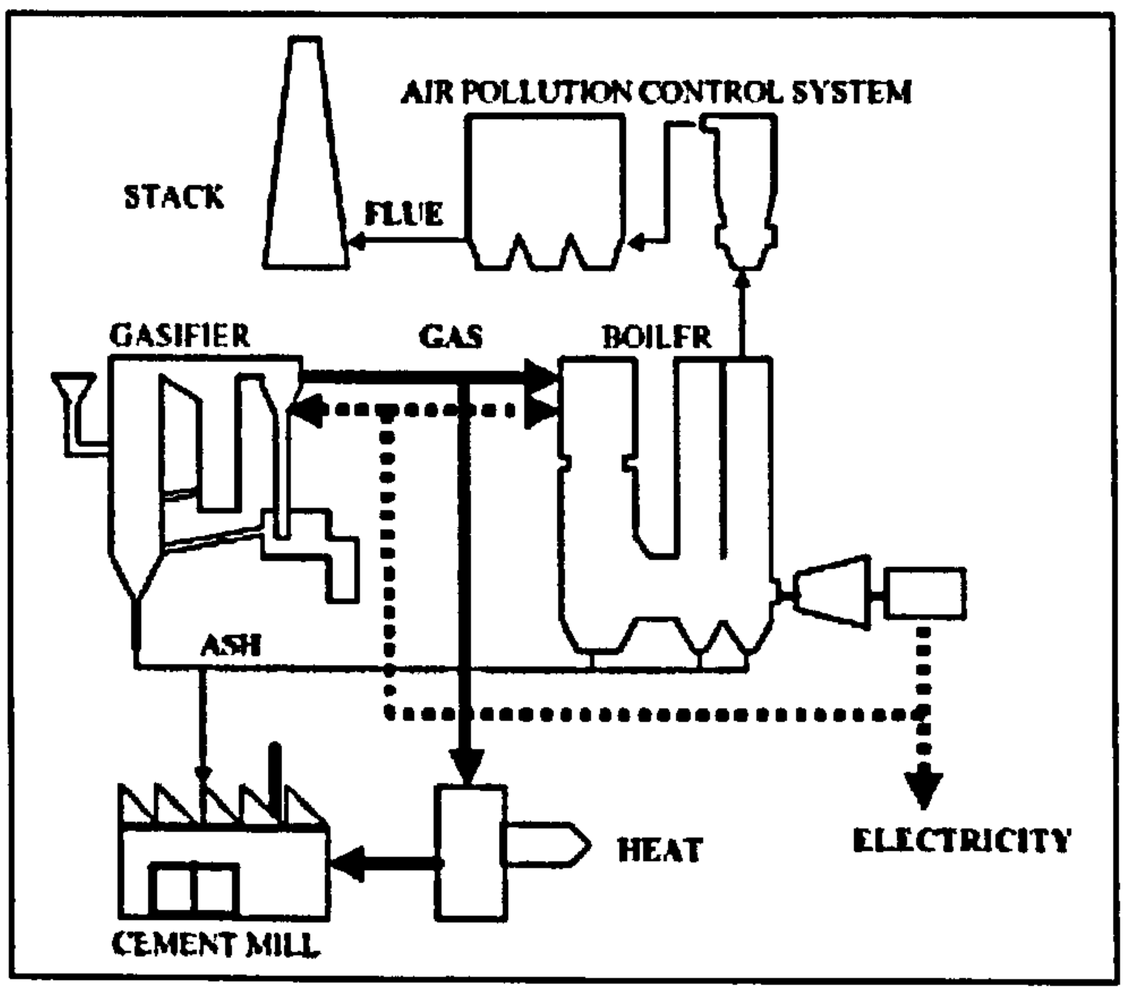

Figure 2.15: TPS gasification plant in Greve in Chianti (Italy) (Belgiorne V, 2003; De Feo, 2000).

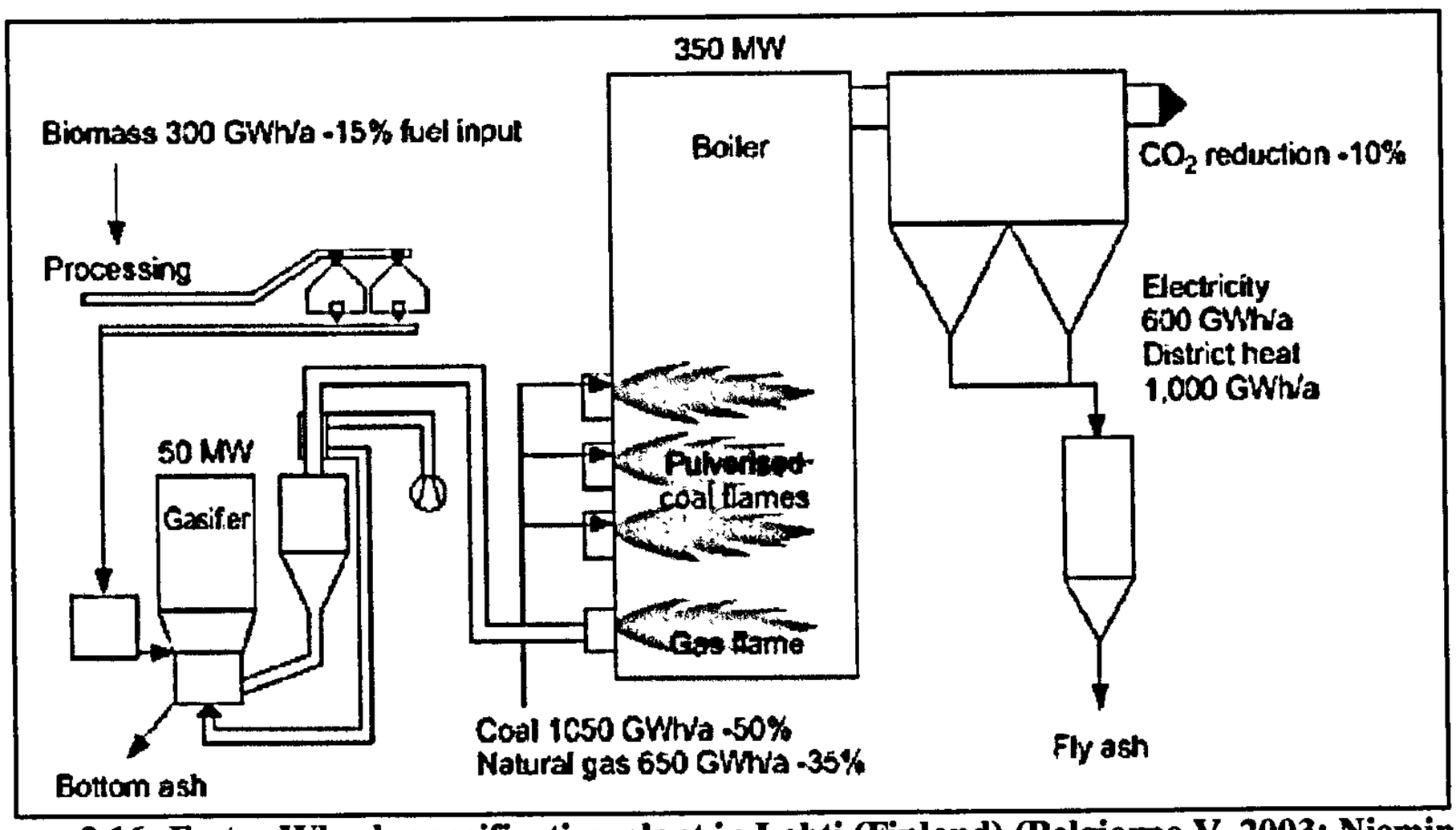

Figure 2.16: Foster Wheeler gasification plant in Lahti (Finland) (Belgiorno V, 2003; Nieminen, 1999).

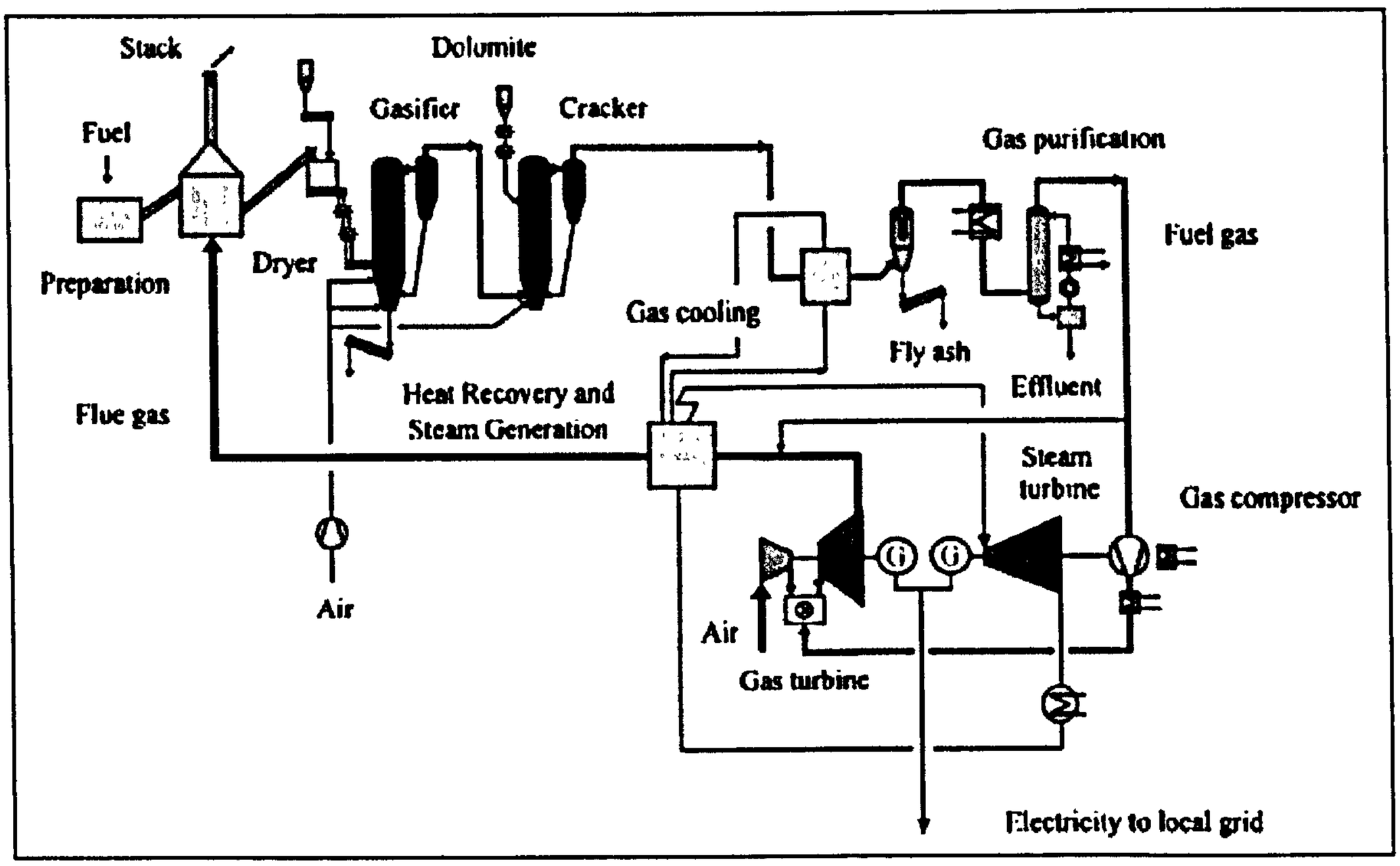

Figure 2.17: TPS/ ARBRE gasification plant in Eggborought (UK) (Belgiorno V, 2003; *Faaij et al*, 1997).

Combined Heat and Power

The combined cycle power plant utilizes the coupling of a gas turbine and steam turbine through a heat recovery steam generator. The high temperature exhaust gases of the gas turbine are discharged into a heat-recovery boiler that provides steam for the steam turbine. Heat is converted to power at a higher temperature than in a simple steam turbine cycle thus giving higher efficiency. The energy saving of a small scale CHP is 30% when its power generation replaces a conventional power plant, and 15% compared to a natural gas-fired combined cycle (Hendriks and Blok, 1996). The electricity generated can be transported to other users through the grid although back-up is required for periods that the CHP unit is not operational. Heat is the most important energy needed in the EU as 46% of electricity is used for heating. The efficiency of current system to transform chemical energy using fossil fuels averages below 40-50%. Therefore, it is a waste of primary energy to produce electricity in power stations without cogenerating electricity for heating (Aebiom, 1999).

CHP capacity increased by over 80% between 1991 and 1999. In 1999, it provided 6% of the overall UK electricity generating capacity. The UK target is 10,000MWe of CHP capacity by 2010. The proportion of electricity generated from renewable has risen from 1.7% in 1989 to 2.8% in 1999. The UK targets an increase in the amount of electricity from renewable sources from 5% in 2003 to 10% in 2010 (DTI, 2001). The amount of combusted waste is also expected to increase and CHP is predicted to increase. The waste used in combined power and heat plants will increase from 31Mtons in 1990 to about 56Mtons because of the increase in generated waste and decrease of landfill waste (Carlsson, 1999).

Capacity

Currently, biomass supplies 12% of the world energy supply. A large power plant (200MW) has relatively efficient energy conversion compared to a smaller biomass-fired steam turbine system. A large scale combined gas and steam turbine has ~58% efficiency, while for small sizes (5-20MW) efficiency is over 40% (Jurado *et al*, 2003). In Europe, small scale CHP provides 1kWe-5MWe by mini-grids (Morris and Waldheim, 1998). While it is feasible to build larger scale plant at a size of 25 to 30MWe in more arable parts of the UK, smaller plant is more suitable in farming areas. There is a demand for small-scale distributor power at sizes of a hundred or less kilowatts (Barker, 1996). The waste fuelled district-heating scheme in Sheffield has 150MW of heat load connected and a similar system operates in Nottingham (Swithenbank *et al*, 1999).

2.3 SUMMARY

Coal, oil and gas have been the main fuels generating electricity but this will not last as they contribute to climate change. The urgent need for green and sustainable fuel prompted this research into energy crops as an alternative to fossil fuel. The review of the literature reveals that the use of energy crops for the combustion industry is fairly novel in the UK compared to other European countries. The application of energy crops as a source of fuel is hindered by the lack of experience, economic viability and environmental cost, plus the relatively low density of the fuel (compared to solid and liquid fossil fuels) imply that it cannot be transported for long distances.

The implementation of incineration technology is hindered by social acceptance creating a need for an alternative route. The gasification process has been identified as the most favourable thermo-chemical biomass conversion process due to its higher thermal efficiency compared to combustion. The gasification of char produces synthesis gas that can also be used as feedstock for chemical synthesis, production of liquid fuel via Fisher-Tropsch technology, electric power in fuel cells or combustion in a gas turbine combined cycle (CCGT). Although work on gasification can be dated back to the 16^{th} century, there has been little technological progress since then, leaving an urgent demand for this research work especially with the current state of diminishing fossil fuel. The review showed that there are many types of gasification processes with a broad range of reactor types and operating conditions. The end use of the product and economic factors are the primary factors that govern the selection of a particular type of gasification process. The high level of contaminants and tar has traditionally ruled out the use of the up-draft or counter-current gasification especially in the case of a gas-turbine cycle although the overall efficiency of the process is higher compared to the co-current gasification. The three main parameters in the operation of a gasifier are the pressure, temperature and reactants. High calorific value syngas can be achieved if there is no dilution by nitrogen. The review showed that the efficiency of the fixed bed gasification process can be further enhanced by manipulating the reactants and temperature and further study is needed to understand and optimize the system. There is also a need to tackle the problem of high tar content in the flue gas as this limits its application in an energy recovery system and increases plant cost for gas clean-up.

CHAPTER 3

THEORETICAL BACKGROUND

This chapter aims to put the research on fixed bed combustion and gasification into context. Both fixed bed combustion and gasification processes are discussed, beginning with the background theory, and proceeding to review the experimental and modelling work that has been carried out previously. The purpose is to show the current progress of research in this field. The gasification section includes a review on the use of catalysts in gasification to enhance the decomposition of tarry constituents in fuel gas or to increase carbon conversion. This chapter concludes with the identification of the need for further characterisation of energy crops and waste in fixed bed combustion. It also highlights the urgent need for a deeper understanding of the gasification process and particularly a gasification system yielding low tar producer gas.

3.1 COMBUSTION IN THE BED REGION

The combustion of a fuel batch in a pot furnace has traditionally been used to study the combustion on a travelling grate. The combustion time for a fuel batch in a pot furnace corresponds to a certain transport distance on a reciprocating grate where progress of combustion is comparable to that of a fuel batch in the pot furnace. The concept of a travelling pot furnace is a conventional approach, which is deemed suitable when the horizontal velocity of the bed along the grate is faster than the vertical velocity of the propagating reaction front inside the bed, making the two-dimensional effects negligible (Thunman and Leckner, 2001).

The combustion in an incinerator occurs in two distinctive regions: the solid-bed region, where the combustion process occurs within the bed on top of the grate and in the freeboard region. Waste incineration is a complex process as inhomogeneous waste composition and arbitrary physical characteristics cause difficulty in predicting the combustion behaviour. During incineration, the fuel undergoes complicated processes involving drying, pyrolysis, solid-phase and gas-phase combustion with conductive, convective and radiative heat transfer, mass transfer and gas flowing through randomly packed beds of various material size, shape

and orientation (Shin and Choi, 2000; Hisaki, 2003). *Figure 3.1* shows the conceptual view of waste bed combustion above a grate.

The radiation from the gaseous flame and furnace wall heats the waste, evaporates the moisture and ignites the waste from the bed top. Preheated air is supplied from under the grate and moves upward, crosswise from the moving direction of the waste bed. The typical solid fuel combustion process would be waste solid fuel heat-up followed by moisture evaporation. The fuel then undergoes pyrolysis, gas phase combustion and char reaction. The evaporation and combustion zone formed at the bed surface would descent to the bottom of the bed as the reaction proceeds. The ash from the combustion is cooled by convection of air supply and thrown into the ash hopper when the combustion is completed.

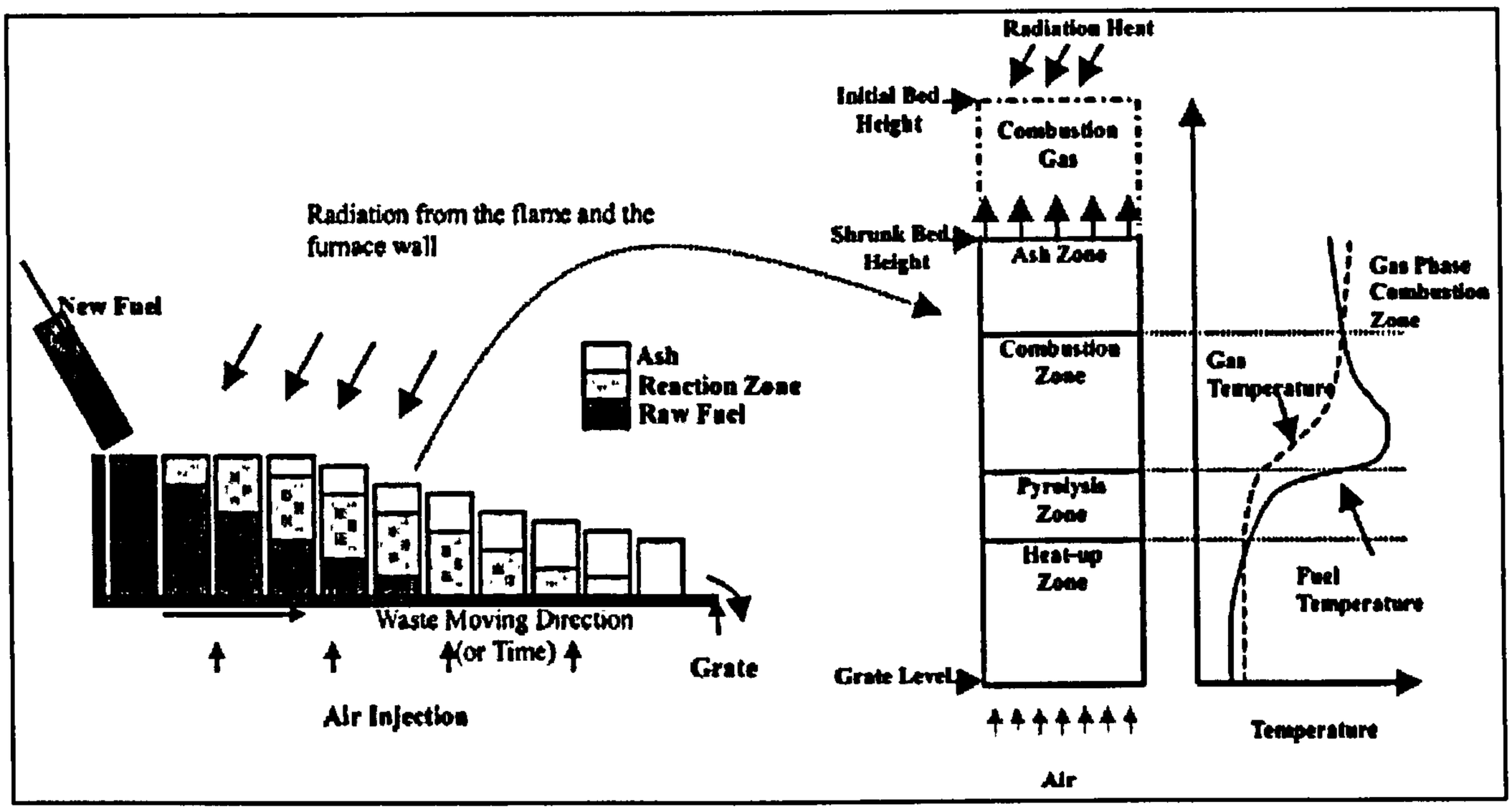

Figure 3.1: Schematic view of solid fuel bed combustion (Shin and Choi, 2000).

Solid fuel is assumed to consist of four components; *moisture, volatile matter, fixed carbon* and *ash*. The whole combustion process in the bed is divided into three stages:

1) Ignition stage
2) Steady-state combustion stage
3) Char burning stage.

The steady-state stage involves simultaneous moisture evaporation, release and burning of pyrolysis gases and char combustion. This is followed by the char burning stage which is the

final stage where all the moisture and volatile matter have left the bed and only the char reaction proceeds (Yang *et al*, 2003).

Solid fuels are first heated up by over-bed radiation when they enter the incinerator and moisture is released as evaporation proceeds. Moisture can also be driven out by mass exchange between the wet solids and the drier airflow from under the grate. Volatile matter in MSW could range from 10% to as high as 70% of the original mass and the gases released are composed mainly of hydrocarbon (C_mH_n), CO, CO_2 H_2, O_2 and other trace compounds:

Waste ⟶ Volatile (C_mH_n), CO, CO_2 H_2, O_2, etc.) + char

The release of volatile gases from the solid is proportional to the bed temperature and the remaining volatiles in the solid. Volatile hydrocarbon, $C_mH_nO_l$ is oxidized to produce CO and H_2. The CO is then burned by further oxidation to form CO_2 and H_2 to form H_2O.

$$C_mH_nO_l + (m/2 - l/2)O_2 \rightarrow mCO + n/2\,H_2$$
$$CO + 1/2\,O_2 \rightarrow CO_2$$
$$H_2 + 1/2\,O_2 \rightarrow H_2O$$

Gaseous fuels released from the devolatilisation process have to mix first with the surrounding air before the combustion takes place. The burning of volatile hydrocarbon is limited by the reaction kinetics and the mixing-rate of the gaseous fuel with the under-fire air. Char is formed as the volatiles escape from the particles. The primary products of char combustion are CO and CO_2. The moisture level in the fuel affects the percentage of char burned in the final stage.

3.1.1 Fixed Bed Combustion Regime

Gort (1995) and Shin and Choi (2000) proposed three modes of combustion in the bed, depending on the air supply rate; *oxygen limited combustion, reaction-limited combustion* and *extinction by convection*. The combustion in the bed region was characterized by the stoichiometry between fuel and oxygen as shown in *Figure 3.2*.

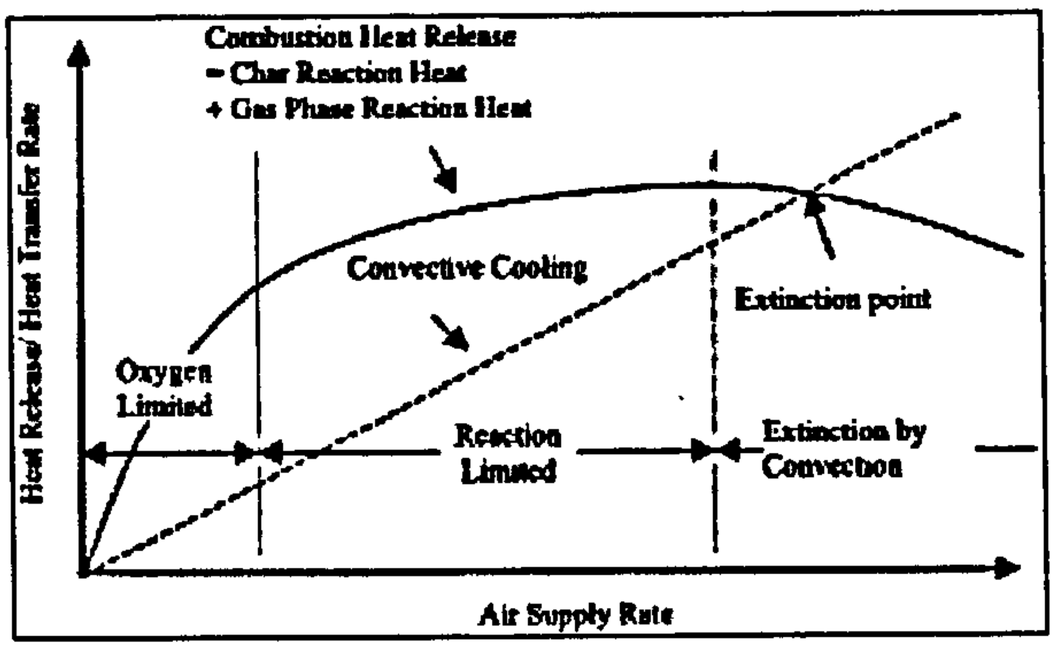

Figure 3.2: Effects of air supply rate on the combustion of a bed (Shin and Choi, 2000).

In the first regime, the low air supply limits the reaction rate. The high fuel-air ratio results in the complete consumption of oxygen by char and reacting volatile material. The reaction rate is then dependent on the oxygen supply rate. As the air supply increases, the flame propagation speed increases, however, the flame propagation is now limited by the reaction rate of the fuel. The limited combustion rate causes an increase of oxygen concentration at the exit and thus the excess air cools the bed and extinguishes the flame. If the heat release in the bed is higher than the convective cooling by air supply, the flame is then sustained but if the air supply is further increased beyond this point, the gas phase combustion zone is swept away and the flame is extinguished.

The boundary between complete gasification and combustion is defined by the stoichiometric fuel-air ratio. The stoichiometry is determined by oxygen supply rate and ignition speed. The ignition speed varies for different fuel depending on the fuel properties such as moisture and proportion of fixed carbon and volatiles. Therefore, it is especially important in this research to investigate the stoichiometric fuel-air ratio for new energy crops or biomass material for optimal combustion operation.

3.2 DEVELOPMENT IN THE FIXED BED COMBUSTION MODEL

As a combustion test in a large-scale MSW unit is difficult and costly, most experimental investigations were carried out in smaller laboratory scale units. The experimental investigations include both the design features and combustion parameters for efficient bed combustion.

As explained in *Section 3.1.1*, the ignition propagation speed increases almost linearly with air supply in the oxygen limited mode. The slope in *Figure 3.2* decreases in the reaction-limited mode and ceases in flame extinction zone due to convection from the air. Yang *et al* (2002) found that the burning rate with large scale MSW is less sensitive to variation in air flow rate although the flammability range becomes much wider. For low under-grate air (low air to fuel ratio), the supply of oxygen to the reaction layer is insufficient and a large amount of volatile gases escape without burning. This was found to lower the bed temperature and inhibit the devolatilization process. Rogaume *et al* (2002) studied the effect of air flow rate on the formation of pollutants during waste incineration including the yield of carbon monoxide and nitrogen oxide. Primary air flow rate below the stoichiometric requirement leads to an oxygen deficient combustion region. This regime is characterized by low reaction temperatures, favouring endothermic pyrolysis and enhances CO yield. The influence of primary air flow rate was also reported by Swithenbank *et al* (1999), in which they explained that CO was produced at low air flow rate due to the combustion and gasification of char. For higher air flow rates, sufficient oxygen was available to ensure that the char burn-out occurred as rapidly as ignition.

In her research using a pot burner, Goh *et al* (1999) described that a large volume of excess air is required for a good burnout but this advantage is set off by problems caused in gas phase combustion; overloading of electrostatic precipitators and scrubbers and high particulate emissions. In her work, Goh monitored the behaviour of NO_x during the pyrolysis stage, whereby, the NO_x concentration increased to a maximum value of 150ppm before reducing to 100ppm. The increase in NO_x is due to the devolatilisation of waste while a decrease in NO_x occurs when the CO and NO_x in the char layer reacts to form CO_2 and N_2 using carbon in the char as a catalyst. The effect of reduced NO_x emission with a reduction in air flow rate was also reported by Klasen and Gorner (1999) and colleagues. They suggested an additional source of combustion air; using both primary and secondary air. The mixing of the secondary air in the furnace was found to promote uniform oxygen, temperature and velocity distribution. Jorgensen and Madsen (1999) and Rogaume et al (2002) described similar benefits from using secondary air flow to promote mixing but highlighted the effect of fuel dilution leading to reduction in temperature in the case of high secondary air flow rate.

Recent work on particle emission was carried out by Gomez *et al* (2003). Their work focussed on the particle emission generated during different stages of pyrolysis/incineration of refused derived fuel at a pilot scale incinerator. As RDF incineration is not a stationary process, the aerosol properties are a function of the process stage and charge of the furnace. The incinerator design and operation influences the particles formation. The mass

concentration of particles emitted increases during the pyrolysis phase, reaching the maximum during transition between pyrolysis and combustion and then decreases during the char combustion phase. Research on the formation and decomposition behaviour of a critical pollutant, dioxin was carried out by Tagashira *et al* (1999). They investigated the combustion characteristic of different materials; municipal waste, waste plastic and refuse derived fuel (RDF). Dioxin control was found possible by sustaining a stable combustion temperature with longer gas residence time.

Saastamoinen *et al* (2000) carried out extensive research on the influence of combustion parameters; *air flow rate, moisture content, particle size, bed density* and *wood type* on fixed bed combustion. Their investigation showed that moisture above 30% was found to significantly lower the ignition speed because of a decrease in temperature of the ignited region. This was due to dilution and the increased energy needed to heat particles to the ignition temperature. Particle size proved to have no effect on ignition front speed but larger particle sizes were associated with an increase in maximum bed temperature. The front velocity was found to be inversely proportional to fuel bed density and the specific heat of wood. The influence of primary air flow rate and particle properties on the ignition front, temperature and gas composition were also studied by Ronnback (2000). Thermally thin fuel was found to have a higher devolatilisation rate, leading to a sub-stoichiometric regime with full oxygen consumption sustained at high air flow. The resistance towards heat flow into the particles increases with diameter, and more of the heat produced is transported to new layers of fresh fuels and not towards the centre of the fuel particles. The larger particles are thermally thicker and the devolatilization rate is lower. Therefore, the sub-stoichiometric regime with complete consumption starts at a higher airflow for larger diameter fuel. In 1972, Rogers (1972) reported that the ignition velocity decreases with increasing bulk density. It was explained by Hisaki (2003) that there is a slower heat transfer from the ignition part to the unburnt fuel with increasing bulk density. The more open packing in lower bulk density fuel allows the ignited particles to radiate further into unburnt fuel increasing the radiation heat transfer.

Zakaria (2000) extended the investigation of the primary and secondary air flow rate on wood and simulated waste consisting of wood, cardboard, paper and vegetable matter with 48% moisture content. His findings supported Saastamoinens' work whereby the combustion rate varied linearly with primary air flow rates. Zakaria (2000) concluded that the temperature of the primary air has little effect on waste combustion because heat transfer within the bed was mainly by radiation and very little by convection and conduction. In the modelling work conducted by van der Lans *et al* (2000), a high air inlet temperature was found to increase the

front propagation rate at the expense of a lower maximum bed temperature. The high propagation rate heats up more bed material per unit time. Although more heat is supplied by a hotter inlet air, the effect is smaller causing lower bed temperature.

Yang *et al* (2003) carried out detailed mathematical simulations and experiments on the combustion of wood chip and incineration of municipal solid waste in a bench-top stationary bed. The major mass loss from the bed was determined by the moisture evaporation and volatile release from the waste solids. One of the key findings in their work was that wetter fuels and slower devolatilisation kinetic rates produced lower emissions of CO and H_2. If the fuel is very dry, there is a large amount of un-burnt volatile gases. With increasing moisture levels, combustion becomes fuel-lean as the moisture evaporation slows down the devolatilisation rate. Nevertheless, the char-burning rate decreased due to less oxygen available. Therefore, dryer fuel is preferred to wetter, as it is more easily converted to combustible gases than wet fuels.

3.2.1 A Numerical and Mathematical Model of Fixed Bed Combustion

The modelling of an incinerator requires careful consideration. The prediction must be limited to not only plants with identical designs but also similar operating conditions and waste composition. A commonly used technique in modelling is to combine both experimentally measured data and theory. Modelling in the earlier years was carried out in a one-dimensional form and was mostly semi-empirical. However, recent advances enable 2D modelling and determination of the boundary conditions for the freeboard area through the successful computation modelling of the bed region.

Kuo (1997) constructed a simple one-dimensional model to derive a correlation of combustion rate as a function of flue gas temperature and oxygen concentration. The model was relatively simple as many of the chemical and physical process of combustion were not considered. Kuos' model involved only the combustion of volatiles and the theoretical work did not include a detailed enough simulation of MSW conversion. The combustion model was constructed based on the theory that the combustion rate was proportional to the oxygen consumption rate in the fuel bed. The oxygen concentration was assumed to vary one-dimensionally through the fuel bed under steady-state. The calculation prediction provided a theoretical basis for estimating the combustion rates based on temperature and excess oxygen measurement.

Goh et al (1998) improved on Kuos' work to provide a more accurate representation of the combustion process. Goh referred to Kuo (1970) illustration on how the various processes of combustion propagates as waves through the waste bed as shown in *Figure 3.3*. This forms the basis on which the mathematical model for solid phases was built. Goh developed the model based on different zones for virgin, dried and pyrolysed fuel and ash to calculate the boundary conditions for a CFD code. The model included the processes within a burning refuse bed such drying, pyrolysis, solid-phase and gas-phase combustion, conduction, convection and radiative heat-transfer, mass transfer and gas flowing through randomly packed beds of material.

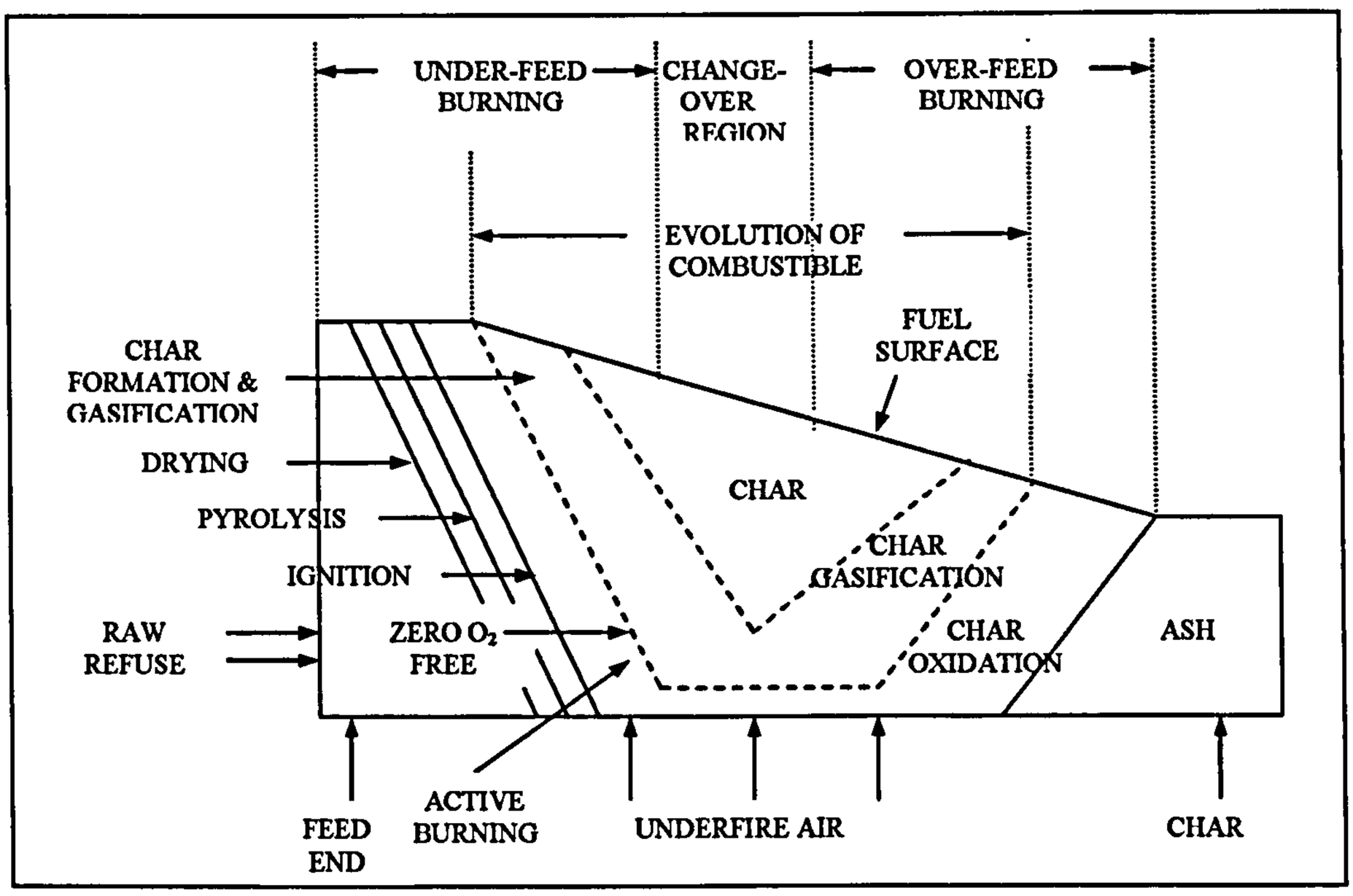

Figure 3.3: The waste-bed combustion zone (Kuo, 1970)

One of the main assumptions made in the model was that there was no heat transfer within the bed material parallel to the direction of the grate movement. The steady-state moving bed was modelled as an unsteady-state static bed in which heat was only transferred normal to the grate. The variation with respect to time t, using the unsteady-state static bed model can be employed to predict variation with distance x from the point of refuse input in the steady-state moving bed model using $x = v_x t$ whereby v_x represents the steady velocity of material caused by the grate movement. The use of an unsteady-state bed model is as shown in *Figure 3.4*.

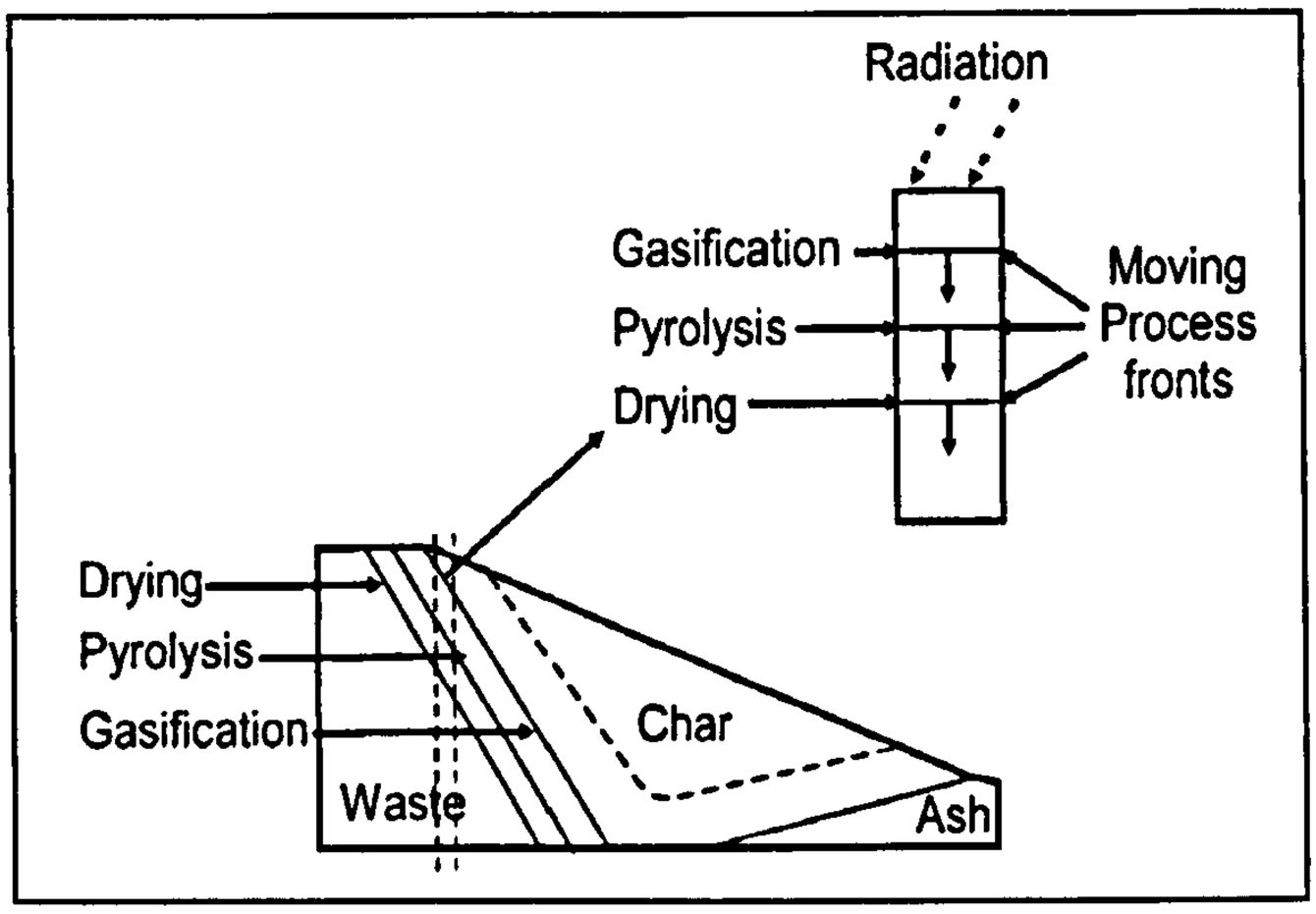

Figure 3.4: A fixed bed model for waste bed.

The modelling carried out by Goh provided a fairly accurate representation of the bed volume as it took into consideration the internal pore space and allowed for an increase in space during the drying and pyrolysis and its removal during char gasification. The transfer of energy occurring normal to the grate was accounted for through convection and effective conductivity. Goh used a high value of `effective` thermal conductivity to compensate for the effect of radiation as the radiation that penetrates through the channels and is absorbed in the bed was unknown. Gohs' modelling required empirical correlations, which were determined experimentally for each fuel to describe the thermal conversion adequately.

The combustion of wood on a fixed grate with a separate supply of combustion air was presented by Oman (1999). In their work, the fixed carbon was burned in the primary combustion chamber in the presence of primary air, whereas the volatiles were burned subsequently in the secondary combustion chamber in the presence of secondary air. Drying and pyrolysis was assumed to have taken place in the upper part of the layer while char was burned in the lowest segments of the layer. Drying was without volume reduction, while pyrolysis and combustion of char was with volume reduction. The influence of ash was neglected. Heat transfer in the control volume was the consequence of mass transport and the temperature difference between the solid and gaseous phases. The heat transfer through the contact areas of the neighbouring solid pieces was taken into account.

Cooper and Hallett (2000) presented a numerical model for the combustion of char particles in an overfed packed bed. The one-dimensional model accounted for the heterogeneous reactions for the production of CO, the oxidation of CO in the gas phase, heat transfer in the gas and solid phases as well as between phases, particle motion and shrinkage within the bed, heat transfer in the grate, and the behaviour of ash. The radial variations of temperature and composition were neglected. The authors took into account the heat transfer between two different phases, the gas and solid phase, as well as the particle shrinkage. In contrast to the previous work carried out by Goh (1998) that assumed equal gas and solid temperature, Cooper used separate energy equations for the two phases. In older models, char surface reactions were assumed to be typically diffusion controlled and the kinetics of the gas phase oxidation of CO was neglected. However, Cooper's investigation showed that although char oxidation was primarily diffusion-controlled in steady state combustion, the gas phase CO oxidation reaction was sufficiently kinetically controlled that finite-rate CO kinetics proved to be necessary for accurate temperature prediction in the oxidation zone.

Shin and Choi (2000) developed a mathematical model by separating the combustion reactions in the bed into solid and gas phases. Each phase of the bed was modelled numerically as shown in *Figure 3.5*. The mass of the bed in the control volume exchanges heat with the material in the upper and lower control volume via conduction and radiation, and also with the gas flow via convection. The shrinking of the control volume, the loss of mass and density changes as the reaction in the bed proceeded were taken into account. The reaction of char and evaporation of moisture also were included in the solid phase and the reactions of carbon monoxide and volatiles were included in the gas phase. A heat balance was carried out on the solid and the gas phases and the discretized form for both of the equations were applied by assuming constant specific heats for the temperature limited range. As radiative heat transfer is important in initiating the flame front and transferring heat to the cold bed, a two-flux model was employed to predict the radiative heat transfer in the bed.

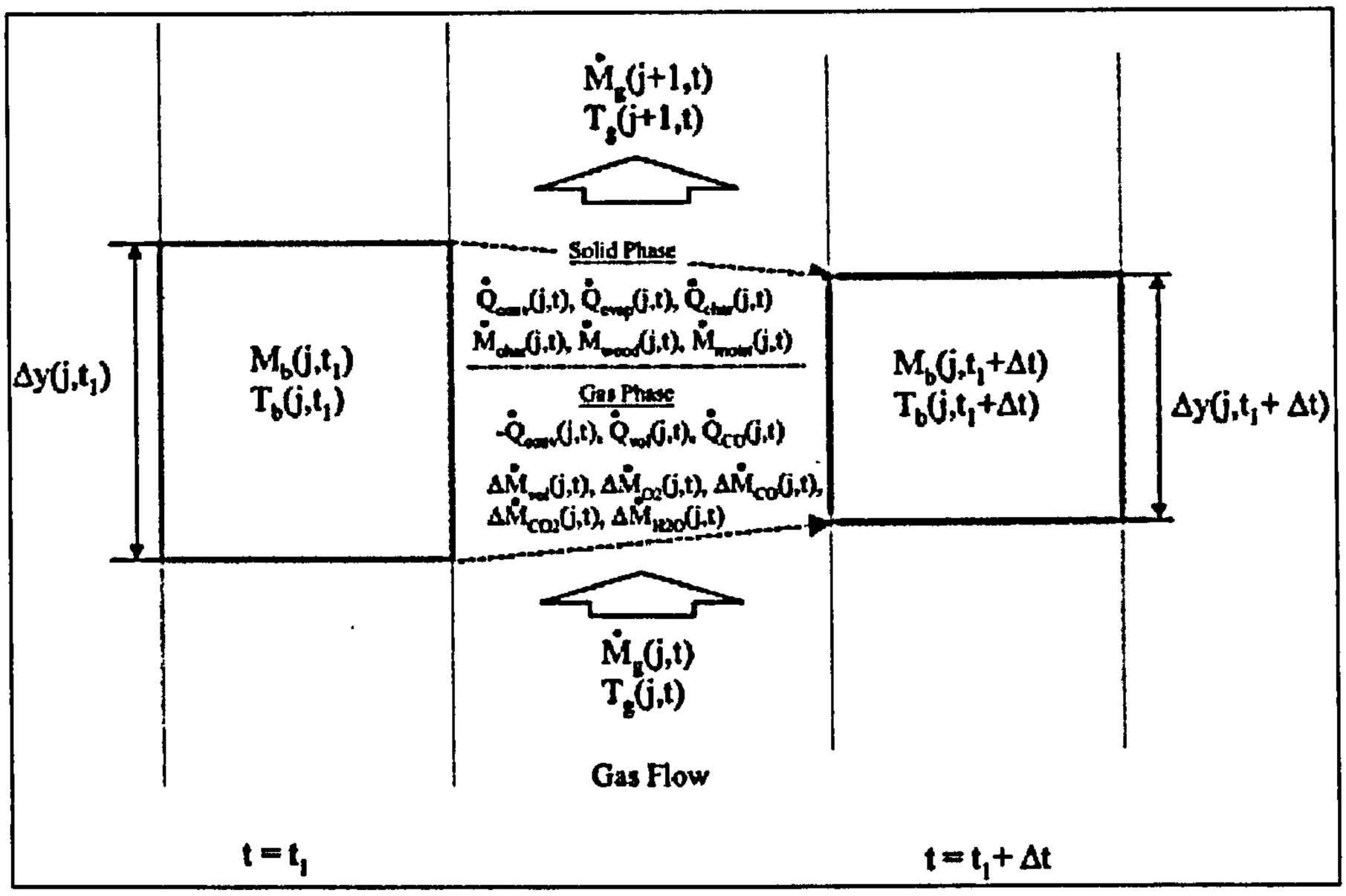

Figure 3.5: Numerical modelling concept of the solid and gas phases.

Shin and Choi made an approximation to the absorption coefficient based on the assumption that the fraction of the radiation transmitted through the layer of particles was assumed to be the void fraction, f_v of the bed as in *Figure 3.6*. The approximation has limitations as the actual bed was not arranged so ideally and the void fraction changed while combustion progressed. Further work on the shrinking factor of the bed was therefore required.

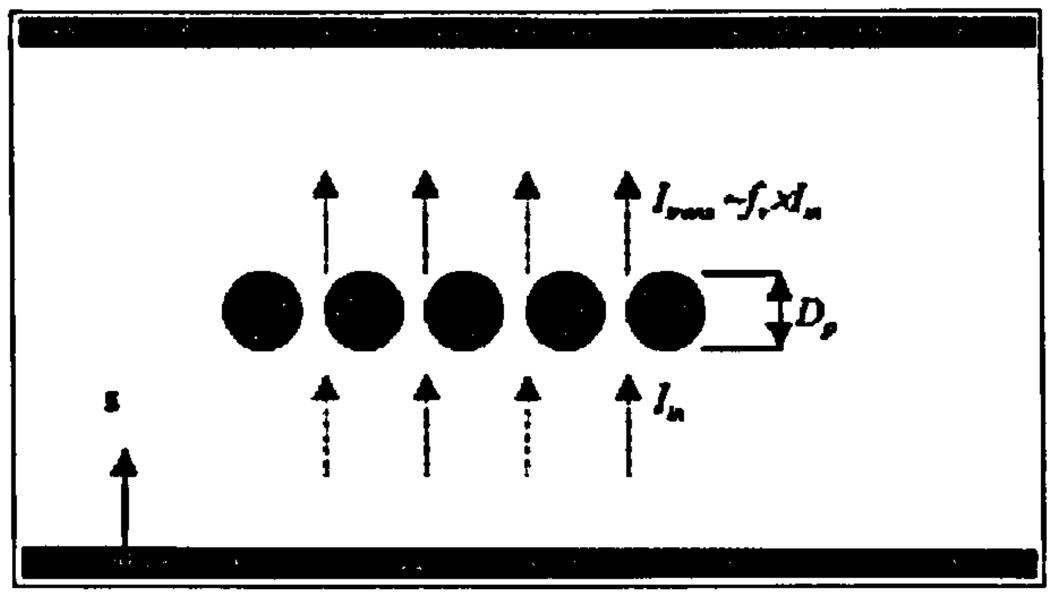

Figure 3.6: Radiation absorption by the bed particle.

Peters (1995) has summarised the general governing equations for both the gas and solid phases in a moving bed. For a stationary bed, the source term in gas and solid continuity equations accounts for the conversion rate from solid to gas due to moisture evaporation, devolatilisation and char combustion.

Yang (2002) extended the numerical calculation in a stationary bed of solid waste material carried out initially by Goh (1998). The governing equations for mass, momentum and heat transfer for both solid and gaseous phases in a moving packed bed of waste solids were described. A 2-D interactive computer program was developed to solve all the concerned equations numerically. The work carried out by Yang provided more spatial details of the incineration processes within bed as most of the previous work was on the empirical side. In his model, the individual process rates such as moisture evaporation, volatile devolatilization and char burning can be monitored and analysed. The incineration process of solid waste was divided into four successive sub-processes: *evaporation of moisture from the solids, volatile release/char formation, burning of the hydrocarbon volatiles in the gaseous space,* and the *gasification of char particles*. These processes may overlap to some extent. In the calculation, the burning of volatile hydrocarbon gases was limited not only by the reaction kinetics but also by the mixing-rate of gaseous fuel with the under-fire air. The bed radiation was simulated by a four-flux model. The cell-averaged mixing in the freeboard area was correlated to a number of parameters including local void fraction, gas velocity and length scale comparable to particle size or size of the void space. The work carried out by Yang forms the basis for the FLIC calculation used in this research work.

A homogeneous two-dimensional mathematical model was developed for combustion of straw in a cross-current moving bed by van der Lans (2000). The model was used to predict the ignition front temperature and front propagation rate. In the model, Lans (2000) assumed that only the reaction of O_2 with char took place in the bed. The particle shrinkage was not taken into account as he assumed that the outer surface area of the char corresponds to that of straw before reaction. As the theoretical prediction of CO_2/CO ratio was incorrect, the ratio was then fixed in the model. Further development in the gas-phase chemistry was required as van der Lans work lacks other reactions in the char oxidation period such as the formation of carbon monoxide and the reverse reaction to account for the dissociation of carbon dioxide at high temperature.

Previous modelling had mostly been based on the transient, one-dimensional model as a representation of the two-dimensional steady-state model. Heat was assumed to be absorbed symmetrically on the surfaces of the particle. All the studies-mentioned above only access the

ideal case of surface reactions on a particle without temperature and species profiles inside the particles. The models could not predict thermal conversion very accurately and required several empirical correlations to compensate.

Thunman and Leckner (2003) developed a model to investigate the conversion of thermally large wood particles in a fixed fuel bed on a grate. The model is formulated in a general way and can be applied for co-current and counter-current combustion of any solid fuel. The bed voidage was assumed to be constant and the absorption of radiation in the gas is negligible. In contrast to other models previously developed, the derivation in this case includes irregularly shaped, shrinking, thermally large particles, elutriation of solids, solids mixing in the bed expressed as dispersion, and heat transport by diffusion of gas species or by dispersion of solids. A shrinkage factor was determined empirically from experiment. In the mathematical modelling of solid waste, Yang (2003) compensated for non-isothermal behaviour of a single particle by reducing the cell size to a size-scale much smaller than the fuel particle.

For the past years, there has been very little research on the channelling phenomenon. The current theory adopted by most researchers was to assume a uniform bed where combustion and incineration of municipal solid waste occurs. Yang (2003) worked on the experimental observations of channelling in the burning bed of municipal solid waste incinerator. A detailed numerical simulation of the growth of an individual burning channel was carried out. Yang discussed the formation of channels by `push` and `loose` circles of the bed induced by the grate movement. Channelling was found to present a chaotic and three-dimensional pattern. The temperature profile was not orderly and the flame front reaches the bed bottom much earlier while a significant part of the bed is still to be ignited. The detailed mathematical simulation showed that the bulk of the oxidation processes took place inside the channel where local temperature was 100-200°C higher than the bed temperature in the neighbouring areas. The flame front was found to travel faster inside the channel and a hollow formed in the bed centre grew deeper and bigger as the burning process proceeded.

The approach taken by Peters (2002) was slightly different from the rest of the numerical modelling carried out previously. The packed bed was considered to be composed of a finite number of individual particles with different sizes and properties. Each of the particles undergoes a sequence of processes such as heat-up, drying, pyrolysis or gasification and oxidation. The sum of these processes represents the conversion of a packed bed. A single particle model was developed and applied to each particle in the bed to present the entire

conversion of a packed bed in the Discrete Particle Model (DPM). The single particle model is based on a system of one-dimensional transient conservation equations for mass and energy to predict major properties such as temperature and distribution of species inside a particle. The numerical model for the packed bed was carried out in two parts; the conversion of a single particle and the model of the void space of a packed bed. The particles are coupled to the surrounding gaseous phase by heat and mass transfer.

A similar modelling approach was taken by Bruch (2003). The packed bed was taken to consist of a finite number of particles where an individual particle undergoes a thermal conversion process, described by a one-dimensional and transient model. Brunch aimed at developing a general model to cover the entire conversion process of biomass fuels, from drying to char conversion, which can be used to determine limiting rate. A compromise is required between the computational time and accuracy of description, therefore a general approach was taken to which the chemical reactions; pyrolysis, char conversion and the homogeneous reactions within a particle were neglected. Such application of a single particle to an entire packed bed requires some form of simplification as more detailed models would exceed the acceptable numerical effort. The bed mesh is filled up with solid particles by assuming a constant porosity and a certain number of neighbouring particles. The position of the solid particles may change and is recomputed during the conversion process, due to the depletion of solid and shrinkage of the particles.

3.3 GASIFICATION

Gasification involves many chemical reactions, the two main types being; (1) the transition of biomass to char and (2) the subsequent gasification of the char itself.

The overall reactions that can occur during the initial gasification stages for coal are given in *Figure 3.7* (Johnson, 1979). The devolatilization reactions represented were similar to a pyrolysis model. Primary devolatilization in an inert atmosphere illustrated by reactions I-VIII involves the evolution of coal oxygen as carbon oxides and water, in addition to the formation of other gaseous hydrocarbons, heavy oils, tar, and some gaseous hydrogen. The solid product of this reaction stage is semichar. Secondary devolatilization is illustrated by reaction IX, in which semichar is converted to char through the evolution of hydrogen. Methane formation from the direct reaction of gaseous hydrogen and coal is indicated by reaction II, which occurs concurrently with primary devolatilization reactions. Reaction VIII, illustrates another path for the formation of methane in hydrogen, which results from the

heterogeneous interaction during secondary devolatilization concurrent with the conversion of semichar to char. In an inert atmosphere, the various hydrocarbon products and carbon oxides are then cracked to form carbon and char in the secondary reactions. In a hydrogen atmosphere at elevated pressure (reaction VII) higher yields of evolved oils and tars are promoted during the initial reactions. The hydrogenated products can then undergo further hydrogen enrichment, leading to the formation of light oils, gaseous hydrocarbons and eventually methane.

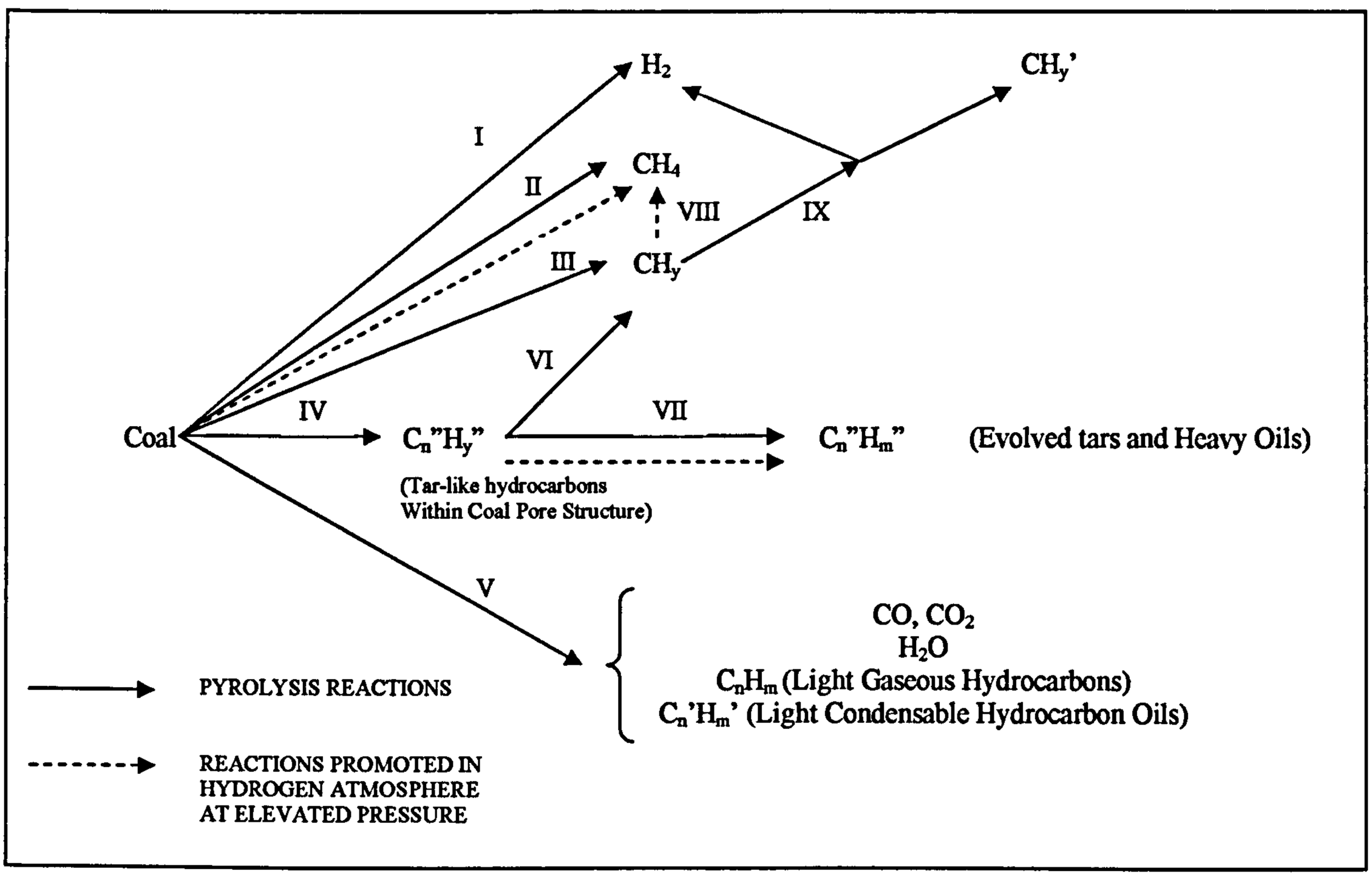

Figure 3.7: Simplified reaction scheme. Direct coal reactions during initial gasification regime.

3.3.1 Gasification Reactions

Combustible gases can be produced by the reaction of the coal, char or volatile matter with oxygen, carbon dioxide, hydrogen or steam. The principal components in the producer gas or flue gas from an air-blown gasification process are carbon monoxide and nitrogen. Hydrogen is present in significant amounts when air and steam are used in place of air alone. The reactions taking place in the gasifier can be summarised in *Table 3.1* (Higman, 2003):

Heterogeneous reaction		
Partial combustion	$C + \frac{1}{2}O_2 = CO$	-111 MJ/kmol
Boudouard reaction	$C + CO_2 \leftrightarrow 2CO$	+266 MJ/kmol
Water gas reaction	$C + H_2O \leftrightarrow CO + H_2$	+131 MJ/kmol
Hydro-gasification reaction	$C + 2H_2 \leftrightarrow CH_4$	-75 MJ/kmol
Homogenous Reaction		
Oxidation reaction	$CO + \frac{1}{2}O_2 = CO_2$	-283 MJ/kmol
Oxidation reaction	$H_2 + \frac{1}{2}O_2 = H_2O$	-242 MJ/kmol
Methanation reaction	$CO + 3H_2 \leftrightarrow CH_4 + H_2O$	-75 MJ/kmol
Water gas shift reaction	$CO + H_2O \leftrightarrow CO_2 + H_2$	-41 MJ/kmol

Table 3.1: Gasification reactions.

The arrows indicate that the reactions are in equilibrium and can proceed in either direction, depending on the temperature, pressure and concentration of the reaction species. All the reactions above are exothermic except the Boudouard and water-gas shift reaction.

Three product gas qualities with different calorific value can be produced by varying the gasifying agent, method of operation and process operating condition (McKendry, 2002):

Low CV	4-6 MJ/Nm³	Using air and steam/air
Medium CV	12-18 MJ/Nm³	Using oxygen and steam
High CV	40 MJ/Nm³	Using hydrogen and hydrogenation

The principal reactions in an air-blown gasifier are the partial combustion, oxidation and Boudouard reactions. Carbon dioxide formed in the presence of excess oxygen is reduced into carbon monoxide by the Boudouard reaction. This reaction is the most important reaction controlling the process. Its equilibrium constant greatly increases with a rise in temperature but reduces with increase in pressure. The type of carbon does not disturb the equilibrium content of carbon monoxide but influences the kinetics of the reaction. Producer gas is favoured by a high fuel bed temperature, reactive fuel and adequate time of contact (thick fuel bed) (Sarkar, 1990).

The demerits of an air-blown gasification can be overcome by the addition of steam to the blast of air. This increases the two reactions between the carbon and steam:

$$C + H_2O \leftrightarrow CO + H_2 \ldots\ldots\ldots\ldots\ldots \Delta H = +28{,}440 kcal \qquad \text{Reaction 3.1}$$

$$C + 2H_2O \leftrightarrow CO_2 + H_2 \ldots\ldots\ldots\ldots\ldots \Delta H = +18{,}600 kcal \qquad \text{Reaction 3.2}$$

The water gas reaction is active at and above 1,000°C while the shift reaction predominates between 500-600°C (Table 3.1). Both reactions are endothermic and convert the sensible heat liberated by carbon in the bed into potential heat in combustible form, namely CO and H_2. The formation of carbon dioxide (Reaction 3.2) can be suppressed by maintaining a high bed temperature. Similar to the Boudouard reaction, Reaction 3.1 is inhibited at high pressure.

In addition to the above reactions, there is also methane formation or methanation reaction between carbon and hydrogen. It has been reported that 80% of the methane formed appears as result of hydrocracking of primary tar and only 20% from hydrogasification of char (Merrick, 1984). The hydrogasification reaction is an exothermic reaction and is largely suppressed by high temperature conditions in the bed but is favoured at high pressure.

Carbon-steam and carbon-CO_2 reactions compete at temperatures above the transition range of 700-1200°C, wherein the rates become about the same. Below the transition range, the carbon-steam reaction is much faster. The addition of oxygen to the steam-carbon reaction (to supply endothermic heat) will yield less H_2 and thus give lower H_2/C ratios. Sulphur in a gaseous phase tends to appear as H_2S in a reducing atmosphere whereas in an oxidizing atmosphere, sulphur will appear as SO_2 (Hoffman, 1978).

Therefore, it can be summarised that the formation of methane, steam and carbon dioxide in the product gas is favoured by low temperatures and high pressures whereas the presence of hydrogen and carbon monoxide points towards a high temperature and low pressure operation.

Figure 3.8 gives an example of the equilibrium trend in a C-H-O gasification system for a hydrogen-oxygen ratio of 1. Thermodynamic consideration related to gasification is important to evaluate the limiting performance and, also for the practical design of experimental and commercial reactor systems.

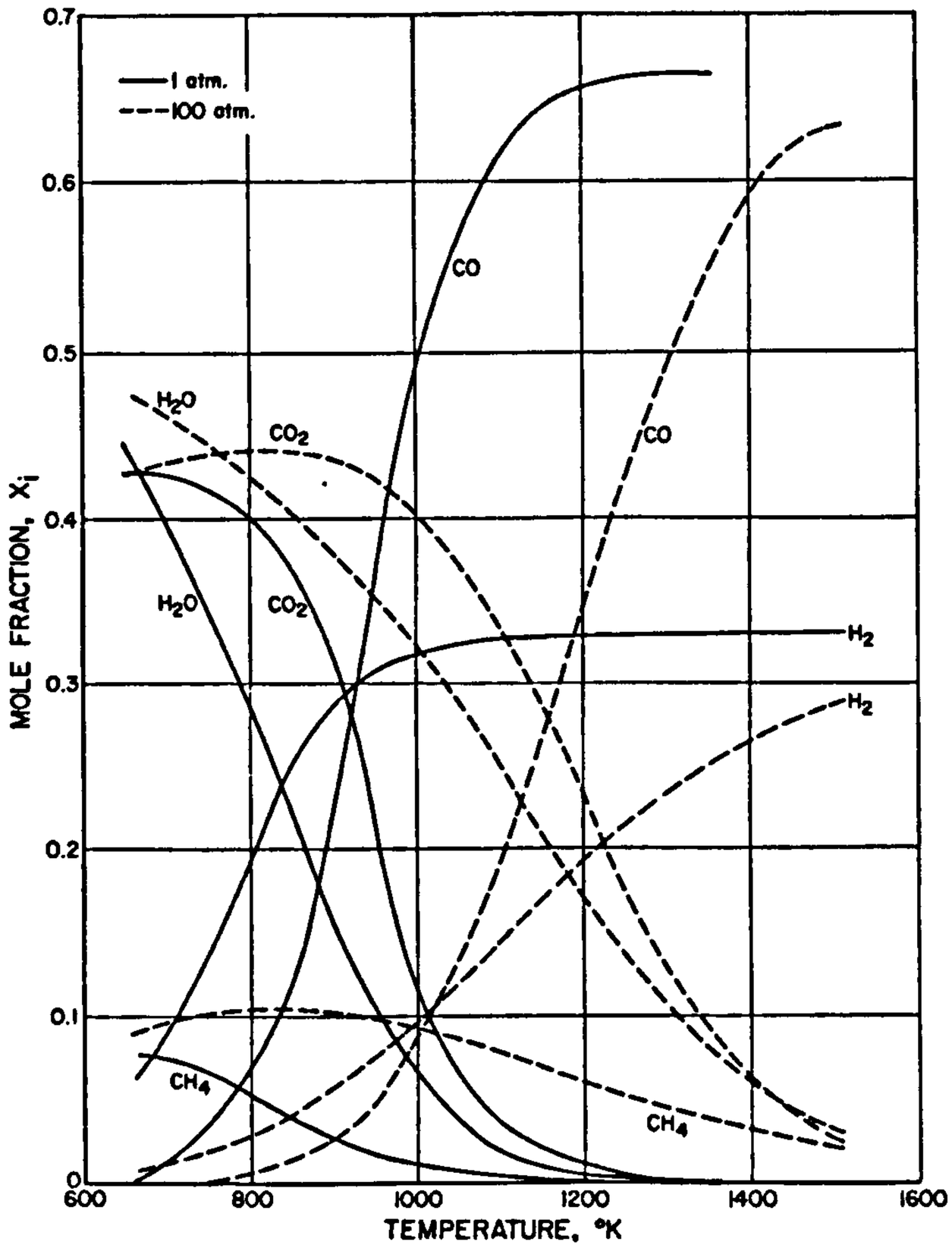

Figure 3.8: Equilibrium characteristics for C-H-O system (hydrogen:oxygen=1 g-atom/g-atom) (Johnson, 1979)

3.3.2 Reaction Kinetics

The speed of the gasification reactions discussed in *Section 3.3.1* influences the time required to achieve equilibrium. For gas-solid reactions, the two rate controlling processes are; *the diffusion of the gaseous reactants and products from the particle surface* and *the chemical reaction at the particle surface*. For gas-phase reactions, the chemical reaction rates are the main controlling factor. In general, the diffusion rate only becomes important when the reaction rates are high.

Reactions tend to be chemically rate controlled at low temperature, changing to diffusion rate controlled at high temperature. Diffusion-limited combustion occurs at about 1000-1400°C (Hoffman, 1978). The operating pressure imposes negligible effect on the diffusion rate but a significant effect on both the gas-solid reaction and the gas-phase reaction. Char of high reactivity increases the chemical reaction rate while a high diffusion rate is favoured by fine particles and turbulent gas-solids mixing. Chemical reaction rates vary widely depending on

the type of reactants as combustion and pyrolysis reactions are extremely quick, compared to the water-gas and shift reactions. For air gasification, the high combustion rate causes the process to shift towards a diffusion controlled reaction, however, the other reactions such as the Boudouard, hydrogasification, water-gas, shift and methanation are generally chemical reaction controlled at non-slagging temperature (<1200°C) (Merrick, 1984).

3.4 DEVELOPMENTS IN GASIFICATION MODELLING

Goetz *et al* (1983) carried out gasification tests on four commercial types of coals ranking from bituminous coal to lignite in a drop tube furnace system, to determine the kinetic parameters of these coals. Some of the main conclusions drawn from their findings are that temperature and CO_2 partial pressure play important roles during the gasification of coal. Char combustion and gasification could be assumed to proceed by a "shrinking core" mechanism. The reaction rate was found to exhibit near first order dependency on carbon dioxide partial pressure. Tancredi *et al* (1996) investigated the reactivity of chars from Eucalyptus sawdust prepared under different carbonisation temperatures. Char prepared at a low carbonisation temperature showed higher reactivity. The gasification of the lower carbonisation char seems to start at lower temperature. The reactivity of char increases with conversion, which, at low and intermediate conversion can be attributed to the increase in surface area as the gasification proceeds. At high conversion levels, a steeper increase in reactivity was observed due to the increasing catalytic effect of the metallic constituents (mainly Na and K) of the inorganic matter present in char. The influence of the treatment condition during pyrolysis on the reactivity of char was further investigated by Chen *et al* (1997) using a tubular reactor. A rapid heating of char from biomass gave high reactivity in reaction with both CO_2 and steam compared to char formed under slow heating. The reactivity of chars from rapid pyrolysis is 2.4-3.3 times the value of the rate constant from slow pyrolysis.

Fushimi *et al* (2003) carried out work on the effect of heating rate on the final conversion and reaction rate of char. The steam gasification was carried out using biomass materials (cellulose, lignin and bagasse) in a thermobalance reactor. In the rapid pyrolysis experiments conducted, the evolution of low molecular weight gases such as H_2, CO, CO_2 and CH_4 occurred at about the same time. One important finding in their study was the decrease of tar and increased yield of carbon in the gas with rapid heating due to enhanced decomposition of tar. The importance of the water-gas shift reaction in affecting the overall gas composition was highlighted as rapid heating or high temperatures were seen to encourage the evolution of CO.

de Jong *et al* (2003) studied the characteristics of two biomass fuels (pelletised Miscanthus Giganteus and wood) at three heating rates (10, 30, 100°C/min) using thermogravimetric analysis with a final temperature of 900°C. Contradicting the results obtained by Fushimi (2003), Jong found that the tar yields increase at the expense of lighter gaseous species (mostly, CO, CO_2, and acetaldehyde) as the heating rate increases. It was explained that at high heating rates, there is insufficient time for the evolution of light species, and thus, tar fragments leaving the biomass carry with them precursor material that could result in light gas compound formation. The pyrolysis of miscanthus was found to produce higher yields of char and lower yields of volatile matter compared to wood due to the difference in biochemical composition.

Na *et al* (2003) studied the oxygen-blown fixed bed gasification of waste pellets (Φ=2-3cm) in the temperature range of 1100-1450°C. A higher methane concentration was produced by PE (plastic) gasification compared to the mixed-waste gasification due to the increased cracking. His experimental study showed that the product gas composition was sensitive to the O_2/waste ratio. The CO concentration in the product gas was found to increase to a maximum at an O_2/waste ratio of 0.35-0.45 and then decreases. For an O_2/waste ratio above 0.45, the concentration of H_2, CH_4 and CO decreased while CO_2 increased.

Di Blasi (1993) reviewed the thermal degradation processes of charring and non-charring materials. Cellulosic material pyrolysis was said to occur under two different regimes: (1) the chemical regime, and (2) the heat transfer regime. The pyrolysis of wood and biomass materials was described in two stages, primary reactions of virgin solid degradation and secondary reactions of evolved degradation products. Blasi outlined the three main classes of pyrolysis kinetic studies:

1) *one step global models*, when a one-step reaction is used to describe degradation of solid fuel by means of experimentally measured rates of weight loss:

$$SOLID \xrightarrow{k} VOLATILES + CHAR$$

2) *One-stage, multi-reaction models*, used to correlate reaction product distribution. These are one-stage simplified kinetic models, made of several reactions, describing the degradation of the solid to char and several gaseous species. The proposed models

assume that the virgin solid fuel decomposes directly to each reaction product *i*, except tar, by a single independent reaction according to:

$$VIRGINFUEL \xrightarrow{k_i} PRODUCT_i$$

The kinetics is modelled through a unimolar-first order reactions rate which was expressed as:

$$\frac{dV_i}{dt} = A_i \exp(-E_i / RT)(V_i^* - V_i)$$

Where V_i is the yield of the product i, and A_i and E_i are the pre-exponential factor and apparent activation energy, respectively.

3) *Two-stage, semi-global model,* when the kinetic mechanism of solid degradation includes both primary and secondary reactions. Below is an example of the first semi-global models proposed for the degradation of cellulose:

$$CELLULOSE \xrightarrow{k_1} ANHYDROCELLULOSE$$
$$CELLULOSE \xrightarrow{k_2} TAR$$
$$ANHYDROCELLULOSE \xrightarrow{k_3} GAS + CHAR$$

Di Blasi (1999) employed counter-current air blown fixed-bed gasification to compare the gasification characteristics of several biomass materials (beechwood, nutshells, olive husks and grape residues). The gas-heating values of the product gas were reported to be in the range of 5-5.5 MJ/Nm³ with 28-30%CO, 5-7% CO_2, 6-8% H_2, 1-2% CH_4 and small amounts of C_2-hydrocarbons (apart from nitrogen). High density fuel (olive husks) led to poor flow distribution with high amplitudes in the temperature oscillations. The non-uniform bed properties of the grape residues caused the formation of bridges and large voids. The experimental results also showed that the rate of fuel consumption increased with air flow rate. A higher amount of fuel consumed led to a higher bed temperature and higher rate of heat transfer to the fuel, promoting further char gasification, pyrolysis and drying process. Findings indicated that the optimum gasification condition for grape and olive residues are established at a higher air flow rate compared to wood.

3.5 CATALYZED GASIFICATION

Catalysts have been increasingly used in gasification processes to enhance desired reactions and to upgrade primary products to higher quality fuels. One important effect of the catalyst is that it permits a lowering of reaction temperature. Catalysts are used in two major reactions in gasification processes:

- Carbon-Steam Reaction

In this case, the catalyst is used to improve the quality of the product gas in terms of composition to make the synthesis of a higher value product, more efficient and cost effective. For example, the increased production of syngas that serves as an intermediate fuel. It could also be used to change the ratio of carbon monoxide to hydrogen for methanol synthesis.

- Tar Breakdown

The gasification of biomass is proposed to be the future technology in gaining access to electricity or other fuels while simultaneously maintaining the environmental quality. However, the formation of tar in the gasification processes, particularly with updraft gasifiers greatly affects the practical application of the process. The high tar content in the synthesis gas or biomass-derived fuel is a barrier to the application of these fuels in engines, turbines or compressors. Higher thermal value of dry gas is obtained from the catalytic reforming of tar as it decomposes to hydrogen and intermediate carbon compounds, which in turn will react with water, forming carbon monoxide, carbon dioxide and hydrogen. Conventional methods of filtration are inadequate to complete the separation of tar. Physical tar removal by water scrubbing creates more problems through generation of dirty water requiring extensive biological or thermal treatment.

Catalytic substances such as lime or caustic soda, hydrates or carbonates, chlorides, sulphates, sulphides, silicates, metallic oxides, alkalis and metallic couples such as copper-ion have been used to lower the carbon-steam reaction temperature. Taylor (1921) found potassium and sodium carbonates to be the best materials, particularly potassium carbonate. In the experimental work conducted by Li and Cheng (1995) on the catalytic gasification of gas-coal char in CO_2, it was also found that potassium carbonate proved to be superior compared to sodium carbonate. The alkali metals in the ashes of many biomass species and some waste could act as a natural form of catalyst.

Ferric oxide was found to be only about one-tenth as effective as alkali carbonates for the steam-carbon reaction although it was found to be very effective for the CO-shift (Hoffman, 1978). Ponder and Richards (1994) carried out an experimental study on the oxygen and CO_2 gasification of chars from wood treated with iron (II) and iron (III) sulfates. Samples of cottonwood and sapwood were sorbed with iron sulphate salt solutions. In this research, the char samples were prepared at different heat treatment temperatures (HTT). Results showed that sorbed ferrous and ferric sulphates are only superior to indigenous inorganic in cottonwood as catalysts in O_2 gasification, only in the case of low-HHT chars. The opposite situation was seen with CO_2 where the iron sulphates are superior to the indigenous species. For both type of gasification, ferric sulphate appears to be superior to the ferrous sulphate as a catalyst.

In the review carried out by Hoffman, he pointed out several research studies that indicated use of alkali carbonates as catalysts for carbon-oxygen steam reactions. Li and Cheng (1995) investigated the catalytic effect of both Na_2CO_3 and K_2CO_3 in gas-coal char CO_2 gasification using a fixed-bed reactor at 790°C-1020°C and 0.2MPa. The catalytic effect of K_2CO_3 was proven to be greater than that of Na_2CO_3. The reaction rate increased with loading above 9 wt% Na_2CO_3 and 5 wt% K_2CO_3 and starts to decrease above 25 wt% Na_2CO_3 and 20 wt% K_2CO_3 indicating a saturation effect. The catalytic steam gasification of Illinois No. 6 coal was carried out using binary Na_2CO_3 - K_2CO_3 (NK) and ternary Li_2CO_3-Na_2CO_3 - K_2CO_3 (LNK) eutectic salt mixtures in a fixed bed reactor by Godavarty and Agarwal (2000). The catalyst was physically mixed in different amounts of 5 wt%, 10 wt% and 15wt% of the raw coal. Experimental findings showed that for both LNK and NK catalysts, 10 wt% is the optimum amount of catalyst as any further increase beyond this point showed negligible increase of carbon conversion because the coal was physically saturated with catalyst. The gasified char particles having NK catalyst coalesce indicated liquid-phase sintering whereas the ternary catalyst showed highly porous and crystalline morphology.

Asadullah (2004) investigated the effectiveness of a newly developed catalyst $Rh/CeO_2/SiO_2$ in both a single and dual-bed gasifier system. The $Rh/CeO_2/SiO_2$ catalyst proved to exhibit a higher performance compared to the commercial steam-reforming catalyse G91 (14mass% Ni, 65-70mass% Al2O3, 10-14 mass%CaO, and 1.4-1.8 mass%K2O).

Cobalt compounds have been used in the Fischer-Tropsch reaction between CO and H_2 to produce hydrocarbons. It was found that cobalt oxide reduced in hydrogen would catalyse the CO-shift, even at very low temperature. The effect of cobalt catalysts on the carbon dioxide gasification of wood chars is also discussed by DeGroot and Richards (1988). Their work

placed a strong emphasis on the effect of heat treatment temperature (HTT) on the rate of gasification. The chars were prepared from wood treated at and beyond the ion exchange capacity with cobalt and compared with those prepared using calcium and potassium. Cobalt-exchanged woods enable gasification at lower temperature whereas chars prepared from calcium and potassium-exchanged wood was completely unreactive at this temperature. The most reactive chars were those prepared and gasified at 600°C.

Carbonate rocks such as limestone and dolomite have been known to decompose tar efficiently in gasification processes. Simell (1992) compared the tar decomposing activity of potential low cost materials suitable for bulk use in gasification processes. The catalyst increases both the tar decomposing and gas reactions such as the water-gas shift and water-gas reactions. The tested materials were divided according to their hydrocarbon decomposing activity:

- High activity: ankerite and dolomite
- Intermediate activity: limestone, calcitic dolomite and dolomite limestone
- Low activity: sinter and pellet

The amounts of the most problematic tar compounds, polyaromatic hydrocarbons (PAH) and monocyclic compounds, such as phenol, were reduced significantly even by the low activity material. The effect of ankerite and dolomite were found to be comparable to that of commercial nickel catalyst. The formation of CO was high with high activity materials and limestone. Nickel-catalyst and iron-containing materials (ankerite, sinter, pellets) decomposed ammonia and hydrogen cyanide efficiently. Carbonate rocks decomposed hydrogen cyanide to some extent, but increased the content of ammonia. The tar composition changes were similar with all the tested materials. The ferrous materials were not as reactive but the content of most problematic tar fraction decreased significantly. Gases were apparently formed in the tar decomposition reactions, the water-gas shift reaction and water-gas reaction.

3.5.1 Catalyst Application

The use of catalyst could be applied in a single bed or dual-bed gasifier system. Catalysts tend to deactivate due to the deposition of coke and ash on the catalyst surface. This decreases the catalyst activity as large amount of ash powder interacts with the catalyst surface and cover the active sites on the catalyst. Therefore, it is necessary to separate the catalyst from ash in the gasification of biomass with high ash content. The dual bed gasifier has two separate

reactors for the secondary-bed reforming of tar and an ash separator used between the reactors. The advantage of increased catalyst activity is offset by higher complexity in the system. For biomass containing low amount of ash such as wood, the single-bed gasifier system could be used.

Catalysts are usually used with promoters and carriers to enhance the activity of the given catalyst. Alkali or alkali carbonates are effective promoters. Other carriers used include silica gel, alumina, silica and dolomite. The catalysts may be prepared by impregnation from solution, by binding agents or even physically mixed with the bed materials. Catalyst can also be sprayed on surfaces (e.g, Raney nickel) and are produced by spray drying. The process or preparation affects the interstitial pores and the activity. The effect of the different methods of catalyst application was studied by Mudge (1979). Two methods for wood catalyst contacting were used here: dry mixing of wood and solid catalyst and impregnation of wood with catalyst. The catalysts used in his study were potassium carbonate, sodium carbonate, trona and borax, in order of their effectiveness at all temperature. Impregnation produced about 10% more gas than dry mixing with a slight increase in rate of gas production although both contacting methods significantly increase the total gas production.

3.6 SUMMARY

The combustion on the travelling grate in a biomass plant is simulated using a laboratory scale pot furnace to abate high cost and complex design. The literature shows that extensive experiments have been carried out using wood as a fuel source to investigate the influence of combustion parameters such as; *air flow rate, moisture content, particle size* and *bed density* on fixed bed combustion. The behaviour of new energy crops and processed waste should be investigated experimentally before their use in commercial applications as the physical and chemical properties of the fuel source significantly affects the combustion efficiency. The review showed that the use of numerical modelling helped to further understand the mechanism of the combustion process. The bed calculation was based on a transient, one-dimensional model as a representation of the two-dimensional steady-state model. One of the main assumptions made in the model was to assume negligible radiation variation with temperature and composition, limiting the model to small particles. The Discrete Particle Model (DPM) on the other hand, accounts for all processes in a single particle but the application of the model to an entire bed of particles is limited by computational time and requires some form of simplification.

The interest in gasification is driven by the fact that it yields an intermediate fuel that could be used in an energy recovery system. The use of steam in gasification was found favourable as it leads to a higher yield of hydrogen. Nevertheless, the requirement for additional heat input into the process has previously rendered this system economically unviable. The literature reveals concerns regarding the problematic tar content in the synthesis gas barring its direct application in gas turbines. Catalytic gasification has been proven useful in tackling tarry fuel gas but at the expense of a more complicated system and higher cost. A lot of the gasification research was carried out in a drop-tube furnace and focussed on the heating-up of the biomass. The temperature and heating up rate of biomass materials prior to the gasification was found to significantly affect the reactivity of the char during the gasification. The product gas composition from the gasification was to found to be sensitive to the air/fuel ratio. From the literature, the gasification reactions were found to be chemically controlled at low temperatures but diffusion limiting at high temperatures (>1000-1400°C) rendering the use of kinetic models appropriate in gasification calculations.

CHAPTER 4

FIXED BED COMBUSTION

This chapter presents the experimental programme, results and discussions of the fixed bed combustion of 3 main types of biomass materials (herbaceous plants, woody plants and waste) under fuel-rich gasification conditions. The experimental setup, measurement accuracy and experimental procedures carried out in this study are presented in detail.

The experimental results are reported in different sections corresponding to the characteristic investigated (air flow rate, fuel type and particle size). The primary air flow rate was varied in the range of 281-468kg/m^{2}hr to compare the performance of the fixed bed combustion under varying conditions. This effect was tested with willow wood (woody plants), refused-derived fuel (RDF) and pelletised miscanthus (herbaceous plants). In the investigation of the effect of particle size, all experimental conditions for the 4 cases except for the size of wood cubes (5mm, 10mm, 20mm and 35mm) were similar. A series of combustion tests was also carried out for three herbaceous crops (straw, switchgrass and reed canary grass) at different air flow rates (237-1170kg/m^{2}hr). The combustion experiments for straw were repeated with different straw length to investigate the influence of bed packing on the combustion profile.

The temperature along the bed height, flue gas composition and mass loss were measured as the combustion progressed and the key results on the ignition front speed, burning rate, percentage mass loss, equivalence ratio and temperature gradient were evaluated.

4.1 EXPERIMENTAL WORK

4.1.1 Experimental Setup

Figure 4.1 shows the schematic of the experimental rig constructed for this work. The fully constructed rig is as shown in *Figure 4.2* and *Figure 4.3*.

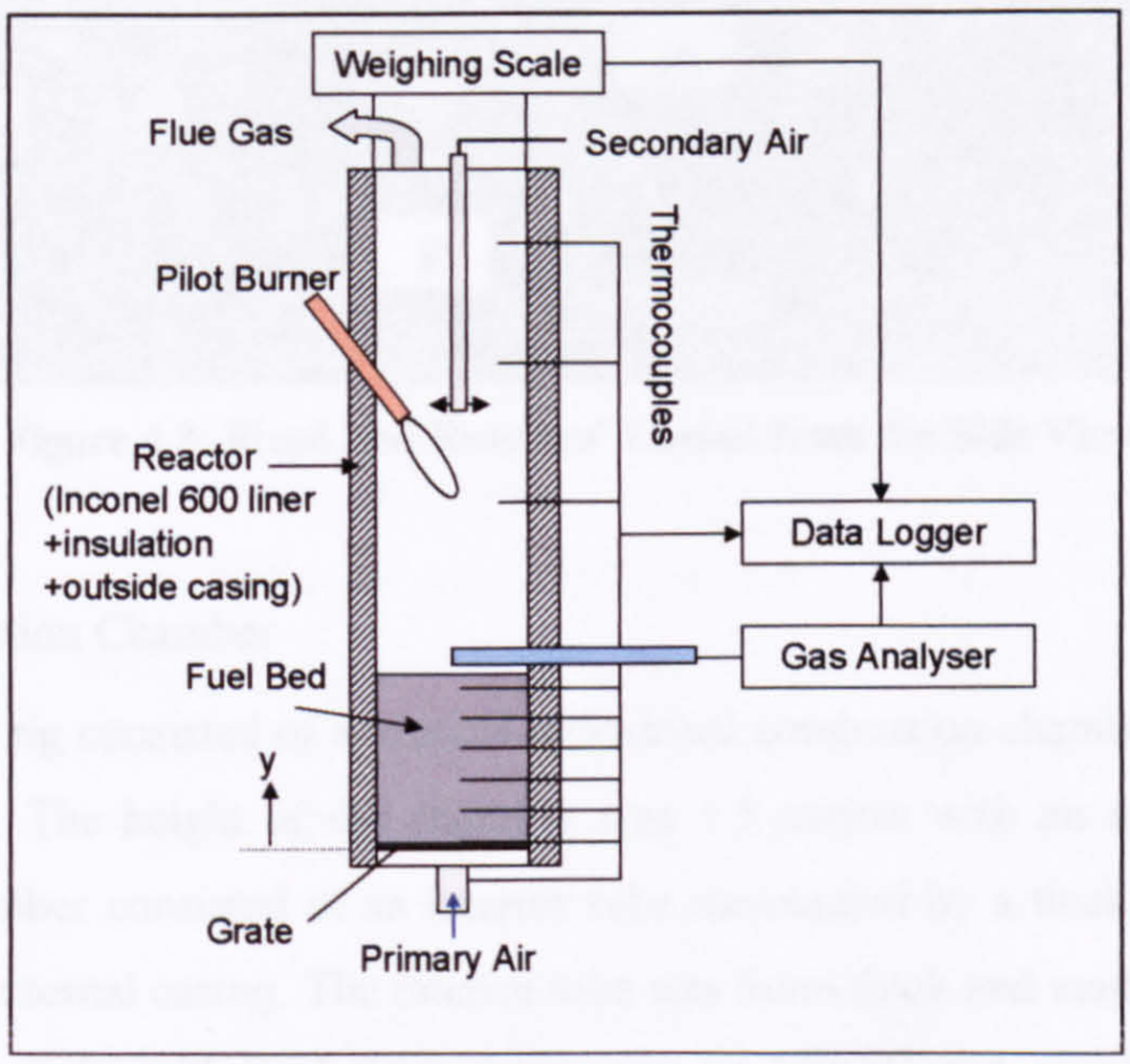

Figure 4.1: Schematic of Fixed Bed Reactor.

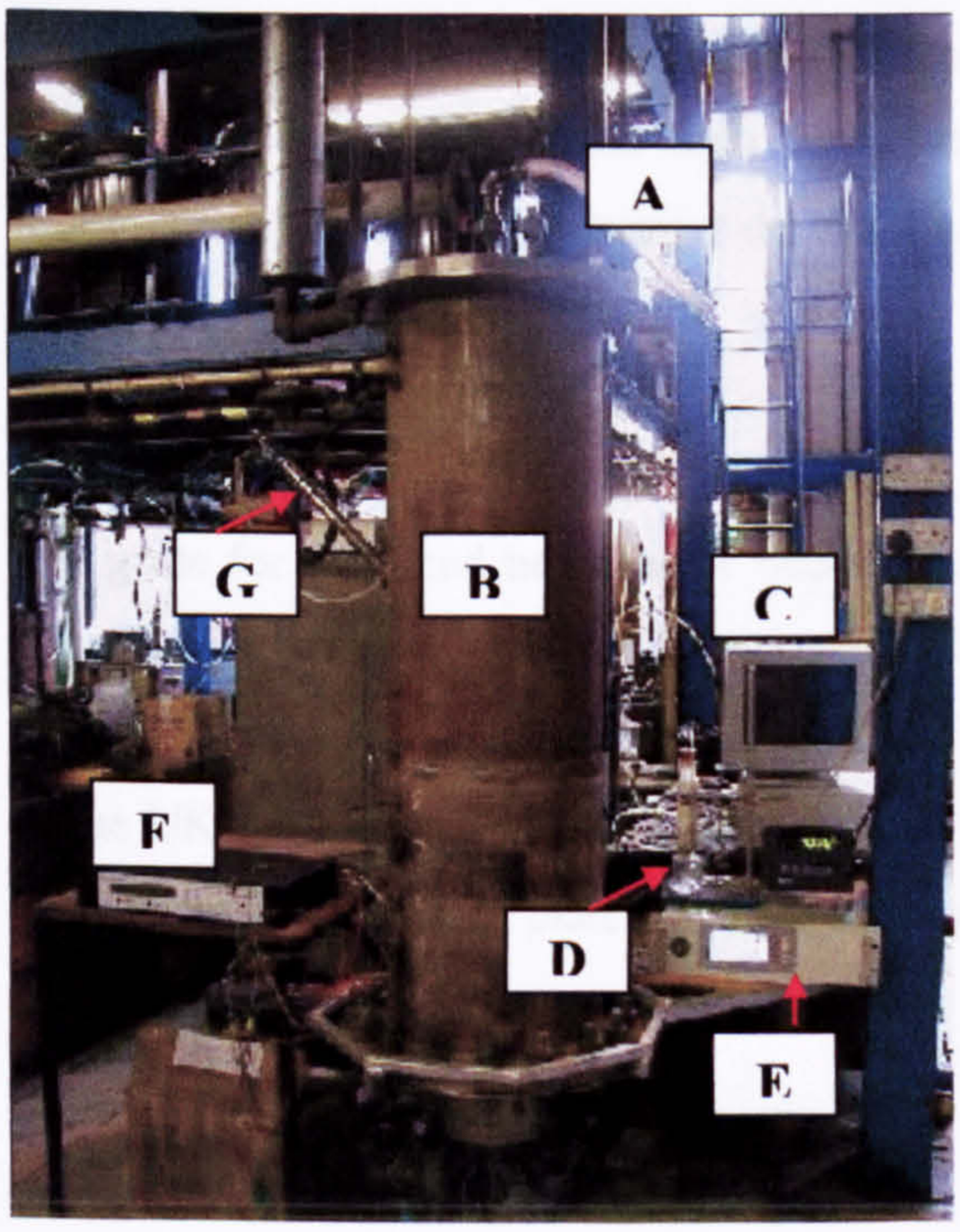

A – Flexible Hose

B – Furnace

C – Computer

D – Weight Indicator

E – Gas Analyser

F – Data Logger

G – Gas Burner

H - Rotameter

Figure 4.2: Fixed Bed Reactors' Layout from the Front View.

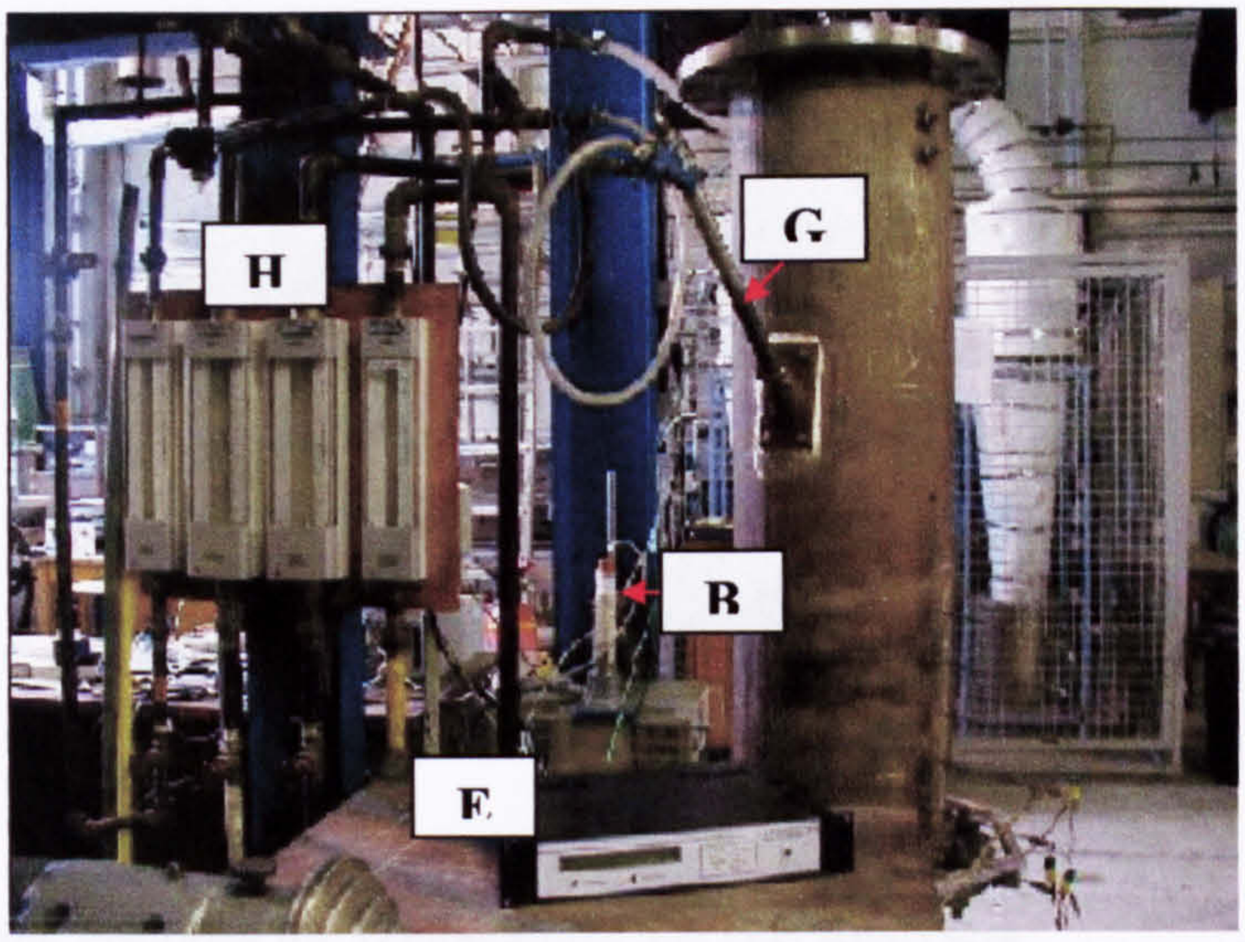

Figure 4.3: Fixed Bed Reactors' Layout from the Side View.

4.1.1.1 Combustion Chamber

The experimental rig consisted of a vertical cylindrical combustion chamber, suspended from a weighing scale. The height of the chamber was 1.5 metres with an internal diameter of 200mm. The chamber consisted of an interior tube surrounded by a thick layer of insulating material and the external casing. The interior tube was 8mm thick and made from Inconel 600 nickel alloy and could withstand temperatures up to 1200°C and resist corrosion at high temperature. The middle part is made of 80-mm-thick insulating material made from thermal ceramic blanket. The insulating material used was Kaowool Blanket S thermal ceramic blanket, which can withstand high temperature up to 1260°C. The external casing was stainless steel with 420-mm outside diameter and 30-mm thick wall.

4.1.1.2 Grate

The grate for the fixed bed reactor was a perforated plate, with approximately 700 holes of 2mm diameter, representing 7% open area. This was placed at the bottom of the combustor. The open area was taken as 7% open area as it represents the grate open area of an incinerator in the UK (Nasserzadeh, 1990). In order to withstand a temperature in the order of 500°C, a stainless steel perforated plate was used. The grate used in this experiment is shown in *Figure 4.4*.

Figure 4.4: Grate Used in the Fixed Bed Reactor.

4.1.1.3 Sampling Positions for Temperatures and Gas Analysers

There were 11 sampling holes on the wall of the combustion chamber for measurements of temperature and gas composition. The positions of the sampling holes are given in *Table 4.1*. Sampling holes 1, 10 and 11 were for measuring the temperature of the primary air, the flame of the burner and the flue gas respectively. The gases inside the chamber were sampled at 430m above the grate. The measurements were made at the centre line of the bed.

No	Position above the grate (mm)
1	Below grate
2	0
3	90
4	160
5	250
6	340
7	430
8	520
9	610
10	855
11	1305

Table 4.1: Position of Thermocouples on the Combustion Chamber.

Ni/Cr-thermocouples (type K) were used to measure the gas temperature inside the reactor, the flue and the primary air. The thermocouples were placed inside the chamber so that the tips of the thermocouples were at the centre of the internal tube. This was to ensure that measurements made were least affected by the channelling flow that occurred near the wall of the chamber. All the thermocouples were connected to a data logger, which was connected to a computer for automated temperature recording.

The main components of gas measurements were O_2, CO, CO_2. The probes were connected from the tapped holes to the gas analysers for gas measurement. The analysers were also connected to the data logger for storing of data.

4.1.1.4 Gas Burner

A gas burner was placed at a 45° angle toward the waste at 750mm above the grate. The gas burner was use to initiate the burning process of the waste sample and to maintain the freeboard combustor temperature during the experiment.

4.1.1.5 Weighing Beams

The fixed bed reactor was suspended from 2 weighing beams, which 4 load cells that could take up to a total maximum load of 2000kg. The weighing beams were used to monitor the weight changes (loss) of the sample during the combustion experiment. The pipes connected to the combustion chamber were made from flexible hoses to avoid interferences with the weight measurement. Continuous measurement of weight was performed using computerised recording of the data. *Figure 4.5* shows the weighing beams (1200 x 110 x 70mm) that were used to suspend the experimental rig.

Figure 4.5: Weighing Beams.

4.1.1.6 Combustion Air

The primary air was supplied from a compressor. The air flow rates were controlled by manual valves and volume flow rates measured by Rotameters Series 2000 by KDG Mobrey Ltd. Primary air was fed from the bottom of the fixed bed reactor through the grate.

4.1.1.7 Gas Analyser

The gas analyser was used for continuous monitoring of the flue gas concentration within the bed. The gas analyser used in this experiment is shown in *Figure 4.6*. *Table 4.2* gives detailed specification of the analyser used.

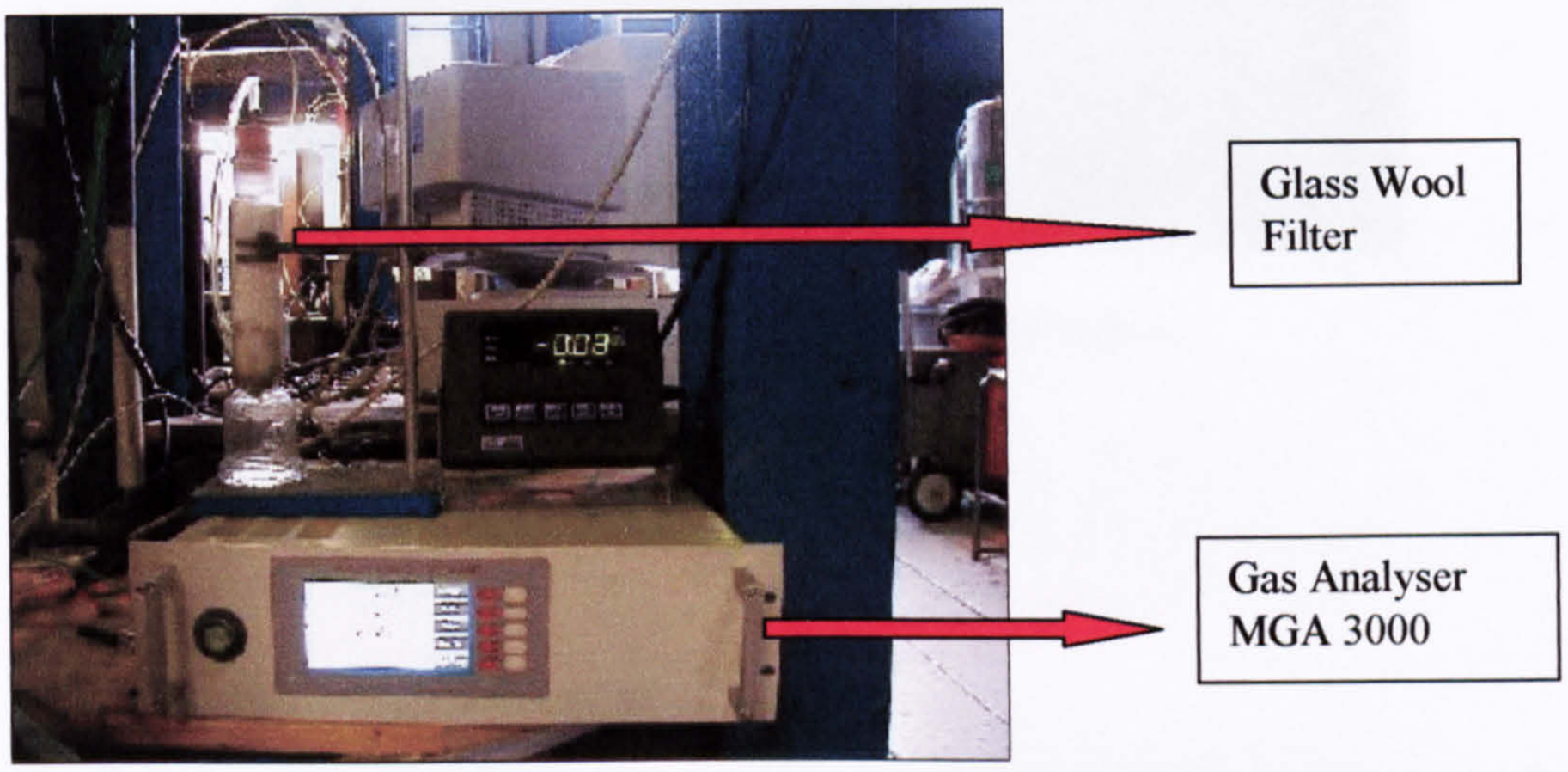

Figure 4.6: MGA 3000 Gas Analyser and Glass Wool Filter.

Manufacturer	Analyser	Detector	Range (%)
Analytical Development Co, Ltd	O_2	Chemical oxygen sensor	25
MODEL:	CO	Infrared	30
MGA 3000 Multi- Gas Analyser	CO_2	Infrared	20

Table 4.2: Specification of the MGA 3000 Gas Analyser.

A stainless steel probe was positioned above the fuel bed to continuously extract a sample of the combustion gas from the chamber. The combustion gas was passed through a glass wool filter, followed by a drier consisting of calcium chloride granules before entering the gas analyser. This is to prevent dust and water from entering the analyser and affecting the measurements.

4.1.1.8 Data Logging System

A Data Acquisition Board was used to automatically record the continuous data from the gas analysers and the thermocouples. The data logger used in this experiment is shown in *Figure 4.7*. It was designed with 24 channels of which 16 were for thermocouples and 8 were for inputs from the gas analysers. The data coming from the thermocouples and analysers were recorded at 0.5 sec interval between each channel. A lapse time of 2-60secs can be specified

between each set of 24 channel readings. The file can then be imported to the Excel program for data analysis.

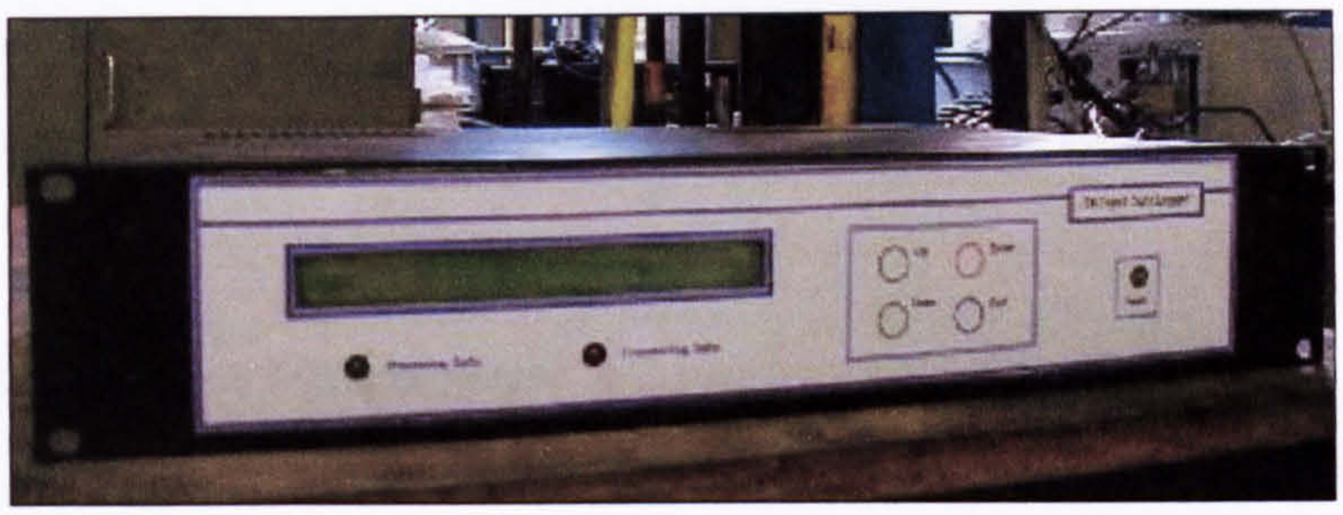

Figure 4.7: Input Channel Data Logger.

4.1.2 Experimental Measurement Accuracy

4.1.2.1 Temperature Measurement

The thermocouples used for temperature measurement were type K thermocouples from RS Components Ltd. These insulated nickel alloy probes could measure continuous temperature in the range of 270°C to 1379°C making it suitable for high temperature bed measurements. The thermocouples conform to accuracy class 2 or better specified by IEC 584 (International thermocouple reference tables Nickel – Chromium/Nickel- Aluminium thermocouples type K). Thus, the thermocouples have an accuracy of ±0.0075 of the actual temperature or ±2.5°C.

The radiation effect could cause significant errors for temperature measurement of gases above 1000°C (Fristrom, 1995). This is because the thermocouples` reading is affected by radiation exchange with the surroundings. However, this did not affect the analysis and conclusion of the study as the flue gas measurements were only used to indicate if there was a significant combustion process above the bed. A higher flue gas temperature than the bed temperature indicated that the combustion process was not complete in the bed and a certain fraction of the gaseous fuel escaped the bed and continued to burn in the freeboard. Analysis of the fraction of energy transfer from the gaseous fuel to the bed was based on the bed temperature measurements.

The bed temperatures were measured inside the bed where the thermocouple probes were totally immersed in the bed. The thermocouple probe temperature was the same as bed temperature because the heat transfer from the bed to thermocouples was predominantly by

conduction. In addition, the bed was practically opaque to thermal radiation thus the radiation heat loss to the surroundings was negligible As a result, the temperature measurements of the bed represent the actual temperature of the bed and the measurement errors were only due to the accuracy of the thermocouples as has been discussed above. The thermocouples have been used in previous fixed bed combustion studies (Zakaria, 2000).

4.1.2.2 Combustion Gas Measurement

The accuracy of the gas analyser, MGA3000 (ADC) depended on the accuracy of the span gas. The span gas used for calibration had an accuracy of 2%. The gas analyser has a repeatability and linearity of ±1% and a resolution of 0.1%. The gas emitted from the furnace flows through tube piping, joints and filter before reaching the sample input of the gas analyser. This caused a time delay between gas emission from the furnace and the gas sampling into the gas analyser.

The response time is given by:

$$= \frac{\text{Total volume of sampling line (from probe to analyser)}}{\text{Sampling flow rate}}$$

In this experiment, a pump was used to increase the sampling flow rate, reducing the response time. The maximum response time including the instrument response was timed to be 37seconds.

4.1.2.3 Air Flow Measurement

The air flow rates for the combustion test were measured using Rotameter Series 2000 instruments by KDG Mobrey Ltd, which were factory calibrated using air at 15°C and 1013 mbars abs. The accuracy of the rotameters given by the manufacturer was 2.5% of their full-scale reading (FSR).

The maximum and minimum rotameters scale ranges with the reading errors are summarize *Table 4.3*.

	Rotameter Scale Ranges (lit/min)			
	Maximum	Error	Minimum	Error
Burner	500	12.5	50	1.25
Primary Air	500	12.5	25	0.62

Table 4.3: Reading errors for the maximum and minimum rotameter scale ranges.

The error due to the temperature difference of air is very small. Correction for temperature difference can be made by multiplying the flow rate reading by $(T_m/T_c)^{1/2}$, where T_m is the temperature of the metered air and T_c is the temperature of the calibration air. The average room temperature during the combustion test was 18°C, thus error due to temperature difference was 0.09, which was considered negligible.

4.1.2.4 Weight Measurement

The weight of the biomass material was measured using a calibrated scale which measures accurately to the nearest ±20g. Thus, 2.0kg of material has a weight of 2000 ± 20g. The scale used consisted of a pair of weigh beams (incorporating four load cells) where the combustion chamber was suspended and the digital display of the readings was located at the lower level. For improved accuracy, the initial weight of the waste before and after the test was measured using a digital scale which could accurately weigh to the nearest 0.1g for confirmation of the reading of the weight loss during combustion.

The weight measurement is affected by the thermal expansion of the furnace. The heat during the experiment caused the furnace to expand. However, the expansion is restricted as the bottom of the furnace was connected to the primary air pipeline. The air pipeline resisting the furnace expansion will lift the furnace.

Thermal Expansion Coefficient of Stainless Steel (20-540°C): 16.0×10^{-6}mm/mm°C
Room Temperature: 19°C
For a furnace of 1.5m and a maximum temperature of 1200°C, the maximum expanded length would be = $1.5\ (16.0 \times 10^{-6})\ (1200\text{-}19) = 2.88$cm

In practise, the average metal temperatures will be significantly lower than 1200°C. The weight of materials loss was determined after the cooling down of the furnace to room temperature.

4.2 BIOMASS SAMPLES

4.2.1 Preparation of Samples

The materials selected for the tests are from three primary classes of biomass fuels including one sample from a segregated waste having a large fraction of cellulosic materials. *Figure 4.8* illustrates the biomass samples used for the combustion experiments.

Woody Plants

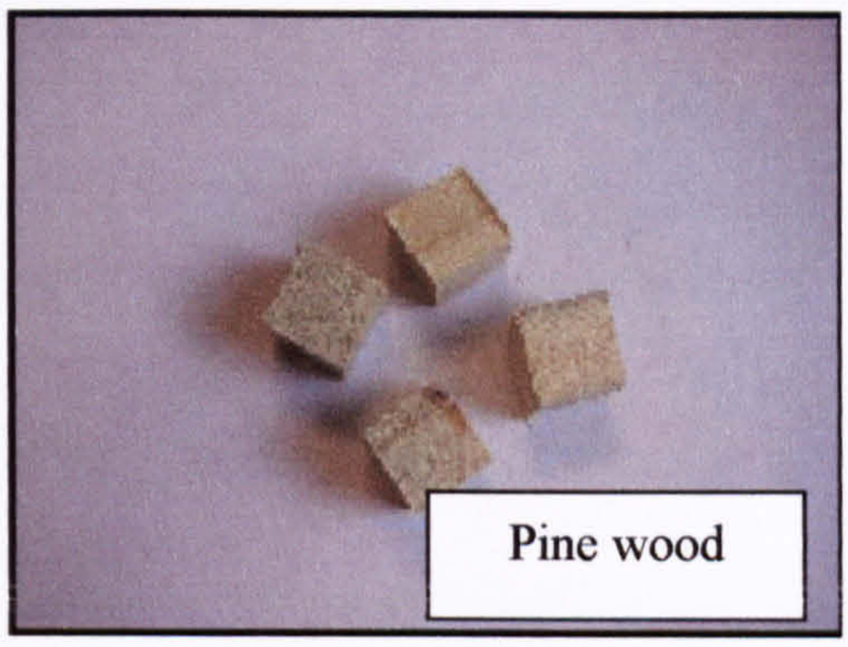

Herbaceous Plants

Waste

Figure 4.8: Biomass samples used in this experiment.

Laboratory Analysis by standardised techniques; proximate and ultimate analyses were conducted prior to the experiments. The carbon and hydrogen content of the biomass sample were carried out according to the ASTM D-3178 and the proximate analysis was based on the D-3173-3175 (American Society of Testing Material) analytical method. The analyses were carried out in the analytical laboratory at the Department of Chemical and Process Engineering, University of Sheffield. The proximate analysis determines the moisture evolved at 105°C, volatile matter (VM) released on heating to 925°C in a closed crucible, ash residue on combustion at 800°C and the fixed carbon (FC). The results were expressed in weight %. The ultimate analysis gave the carbon, hydrogen and oxygen composition present in the biomass fuel expressed as weight %. The calorific value determinations were made using the adiabatic calorimeter method as described by *British Standard 1016 Part 5*. Based on the proximate and ultimate analysis, the biomass used in this work had the composition as tabulated in the Table 4.4 to 4.10.

Woody Plants

Willow wood		Sample 1	Sample 2	Sample 3	Average
Proximate Analysis (%wt)	Moisture	6.8	8.3	6.4	7.2
	Volatile	79.2	78.5	76.6	78.1
	Ash	1.0	0.9	1.2	1.1
	Fixed Carbon	12.9	12.3	15.9	13.7
Ultimate Analysis (%wt)	Carbon	45.2	46.2	46.1	45.8
	Hydrogen	6.5	6.5	6.9	6.6
	Oxygen	40.1	39.1	38.9	39.3
Gross Calorific Value (MJ/kg)		17.4	18.1	17.8	17.8
Particle Type		Length: 35mm			

Table 4.4: Properties of willow wood samples.

Pine Wood		Sample 1	Sample 2	Sample 3	Average
Proximate Analysis (%wt)	Moisture	6.6	4.5	6.4	5.9
	Volatile	80.8	81.7	78.9	80.5
	Ash	1.4	0.9	0.5	1.0
	Fixed Carbon	11.3	12.8	14.0	12.7
Ultimate Analysis (%wt)	Carbon	47.9	46.6	47.1	47.2
	Hydrogen	7.1	5.4	7.1	6.6
	Oxygen	38.2	41.1	38.8	37.4
Gross Calorific Value (MJ/kg)		18.3	19.9	18.3	18.9
Particle Type		Cube: 5, 10, 20, 35mm			

Table 4.5: Properties of Pine Wood Samples.

Herbaceous Plants

Pelletised Miscanthus		Sample 1	Sample 2	Sample 3	Average
Proximate Analysis (%wt)	Moisture	5.5	5.6	7.2	6.1
	Volatile	68.4	68.2	66.8	67.9
	Ash	12.9	12.8	12.8	12.9
	Fixed Carbon	13.0	13.2	13.1	13.1
Ultimate Analysis (%wt)	Carbon	39.8	39.8	39.1	39.6
	Hydrogen	5.9	6.7	4.9	5.9
	Oxygen	35.1	34.4	36.8	35.5
Gross Calorific Value (MJ/kg)		15.4	15.4	15.4	15.4
Particle Type		Pellets: Φ4mm			

Table 4.6: Properties of Pelletised Miscanthus Samples.

Switchgrass		Sample 1	Sample 2	Sample 3	Average
Proximate Analysis (%wt)	Moisture	6.4	6.4	6.4	6.4
	Volatile	82.6	82.4	83.4	82.8
	Ash	3.4	3.6	3.4	3.5
	Fixed Carbon	7.4	7.4	6.8	7.6
Ultimate Analysis (%wt)	Carbon	44.4	43.6	44.3	44.2
	Hydrogen	7.1	7.1	6.6	6.9
	Oxygen	38.3	39.2	39.3	38.9
Gross Calorific Value (MJ/kg)		17.2	17.3	17.2	17.3
Particle Type		Length:20cm			

Table 4.7: Properties of Switchgrass Samples.

Straw		Sample 1	Sample 2	Sample 3	Average
Proximate Analysis (%wt)	Moisture	7.9	7.8	7.9	7.9
	Volatile	80.5	79.7	80.0	80.1
	Ash	5.7	5.3	4.8	5.3
	Fixed Carbon	5.9	7.1	7.2	6.8
Ultimate Analysis (%wt)	Carbon	41.5	40.0	41.7	41.1
	Hydrogen	6.7	6.9	7.0	6.8
	Oxygen	38.3	39.9	38.6	38.9
Gross Calorific Value (MJ/kg)		16.4	16.4	16.3	16.4
Particle Type		Length: 3-4cm (cut) 12-13cm(uncut)			

Table 4.8: Properties of Straw Samples.

Reed Canary Grass		Sample 1	Sample 2	Sample 3	Average
Proximate Analysis (%wt)	Moisture	7.9	8.0	8.2	8.1
	Volatile	83.9	83.9	83.8	83.9
	Ash	4.5	4.4	4.1	4.3
	Fixed Carbon	3.7	3.7	3.9	3.8
Ultimate Analysis (%wt)	Carbon	41.7	41.8	41.5	41.7
	Hydrogen	7.7	5.9	7.6	7.1
	Oxygen	38.2	39.9	38.6	38.9
Gross Calorific Value (MJ/kg)		16.4	16.5	16.4	16.4
Particle Type		Length:10mm			

Table 4.9: Properties of Reed Canary Grass Samples.

Waste

Refused Derived Fuel (RDF)		Sample 1	Sample 2	Sample 3	Average
Proximate Analysis (%wt)	Moisture	1.8	1.8	2.1	1.9
	Volatile	71.2	73.4	65.1	69.9
	Ash	18.2	19.4	18.6	18.7
	Fixed Carbon	8.8	6.4	14.2	9.8
Ultimate Analysis (%wt)	Carbon	44.3	45.1	48.5	45.9
	Hydrogen	6.3	5.1	6.5	5.9
	Oxygen	28.8	29.2	24.4	27.5
Gross Calorific Value (MJ/kg)		20.3	21.4	22.3	21.3
Particle Type		Pellets: Φ7mm			

Table 4.10: Properties of Refused-Derived Fuel Samples.

4.2.2 Pelletisation

The refused-derived fuel (RDF) is processed waste mixtures comprised mainly of paper, plastic and textiles. The breakdown of materials used in the production of the RDF is shown in *Figure 4.9*.

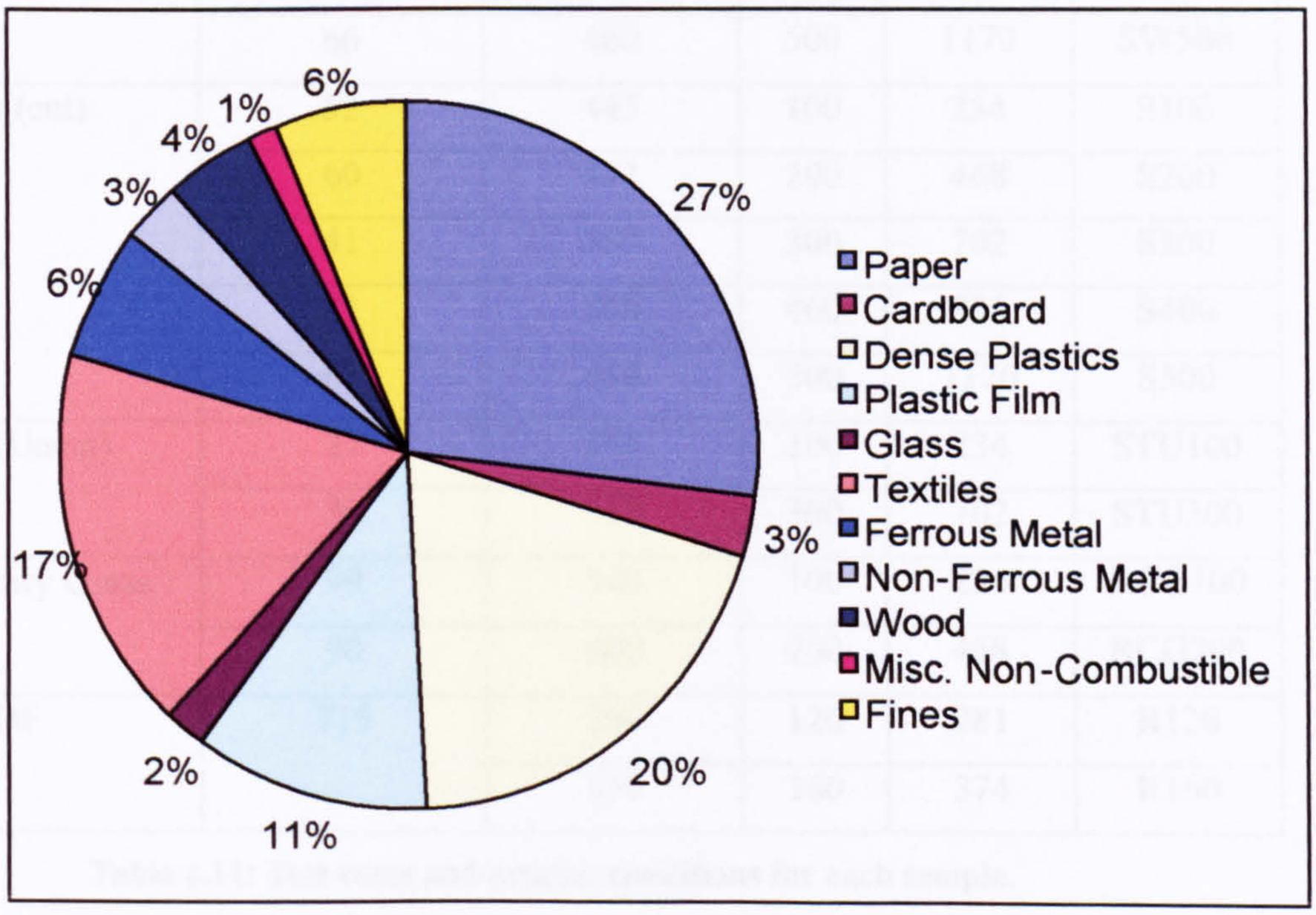

Figure 4.9: Breakdown of Materials used in the RDF Production.

4.3 OPERATING CONDITIONS

Table 4.11 lists the bulk density, bed height and operating conditions for the tests.

Samples	Bulk Density (kg/m^3)	Bed Height (mm)	Air flow rate		Case name
			(l/min)	(kg/m^2hr)	
Willow wood	181	520	120	281	W120
		410	160	374	W160
		400	200	468	W200
Pine wood, 5mm	285	350	160	374	P-5
Pine wood, 10mm	272	375	160	374	P-10
Pine wood, 20mm	285	360	160	374	P-20
Pine wood, 35mm	295	360	160	374	P-35
Pelletised Miscanthus	660	400	120	281	M120
		350	160	374	M160
		400	200	468	M200
Switchgrass	55	500	100	234	SW100
	68	450	200	468	SW200
	58	540	300	702	SW300
	57	560	400	936	SW400
	66	460	500	1170	SW500
Straw (cut)	52	445	100	234	S100
	60	471	200	468	S200
	41	550	300	702	S300
	41	550	400	936	S400
	65	450	500	1170	S500
Straw (Uncut)	27	550	100	234	STU100
	39	550	300	702	STU300
Reed Canary Grass	99	540	100	234	RCG100
	90	600	200	468	RCG200
RDF	715	360	120	281	R120
		350	160	374	R160

Table 4.11: Test cases and process conditions for each sample.

In some cases, the maximum primary air-flow rate was limited as a consequence of the high bed temperature of over 1000°C. The secondary air was used in some cases to increase mixing and agitation in the bed. However, the secondary air did not interfere with the bed burning rate (Zakaria, 2000).

The calculation of the bulk density might be subjected to slight error caused in the measurement of the bed height. The location of the thermocouples at the centre of the furnace affects the distribution of particles during the loading of samples. This causes a non-uniform bed height across the cross-sectional area of the furnace. Another cause of error could be due to the feeding of dust accumulated during the preparation of the materials together with the experimental samples.

4.4 EXPERIMENTAL PROCEDURES

The flow diagram of the experimental setup of the rig is shown in *Figure 4.10*. The start up and shut down procedures are described in the following sections.

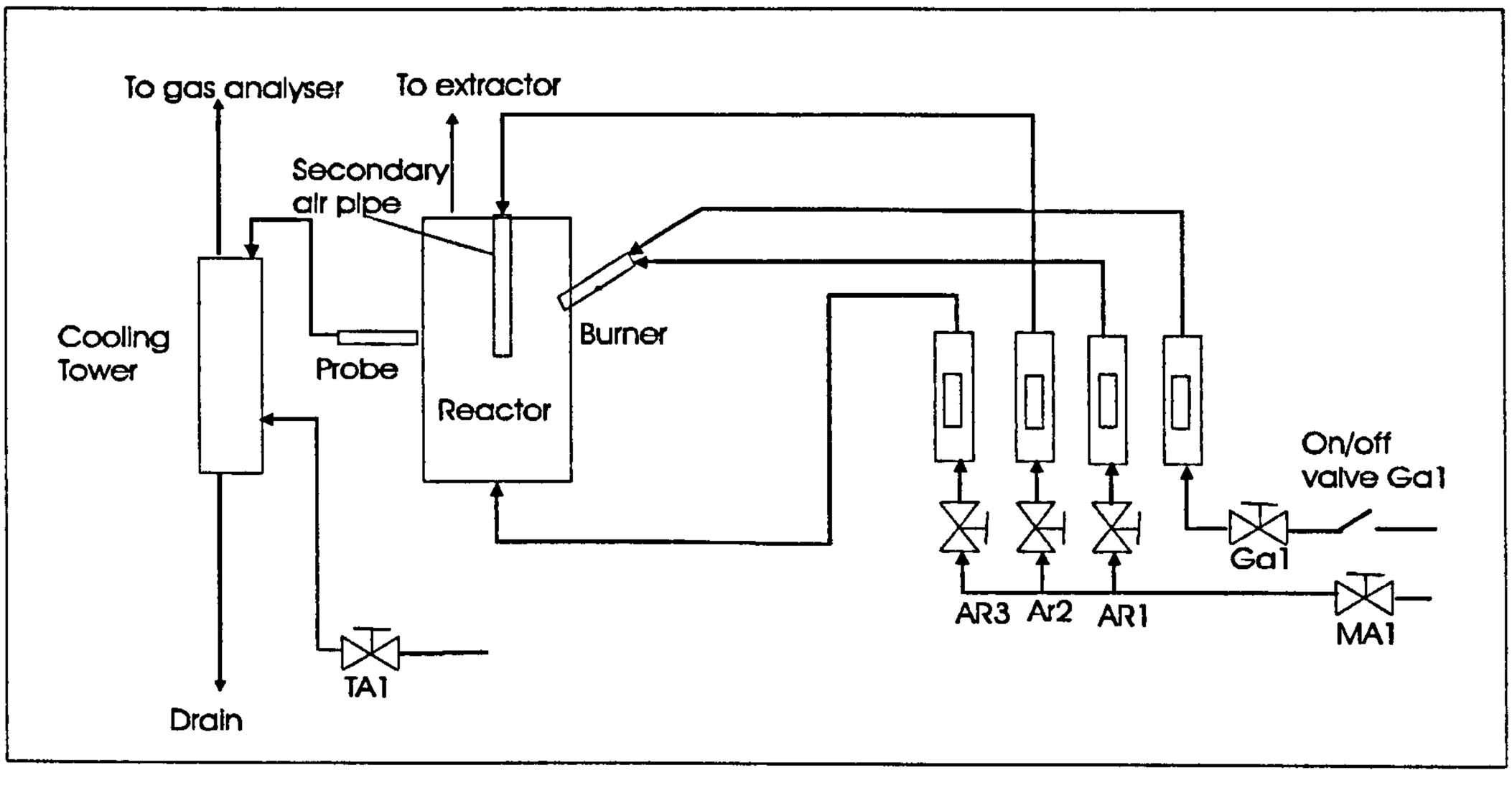

Figure 4.10: Flow Diagram of the Experimental Setup.

4.4.1 Start Up Procedure

1. The analysers and pumps were switched on and left to warm up for an hour.
2. The tap water (valve TA1) to the cooling tower was turned on.
3. The scale indicator was switched on and set to zero.
4. A known weight of pre-prepared biomass sample was fed into the combustor through the waste inlet point on the top of the combustor. The lid was screwed on tightly.
5. The weight shown on the indicator was checked to ensure that the increase was the same as the sample weight.
6. All measuring ports were checked to ensure that they were air tight.
7. The data logger was switched on and the thermocouple readings were checked by manually going through the channels to ensure that all the thermocouples gave correct readings. The thermocouples were then connected to a temperature indicator to check that the readings from the data logger were correct.
8. When all the analysers were warmed up, they were calibrated with calibration gas according to the instruction given by manufacturers. The readings of the analysers were then compared with the calibration gas as well as with the readings logged from the data logger.
9. The data logger was then switched off. This is to avoid the shock from the high current when the burner is ignited.
10. The exhaust extraction fan was then switched on.
11. All the valves to the rotameters were checked to ensure that they were shut. The main compressed air valve, MA1 was first opened followed by valves for primary air (AR3).
12. The valve for air to the burner (AR1) was turned to let 250lit/min air pass through.
13. The power supply to the burner ignitor was switched on (SW1), and the valve for gas to the burner (GA2) was fully opened. While the ignitor was fired, the on/off valve (GA1) was open and the flame was checked. (this requires two persons)
14. As soon as the ignitor was fired off, the weight logging was started. The data logger for the temperature and gas was switched on. Each channel on the data logger was recorded at every 0.5secs and the time elapse between each set of readings (24channels) was set according to the length of the experiment. A longer time elapsed was chosen if the experiment were to be carried out for a longer period of time. This is to avoid over-flooding of the data loggers` memory ram.
15. The readings of the temperatures in the freeboard were checked to ensure that the thermocouple was working.

4.4.2 Shut Down Procedure

1. The valves supplying gas to the burner (GA1 and GA2) were shut off followed by the valve supplying air to the burner (AR1).
2. The power was switched off (SW2)
3. The valves for primary air (AR3) and secondary air (AR2) were shut off, followed by the valve for main air supply (MA1).
4. The logging of weight, temperature and gas were stopped.
5. The analysers` connections were disconnected from the combustion port.
6. The analyser was left to flush out all the gas in it before switching off, usually for half an hour or so.
7. The exhaust extraction fan was switched off followed by the tap water (valve TA1) to the cooling tower.

4.5 EXPERIMENTAL RESULTS AND DISCUSSION

4.5.1 Temperature, Gas Composition and Mass Loss

This section gives an overview of the biomass combustion process in a fixed bed reactor. *Figure 4.11* and *Figure 4.12* shows the temperature within the bed and gas concentration at the bed top (y=43cm) for the combustion of 20mm pine wood samples (Case P-20).

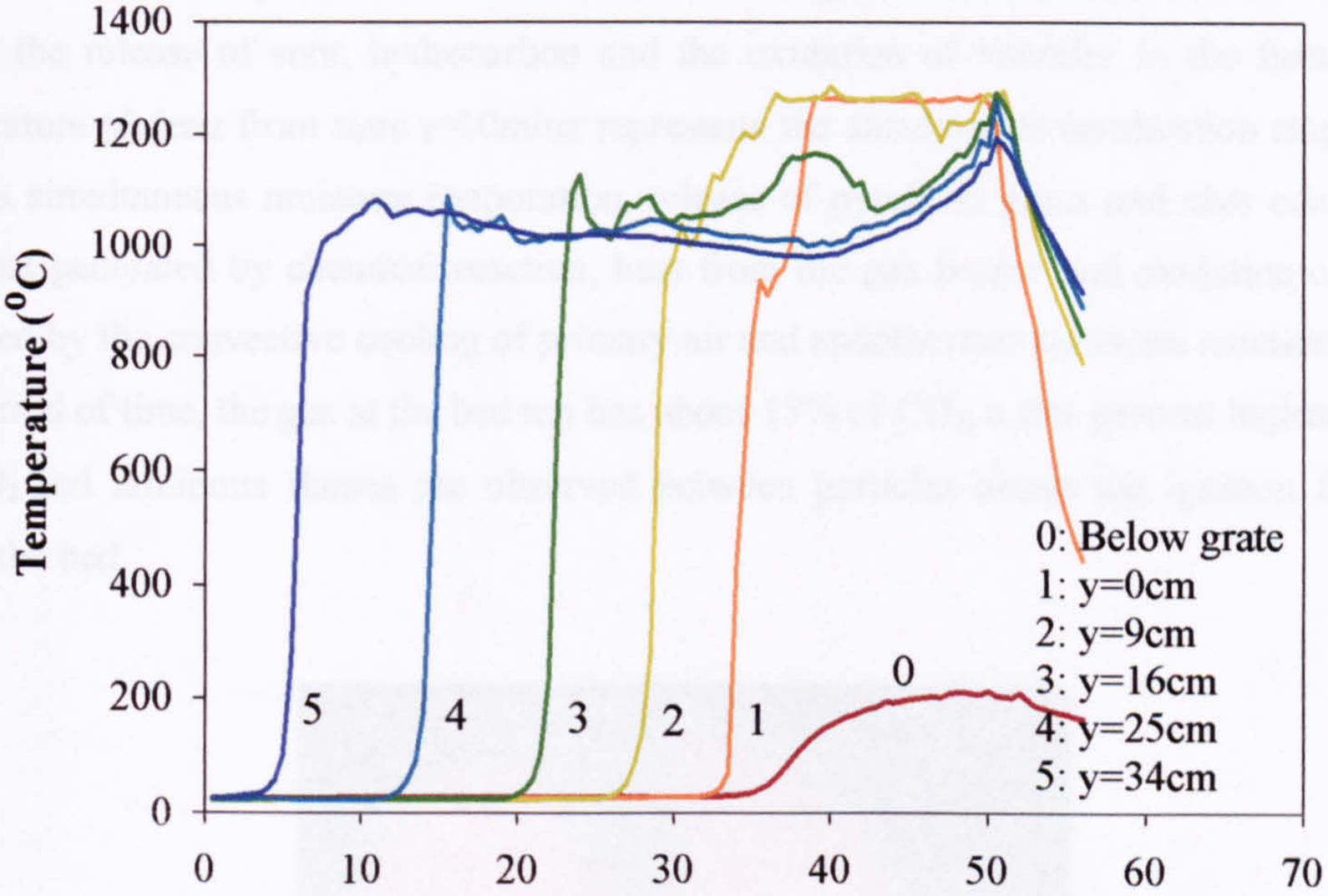

Figure 4.11: Temperature history at the bed top for Case P-20.

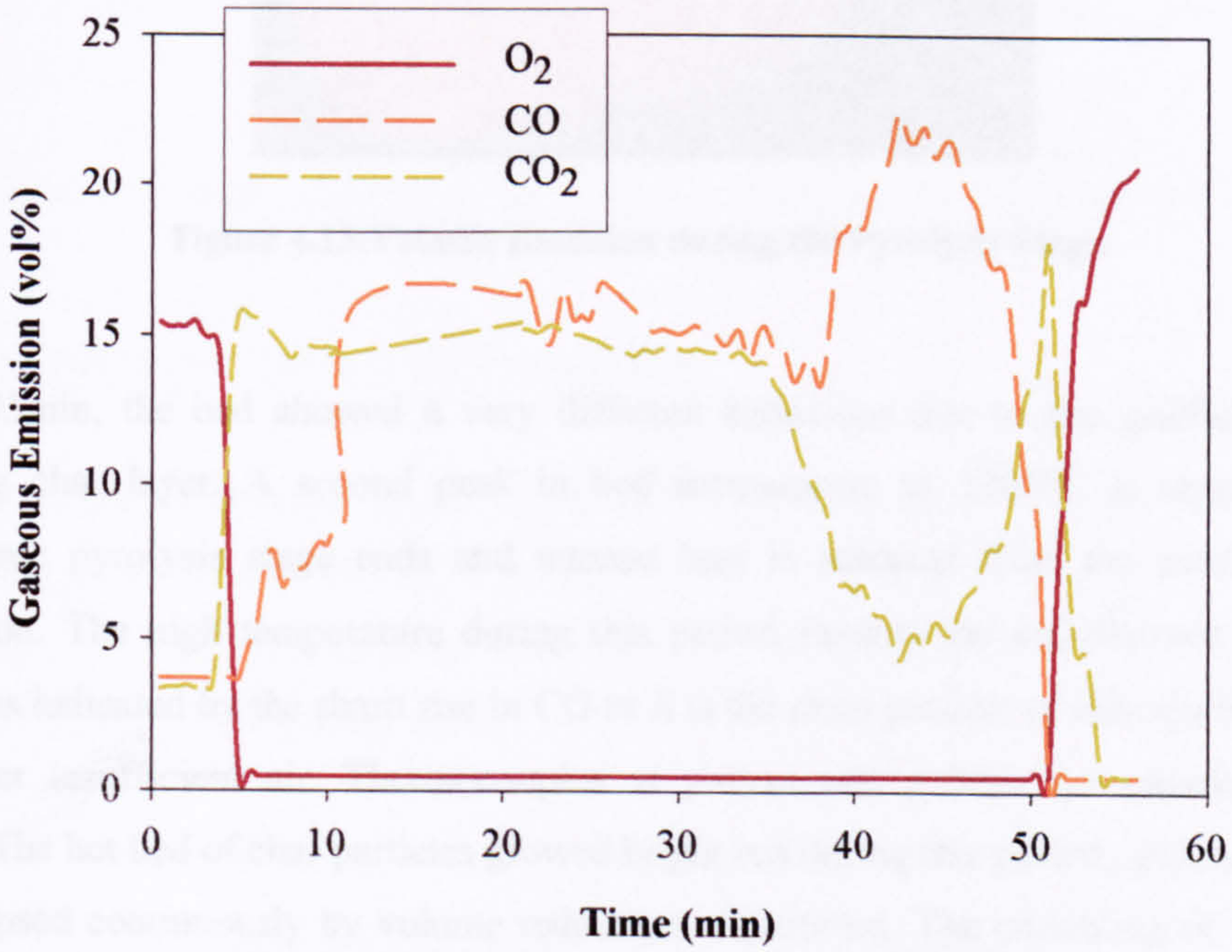

Figure 4.12: Gas composition in the flue gases out the bed top vs. reaction time for Case P-20.

The temperature in the freeboard area rose as soon as the gas burner was ignited. The heat from the gas burner reached the first measurement point just 20mm below the bed top (Position 5: 340mm) 6mins after the start of the experiment. The temperature at consecutive measuring ports below the bed soars up to 1000°C when the ignition front progresses from the top of the bed to the bottom. The bed temperature then stabilized at around 1000°C. The ignition front reaches the bed bottom at around t=35min. During the propagation of the ignition front, a smoky luminous flame as shown in *Figure 4.13* was observed above the bed due to the release of soot, hydrocarbon and the oxidation of volatiles in the furnace. The temperature plateau from time t=10mins represents the steady-state combustion stage where there is simultaneous moisture evaporation, release of pyrolysis gases and char combustion. The heat generated by chemical reaction, heat from the gas burner and oxidation of char is balanced by the convective cooling of primary air and endothermic pyrolysis reaction. During this period of time, the gas at the bed top has about 15% of CO_2, a few percent higher CO and zero O_2 and luminous flames are observed between particles above the ignition front and above the bed.

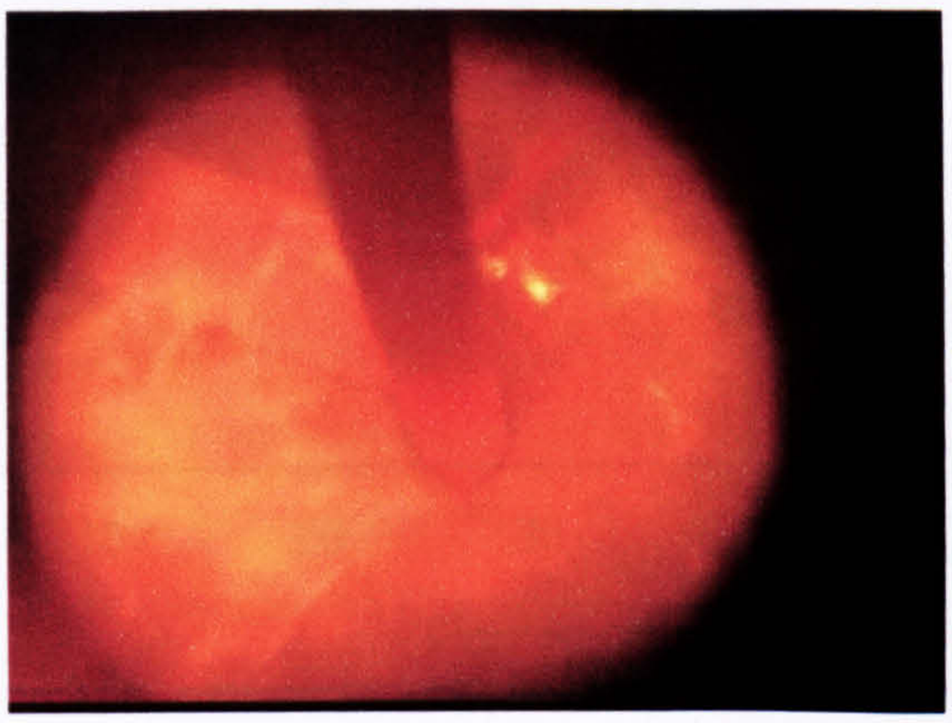

Figure 4.13:Volatile Emission during the Pyrolysis Stage.

From t=35min, the bed showed a very different behaviour due to the gasification of the remaining char layer. A second peak in bed temperature to 1200°C is observed as the endothermic pyrolysis stage ends and intense heat is released from the exothermic char combustion. The high temperature during this period favours the endothermic gasification reaction as indicated by the sharp rise in CO as it is the main product of char gasification with CO_2 under insufficient air. Thermocouples at y=0cm and y=9cm are saturated at about 1280°C. The hot bed of char particles glowed bright red during this period, and the whole fuel bed collapsed continuously by volume reduction of particles. The crumbling of the fuel bed

resulting in a tightly packed and higher temperature environment around the thermocouples during the later stage of combustion was suggested by Kuo (1970).

The combustion process involves 3 main stages: the evaporation of moisture from the solid, ignition propagation and combustion of volatile gases and char particles. *Figure 4.14* shows the two main stages of the combustion process. The mass left on the bed decreased with a uniform slope during the ignition propagation period. A large percentage of mass (70-80%) is lost during this period of time corresponding to the volatile content in the biomass sample used. As the char oxidation period commences, the mass loss slows down.

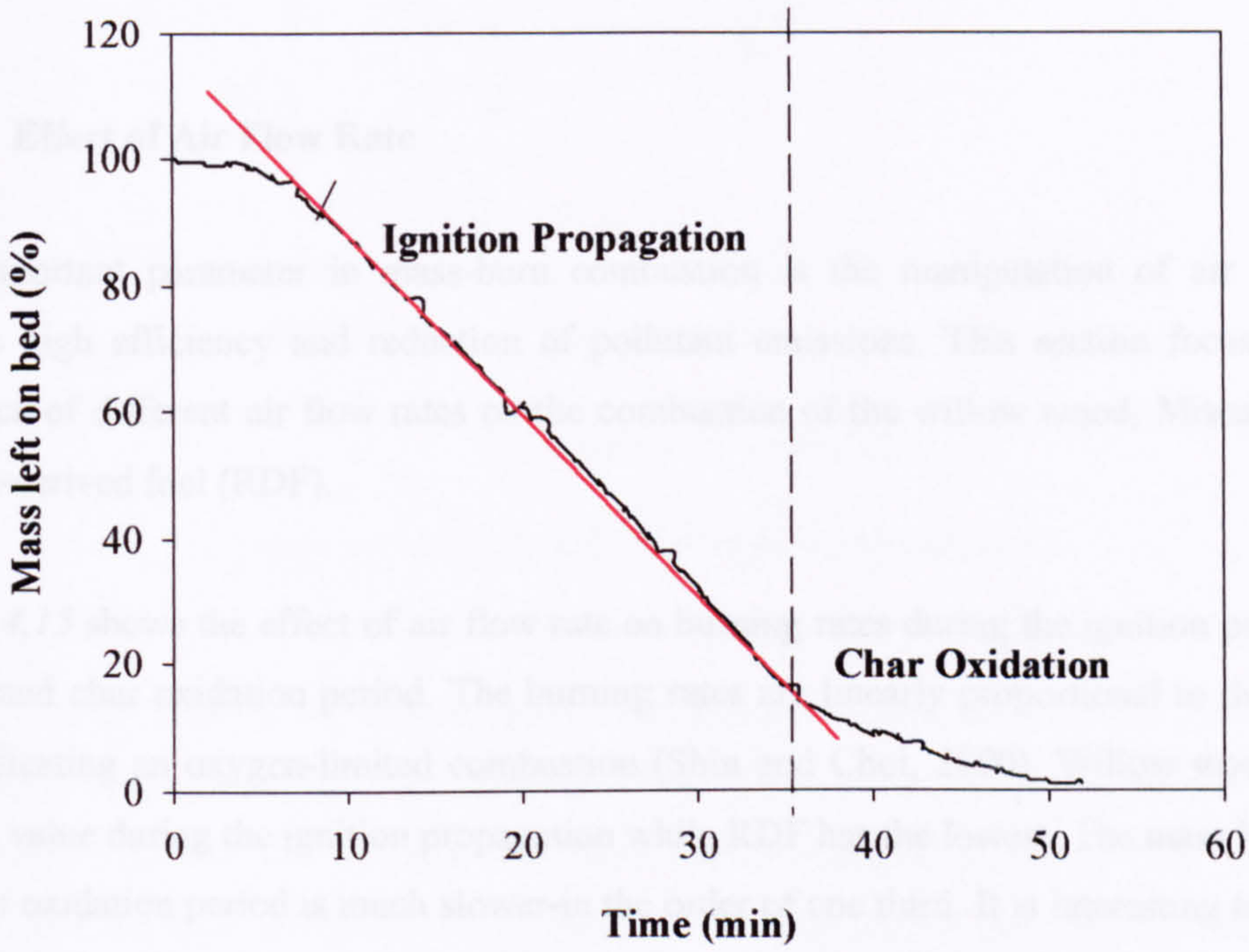

Figure 4.14: Percentage mass left on the bed representing the different stages of combustion.

4.5.2 Ignition Front Speed and Burning Rate

In this investigation, the ignition velocity is taken as the distance in m (metres) between two temperature ports divided by the time in s (seconds) taken for the ignition front (at a temperature of 300°C (573K)) to move between the temperature ports. This can be represented by the following equation:

$$\text{Ignition Front Speed} = \frac{\text{Distance between ports (m)}}{\text{Time (s)}}$$

The ignition rate is the rate of mass per unit cross-sectional area through which the ignition front passed. It is calculated by multiplying the ignition front speed by the bulk density of the bed. The burning zone thickness is calculated based on the distance between the bed height and position of the ignition front at that instant. This calculation is only an approximation for the bed density changes as the combustion progresses.

The burning rates are quantified as the average burning rate or the burning rate during a specified stage. For example, the burning rate during the ignition propagation stage represents the mass loss during the period of time the ignition front moves from the top of the bed to the grate per unit area of grate.

4.5.3 Effect of Air Flow Rate

One important parameter in mass-burn combustion is the manipulation of air supply to achieve high efficiency and reduction of pollutant emissions. This section focuses on the influence of different air flow rates on the combustion of the willow wood, Miscanthus and refused-derived fuel (RDF).

Figure 4.15 shows the effect of air flow rate on burning rates during the ignition propagation period and char oxidation period. The burning rates are linearly proportional to the air flow rate indicating an oxygen-limited combustion (Shin and Choi, 2000). Willow wood has the highest value during the ignition propagation while RDF has the lowest. The mass loss during the char oxidation period is much slower-in the order of one third. It is interesting to note that the Miscanthus has a lower burning rate compared to the RDF during the char oxidation stage. This is due to the agglomeration of the Miscanthus ashes in the later stage that blocks the diffusion of oxygen into the particles.

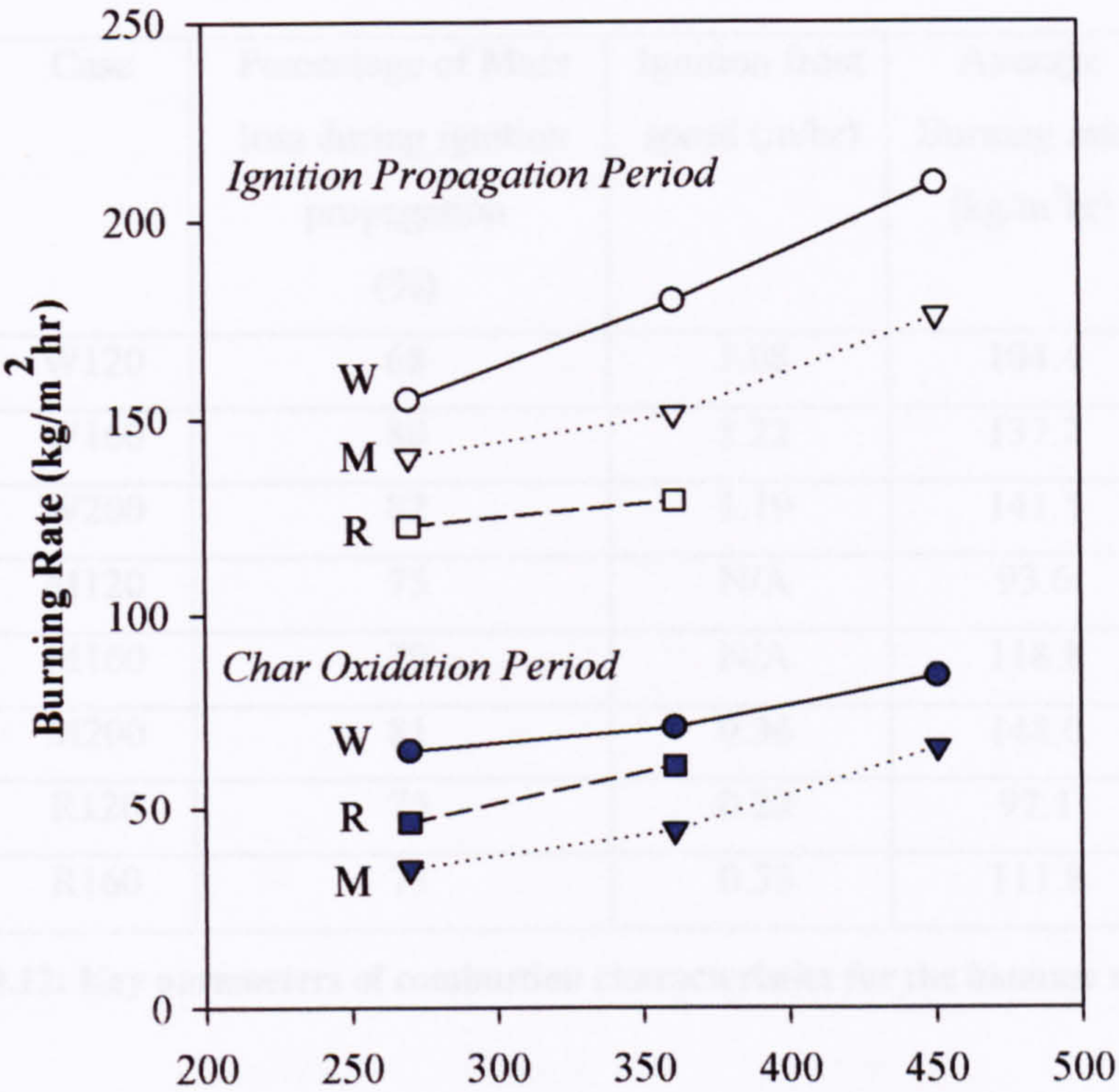

Figure 4.15: Effect of air flow rates on burning rates.

Table 4.12 lists some of the key results of combustion characteristics for the test cases. The equivalence ratio is a quantitative indication of whether the fuel oxidizer mixture is rich, lean or stoichiometric. For fuel-rich mixtures, $\Phi>1$, and for fuel-lean mixtures, $\Phi<1$. The average burning rate and equivalence ratio are based on the mass loss of the whole periods. All the test cases are in fuel-rich conditions with average equivalence ratios of 1.9-4.1. The available oxygen in the primary air is insufficient to achieve complete combustion. Therefore, reactions proceed in the oxygen-limited region, controlled by the air supply. The value for Cases M120 and M160 are not given as the thermocouples were damaged or erratic at severe bed temperatures.

Sample	Case	Percentage of Mass loss during ignition propagation (%)	Ignition front speed (m/hr)	Average Burning rates (kg/m^2hr)	Average Equivalence Ratio
Willow	W120	68	1.08	104.4	4.13
	W160	80	1.22	137.2	3.52
	W200	82	1.19	141.5	2.90
Miscanthus	M120	75	N/A	93.6	2.33
	M160	79	N/A	118.8	2.26
	M200	81	0.36	148.0	2.07
RDF	R120	75	0.22	97.1	2.40
	R160	73	0.33	111.8	2.15

Table 4.12: Key parameters of combustion characteristics for the biomass samples.

The percentage of mass loss during ignition propagation increases for willow and miscanthus with increasing air flow rates. This means that the remaining char layer becomes thicker as the ignition front propagates faster. *Figure 4.16* shows that both the maximum flame temperature and calculated burning zone thickness increases for combustion processes carried out under high primary air flow rate. For sub-stoichiometric combustion, the oxygen is completely consumed by the char and reaction volatile material as the char oxidation requires more time compared to the pyrolysis and gas reaction. The higher primary air flow rate increases both the gas reaction and release of heat. The higher temperature in the ignition front would then lead to more heat transferred down the bed and a faster flame propagation speed. This explains the thicker burning zone thickness as more char is left above the ignition front.

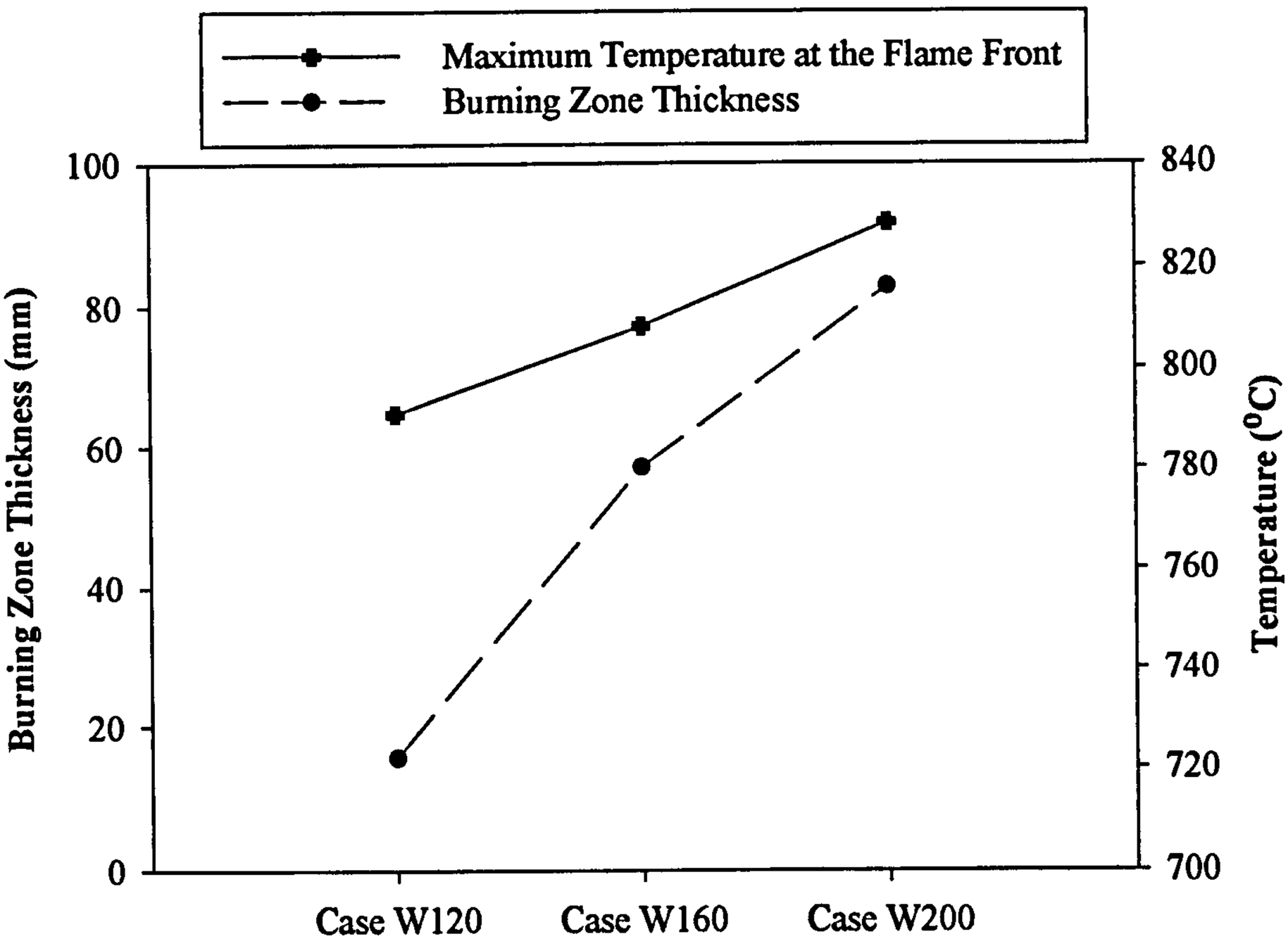

Figure 4.16: Calculated burning zone thickness and the maximum temperature at the flame front for the combustion of willow wood.

Figure 4.17 shows the temperature within the bed for Case W120, Case W160 and Case W200. For Case W200, the temperature at all the consecutive measuring port increases to about 1000°C as the ignition front passes through the bed. This phenomenon was not observed in Case W120 and Case W160 where the temperature rise at each thermocouple port was variable during the ignition propagation period. The increase of primary air flow rate caused a uniform peak temperature during the ignition propagation period. Another distinct difference that follows the increase of primary air flow rate is the higher plateau temperature observed in Case W200. The plateau temperature hovered around 850-900°C during the steady-state for Case W200 and is about 60°C higher compared to Case W160. The step-up in air flow rate increases both the burning rate and ignition velocity causing a larger amount of fuel burning in this period and thus releasing additional heat. The additional supply of primary air encourages the combustion of volatiles offsetting the endothermal nature of the pyrolysis reaction. The higher volume of air flow promotes the heat distribution in the reactor producing a smoothing effect on the temperature variation. As expected, the peak temperature during the char oxidation period is about 150°C lower in Case W200 compared to the other two cases as only 17% of the fuel is combusted during this period compared to 31% in Case W120.

a)

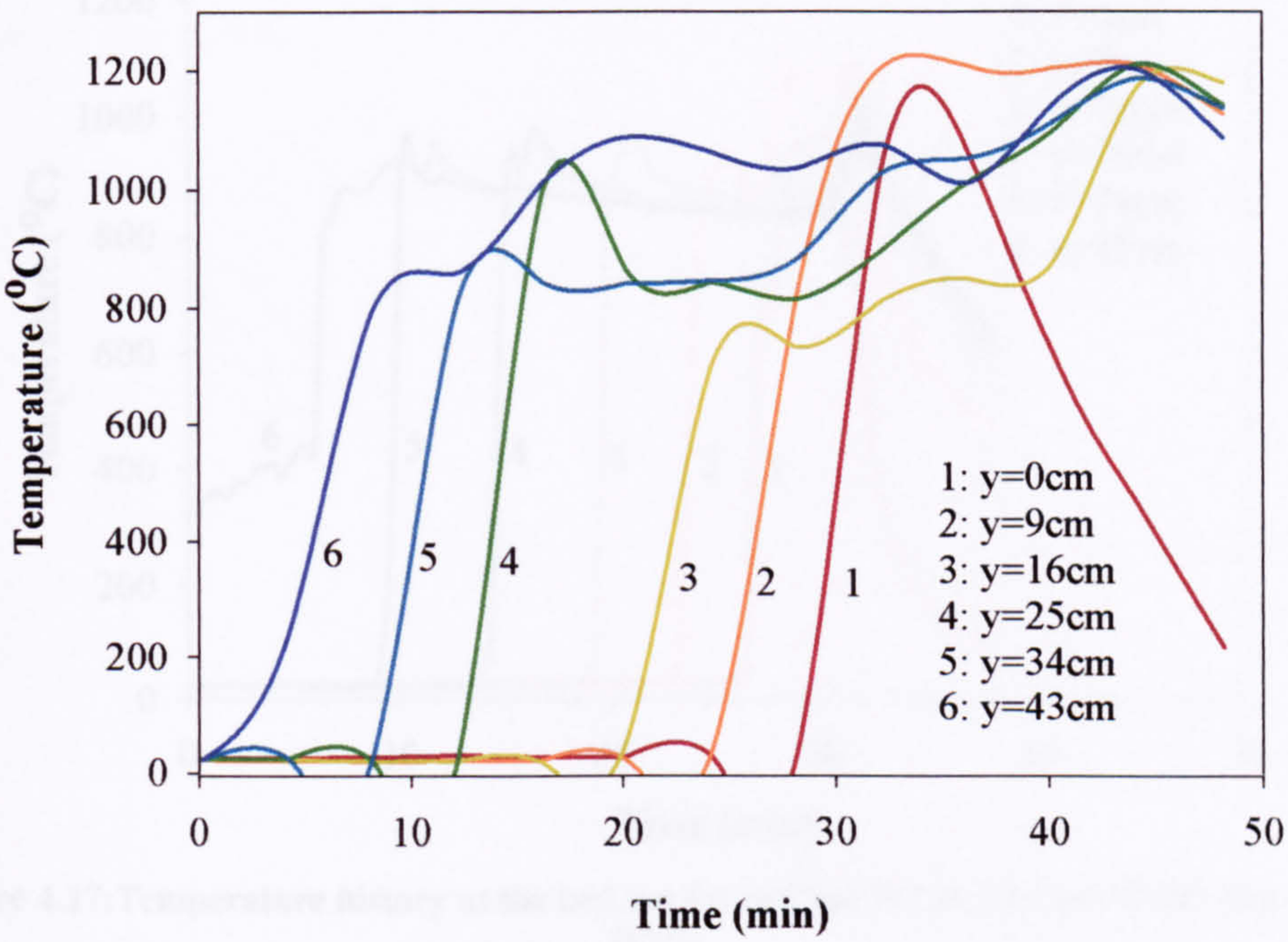
Temperature (°C)
0
200
400
600
800
1000
1200
0
10
20
30
40
50
Time (min)
1
2
3
4
5
6
1: y=0cm
2: y=9cm
3: y=16cm
4: y=25cm
5: y=34cm
6: y=43cm

b)

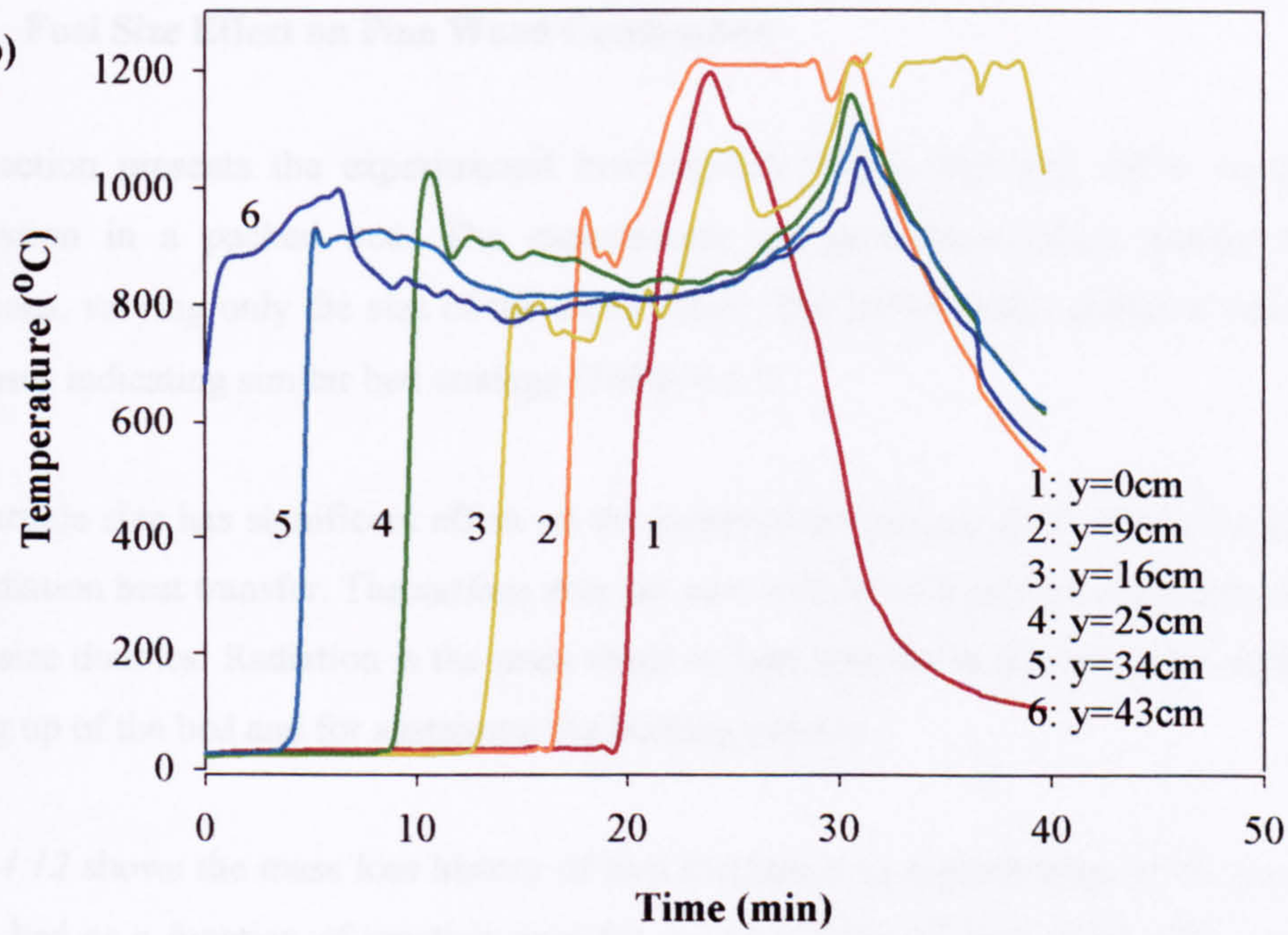
Temperature (°C)
0
200
400
600
800
1000
1200
0
10
20
30
40
50
Time (min)
1
2
3
4
5
6
1: y=0cm
2: y=9cm
3: y=16cm
4: y=25cm
5: y=34cm
6: y=43cm

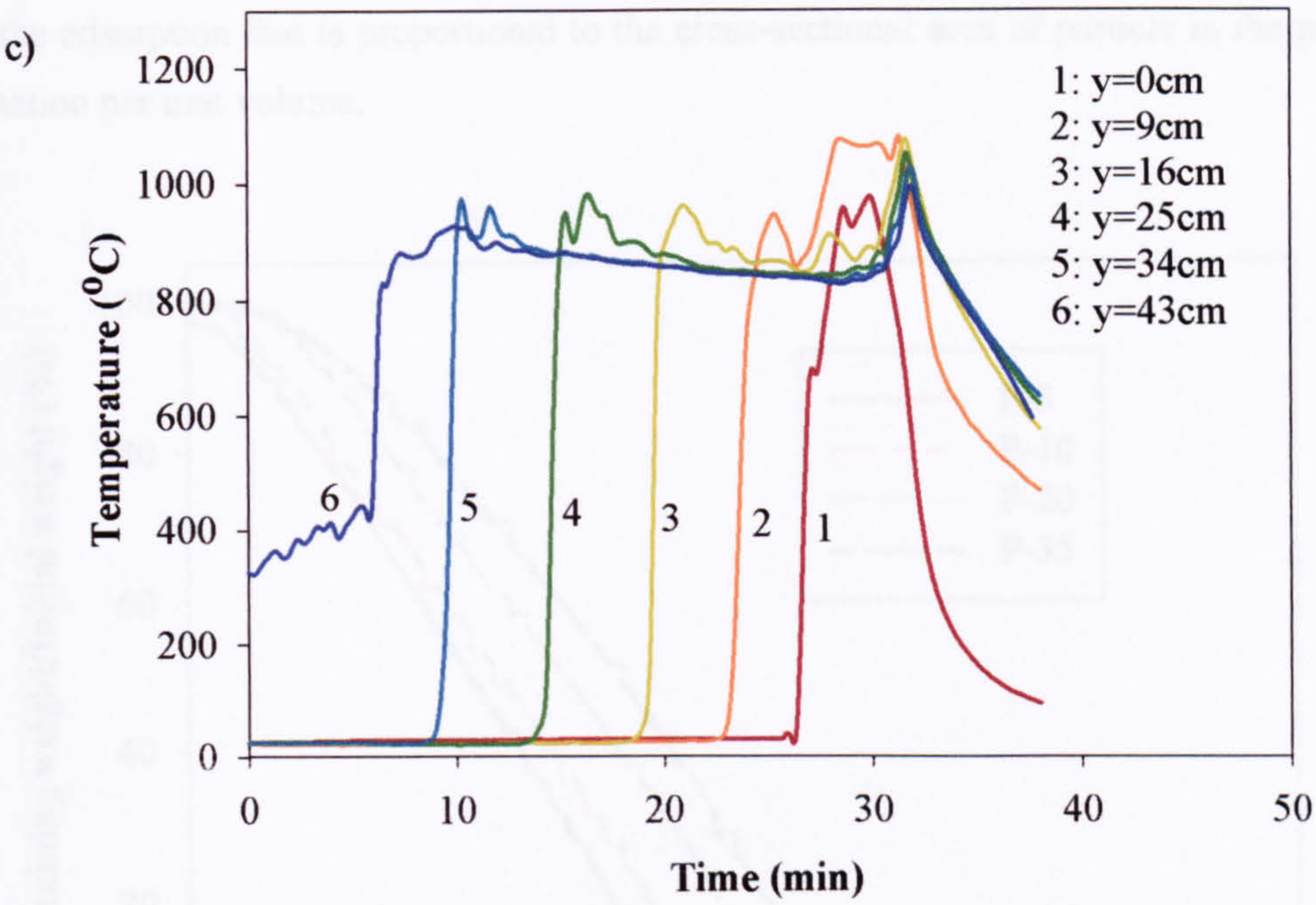

Figure 4.17:Temperature history at the bed top for a) Case W120, b) Case W160 and c) Case W200.

4.5.4 Fuel Size Effect on Pine Wood Combustion

This section presents the experimental investigation of the fuel size effect on pinewood combustion in a packed bed. The experiments are performed under similar operating conditions, varying only the size of the wood cubes. The bulk density is almost similar in all four cases indicating similar bed voidage (*Table 4.11*).

The particle size has significant effect on the combustion process as it affects the heat, mass and radiation heat transfer. The surface area per unit volume of a particle decreases twice-fold as the size doubles. Radiation is the main mode of heat transfer in the bed, providing heat for heating up of the bed and for sustaining the burning process.

Table 4.12 shows the mass loss history of fuel expressed as a percentage of remaining mass on the bed as a function of reaction time for the four cases of pine wood with varying fuel size. For Case P-5, the initial mass loss was quick, reaching a steady stage at t=2min. For 10mm pine wood cubes, the initial mass loss rate was slightly slower, reaching steady-state at t=3.5min; for the 20mm particle size, it was only after t=7min that the mass loss reached a steady state. The 35mm pinewood produces the longest ignition period (15min) before a fully steady combustion stage was reached. The shorter ignition time for small fuel size shows that a bed of smaller particles absorbs radiation more quickly. The radiation heat transfer depends

on the adsorption that is proportional to the cross-sectional area of particle in the path of the radiation per unit volume.

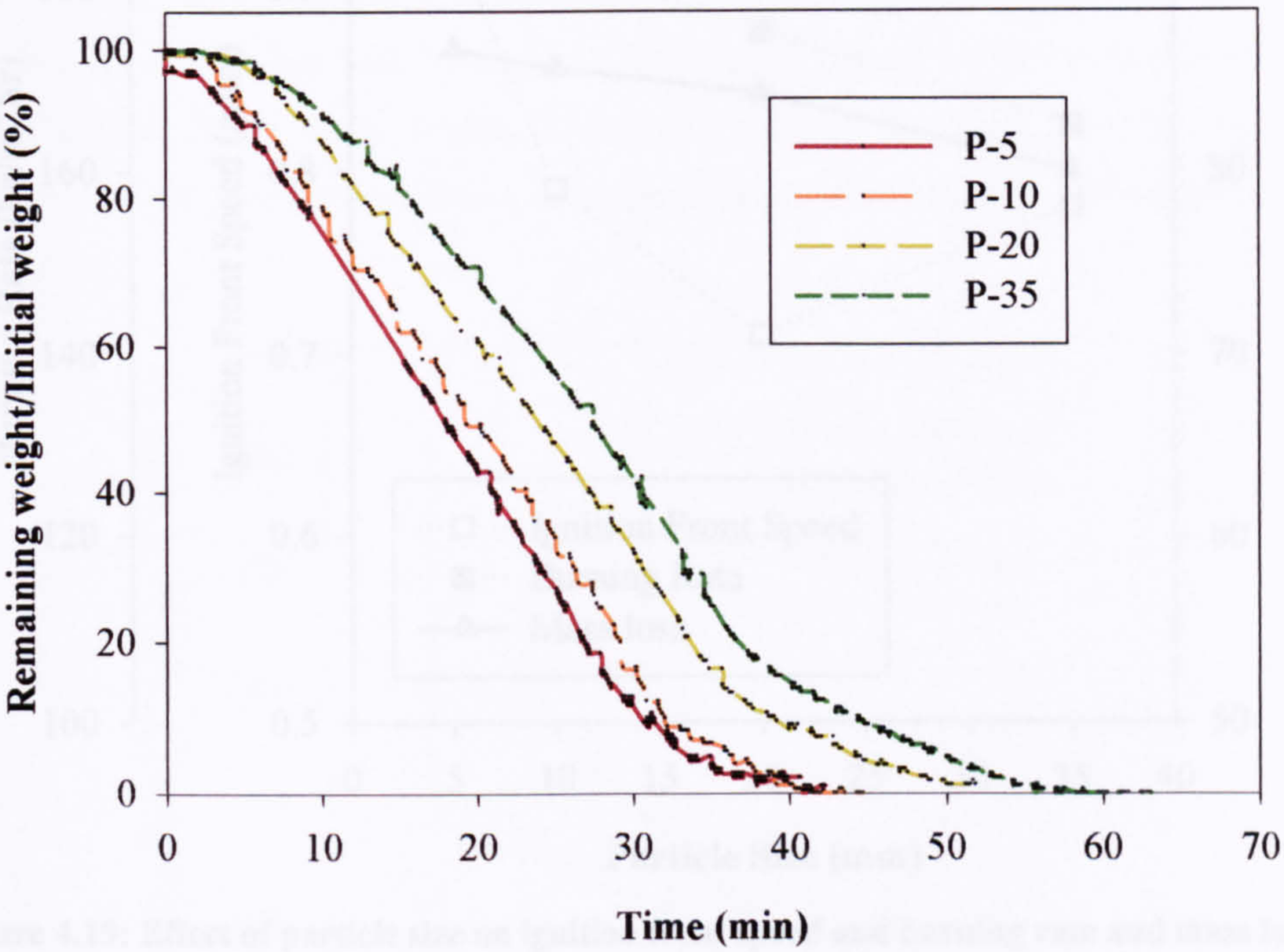

Figure 4.18: Mass loss curve for pine wood.

After the initial ignition period, a linear decrease in total mass of bed fuel was observed. The length of the ignition propagation period ranged from between 23 to 15min, with the largest fuel having the shortest time. The shorter time period for the largest fuel resulted in the smallest mass loss during this period as shown in *Figure 4.19*. The mass loss during the ignition propagation decreases as the fuel size increases. Therefore, this leaves a higher proportion of char left above the ignition front and a longer char oxidation period for larger fuel sizes. For Case P-5, the char oxidation period was about 13 min and for Case P-10, this increased to 15 min. The final burning stage was prolonged to 18 min for the Case P-20 and 25 min for Case P-35.

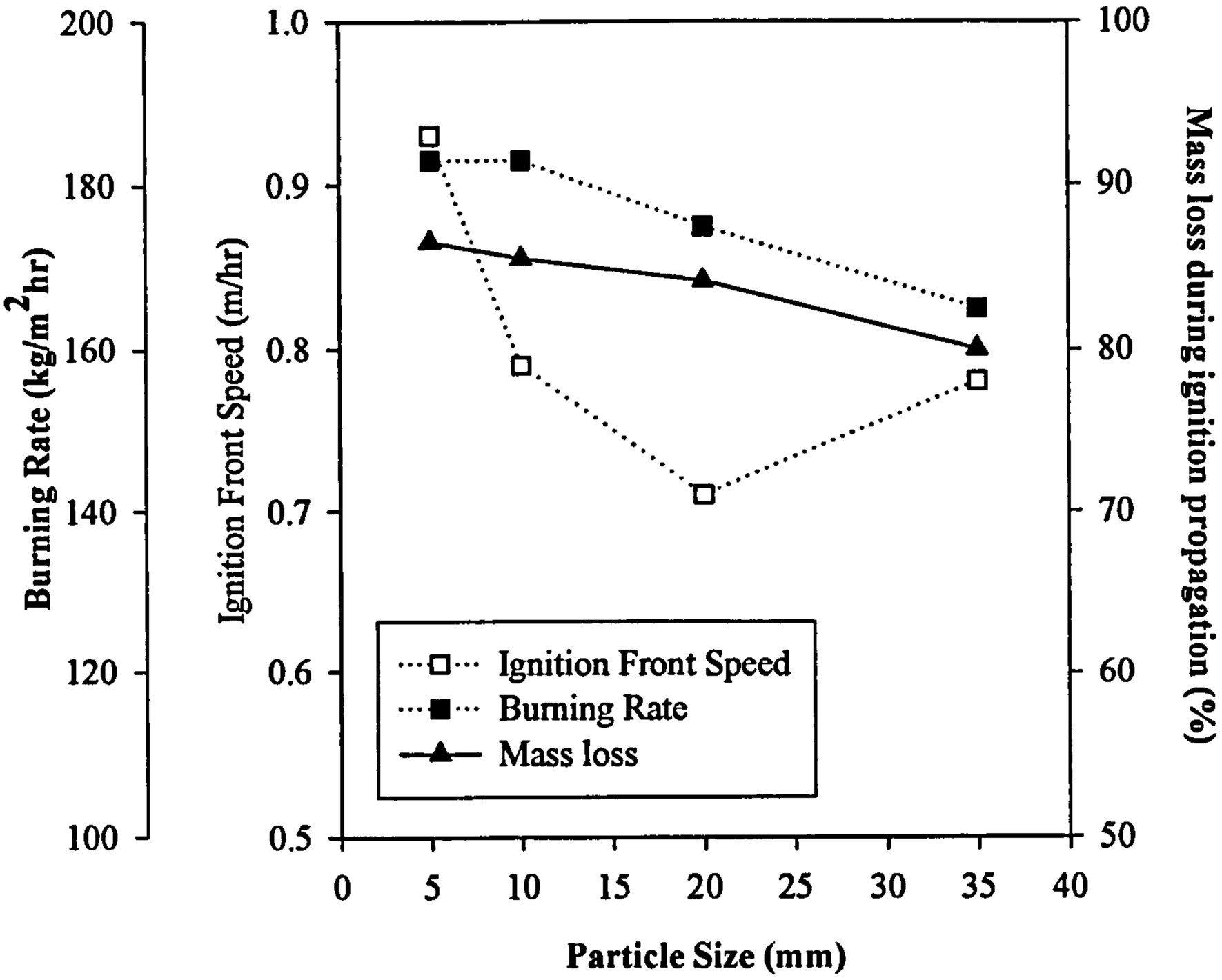

Figure 4.19: Effect of particle size on ignition front speed and burning rate and mass loss during the ignition propagation period.

Figure 4.19 also compares the ignition front speed and burning rate during the ignition propagation period for the four different fuel sizes of pine wood. Smaller particles have higher burning rates and ignition front speeds. Particle size affects the two-phase heat and mass transfer (between the gas and solid). Convective processes such as drying occur at the particle external surfaces and the rates are proportional to the surface area. Therefore, reduction of size results in fast and intense moisture evaporation. Smaller particles further enhance the radiation heat transfer leading to quicker heat absorption and faster char burning rates in the bed. In Case P-35, the ignition front speed is higher than P-20, while the mass loss and burning rate are lower. This can be explained by the channelling effect becoming significant for this case due to larger voids within the bed, which is described later.

Smaller particles have a larger surface area per unit volume and this encourages the propagation of heat throughout the particle. For small particles, the heat and mass transfer through the cross-sectional area would be negligible compared to the heat and mass transfer in the direction of the bed height. For large thermally thick particles, the individual heat and mass transfer in the direction of the bed would be as important due to the higher temperature and species gradient in the particle. Thermally thick particle causes a non-uniform temperature distribution inside a particle resulting in a low transient temperature gradient.

Figure 4.20 shows the transient temperature gradient (ΔT/Δt, °C/min) between 200°C and 800°C at each thermocouple calculated when the ignition front passes. The spatial temperature gradient is calculated by dividing the transient temperature gradient by the ignition speed. Both the spatial and transient temperature gradients decrease with increasing particle size. It takes less than 1 minute for the 5mm size particles size to increase temperature of 800°C from 200°C while it takes 3 minutes for 35mm size particles. This corresponds to about 10mm and 33mm respectively, in terms of height-about the order of the particle size.

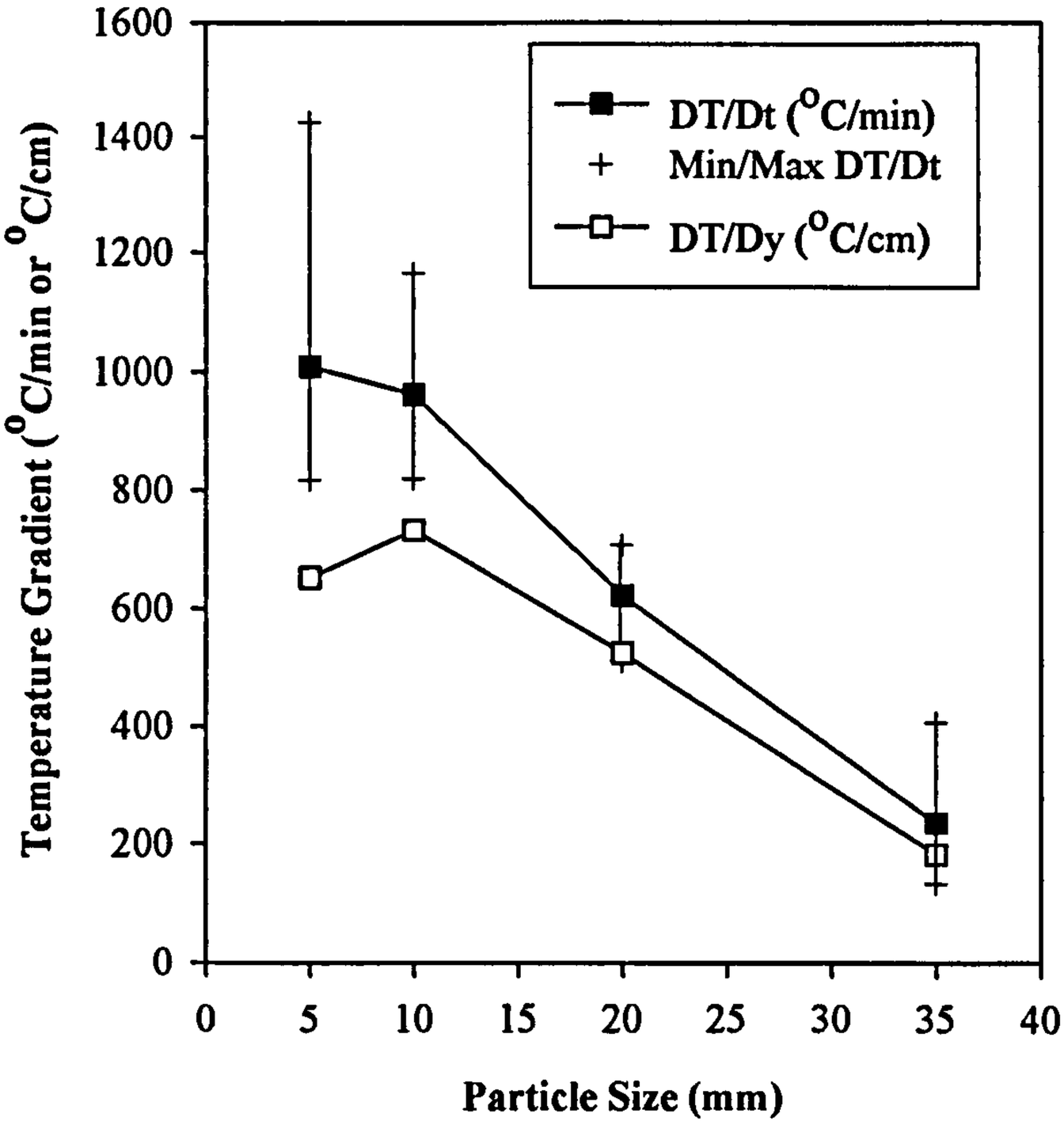

Figure 4.20: Transient and spatial temperature gradients at the ignition front.

Figure 4.21 shows the measured bed temperature against time at different bed heights above the grate for pine wood sizes of 5 mm, 10 mm, 20 mm and 35 mm. The temperature history for all the cases shows similar behaviour of increasing to a peak temperature in the initial stage then falls to form a plateau. For Case P-5, the local bed temperature rose sharply from room level to a peak value as high as 1080°C as the ignition front propagates and then dropped to a stable level of about 950°C. The local temperature peaks to a temperature higher than the temperature measure at the position above it. For Case P-35, the local bed temperature shows a more erratic pattern as the ignition front propagates down the bed and stabilizes about 1070°C after the ignition front passes. A contributing factor to the higher

flame and bed temperature produced with larger fuel size is the earlier start in char ignition and combustion, which is described in the modelling chapter.

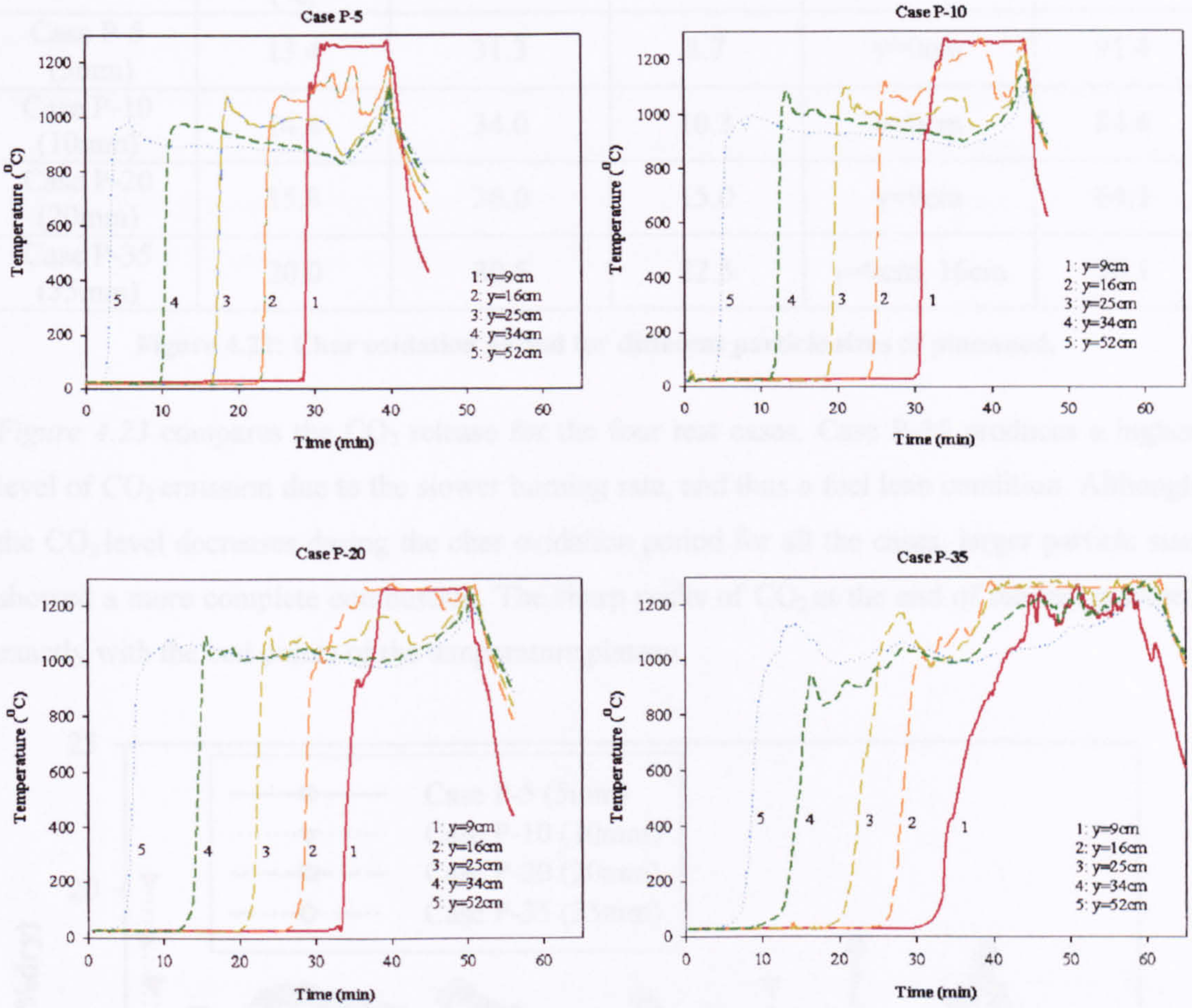

Figure 4.21: Temperature history at different bed heights above the grate for pine wood combustion with different particle sizes.

The particle size also affects the char oxidation period. For Case P-35, the temperature plateau lasted for 22.5 minute starting at t = 40 min. The reaction zone during this period stretched as far as y = 16 cm from the grate. As for Case P-5, the duration of the plateau temperature was only 8.7 minute and the reaction zone was only at the bottom of the bed. The increased thickness of char layer in Case P-35 explains the higher proportion of mass loss during this period. This agrees well with theory as larger particle have greater radiation flux as less is absorbed and thus radiation penetrates further. The effective thermal and fluid dispersion coefficients are proportional to particle diameter. Therefore, a larger particle size produces turbulence in the local bed structure inducing cross flow and mixing. *Table 4.12* lists the key experimental results for the char oxidation period.

Particle size	Proportion of Mass loss (%)	Temperature plateau			Burning rate (kg/m^2hr)
		Starting time (min)	Duration (min)	At thermocouple	
Case P-5 (5mm)	13.4	31.3	8.7	y=0cm	91.4
Case P-10 (10mm)	14.4	34.0	10.3	y=0cm	84.6
Case P-20 (20mm)	15.8	36.0	15.0	y=9cm	64.1
Case P-35 (35mm)	20.0	39.5	22.5	y=9cm, 16cm	56.1

Figure 4.22: Char oxidation period for different particle sizes of pinewood.

Figure 4.23 compares the CO_2 release for the four test cases. Case P-35 produces a higher level of CO_2 emission due to the slower burning rate, and thus a fuel lean condition. Although the CO_2 level decreases during the char oxidation period for all the cases, larger particle size showed a more complete combustion. The sharp peaks of CO_2 at the end of the test matches exactly with the end points of the temperature plateau.

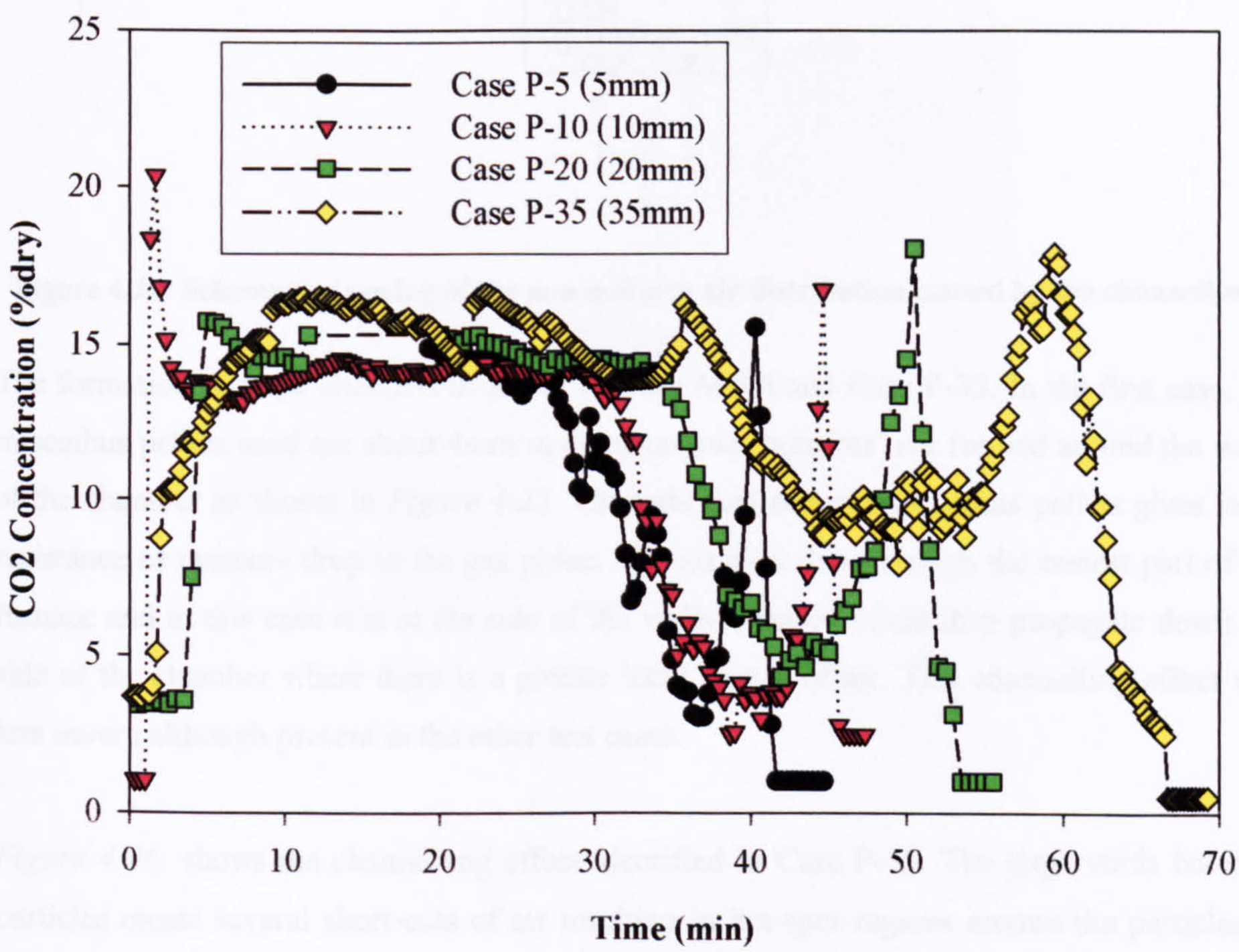

Figure 4.23: CO_2 concentrations for pinewood samples for pinewood combustion with different particle sizes.

4.5.5 Channelling and Non-Uniform Temperature Distribution

Channelling is a phenomenon that causes the air flow to pass through short-cuts or bigger holes in the bed without the expected combustion reactions, since it reduces the contact between the primary air and the burning fuel. The air flow varies across the cross-section area of the bed, producing non-uniform burning as shown in *Figure 4.24*. Channels appear as a 'hot-spot' when viewed from above the bed as these areas become hotter than the rest. The ignition front propagates much faster around the channel. It causes large transient or spatial fluctuations of temperatures and chaotic burning patterns (Yang, 2003).

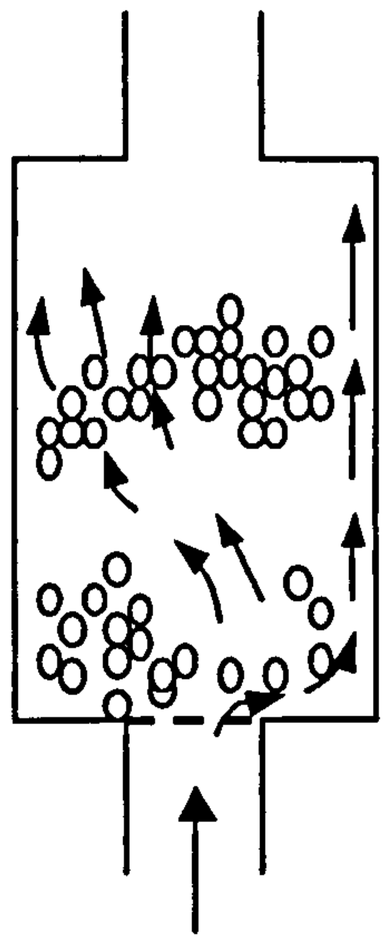

Figure 4.24: Schematic drawing of the non-uniform air distribution caused by the channelling.

The formation of large channels occurred in Case M200 and Case P-35. In the first case, the miscathus pellets used are about 4mm in diameter and 'hotspots' are formed around the walls of the chamber as shown in *Figure 4.25*. The tight fuel bed of miscanthus pellets gives large resistance or pressure drop to the gas phase. The air then flow through the easiest part of the furnace and in this case it is at the side of the walls. Flames would then propagate down the side of the chamber where there is a greater local supply of air. This channelling effect was less severe although present in the other test cases.

Figure 4.26 shows the channelling effect identified in Case P-35. The large voids between particles create several short-cuts of air resulting in hot-spot regions around the particles as indicated by the arrows. A series of photos taken as the combustion progresses show that numerous new channels appear at different locations once the previous channels collapse by volumetric shrinkage. The channelling causes uneven temperature distribution across the bed

and could cause the flame front to reach the bed bottom earlier. The temperature history for this case is relatively erratic with severe fluctuations as shown in *Figure 4.21*.

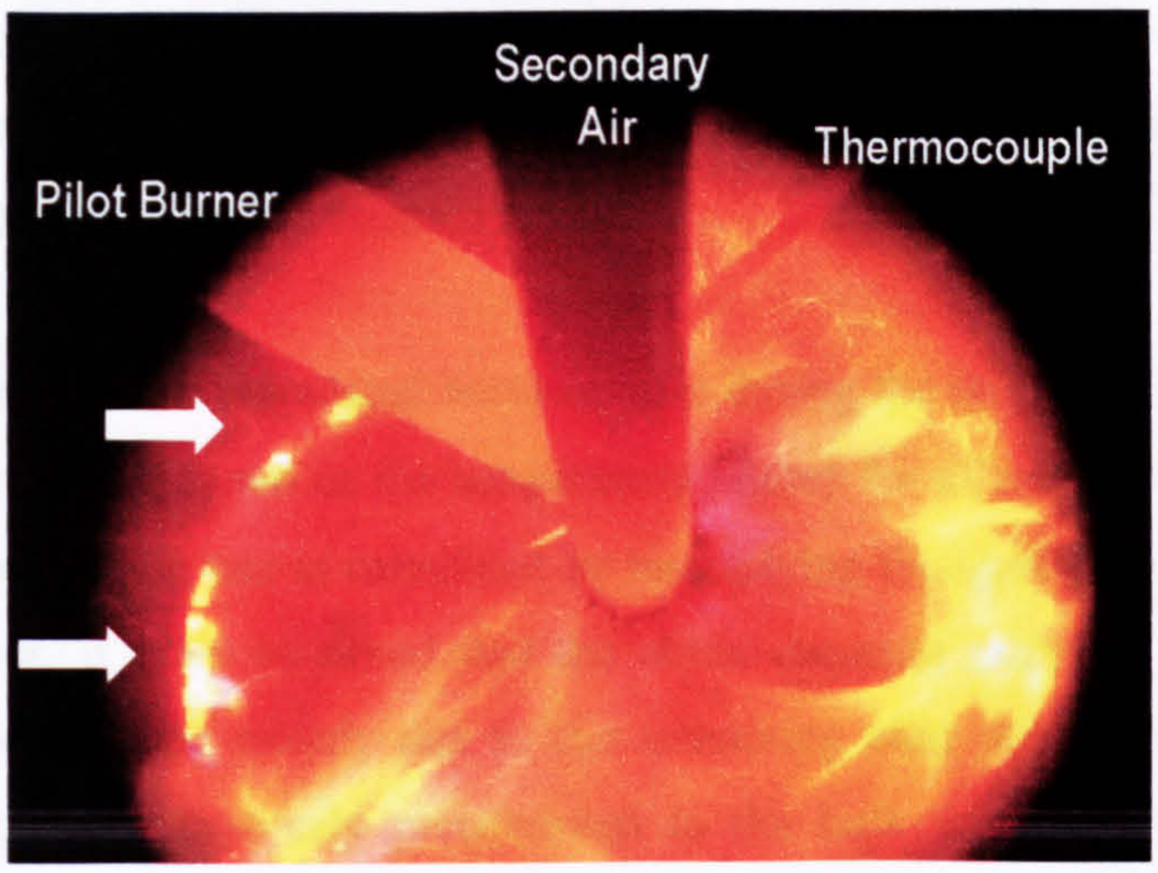

Figure 4.25: Case M200 during ignition propagation.

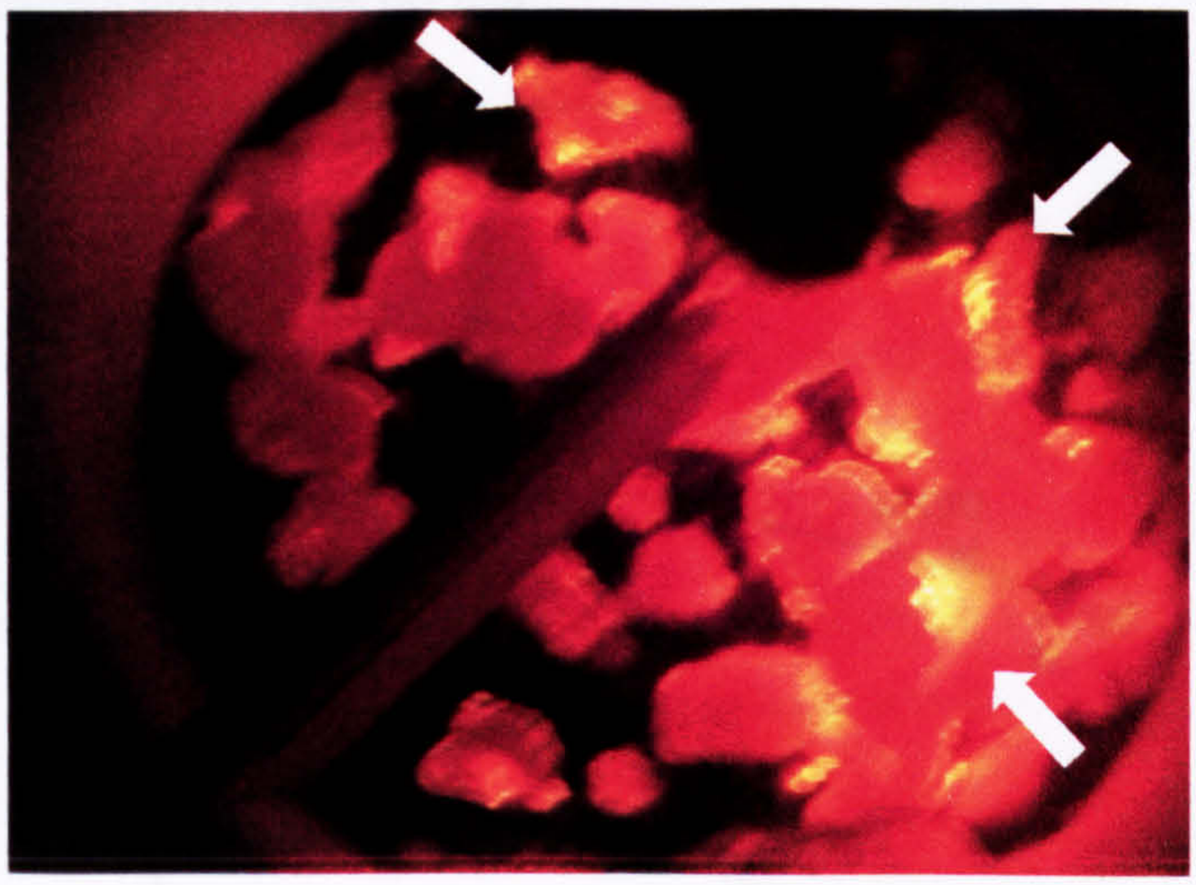

Figure 4.26: Photo of fuel bed for Case P-35.

4.5.6 Fuel Type

This section compares the performance of the different biomass materials used in the test cases. Each biomass material shows a different combustion behaviour as it differs in composition and properties. The bulk density of the material is found to be one of the main controlling factors dictating the burning rate.

Figure 4.27 compares the calculated burning rates during the ignition propagation period and the ignition front speeds based on the temperature history for all cases with the air flow rate of 274kg/m²hr. The burning rate is calculated by multiplying the ignition front speed by the bulk density. However, it must be noted that the actual burning rates are much smaller in the oxygen-controlled regime mainly due to the remaining char above the ignition front. The ignition front speed is inversely proportional to the bulk density, while the burning rate decreases linearly. The flame propagates 4 times faster for willow wood (bulk density: 181 kg/m³) compared to the RDF (bulk density: 715 kg/m³). The dense RDF material results in a thicker layer of thermal resistance towards the flame propagation zone reducing the heat transfer throughout the individual particles and the bed. A more open bed packing allows the radiation to propagate further into the bed.

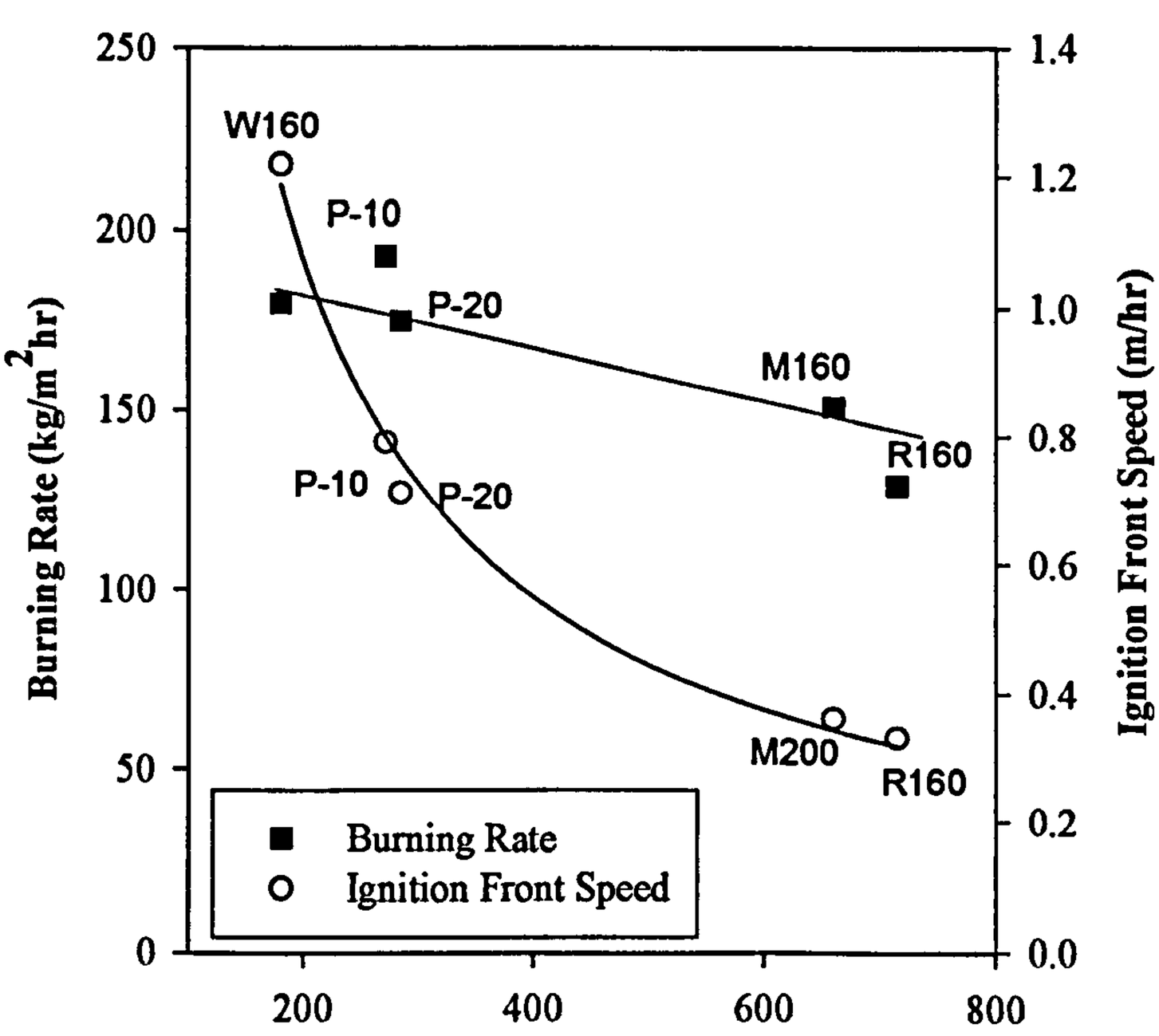

Figure 4.27: Effect of bulk density on ignition front speed and burning rate during ignition propagation.

4.5.7 Straw Combustion

This section presents the research into the performances of these 3 dedicated herbaceous energy crops (switchgrass, straw and reed) in a fixed bed reactor. The work provides an increased understanding of the behaviour of herbaceous crops to which there is still a lack of detailed experimental investigation. The combustion tests were carried out for a range of air flow-rates (234-1170kg/m²hr). The combustion process was evaluated in terms of temperature profiles and gas composition, and then quantified into ignition rate, burning rate and equivalence ratio. Results for the cases with the lowest and highest air flow rate (ST1 and ST5) are compared and discussed. The effects of straw packing conditions and the channelling phenomenon were discussed with visual illustration from the experiments.

Figure 4.28 shows the mass loss history of fuel expressed as a percentage of the remaining mass on the bed as a function of reaction time. The reactions began as soon as the over-bed gas burner was switched on as indicated by the instantaneous mass loss. For Case ST5, there was an initial ignition period of about 2min before the steady-state stage began. The high volume of under-grate air initially prevented and delayed the ignition of the fuel bed. A sharp linear decrease in the total mass of the bed fuel was seen after the bed was ignited for all the cases. The length of this linear period of mass decrease depends on the air flow rate.

The gradient of the curves increased as the air flow rate increased from the air flow rate of 234kg/m²hr to 702 kg/m²hr (ST1-ST3) and then decreased at higher air flow rates. At the end of the steady mass loss period, the mass loss slowed down gradually which indicates the second combustion stage; that is the char oxidation stage. This stage was very short at high air flow rates (Cases ST4 and ST5). This differs from previous experimental investigation of waste and wood fixed bed combustion where the 2 main combustion stages can be distinctly identified on the mass loss curve.

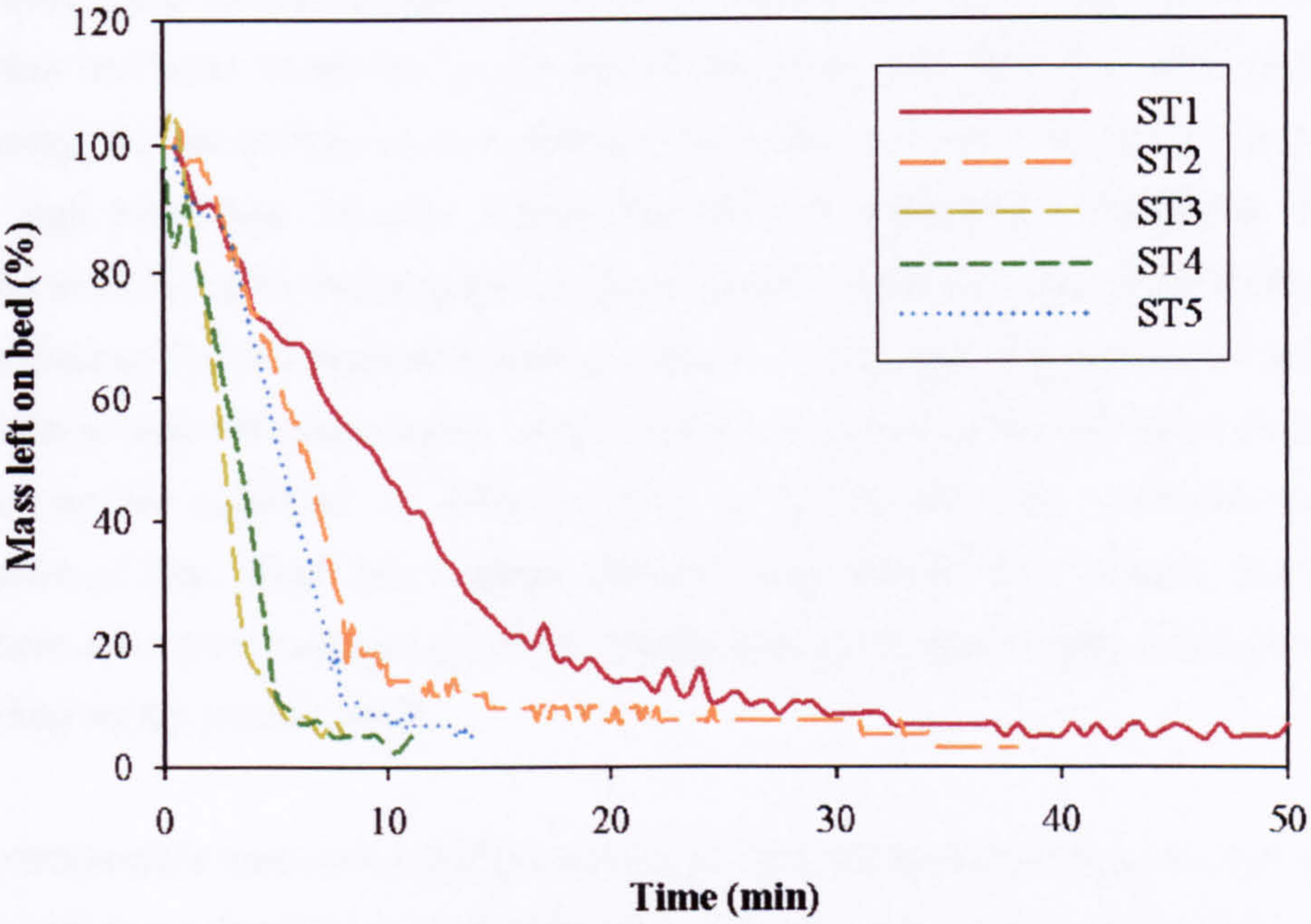

Figure 4.28: Mass loss history as a function of reaction time.

4.5.7.1 Case ST1

Case ST1 and Case ST5 referred to the combustion carried out with straw at 100l/min and 500l/min primary air flow. *Figure 4.29* shows the measured bed temperature against reaction time at different bed heights above the grate for Case ST1. The local bed temperature rose sharply from room level to a peak value of 550°C as the flame front passed, and then dropped as the flame propagated lower down the bed. The average time span required for the local bed temperature to rise from ambient to the first peak value was 1.5mins. This time span was shorter (1min) at a lower bed depth indicating a faster increase in temperature.

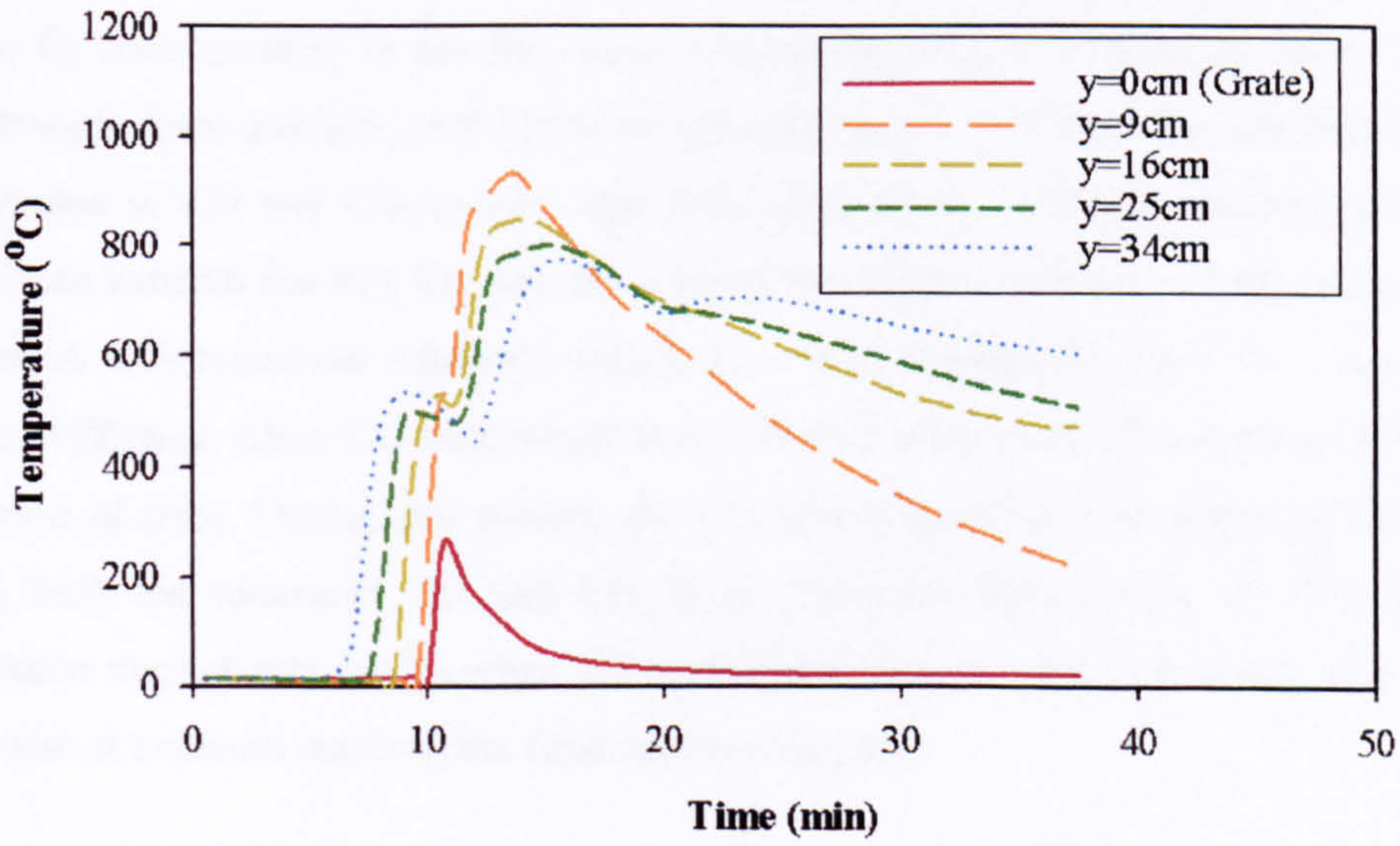

Figure 4.29: Bed temperature profile for Case ST1.

The ignition front reached the grate (y=0cm) at t=11min. The mass loss curve (*Figure 4.28*) shows that the mass remaining in the bed at this point was still very high (about 60%). Considering that the amount of char after pyrolysis above 300°C is typically less than 30%, such a high percentage of mass implies that the bed contained a significant amount of unignited material. After the propagation of the ignition front, the bed temperatures began to rise simultaneously and reached a peak at around t=13.5 min. The maximum temperature appeared at y=9cm indicating active combustion at the bottom of the bed. Such a temperature increase can be explained as follows. First, as the oxygen was consumed mostly by combustion of char, which has a higher calorific value than the raw material and secondly, when there is no fresh material below so that the heat generated by char combustion is used only to heat up the particle itself.

As the combustible mass in the bed decreased, the bed temperatures began to drop gradually. *Figure 4.28* shows that the mass left at the peak temperature point was 22% and the mass loss slowed down significantly after this point.

It was visually observed during the experiment that the herbaceous fuel bed largely maintains its original structure and the collapse of the bed as seen in the combustion of other biomass materials in the *Section 4.5* did not occur. The entanglement of the long, fibrous straws formed a 'nest-like' bed within the small laboratory furnace and the light weight of the straw enables it to maintain its structure. After the ignition front propagation stage, a bright yellow glow was seen at the bottom of the bed beneath the layer of pyrolysed char. The bed height gradually decreased as the pyrolysed char was combusted at the bottom.

Figure 4.30 shows the gas emission profile as a function of reaction time obtained for Case ST1. The O_2 concentration in the flue gases dropped quickly in a space of 3mins from t = 1min to t=4min from ambient level (21%) to a minimum level (<1%). This was followed by a sharp increase in CO and CO_2 to 17% and 20% respectively. The gas sampling probe was buried 15mm beneath the bed top and this caused the delay in the drop of O_2 concentration. The level of CO_2 remained relatively steady at a concentration of 20% for 11mins from t=9min to t=20mins, while CO concentration declined steadily from 17% to about 10% in the same period of time. During this period, the CO was progressively oxidised to CO_2. From t=20min, both the measured CO and CO_2 level decreased from levels of 10% and 20% concentration respectively to 0% when the combustion process was completed. The O_2 level began to rise at t=26min marking the final combustion stage.

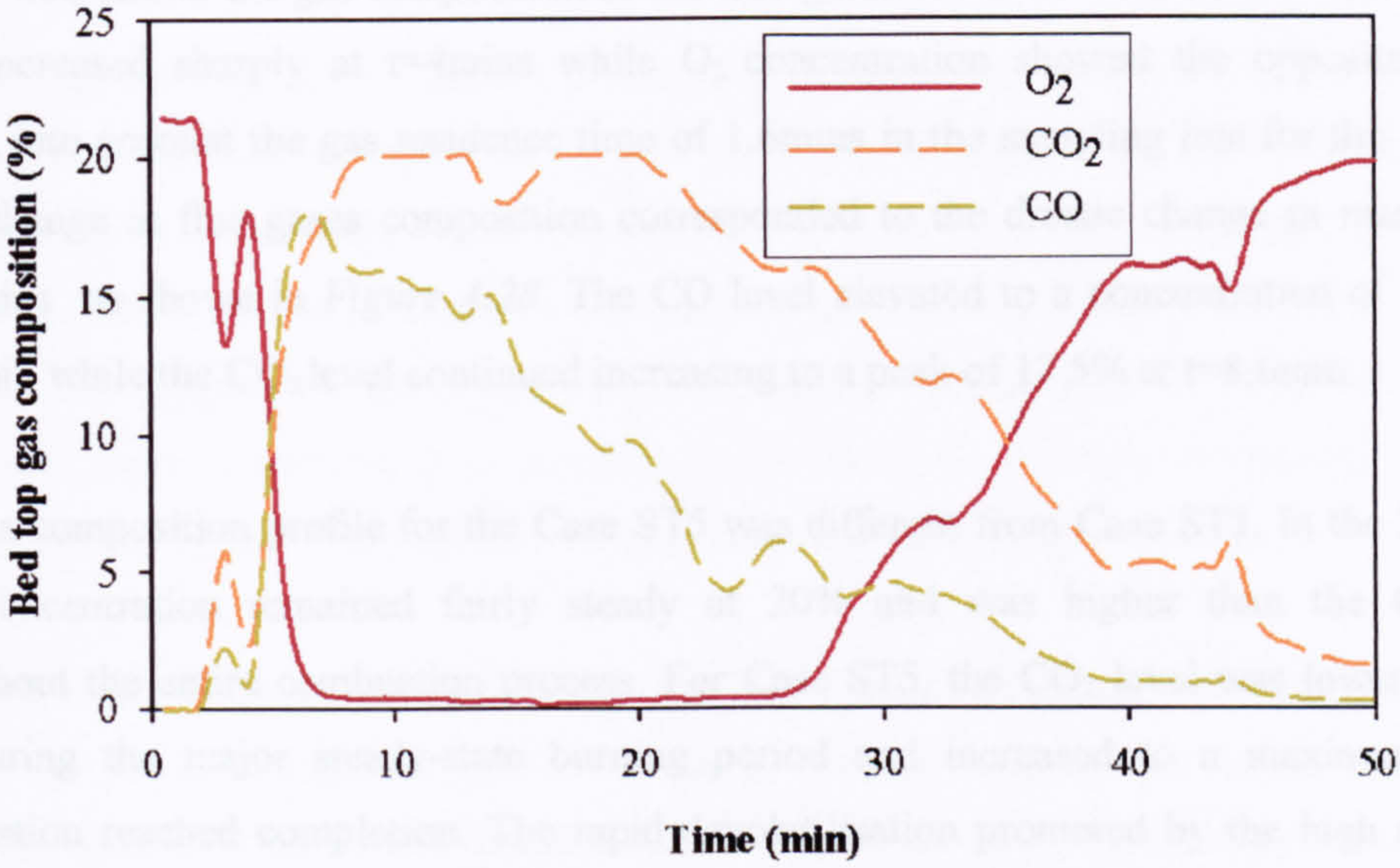

Figure 4.30: Gas composition measured at the bed top for Case ST1

4.5.7.2 Case ST5

Figure 4.31 shows the measured bed temperature profiles for Case ST5. The temperature just below the bed top increased sharply at t=2.5mins to 1064°C in less than 1min. The high temperature gradient indicates that the heat release in the bed was more intensive than in Case ST1. In contrast to the case ST1 no further increase of temperature was observed after the ignition propagation stage. The whole combustion occurred in a single stage, as the fuel was thermally thin with a large surface area per unit volume and the air supply was sufficient to oxidise char simultaneously with reaction of volatiles.

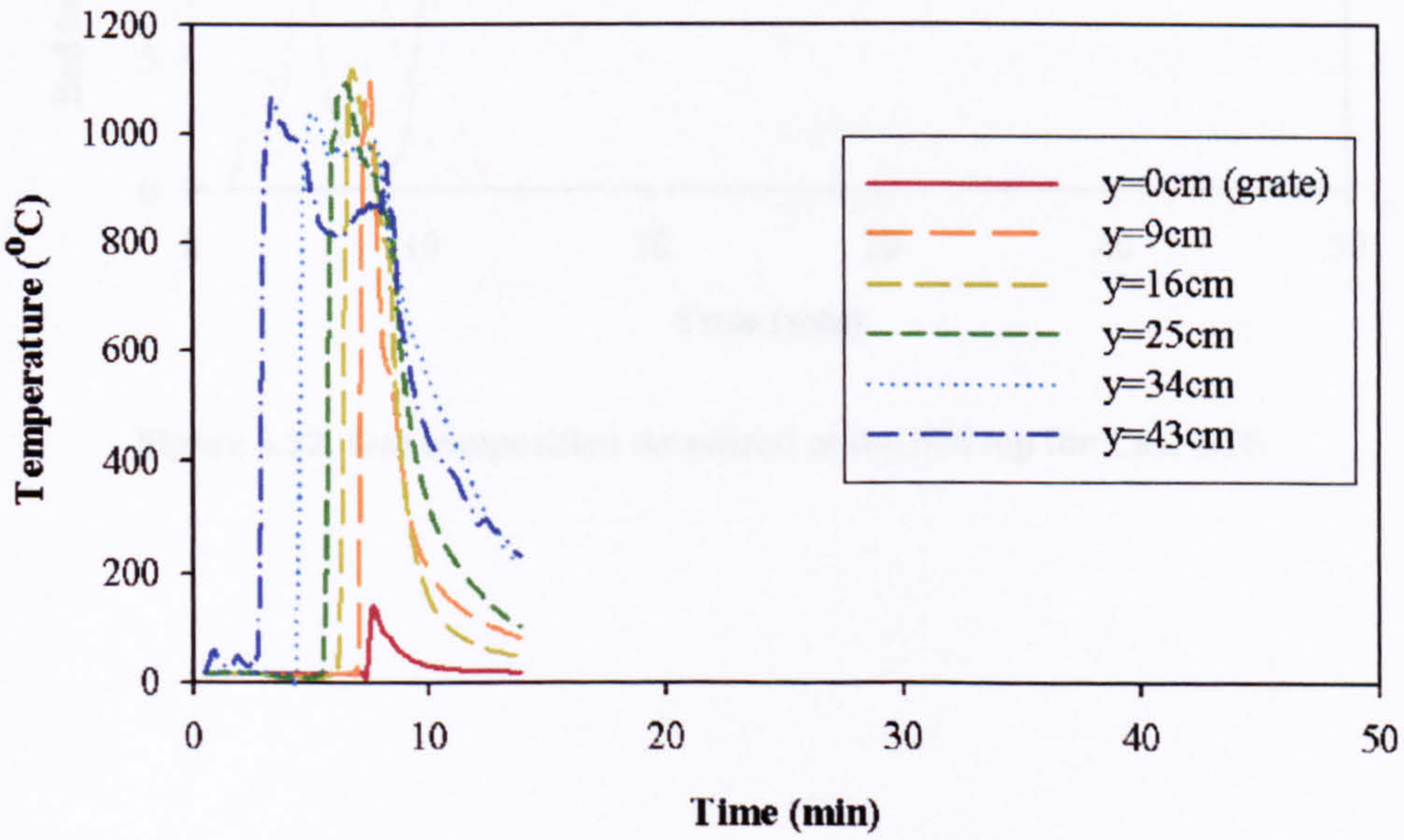

Figure 4.31: Bed temperature profile for Case ST5

Figure 4.32 shows the gas composition in the flue gases for the Case ST5. The CO and CO_2 level increased sharply at t=4mins while O_2 concentration showed the opposite pattern. Taking into account the gas residence time of 1.6mins in the sampling line for this case, the rapid change in flue gases composition corresponded to the drastic change in mass loss at t=2.5mins as shown in *Figure 4.28*. The CO level elevated to a concentration of 16.5% at t=6.5min while the CO_2 level continued increasing to a peak of 17.5% at t=8.6min.

The gas composition profile for the Case ST5 was different from Case ST1. In the latter, the CO_2 concentration remained fairly steady at 20% and was higher than the CO level throughout the entire combustion process. For Case ST5, the CO_2 level was lower than the CO during the major steady-state burning period and increased to a maximum as the combustion reached completion. The rapid devolatilisation promoted by the high supply of primary air flow resulted in a spike in the CO level. The CO level then decreases as it is oxidised to CO_2. The decrease of CO with reaction time was more intensive in this case (t>6.5min) resulting in a rise of CO_2. The average CO and CO_2 concentration in case ST1 was 10% and 16% respectively which was higher compared to the 6.5% and 8.5% in Case ST5.

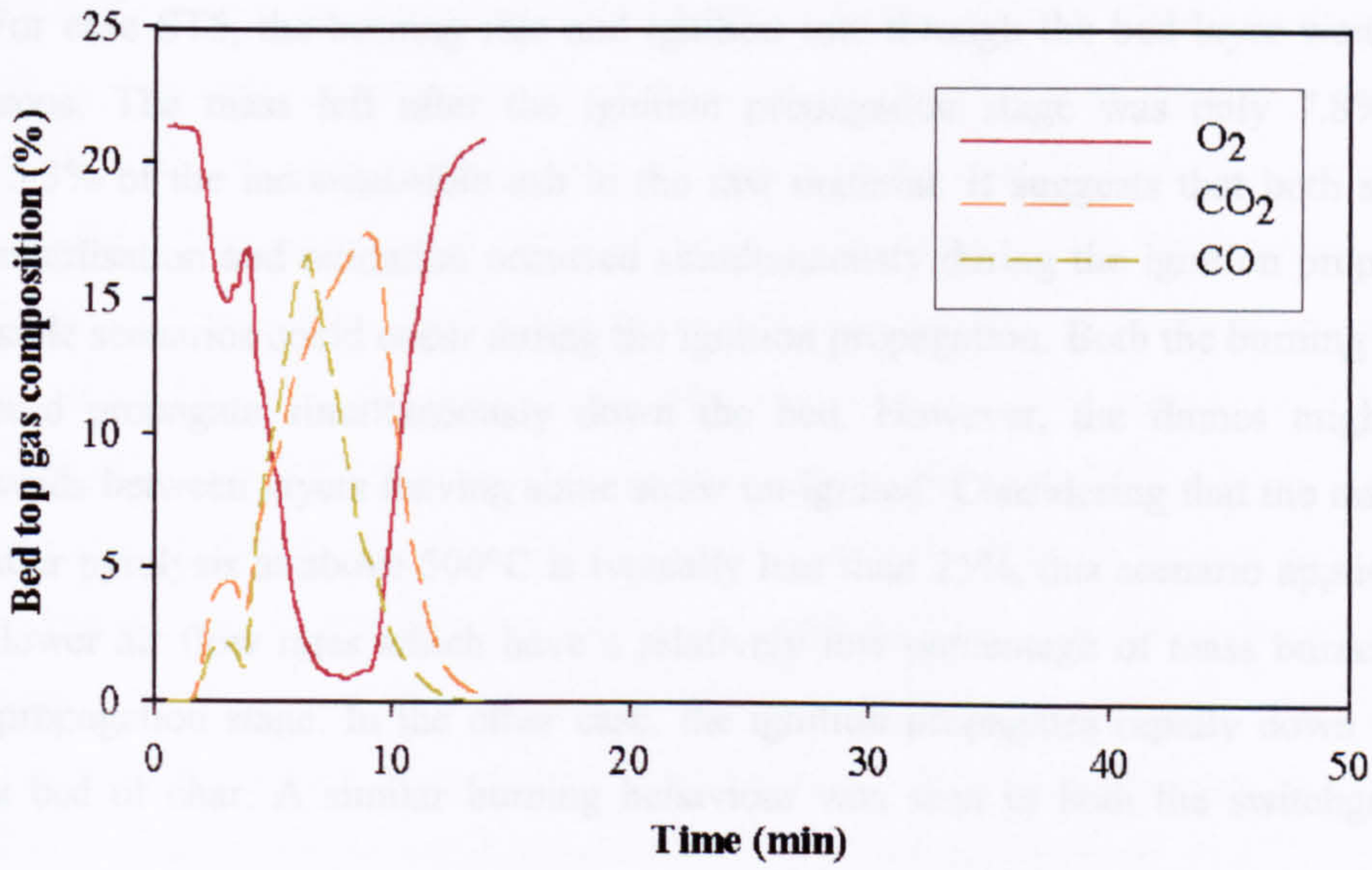

Figure 4.32: Gas composition measured at the bed top for Case ST5

4.5.7.3 Burning Rate and Ignition Front Speed

The burning rate during the ignition propagation stage represents the mass loss during the period of time the ignition front moves from the top of the bed to the grate per unit area of grate. *Figure 4.33* shows the effect of air flow rate on the burning rates during the ignition propagation stage. As the combustion occurred almost in a single stage, the burning rate after the ignition propagation stage is very slow, fluctuating in the range of 20-80kg/m²hr for both herbaceous fuels. Therefore, it is desirable to minimise the duration of the char oxidation stage by increasing the consumption of mass in the ignition propagation stage.

Figure 4.33 also compares the burning rate and ignition rate calculated for the ignition propagation stage. The ignition rate is the rate of mass per unit cross-sectional area through which the ignition front passed. It was calculated by multiplying the ignition front speed by the bulk density of the bed. In general, the ignition rates for both straw and switchgrass are higher than the actual burning rate in that period. The difference between the ignition rate and burning rate shows that un-burnt or carbonised material was left in the bed after the ignition propagation. The mass of fuel loss during the ignition propagation was about 36%. This was expected as the ignition rate was 2.6 times faster than the burning rate of straw during that period. For case ST5, the burning rate and ignition rate through the bed layer were almost simultaneous. The mass left after the ignition propagation stage was only 7.8% which includes 5.3% of the incombustible ash in the raw material. It suggests that both stages of char devolatilisation and oxidation occurred simultaneously during the ignition propagation. Two possible scenarios could occur during the ignition propagation. Both the burning rate and flame could propagate simultaneously down the bed. However, the flames might travel through voids between layers leaving some straw un-ignited. Considering that the mass yield of char after pyrolysis at above 500°C is typically less than 25%, this scenario applies to the cases at lower air flow rates which have a relatively low percentage of mass burned in the ignition propagation stage. In the other case, the ignition propagates rapidly down the bed, leaving a bed of char. A similar burning behaviour was seen in both the switchgrass and straw.

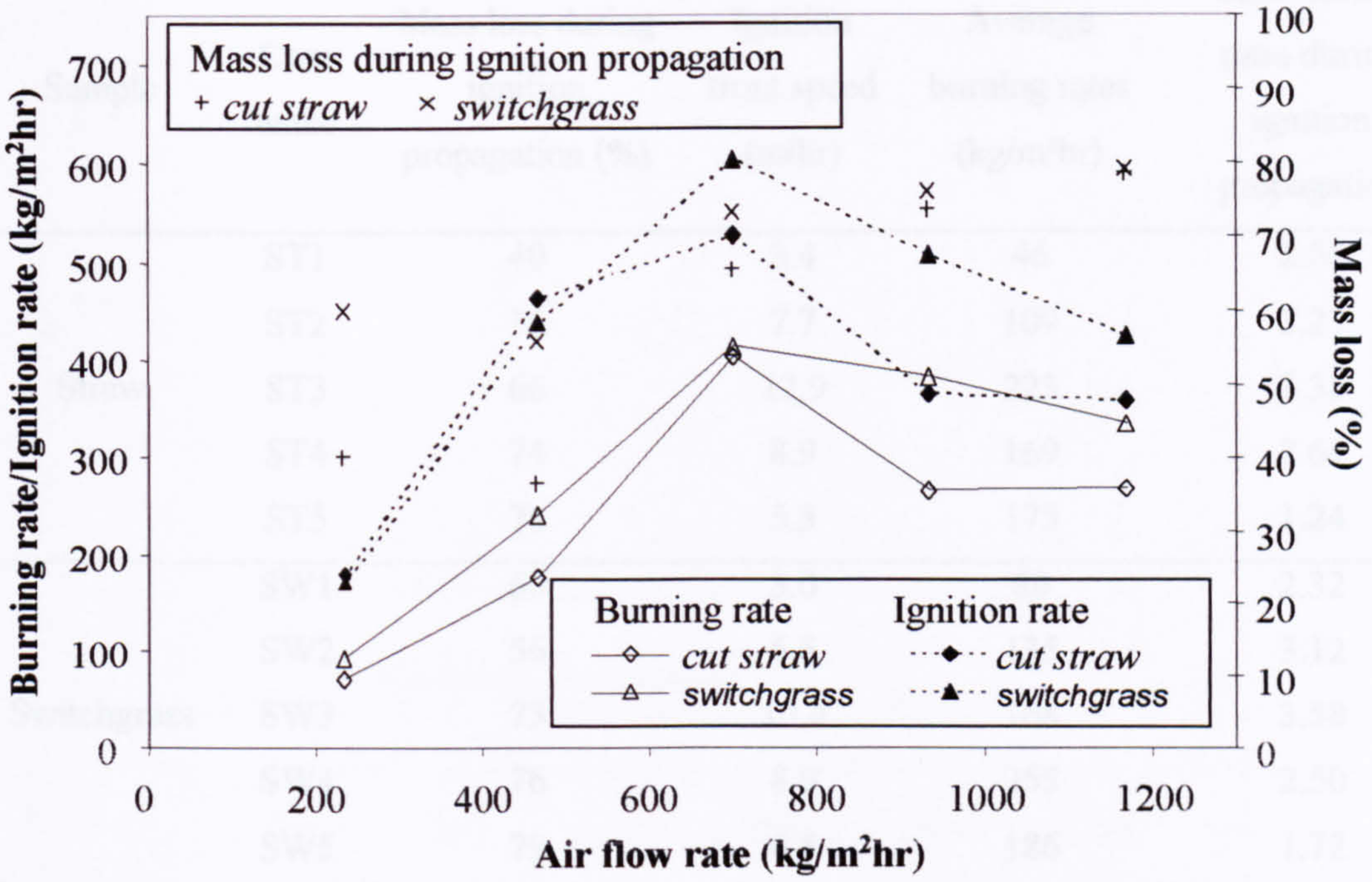

Figure 4.33: Effect of air flow rate on the burning rate, ignition rate and mass loss during the ignition propagation stage.

Table 4.13 lists some of the key results for the combustion characteristics calculated for the various cases. The equivalence ratio was calculated for the period of ignition propagation. The rapid ignition propagation resulted in a fuel-rich condition in the bed as indicated by the equivalence ratios that were in the range of 1.2-3.7. This explains the high emission of CO during the initial stage of the combustion process. The fuel-rich conditions were extreme in cases SW3 and ST4 where the equivalence ratio was 3.58 and 3.69 respectively. High CO emission of 28% and 21.5% was measured in cases SW3 and ST4, during the initial combustion stages, due to the fuel-rich condition, as only 28% of the air required was supplied. The burning process after the ignition propagation stage was in a fuel-lean condition as only a small percentage of fuel was left and the burning rate was much slower. Therefore, the gas composition shows a decrease in CO with reaction time, while CO_2 emissions remain fairly steady forming a plateau in the range of 15-20% for all the cases except ST5.

Sample	Case name	Mass loss during ignition propagation (%)	Ignition front speed (m/hr)	Average burning rates (kg/m²hr)	Equivalence ratio during ignition propagation
Straw	ST1	40	3.4	46	2.58
	ST2	36	7.7	109	2.23
	ST3	66	12.9	223	3.38
	ST4	74	8.9	169	3.69
	ST5	78	5.5	175	1.24
Switchgrass	SW1	60	3.0	60	2.32
	SW2	56	6.5	135	3.12
	SW3	73	10.4	168	3.58
	SW4	76	8.9	253	2.50
	SW5	79	6.5	186	1.72
Reed canary grass	RCG1	50	1.4	60	2.29
	RCG2	47	5.3	164	2.25

Table 4.13: Key parameters of combustion characteristics for the biomass samples.

In general, the experimental investigation showed that the ignition flame front propagation rate increases rapidly with air flow rate (for primary air flow-rate less than 700kg/m²hr). The experiments conducted prove that an ideal air flow rate for straw and switchgrass combustion would be in the range of 700-900kg/m²hr as this gives a maximum burning rate and a short char oxidation stage. The average burning rate is taken as the mass loss per unit cross-sectional area in between the start and the end of the experiment, divided by the time in hours. The end point of the experiment was determined by the increase in oxygen measurement by the gas analyser.

Figure 4.34 shows the relationship between the maximum CO/CO_2 ratio and maximum bed temperature as a function of air flow rate for the combustion of cut straw. The CO/CO_2 ratio was found to be inversely proportional to the maximum bed temperature. The CO combustion that is active at high temperature causes a high maximum temperature of 1126°C at 0.32kg/m²s.

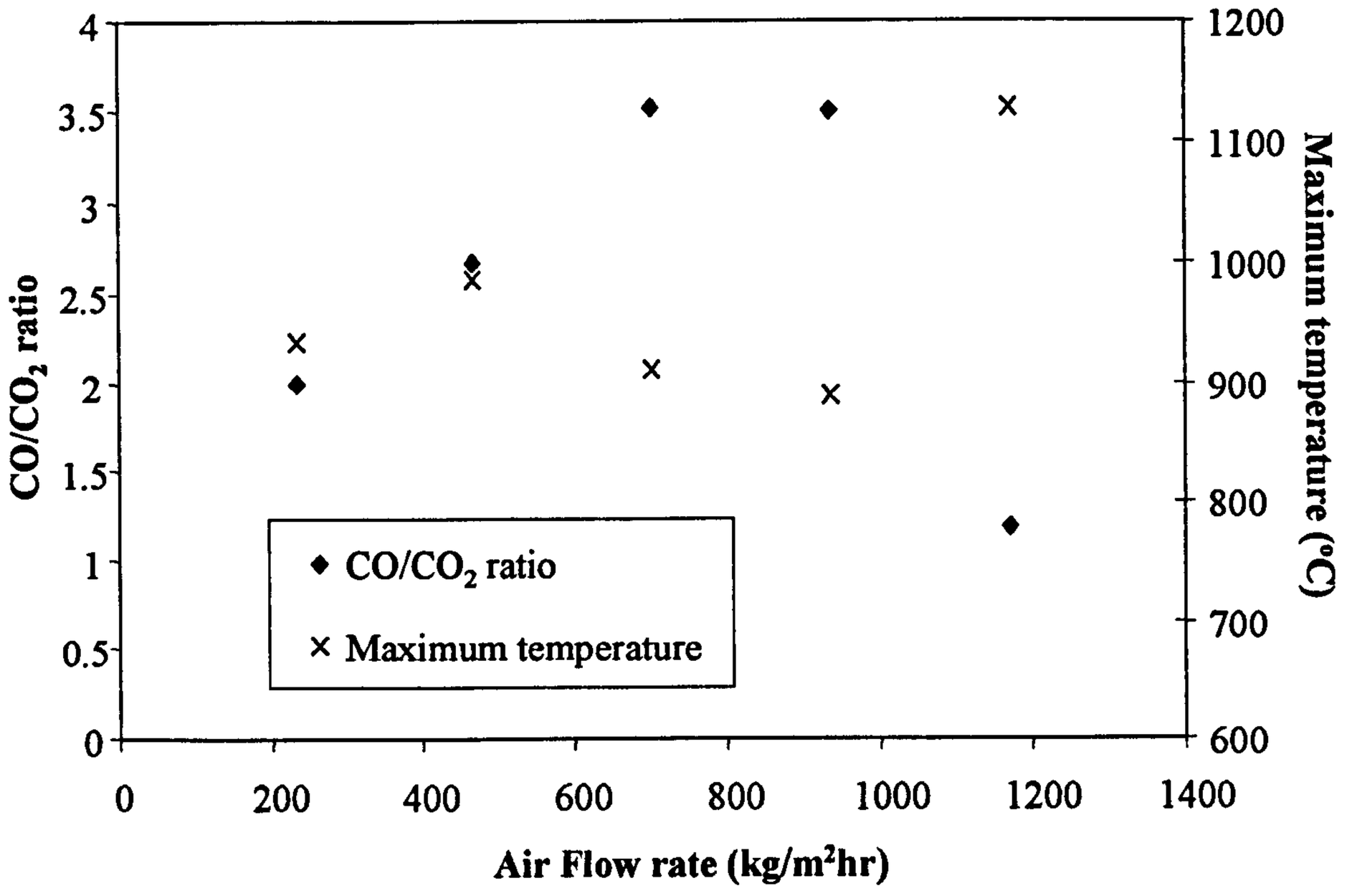

Figure 4.34: Experimental results of CO/CO_2 ratio as a function of primary air flow rate.

4.5.7.4 Combustion of Uncut Straw

The combustion experiments were repeated at air flow rates of 234kg/m²hr and 702kg/m²hr for uncut straw (12cm) in order to investigate the influence of the straw bed packing on the combustion profile. *Figure 4.35* shows the measured bed temperature against time at different bed heights for Case STU1. Both the cases, STU1 and STU2 showed a similar pattern. Unlike the cases for cut straw, the temperature profiles for the two cases of uncut straw were erratic. The temperature between y=0cm to 25cm began to rise simultaneously which can not be explained by progressive propagation of an ignition front. Two plausible scenarios for this are: i) the air channels develop randomly and cause irregular propagation of the ignition front, ii) some ignited particles drop through the loosely packed bed and ignite the lower part of the bed. The observation in the glass tube confirmed that both scenarios are active for the uncut straw. This results in a significant amount of unburned fuel above the ignition front. After the ignition front reached the grate (y=0cm) in STU1, the temperatures at y=9cm and then y=34cm peaked. This means that the middle part of the bed was undergoing active combustion.

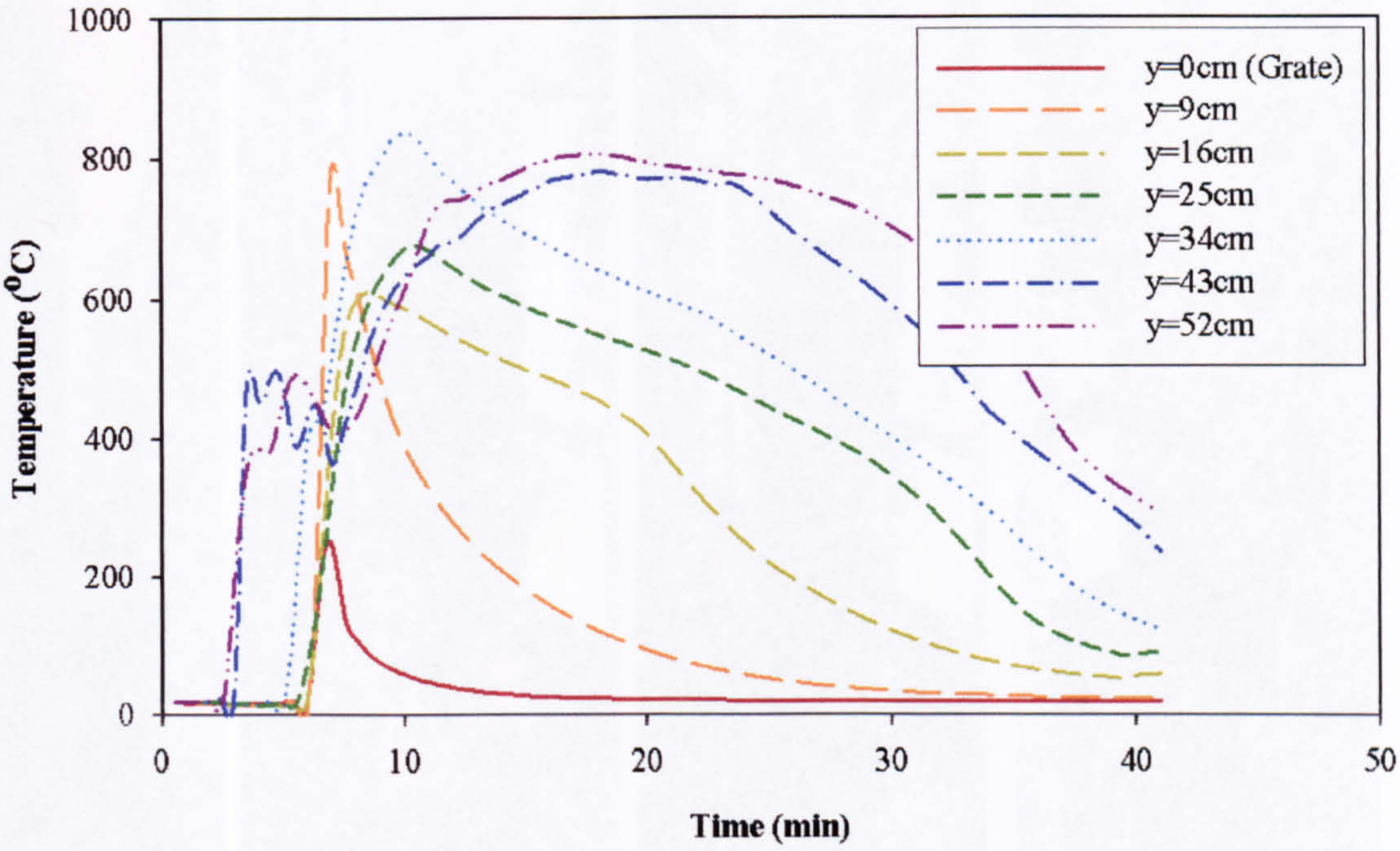

Figure 4.35: Bed temperature profile for Case STU1

Figure 4.36 shows the four photos taken during the glass tube test for the uncut straw combusted at 280kg/m²hr. In *Figure 4.36(a)*, another ignition front appeared 20cm below the existing one on the right hand side. This happened several times and the lowest ignition front continued to develop consuming the air from below and leaving a large amount of partially unburned and carbonised material, as shown in *Figure 4.36(b)*. *Figure 4.36(c)* shows that the ignition front is not flat due to randomly developed air channels. After the ignition front reached the grate in *Figure 4.36(d)*, the purple flame can be seen through the air channels across the bed. The findings from the observation matched well with the measured results in *Figure 4.35*. *Figure 4.36(a)* also shows that the glass tube above the bed was filled with white smoke, and the flame was formed on top of the tube as the combustion gas met the ambient air. The white smoke consists of oil droplets. These are generated by pyrolysis of the large molecules forming the biomass that decomposes thermally into gas, oil and char.

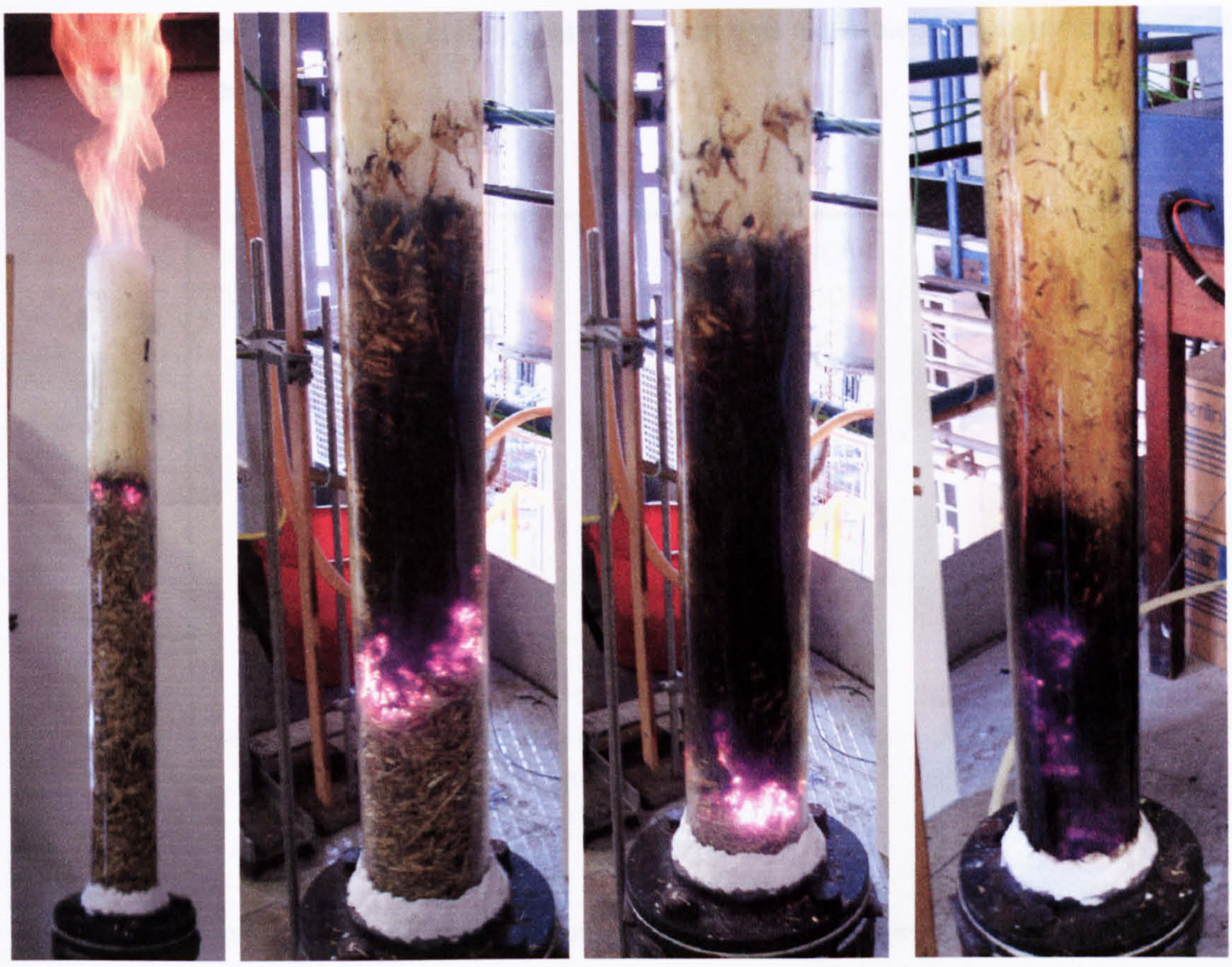

Figure 4.36: Burning of uncut straw in a glass tube at 280kg/m²hr; (a) t=20sec (b) t=106sec (c) t=194sec (d) t=207sec

The temperature profile suggested that the flame does not propagate in a single direction down the bed but also upwards. This indicated a lower level burnt before an upper level. It can be seen that at t = 6.5min, the temperature at y=9cm is higher than the temperatures at y=16cm, 25cm and 45cm. This effect is caused by the non-uniformity of straw distribution and big voids in the packed bed. Air penetrates through the easier path in the straw bed, igniting and burning the fuel as it propagates whilst by-passing sections of denser packed fuel. As straw contains fine material, some ignited straw fragments in the bed might fall through the bed and ignite the un-burnt denser packed material causing it to further smother due to the lack of air and the presence of heat. The straw size clearly plays an important role in the burning profile as it affects the packing of the bed, thus, causing channelling and non-uniform burning.

Figure 4.37 shows the gas composition in the flue gases for Case STU1. The behaviour of the flue gas composition in Case STU1 showed close qualitative similarity to Case ST1 (*Figure 4.30*). In both cases, the CO_2 composition peaked and remained fairly stable at a plateau while the CO concentration declined. However, the CO concentration in Case ST1 was lower

compared to Case STU1 and a few percent of oxygen was available for a significant part of the combustion period.

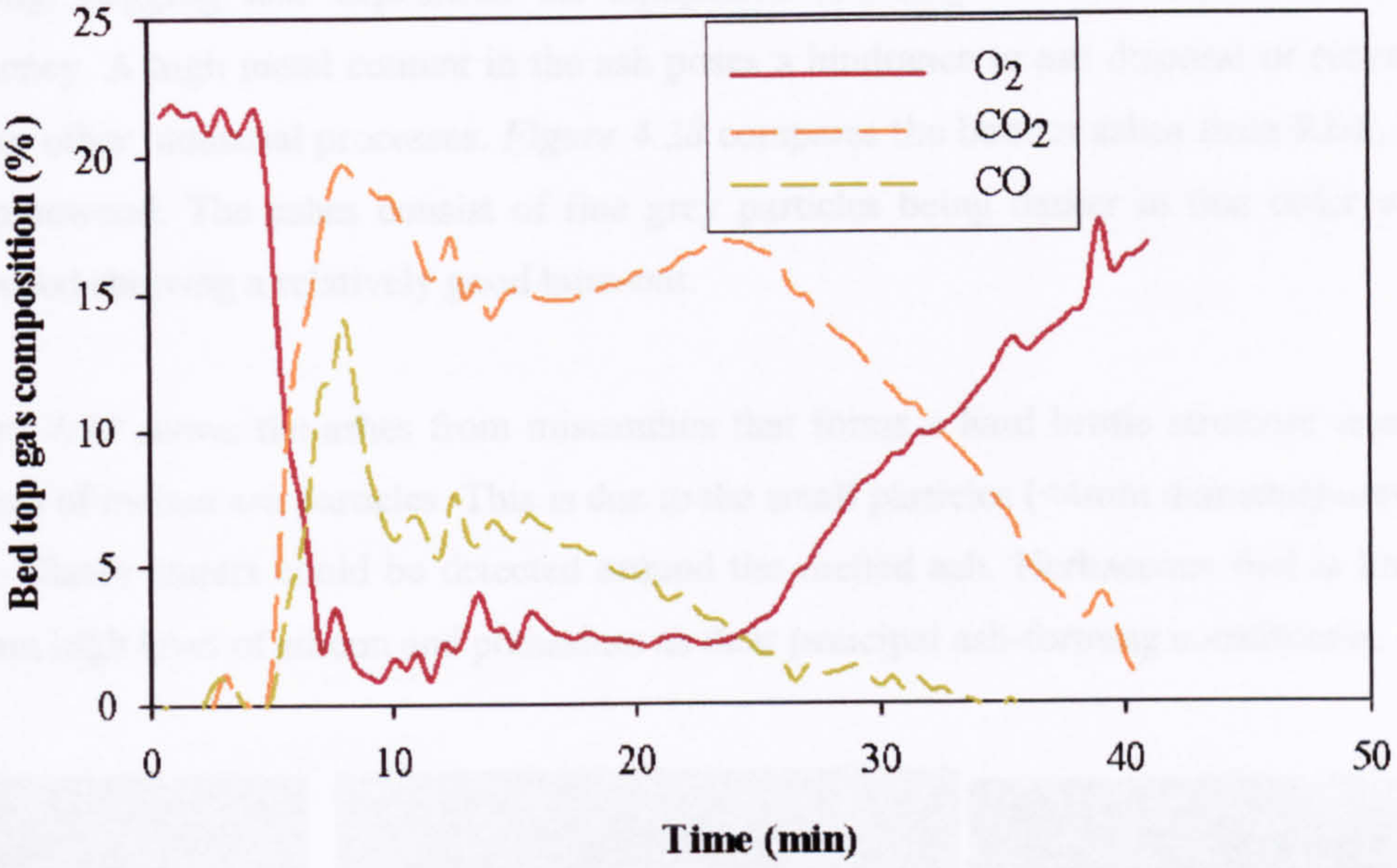

Figure 4.37: Gas composition measured at the bed top for Case STU1

Table 4.14 shows the key parameters for the uncut straw combustion. The average burning rates for the two cases of uncut straw (STU1 and STU3) are slightly higher than the corresponding cases of cut straw (ST1 and ST3). The higher oxidant to fuel ratio indicated by the equivalence ratio promotes the burning rate of the bed. The loosely packed bed in cases STU1 and STU3 caused rapid ignition propagation. However, the mass loss during ignition propagation indicated an incomplete pyrolysis of fuel during this period as straw consisted of about 80% volatile content.

Case name	Mass loss during ignition propagation (%)	Ignition front speed (m/hr)	Ignition rate (kg/m²hr)	Average burning rates (kg/m²hr)	Equivalence ratio during ignition propagation
STU1	52	8.9	240	33	1.48
STU3	37	20.8	811	186	2.39

Table 4.14: Key parameters of combustion characteristics for uncut straw.

4.5.8 Ash Characterisation

Ash residues from biomass could pose significant problems to the process operation by creating slagging and deposition on equipment reducing the life-time and combustor efficiency. A high metal content in the ash poses a hindrance to ash disposal or recycling of ash for other industrial processes. *Figure 4.38* compares the bottom ashes from RDF, willow and pinewood. The ashes consist of fine grey particles being darker in that order with the pinewood showing a relatively good burn-out.

Figure 4.39 shows the ashes from miscanthus that forms a hard brittle structure resembling clusters of melted ash particles. This is due to the small particles (<4mm diameter) used in the tests. Glassy sinters could be detected around the melted ash. Herbaceous fuel is known to contain high level of silicon and potassium as their principal ash-forming constituents.

Figure 4.38: Ash residues obtained from the combustion of RDF, willow and pinewood.

Figure 4.39: Sintered agglomerates of the bottom ash from miscanthus.

The ashes were sent to the Engineering Materials Department, Sheffield University for the analysis of elemental composition. *Figure 4.40* shows the elemental composition of the bottom ash for each sample. Silica forms a major fraction (74%) of the deposit in the

miscanthus ash with high concentration of Ca, Fe and K in the remainder. The two wood materials have similar composition with high presence of Ca, Fe, P and K and significantly low Si. There is a relatively large fraction of Si (45%) and Al (75%) found in the RDF ashes. This is due to the kitchen foils used in the makeup of the fuel.

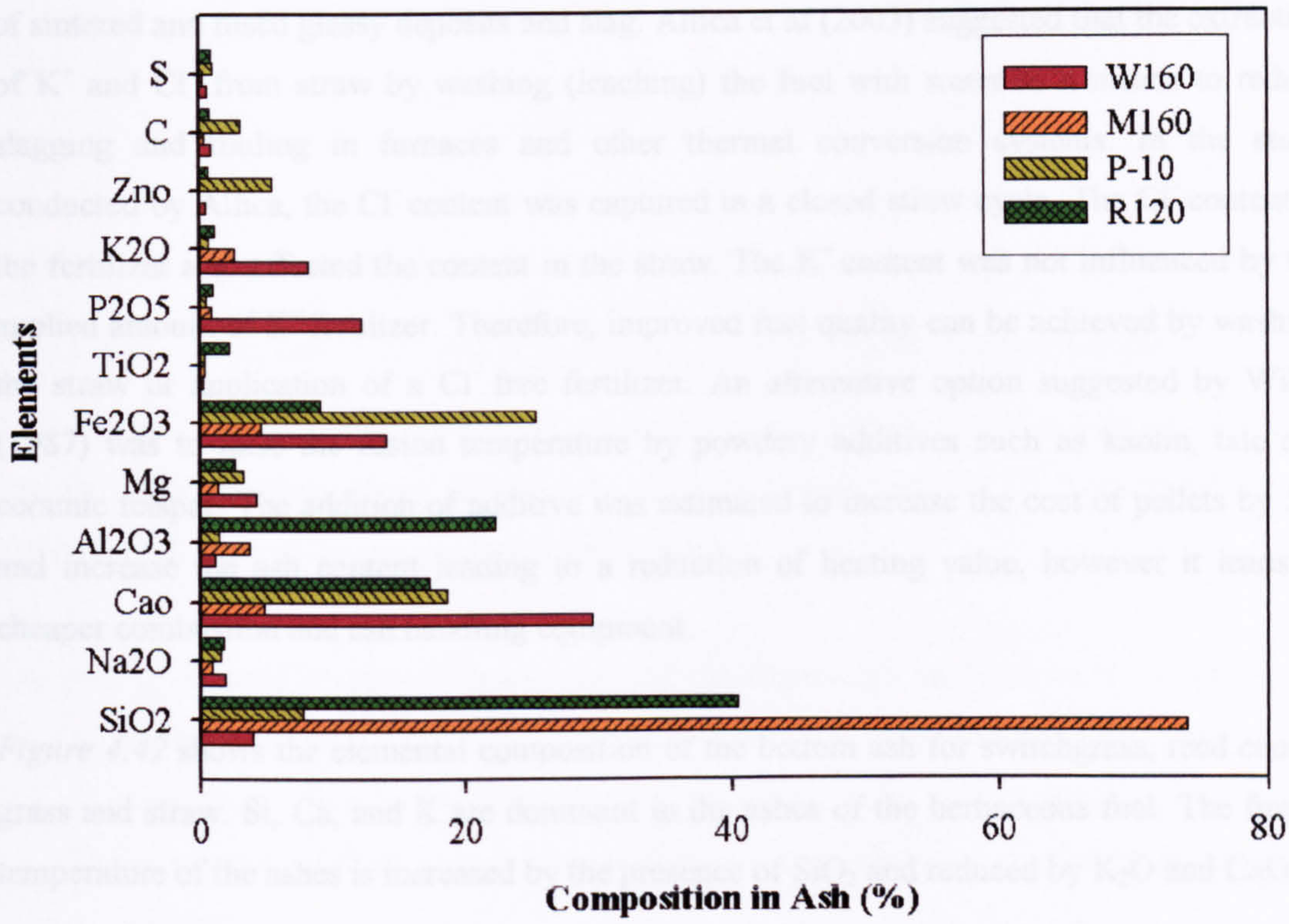

Figure 4.40: Elemental composition of the bottom ashes.

Figure 4.41 compares the major constituents of the miscanthus ash with the composition of glass obtained from Jenkins (1998). The constituents of ash material in the miscanthus used in these test cases resemble the composition in an ordinary glass. This explains the glassy sinters found around the melted ash of the miscanthus.

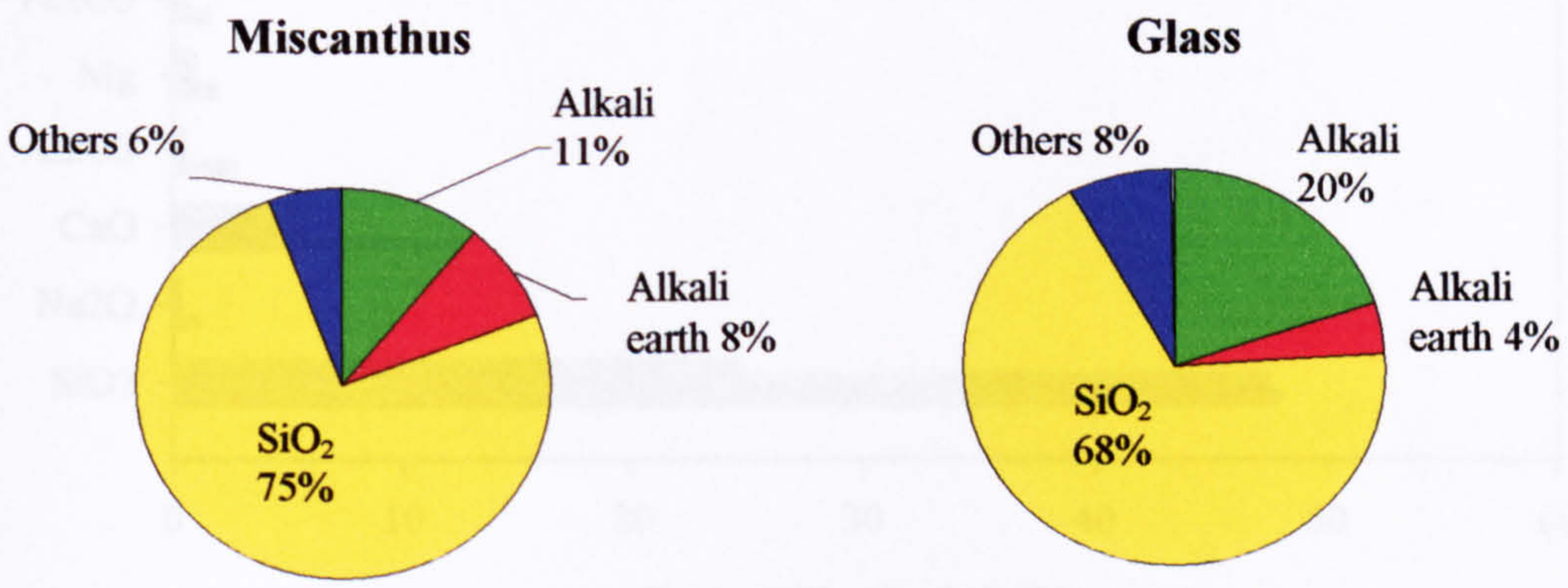

Figure 4.41: Major composition for miscanthus and glass.

The combustion of herbaceous fuels is known to be hampered by high ash content and the fusion of the ash at low temperature leading to difficulty in grate operation and ash handling. Although the actual mechanism is still under investigation, it is well known that the reactions between K^+ and silicon (in the form of silica), with Cl^- as a facilitator, leads to the formation of sintered and fused glassy deposits and slag. Allica et al (2003) suggested that the extraction of K^+ and Cl^- from straw by washing (leaching) the fuel with water as a means to reduce slagging and fouling in furnaces and other thermal conversion systems. In the study conducted by Allica, the Cl^- content was captured in a closed straw cycle. The Cl^- content in the fertilizer also affected the content in the straw. The K^+ content was not influenced by the applied amount of K^+ fertilizer. Therefore, improved fuel quality can be achieved by washing the straw or application of a Cl^- free fertilizer. An alternative option suggested by Wilen (1987) was to raise the fusion temperature by powdery additives such as kaolin, talc and ceramic felspar. The addition of additive was estimated to increase the cost of pellets by 5% and increase the ash content leading to a reduction of heating value, however it leads to cheaper combustion and ash handling equipment.

Figure 4.42 shows the elemental composition of the bottom ash for switchgrass, reed canary grass and straw. Si, Ca, and K are dominant in the ashes of the herbaceous fuel. The fusion temperature of the ashes is increased by the presence of SiO_2 and reduced by K_2O and CaO.

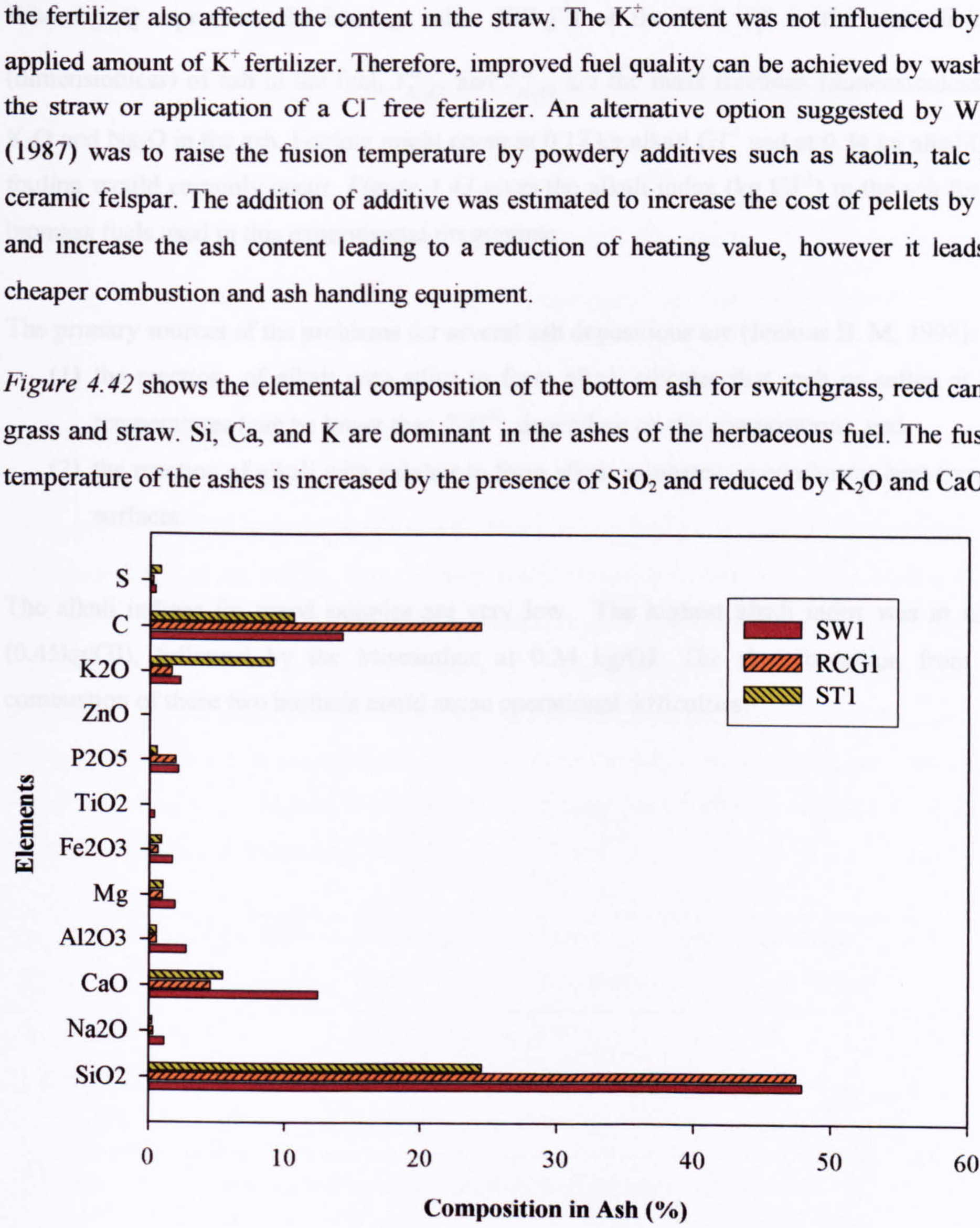

Figure 4.42: Elemental analysis of bottom ash for switchgrass, reed canary grass and straw.

The alkali index, has been used in recent years as a threshold indicator for fouling and slagging. All biomass fuels exhibit fouling behaviour but at different rates depending on the composition and ash content. The alkali index expresses the quantity of alkali oxide in the fuel per unit of fuel energy (kg alkali GJ^{-1}). It is given as:

$$\left(1/Q\right)Y_f^a\left(Y_{K_2O}^a + Y_{N_2O}^a\right)$$

Whereby Q represents the heating value ($GJkg^{-1}$) of the fuel, Y_f^a is the mass fraction (dimensionless) of ash in the fuel, $Y_{K_2O}^a$ and $Y_{N_2O}^a$ are the mass fractions (dimensionless) of K_2O and Na_2O in the ash. Fouling might occur at 0.17 kg alkali GJ^{-1} and at 0.34 kg alkaliGJ^{-1}, fouling would certainly occur. *Figure 4.43* gives the alkali index (kg GJ^{-1}) in the ash for the biomass fuels used in this experimental programme.

The primary sources of the problems for several ash depositions are (Jenkins B. M, 1998):

(1) the reaction of alkali with silica to form alkali silicates that melt or soften at low temperatures (can be lower than 700^{oC}, depending on the composition), and

(2) the reaction of alkali with sulphur to form alkali sulphates on combustor heat transfer surfaces.

The alkali indices for wood samples are very low. The highest alkali index was in straw (0.45kg/GJ), followed by the Miscanthus at 0.34 kg/GJ. The slag formation from the combustion of these two biofuels could cause operational difficulties.

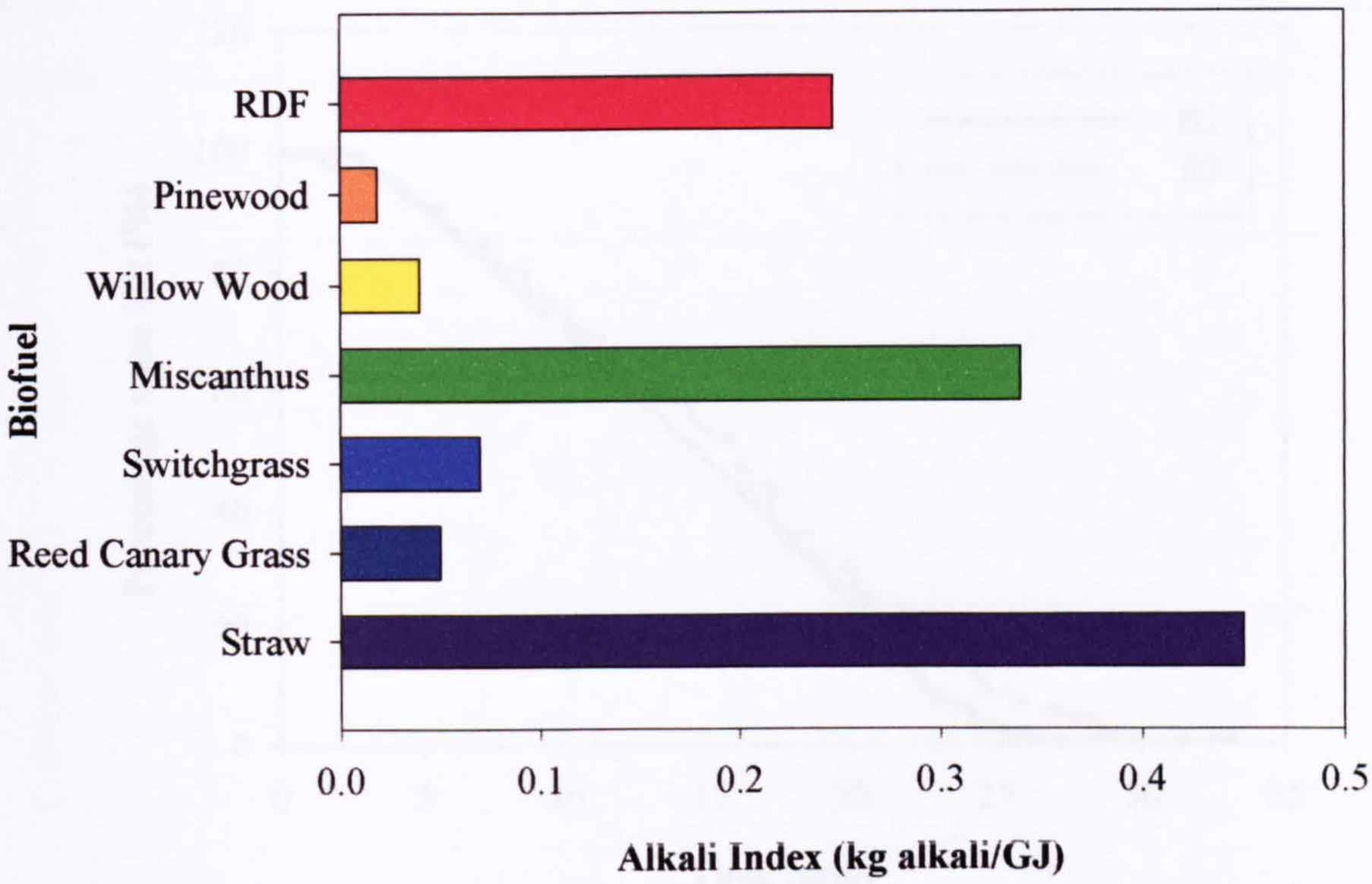

Figure 4.43: Alkali index and sulphur concentration of the bottom ashes

4.5.9 Repeatability

The combustion tests were repeated using similar conditions as in Case W200 to investigate the repeatability of the results obtained from the experimental work. The experiments should be repeated for all biomass samples for an accurate representation but due to the limitation of time and material, Case W200 was chosen. The non-uniformity of the size of the willow wood particles is higher compared to the Miscanthus and the pine wood. The highest primary air flow used in the test was chosen as this results in the most rapid burning rate and a more variable combustion compared to a slower burning rate. The conditions carried out for all the cases are tabulated in *Table 4.15* below:

Case	Mass (kg)	Bed Height (mm)	Primary Air Flow (l/min)	Secondary Air Flow (l/min)
R1	2.36	400	200	100
R2	1.73	270	200	100
R3	2.82	440	200	100

Table 4.15: Experimental conditions for the repeated tests.

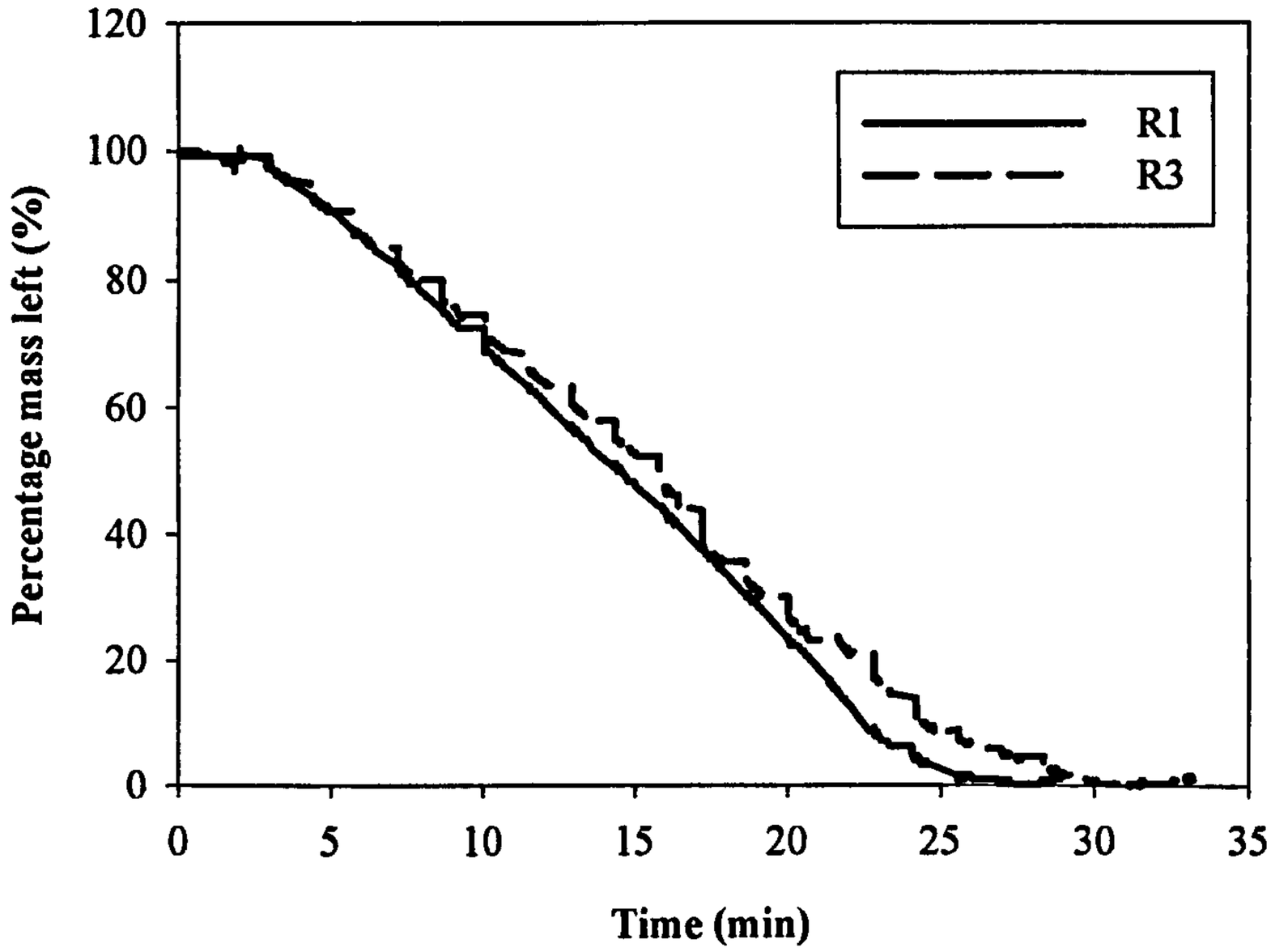

Figure 4.44: Mass loss as a function of reaction time for Case R1 and R3.

From *Figure 4.44*, it is observed that the mass loss curve for *Case R1* and *Case R3* shows remarkable agreement. The slight fluctuation in the mass loss curve for *Case R3* at t= 16.5min to 20min is to due to movement of the furnace as the gas sampling port was removed and cleaned. Discrepancy between the two curves at the steady-state was found to be highest at t=12.5min of about 3%. The difference between the two curves increased towards the end of the combustion; the char oxidation period. The difference between the mass left for Case R1 and Case R3 is about 7.6% at t =25min. The weight measurement is affected by the thermal expansion of the primary air flow pipe as explain in *Section 4.1.2*. Therefore, this caused a slight variation between the two mass loss curves towards the end of the combustion.

Figure 4.45 shows the temperature profile obtained in the fixed bed combustion of all the three cases; Case R1, Case R2 and Case R3. The rise in temperature detected at each position along the bed occurred almost at the same time period for all the three cases; Case R1, Case R2 and Case R3. It can be postulated that the flame propagation speed is uniform for all the three cases. Case R1 shows a slightly earlier bed ignition compared to Case R2 and Case R3. This is due to the earlier start of the recording time by the data logger as the start-up of each equipment was carried out in batches. Measurement of the temperature profile for Case R1 was taken earlier compared to Case R2. This caused the entire temperature profile graph for Case R1 to shift slightly towards the left. The difference in the peak flame temperature measured by Case R2 compared to Case R3 is about 1.5%. The temperature measured in all

three cases showed a peak temperature above 1200°C and thermocouple saturation. In general, the three cases repeated shows close similarity in behaviour and performance.

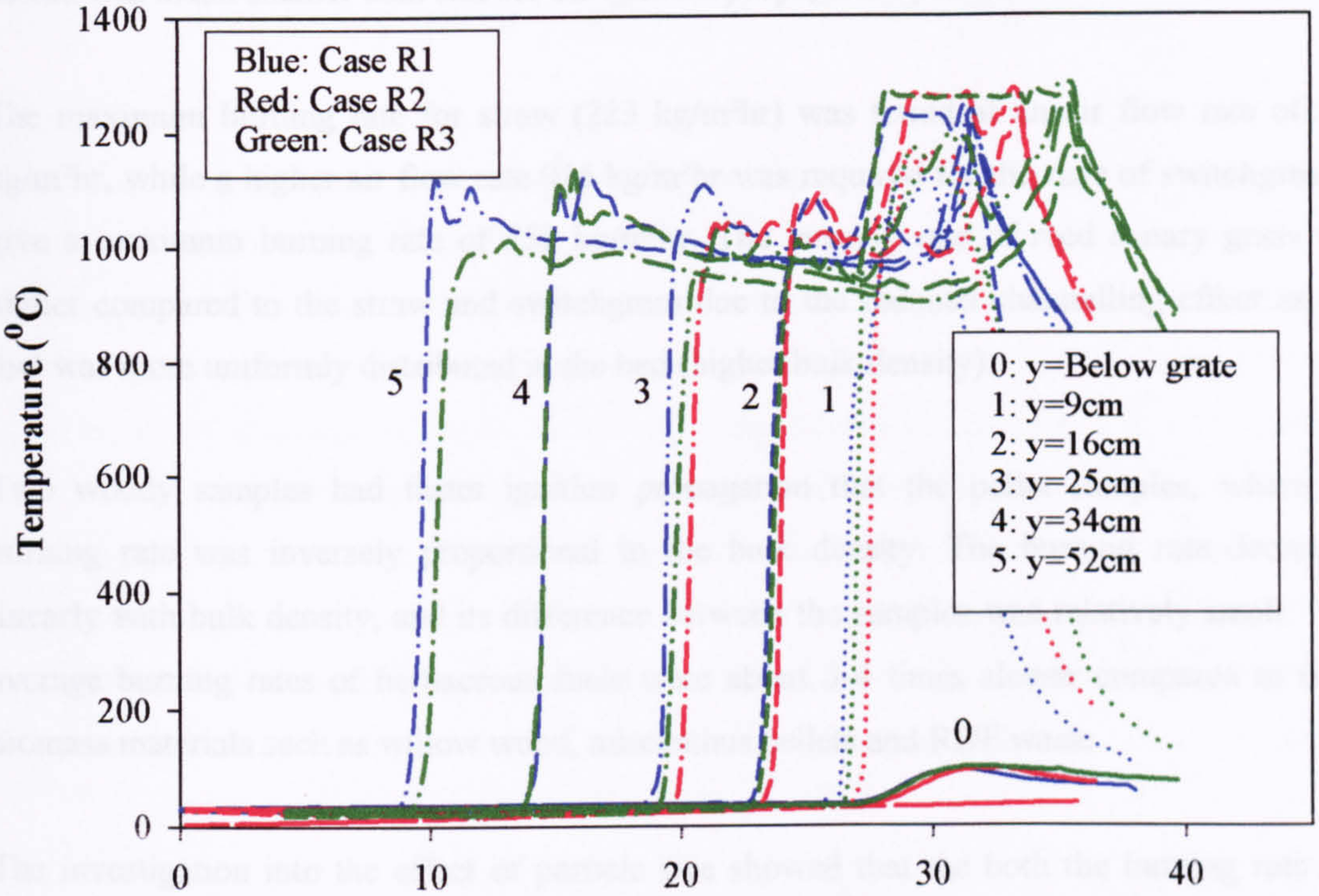

Figure 4.45: Bed temperature profile for Case R1, Case R2 and Case R3.

4.6 SUMMARY

The fixed bed combustion of biomass with different particle types and properties was investigated. For the tested range of air flow rates (234-1170kg/m²hr), all the samples were burned in the fuel rich conditions (equivalence ratio (1.2-4.1)). The progress of combustion in the bed had two distinctive stages: ignition propagation stage and slow char oxidation stage that were present at lower air flow rates. In the test cases with herbaceous fuels, (straw, switchgrass and reed canary grass), single-stage combustion occurred at higher air flow rate as the increased air supply oxidised the char remaining above the ignition front.

The ignition front speed and the burning rate increased with increasing air flow, leaving a smaller amount of char above the ignition front and then decreased as the air flow rate was further increased due to the cooling of the bed. In the combustion of straw, the ignition front speed and burning rate peaked at an air flow rate of 702kg/m²hr and then decreased as the air flow rate was further increased. As the burning rate during the ignition propagation matched

the ignition rate at high air flow rates (936-1170 kg/m²hr), less unburnt material was left behind. The study also showed that the maximum flame temperature and burning zone thickness increased with high primary air flow. The burning rate during the char oxidation period was much smaller than that for the ignition propagation period.

The maximum burning rate for straw (223 kg/m²hr) was found at an air flow rate of 702 kg/m²hr, while a higher air flow rate 936 kg/m²hr was required for the case of switchgrass to give a maximum burning rate of 253 kg/m²hr. The burning rate of reed canary grass was higher compared to the straw and switchgrass due to the reduced channelling effect as this fuel was more uniformly distributed in the bed (higher bulk density).

Two woody samples had faster ignition propagation that the pellet samples, where the burning rate was inversely proportional to the bulk density. The burning rate decreased linearly with bulk density, and its difference between the samples was relatively small. The average burning rates of herbaceous fuels were about 3-4 times slower compared to other biomass materials such as willow wood, miscanthus pellets and RDF waste.

The investigation into the effect of particle size showed that the both the burning rate and ignition front speed were reduced as larger particles were used. This caused a larger amount of char left above the ignition front and the char oxidation period lasted longer. The temperature gradient at the ignition front also decreased with increasing particle sizes, and the thickness of the ignition front from 200°C to 800°C was about the order of the particle size.

The channelling phenomenon was visually observed around the side wall in the reactor for the small miscanthus pellets and at several locations in the bed for larger pinewood particles (35mm cube). The latter case resulted in a faster propagation of the ignition front to the bed bottom than the case with 20mm cubes, but the effect of channelling on the burning rate was not significant. The observed channelling effect was severe in the test cases of uncut straw as indicated by the rapid ignition rate. However, there was no significant difference in the burning rate between uncut and cut straw.

The alkali index based on the elemental composition of the bottom ash indicated that straw and miscanthus has a high potential for fouling and slagging. This explained the sintered agglomerates of ashes found in the combustion of pelletised miscanthus. However, this was not seen in the case of straw. This might be due to the lower density of the unpelletised herbaceous fuel that avoided the sintering ashes as the fuel bed has a high voidage.

CHAPTER 5

COUNTER-CURRENT GASIFICATION

This chapter presents the gasifier design, experimental setup, results and discussion of the fixed bed gasification of commercial charcoal. The experimental work involves the gasification of char in a counter-current gasifier under varying mass flow rates of steam and air. The percentage of steam in the total reactants was in the range of 30-55%wt. As known from literature, gasification can be carried out using either air and/or steam as a reactant. The use of steam increases the hydrogen content of the combustible gases at the expense of a lower operation temperature. Therefore, a heated furnace was used to increase or maintain the bed temperature to encourage crucial gasification reactions as the gasification process comprises of both endothermic and exothermic reactions. The temperature at different locations, gas composition and mass of charcoal were measured as the gasification progressed.

5.1 GASIFIER DESIGN AND CONSTRUCTION

5.1.1 Introduction

This section presents the design and construction of the novel gasifier used in this experimental work. The fundamental designs and problems associated with conventional gasifiers are highlighted in the chapter on literature review. As commonly known, producer gas from biomass gasification contains particulate and organic contaminants (tars) which limits the end use of the product gas and causes operational problems. The performance as well as the investment and operational cost of gas cleaning systems are determined by the gasifier performance and the gas cleaning systems (Hasler, 1999). The design of the updraft gasifier successfully tackles the conventional challenges faced by traditional gasifiers:

1. Countercurrent gasifiers are not considered as an option for IC engine application due to the high tar content >100mg/Nm^3. If tar cleaning is carried out, valuable energy is lost when tar is taken from the gas. The newly designed gasifier differs from conventional updraft and downdraft gasifier and produces practically tar-free gas. The high operating temperature of this gasifier (about 800°) is one of the unique and important features as this acts as a catalyst to pyrolyse tar to carbon and gas.

2. The newly developed gasifier provides the opportunity to combine thermal gasification with a Stirling engine for use in small combined heat and power plants based on biomass. The high temperature gas has the advantage of improving the overall electricity generation efficiency. Under normal operating conditions of existing updraft gasifiers the temperature of the producer gas is low.

The design of this gasifier is part of an integrated two-stage unit. This PhD project focuses on this novel design and developing an understanding of the operation of the gasification chamber that will be directly coupled to a pyrolysis chamber.

The steam and preheated air flow rate are operating parameters that are of interest in this investigation. The application of steam requires prudent design to maintain its' temperature above 100°C in all parts of the furnace and pipelines to avoid steam condensation. As the gasifying steam and air were introduced into the bed at the same inlet location, it was important to ensure that condensation did not occur as this would flood the pipelines leading to a stop in the experiments. The small scale experiment would also require an accurate steam measurement method for low steam flow rate (<10kg/hr). This proves challenging as the standard commercial steam flow meter is mainly designed for steam flow rates of <100kg/hr. The high operating temperature (≈1000°C) gives rise to two engineering difficulties. One is the selection of a suitable material of construction that will withstand the high temperature encountered with the appropriate heaters to provide the heating power demanded. Another feature that is necessary in the gasifier for efficient operation is a continuous or batch ash discharge system. The quantity of ash produced in this experiment using commercial char is low but the quantities may become significant for other biomass residues as observed by Di Blasi (1999). The gasifier design and auxiliary equipments are discussed in detail in the following sections.

5.1.2 Experimental Setup

Figure 5.1 shows the schematic of the experimental rig constructed for this work. The fully constructed rig is as shown in *Figure 5.2* and *Figure 5.3*. *Figure 5.3* presents the setup of the pipe-lines for the reactants (steam, air and nitrogen) into the furnace.

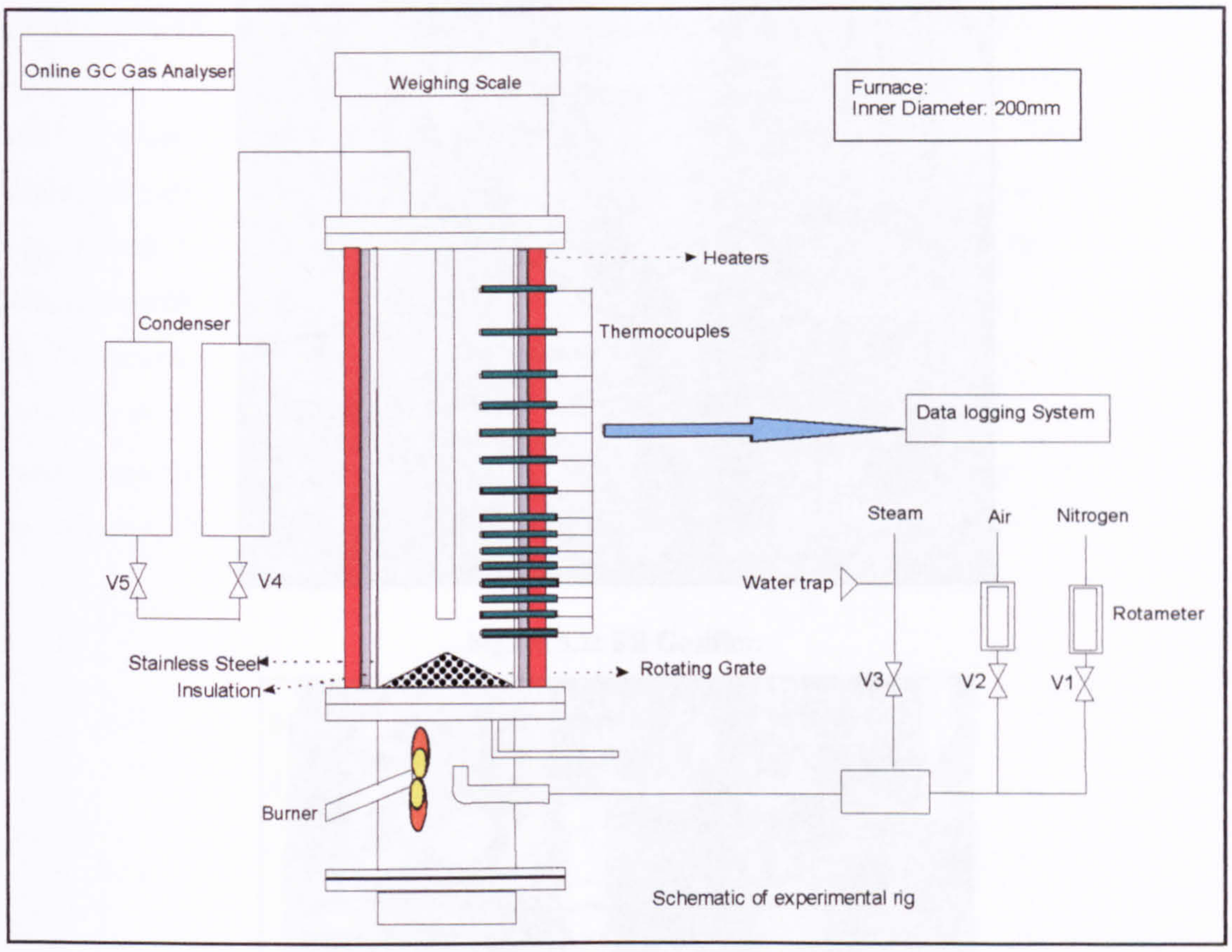

Figure 5.1: Schematic of Fixed Bed Gasifier.

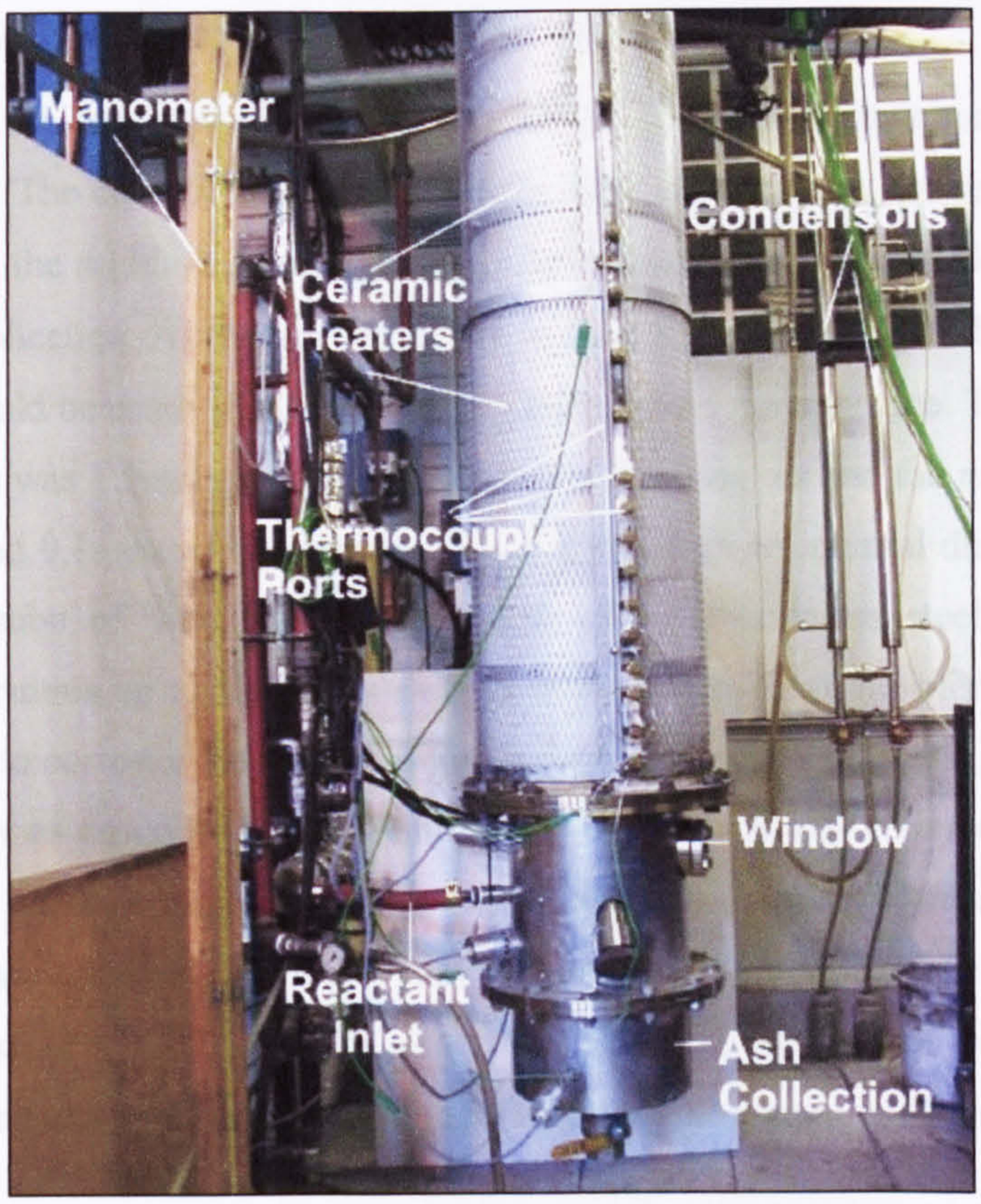

Figure 5.2: FB Gasifier.

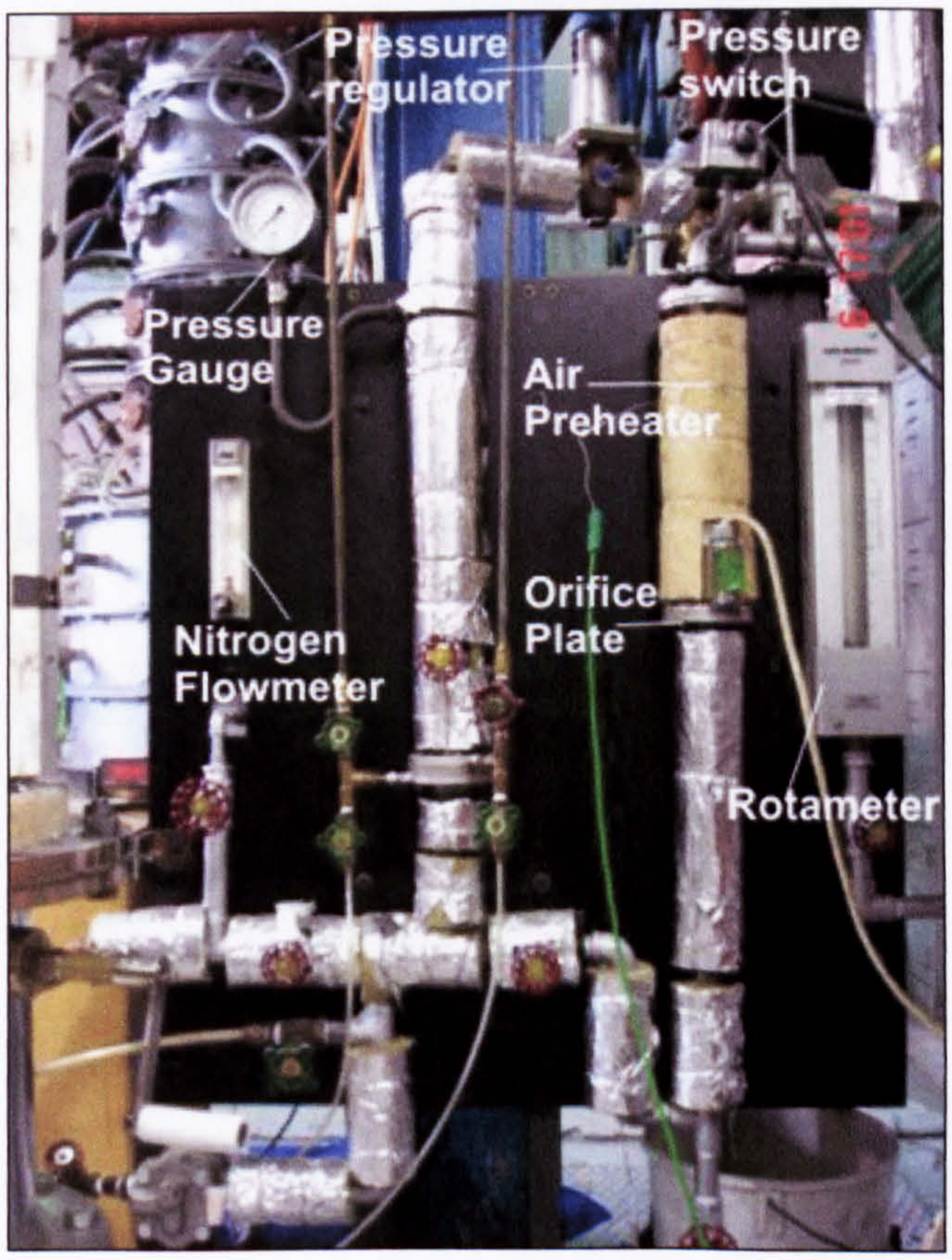

Figure 5.3: Reactant (steam, air and nitrogen) pipelines.

5.1.2.1 Gasification Chamber

The experimental rig consisted of a vertical cylindrical gasification chamber, suspended from a weighing scale. The chamber divided into three main sections; the top section, which was the main furnace, the middle section containing the reactants and burner inlet and the bottom section for ash collection. All the sections were secured together and sealed with flanges and bolts so that it could be easily disassembled for cleaning and maintenance. The total height of the entire furnace was 1.9metres with the top section at 1.5metres and the middle and bottom sections at 0.3 and 0.1metres respectively. The chamber had an internal diameter of 200mm and an interior tube of 4mm thick constructed with 316-stainless steel. This alloy can withstand temperatures up to 1200°C with high tensile strength at elevated temperature and higher resistance to corrosion compared to the conventional stainless steels. The chamber was heated electrically as described in Section 5.1.2.3. The furnace was covered with two layers of 25-mm-thick insulating material made from thermal ceramic blanket The insulating material used was Kaowool Blanket S thermal ceramic blanket that can withstand high temperature up to 1260°C. *Figure 5.4* shows the different sections of the gasifier before assembling. The exact dimensions of the experimental rig are shown in *Figure 5.5*.

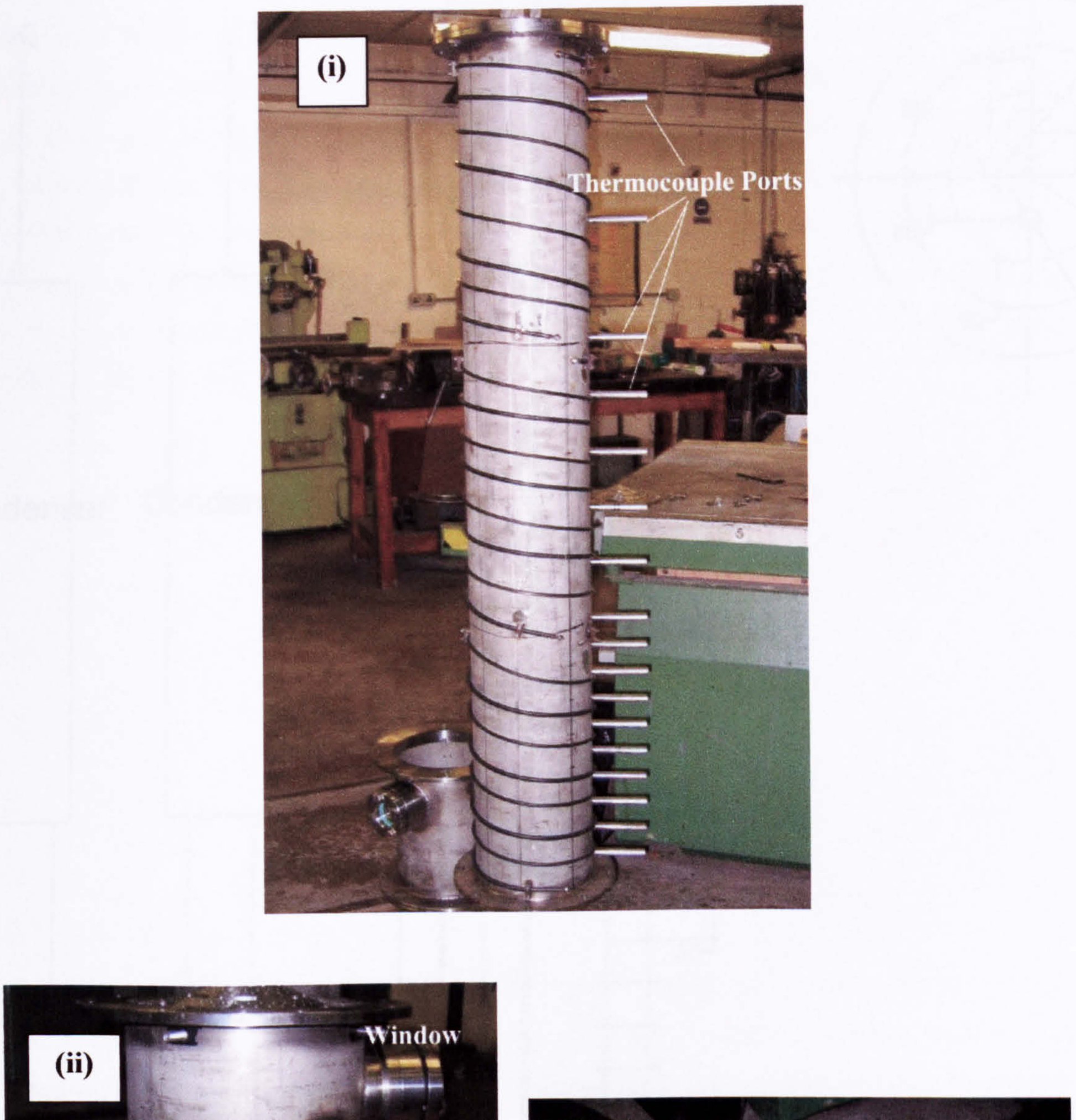

Figure 5.4: Gasifier before assembling; top section of the furnace (before insulation) from the front view (i), bottom Section of the furnace from the front view (ii) and the Top View (iii).

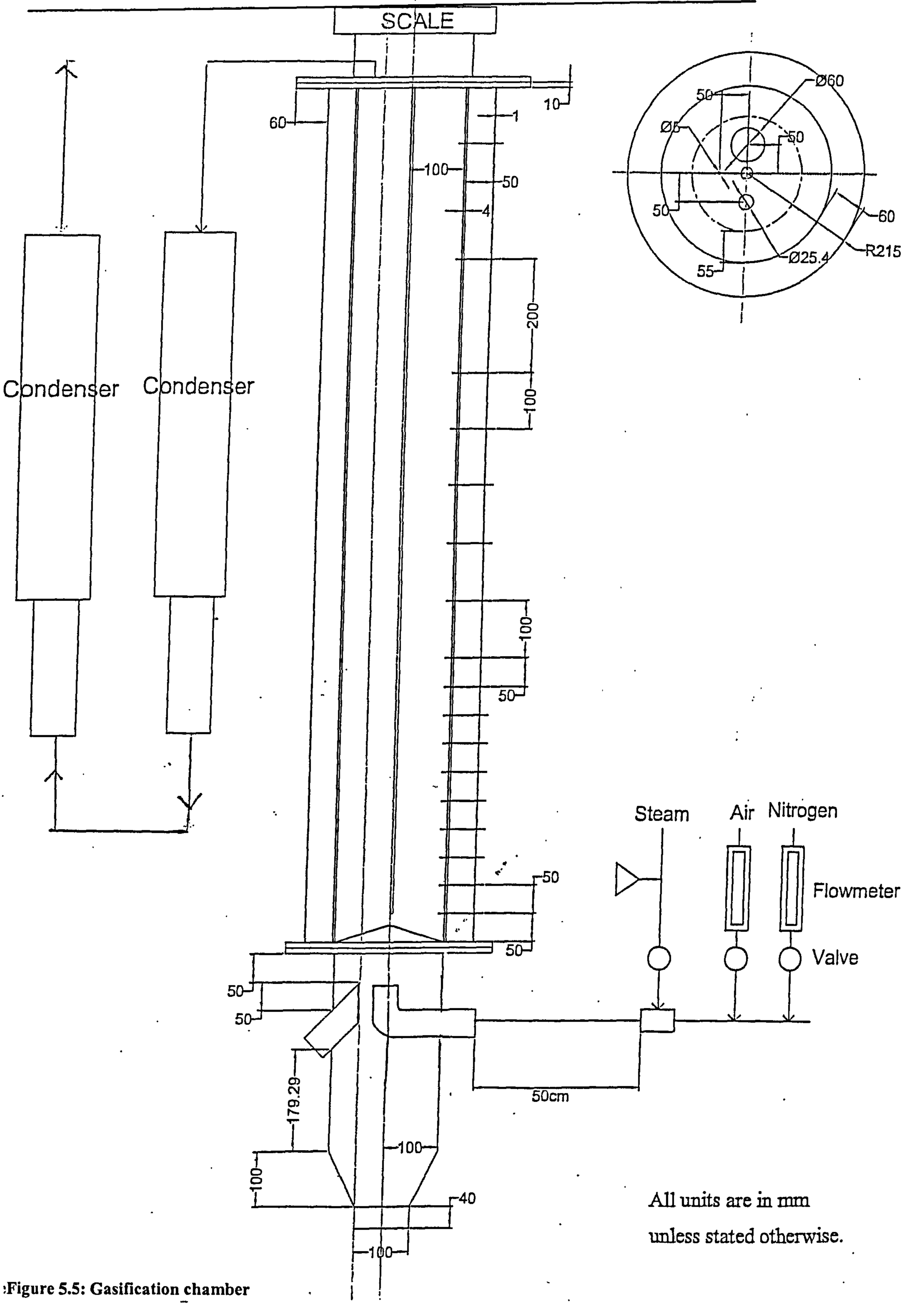

All units are in mm unless stated otherwise.

Figure 5.5: Gasification chamber

5.1.2.2 Grate

The grate for the gasifier was a perforated cone made of stainless steel, with the centre slightly higher than the sides and placed at the end of the first section of the furnace. The grate had approximately 185 circular holes of 3mm diameter and 45 rectangular holes of 20-35mm length and 5mm width, representing 21% open area. A gear was fastened to the grate so that it could be rotated manually from outside the furnace using a handle (*Figure 5.4 (iii)*). The rotating and inclined grate combined with a large open area was to facilitate the dropping of ash to the bottom section for collection. The design of the grate enabled it to be easily removed for cleaning. The grate used in this experiment is shown in *Figure 5.6*.

Figure 5.6: Grate used in the gasifier.

5.1.2.3 Heating Elements

The gasification furnace was heated by ultra-high temperature, helically wound ceramic ribbon heaters as shown in *Figure 5.7*. Six units of the semi-cylindrical heaters were combined to form a full cylinder of heating elements for the entire furnace length. Four of the heating elements provide heating power up to 4500W while the other two provide power of 3375W. The ceramic heaters provide effective radiant heating energy, rated to a temperature of 900°C. The full specifications of the heaters are as tabulated in *Table 5.1*.

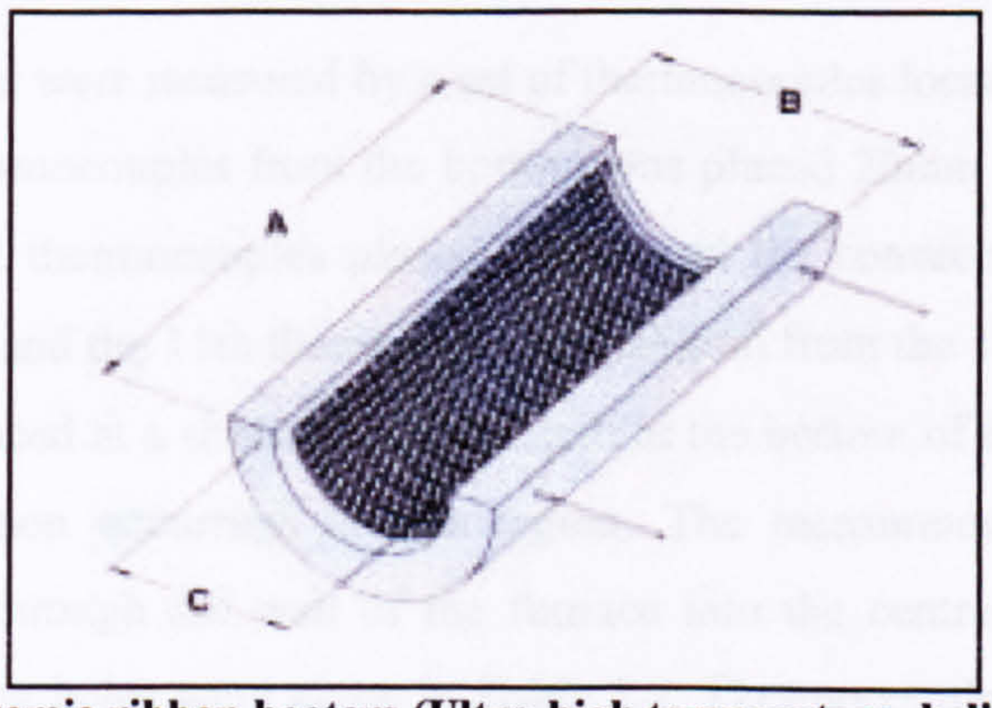

Figure 5.7: Ceramic ribbon heaters (Ultra-high temperature, helically wound).

No of Units	Watts	Volts	Dimensions are in Inches		
			A	B	C
4	3375	240	18	14	10
2	4500	240	24	14	10

Table 5.1: Specification of the Semi-Cylindrical Helically Wound Ribbon Heaters.

5.1.2.4 Temperature Controller

A temperature controller manufactured at the University of Sheffield was used to automatically control the heating power of the ceramic heaters. Three separate controllers were used to regulate the temperature of the bottom furnace section, middle section and top section of the furnace. *Figure 5.8* shows the block diagram of the temperature controller used. The solid state relay-50amp would take a maximum power of 12 000W. The electrical drawing of the temperature controller can be found in *Appendix A.1*.

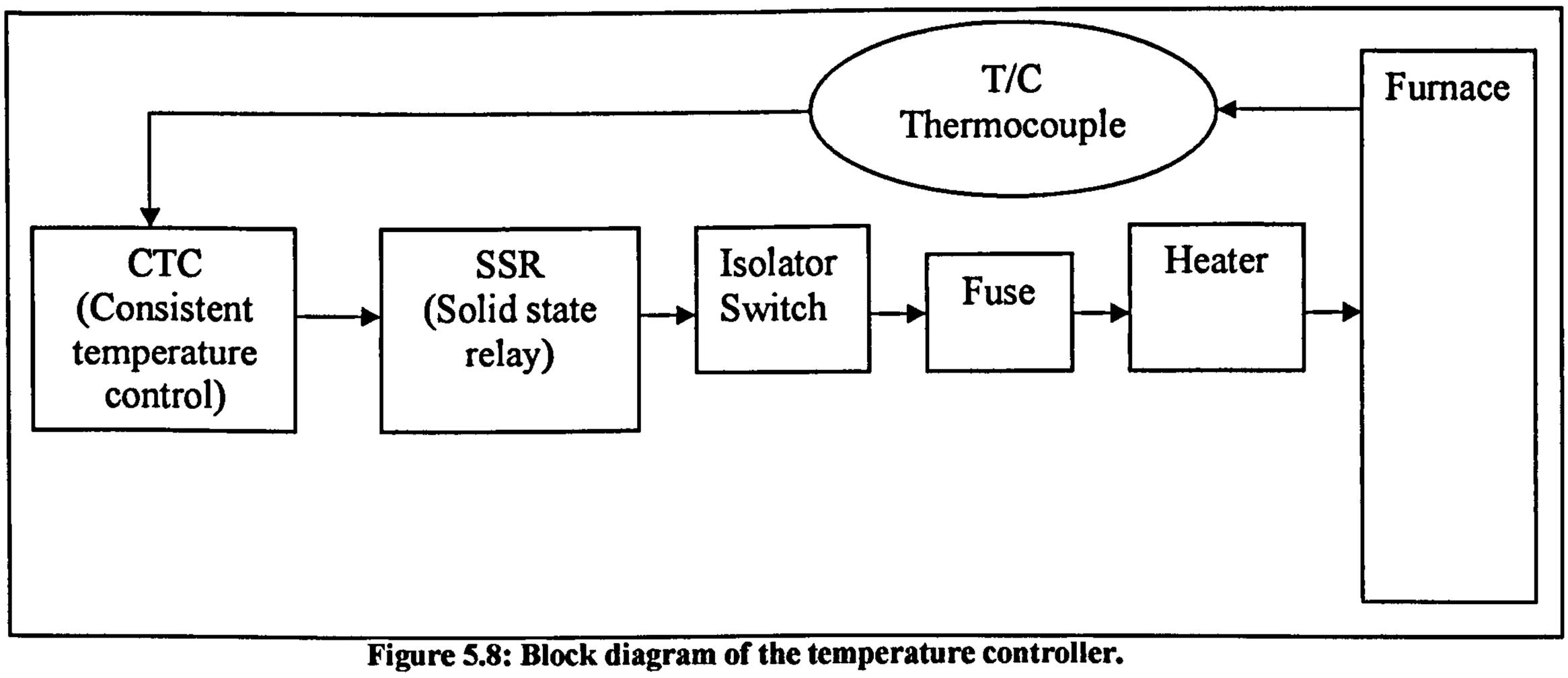

Figure 5.8: Block diagram of the temperature controller.

5.1.2.5 Sampling Position for Temperature

The temperature profiles were measured by a set of thermocouples located in the centre of the gasifier. The first 6 thermocouples from the bottom was placed 20mm apart from each other followed by the next 2 thermocouples placed 50mm and the consecutive two placed even further apart at 200mm and the 11th thermocouple at 400mm from the 10^{th} thermocouple. The thermocouples were placed at a shorter distance apart at the bottom of the furnace because of the more intense reaction occurring in that region. The measurements were made with thermocouples placed through the wall of the furnace into the centre line of the bed. The positions of the sampling holes were given in *Table 5.2*. Thermocouples were also located at the chamber surface as a sensory to provide feedback to the temperature control system.

Sampling ports were also located on the wall of the gasification chamber to provide an alternative method for measurements of temperature. The first thermocouple was placed just above the grate with consecutive thermocouples placed 100mm apart from each other.

No	Position above the grate (mm)
1	6
2	26
3	46
4	66
5	86
6	106
7	156
8	206
9	406
10	606
11	1006

Table 5.2: Position of Thermocouples on the Gasification Chamber.

The thermocouples used were type-K Chromega Alomega 304 SS Sheath by Omega Ltd. The K-type thermocouples were protected with a stainless steel sheath of 0.15 inches diameter giving it a general mechanical protection and therefore, can withstand extensive temperature (1260°C) and reducing atmosphere in the gasifier.

5.1.2.6 Gas Burner and Window

A gas burner was placed at a 45° angle towards the grate at 100mm below the grate in case the initiation of the burning process of the sample is required.

A 5mm diameter window constructed from high-temperature glass was installed 10cm below the grate to monitor the falling of ash into the bottom of the furnace. The monitoring was important, as the grate rotation was stopped as soon as specks of ignited particles were visually seen in this section, as this indicates that most of the ashes above the grate have been removed.

5.1.2.7 Reactant Supply System

The reactant was fed into the gasifier through an L-shaped stainless steel tube (i.d 15mm) that was also located 100mm below the grate. The top of the tube was sealed and the inlet holes were instead located at the side of the tube to prevent blockage due to falling ashes or dust from the grate. This also improved the distribution of air and steam across the cross-section area of the grate and prevented a channelling effect in the centre of the furnace. The outlet holes were arranged in three layers with each layer containing 6 holes of 4mm diameter. *Figure 5.9* shows the L-shape stainless steel tube and the reactant outlet (holes).

Figure 5.9: L-Shape Stainless Steel Tube and Reactant Outlet.

5.1.2.8 Rotameter & Flowmeter

The primary air was supplied from a compressor and the air flow rates were controlled by manual valves and volume flow rates measured by a Rotameter Series 2000 by KDG Mobrey Ltd. Primary air was fed from the bottom of the fixed bed reactor through the grate.

5.1.2.9 Air Preheater

The air heater used was suitable for low pressure, high flow air heating. This air heater was designed with a 2.4inch outer diameter aluminium tube and a cross frame heating element for minimum resistance to air flow. The heated length is 10inches and 500Watts of power is required for operation. The heating element was made from nickel-chrome and insulated with ceramic beads. The heater has a practical operating range of up to 200CFM (cubic feet per minute) and can be operated to temperature up to 315°C. A temperature controller was used to set and maintain the temperature of the heated air. A pressure switch was installed prior to the heater to avoid overheating the heater. The pressure switch reacts to overpressure and closes, opens or switches over a current circuit when the specified pressure set-points are overshot or undershot. *Figure 5.10* shows the set-up of air heaters with the in-built temperature control.

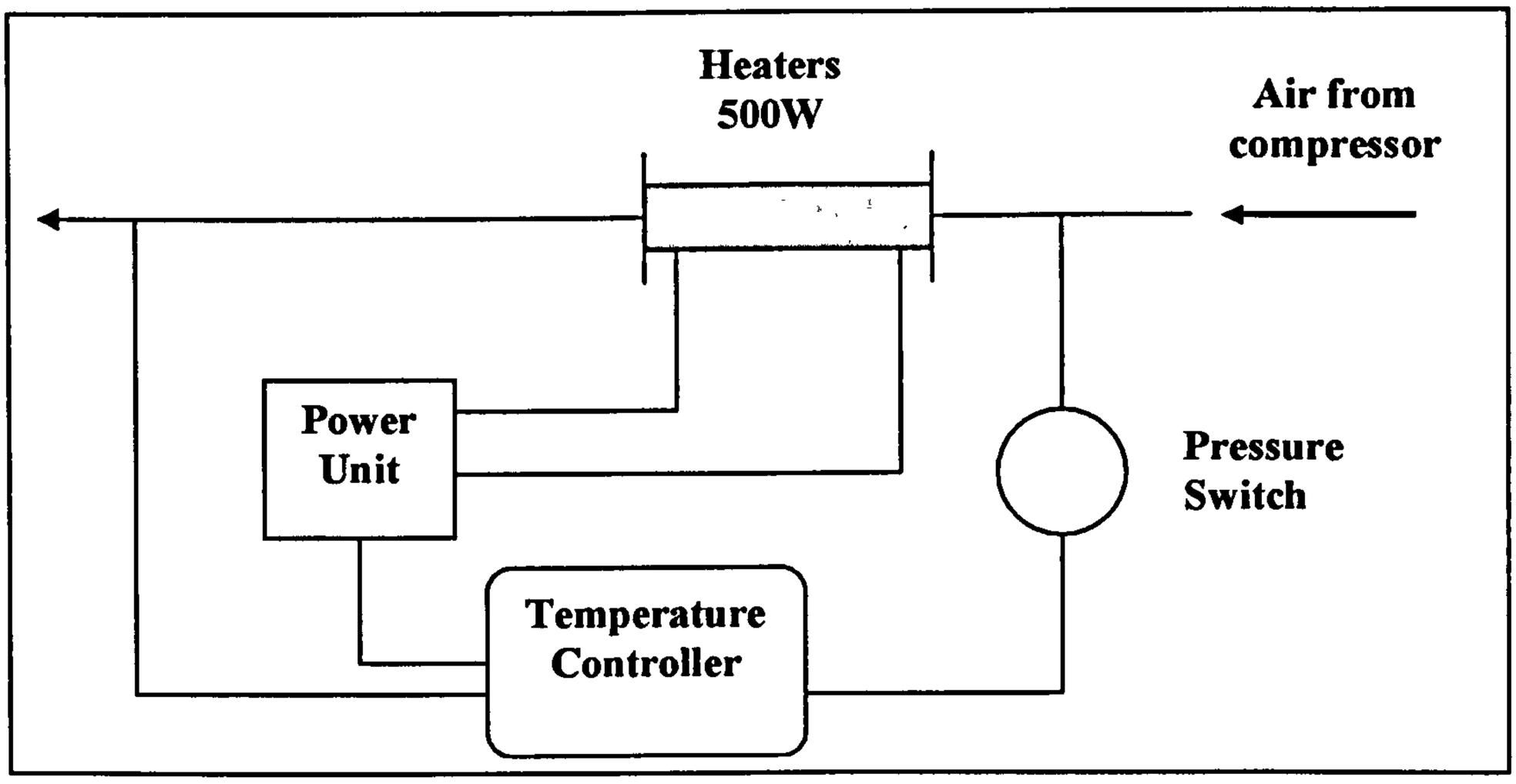

Figure 5.10: The set-up of air heaters with in-built temperature control.

5.1.2.10 Flow Meter

The nitrogen was supplied from a compressed nitrogen cylinder. The nitrogen flow rates were controlled by Platon LG series of miniature Glass Tube VA flowmeters. The glass flow tubes have 30mm scale length and measure air flow range up to a maximum of 25l/min and an accuracy of ±5% FSD.

5.1.2.11 Steam Supply Line

Saturated steam at temperatures of 103-105°C and absolute pressures of 1.13-1.18bar was supplied from the boiler through well insulated pipelines as shown in *Figure 5.11*. The steam was superheated on entry to the furnace as the furnace temperature was maintained above 400°C. Stream traps were placed at the pipes before valve V3 and V12 to drain any condensed water from the steam. A pressure regulator (PR) was installed just before valve V7 to maintain a stable flow of steam and avoid any surge increase or decrease of steam from affecting the flow. Valve V11 is used during the calibration of the flow through the orifice plate. The steam pipelines were insulated from the boiler to the fixed bed gasifier unit. The differential pressure or "head" created by the orifice plate was measured using a water manometer. An air trap between the pipeline from the orifice and the manometer avoided steam flowing into the manometer and condensing.

One of the main problems encountered is the formation of condensate on the pipe line connecting valve V5, V6, V8 and V9. The small diameter pipelines provide a high surface

tension in the condensed water droplets, causing a blockage in the pipelines. This affects the reading of the manometer. Therefore, valves V6 and V9 were installed to flush or drain any condensate formed before manometer measurements were taken.

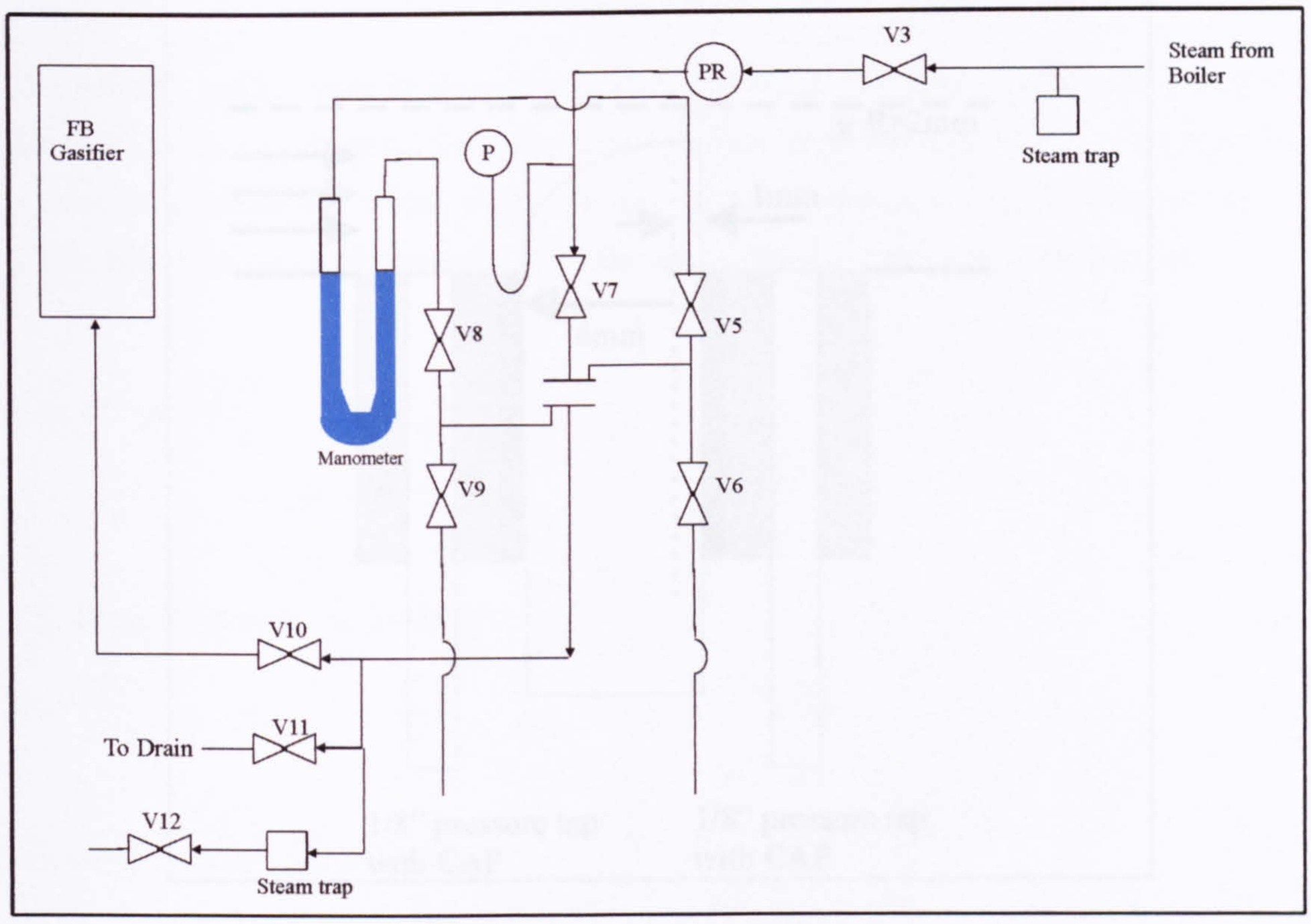

Figure 5.11: Schematic diagram of steam pipelines to the fixed bed gasifier.

5.1.2.12 Steam Orifice Plate

For simplicity in design and economic reasons, an orifice plate was used to create a differential pressure that is measured using a water manometer. The differential pressure across the restriction created by the orifice plate was calibrated to the fluid flow rate. One of the important tasks during the design was to select the appropriate orifice plate and size. Due to the small flow rate of steam (<0.15m³/min), the quadrant orifice was chosen. Calculations were carried out to determine the appropriate orifice size. An orifice size that is too large in diameter will result in too small a differential pressure to be measured accurately and vice versa. *Figure 5.12* shows a sketch of the dimensions of the steam orifice plate. The steam orifice plate was inserted into a pipe of 19.05mm in diameter and the pipe was clear of bends and tees to avoid any disruption to the flow.

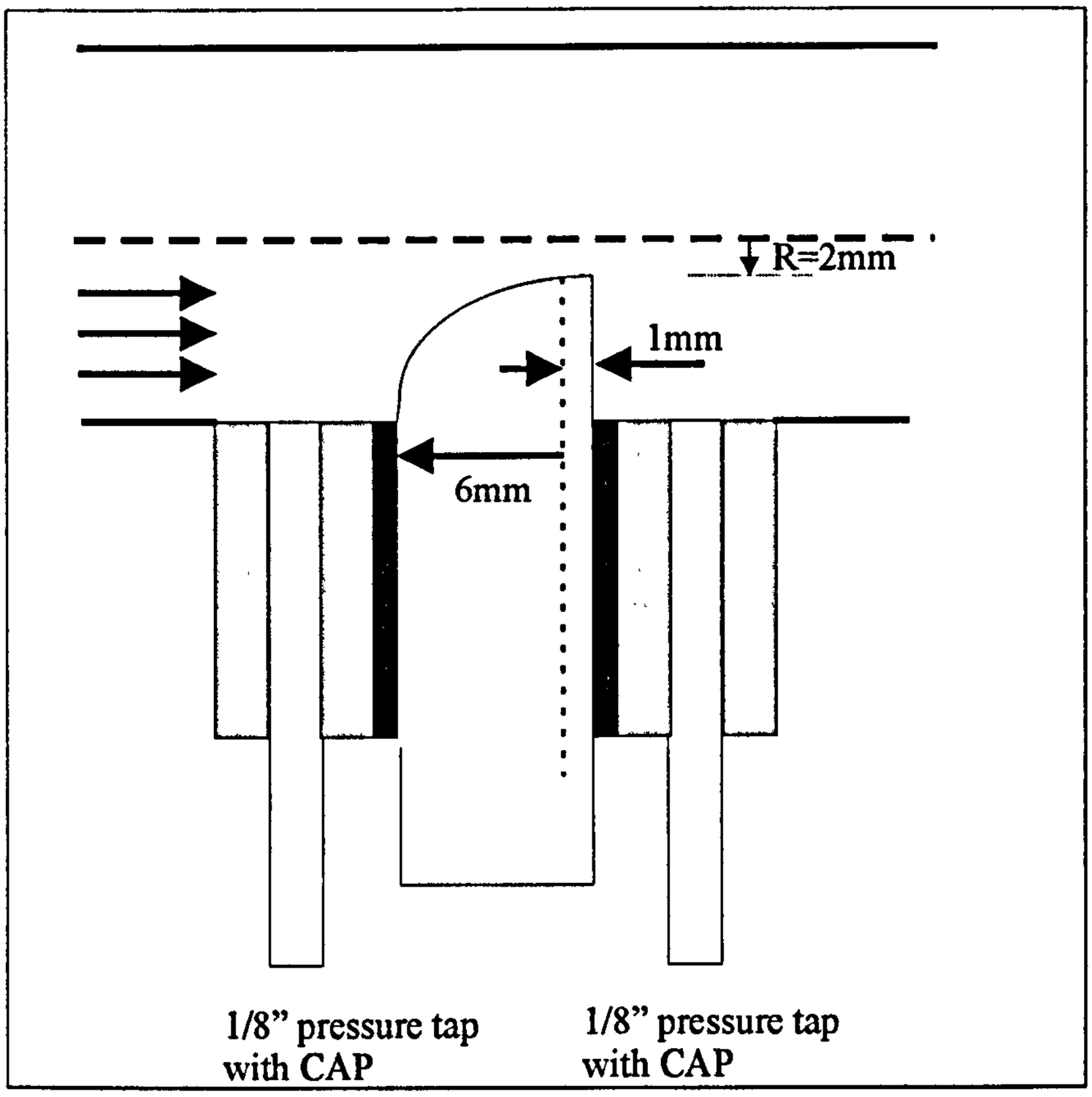

Figure 5.12: Sketch of steam orifice plate.

5.1.2.13 Design Equations

The design of the orifice plate was calculated using equations given by Ower (1984). An initial value of orifice diameter was assumed to calculate the differential pressure head. The manometer height used measures a differential pressure head of 2m. Therefore, iterations of the calculation with different orifice diameter were carried out to obtain a differential pressure head of <2 m. The equations below shows the calculation carried out in Microsoft Excel.

Diameter of the pipe, D = 0.01905 m

Diameter of the Orifice Bored, d = 0.005 m

Area of pipe, a1 $= \pi\left(\frac{D}{2}\right)^2$

$= 2.85 \times 10^{-4}\ m^2$

Orifice area, a2 $= \pi\left(\frac{d}{2}\right)^2$

$= 1.96 \times 10^{-5} m^2$

Ratio of pipe area to orifice area $= \frac{a1}{a2}$

$= 6.89 \times 10^2$

The velocity and pressure levels as the fluid leaves the orifice with kinetic energy partially converted back into potential energy according to the laws of conservation of energy. The permanent pressure loss is due to friction and the loss is a function of the diameter of the orifice bore (d) to the pipe diameter (D). This ratio (d/D) is known as the beta (β) ratio.

$$\text{Beta } (\beta) \text{ ratio} = \frac{d}{D}$$

$= 0.26$

The Reynolds number is given by:

$$\text{Re} = \frac{\rho u d}{\mu}$$

Where, ρ = density of steam (kg/m^3)

u = flow velocity (m/s)

d = orifice diameter (m)

μ = viscosity of steam (Ns/m^2)

The Reynolds Correction is given by:

$$0.0029(\beta)^{1.25}\left(\frac{10^6(\beta)^{0.5}}{\text{Re}}\right)^{0.75}$$

The coefficient of discharge C is defined in the following equation:

$$\text{Discharge Coefficient, } C = 0.5959 + 0.312(\beta)^{1.05} - 0.184(\beta)^4$$

The differential pressure or "head" developed between the two measurement locations is as follows:

$$\text{Head meter} = \left(\frac{m}{C(a_2)}\right)^2\left(\frac{1-\beta^2}{2\rho}\right)$$

Where m = mass flow rate of steam (kg/s)

The calculations were repeated using different orifice size and steam flow rate (based on temperature of 100°C and atmospheric pressure) and the results are as tabulated in *Table 5.3*.

Orifice Diameter (mm)	Pressure head (m)		
	Steam flow rate = 0.5 m^3/min	Steam flow rate = 0.1 m^3/min	Steam flow rate = 0.15 m^3/min
4.0	34.05	136.29	306.73
4.5	21.19	84.84	190.96
5.0	13.84	55.45	124.85
5.5	9.40	37.69	84.89
6.0	6.59	26.96	59.61
6.5	4.74	19.07	42.98
7.0	3.49	14.05	31.69
7.5	2.61	10.55	23.81
8.0	1.99	8.04	18.00

Table 5.3: Calculated pressure head for various orifice diameters and steam flow rate.

A literature review was carried out to provide a guideline in selecting the appropriate range of steam flow rate. Hobbs (1992) presented the operating parameter for different gasifiers ie, Lurgi, Absoloka and Jetson. The volume ratios of steam to air used are in the range 25-45%.

Based on the calculations and literature review, the orifice size was designed with a 4mm diameter as it provides the operating range required by the gasifier and a "head" of liquid within the measurement of the manometer.

The theoretical design of the steam orifice plate was confirmed with experimental calibrations. The flow restriction through the orifice plate causes a differential pressure to be developed and this differential pressure was measured using a manometer. The calibration was carried out by measuring the differential pressure/ head meter across the orifice and collecting the steam flow, which has passed through the orifice plate, into a bucket of water for a certain period of time. The bucket of water was weighed before and after the collection of steam in order to measure the steam flow rate. This was repeated for different steam flow rates.

The flow rate through an orifice can be said to be proportional the square root of the head pressure, *h* exerted by the liquid at the orifice. It was found from *Figure 5.13* that the experimental steam-flow rate obtained agreed well with the theoretical prediction that the steam flow rate is proportional to the square root of the head pressure.

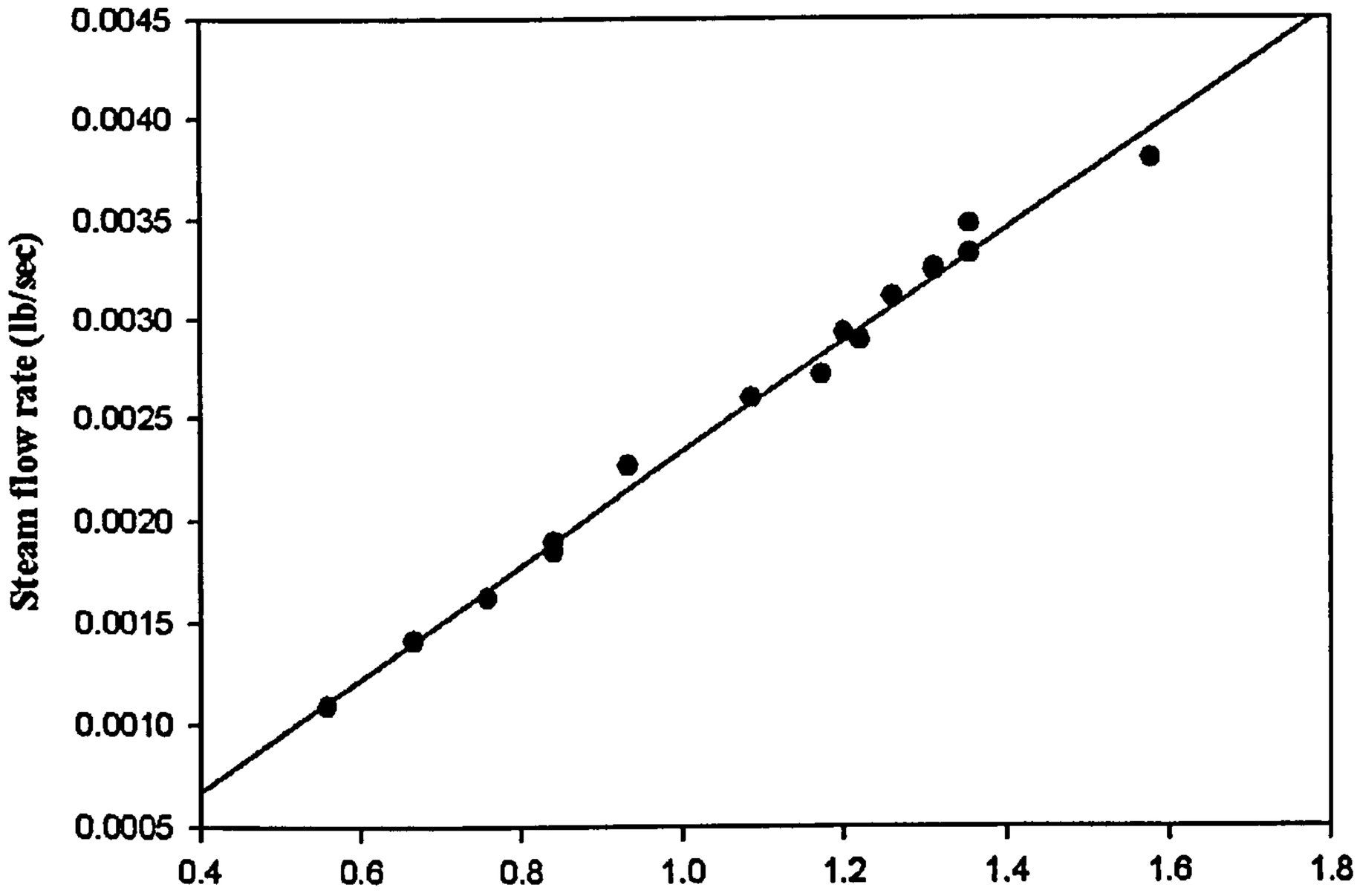

Figure 5.13: Experimental data for steam orifice plate calibration.

5.1.2.14 Condenser and Cooler

The flue gases exit from the top of the furnace and flow through a 1-inch diameter pipe to the two condensers. The condensers used are shell and tube units (single pass with i.d. 2.54cm and a total exchange surface area of 0.08m² for each unit). Valves were located at the bottom of each condenser to discharge the liquid phase. A gas sampling port was placed at the top of the second condenser in case the collection gases were required for analysis. The gases from the condenser are directed to the gas-chromatogram (GC) and MGA gas analyser. The mechanical drawing of the condenser is found in *Figure 5.14*.

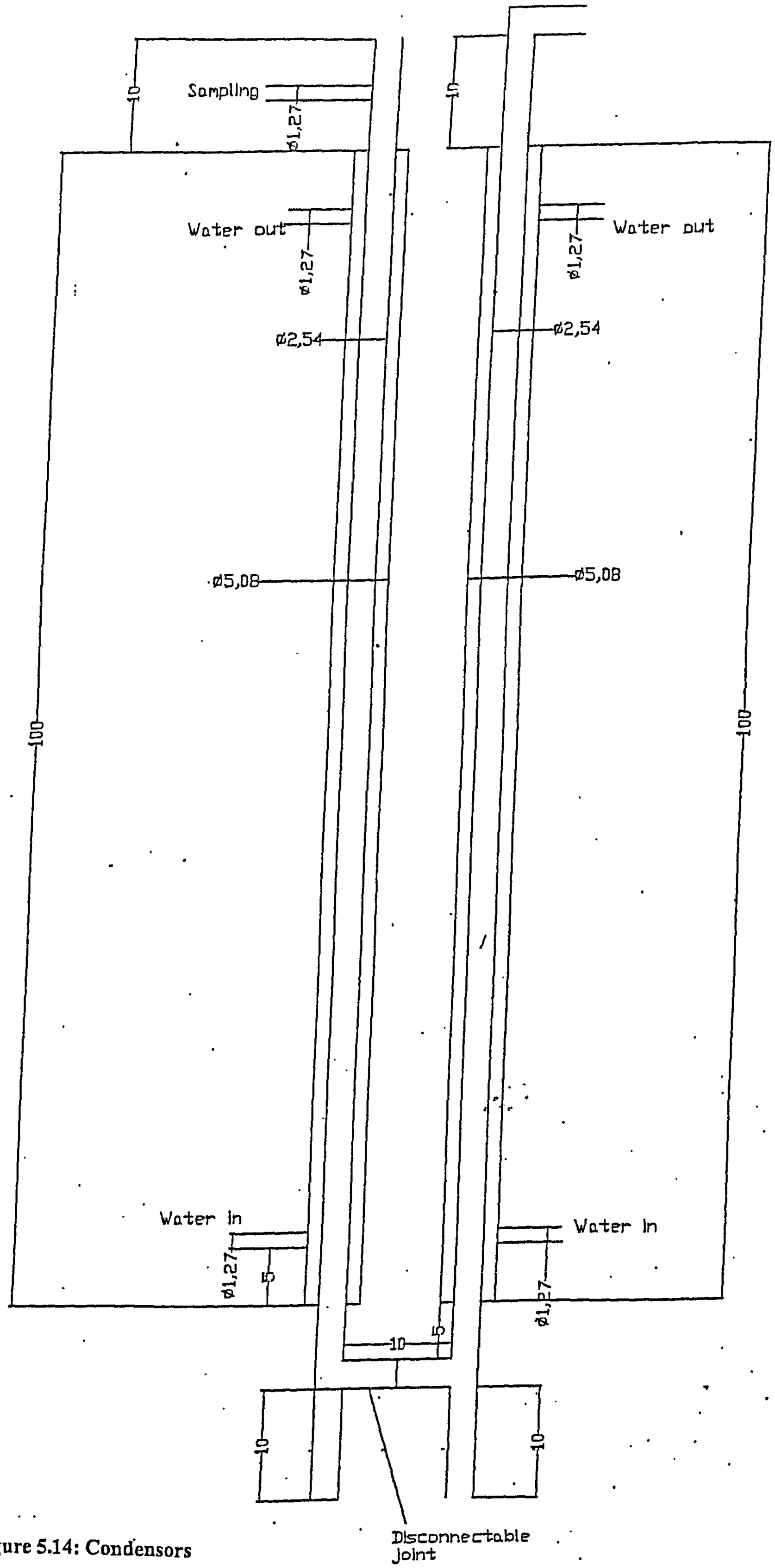

Figure 5.14: Condensors

All units are in cm.
25/10/04

5.1.2.15 Weighing Beams

The gasifer was suspended from 2 weighing beams, which incorporated 2 x 100kg capacity load cells per beam giving a total maximum load of 400kg. The weighing beams were used to monitor the weight changes (loss) during the gasification process. The pipes connecting the air supply to the gasification chamber were made from flexible hoses to prevent the thermal expansion of the furnace from interfering with the weighing equipment. Continuous measurements of weight were performed with computerised recording of data. The weight was also shown on an indicator and monitored throughout the experiment.

5.1.2.16 ABB Gas Chromatograph

An online process gas chromatograph (PGC2000) by ABB was used for continuous monitoring of the flue gas concentration. The gas chromatograph separates and measures the individual components of gas samples. Two types of thermal conductivity detector (TCD) are used in this analyser, a filament TCD and a thermistor TCD.

The filament TCD works on the principle that a heated body loses heat dependent on the composition of the surrounding gas. Filaments sense the rate of heat loss so that any change in filament current results in a bridge output proportional to the change. The TCD contains a reference filament and a measurement filament. When the reference carrier gas flows across both filaments, the two filaments have the same filament temperature and the bridge has a zero output. During a measurement cycle a sample flows past the measurement filament, changing thermal conductivity and the filament temperature, thereby, causing a corresponding change in electrical resistance. The bridge senses this change in current and increases or decreases current flow through the bridge to compensate for the temperature change. The change in current flow sensed by the bridge is proportional to the component concentration in the sample being measured.

Hydrogen, nitrogen and helium were used as carrier gases to purge the columns and cell prior to introducing a sample, to sweep the sample into the detector cell, and to backflush the backflush column. The gas chromatograph has 10 columns and each column has one of the four types of coating, Hayesep Q 60/80, 5A Sieves 40/60, Chromosorb 103 (KOH washed tubing) or Hayesep T, 60/80 and 0.3% Carbowax 20M/0.1% H_3PO_4 Carbopack C, 60/80. The carrier gas pressures were set to 49.5PSIG for nitrogen, 57.5PSIG for hydrogen and 46.5 and 88 PSIG for helium while air supply was set to a pressure of 60PSIG.

The electrical output signal from the detector represents the component inputs proportionally. The accuracy of the measurements is dependent on the accuracy of the span gas which in this case is 5% of the range. The 10 components were measured using two method tables that run simultaneously on a master and slave loop to reduce the cycle time. Method table 1 and 2 operates on a cycle time of 570s and 530s respectively. These two method tables are listed in *Table 5.4*.

The analyser takes in 4 samples every 9.5 minutes. There are 5 valves in the oven. Valves 1, 2, 4 and 5, besides also back flushing unwanted components from the measured sample, all inject samples into the various columns. Valve 1 injects at 5 seconds for the measurement of H_2. Valve 2 injects at 35 seconds for the measurement of NH_3. The components pass through detector 1 and use method Table 1 (Master). Valve 5 (method 2-Slave) injects at 5 seconds for the measurements of CO_2, H_2S, COS, C_3H_8 and HCN and pass through the second detector.

Both the master and slave methods start at the same time for every analysis cycle. The slave ends a second before the master and then waits for the master to restart its cycle.

Method Table 1		
Time	Component	Span calibration (%)
092	H_2	30
177	O_2	2
204	N_2	77.4
271	CH_4	8
303	CO	20
440	NH_3	4
Method Table 2		
185	CO_2	20
291	H_2S	0.4
348	COS	0.2
414	C_3H_8	1
505	HCN	0.001

Table 5.4: Components measured and the respective span calibration for the gas chromatograph (PGC2000).

5.1.2.17 MGA 3000 Multi-gas Analyser

The MGA 3000 gas analyser used for this experiment is similar to the one used for continuous monitoring of the flue gas concentration in the fixed bed combustion. Detail specification of this equipment is given in *Section 4.1.1*.

5.1.3 Experiment Measurement Accuracy

The accuracy of the equipment used in this experiment are summarised in *Table 5.5*. As some of the equipment employed in the fixed bed gasifier are similar to the ones used for the fixed bed combustion in Chapter 4, only equipments that have no previous examples are described in this section to avoid repetition.

Equipment	Accuracy
K-type thermocouples	±0.0075 of the actual temperature/±2.5°C
Weight measurement	±10g
Platon LG	±5% FSD = ±1.25%lit/min
KDG Mobrey	±2.5% FSR = ±5lit/min
Steam flow rate (from calibration)	Standard deviation of flow = ±0.000812 Linear regression = 0.9917
MGA 3000 gas analyser	Span gas accuracy: ±2% Response time: 90s
ABB Gas Chromatograph	Span gas accuracy: ±5% Samples taken every 10 minutes

Table 5.5: Accuracy of equipment used.

The temperature controllers for both the furnace heaters and air pre-heater operate as a three mode proportional-integral-derivative (PID) controller. This provides quick acting corrective control of the process variables. The PID controller eliminates steady state error, reduce overshoot and settling time. The disadvantage of using this type of controller is that it increases the heating up time.

As explained in *Section 4.1.2*, the weight measurement is affected by the thermal expansion of the furnace. As the furnace was suspended from a weighing scale at the top, the expansion would be restricted by the pipeline connected at the bottom. This results in an upward force

and causes a false reading as it 'reduces' the weight of the furnace as the temperature increases. The readings from the weight measurement are critical in the calculation of the char conversion rate. Two approaches are adopted in the calculation of the conversion rate to minimise the effect of the thermal expansion on the accuracy of the results. In the gasification experiments, the bed temperature is fairly stable, fluctuating in a small range of about 30°C as the bed approaches equilibrium. The burning rate is measured over this period of time when the temperature is fairly constant. To minimise any errors, the burning rate is taken over a longer period of time. As the weight loss due to the gasification reactions increases over time, this reduces the influence of the weight fluctuation caused by thermal expansion and provides a more accurate representation of the actual burning rate. Mass balance calculations were carried out based on the flue gas outlet to further confirm the char conversion rate.

5.2 CHARCOAL SAMPLES

5.2.1 Preparation of Charcoal Samples

The gasification experiments were carried out using commercial lumpwood charcoal that was broken to sizes of 3-4 cm diameter as shown in *Figure 5.15*.

Figure 5.15: Charcoal samples used for the gasification experiments.

5.2.1.1 Composition of Charcoal samples

The proximate analyses were carried out based on the ASTM (American Society of Testing Material) method. The CHN analyses were carried out at the Department of Chemistry, University of Sheffield. The composition of the samples was determined using the Perkin Elmer 2400 CHNS/0 Series II Elemental Analyser, which used a combustion method in a pure oxygen environment to convert the accurately weighed sample into simple gases CO_2,

H_2O, N_2 and SO_2 (*Appendix A.2*). The tolerance levels laid down in this analytical method was 0.3% for organic samples.

Fresh Charcoal		Sample 1	Sample 2	Sample 3	Average	Standard Deviation	95% Confidence
Proximate Analysis (%wt)	Moisture	5.21	4.96	4.84	5.00	0.19	±0.60
	Volatile	18.96	19.73	18.82	19.17	0.49	±1.56
	Ash	6.08	5.97	6.08	6.04	0.06	±0.20
	Fixed Carbon	69.75	69.34	70.26	69.79	0.46	±1.47
Gross Calorific value (MJ/kg)		26.45	26.83	26.69	26.66	0.19	±0.61
CHN Analysis (%wt)	Carbon	72.10 ± 0.3%					
	Hydrogen	2.05 ± 0.3%					
	Nitrogen	0.44 ± 0.3%					
	Oxygen	14.37 *					

*by difference

Table 5.6: Composition of the commercial lumpwood charcoal.

Charcoal Remaining from the Experiment		Sample 1	Sample 2	Sample 3	Average	Standard Deviation	95% Confidence
Proximate Analysis (%wt)	Moisture	2.57	3.22	2.53	2.77	0.39	±1.23
	Volatile	10.60	10.99	10.39	10.66	0.30	±0.97
	Ash	3.75	3.74	3.51	3.67	0.13	±0.43
	Fixed Carbon	83.08	82.05	83.57	82.90	0.77	±2.49
Gross Calorific value (MJ/kg)		30.49	30.56	30.57	30.54	0.04	±0.14
CHN Analysis (%wt)	Carbon	83.63 ± 0.3%					
	Hydrogen	1.55 ± 0.3%					
	Oxygen	8.38*					

*by difference

Table 5.7: Composition of the charcoal remaining from the gasification experiment.

Table 5.6 and Table 5.7 give the composition of the commercial lumpwood charcoal before and after heating. The oxygen and fixed carbon were determined by difference. The proportion of carbon in the charcoal remaining after the gasification experiment increased to about 83% compared to the 72% in the fresh charcoal. About 50% of the initial moisture and volatiles in the fresh charcoal were removed, resulting in a higher calorific value in the char after the gasification. No sulphur was detected in any of the samples. A small trace of nitrogen was found in the fresh charcoal samples.

5.3 EXPERIMENTAL PROCEDURE

Figure 5.16 shows the flow diagram of the experimental setup of the rig. The start up and shut down procedures are described in the following section.

Due to the complex characteristics of this fixed bed gasifier, several trial runs were carried out before determining a start-up procedure. One of the main problems was the formation of condensation in the pipe line connecting valves V5, V6, V8 and V9. Before any measurement of steam was carried out using the manometer, any condensate was flushed/drained out of the pipeline by opening valves, V3, V6, V7, V9 and V11 and shutting valves V5, V8 and V10. Valves V6 and V9 are then shut while valves V5 and V8 are opened to measure the differential "head" developed due to the flow restriction by the orifice plate using the manometer.

Complications were also encountered due to the time limit of the experimental work. For safety reasons, the experimental work could not be conducted out of the normal working hours. Therefore, each experiment was constrained to an 8 hour run. The gasification is a relative slow process compared to combustion or pyrolysis and requires a long period of time to achieve a stable condition. The initial start up period (purging of reactor and heating up of the charcoal bed) requires about 5 hours. However, the bed temperature after this time is only about 500°C and is not high enough for most of the crucial gasification reactions such as the water-gas reaction and water-shift reactions. Therefore, to shorten the preheating time and increase the bed temperature during the start-up, preheated air (175°C) was blown into the reactor for about 20mins to raise the bottom bed temperature to about 700°C.

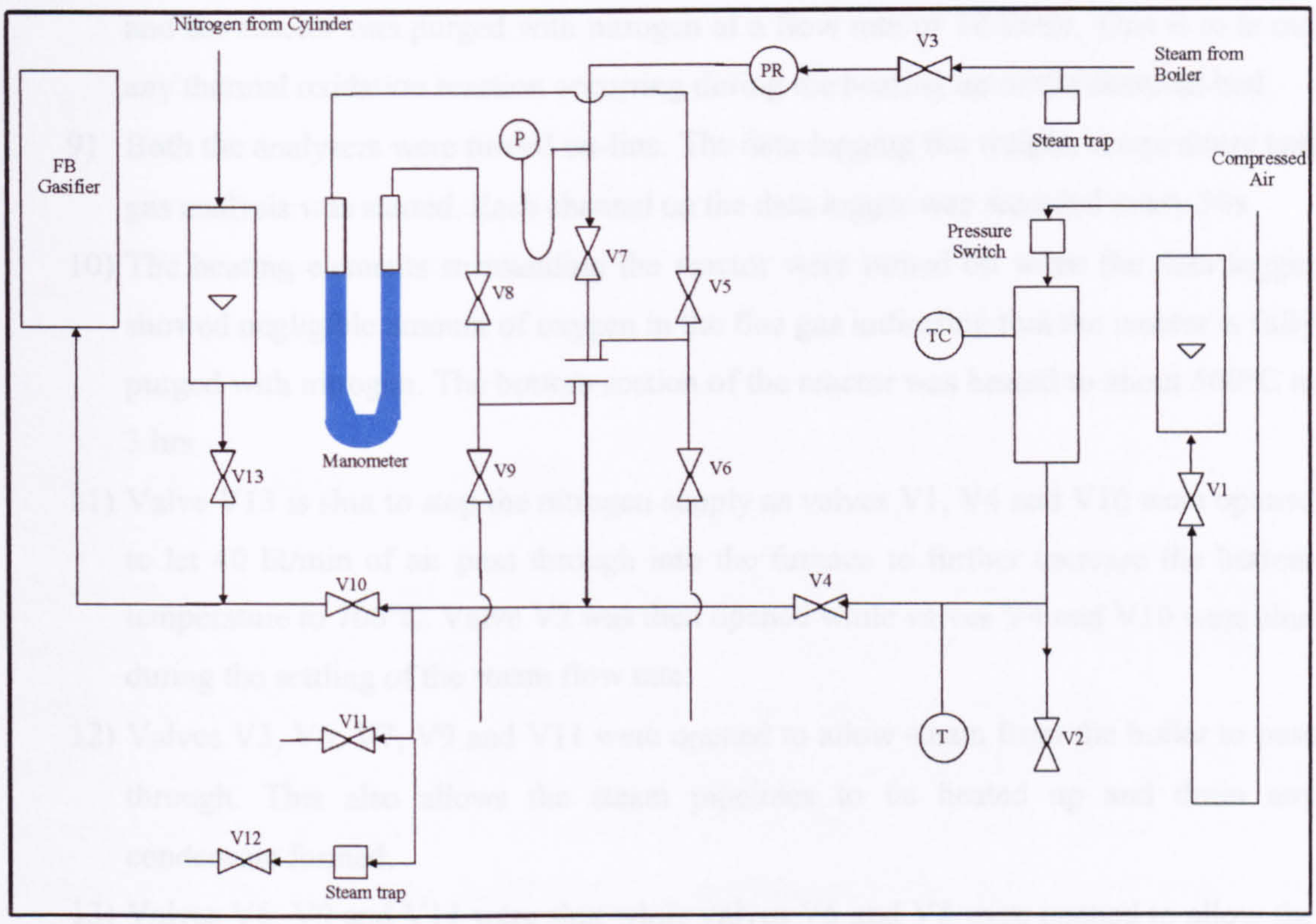

Figure 5.16 : Flow diagram of the fixed bed gasifier.

5.3.1 Start-Up Procedure

1) The analysers and pumps were switched on and left to warm up for 2 hours prior to the experiments. The tap water to the condensers was turned on.
2) The scale indicator was switched on and tare set to zero.
3) A known weight of pre-prepared charcoal sample was fed into the gasifier through the inlet point on the top. The bed height was measured using a long rod and the lid was then screwed on tightly.
4) The weight shown on the indicator was checked to ensure that the increase was the same as the sample weight.
5) The data logger was switched on and the thermocouple readings were checked. The thermocouples were then connected to a temperature indicator to check that the readings from the data logger were correct.
6) The exhaust extraction fan was switched on.
7) When both the MGA 2000 Multi-Gas Analyser and the Process Gas Chromatograph (PGC2000) were warmed up, they were calibrated with the calibration gas according to the instructions. The readings were then compared with the readings logged from the data logger.

8) All the valves were checked to ensure that they were shut. Valve V13 was opened and the reactor was purged with nitrogen at a flow rate of 10 l/min. This is to avoid any thermal oxidation reaction occurring during the heating up of the charcoal bed.
9) Both the analysers were turned on-line. The data logging the weight, temperature and gas analysis was started. Each channel on the data logger was recorded every 30s.
10) The heating elements surrounding the reactor were turned on when the data logger showed negligible amount of oxygen in the flue gas indicating that the reactor is fully purged with nitrogen. The bottom section of the reactor was heated to about 500°C in 3 hrs.
11) Valve V13 is shut to stop the nitrogen supply as valves V1, V4 and V10 were opened to let 40 lit/min of air pass through into the furnace to further increase the bottom temperature to 700°C. Valve V2 was then opened while valves V4 and V10 were shut during the settling of the steam flow rate.
12) Valves V3, V6, V7, V9 and V11 were opened to allow steam from the boiler to pass through. This also allows the steam pipelines to be heated up and drain any condensate formed.
13) Valves V6, V9 and V11 were shut while valves V5 and V8 were opened to allow the differential pressure from the orifice to be measured by the manometer through an air trap in the pipeline. The steam flow rate was manipulated using valve V7. After setting the steam flow rate, valves V5 and V8 were shut and valve V10 was opened to allow steam into the reactor. Valve V1 was used to set the air flow rate and V4 was opened to supply preheated air into the reactor.
14) The steam and preheated air flow rate was varied throughout the experiment by repeating Step 13. The steam and preheated air flow rate were kept constant for about 30-40 minutes for each case until equilibrium was reached.
15) The grate was rotated at intervals to allow for de-ashing. This was stopped as soon as specks of ignited particles were observed through the small window at the bottom of the furnace.

5.3.2 Shut Down Procedure

1) The heating elements surrounding the furnace were turned off.
2) The valves supplying air to the reactor (V1 and V4) were shut off.
3) Valve V3 was then turned off to shut the steam supply from the boiler. Valve V10 was then shut while simultaneously opening valve V11 to drain the remaining steam or condensate formed during the shut down.

4) The logging of weight, temperature and gas were stopped.
5) The analyser's connections were disconnected from the combustion port.
6) The MGA 2000 Multi-Gas Analyser was left for half an hour to flush out all the gas in it before switching off. The Process Gas Chromatograph (PGC2000) was turn off and left to cool down with a small purge of carrier gases.
7) The exhaust extraction fan was switched off followed by the tap water to the cooling towers.

5.4 OPERATING CONDITION

The experiments were carried out with approximately 4kg of fresh charcoal samples and a bed height of 30cm. Two or three cases with varying air or steam flow rates were carried out during each run. The bed height decreased when the experiment progressed, this led to a lower bed height for some of the later cases. According to Encinar (2001), the reaction rates are constant until the charcoal is exhausted as the reactions only occur on the surface in contact with the steam and that surface is approximately constant. Consequently, the influence of the bed height is relatively small as long as the bed depth was sufficient to allow all the gasification reactions to occur. The approximate bulk density of the bed was measured to be about 420kg/m^3.

Detailed measurements were made during the series of gasification experiments at varied air and steam flow rates. The air temperature was heated up to 175°C and steam was supplied at atmospheric pressure. The test runs are named according to the volume of each reactant supplied. For example, the "A40-S45" run refers to the gasification using 40lit/min of preheated air and with steam making up 45%wt of the total input reactants (air and steam). The furnace temperatures throughout the experiments were kept constant by external heaters. Two sets of experiments were conducted with different heating rates. 'S1' refers to the cases with the higher heating rate and a furnace temperature of about 850°C while 'S2' represents cases with a lower heating rate and furnace temperature of 650°C. The operating conditions for the cases are as shown in *Table 5.8*.

Air flow rate (lit/min)	Air flow rate (kg/m²hr)	Steam flow rate (kg/m²hr)	Steam wt%	Case Name
50	122.52	81.81	40	A50-S40 (S1)
70	171.57	140.38	45	A70-S45 (S1)
80	196.03	49.02	20	A80-S20 (S2)
80	196.03	84.03	30	S80-S30 (S2)
80	196.03	130.51	40	A80-S40 (S2)
90	220.60	94.54	30	A90-S30 (S1)
90	220.60	118.73	35	A90-S35 (S1)
90	220.54	147.06	40	A90-S40 (S1)
100	245.04	81.68	25	A100-S25 (S1), A100-S25 (S2)
100	245.04	105.05	30	A100-S30 (S1), A100-S30 (S2)
100	245.04	131.78	35	A100-S35 (S1)
100	245.04	163.30	40	A100-S40 (S1), A100-S40 (S2)
110	269.55	115.55	30	A110-S30 (S1)
110	269.55	145.15	35	A110-S35 (S1)
110	269.55	179.85	40	A110-S40 (S1)
120	293.94	195.96	40	A120-S40 (S1)

Table 5.8: Test cases and process conditions.

5.5 HEATING UP OF CHARCOAL

The analysis of raw charcoal shows that it contains a significant quantity of volatile material which will break down to gas and condensable vapours during initial bed heating. The heating up of the bed materials (fresh charcoal) were performed under an inert environment (a continuous flow of nitrogen was applied to avoid char oxidation) before the gasification experiments were carried out with the introduction of steam and air. Some investigations exist in the literature regarding the effects of pyrolysis on char reactivity. The composition of the product gases were reported to be dependant on the ambient atmosphere of the heat source. Pyrolysis carried out in hydrogen gave C_2H_2 and CH_4 as the main products whereas, the product would mainly be carbon monoxide and hydrogen if steam was used (Albal *et al*, 1989). Char made with high pressures and high heating rates was found to have apparent reaction rates in CO_2, H_2O and O_2 that are orders of magnitude faster than those of char made from the same coal at atmospheric pressure and slow heating rate condition (Roberts et al, 2003). The effect of the pyrolysis of biomass on the product composition was investigated in

detail by Shafizadeh (1985). Pyrolysis at lower temperatures (below 300°C) favours the production of char, water, CO_2 and CO. Whereas heating at higher temperatures (300-500°C) favours the formation of tar that interacts with water and carbon dioxide formed previously to provide a mixture of low-molecular weight gaseous or volatile products. There is also a possibility of the conversion of char directly to low-molecular weight gases. The reaction products are lumped into three main classes (liquids, char and gas) whose relative amounts and composition are strongly dependant on the heating rate, reaction temperatures and also the conversion unit (Di Blasi, 1993; Chen et al, 1997).

Figure 5.17 shows an example of the temperature history within the bed during the heating up of fresh charcoal prior to the gasification for cases (S1). The average heating up rate of 5 tests measured at position T8 in the centreline of the bed (y=206mm) is 10.74±2.16°C/min. This rate was about 4 times faster compared to the heating up rate at T1 (y=6mm) of 2.59±0.98°C/min. A slow rise in temperature was observed at the bottom of the bed. This is due to the lack of insulation in the ash discharge section beneath the bed and also the required sensible heat to heat up the thick layer of charcoal materials at the bottom of the furnace. The heating up rates in this experiment are slow compared to 1000°C/s used in flash pyrolysis processes. Slow heating rates achieved by thick wood maximises the production of char and this is desirable especially for the gasification process (Di Blasi et al, 2001). Chars obtained from rapid pyrolysis possessed higher reactivity in the reaction with carbon dioxide and steam compared with chars obtained from slow pyrolysis (Chen et al, 1997). However, the primary degradation is only weakly affected by external heating condition given the intrabed temperature gradients (Scott et al, 1988). The temperature across the bed (T1 to T8) fell in the range of 500-900°C at t = 220min and this temperature was high enough to cause biomass degradation.

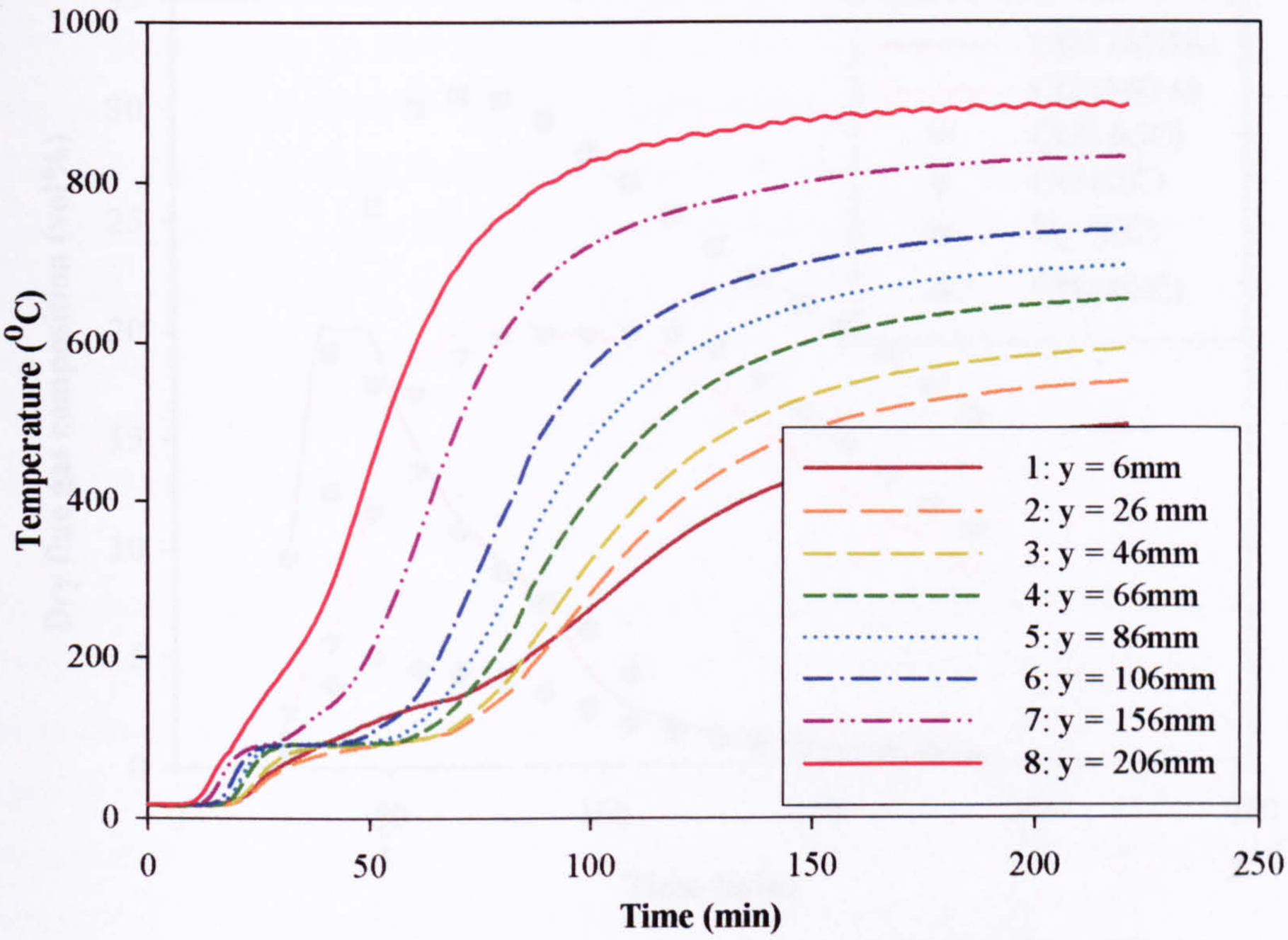

Figure 5.17: Temperature history within the bed during the heating up of charcoal (Case S1).

Figure 5.18 shows the dry flue gas composition as measured by both the gas chromatograph (GC) (dotted symbols) and the multi gas analyser, MGA 2000 (line curve) as a function of the bed temperature for case (S1). The remaining gas from the GC is nitrogen as a continuous supply of N_2 was flowed through the reactor throughout the heating up. The CO_2 measurements from the MGA 2000 showed a plateau from t = 34-46min, indicating instrument saturation as the maximum concentration measured by the analyser was 20%. The deviation in the readings between both the instruments was about 10%. The difference in readings is because of the lagging time (time required by the analyser to detect any changes at the sampling point) that is 30s for the multi-gas analyser and also because the ABB gas analyser measures over a cycle time of 590s. *Figure 5.19* shows the relation between the dry flue gas composition and the bed temperature at 2 positions, y=206mm (T8) and y=6mm (T1) for Case S1. The second x-axis at the top of the graph represents the temperature at y=6mm (T1) corresponding to the temperature at y=206mm (T8) at a particular time. This is to give an indication of the temperature distribution across the length of the bed as T8 is closest to the bed top while T1 is at the bottom of the bed.

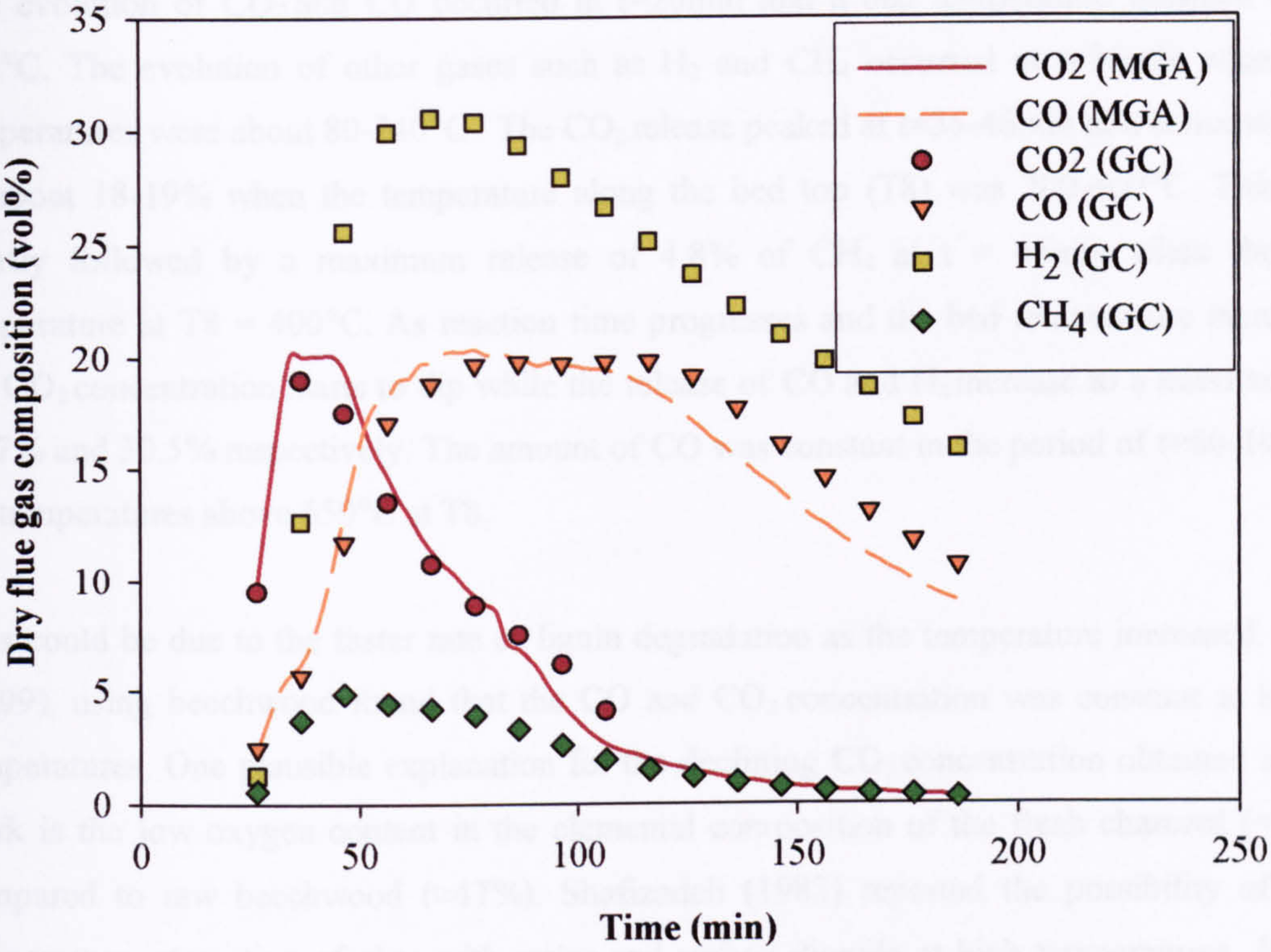

Figure 5.18: Dry flue gas composition vs the reaction time (Case S1).

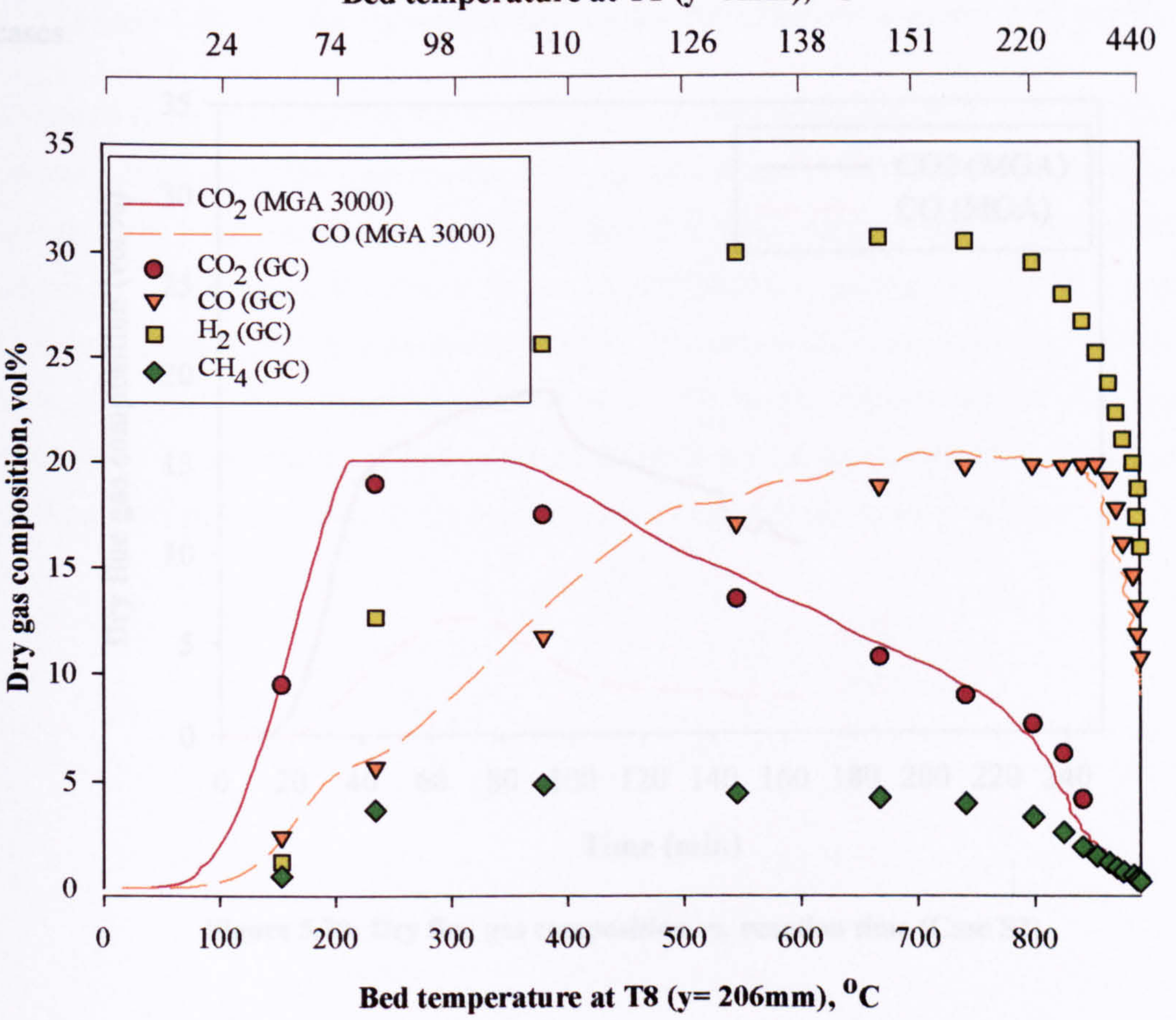

Figure 5.19: Dry flue gas composition as a function of bed temperature at T8 and T1 (Case S1).

The evolution of CO_2 and CO occurred at t=26min and a bed temperature between 60 to 100°C. The evolution of other gases such as H_2 and CH_4 occurred at t=36min when bed temperatures were about 80-240°C. The CO_2 release peaked at t=36-46min at a concentration of about 18-19% when the temperature along the bed top (T8) was 200-400°C. This was shortly followed by a maximum release of 4.8% of CH_4 at t = 46min when the bed temperature at T8 = 400°C. As reaction time progresses and the bed temperature increases, the CO_2 concentration starts to dip while the release of CO and H_2 increase to a maximum of 19.7% and 30.5% respectively. The amount of CO was constant in the period of t=60-100min for temperatures above 650°C at T8.

This could be due to the faster rate of lignin degradation as the temperature increased. Blasi (1999), using beechwood found that the CO and CO_2 concentration was constant at higher temperatures. One plausible explanation for the declining CO_2 concentration obtained in this work is the low oxygen content in the elemental composition of the fresh charcoal (≈14%) compared to raw beechwood (≈47%). Shafizadeh (1982) reported the possibility of high temperature interaction of char with water and carbon dioxide at high temperatures. *Figure 5.20* and *Figure 5.21* shows the dry flue gas composition as a function of reaction time and bed temperature respectively at slower heating rates cases (S2) compared to the previous cases.

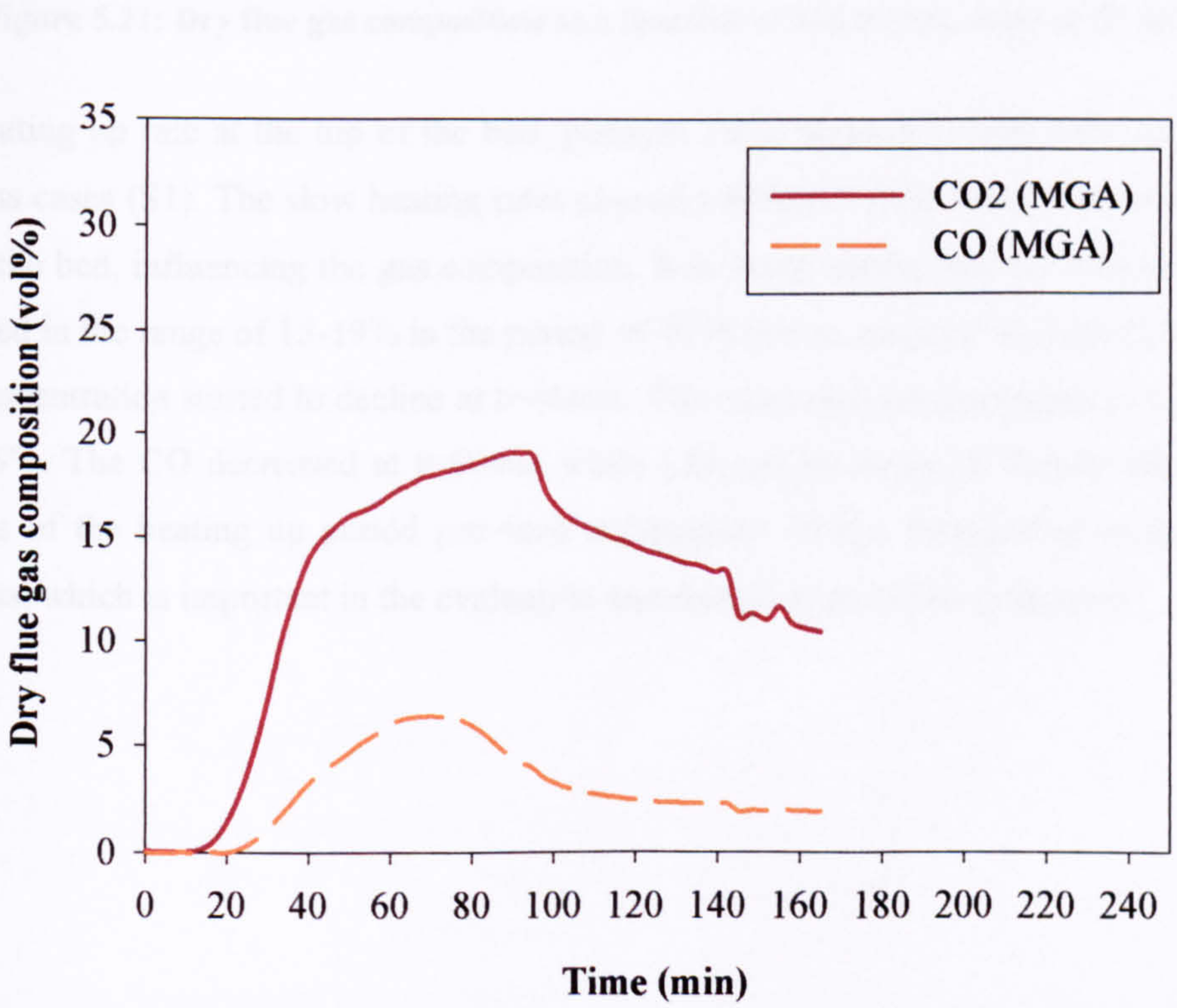

Figure 5.20: Dry flue gas composition vs. reaction time (Case S2).

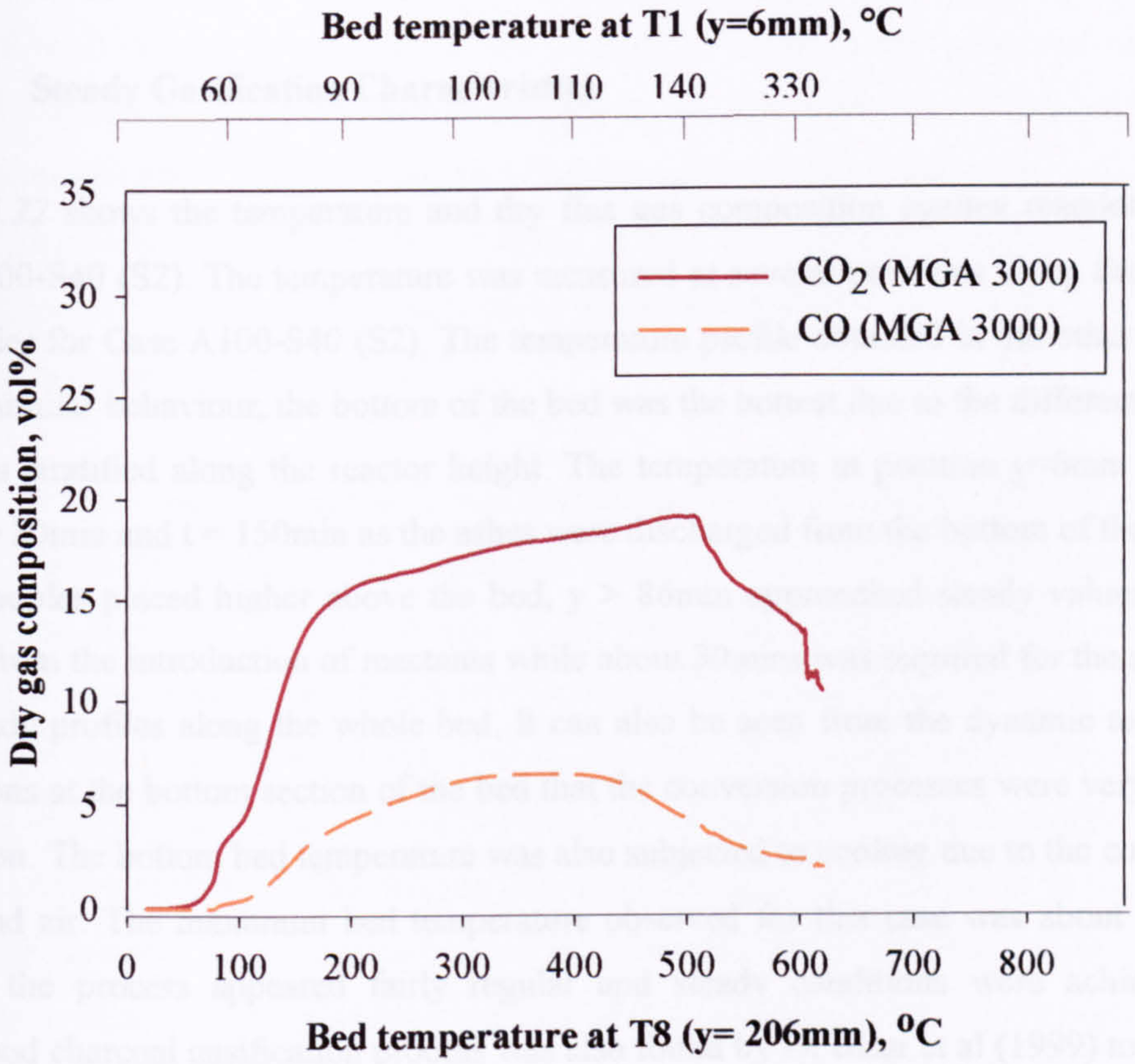

Figure 5.21: Dry flue gas composition as a function of bed temperature at T1 and T8.

The heating up rate at the top of the bed, position T8 is about 6°C/min, half the rate of the previous cases (S1). The slow heating rates caused a different differential temperature profile across the bed, influencing the gas composition. It is worth noting that the CO_2 concentration remained in the range of 15-19% in the period of 40-80min in contrast to cases (S1) where the CO_2 concentration started to decline at t=46min. The maximum concentration of CO was only about 6%. The CO decreased at t=80min while CO_2 release dropped 10mins after that. The analysis of the heating up period provided information on the distribution of the pyrolysis products, which is important in the evaluation and design of pyrolysis processes.

5.6 EXPERIMENTAL RESULTS AND DISCUSSION

5.6.1 Steady Gasification Characteristics

Figure 5.22 shows the temperature and dry flue gas composition against reaction time for Case A100-S40 (S2). The temperature was measured at several positions along the centre of the gasifier for Case A100-S40 (S2). The temperature profile obtained in the other test cases showed similar behaviour, the bottom of the bed was the hottest due to the different chemical processes stratified along the reactor height. The temperature at position y=6mm dipped at about t = 30min and t = 150min as the ashes were discharged from the bottom of the bed. The thermocouples placed higher above the bed, y > 86mm approached steady values in about 15mins from the introduction of reactants while about 30mins was required for the attainment of a steady profiles along the whole bed. It can also be seen from the dynamic temperature oscillations at the bottom section of the bed that the conversion processes were very active in this region. The bottom bed temperature was also subjected to cooling due to the contact with steam and air. The maximum bed temperature observed for this case was about 920°C. In general, the process appeared fairly regular and steady conditions were achieved. The beechwood charcoal gasification process was also found by Di Blasi et al (1999) to be highly reproducible with uniform bed structure.

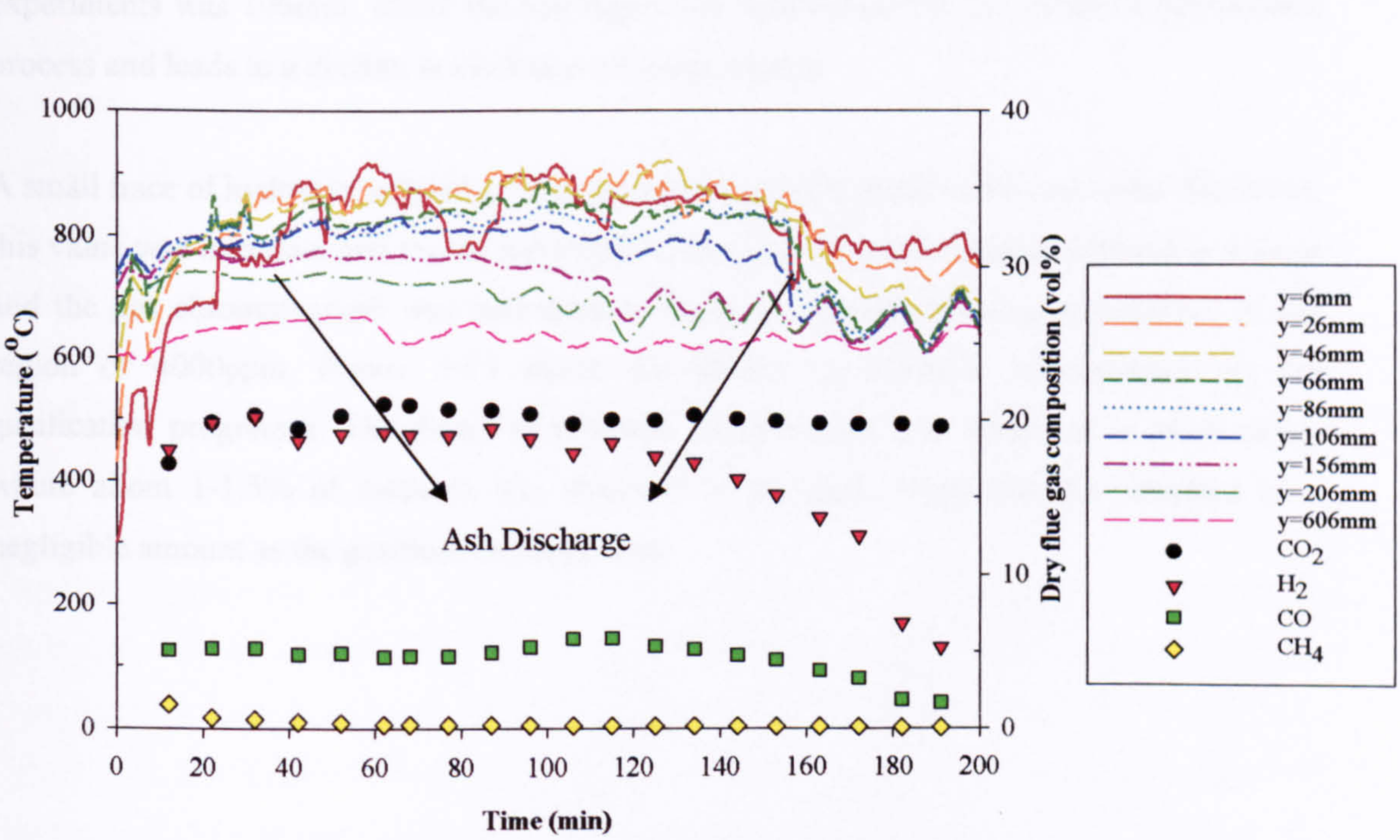

Figure 5.22: Temperature and dry flue gas composition as a function of reaction time (Case A100-S40 (S2)).

The thermocouple measurements reflect the cyclic heating of the furnace as the temperature controller regulates the temperature in the furnace to maintain the minimum set point of 650°C. Temperature at position y=606mm reflects the temperature in the freeboard region that is about 630-650°C. The consecutive thermocouples at y= 206mm, 156mm and 106mm were progressively exposed at time, t=84min, 114min and 120min respectively as the char was continuously consumed. The temperature measured by the thermocouples exposed to the freeboard oscillated in a range of 50°C.

Figure 5.22 also shows an example of the dry flue gas evolution during charcoal gasification (Case A100-S40(S2)). The gases contained the combustible and non-combustible gases, moisture and soot. The dry gas consists, apart from nitrogen, of carbon monoxide, carbon dioxide, hydrogen and a small amount of methane. The concentrations of CO, CO_2 and H_2 remained in the range of 4.5-5.5%, 19.5-20.5% and 17-20% and were fairly stable until t=270min. From *Figure 5.22,* CO and H_2 started to decline at t=155min from 6% and 19% to 5% and 1.6% at t=190min. The drop in CO_2 was less significant compared to the other two gases. The decrease in gas concentration that occurred when the bed height was below 106mm is confirmed in many of the cases carried out. In consequence, although the influence of bed height was relatively small, there is a minimum bed height, which in the case of these experiments was 106mm, where the bed depth was insufficient for the stratified gasification process and leads to a decline in evolution of product gases.

A small trace of hydrogen sulphide, <10ppm was detected in some of the test cases. However, this value was uncertain and maybe subjected to errors as the concentration detected is minute and the gas chromatograph was calibrated to measure a much higher concentration, in the region of 4000ppm. *Figure 5.23* shows the decline in methane concentration as the gasification progresses. The decay in methane concentration was observed in most cases, where about 1-1.5% of methane was detected in the early stage and this dropped to a negligible amount as the gasification progresses.

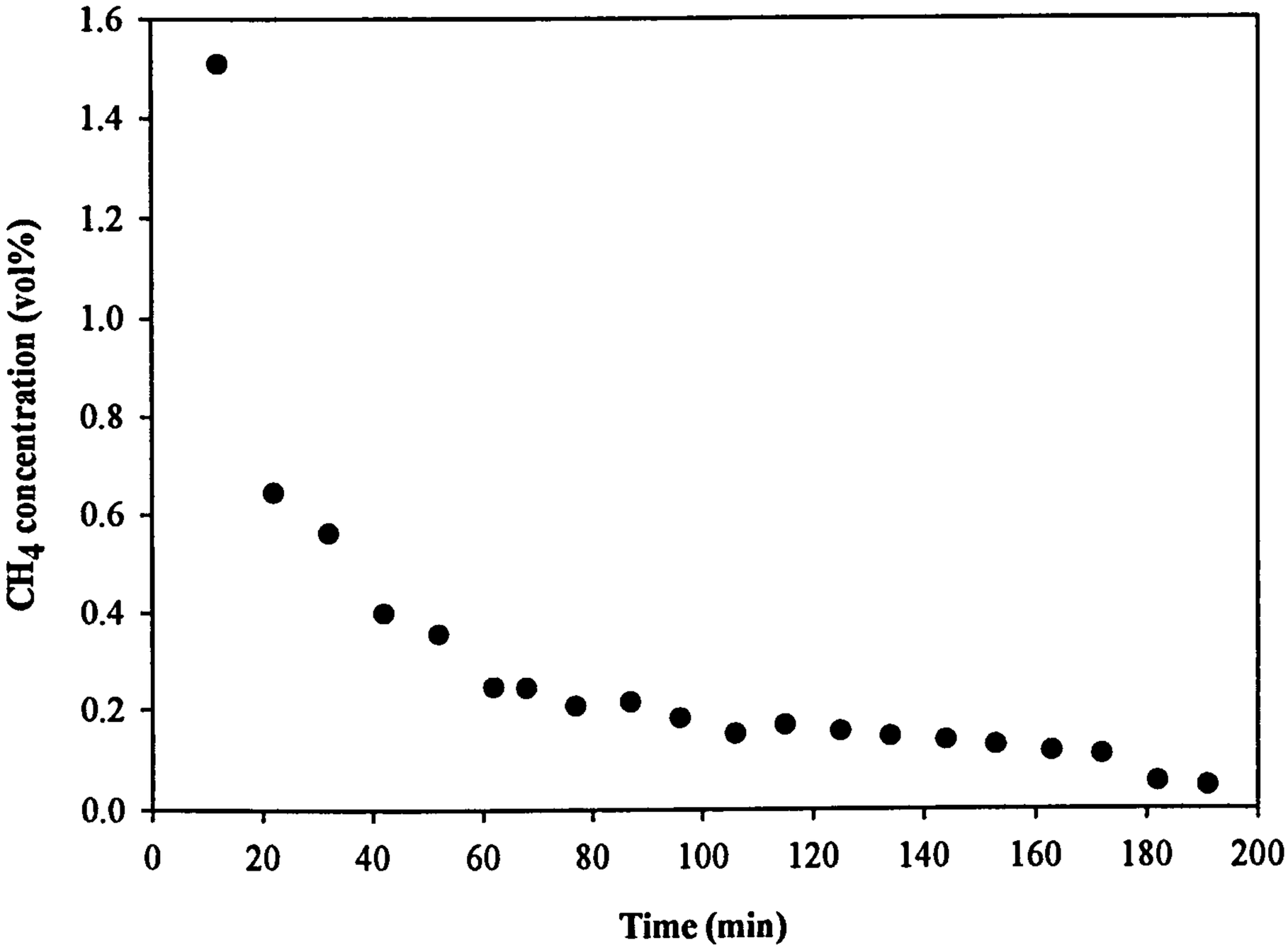

Figure 5.23: Methane concentration as a function of reaction time.

The measurement of the mass left on the bed was affected by the temperature of the furnace as the thermal expansion of the chamber is restricted due to the connection with a steam and air supply pipe line. As the temperature of the furnace increased, the chamber expanded and exerted a force on the pipe line which then produces an opposite force causing the weight measured to be less as the measurements were made from a chamber suspended on a weighing scale. More information on the effect of the thermal expansion on the weight measurement can be found in *Appendix A.3*. The load cells used in the weighing beams are also affected by temperature change but inaccuracy caused would be small as the load cells were placed at a considerable distance from the hot furnace in a well-ventilated room.

Therefore, it was important that the carbon conversion rate was determined over a long period of time whereby the temperature of the furnace was stable in order to obtain a higher accuracy. Example of the measured mass left on the bed as the gasification progressed is shown in *Figure 5.24*. The mass left on the bed fluctuated at 40 and 160min due to the movement of the furnace as the ashes were discharged. The mass loss decreased linearly with time and the standard estimate of error (SEE) which is a description of the scatter of the data about the linear line is low, 0.0176. The carbon conversion rate is defined as the rate of mass loss per unit area of grate per hour and is calculated from the slope of the graph. For this Case A100-S40(S2), the carbon conversion rate is found to be 28.65kg/m^{2}hr.

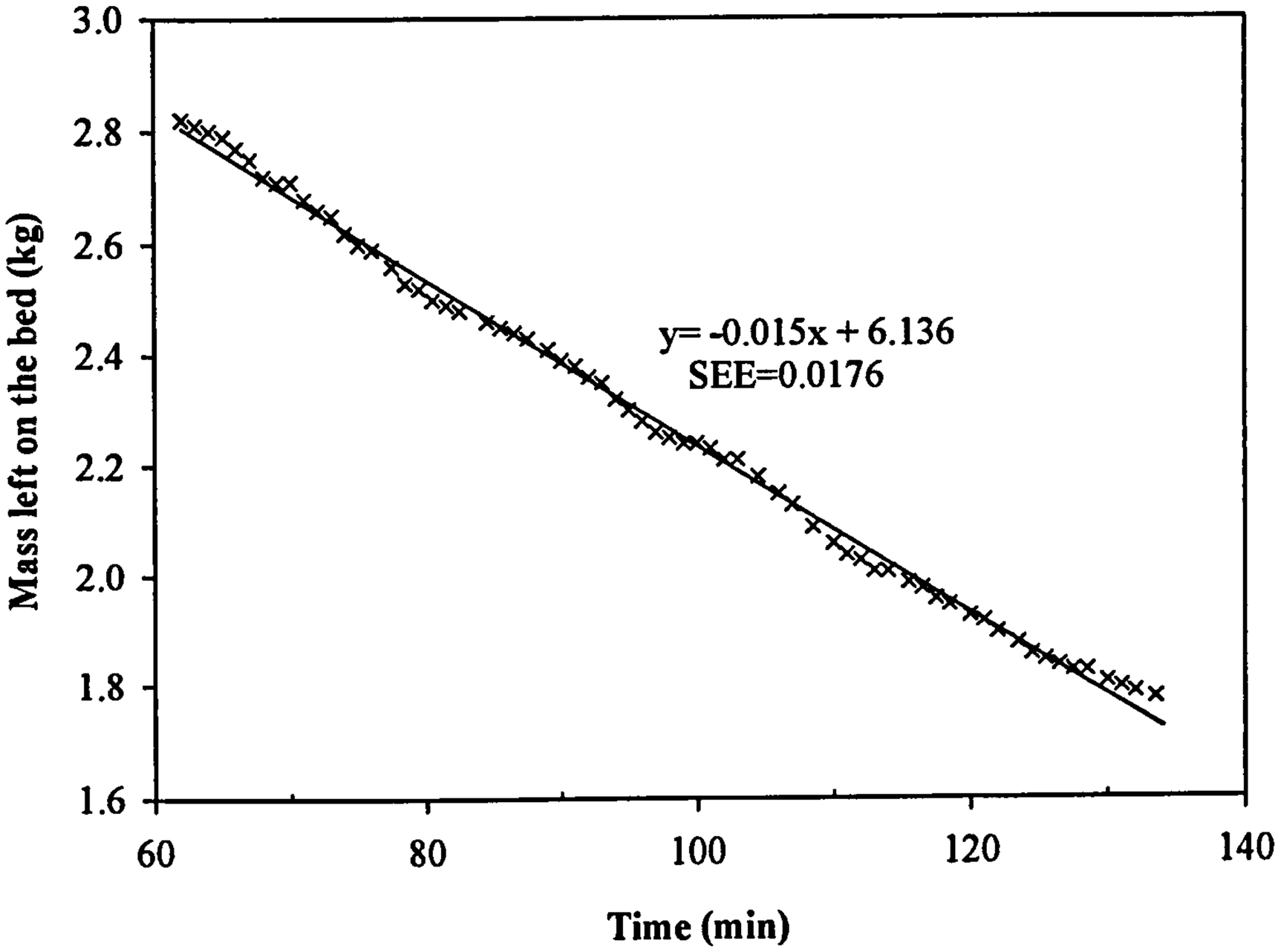

Figure 5.24: Mass left on the bed vs. reaction time (Case A100-S40 (S2)).

5.6.2 Effect of Reactants (steam/air) Flow on Gasification of Chars

5.6.2.1 Temperature

Figure 5.25 and *Figure 5.26* show the measured temperature across the bed height for Case A100-S25 (S1) and A100-S40 (S1) while *Figure 5.27* and *Figure 5.28* show the measured temperature during the gasification test at similar reactant flow rates but a lower heating rate (S2). The temperature profiles were given for time t=10, 20 and 30minutes after a steady condition was reached. The air flow rate was kept constant at 100l/min (245kg/m²hr) for all the four cases but the steam flow rate was increased from 25%wt (81kg/m²hr) to 40%wt (163kg/m²hr) at two different heating temperatures (S1) and (S2). As explained in Section 5.4, the heating temperature for (S1) is about 850°C and 650°C for (S2). The temperature profile above 200mm was not extrapolated as there was another data point at a distance of 606mm.

With reference to *Figure 5.25*, the hottest temperature was measured at the bottom of the bed, y=6mm in the range of 830-940°C. The temperature fell as the distance from the grate increased to about 150mm above the grate. However, further along the bed >150mm, the temperature started to escalate as it approached the bed top due to the heat from the freeboard. The temperature above the bed >300m varied in a close range for time t=10, 20 and 30min as

this temperature is determined by the external heaters. From *Figure 5.26*, the temperature at the bottom of the bed (y=6mm) increases from 730-760°C in 30minutes. The bottom temperature is about 100°C lower compared to the previous case of a lower steam flow rate, Case A100-S25(S1) *(Figure 5.25)*. Contrary to Case A100-S25(S1), a higher bed temperature was measured as the distance from the grate increased to about 50mm and this was followed by a decrease in temperature above 50mm from the grate. In both the cases; low and high steam flow rate (*Figure 5.25, Figure 5.26)*, the temperature at a distance of 150mm was about 750°C.

The influence of steam on the temperature profile in the bed was confirmed at a lower heating temperature (S2) as shown in Figure 5.27 and Figure 5.28. The bottom bed temperature for the case with 40%wt steam (A100-S40 (S2)) is almost 100°C lower compared to the case with 25%wt of steam.

The results obtained so far suggest that a high steam to air ratio (40%wt steam) reduced the temperature at the bottom of the bed and also caused a shift of the active combustion phase further up the bed. Two possible scenarios that could explain the low temperature at the bottom of the bed are:

a) cooling due to the direct contact with a higher flow rate of lower temperature reactant (steam and air)

b) enhanced endothermic water gas reaction ($C + H_2O \leftrightarrow CO_2 + H_2$) as the steam feed was increased. The amount of reactants changes the behaviour of the stratified temperature along the bed. The higher temperature attained in the case of a lower steam flow rate implied a more active combustion phase at the bottom of the bed. This is expected to lead to a higher carbon conversion for cases with lower steam flow rate.

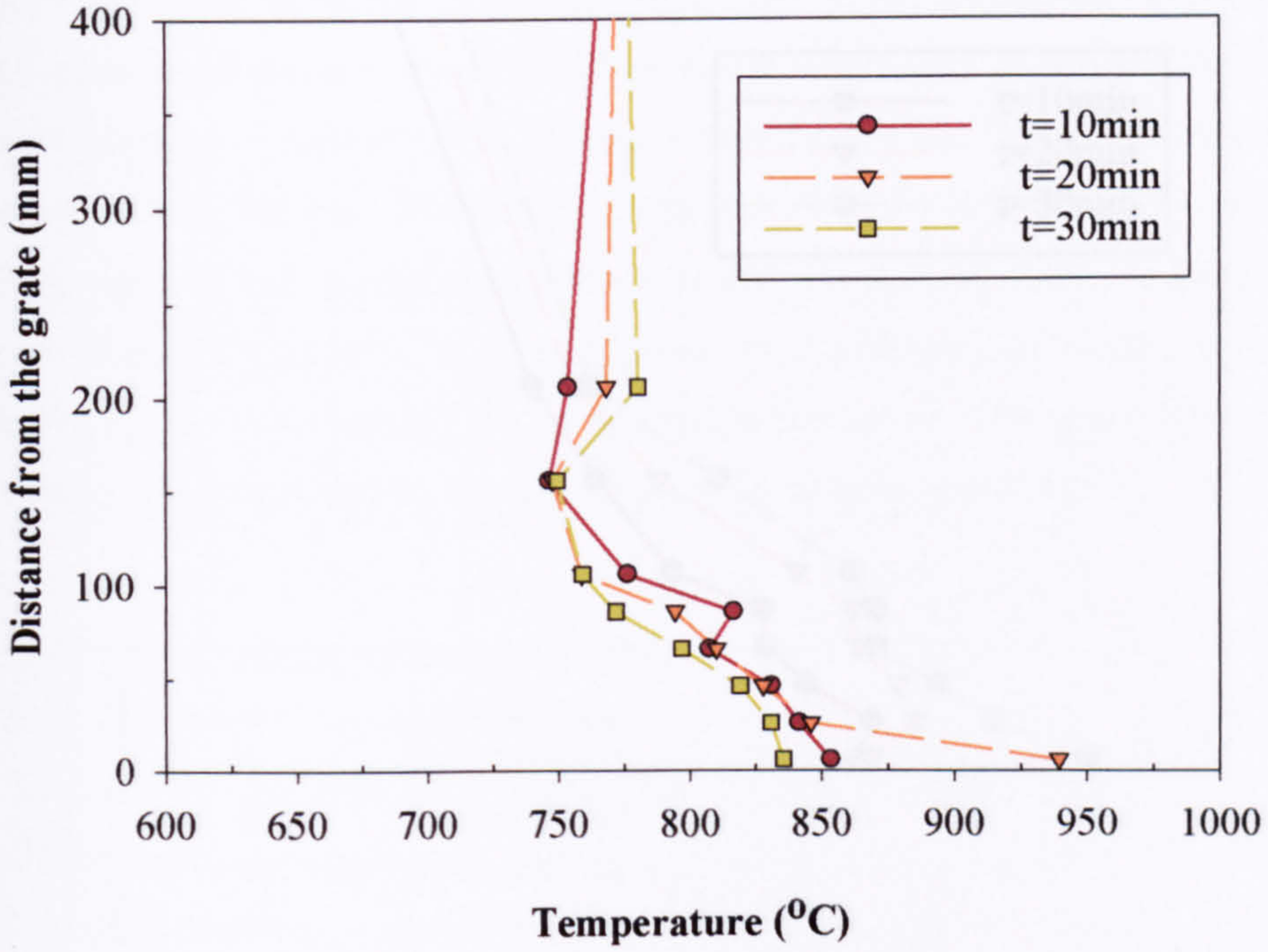

Figure 5.25: Distance from the grate vs. temperature for 10, 20 and 30 minutes after the steady phase was reached (Case A100-S25 (S1)).

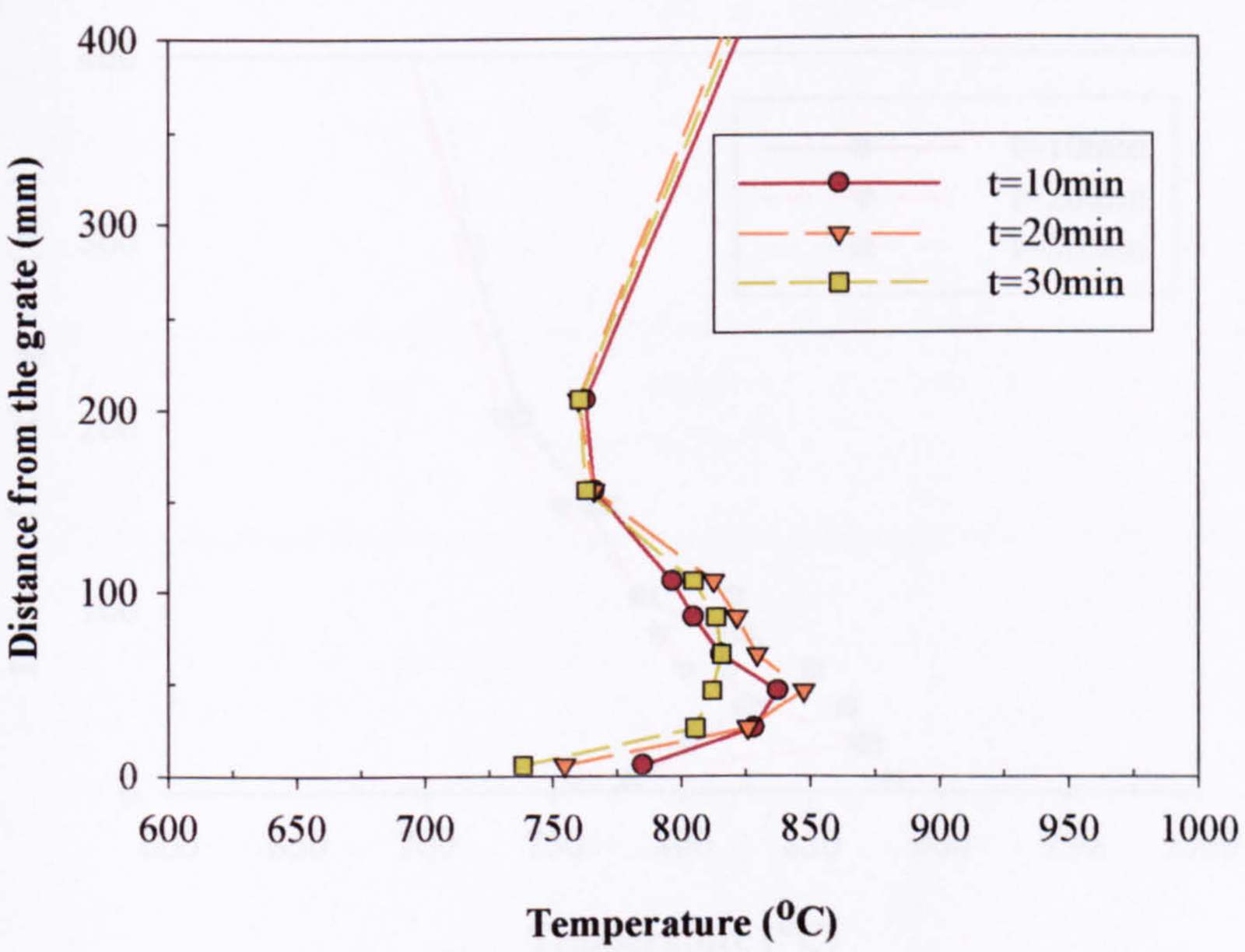

Figure 5.26: Distance from the grate vs. temperature for 10, 20 and 30 minutes after the steady phase was reached (Case A100-S40 (S1)).

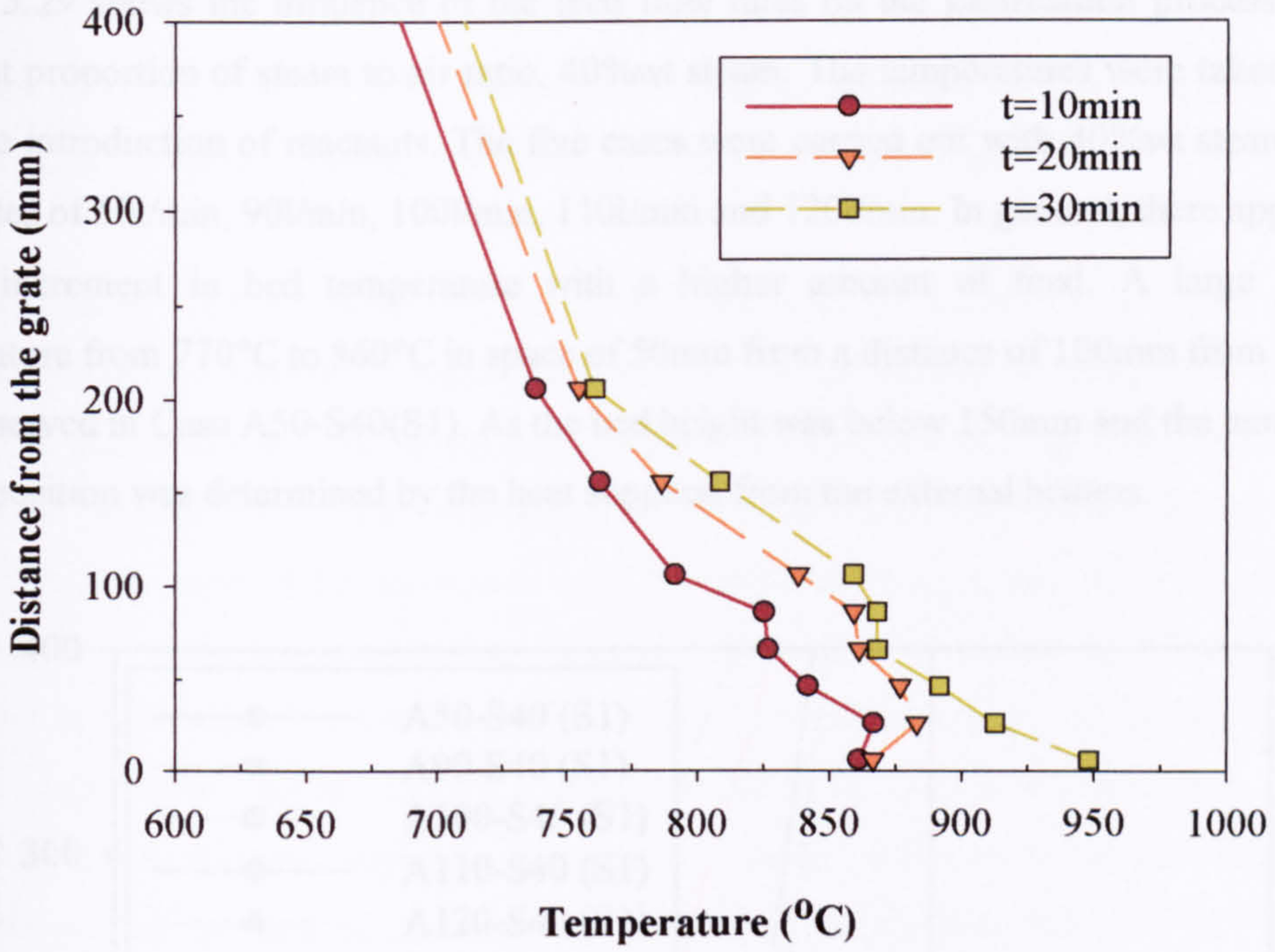

Figure 5.27: Distance from the grate vs. temperature for 10, 20 and 30 minutes after the steady phase was reached (Case A100-S25 (S2)).

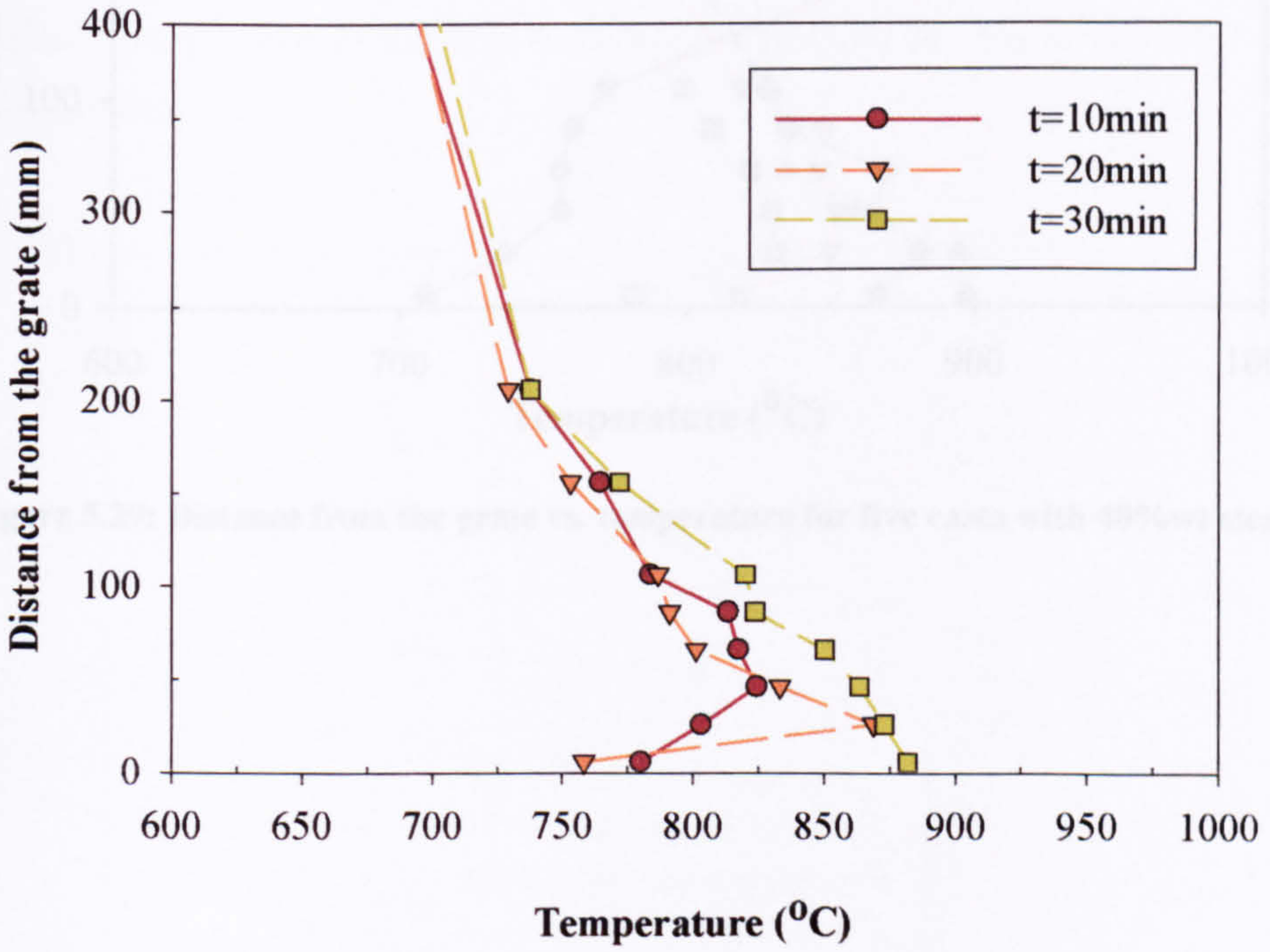

Figure 5.28: Distance from the grate vs. temperature for 10, 20 and 30 minutes after the steady phase was reached (Case A100-S40 (S2)).

Figure 5.29 shows the influence of the feed flow rates on the gasification process under a constant proportion of steam to air ratio, 40%wt steam. The temperatures were taken 30mins after the introduction of reactants. The five cases were carried out with 40%wt steam and air flow rates of 50l/min, 90l/min, 100l/min, 110l/min and 120l/min. In general, there appeared to be an increment in bed temperature with a higher amount of feed. A large jump in temperature from 770°C to 860°C in space of 50mm from a distance of 100mm from the grate was observed in Case A50-S40(S1). As the bed height was below 150mm and the temperature at that position was determined by the heat supplied from the external heaters.

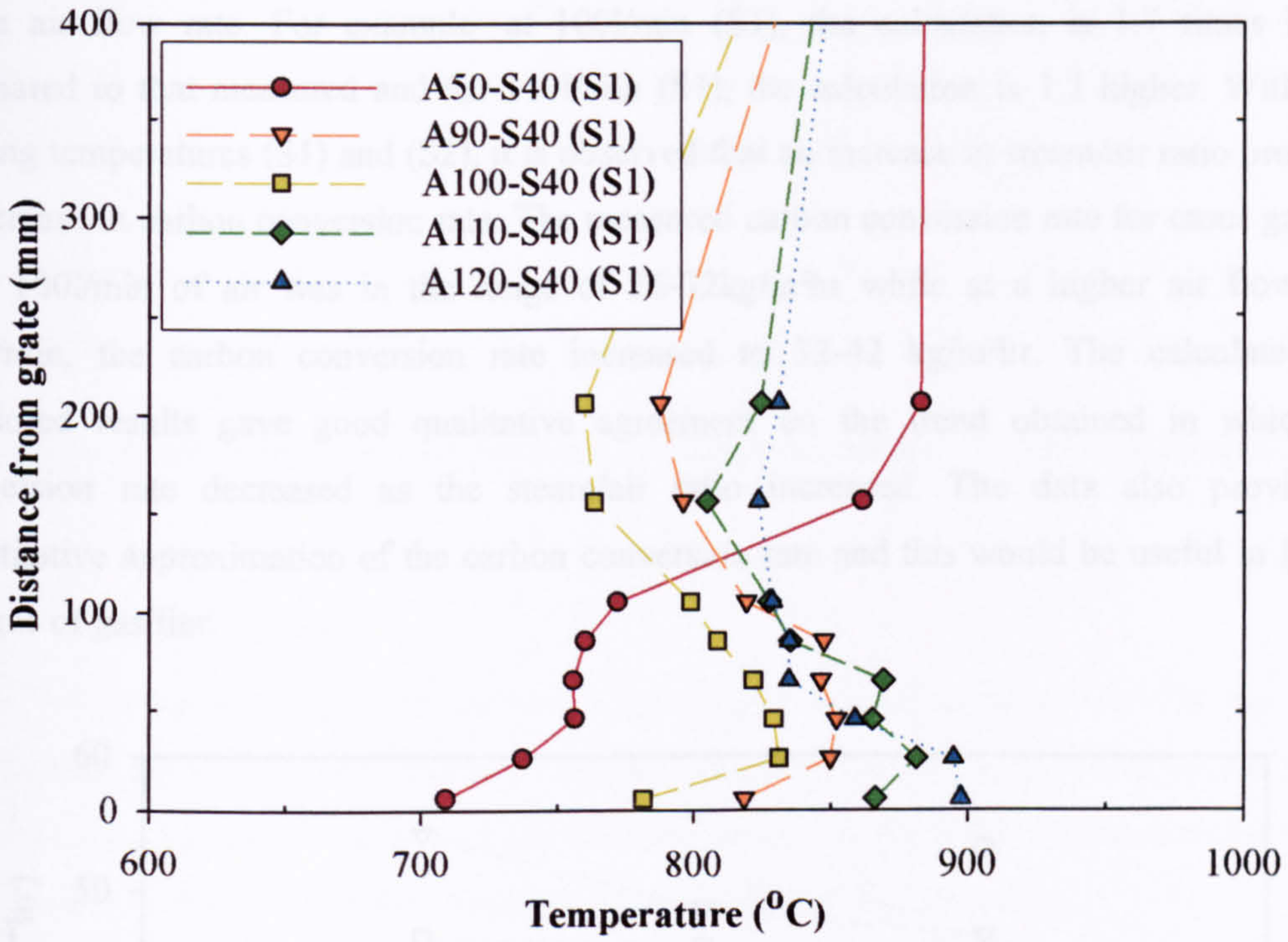

Figure 5.29: Distance from the grate vs. temperature for five cases with 40%wt steam.

5.6.2.2 Carbon Conversion

In *Figure 5.30* and *Figure 5.31*, the measured and calculated carbon conversion rates are shown versus the mass percentage of steam at different air flow rates.

The "calculated" carbon conversion rate was determined by mass balance over the input reactants and output concentrations (*Appendix A.4*). The uncertainty concerning the calculated conversion rates was due to the uncertainty of the exact char composition that lies in between the values obtained for fresh charcoal and charcoal remaining from the gasification experiment. The ratio of the calculated over the measured values are fairly constant for a given air flow rate. For example: at 100l/min (S1), the calculation is 1.7 times higher compared to that measured and for 110l/min (S1), the calculation is 1.1 higher. With both heating temperatures (S1) and (S2), it is observed that an increase in steam/air ratio produced a decrease in carbon conversion rate. The measured carbon conversion rate for cases gasified with 100l/min of air was in the range of 26-32kg/m²hr while at a higher air flow rate, 110l/min, the carbon conversion rate increased to 32-42 kg/m²hr. The calculated and measured results gave good qualitative agreement on the trend obtained in which the conversion rate decreased as the steam/air ratio increased. The data also provides a quantitative approximation of the carbon conversion rate and this would be useful in further designs of gasifier.

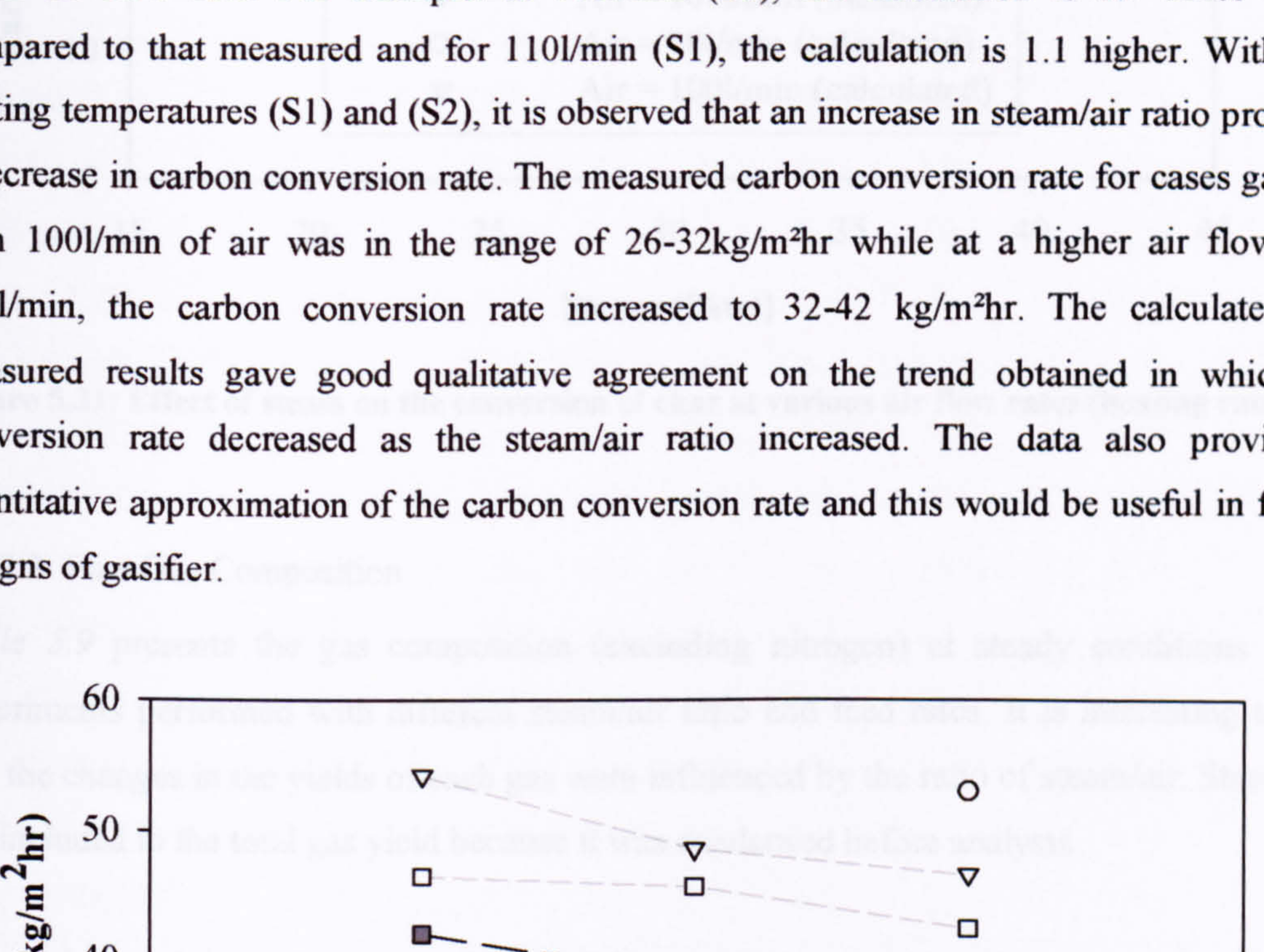

Figure 5.30: Effect of steam on the conversion of char at various air flow rates (heating rate=S1).

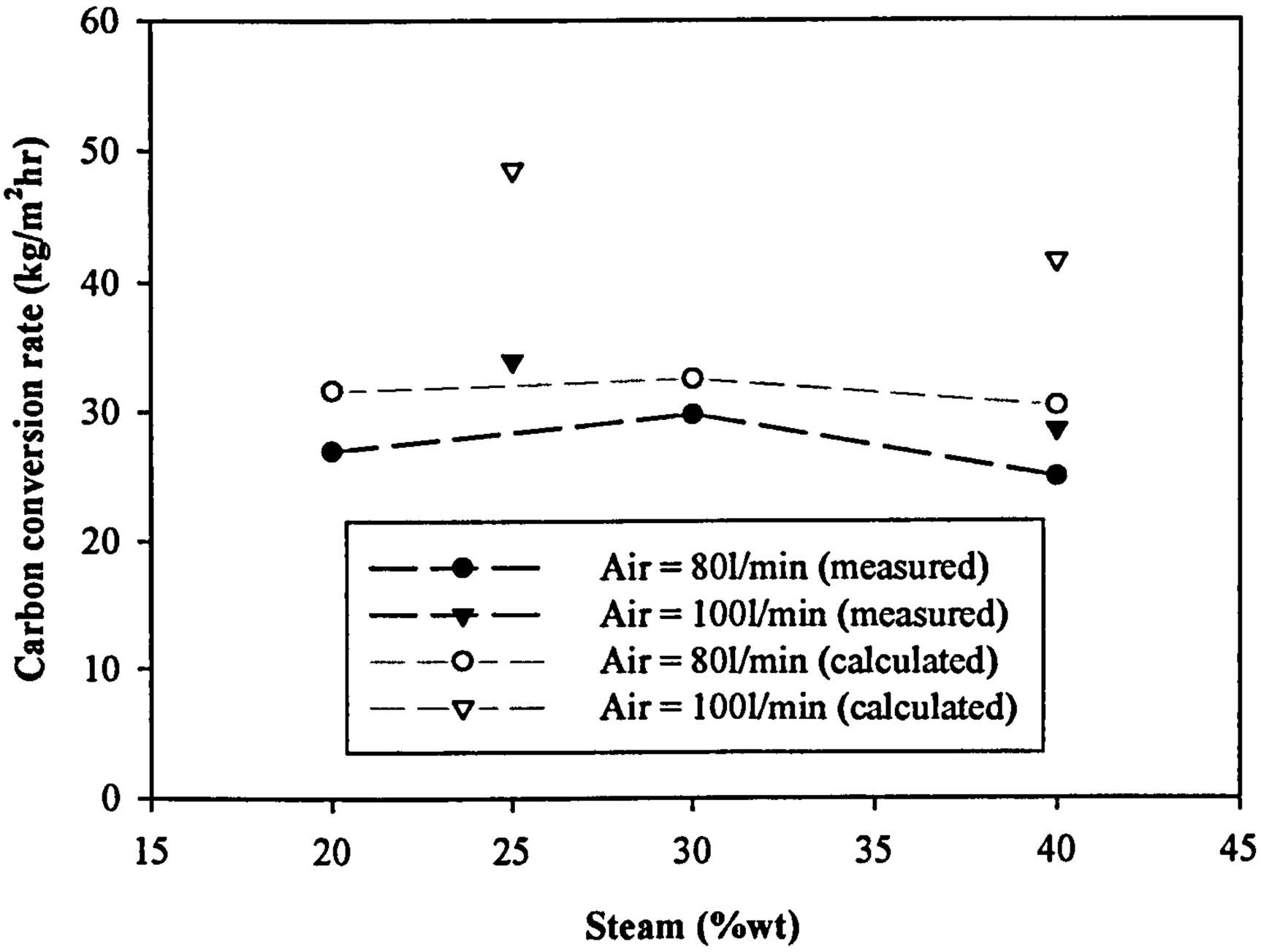

Figure 5.31: Effect of steam on the conversion of char at various air flow rates (heating rate = S2)

5.6.2.3 Flue Gas Composition

Table 5.9 presents the gas composition (excluding nitrogen) at steady conditions in the experiments performed with different steam/air ratio and feed rates. It is interesting to note that the changes in the yields of each gas were influenced by the ratio of steam/air. Steam was not included in the total gas yield because it was condensed before analysis.

It was observed that a higher yield of H_2 (20% to 25%) was attained as the ratio of steam in the feed was increased from 30% in Case A100-S30 (S1) to 40% in Case A100-S40 (S1). The concentration of CO decreased at the expense of increased CO_2. The two main gasification reactions that have significant effects on the formation of H_2 are:

Water gas reaction: $\left(C_{(s)} + H_2O_{(g)} \rightarrow H_{2(g)} + CO_{(g)}\right)$ (1)

Water-gas shift reaction: $\left(CO_{(g)} + H_2O_{(g)} \leftrightarrow CO_{2(g)} + H_{2(g)}\right)$. (2)

The increase in H_2 is favoured by the increase of the exothermal character of the water-gas shift reaction which begins and predominates between 500 to 600°C, and the water gas reaction which becomes significant at temperatures from 1000°C upward (Midilli, 2001). The higher formation of H_2 with increasing steam was also reported in the work carried out by

Lucas (2004) where the steam-biomass reaction rate was enhanced relative to the competing reactions by increasing the reactive agent steam in the feed gas. A parallel increase in H_2 yield with increasing steam/biomass was found in the gasification experimental investigation by (Turn 1998).

Case	Equivalence ratio (λ)	Dry product gas composition (vol%)					Heating Value (MJ/kg-dry)	H_2/CO
		H_2	CO	CO_2	CH_4	H_2+CO		
A50-S40(S1)	-	16.8	2.6	21.6	-	19.4	2.04	6.5
A70-S45(S1)	-	27.4	7.5	21.6	0.2	34.9	4.10	3.7
A90-S30(S1)	-	25.2	11.6	18.6	0.2	36.8	4.27	2.2
A90-S40(S1)	1.35	27.5	9.7	19.9	0.2	37.2	4.52	2.8
A100-S30(S1)	1.30	21.3	8.2	18.5	0.3	29.5	3.38	2.6
A100-S35(S1)	1.24	21.8	8.4	19.8	0.2	30.2	3.38	2.6
A100-S40(S1)	1.09	25.0	7.7	20.4	0.4	32.7	2.78	3.2
A110-S30(S1)	1.58	17.1	5.7	20.4	0.1	22.8	2.43	3.0
A110-S35(S1)	1.45	20.6	7.0	19.2	0.2	27.6	3.08	2.9
A110-S40(S1)	1.21	18.4	5.4	21.1	0.1	23.8	2.56	3.4
A120-S40(S1)	0.70	17.1	5.7	20.4	0.1	22.8	2.43	3.0
A80-S20(S2)	1.39	16.0	8.8	18.4	0.2	24.8	2.65	1.8
A80-S40(S2)	1.22	17.3	4.4	20.8	0.4	21.7	2.31	3.9
A100-S25(S2)	1.40	19.5	9.4	17.6	0.6	28.9	3.21	2.1
A100-S40(S2)	1.18	19.1	5.0	20.1	0.4	24.1	2.62	3.8

Table 5.9: Results on the equivalence ratio, dry product gas composition, heating value, and H_2/CO ratio obtained during steam gasification of char at various steam and air flow rates.

The H_2 concentration declined to 18% when the steam feed rate was further increased to 40% from 35% in Case A110-S35 (S1). The drop in H_2 evolution could be due to the influence of a lower bed temperature. Reactor temperature and feed temperature were proven to have an effect on H_2 yield (Turn et al, 1998; Chaudhari et al, 2003; Franco et al, 2003) as the water-gas and Boudouard reactions are endothermic and thermodynamically favourable at high temperature.

Boudouard: $(C + CO_2 \leftrightarrow 2CO)$ (3)

The lowering of bed temperature due to the addition of steam as in Case A110-S40 could possibly have reduce the influence of either reactions (1) or (3) resulting in a slower char conversion rate and lower H_2 and CO evolution. A similar trend was reported by Franco et al (2003) whereby the H_2 formation reached a maximum with increasing steam/biomass ratio and then declined as the ratio was further increased. In his work, the CO was found to decrease significantly while no significant change was observed for CO_2.

The equivalence ratio (λ) is a quantitative indication of whether the fuel-oxidizer mixture is rich, lean or stoichiometric. For fuel-rich mixtures, λ>1, and for fuel lean mixtures, λ<1. Therefore, the equivalence ratio (λ) is defined as the ratio of the actual fuel-oxidant ratio (F/O) to the ratio for a stoichiometric condition $(F/O)_{st}$. It was calculated from the air flow rate (m_{air}, kg/m²hr), the carbon conversion rate (CC, kg/m²hr) and the fuel elemental composition combusted ($w(H_2O).C_xH_yO_z$).

$$\lambda = (F/O)/(F/O)_{st} = m_{air/st}/m_{air}$$

$$m_{air,st} = [32(x + y/4 - z/2)CC]/0.233(18w + 12x + y + 16z)$$

In the calculations, the portion of mass combusted was assumed to take the composition of the gasified material as given in *Table 5.7* (w=0.16, x=7.24, y=1.61, z=0.54). However, in practise there is slightly less C in the composition and more H and O. Hence, the actual equivalence ratio is marginally lower than in *Table 5.9*. All the experiments except A120-S40(S1) were in fuel-rich mixtures in an ER range of 1-1.58. The equivalence ratio reduced from 1.30 to 1.09 as the ratio of steam with 100l/min of air was increased from 30% to 40%. The steam gasification reaction (2) becomes important as the steam content increased. This explains the result that the content of CO decreases and CO_2 increases. The lower bed temperature associated with a higher steam input reduces the influence of endothermic reaction (1). Therefore, the lower carbon conversion rate gave the impression of a fuel lean condition. The total concentration of H_2 and CO (22-27%) in the product gas obtained in the cases gasified with 110l/min of air was lower compared to the 29-33% obtained in the cases run with 100l/min of air. The 10% addition in air supplied was accompanied by a higher amount of nitrogen entering the gasifier leading to a dilution in the product gas and a lowering of heating value. A possible reason why the addition of steam in cases run with 110l/min did not result in a higher percentage of H_2 is that the equilibrium consideration for reaction (2) suggests that it proceeds in the opposite direction at high temperatures (Merrick, 1984).

The total production of H_2 and CO was highest in Case A90-S40 (S1) whereby the product gas contained 28% H_2 and 10% CO. Comparing cases with 40% steam ratio [A90-S40 (S1), A100-S40 (S1), and A120-S40 (S2)], the production of H_2 and CO declined as the total flow rate of reactant increased. *Figure 5.29* showed that the bed temperature increased with a higher input of reactants. It can be postulated that the decrease in H_2 and CO arises from more air entering the reactor resulting in the exothermic burning of these two gases in the oxidation zone, thus, contributing to the increase in bed temperature. The results obtained in this study agrees with the observations made by Midilli (2001) in their experiment with an air-blow downdraft gasifier where the flow rate of hydrogen gas and temperatures at the oxidation zone decreased from more air entering the reactor bed. Thus, combustion was said to occur in the reactor bed rather than gasification. The heating value of the product gas decreased from 4.27MJ/kg to 2.43 MJ/kg as the air flow rate increased from 90l/min (220kg/m²hr) in Case A90-S40 (S1) to 120l/min (294kg/ m²hr) in Case A120-S40 (S1).The evolution of H_2 and CO was very low for Case A50-S40 (S1) due to the limited amount of reactant supplied. It can be concluded that control of the air flow rate is crucial in the operation of air-steam gasification. A low air flow rate will lower the reaction temperature, which is not favourable while an air flow rate that is too high promotes the combustion of the product gas, lowering the heating value.

The H_2/CO ratio for steam-air gasification of commercial char ranges up to 3.7 (excluding Case A50-S40 (S1)). The results in *Table 5.9* showed that the H_2/CO ratio increased as the proportion of steam in the feed was increased. The increase in H_2/CO is mainly due to the decrease in CO with increasing ratio of steam in the feed. Therefore, the H_2/CO ratio in the synthesis gas can be adjusted to suit different application by manipulating the steam input.

The heating values were calculated based on the heat of combustion values (kcal/kmol) given by Sarkar (1990) (carbon: 97000kcal/kmol, hydrogen: 68317kcal/kmol, carbon monoxide: 67636kcal/kmol, methane: 212798kcal/kmol). The presented heating values were calculated in units of MJ/kg by division of the total heat of combustion by the molecular weight of the dry product gas.

Table 5.10 presents the conversion ratios of hydrogen gas from char gasification. The flow rate of H_2 and combustible gas from char was calculated from the mass balance of the input reactants and product gas concentration. The production ratio of the gases was based on the mass of gases produced per mass of char converted. In Case A90-S40, the combustible gas production ratio was over 100% as steam contributed to the H_2 formed. The average production ratio of H_2 is 0.12 (kg H_2 /kg char). The average production ratio of hydrogen

energy is 17MJ/kg of char. The data are useful in the approximate estimation of the char required in power generation from either hydrogen or combustible gas.

Case	Hydrogen production rate (kg/h)	Combustible gas production rate (kg/h)	Hydrogen production ratio (%)	Combustible gas production ratio (%)
A70-S45 (S1)	0.16	0.80	14	68
A90-S40 (S1)	0.20	1.72	12	103
A100-S30 (S1)	0.20	1.40	12	82
A100-S35 (S1)	0.17	1.09	11	71
A100-S40 (S1)	0.22	1.17	15	79
A110-S35 (S1)	0.16	0.89	11	62
A110-S40 (S1)	0.14	0.70	10	53
A100-S25 (S2)	0.16	1.28	11	84
A100-S40 (S2)	0.14	0.69	11	50
A80-S20 (S2)	0.09	0.77	8.72	78
A80-S40 (S2)	0.10	0.43	11	47

Table 5.10: The conversion ratios of hydrogen produced to char converted.

5.6.2.4 Effect of Freeboard Temperature

The reactor temperature plays an important role in the gasification process. In the present work, the reactor temperature was decreased from 850°C (S1) to 650°C (S2) to investigate the effect of temperature on gas composition and hydrogen yield.

Comparing Case A100-S40(S1) and Case A100-S40(S2) in *Figure 5.32*, it can be found that the H_2 concentration decreased appreciably from 25% to 19% with temperature. This was accompanied by a slight decrease in CO indicating that less char reacts with steam to produce the added H_2 through reactions (1). However, the carbon conversion rate, 28kg/m²hr in Case A100-S40(S2) was slightly lower compared to 26kg/m²hr in Case A100-S40(S1). As the reactor temperature was lowered, the preferred char reaction would be reaction (4) instead of reaction (1). This can also explain the higher value of bottom bed temperature found in Case A100-S40(S2) at 750-875°C compared to Case A100-S40(S1) at 725-775°C.

$$C_{6.97}H_{1.55}O_{0.52} + O_2 \rightarrow 6.97CO_2 + 0.78H_2O \quad (4)$$

In the cases where the reactor temperature was 850°C(S1), the H_2 yield increased as the steam ratio varied from 30%wt to 40%wt but a higher ratio steam/air was found to have less influence in a lower temperature reactor, 650°C (S2).

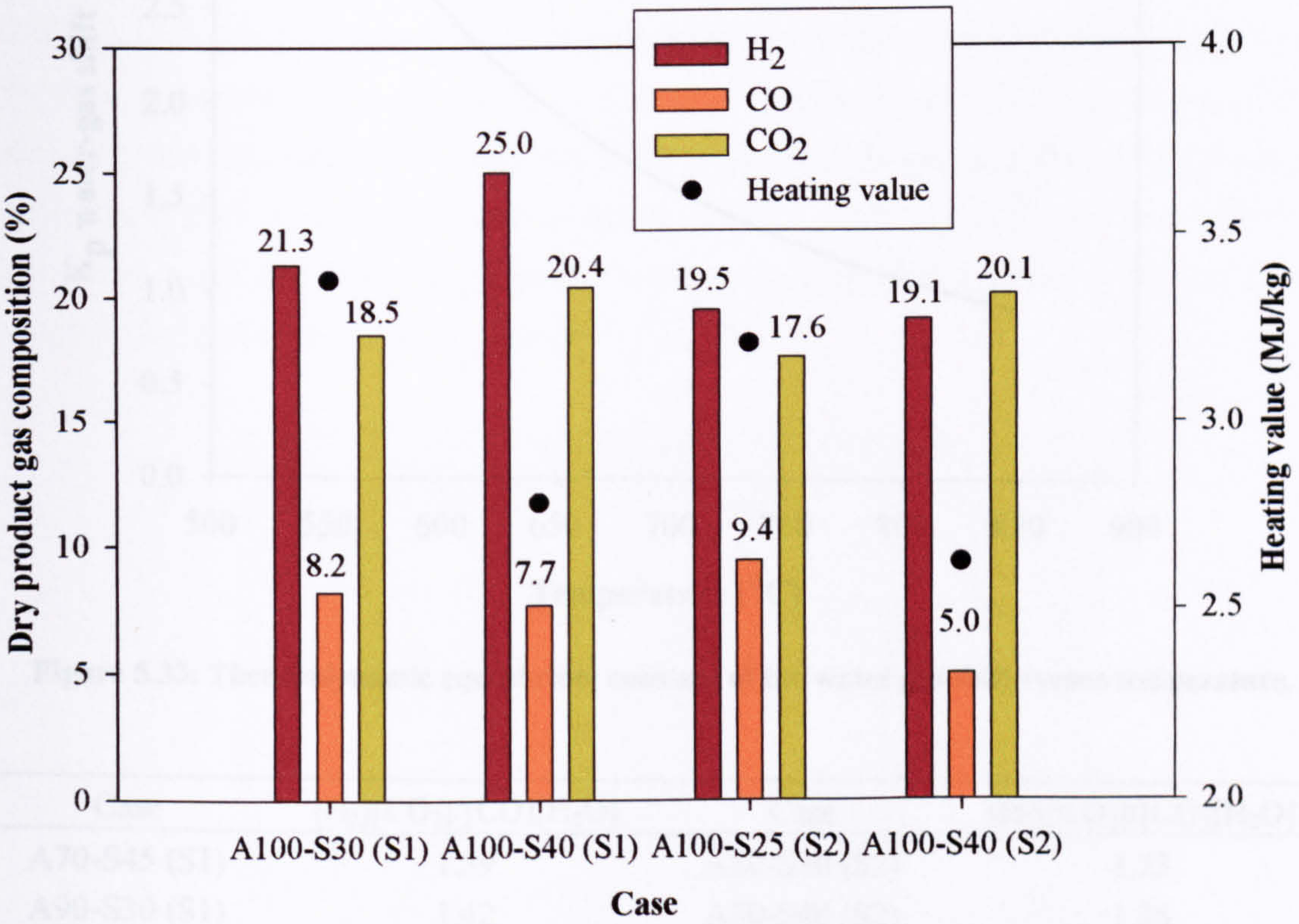

Figure 5.32: Dry product gas composition for Case A100-S30(S1), A100-S40(S1), A100-S25(S2), A100-S40(S2).

5.6.2.5 Water Gas-Shift, K_p

Figure 5.33 shows the equilibrium value for the water-gas shift reaction given by Yoon et al, (1978). *Table 5.11* shows the molar ratio of $[H_2][CO_2]/[CO][H_2O]$ in the gas phase for the experimental investigations. The molar concentration ratios for the cases were in the range of 0.8-1.7, corresponding to a temperature range in between 680°C to 890°C in *Figure 5.33*. The reactor temperature for (S1) varied in the range of 750-850°C while S2 in the range of 650-750°C. Therefore, it can be deduced that the calculated molar concentration ratio lies close to the equilibrium value for the water-gas shift reaction for the given temperature range. For cases with high input of reactants (A110-S30(S1), A110-S35(S1), A110-S40(S1)) and cases in the lower heating rates (S2), the molar concentration ratio decreased with increasing mass flow of steam as under such conditions, the H_2 yield decreased and a larger amount of steam was found in the product gas.

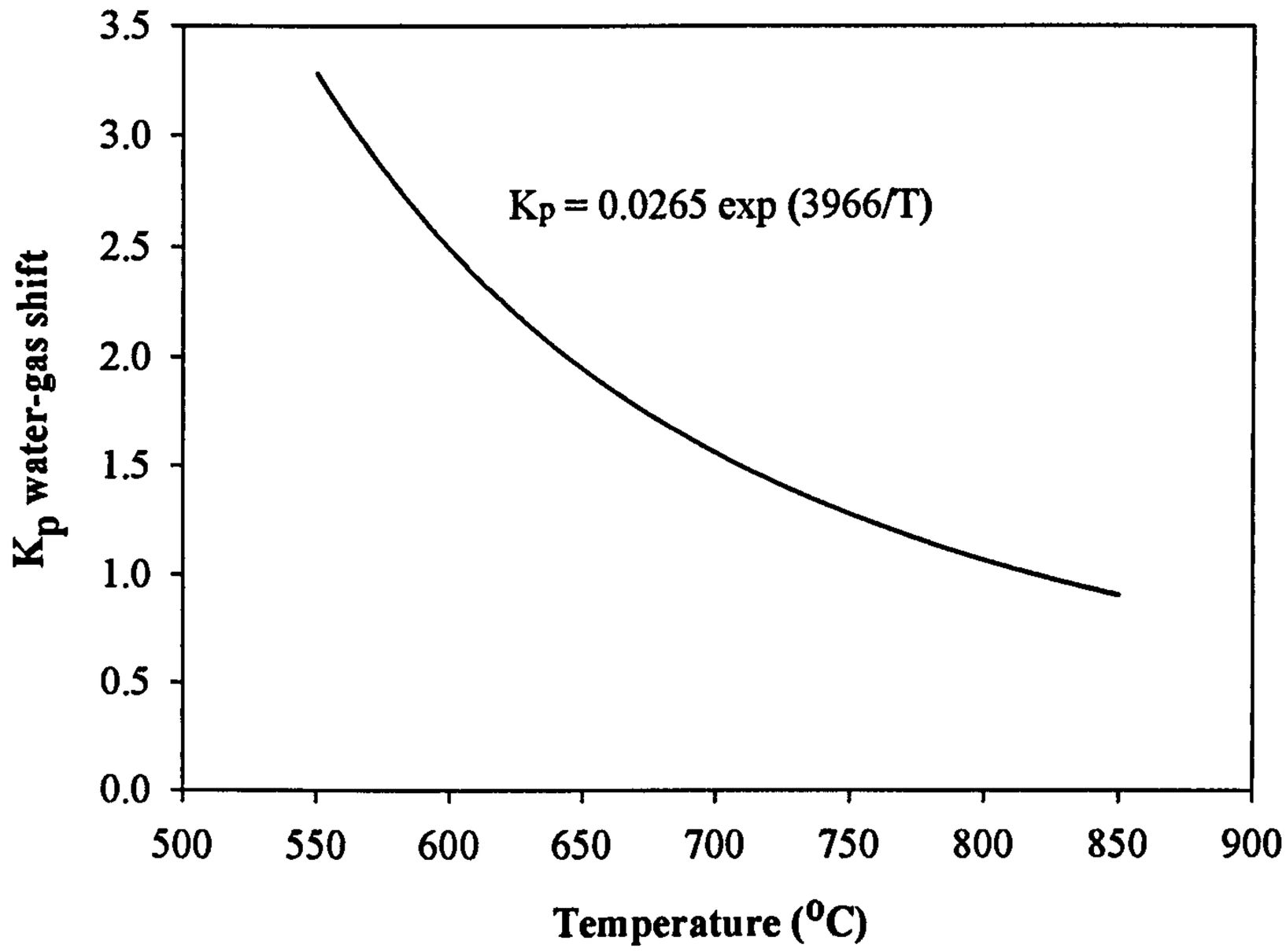

Figure 5.33: Thermodynamic equilibrium constant of the water gas shift versus temperature.

Case	$[H_2][CO_2]/[CO][H_2O]$	Case	$[H_2][CO_2]/[CO][H_2O]$
A70-S45 (S1)	1.39	A80-S20 (S2)	1.73
A90-S30 (S1)	1.42	A80-S40 (S2)	1.26
A90-S40 (S1)	0.78	A100-S20 (S2)	1.71
A100-S30 (S1)	1.21	A100-S40 (S2)	1.41
A100-S35 (S1)	1.26		
A100-S40 (S1)	1.52		
A110-S30 (S1)	1.12		
A110-S35 (S1)	1.52		
A110-S40 (S1)	1.07		
A120-S40 (S1)	0.98		

Table 5.11: Molar concentration ratio $[H_2][CO_2]/[CO][H_2O]$.

5.6.3 Gasification of Pyrolysed Wood Chip

The effect of fuel size on pinewood combustion was discussed in Chapter 4. The size of the particle affects the heating rate and the available surface area for reaction. Smaller fuels have a thinner reaction zone and result in a higher CO concentration in the product gases while larger particles produced a higher flame temperature.

Figure 5.34 shows the size of the pyrolysed wood chips. While the charcoal is about 4cm wide and almost spherical in shape, the pyrolysed wood chips were very thin, as the width measured only 2mm and 2-3cm long.

Table 5.12 shows the composition of the pyrolysed wood chips that were used to investigate the role of particle size in the gasification process. The pyrolysed wood chips have a fairly similar elemental composition compared to the fresh charcoal samples. The main differences lie in the slightly lower oxygen content as the value for the charcoal samples was 14%. The pyrolysed wood chips have a marginally lower ash content and moisture compared to 5% moisture and 6% ash in the fresh charcoal.

Figure 5.34: Pyrolysed wood chips.

Wood Chips		Sample 1	Sample 2	Sample 3	Average	Standard Deviation	95% Confidence
Proximate Analysis (%wt)	Moisture	3.34	3.26	2.60	3.06	0.41	±1.29
	Volatile	24.29	23.52	22.61	23.47	0.84	±2.68
	Ash	4.64	4.69	4.63	4.65	0.03	±0.10
	Fixed Carbon	67.73	68.53	67.56	67.94	0.52	±1.65
Gross Calorific value (MJ/kg)		27.38	27.97	28.81	28.05	0.72	±2.29
CHN Analysis (%wt)	Carbon	77.59 ± 0.3%					
	Hydrogen	2.62 ± 0.3%					
	Oxygen	12.08*					

Table 5.12: Composition of wood chip.

The gasification of the pyrolysed wood chips was conducted under similar conditions to Case A100-S40(S2). *Figure 5.35* and *Figure 5.36* shows the temperature profile as a function of distance from the grate obtained in the gasification of pyrolysed wood chips and lumpwood charcoal respectively. The spatial temperature gradient in the bed during the gasification of pyrolysed wood chips is much larger compared to charcoal. The temperature decreased about 300°C in a distance of 200mm from the bottom of the bed. The spatial temperature gradient ($\Delta T/\Delta y$) in a 200mm distance is about 20°C/cm for the pyrolysed wood chips and 7°C/cm for charcoal.

The temperature profile obtained across the bed changed with particle size. The highest temperature was measured at the bottom of the bed compared to the experiment with charcoal, where the bottom of the bed was cooled by contact with steam. A hotter bed temperature (≈900°C) was also obtained in the gasification of pyrolysed wood chips.

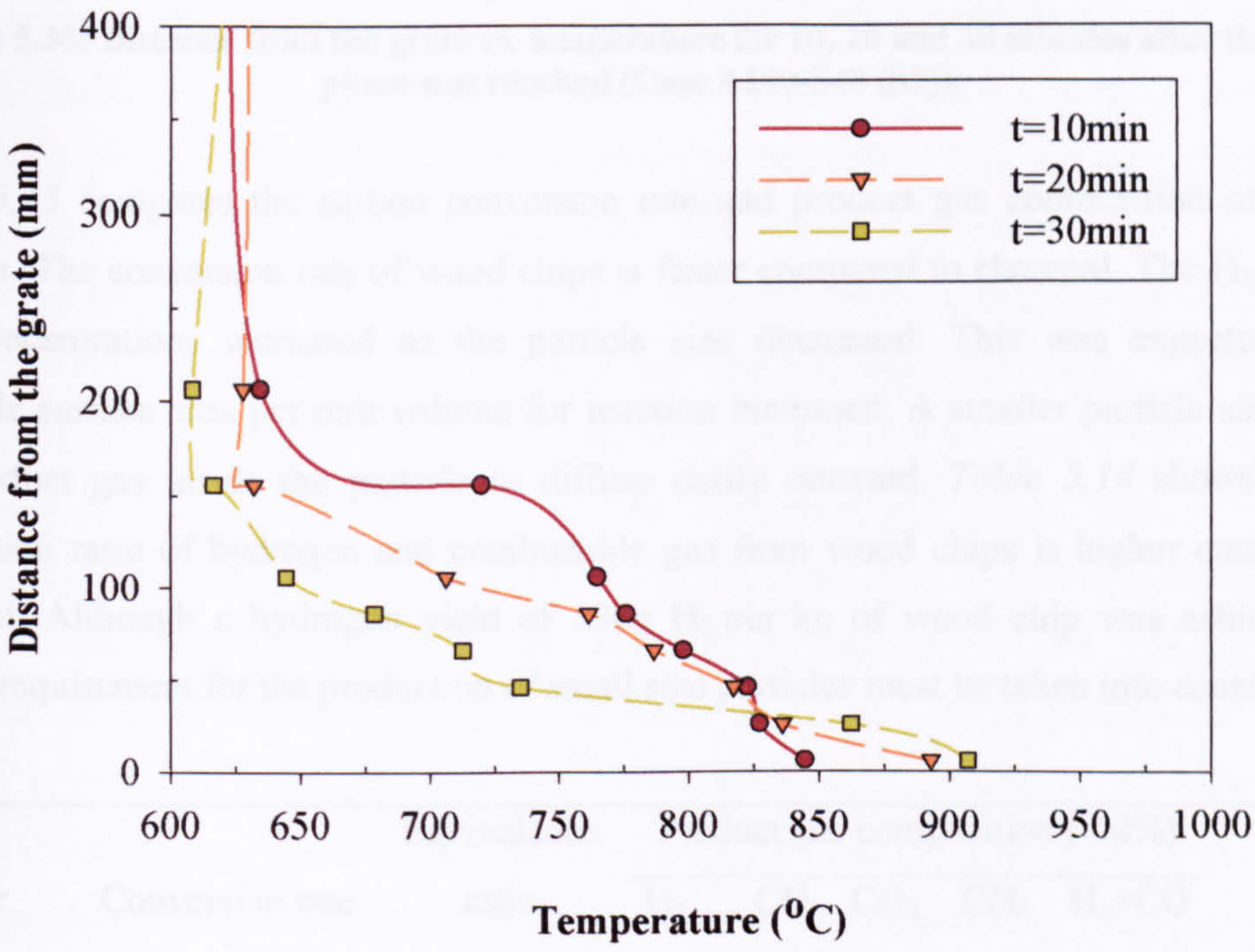

Figure 5.35: Distance from the grate vs. temperature for 10, 20 and 30 minutes after the steady phase was reached (Case WA100-S40 (S2)).

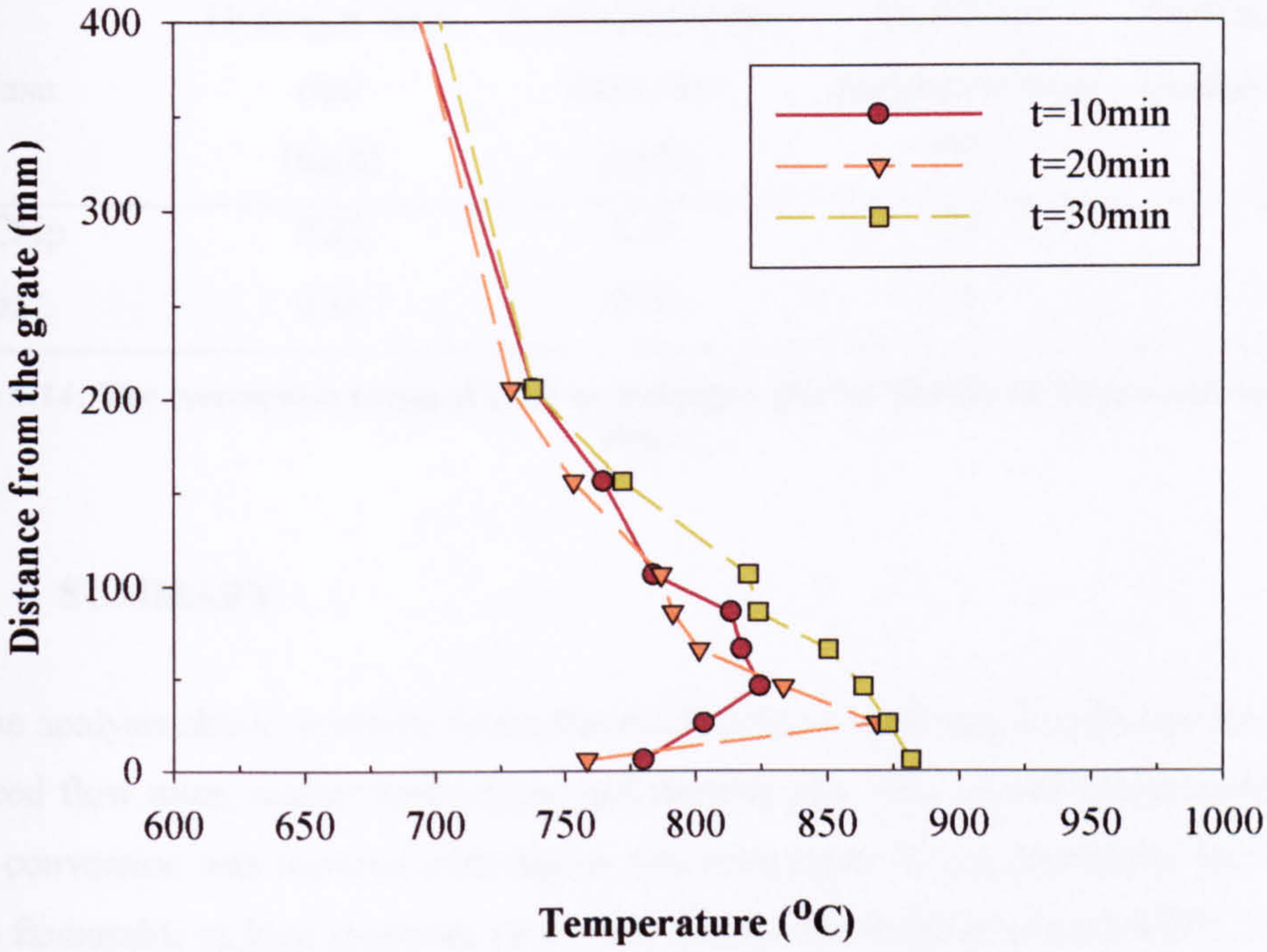

Figure 5.36: Distance from the grate vs. temperature for 10, 20 and 30 minutes after the steady phase was reached (Case A100-S40 (S2)).

Table 5.13 compares the carbon conversion rate and product gas composition of the two samples. The conversion rate of wood chips is faster compared to charcoal. The H_2, CO and CO_2 concentrations increased as the particle size decreased. This was expected as the available surface area per unit volume for reaction increased. A smaller particle also allows the product gas inside the particle to diffuse easily outward. *Table 5.14* shows that the production ratio of hydrogen and combustible gas from wood chips is higher compared to charcoal. Although a hydrogen yield of 130g H_2 per kg of wood chip was achieved, the energy requirement for the production of small size particles must be taken into consideration.

Case	Conversion rate (kg/m²hr)	Equivalence ratio (λ)	Product gas composition (vol%)					Heating Value (MJ/kg)
			H_2	CO	CO_2	CH_4	H_2+CO	
Wood chip	33.04	1.31	25.4	7.5	20.8	0.5	32.9	3.81
Charcoal	28.65	1.18	19.1	5.0	20.1	0.4	24.1	2.62

Table 5.13: Results on the equivalence ratio, dry product gas composition, heating value, and H_2/CO ratio obtained during steam gasification of char from lumpwood and wood chips.

Case	Hydrogen from char (kg/h)	Combustible gas from char (kg/h)	Hydrogen production ratio (%)	Combustible gas production ratio (%)
Wood Chip	0.22	1.15	13	70
Charcoal	0.14	0.69	11	50

Table 5.14: The conversion ratios of char to hydrogen gas for char from lumpwood and wood chips.

5.7 SUMMARY

From the analysis above, it can be found that the hydrogen yield was sensitive to the steam/air ratio, feed flow rates, reactor temperature and particle size. The overall bed temperature and carbon conversion was lowered with higher steam/air ratio. It was found that the hydrogen yield is favourable at high steam/air ratio for a reactor temperature around 850°C. However, an increase in reactants flow rates (steam & air) does not necessarily result in the increase of hydrogen yield. The addition of steam could lower the bed temperature resulting in a decrease in synthesis gas production. The optimum conditions to produce high calorific value gases is with 220kg/m²hr air and 147kg/m²hr steam and at a reactor temperature of 850°C. This was found to produce the highest combustible gas yield. The highest hydrogen production ratio obtained in the counter-current reactor was 15kg/hr of hydrogen from 100kg/hr of char when the gasification was conducted with 245kg/m²hr of air and 163kg/m²hr of steam. It was also established in the experiments carried out that a higher reactor temperature will be more favourable for gas and hydrogen yield. All the cases with a lower reactor temperature (650°C) showed a much slower conversion rate and the hydrogen production was significantly decreased. Biomass particle size also has an influence on the gas composition and hydrogen yield. The conversion rate found in this experimental work ranged in the region of 26-42kg/m²hr depending on the reactant input. The rotating grate used in the counter-current reactor successfully reduced the sensible heat losses in the ashes and helped maintain a high temperature and active region at the bottom of the bed. The production of methane was negligible and no higher hydrocarbons were detected. Therefore, the proposed combination of the gasification chamber with a first stage tar-cracking pyrolyser would allow a low tar content in the synthesis gas.

CHAPTER 6

MATHEMATICAL MODEL FOR THE FIXED BED COMBUSTION AND GASIFICATION OF BIOMASS

Mathematical modelling has always been a useful tool that provides useful information on the temperature profile, gas composition, bed height decrease, pollutant formation and combustion stoichiometry. This chapter presents the theoretical foundation used in the modelling of a one-dimensional fixed bed reactor and proceeds to the mathematical calculation employed. The fixed bed combustion and gasification were modelled using the FLIC (Fluid Dynamics of Incineration Combustion code). A second mathematical approach, Chemical Equilibrium with Application was also adopted to model the gasification process. FLIC, developed at Sheffield University Waste Incineration Centre (SUWIC) was used to model the influence of particle size on pinewood combustion in a stationary packed bed and the influence of steam on the fixed bed gasification. The two main sections in this chapter focus on the modelling of the fixed bed combustion and also the fixed bed gasification process where the experimental work of these processes were given in Chapter 4 and Chapter 5 respectively.

6.1 INTRODUCTION

The solid fuel can be divided into four main components: *free moisture, volatiles, bound ash* and *solid carbon* or *char* as illustrated in *Figure 6.1* (Goh, 1998).

The combustion process can be divided into four successive sub-processes: *evaporation of moisture from the solids, volatile releases/char formation, burning of the hydrocarbon in the gaseous space*, and the *combustion of char particles*. A mass exchange of moisture between the wet solids and the drier air flow occurs as primary air is first supplied to the bed. Simultaneously, the solid fuel will be heated up by the over-bed radiation and moisture is released through evaporation when the solid fuel in the bed reaches a temperature of 373K. As the temperature increases to 533K, the solid fuel is pyrolysed and volatiles consisting of carbon, hydrogen and oxygen are released. In the absence of oxygen, the gaseous volatiles released are assumed to consist of hydrocarbon (e.g. C_xH_y), CO and water. The moving

pyrolysis front is assumed to remain at the pyrolysis temperature until all the volatiles have been driven out.

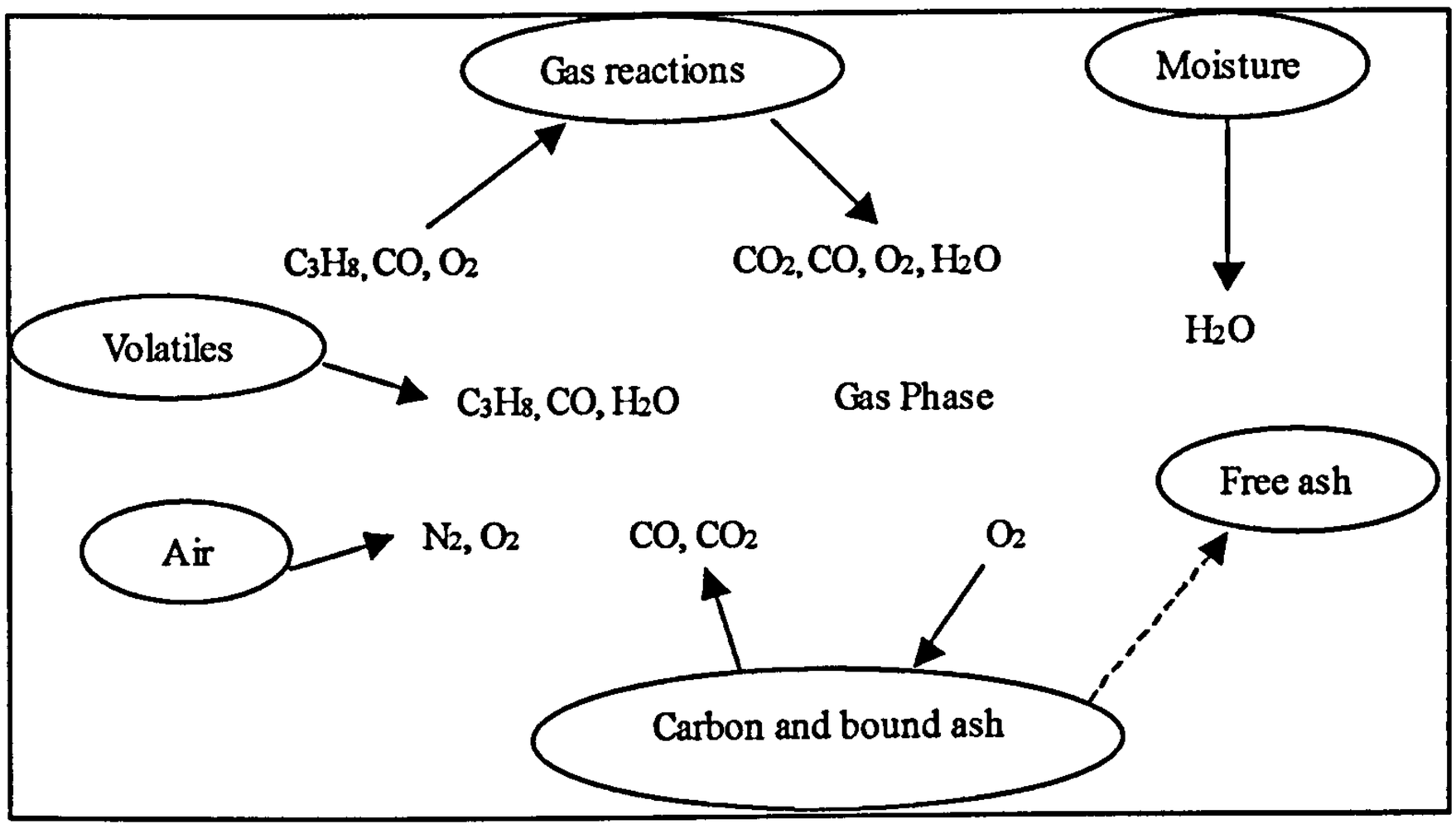

Figure 6.1: Processes that occur during incineration.

As all the moisture and volatiles are driven off, the remaining solid consists of only carbon char and bound ash. The carbon is assumed to react with the available oxygen and carbon-monoxide to form carbon-dioxide eventually. The bound ash would become free ash during the char oxidation process. The rate of ash shedding from the solid surface will be in comparable proportion to the rate of carbon reacted at the solid surface as the proportion of bound ash and carbon in the solids are assumed to remain in the constant. The combustible components released during the pyrolysis and devolatilisation are transferred to the gaseous phase of the void space in the packed bed and burned. The bulk volume of the solid fuel is reduced towards the end of the process.

The mathematical model was developed to mathematically link the reduction of bed height and volume with the processes occurring in the solid fuel combustion. Goh (1998) introduced an additional component known as the internal pore space to account for the void space due to the drying and devolatilisation. This was to differentiate it from the void spaces occupied by the gas phase at the outer surface of the solid fuel. The pore space increases during drying and pyrolysis to compensate for the volume of moisture and volatiles removed. This pore space is removed in the char gasification or oxidation phase, reducing the bulk volume of the bed.

6.1.1 Mathematical Description of the Fixed Bed

The mathematical model was developed based on different zones for the initial state of the fuel, dried and pyrolysed fuel and layer of ash free. The results of this mathematical model could be use to provide the calculated boundary conditions for a CFD (Computational Fluid Dynamic Code).

The packed bed consist of an assembly of individual particles where the combustion reactions can be separated into the solid and gas phases. As the theoretical calculation of an entire packed bed is challenging without some form of simplification, a few assumptions were made:

- The temperature of gas and solid phases inside the bed, gas composition and solid compositions can be described one dimensionally as functions of bed height.
- The temperature and concentration gradients of chemical species in the direction across the cross sectional areas of the bed are negligible compared to those in the direction of gas flow.
- The bed is treated as a porous medium where mass and heat transfer takes place between the solid and gas phases.
- The four successive sub-processes: evaporation of moisture from the solids, volatile release/char formation, burning of the hydrocarbon volatiles in the gaseous space, and the combustion of char particles occurs layer by layer from the bed top to the bottom.

Therefore, the whole bed is divided into many thin layers along the bed height (the thickness of each layer much smaller than the particle size) and inside each layer, the major bed parameters are assumed uniform.

Figure 6.2 shows the representation of the four succesive sub-processes taking place in four subsequent layers of the bed. Layer B represents the fuel in its initial state, layer C consists of the dried materials, layer D is the dried and pyrolysed material and layer A is the layer of the free ash. The drying front lies between layer B and C, the pryolysis front between C and D and the gasification front between D and A. The bed is heated from the top by radiation and under-grate air supplied at the bottom. The processes occur layer by layer down the bed. If no reaction occurs within each layer, each process condition can be considered the boundary condition for the layers immediately next to the process.

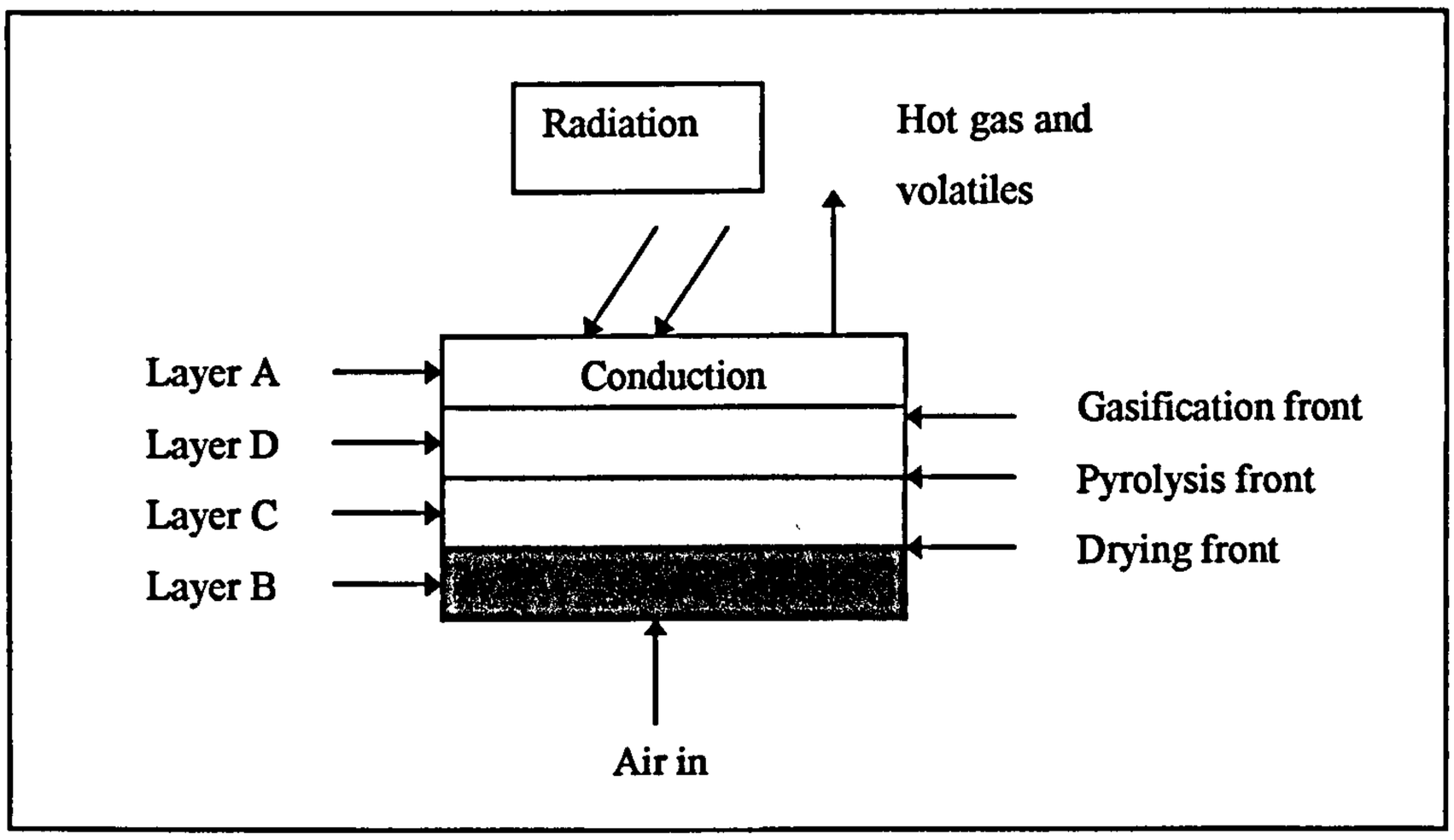

Figure 6.2: Processes in a fixed bed (Goh *et al*, 1998).

6.1.2 Background: Bed Model (FLIC)

A step change method is used to physically represent the change in the volume of the burning fixed bed as shown in *Figure 6.3.* Each layer of the bed undergoes the processes in stages as the burning proceeds. State A represents the layer of the bed in its initial state and state B consists of the dried material after the moisture evaporation. As the combustion proceeds, the layer is fully dried and pyrolysed, reaching state C. The last stage is the gasification, where only ash is left in state D.

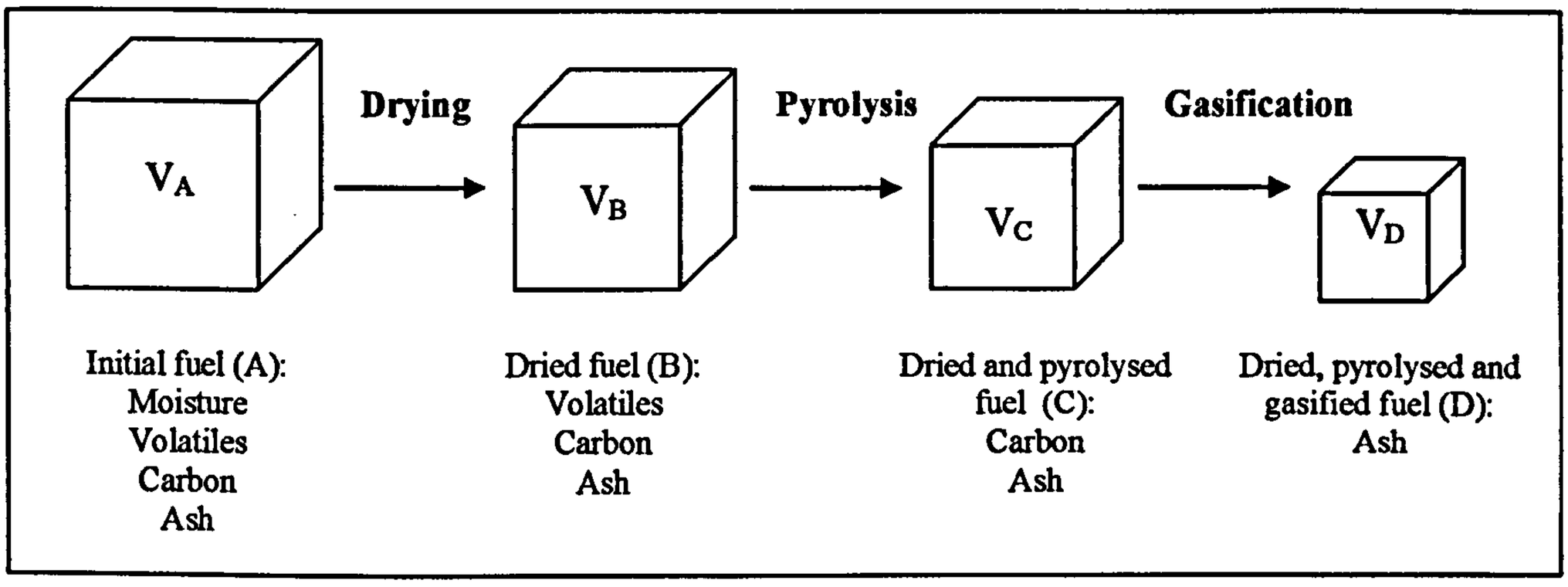

Figure 6.3: Step change model for the fixed bed combustion (Goh, 1998).

The initial volume of fuel A is given by:

$$=(1-\varepsilon_A)V_A \qquad \textit{Equation 6.1}$$

The volume of moisture in fuel A:

$$=(1-\varepsilon)V_A w_{2,A} \qquad \textit{Equation 6.2}$$

When the fuel A is fully dried, the remaining fuel has a volume of V_B. For each unit volume of moisture removed from V_A, the interior pore space increased by F_2. Therefore, the solid volume would decrease by $(1\text{-}F_2)w_{2,A}$. F_2 would have a value between 0 and 1.

For the two extreme cases, where F_2 equals to 0, there would be no increase of pore space during drying or in the other cases where F_2 is equal to 1, the increase in pore space is equal to the moisture removed. When the moisture in fuel A is fully evaporated, it would form the dried fuel B which volume is given by:

Initial volume of fuel A - volume of moisture in fuel A + volume of pores formed:

$$=(1-\varepsilon_A)V_A-(1-\varepsilon_A)V_A w_{2,A}+(1-\varepsilon_A)V_A F_2 w_{2,A}$$

$$=(1-\varepsilon_A)V_A\left[(1-F_2)w_{2,A}\right] \qquad \textit{Equation 6.3}$$

Therefore V_A is related to V_B by:

$$\frac{V_B}{V_A}=\frac{(1-\varepsilon_A)}{(1-\varepsilon_B)}\left[1-(1-F_2)w_{2,A}\right] \qquad \textit{Equation 6.4}$$

Whereby, ε_A and ε_B represents the void fraction in the fuel in state A and B respectively and $w_{2,A}$ represents the volume fraction of moisture in fuel A. The volume fraction of moisture ($w_{2,A}$), volatile matter ($w_{3,A}$), carbon ($w_{4,A}$) and ash ($w_{5,A}$) can be estimated from the proximate and ultimate analysis. The volume fraction of the each individual component in the initial fuel can be calculated using the following equation:

$$w_{n,A}=\frac{\rho_A X_n}{\rho_n(1-\varepsilon_A)} \qquad \textit{Equation 6.5}$$

Whereby, n = 2, 3, 4, 5 for the moisture, volatile matter, fixed carbon and ash respectively. ρ_A is the bulk density of the solid fuel and X represents the mass fraction of each individual

component. The volume fraction of the volatile component in the initial fuel can be found by difference as the sum of the volume fraction is equal to 1.

Table 6.1 shows the equation relating the volume fraction of each component in the fuel at state B, C and D to the volume fraction in A.

Component	FUEL A (V_A)	FUEL B (V_B)	FUEL C (V_C)	FUEL D (V_D)
Gas	$V_{1A} = \varepsilon_A V_A$	$V_{1B} = \varepsilon_B V_B$	$V_{1C} = \varepsilon_C V_C$	$V_{1D} = \varepsilon_D V_D$
Moisture	$V_{2A} = w_{2A}(1-\varepsilon_A)V_A$	$V_{2B} = 0$	$V_{2C} = 0$	$V_{2D} = 0$
Volatile	$V_{3A} = w_{3A}(1-\varepsilon_A)V_A$	$V_{3A} = V_{3B} = w_{3B}(1-\varepsilon_B)V_B$	$V_{3C} = 0$	$V_{3D} = 0$
Carbon	$V_{4A} = w_{4A}(1-\varepsilon_A)V_A$	$V_{4A} = V_{4B} = w_{4B}(1-\varepsilon_B)V_B$	$V_{4B} = V_{4C} = w_{4C}(1-\varepsilon_C)V_C$	$V_{4D} = 0$
Ash	$V_{5A} = w_{5A}(1-\varepsilon_A)V_A$	$V_{5A} = V_{5B} = w_{5B}(1-\varepsilon_B)V_B$	$V_{5B} = V_{5C} = w_{5C}(1-\varepsilon_C)V_C$	$V_{5C} = V_{5D} = w_{5D}(1-\varepsilon_D)V_D$
Internal pore space	$V_{6A} = 0$	$V_{6B} = w_{6B}(1-\varepsilon_B)V_B$ $V_{6B} = V_{6A} + F_2 w_{2A}(1-\varepsilon_A)V_A$ $V_{6B} = F_2 w_{2A}(1-\varepsilon_A)V_A$	$V_{6C} = w_{6C}(1-\varepsilon_C)V_C$ $V_{6C} = V_{6B} + F_3 w_{3B}(1-\varepsilon_B)V_B$ $V_{6C} = F_3 w_{3B}(1-\varepsilon_B)V_B$	$V_{6D} = 0$

Table 6.1: Volume fraction of components in the fuel.

The volume of fuel C is related to fuel B in the same way fuel B is related to A. For each volatile matter removed from the dried fuel (B), the interior pore space is increased by F_3 and the solid volume is decreased by $(1- F_3)w_{3,B}$. The relationship between V_B and V_C is given by:

$$\frac{V_c}{V_B} = \frac{(1-\varepsilon_B)}{(1-\varepsilon_C)}[1-(1-F_3)w_{3B}] \qquad \textit{Equation 6.6}$$

As the volume of volatile matter in fuel B is equal to fuel A, the volume fraction of both fuel are related by the following equation:

$$w_{3B} = \frac{w_{3A}(1-\varepsilon_A)V_A}{(1-\varepsilon_B)V_B} \qquad \textit{Equation 6.7}$$

Substituting *Equation 6.7* into *Equation 6.6* gives:

$$\frac{V_C}{V_B} = \frac{(1-\varepsilon_B)}{(1-\varepsilon_C)}\left[1-(1-F_3)\frac{w_{3A}(1-\varepsilon_A)V_A}{(1-\varepsilon_B)V_B}\right] \qquad \textit{Equation 6.8}$$

From *Equation 6.4*, V_A/V_B is substituted in *Equation 6.8*:

$$\frac{V_C}{V_B} = \frac{(1-\varepsilon_B)}{(1-\varepsilon_C)}\left(\frac{1-[(1-F_2)w_A + (1-F_3)w_{3A}]}{[1-(1-F_2)w_{2A}]}\right) \qquad \textit{Equation 6.9}$$

Similarly, the volume fraction of ash in D is related to C:

$$\frac{V_D}{V_C}=\frac{(1-\varepsilon_C)}{(1-\varepsilon_D)}\left(\frac{w_{5C}}{w_{5D}}\right) \qquad \textit{Equation 6.10}$$

As $w_{5D}=1$, therefore:

$$\frac{V_D}{V_A}=\frac{(1-\varepsilon_A)}{(1-\varepsilon_D)}(w_{5A}) \qquad \textit{Equation 6.11}$$

Multiplying *Equations 6.9* and *Equation 6.4*, V_C/V_A is given by the following equation:

$$\frac{V_C}{V_A}=\frac{(1-\varepsilon_A)}{(1-\varepsilon_C)}(1-[(1-F_2)w_A+(1-F_3)w_{3A}]) \qquad \textit{Equation 6.12}$$

V_D is then related to V_C using *Equation 6.11* and *Equation 6.12*:

$$\frac{V_D}{V_C}=\frac{(1-\varepsilon_C)}{(1-\varepsilon_D)}\left(\frac{w_{5D}}{1-[(1-F_2)w_A+(1-F_3)w_{3A}]}\right) \qquad \textit{Equation 6.13}$$

6.1.3 Mathematical Model for the Bed

The step change model in which the bed is divided into 4 layers (*Section 6.1.2*) is applied to the entire fixed bed reactor by dividing the whole bed into many thin layers along the bed height with the thickness of each layer much smaller than the size of a particle. *Figure 6.4* shows the layer L of the bed under a regressing front.

A generalised equation used to represent the volume distribution of each component in the thin layer, L:

$$\varepsilon_L+(1-\varepsilon_L)\sum_{N=2}^{7}w_{N,L}=1 \qquad \textit{Equation 6.14}$$

Where $\sum_{N=2}^{7}w_{N,L}$ is the sum of the volume fractions of the solid components and internal pore space in the solid volume within each layer, and has a value of unity. It should be noted that if component N does not exist in the layer, w_N becomes zero. For example, in layer B, $w_{2,B}$ is zero, and in layer C, $w_{2,C}$ and $w_{3,C}$ are zero.

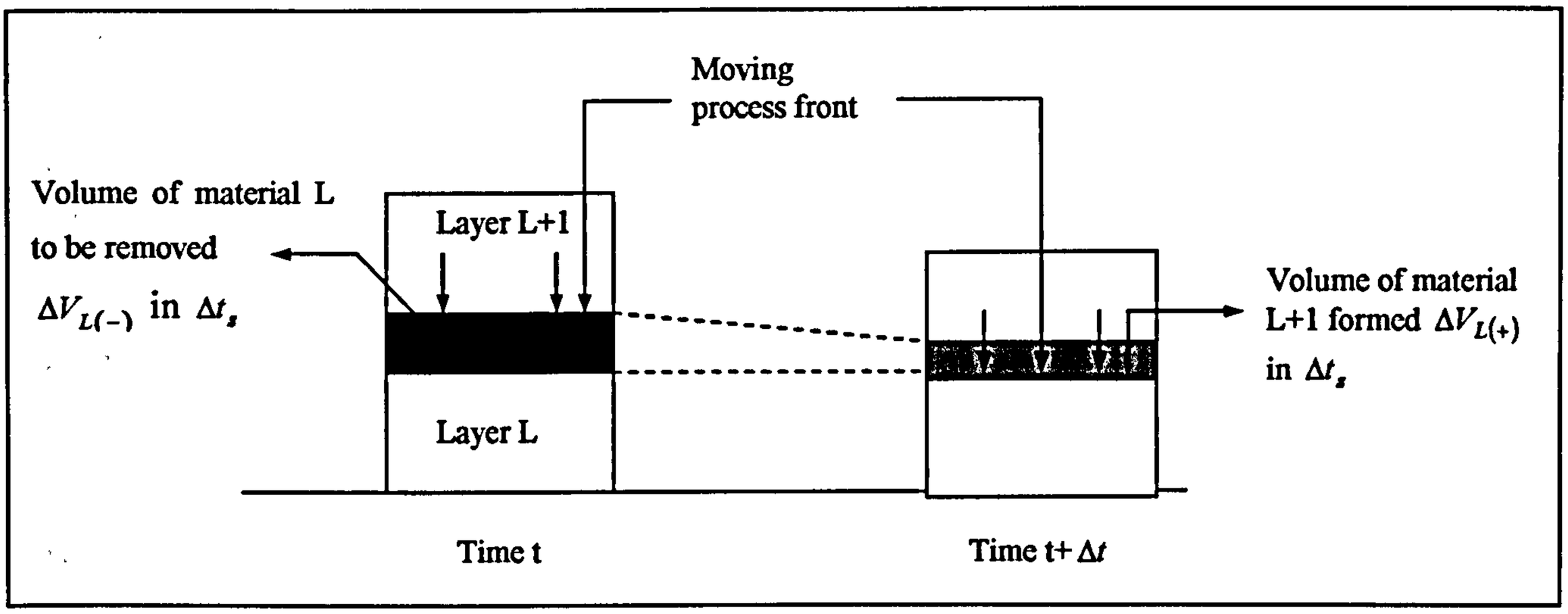

Figure 6.4: Volume change of material due to process front movement.

If the process front above layer L moves a distance ΔY_L in time Δt as shown in *Figure 6.4*, the volume of layer L per unit surface area of bed is decreased by $\Delta V_{L(-)}$. The volume of solid and pores removed due to movement of the process front is given by:

$$\Delta V_{L(-),S} = (1-\varepsilon_L)\Delta V_{L(-)} \qquad \textit{Equation 6.15}$$

The volume of component N removed in the process can be expressed as:

$$\Delta V_{N,S} = w_{N,L}\Delta V_{L(-),S} \qquad \textit{Equation 6.16}$$

Over the same time step Δt, the volume of layer L+1 increases due to addition of material from layer L. The addition of volume due to movement of the process front can be given by the volume of solids added plus the volume of internal pore space generated by the process:

$$\Delta V_{L(+),S} = (1-w_{L,N})\Delta V_{L(-),S} + F_N \Delta V_{L(-),N} \qquad \textit{Equation 6.17}$$

Where F_N is the volume fraction of component N which leaves internal pore spaces as N is being removed from the solid. F_N has a value, which lies between 0 and 1 as previously mentioned. Therefore, the total volume added due to movement of the process front becomes:

$$\Delta V_{L(+)} = \frac{1}{(1-\varepsilon_{L+1})}\Delta V_{L(+),S} \qquad \textit{Equation 6.18}$$

The net reduction in bed volume due to movement of the process front is given by $\Delta V_{L(-)} - \Delta V_{L(+)}$.

For fuel A, *Equation 6.15* can be written as:

$$\Delta V_{A(-),S} = (1-\varepsilon_L)\Delta V_{A(-)} \qquad \textit{Equation 6.19}$$

The volume of moisture removed from fuel A is given by:

$$\Delta V_{2,A(-)} = w_{2,A}\Delta V_{A(-)S} \qquad \textit{Equation 6.20}$$

The mass of moisture removed can be calculated from the rate and time of evaporation:

$$m_{2A} = (R)_2 \Delta t \qquad \textit{Equation 6.21}$$

Therefore, the volume of moisture removed and the volume change of fuel A as drying took place can be written as:

$$\Delta V_{2,A(-)} = \frac{(R)_2 \Delta t}{\rho_2} = w_{2A}\Delta V_{A(-),S} \qquad \textit{Equation 6.22}$$

$$\Delta V_{A(-),S} = \frac{(R)_2 \Delta t}{\rho_2 w_{2A}} \qquad \textit{Equation 6.23}$$

Substituting *Equation 6.19* into *Equation 6.23* gives the volume change of fuel A as the drying took place:

$$\Delta V_{A(-)} = \frac{(R)_2 \Delta t}{\rho_2 w_{2A}(1-\varepsilon_A)} \qquad \textit{Equation 6.24}$$

Fuel B is then formed from each unit volume of A dried. The rate of change of fuel B is the difference between the rates of formation of B from fuel A during drying and the volume of B removed during pyrolysis.

The rate of B formed is taken from Equation 6.4 as:

$$\Delta V_{B(+)} = \Delta V_A \frac{(1-\varepsilon_A)}{(1-\varepsilon_B)}\left[1-(1-F_2)w_{2,A}\right] \qquad \textit{Equation 6.25}$$

Similarly, the volume of fuel B removed as the pryolysis takes place can be obtained by rewriting *Equation 6.24* ($(R)_3$ is the rate volatilisation or pyrolysis).

$$\Delta V_{B(-)} = \frac{(R)_3 \Delta t}{\rho_3 w_{3B}(1-\varepsilon_B)} \qquad \textit{Equation 6.26}$$

Therefore,

Rate change of volume B = Rate of formation of fuel B – Rate of removal of fuel B:

$$\Delta V_B = \Delta V_A \frac{(1-\varepsilon_A)}{(1-\varepsilon_B)}\left[1-(1-F_2)w_{2,A}\right]-\frac{(R)_3 \Delta t}{\rho_3 w_{3B}(1-\varepsilon_B)} \qquad \textit{Equation 6.27}$$

As fuel B is formed from each unit volume of fuel A removed, *Equation 6.27* can be rewritten using *Equation 6.24*:

$$\Delta V_B = \left[\frac{(R)_2}{\rho_2 w_{2A}(1-\varepsilon_B)}\left[1-(1-F_2)w_{2,A}\right]-\frac{(R)_3}{\rho_3 w_{3B}(1-\varepsilon_B)}\right]\Delta t \qquad \textit{Equation 6.28}$$

The rate of change of fuel C could be represented in the same way.

$$\Delta V_C = \left[\frac{(R)_3}{\rho_3 w_{3B}(1-\varepsilon_C)}\left[1-(1-F_3)w_{3,B}\right]-\frac{(R)_4}{\rho_4 w_{4C}(1-\varepsilon_C)}\right]\Delta t \qquad \textit{Equation 6.29}$$

The volume of fuel D formed during gasification is given by *Equation 6.10*:

$$\Delta V_{D(+)} = \Delta V_C \frac{(1-\varepsilon_C)}{(1-\varepsilon_D)}\left(\frac{w_{5C}}{w_{5D}}\right) \qquad \textit{Equation 6.30}$$

As there is no reaction in the ash (fuel D), the volume reduction of fuel D is zero. Therefore, the rate of change of volume D would be equal to the rate of formation of fuel D from the gasification of fuel C. Thus,

$$\Delta V_D = \frac{(R)_4 w_{5C}}{\rho_4 w_{4C}(1-\varepsilon_D)w_{5D}}\Delta t \qquad \textit{Equation 6.31}$$

As $w_{5D} = 1$, *Equation 6.33* can be rewritten as:

$$\Delta V_D = \frac{(R)_4 w_{5C}}{\rho_4 w_{4C}(1-\varepsilon_D)}\Delta t \qquad \textit{Equation 6.32}$$

Table 6.2 summarises the differential equations representing the changes in volume of fuel A, B, C and D where $(R)_2$, $(R)_3$ and $(R)_4$ are the mass rates of drying, pyrolysis and gasification respectively.

Fuel	Differential equations representing the volume changes
A	$\Delta V_A = -\dfrac{(R)_2 \Delta t}{\rho_2 w_{2A}(1-\varepsilon_A)}$
B	$\Delta V_B = \left[\dfrac{(R)_2}{\rho_2 w_{2A}(1-\varepsilon_B)}\left[1-(1-F_2)w_{2,A}\right]-\dfrac{(R)_3}{\rho_3 w_{3B}(1-\varepsilon_B)}\right]\Delta t$
C	$\Delta V_C = \left[\dfrac{(R)_3}{\rho_3 w_{3B}(1-\varepsilon_C)}\left[1-(1-F_3)w_{3,B}\right]-\dfrac{(R)_4}{\rho_4 w_{4C}(1-\varepsilon_C)}\right]\Delta t$
D	$\Delta V_D = \dfrac{(R)_4 w_{5C}}{\rho_4 w_{4C}(1-\varepsilon_D)}\Delta t$

Table 6.2: Differential equations for the volume changes in fuel A, B, C and D.

6.1.3.1 Process Rate Equations

Moisture Evaporation

Solid fuel can be heated up by over-bed radiation when they enter the incinerator and moisture is released as evaporation proceeds. Moisture can also be driven out by the mass exchange between the wet solids and drier airflow from under the grate. The rate of moisture release from solids can be expressed as follows, whereby, $(R)_2$ is the rate of vaporisation or drying rate, given by:

$$R_2 = S_a h_s \left(C_{w,s} - C_{w,g}\right) \qquad \text{when } T_s < 100°C \qquad \textit{Equation 6.33a}$$

or

$$(R)_2 = \frac{Q_{cr}}{H_{evp}} \qquad \textit{Equation 6.33b}$$

Where S_a is the surface area of solid particles, h_s, the convective mass transfer coefficient between solid and gas, $C_{w,s}$, the concentration of moisture at the solid surface, and $C_{w,g}$, the concentration of moisture in the air flow, T_s, the solid temperature, Q_{cr}, the heat absorbed by the solids, and H_{evp} is the evaporation heat of the solid material. Q_{cr} includes both convection and radiation heat transfer which is expressed as

$$Q_{cr} = S_a\left(h_s'\left(T_g - T_s\right) + \varepsilon_s \sigma_b \left(T_{env}^4 - T_s^4\right)\right) \qquad \textit{Equation 6.34}$$

where h_s' represents the convective heat transfer coefficient between solid and gas, T_g, the gas temperature, ε_s, the system emissivity, σ_b, the Boltmann radiation constant, and T_{env} is the environmental temperature (Yang, 2003). The Nusselt number for heat transfer and Sherwood number for mass transfer between the solid and gas phases are calculated as $Nu = 2 + 1.1\,\mathrm{Pr}^{1/3}\,\mathrm{Re}^{0.6}$ and $Sh = 2 + 1.1 Sc^{1/3}\,\mathrm{Re}^{0.6}$ (Wakao, 1982).

Solid Devolatilisation

As the devolatilisation of solid fuel yields a wide range of different gaseous fuels, the one-step global model was applied due to its simplicity. The gases are taken to compose mainly of hydrocarbon (C_mH_n), CO, H_2, CO_2, O_2 (Smoot, 1979).

$$Waste \rightarrow Volatile\left(C_mH_n, CO, H_2, CO_2, O_2, etc.\right) + char$$

The releasing rate of volatile gases from the solid is proportional to the remaining volatiles in the solid and the temperature

$$R_3 = k_v\left(v_\infty - v\right)s^{-1} \qquad \textit{Equation 6.35a}$$

Where

$$k_v = A_v \exp\left(-E_v / RT_s\right) \qquad \textit{Equation 6.35b}$$

For simplification, the volatile hydrocarbons are assumed to consist of a single product, $C_mH_nO_l$, which is oxidised to produce CO and H_2:

$$C_mH_nO_l + \left(m/2 - l/2\right)O_2 \rightarrow mCO + {}^{n}\!/_{2}\,H_2 \qquad \textit{Equation 6.36}$$

CO is then burned by further oxidation to form CO_2

$$CO + \frac{1}{2}O_2 \rightarrow CO_2 \qquad \textit{Equation 6.37}$$

and H_2 to form H_2O

$$H_2 + \frac{1}{2}O_2 \rightarrow H_2O \qquad \textit{Equation 6.38}$$

The temperature-dependent burning rates or kinetic rates, $R_{C_mH_nO_l}$ is assumed to be the same as proposed by Siminski (1972) for C_mH_n.

$$R_{C_mH_nO_l} = 59.8T_g P^{0.3} \exp(-12{,}200/T_g) C^{0.5}_{C_mH_nO_l} C_{O_2} \qquad \textit{Equation 6.39}$$

The kinetic rate for CO, R_{CO} and H_2, R_{H_2} is as given by Howard (1973) and Hautman (1981) respectively.

$$R_{CO} = 1.3x10^{11} \exp(-62{,}700/T_g) C_{CO} C^{0.5}_{H_2o} C^{0.5}_{O_2} \qquad \textit{Equation 6.40}$$

$$R_{H_2} = 3.9x10^{17} \exp(-20{,}500/T_g) C^{0.85}_{H_2} C^{1.42}_{O_2} C^{-0.56}_{C_mH_nO_l} \qquad \textit{Equation 6.41}$$

The original $C_{C_2H_4}$ was replaced with $C_{C_mH_nO_l}$ as an approximation. C_{CO}, C_{H_2O}, C_{O_2}, $C_{C_mH_nO_l}$ represent the species concentrations, and P the pressure (taken as atmospheric for the packed-bed combustion).

Mixing

The volatile products release from the particle surface during the devolatilisation process has to first mix with the surrounding air before combustion could occur. Gas combustion takes place in voids spaces that resemble long inter-connected channels with widths comparable to particle diameters in the bed. The burning of volatiles hydrocarbon gases is limited by both the reaction kinetics (temperature dependent) and the mixing-rate of the gaseous fuel with primary air. The mixing rate inside the bed is assumed proportional to energy loss (pressure drop) through the bed and by recalling Ergun equations (Hunt, 1988; Vafai, 1990) can be correlated as:

$$R_{mix} = C_{mix}\rho_g \left\{ 150\frac{D_g(1-\varepsilon)^{2/3}}{d_p^2\varepsilon} + 1.75\frac{V(1-\varepsilon)^{1/3}}{d_p\varepsilon} \right\} \min\left[\frac{C_{fuel}}{S_{fuel}}, \frac{C_{O_2}}{S_{O_2}}\right] \qquad \textit{Equation 6.42}$$

where C_{mix} is an empirical constant, D_g, the molecular diffusivity of the combustion air, V_g the air velocity, d_p, the particle diameter, ε, the local void fraction of the bed, C, the mass fraction of the gaseous reactants, and S is the stoichiometric coefficients in the reaction.

The actual reaction rates of volatile species are taken as the minimum of the temperature-dependent kinetic rates and their mixing-rates with oxygen:

$$R_{reaction} = \min\left[R_{kinetics}, R_{mix}\right] \qquad \textit{Equation 6.43}$$

Char Combustion

Char forms as volatiles escape from the fuel. The primary products of char gasification are CO and CO_2.

$$C_{(s)} + \alpha O_2 \rightarrow 2(1-\alpha)CO + (2\alpha - 1)CO_2 \qquad \textit{Equation 6.44}$$

with the ratio of CO and CO_2 as (Arthur, 1951):

$$CO/CO_2 = 2500\exp(-6420/T) \qquad \textit{Equation 6.45}$$

The char consumption rate is expressed as (Smooth, 1979)

$$R_{C(s)} = C_{O_2} \Big/ \left(1/k_r + 1/k_d\right) \qquad \textit{Equation 6.46}$$

where k_r and k_d are rate constants due to chemical kinetics and diffusion, respectively.

6.1.3.2 Transport Equations for Gas and Solid Phases

The flow model that is used for the gas phase simulation is based on the hydraulic radium theory of porous media, which allows flows within such a complicated and randomly arranged network to be treated. The early work based on this theory was carried out by Darcy (Peters, 1995) who related flows in porous media to the governing equation pressure gradient through viscosity and porosity as essential parameters of porous media. The continuity and species equations of the gas phase in the packed bed are written as:

Gas continuity: $\dfrac{\partial(\varepsilon\rho_g)}{\Delta t} + \dfrac{\partial(\varepsilon\rho_g V_g)}{\Delta x} = -S_{sg}$ *Equation 6.47*

where, V_g is the gas velocity and x the coordinate along the bed height (x=0 at the bed bottom). The source term S_{sg} is the conversion rate from solid to gas due to moisture evaporation, devolatilisation and char combustion.

Gas species transport: $\frac{\partial(\varepsilon\rho_g Y_{ig})}{\partial t}+\frac{\partial}{\partial x}(\varepsilon\rho_g Y_{ig}V_g)=\frac{\partial}{\partial x}\left(D_{ig}\frac{\partial(\varepsilon Y_{ig})}{\partial x}\right)+S_{Y\,ig}$ *Equation 6.48*

where Y_{ig} is the mass fraction of species 'ig' in the gas (such as O_2, H_2, H_2O, CO, CO_2, C_mH_n, etc.). The source term $S_{Y_{ig}}$ accounts for mass added to the fluid due to evaporation, devolatilization and combustion.

The fluid dispersion coefficient D_{ig} is considered to consist of diffusion and turbulent contributions and is given by the following equation (Wakao, 1982). E^0 is the effective diffusion coefficient.

$$D_{ig}=E^0+0.5d_pV_g \qquad \textit{Equation 6.49}$$

Gas-phase energy conservation

$$\frac{\partial(\varepsilon\rho_g H_g)}{\partial t}+\frac{\partial}{\partial x}(\varepsilon\rho_g h_g V_g)=\frac{\partial}{\partial x}\left(\lambda_g\frac{\partial T_g}{\partial x}\right)+S_a\dot{h_s}(T_s-T_g)+Q_h \qquad \textit{Equation 6.50}$$

where, H_g represents gas enthalpy, λ_g, the thermal dispersion coefficient, Q_h, the heat gain of the gas phase due to combustion. The thermal dispersion coefficient λ_g consists of diffusion and turbulent contributions in a similar way as species dispersion, and can be express as (Wakao and Kaguei, 1982):

$$\lambda_g=\lambda^0+0.5d_pV_g\rho_gC_{pg} \qquad \textit{Equation 6.51}$$

where λ^0 denotes the effective thermal diffusion coefficient.

Solid Phase

The continuity equation is given by:

Solid continuity: $\frac{\partial((1-\varepsilon)\rho_s)}{\Delta t}+\frac{\partial((1-\varepsilon)\rho_sV_s)}{\Delta x}=-S_S$ *Equation 6.52*

where ρ_s is the particle density and V_s is the solid velocity due to the downward movement of the bed caused by mass loss.

The conservation equation of the solid phase components is expressed as:

$$\frac{\partial((1-\varepsilon)\rho_s Y_{is})}{\Delta t}+\frac{\partial((1-\varepsilon)\rho_s V_s Y_{is})}{\Delta x}=-S_{Y_{ig}} \qquad \textit{Equation 6.53}$$

where Y_{is} represents the mass fractions of particle compositions (moisture, volatile, fixed carbon and ash) and $S_{Y_{ig}}$ accounts for the loss of the individual components (moisture, volatile, fixed carbon and ash) during evaporation, devolatilisation and char combustion.

The energy equation for the solid-phase is

$$\frac{\partial((1-\varepsilon)\rho_s h_s)}{\partial t}+\frac{\partial((1-\varepsilon)\rho_s v_s h_s)}{\partial x}=\frac{\partial}{\partial x}\left(\lambda_S \frac{\partial T_S}{\partial x}\right)+S_a h_s^{\cdot}\left(T_g-T_S\right)\frac{\partial q_r}{\partial x}+Q_{sh} \quad \textit{Equation 6.54}$$

where H_s presents the solid-phase enthalpy, λ_S is the effective thermal conductivity of the solid bed, $h_s^{\cdot}$ is the convective heat transfer coefficient between solid and gas and q_r denotes the radiative heat flux. The source term, Q_{sh} accounts for the heat generation due to heterogeneous combustion.

6.1.3.3 Radiation Heat Transfer in the Bed

The gas phase radiation plays a significant role in the heat transfer between the solid particles within a packed bed. Therefore, the flux model (Smoot and Pratt, 1979) for gaseous and entrained flow combustion is used for the gas phase flow prediction. The two-flux radiation model is presented as follows:

$$\frac{dI_x^+}{dx}=-(k_a+k_s)I_x^+ +\frac{1}{2}k_a E_b+\frac{1}{2}k_s\left(I_x^+ +I_x^-\right) \qquad \textit{Equation 6.55a}$$

$$-\frac{dI_x^-}{dx}=-(k_a+k_s)I_x^- +\frac{1}{2}k_a E_b+\frac{1}{2}k_s\left(I_x^+ +I_x^-\right) \qquad \textit{Equation 6.55b}$$

where the two radiation intensities are represented by I_x^+, I_x^-, k_a and k_s denote the absorption and scattering coefficients, respectively. E_b is the black-body radiation.

k_s is assumed zero as the first approximation, and k_a is taken as:

$$k_a=-\frac{1}{d_p}\ln(\phi) \qquad \textit{Equation 6.56}$$

6.1.3.4 Solving the Mathematical Equations

The governing equations described above are generalised into a standard form, except for radiation equation.

$$\frac{\partial \rho \Phi}{\partial t} + \frac{\partial (\rho V \Phi)}{\partial x} = \frac{\partial}{\partial x}\left(\lambda \frac{\partial \Phi}{\partial x}\right) + S_{\Phi} \qquad \textit{Equation 6.57}$$

where ρ represents density, V, velocities, Φ, the parameter to be solved, λ, the transport coefficient, and S_{Φ} is the source term. The whole geometrical domain of the bed is divided into a number of small cells and *Eq. 6.57* is discretised over each cell and solved numerically using the SIMPLE algorithm (Patankar, 1980). The radiation equations are solved by the fourth-order Runge-Kutta method (Bajpai, 1977).

6.2 FUEL SIZE EFFECT ON PINEWOOD COMBUSTION IN A PACKED BED

6.2.1 Input Conditions

The input data for the numerical cases are similar to the experimental conditions so that comparison between the FLIC predictions and experimental results were possible.

The initial bed temperature is taken as room temperature, 288K. The side wall temperature is given as 973K and the side wall heat losses were taken into account in the calculations as the experimental rig was not insulated. The simulations were repeated for particle sizes of 5mm, 10mm, 20mm and 35mm. The fuel is ignited by an over-bed radiation of temperature 1123K with an emissivity of 0.8. The bed porosity is taken as 0.7.

The devolatilisation rate used in this theoretical calculation is given by Pyle and Zaror (1984) in the one-step global model, $k_v = A_v \exp(-E_v / R)$ where A_v = 3.0 x $10^3(s^{-1})$ and E_v = 69(kJ/mol). The kinetic rate of char combustion $k_c = A_c \exp(-E_c / R)$ where A_C = 2.3 x 10^3(kg/m^{2}skPa) and E_c/R = 11000(K) (Smooth, 1985).

The computational zone is extended to the whole length of the bed plus a space height of about 340mm above the bed. The air flow rate and velocity at the bottom of the bed (the lower boundary) are given by the running conditions of the experiment which is 0.145 Nm^3/min and is presented as the standard cubic feet per minute (SCFM) in FLIC.

6.2.2 Numerical Model Prediction

The results obtained from the FLIC computation are presented in contour form with distance above the grate (mm) on the vertical axis, and the wood particle residence time (s) on the horizontal axis.

6.2.2.1 Temperature Profile in the Bed

Figure 6.5(a) and (b) presents the computed solid bed temperature distribution for the fixed bed combustion of 10mm (Case P-10) and 35mm (Case P-35) pine wood particles. The temperature distribution at each specific residence time was calculated as the combustion progresses and the bed of wood particles is gradually burned down towards the grate.

The top of the bed is heated up as soon as the over-bed radiation source was initiated. The bed height decreased to a small extent as moisture in the fuel evaporated. For Case P-10, the temperature at the bed surface is approximately 400K at the start of the calculation and escalated to 674K at t=300secs due to the combustion of the released volatile matter. This is followed by sharp rise in the bed surface temperature to 1200K and a steep decline in bed height at about t=520s as the char oxidation stage commences. The bed was very hot towards the end of the combustion as all the moisture and volatile were driven out leading to an intense char oxidation. The bed surface was the hottest region throughout the combustion process as it was exposed to radiation from the freeboard.

a)

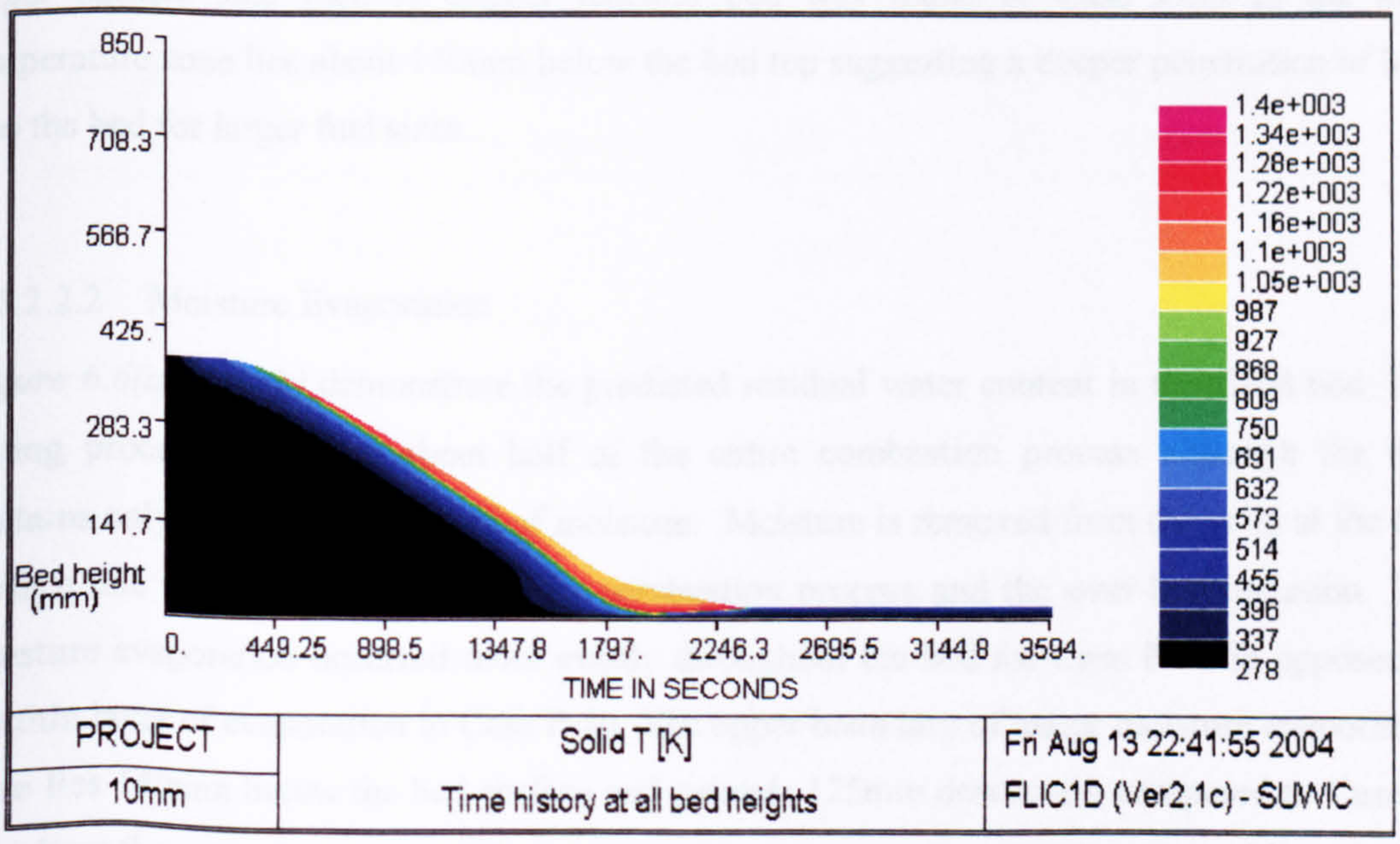

b)

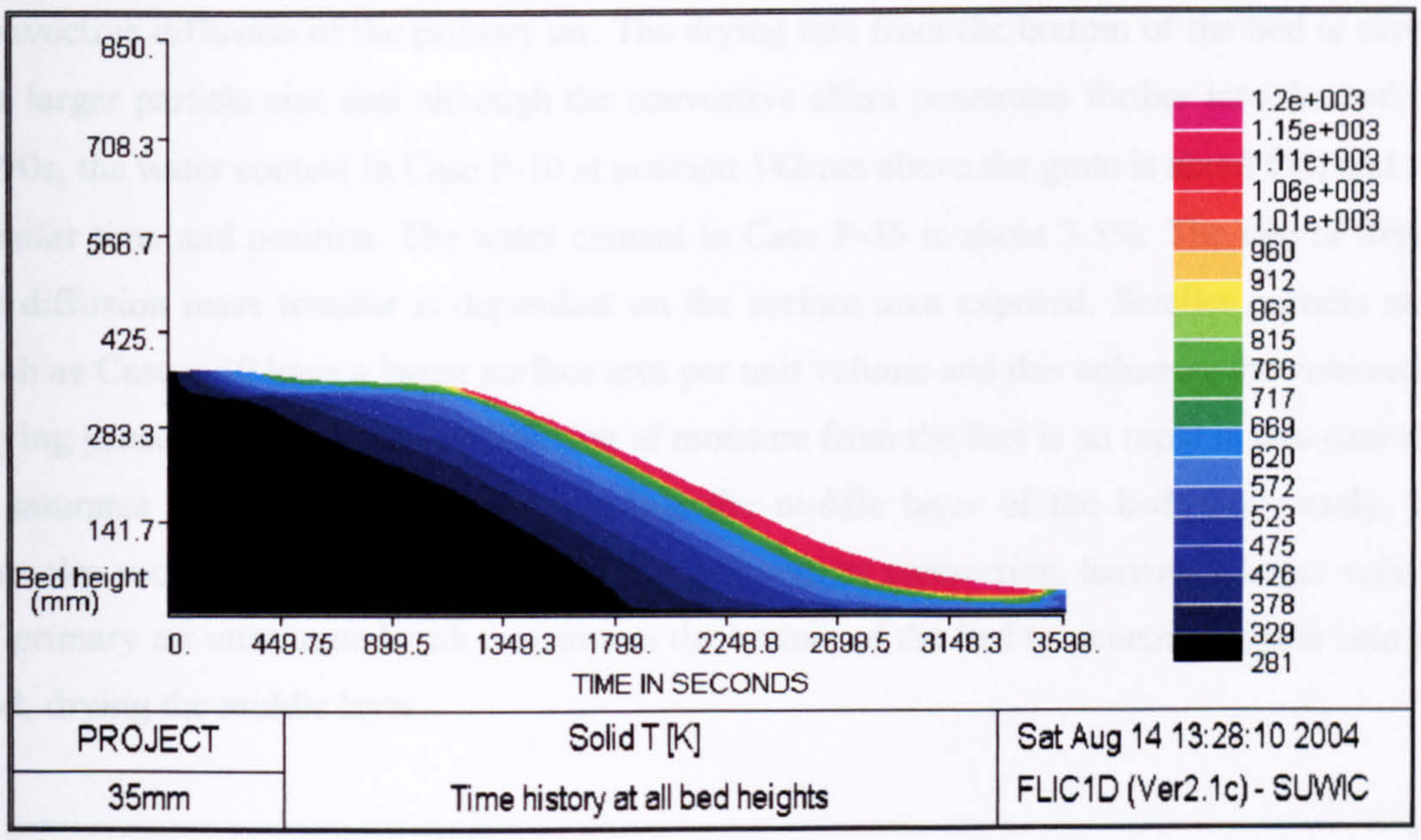

Figure 6.5: Predicted solid bed temperature distribution in the fixed bed. (a) Case P-10 (10mm); (b) Case P-35 (35mm).

Comparing the two cases, one of the most distinctive effects of a large particle size is the extended combustion period. For Case P-10, the entire combustion process ended about 2250s while Case-P4 burning continued for 3600s. As the fuel particle size increases, the bed height decreases gradually with time indicating a slower burning rate. The maximum local bed temperature at the bed surface was 100K lower in Case P-10, taking a value of 1100K. However, the time taken for the bed surface to reach the maximum temperature is longer for larger particle size fuel. A thicker reaction bed was found in Case P-35 as the high temperature zone lies about 140mm below the bed top suggesting a deeper penetration of heat into the bed for larger fuel sizes.

6.2.2.2 Moisture Evaporation

Figure 6.6(a) and (b) demonstrate the predicted residual water content in the fixed bed. The drying process lasted for about half of the entire combustion process although the fuel contains only about 5% by weight of moisture. Moisture is removed from the solid at the bed surface due to intensive heat from the combustion process and the over-bed radiation. The moisture evaporation occurred more evenly throughout the bed for Case P-35 in opposed to the thin layer of evaporation in Case P-10. The upper boundary of major moisture evaporation zone lies 140mm below the bed surface and extends 125mm downward compared to Case P-10 where the upper boundary of the major moisture evaporation zone lies about 50mm below the bed top and the zone extends 70mm downward.

Unlike the bed top, the drying process at the bottom of the bed is largely influenced by the convective diffusion of the primary air. The drying rate from the bottom of the bed is slower for larger particle size fuel although the convective effect penetrates further into the bed. At t=90s, the water content in Case P-10 at position 142mm above the grate is about 5%, and at a similar time and position. The water content in Case P-35 is about 3.5%. The rate of drying by diffusion mass transfer is dependant on the surface area exposed. Smaller particle sizes such as Case p-10 have a larger surface area per unit volume and this enhances the convective drying process. The convective diffusion of moisture from the fuel is so rapid in this case that it saturates the primary air before reaching the middle layer of the bed. Conversely, big particles such as Case P-35 have a slower drying rate by convection, leaving a larger volume of primary air unsaturated with moisture at the bottom of the bed to penetrate higher into the bed, drying the middle layer.

a)

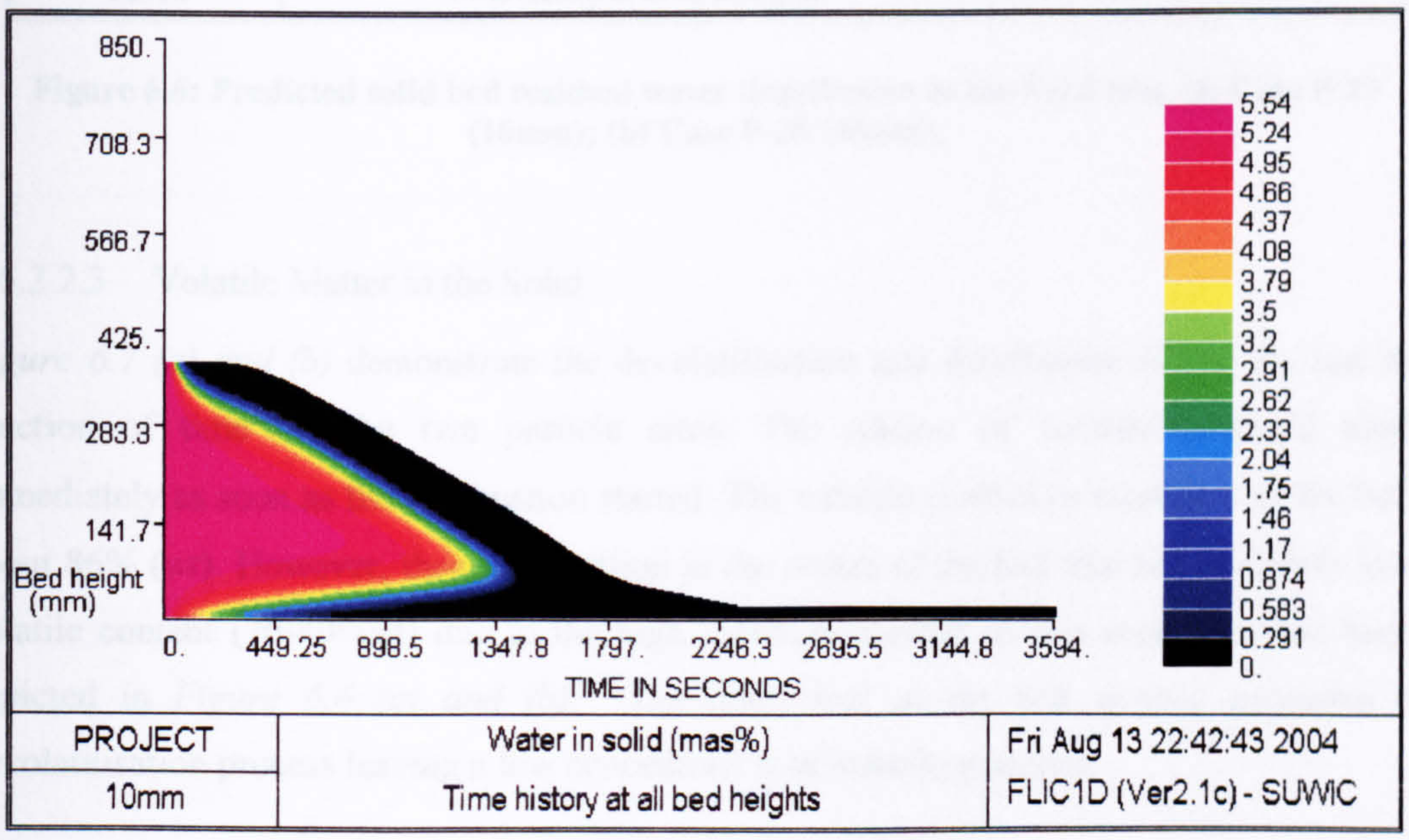

b)

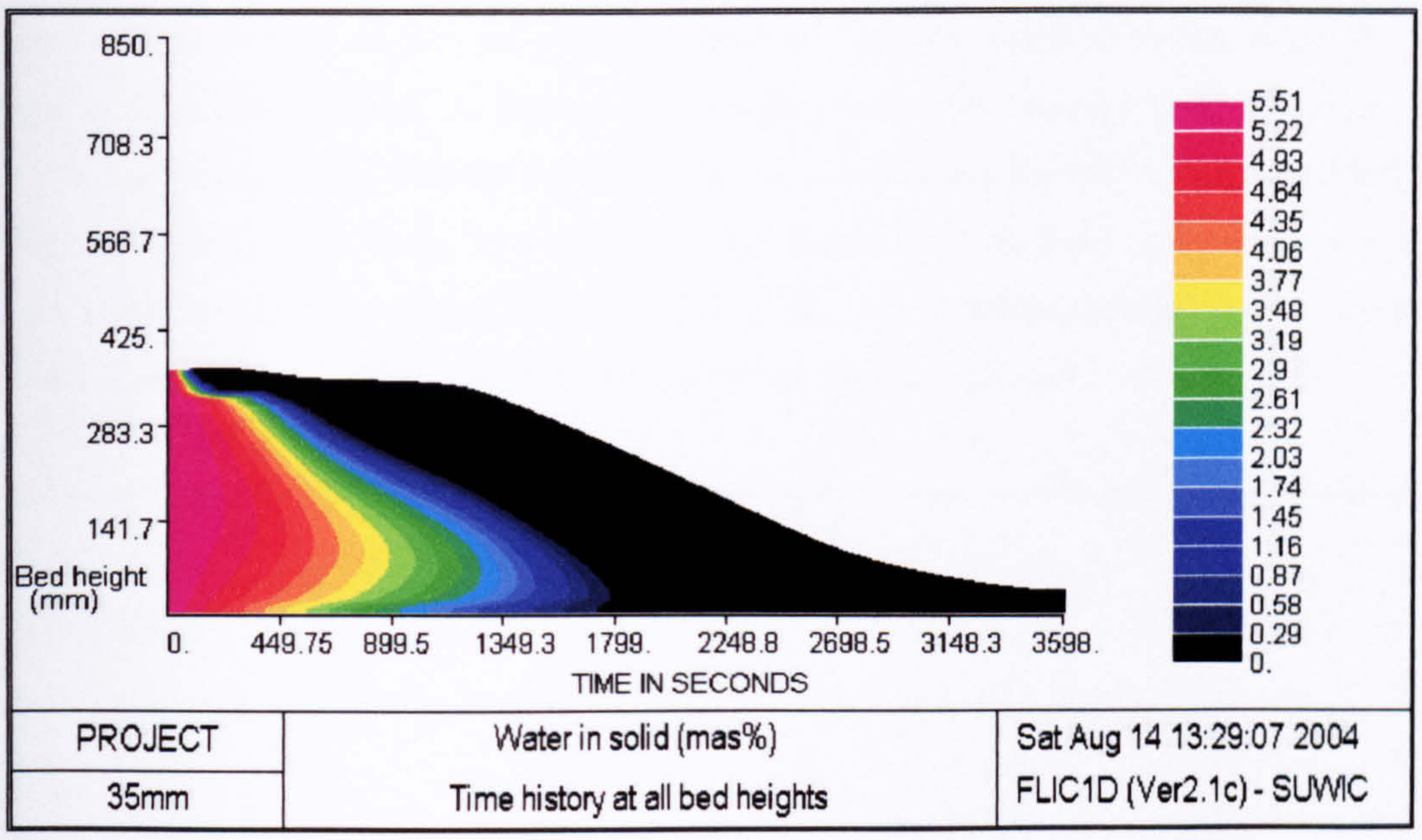

Figure 6.6: Predicted solid bed residual water distribution in the fixed bed. (a) Case P-10 (10mm); (b) Case P-35 (35mm).

6.2.2.3 Volatile Matter in the Solid

Figure 6.7 (a) and (b) demonstrate the devolatilisation rate distribution inside the bed as a function of time for the two particle sizes. The release of volatile occurred almost immediately as soon as the combustion started. The volatile content in most part of the bed is about 86% (wt). However, there is a portion in the centre of the bed that has a slightly lower volatile content (70-80%wt) due to the high moisture content in this section of the bed as depicted in *Figure 6.6 (a) and (b)*. The dried fuel at the bed surface promotes the devolatilisation process leaving a low concentration of volatile material.

For Case P-10, the upper boundary of the major devolatilisation zone moves away from the bed top as the combustion progresses and reaches a maximum 40mm below the bed surface. The thickness of the devolatilisation zone increases about twice-fold to about 75mm for Case P-35. The release of volatile is faster for smaller particle size fuel.

a)

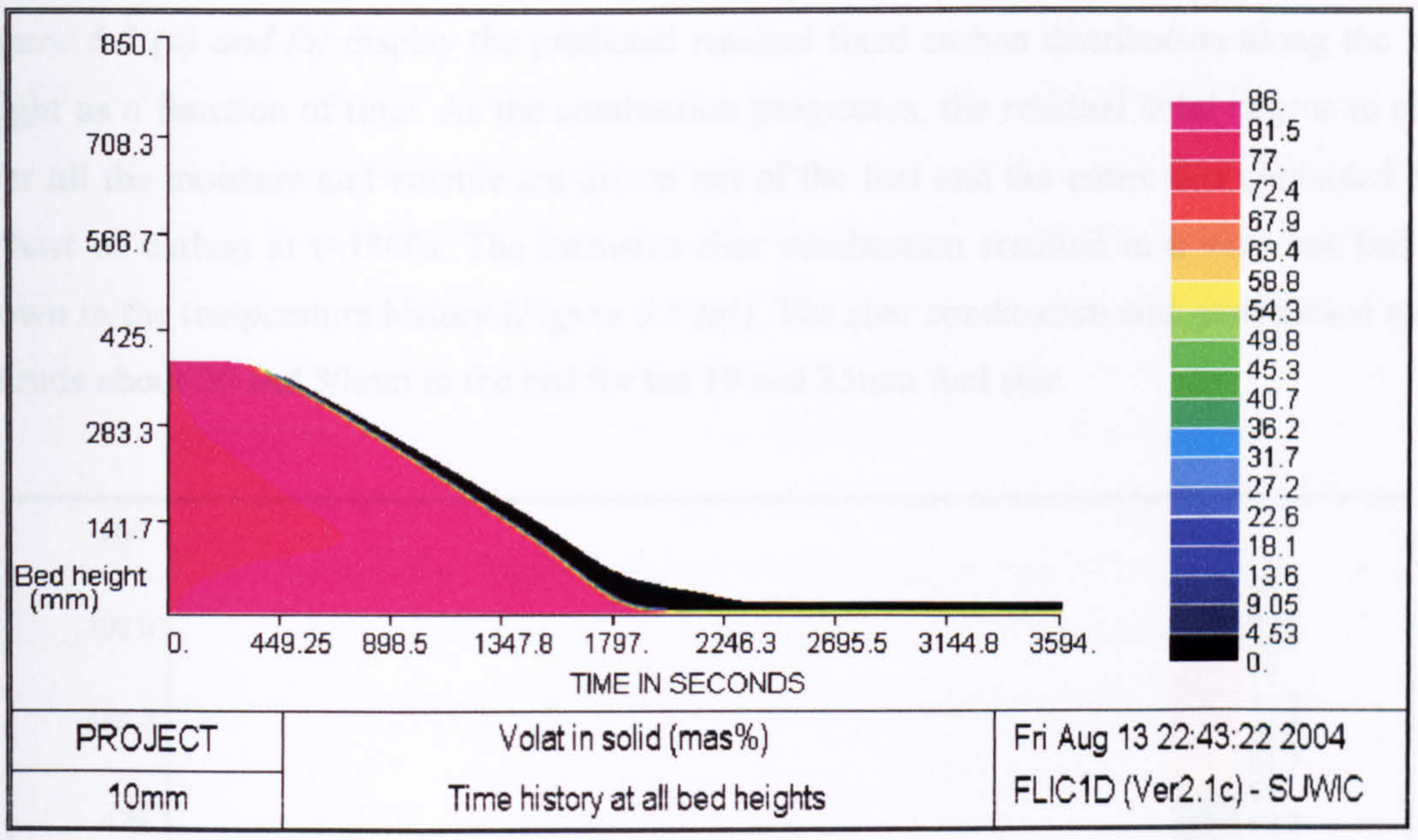

b)

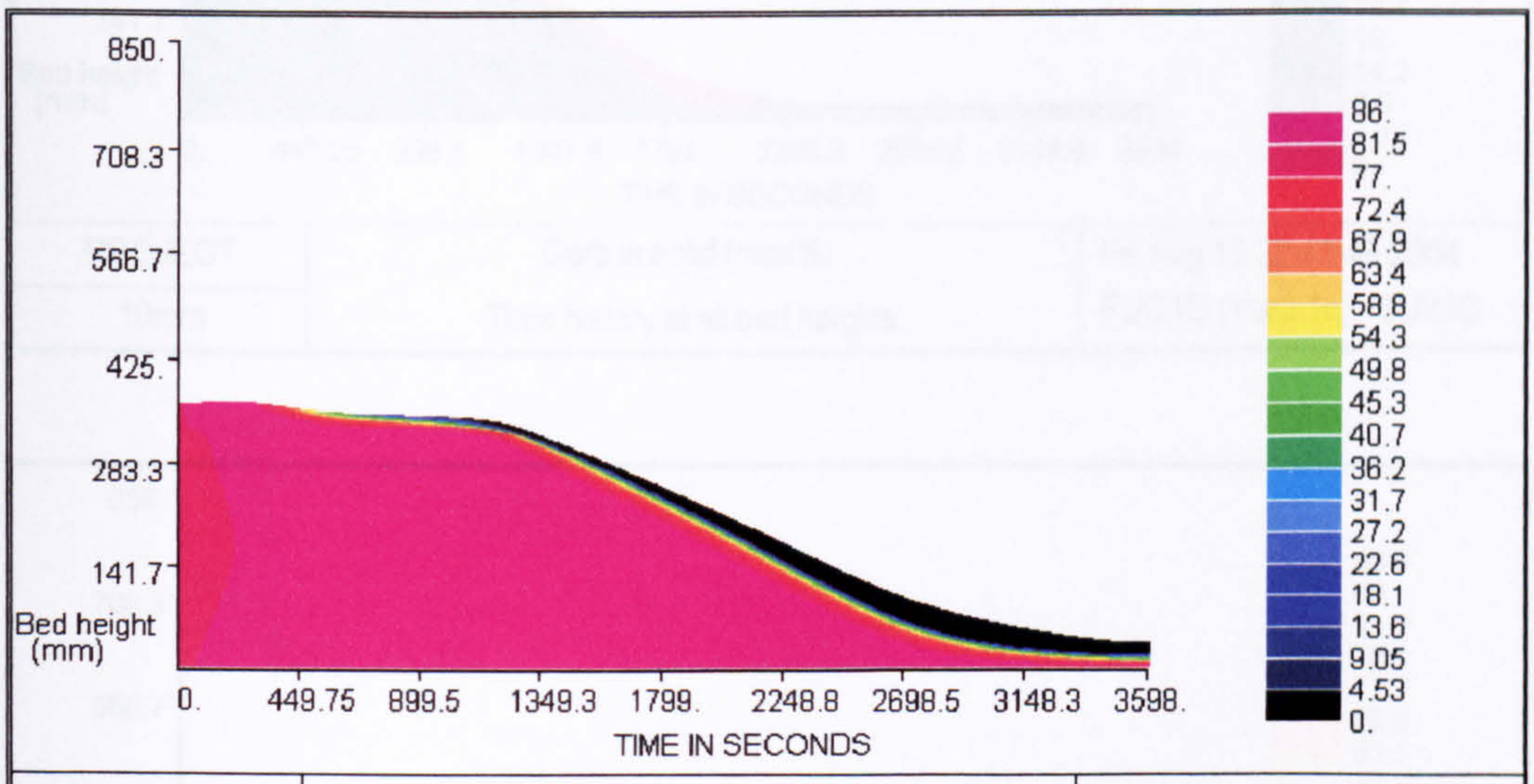

Figure 6.7: Predicted solid bed residual volatile distribution in the fixed bed. (a) Case P-10 (10mm); (b) Case P-35 (35mm).

6.2.2.4 Fixed Carbon in the Bed

Figure 6.8 (a) and (b) display the predicted residual fixed carbon distribution along the bed height as a function of time. As the combustion progresses, the residual solid begins to char after all the moisture and volatile are driven out of the fuel and the entire bed contained 85-90%wt of carbon at t=1800s. The intensive char combustion resulted in a very hot bed as shown in the temperature history (*Figure 6.5 (a)*). The char combustion and gasification zone extends about 20 and 30mm in the bed for the 10 and 35mm fuel size.

a)

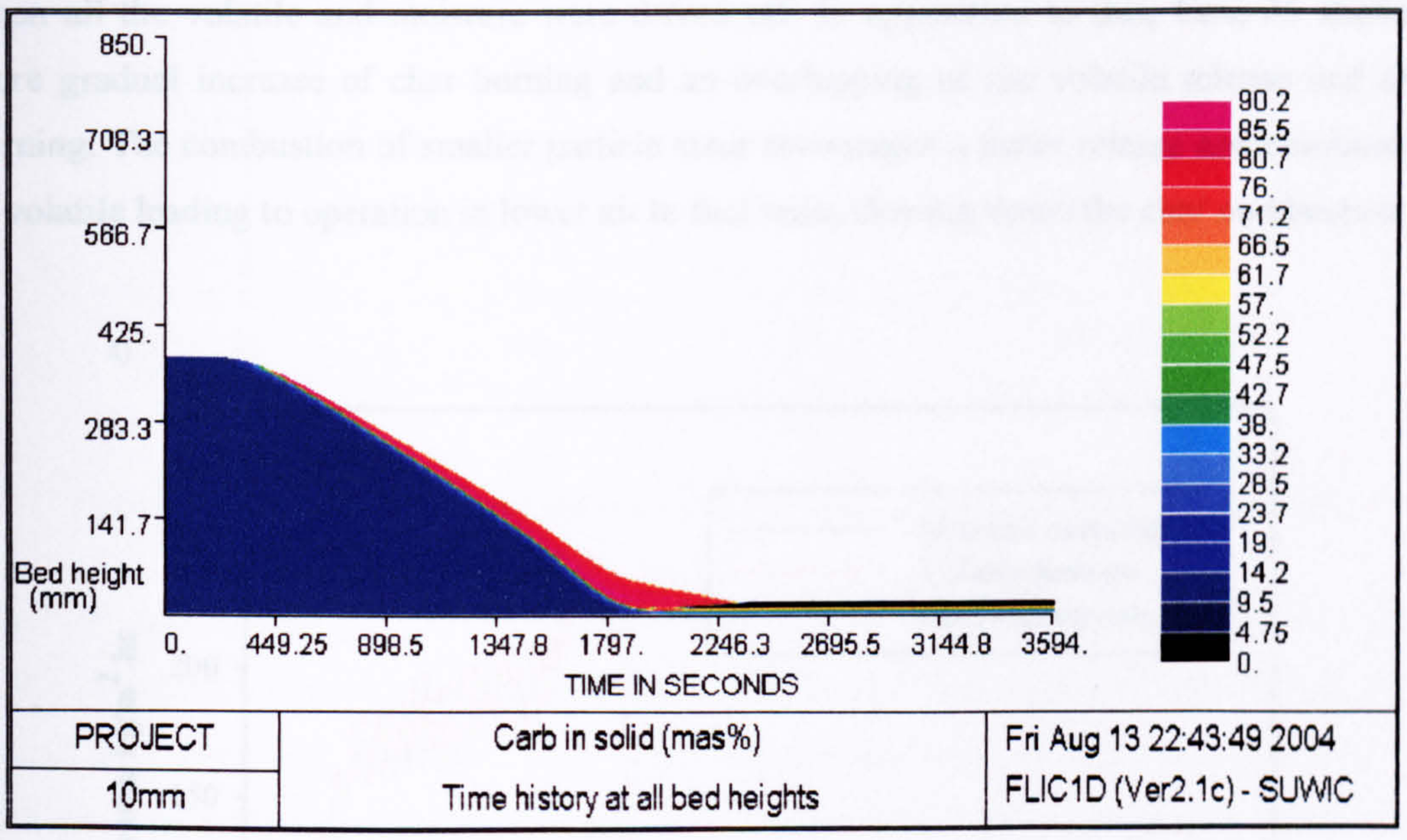

b)

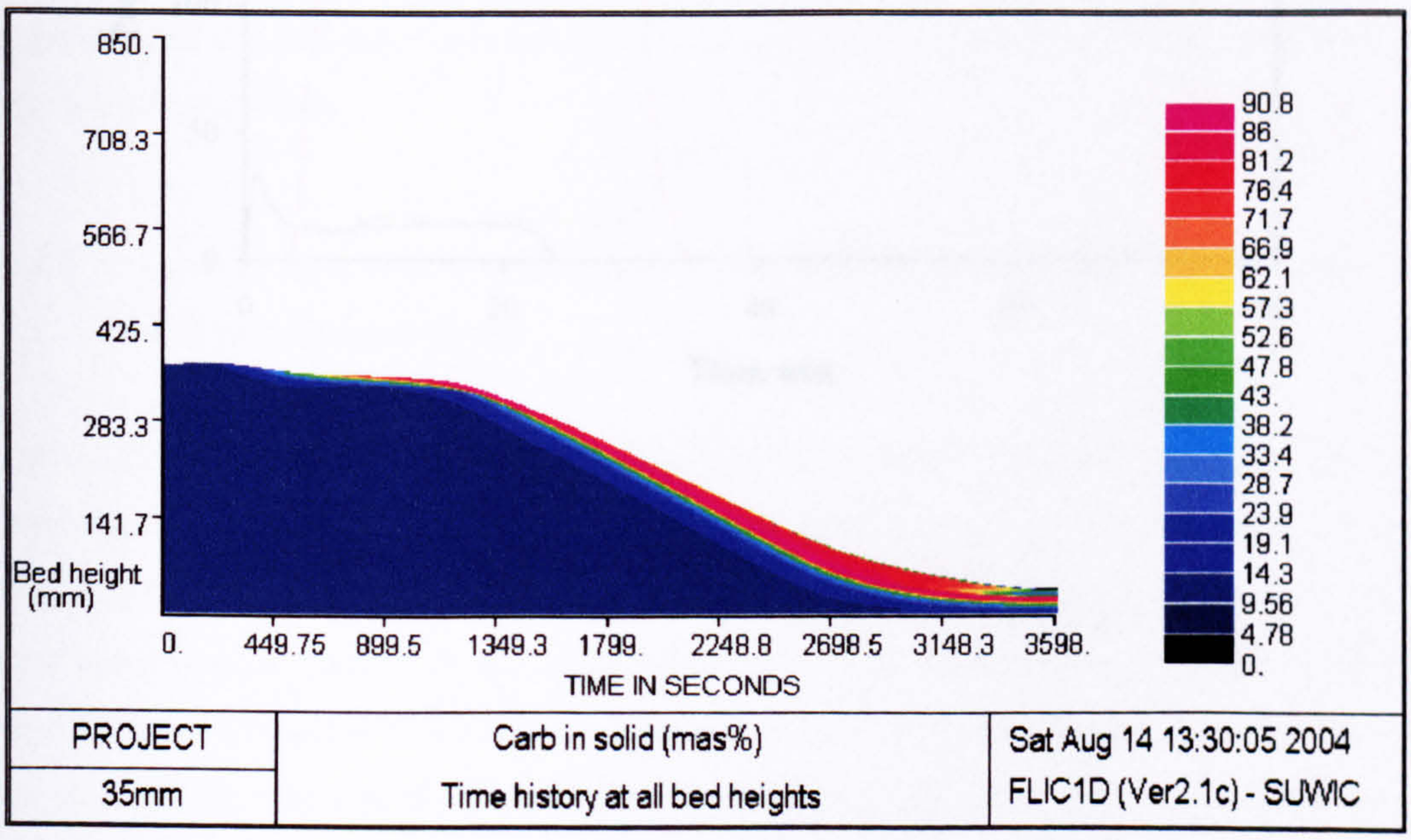

Figure 6.8: Predicted solid bed fixed carbon distribution in the fixed bed. (a) Case P-10 (10mm); (b) Case P-35 (35mm).

6.2.3 Individual Process Rates

Figure 6.9 (a) and (b) show the rates for the three individual sub-processes for Case P-10 and Case P-35. It can be observed that the entire combustion process was 'stretched' towards the right as larger particles were used. Case P-10 features a more constant and steady burning process during the major combustion stage while Case P-35 undergoes gradual changes for most of the combustion period. The particle size plays an important role in the initiation of the char burning rate period. For Case P-10, the char burning increased to a rapid rate at t=1500s when all the volatile and moisture were driven off. In opposition to this, Case-35 shows a more gradual increase of char burning and an overlapping of the volatile release and char burning. The combustion of smaller particle sizes encourages a faster release and combustion of volatile leading to operation in lower air to fuel ratio, slowing down the char combustion.

a)

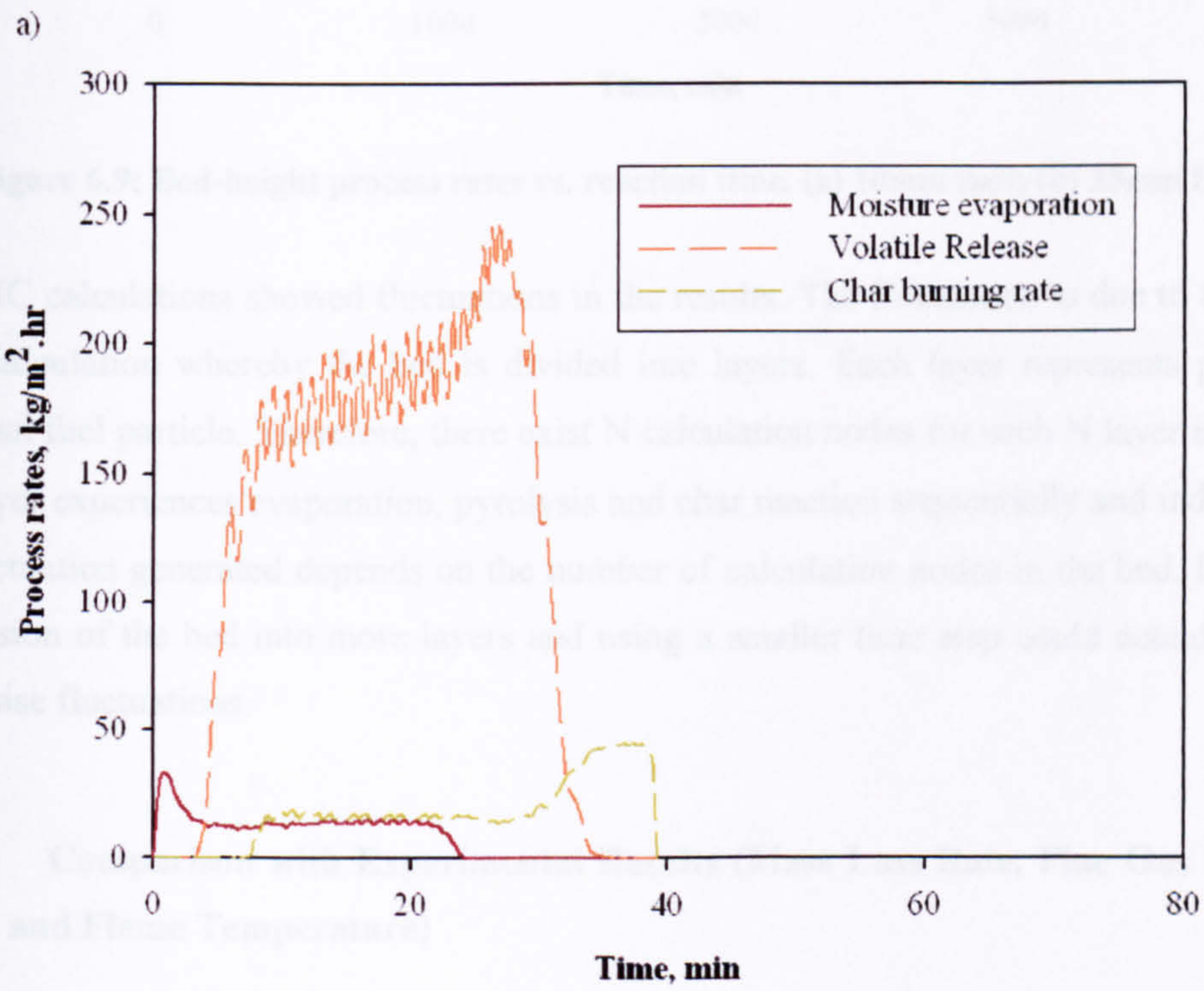

b)

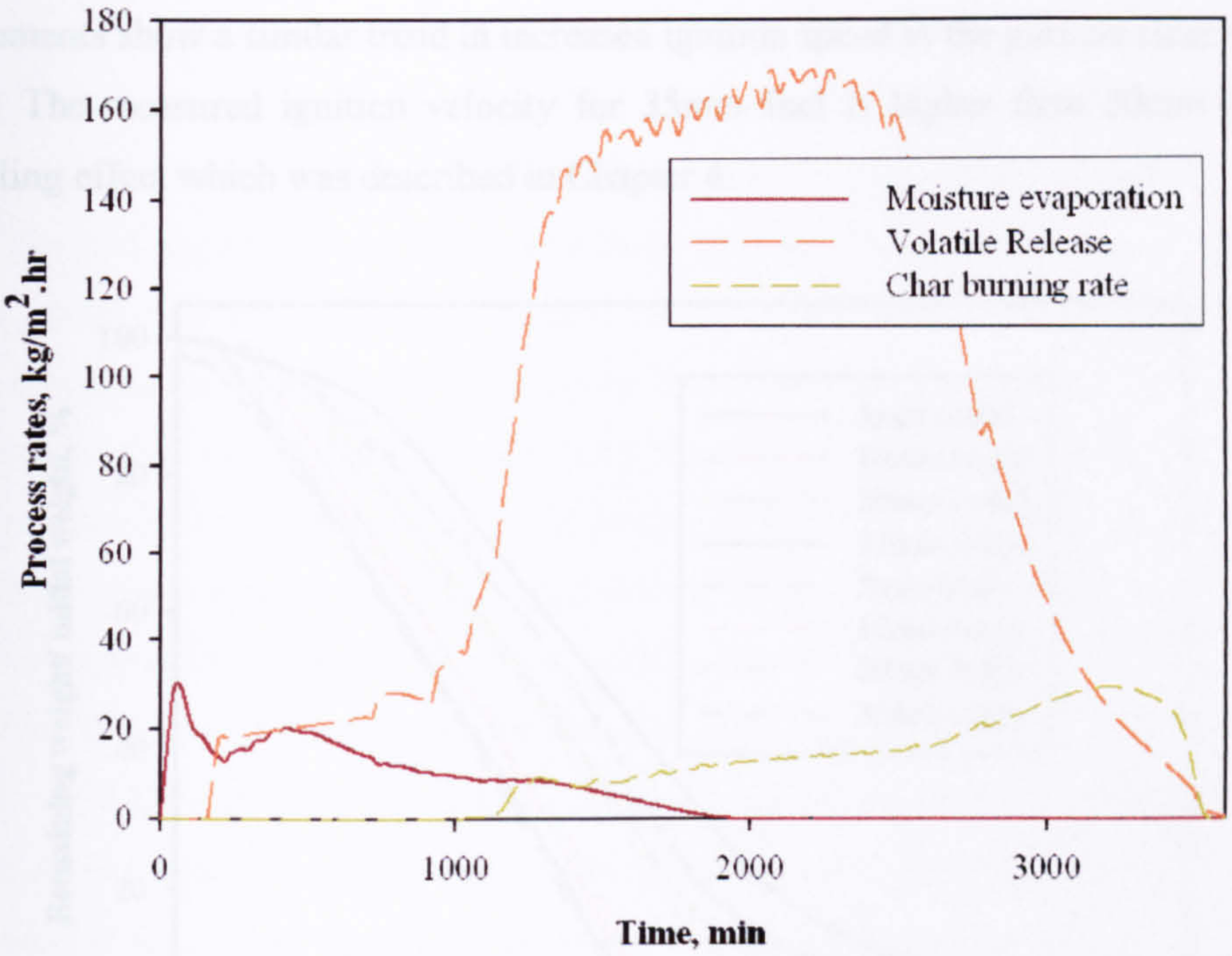

Figure 6.9: Bed-height process rates vs. reaction time. (a) 10mm fuel; (b) 35mm fuel.

The FLIC calculations showed fluctuations in the results. The fluctuation is due to the nature of the calculation whereby the bed is divided into layers. Each layer represents part of an individual fuel particle. Therefore, there exist N calculation nodes for each N layer in the bed. Each layer experiences evaporation, pyrolysis and char reaction sequentially and individually. The fluctuation generated depends on the number of calculation nodes in the bed. Increasing the division of the bed into more layers and using a smaller time step could actually reduce these noise fluctuations.

6.2.4 Comparison with Experimental Results (Mass Loss Rate, Flue Gas Emission and Flame Temperature)

Figure 6.10 shows the measured and calculated mass loss history of fuel expressed as a percentage of remaining mass on the bed as a function of reaction time. The steady state period was reached only after an initiating period. A longer ignition period was observed for larger particle sizes from both the calculations and measurements. The calculated ignition period for size 35mm that occurred only after t=17min was slower compared to the measured ones. A linear decrease in total mass of the bed fuel was observed after the ignition period. The fuel size effect on the average flame velocity is shown in *Figure 6.11*. The calculations indicate a decreasing ignition velocity with increasing particle size and the 35mm fuel

produces the slowest ignition velocity of 0.6m/hr compared to 1.0m/hr for the 5mm fuel. The measurements show a similar trend in increased ignition speed as the particle sizes were made smaller. The measured ignition velocity for 35mm fuel is higher than 20mm due to the channelling effect which was described in Chapter 4.

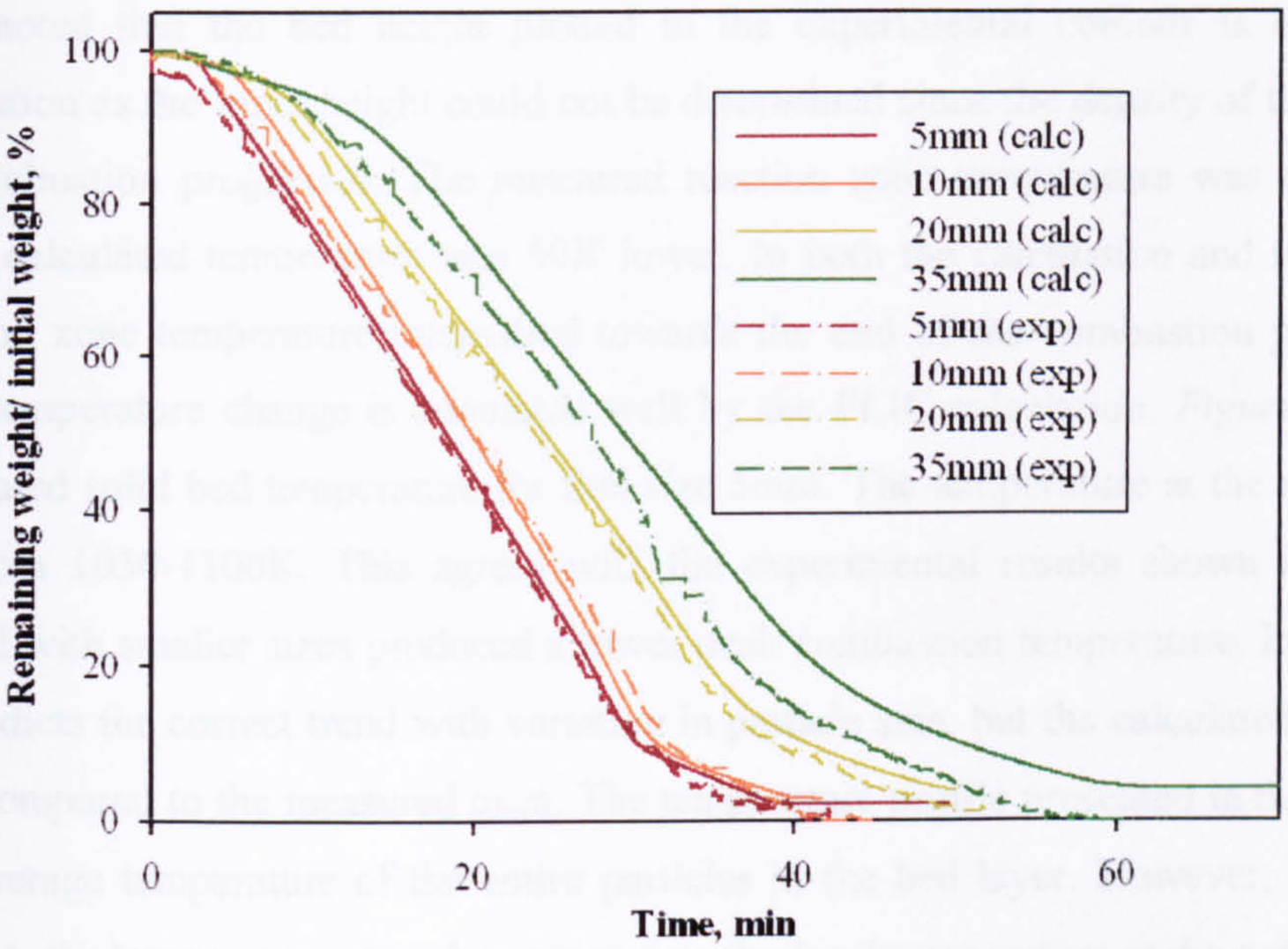

Figure 6.10: Measured and calculated mass loss history as a function of reaction time.

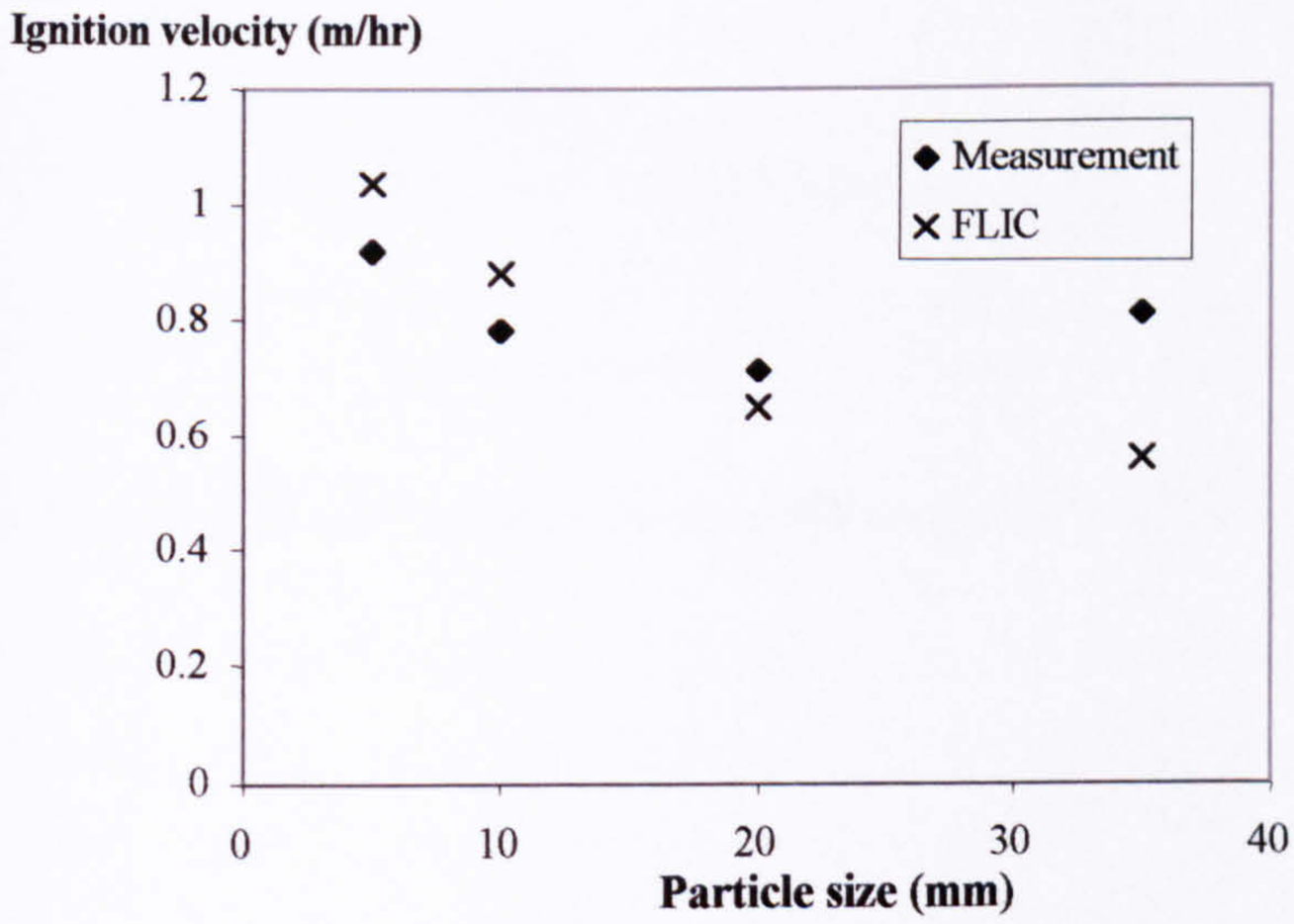

Figure 6.11: Ignition velocity vs. fuel size.

Figure 6.12(a) and *(b)* illustrate the measured and calculated solid bed temperature for fuel size 35mm. The narrow area of temperature change in the measurement represents the reaction zone as seen in the modelling of the fixed bed. The measured temperature contour showed a stepwise pattern because of the limited number of measurement ports along the bed height. The bed height showed the approximate position of the reaction front with time. It must be noted that the bed height plotted in the experimental contour is only a rough approximation as the exact height could not be determined since the density of the fuel varies as the combustion progresses. The measured reaction zone temperature was about 1200K while the calculated temperature was 50K lower. In both the calculation and measurement, the reaction zone temperature intensified towards the end of the combustion progress. The transient temperature change is simulated well by the FLIC calculation. *Figure 6.13* shows the calculated solid bed temperature for fuel size 5mm. The temperature at the reaction zone ranged from 1050-1100K. This agrees with the experimental results shown in Chapter 4 where fuel with smaller sizes produced a lower peak combustion temperature. In general, the model predicts the correct trend with variation in particle size, but the calculated temperature is lower compared to the measured ones. The temperature profile presented in the calculation was an average temperature of the entire particles in the bed layer. However, in the actual experiment, the temperature at each position was the local temperature at the outer surface of the particles. The wall effects and bed channelling were not taken into consideration in the mathematical model.

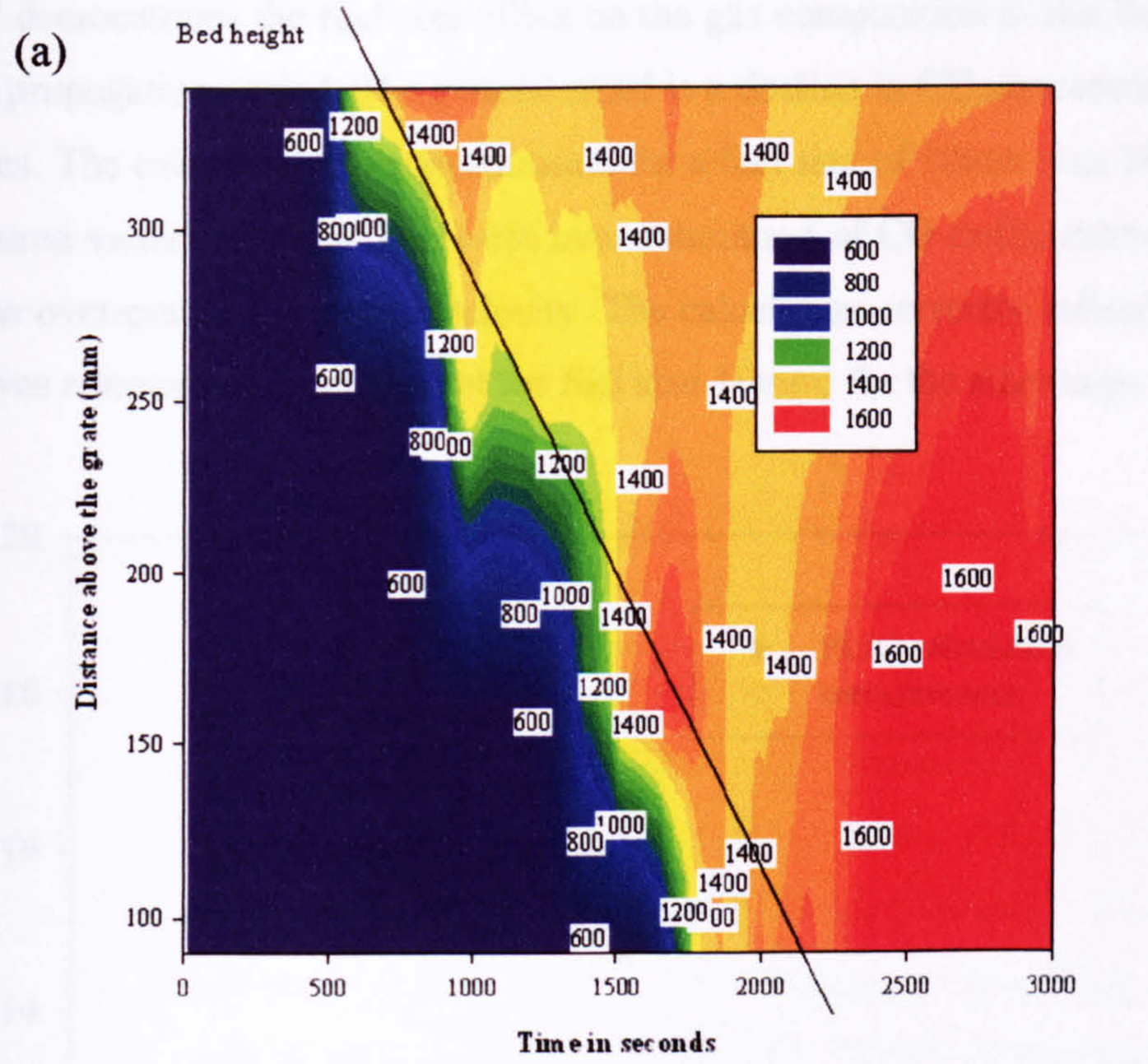

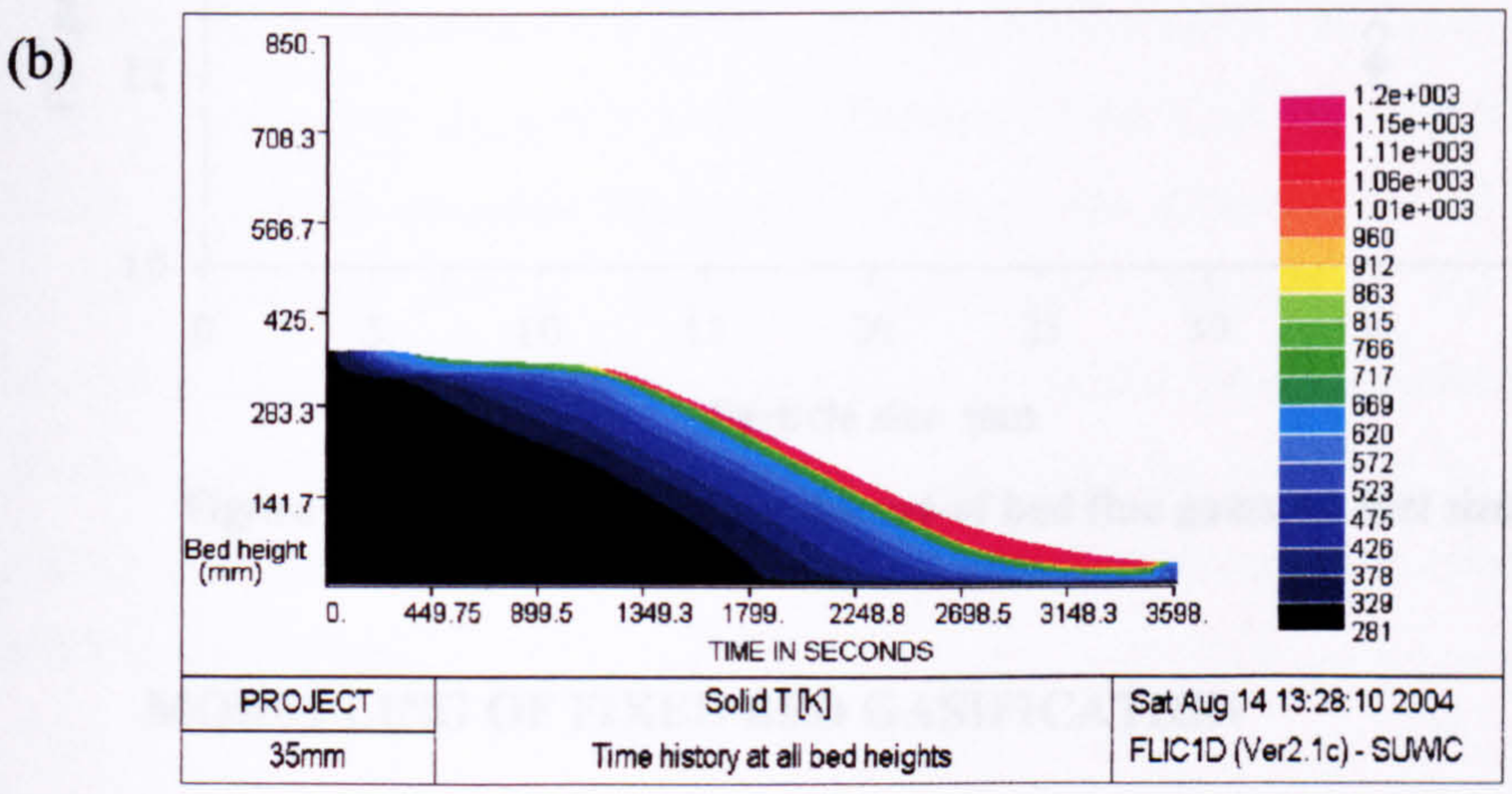

Figure 6.12: Measured (a) and calculated (b) solid bed temperature for fuel size 35mm.

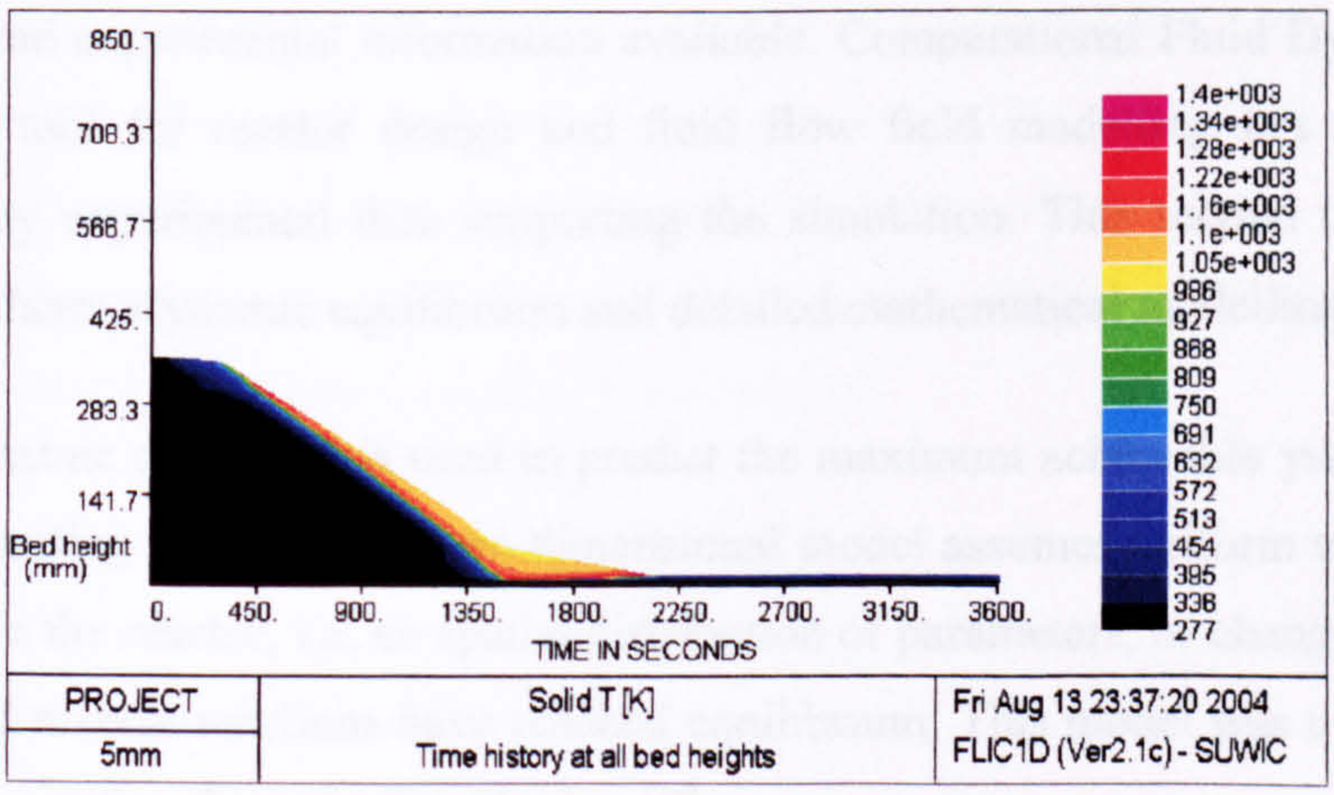

Figure 6.13: Calculated solid bed temperature for fuel size 5mm.

Figure 6.13 demonstrates the fuel size effect on the gas composition in the flue gases during the ignition propagation period. The general trend is a decline in CO concentration as particle size increases. The calculated CO concentration for a fuel size of 10mm was 18.9% compared to the measured value of 17.3%. The 1.6% over estimation of CO in the calculation could be related to the over-predicted ignition velocity. The calculation correctly reflects the measured trend but gives a lower CO level (except for fuel size 10mm) for the size range.

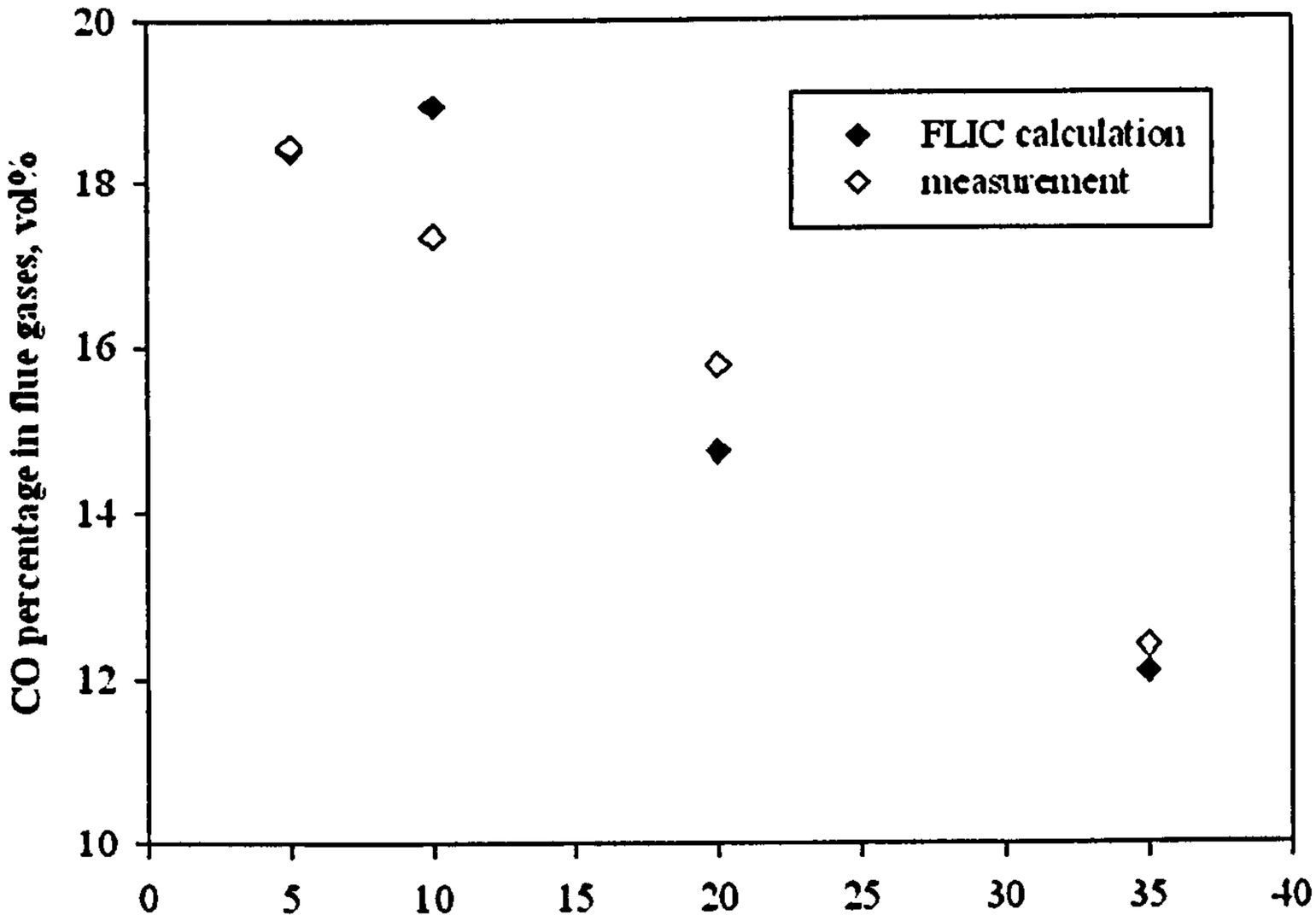

Figure 6.14: CO percentage in the out-of bed flue gases vs. fuel size

6.3 MODELLING OF FIXED BED GASIFICATION

The three main types of models that have been used for gasification systems are the kinetic, equilibrium and Computational Fluid Dynamic (CFD). The type of model chosen depends on the objective and experimental information available. Computational Fluid Dynamics (CFD) is a powerful tool for reactor design and fluid flow field modelling but this should be accompanied by experimental data supporting the simulation. This section presents results from both the thermodynamic equilibrium and detailed mathematical modelling (FLIC).

The thermodynamic modelling is used to predict the maximum achievable yield of a desired product of a reacting system. This zero-dimensional model assumes uniform temperature and concentration in the reactor, i.e. no spatial distribution of parameters, or changes with time as all forward and reverse reactions have reached equilibrium. This model was used to simulate the syngas composition from the fixed bed gasifier.

The detailed mathematical modelling was carried out using the Fluid Dynamics of Incineration Combustion code (FLIC). The mathematical calculation assumes that the major bed properties, i.e. temperatures of gas and solid phases inside the bed, gas composition and solid composition can be described one dimensionally as functions of bed height. FLIC was used to provide information on the reactor temperature, product composition at different positions along the reactor and carbon conversion rate.

6.3.1 Chemical Equilibrium Modelling

The chemical equilibrium for a system is most stable when the entropy of the system is maximized, while the Gibbs free energy is minimized. Two approaches have been developed for equilibrium modelling: stoichiometric and non stoichiometric. The chemical equilibrium calculations were carried out using version 2 of NASA Glenn's computer program *Chemical Equilibrium with Application* (CEA) [2002]. The equations describing the chemical equilibrium and the mathematical solutions used in the CEA2 programme is outline in *Appendix B.1*. The equations are based on the minimisation of Gibbs' energy. The information given is from the user's manual (Gordon, 1994). CEA uses a non-stoichiometric formulation to calculate reaction equilibrium based on the minimisation of the Gibbs free energy. The program obtains chemical equilibrium composition for the assigned thermodynamic state such as temperature and pressure. In the non-stoichiometric calculation, no particular reaction mechanism or species needs to be specified as required with equilibrium constants. This method is suitable for gasification reactions where the reaction mechanism is still unclear.

6.3.1.1 Gasification Reactions

The CEA model was used for the equilibrium calculations of some of the main gasification reactions highlighted by Burgt (2003). A minus sign indicates that heat is generated in the reaction, a positive sign that the reaction requires heat. The individual reactions were modelled at various temperatures using the CEA program to determine the equilibrium gas composition. This allows postulation of the prevailing reactions on the product gas composition at the experimental gasification temperature.

Combustion reactions,

$$C + \tfrac{1}{2}O_2 = CO$$ -111 MJ/kmol

$$CO + \tfrac{1}{2}O_2 = CO_2$$ -283 MJ/kmol

$$H_2 + \tfrac{1}{2}O_2 = H_2O$$ -242 MJ/kmol

Boudouard reaction,

$$C + CO_2 \leftrightarrow 2CO$$ +266 MJ/kmol

Methanation reaction,

$$CO + 3H_2 \leftrightarrow CH_4 + H_2O$$ -75 MJ/kmol

Water gas reaction,

$$C + H_2O \leftrightarrow CO + H_2$$ +131 MJ/kmol

Water gas shift reaction,

$$CO + H_2O \leftrightarrow CO_2 + H_2$$ -41 MJ/kmol

Hydro-gasification,

$$C + 2H_2 \leftrightarrow CH_4$$ -75 MJ/kmol

6.3.1.2 Gas Compositions for Individual Reaction

Figure 6.15 shows the main components of the producer gas for each individual reaction calculated using CEA1. The gas compositions obtained under equilibrium conditions for the gasification of coal chars were calculated by assuming that the solid carbon has the same free energy of formation as that of graphite.

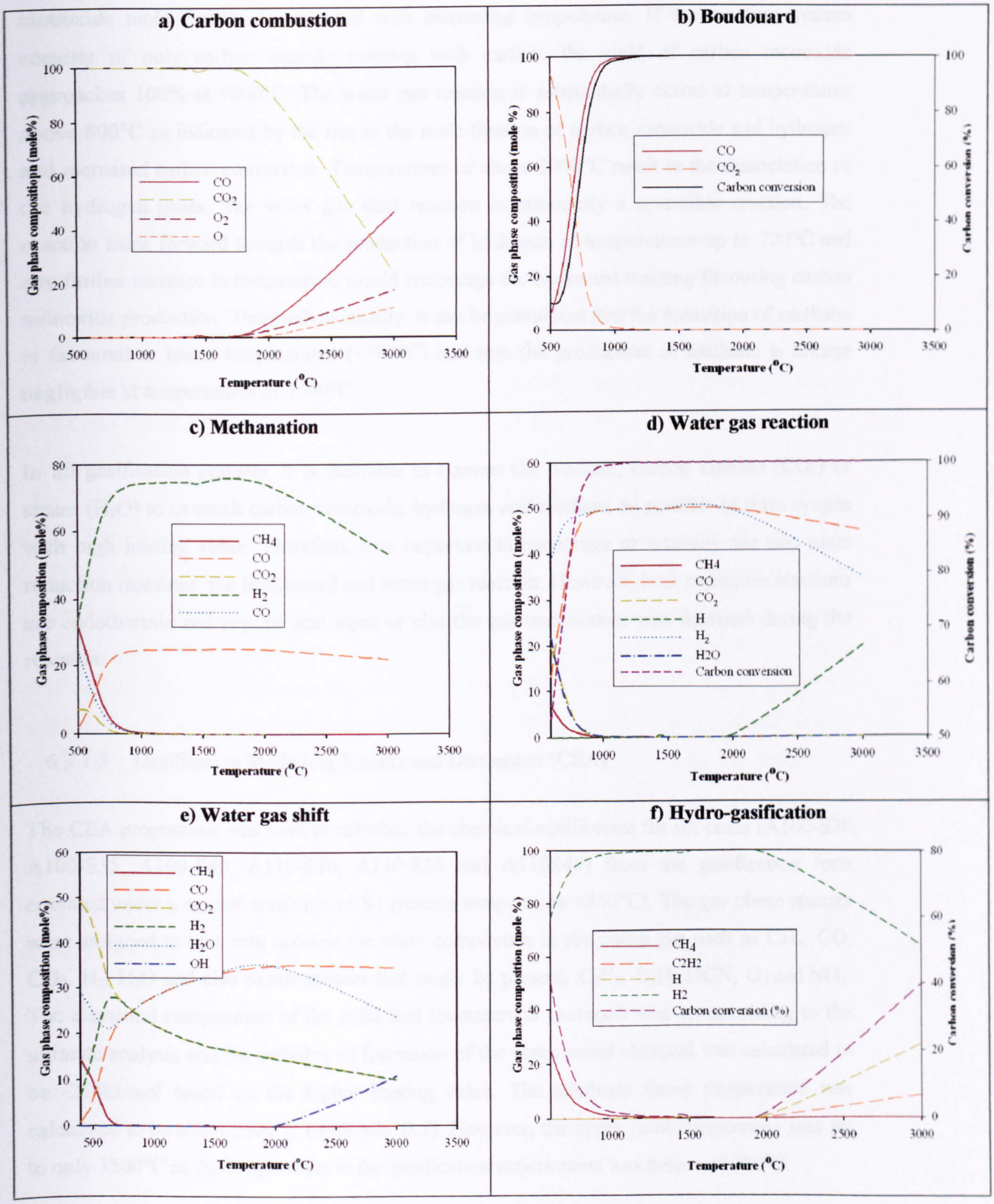

Figure 6.15: Main components of the producer gas calculated for individual reactions using CEA2.

From the carbon combustion and Boudouard reaction in *Figure 6.15 (a)* and *(b)*, the carbon monoxide mole fraction is favoured with increasing temperature. If the reacting system consists of only carbon dioxide reacting with carbon, the yield of carbon monoxide approaches 100% at 1000°C. The water gas reaction is substantially active at temperatures above 800°C as indicated by the rise in the mole fraction of carbon monoxide and hydrogen and increased carbon conversion. Temperatures of above 2000°C result in the dissociation of the hydrogen gases. The water gas shift reaction is essentially a reversible reaction. The reaction leans forward towards the production of hydrogen at temperatures up to 700°C and any further increase in temperature would encourage the backward reacting favouring carbon monoxide production. Thermodynamically, it can be postulated that the formation of methane is favoured at lower temperatures (<700°C) and that the production of methane is almost negligible at temperatures of 1000°C.

In all gasification systems, it is desirable to convert the reactant, carbon dioxide (CO_2) or steam (H_2O) to as much carbon monoxide, hydrogen and methane as possible to form syngas with high heating value. Therefore, it is important to encourage or intensify the two main reduction reactions, the Boudouard and water gas reaction. However, both reduction reactions are endothermic and require heat input or else the gas temperature will decrease during the reaction.

6.3.1.3 Gasification Modelling Results and Discussion (CEA)

The CEA programme was used to calculate the chemical equilibrium for six cases (A100-S30, A100-S35, A100-S40, A110-S30, A110-S35 and A110S40) from the gasification tests operated under a reactor condition of S1 (reactor temperature ≈850°C). The gas phase species were assigned to take into account the main compounds in the outlet gas such as CH_4, CO, CO_2, H_2, H_2O and also minor species that might be present, C_2H_6, C_3H_8, HCN, O_2 and NH_3. The elemental composition of the solid fuel (commercial charcoal) was set according to the ultimate analysis and the enthalpy of formation of the commercial charcoal was calculated to be -254kJ/mol based on the higher heating value. The adiabatic flame temperature was calculated to be about 2600°C (*Appendix B.2*). However, the upper limit temperature was set to only 1500°C as the temperature in the gasification experiments was below <1000°C.

The main objective of this calculation is to give an insight into the chemical equilibrium based on the carbon conversion rate of the gasification experiments. The results from the equilibrium calculations were compared in both the trends and actual values to the

measurements. The experimental gasifier operates at temperature ranging from 750-950°C depending on the flow rate of reactant input (steam and preheated air). Therefore, comparison was made based on the average temperature in the gasifier. The composition of the wet flue gas was calculated through mass balance as experimental measurements were conducted on a dry flue gas basis.

6.3.1.4 Cases: A110-S30, A110-S35, A110-S40

Figure 6.16, Figure 6.17 and *Figure 6.18* compares the calculated and measured wet flue gas composition for Cases A110-S30, A110-S35 and A110-S40. The experimental tests showed close agreement between the calculated CO, CO_2, H_2 and H_2O and the measured value. The measured syngas composition fits the calculated equilibrium composition at a temperature of 850°C for Case A110-S30 and Case A110-S35 and Case A110-S40.

For Case A110-S30, a slight deviation was seen in the measured H_2 concentration that was about 13% compared to the calculated value of 11%. The H_2 concentration fits the equilibrium at about 700°C. As for Case A110-S35, the measured H_2 (12.3%) and CO_2 (14.6%) were slightly higher than the calculated value of 10.4% and 13% while the measured CO (4.1%) and H_2O (28.3) were lower than the calculated value of 4.5% and 33.6%. As the water-gas shift reaction is one of the main gasification reactions, the relationship between H_2 and CO_2 with CO and H_2O is significantly influenced by that reaction. The measured syngas composition fits the calculated equilibrium composition at a much lower temperature of 700°C as forward the shift water-gas reaction was more active in the temperature region of 500-700°C (*Figure 6.15*).

Case A110-S45 shows good agreement between the measured and calculated flue gas composition with deviation only in the measured H_2 concentration that was slightly higher.

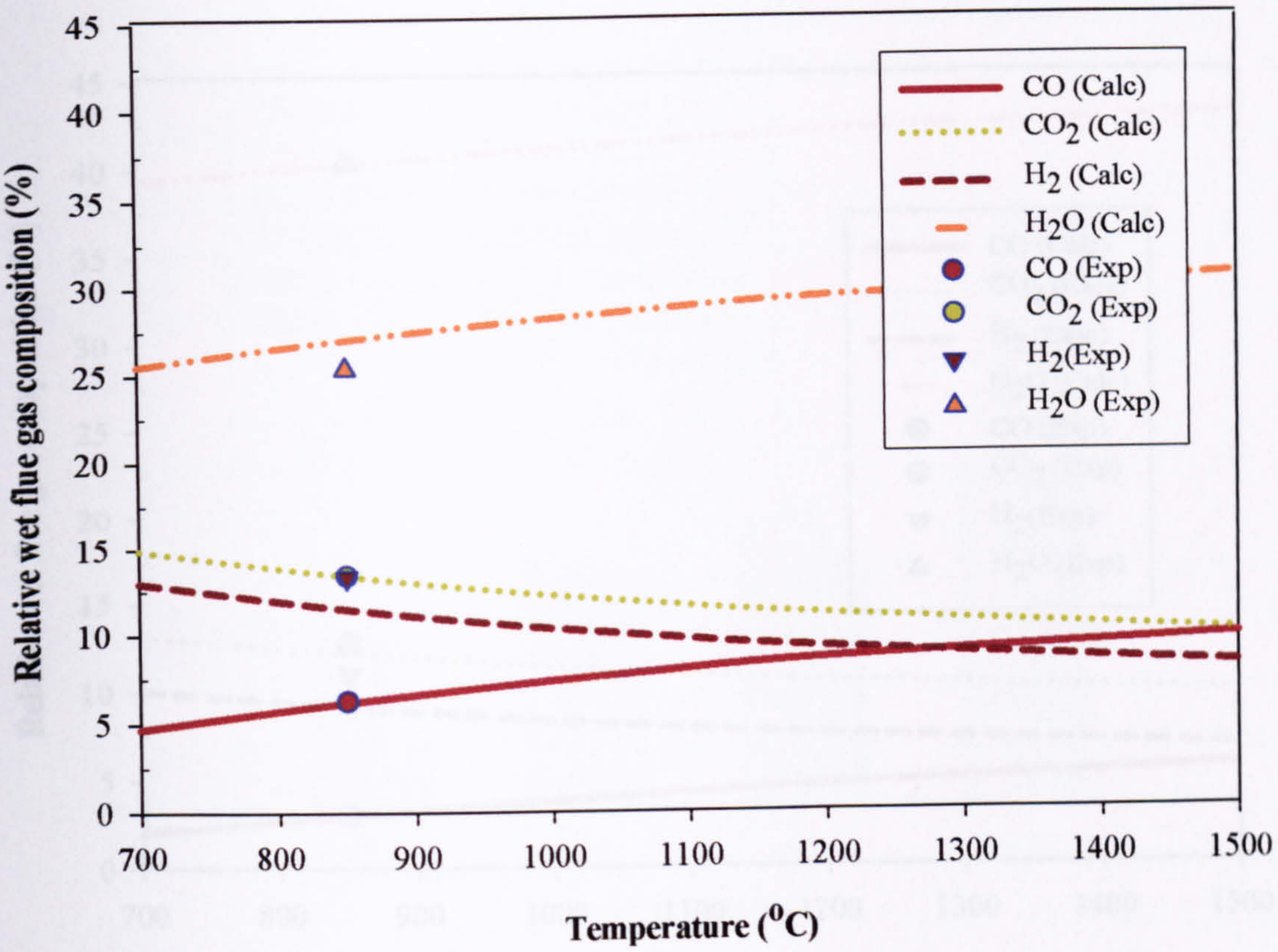

Figure 6.16: Calculated and measured wet flue gas composition for Case A110-S30.

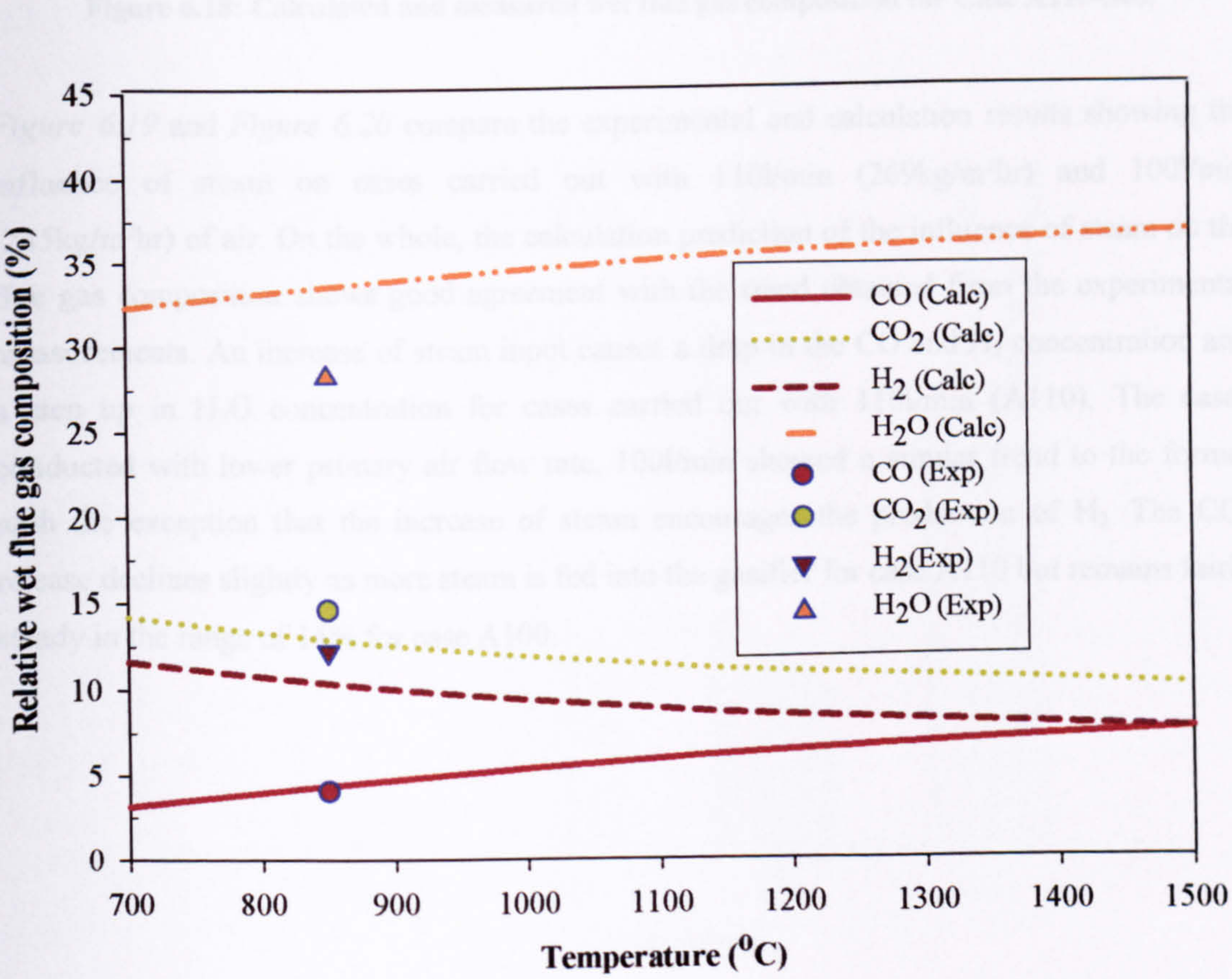

Figure 6.17: Calculated and measure wet flue gas composition for Case A110-S35.

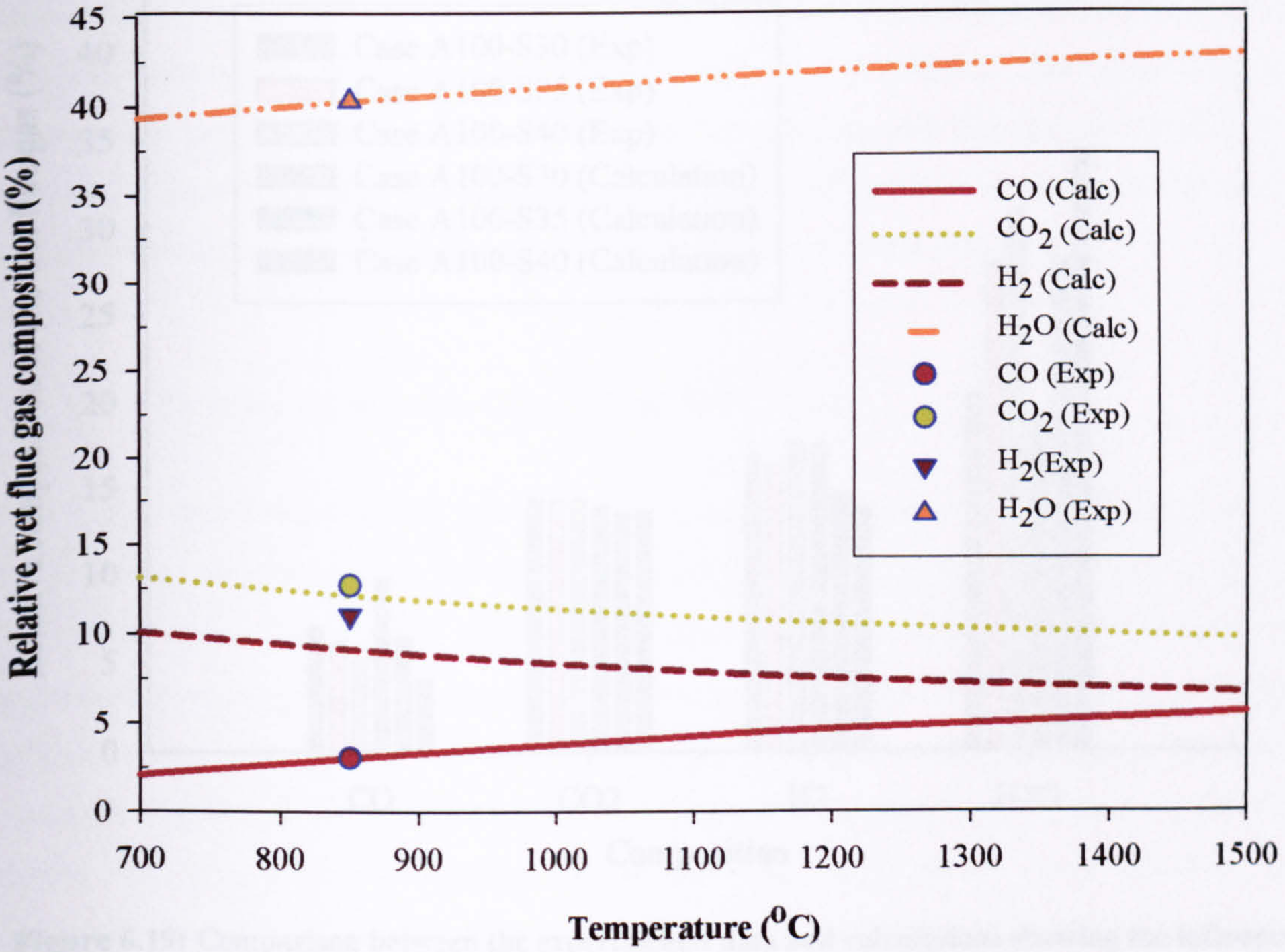

Figure 6.18: Calculated and measured wet flue gas composition for Case A110-S40.

Figure 6.19 and *Figure 6.20* compare the experimental and calculation results showing the influence of steam on cases carried out with 110l/min (269kg/m²hr) and 100l/min (245kg/m²hr) of air. On the whole, the calculation prediction of the influence of steam on the flue gas composition shows good agreement with the trend obtained from the experimental measurements. An increase of steam input causes a drop in the CO and H_2 concentration and a step up in H_2O concentration for cases carried out with 110l/min (A110). The cases conducted with lower primary air flow rate, 100l/min showed a similar trend to the former with the exception that the increase of steam encourages the production of H_2. The CO_2 release declines slightly as more steam is fed into the gasifier for case A110 but remains fairly steady in the range of 14% for case A100.

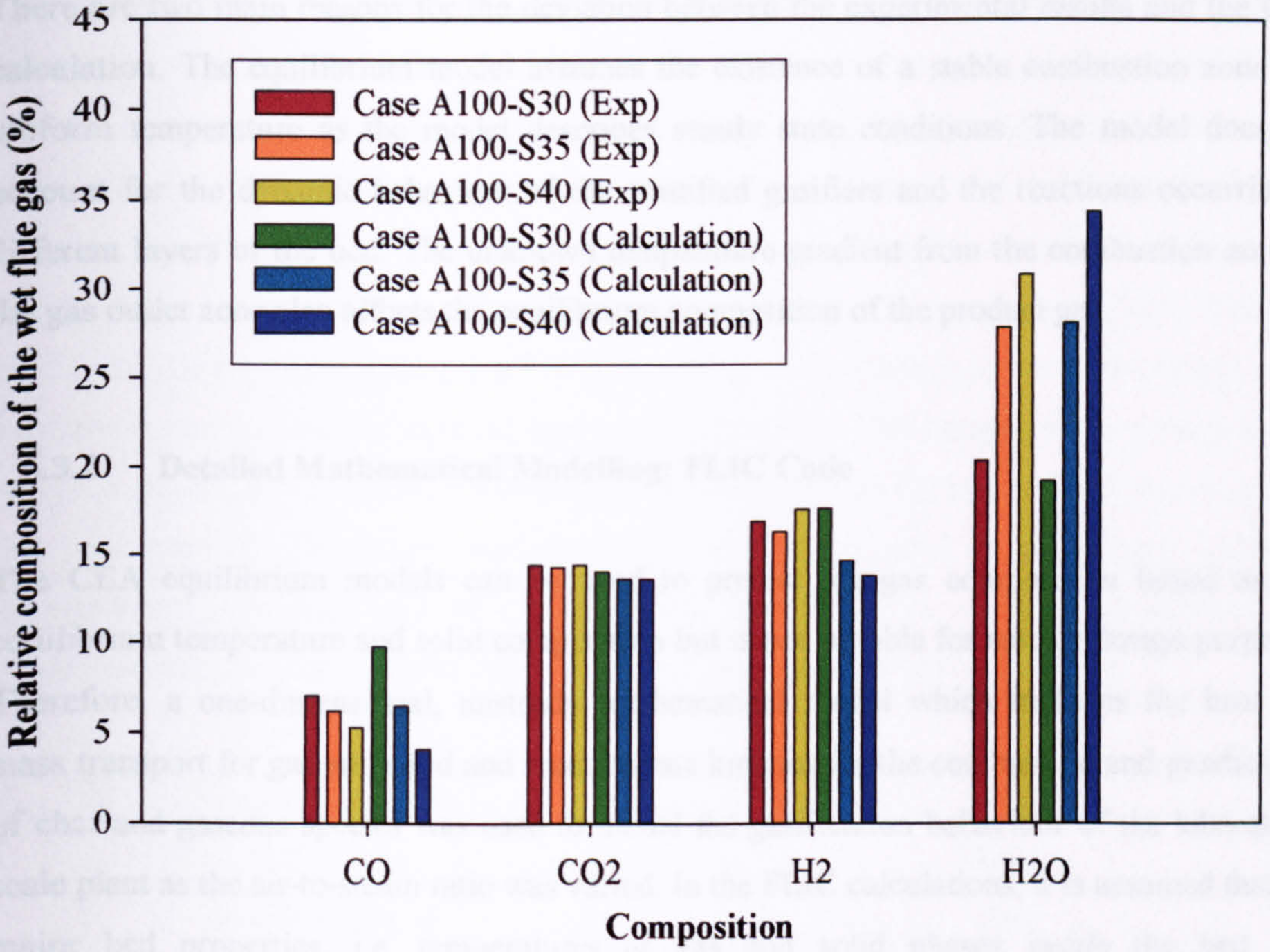

Figure 6.19: Comparison between the experimental data and calculations showing the influence of steam cases with primary air flow rate of 100l/min.

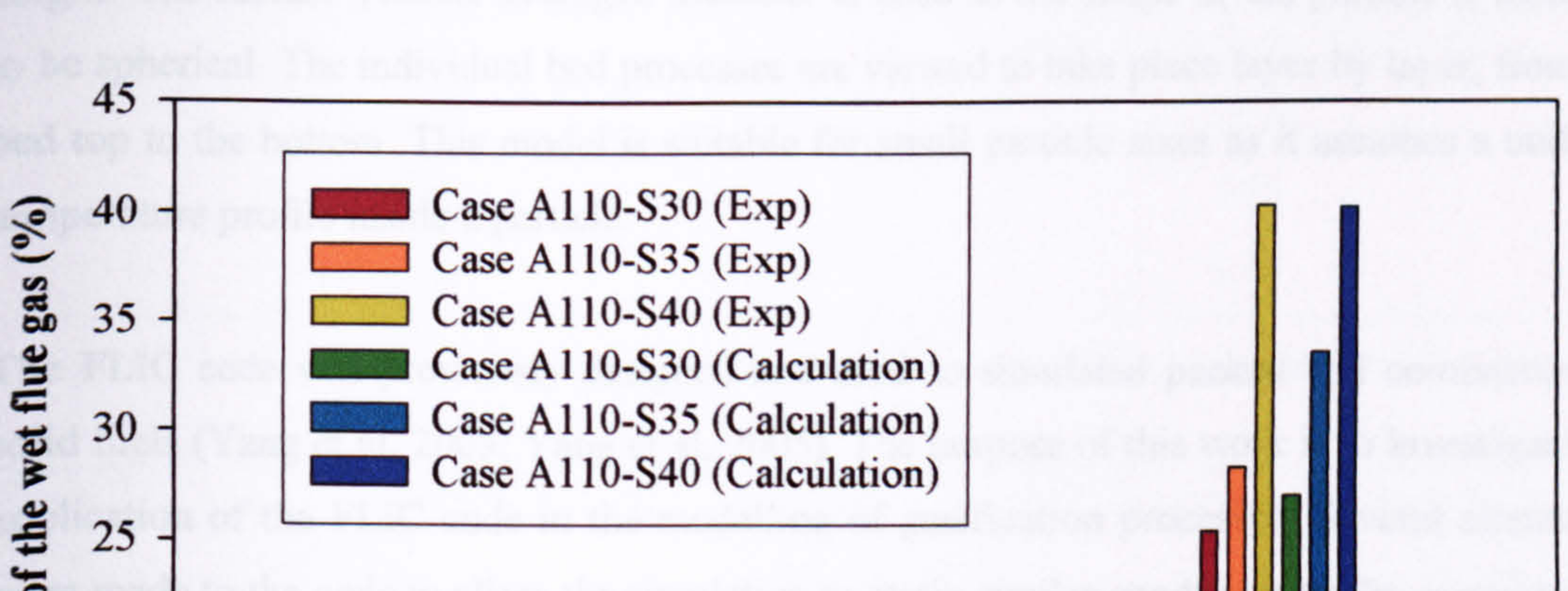

Figure 6.20: Comparison between the experimental data and calculations showing the influence of steam cases with primary air flow rate of 110l/min.

There are two main reasons for the deviation between the experimental results and the CEA calculation. The equilibrium model assumes the existence of a stable combustion zone and uniform temperature as the model describes steady state conditions. The model does not account for the dynamic behaviour of the stratified gasifiers and the reactions occurring at different layers of the bed. The unknown temperature gradient from the combustion zone to the gas outlet zone also affects the equilibrium composition of the product gas.

6.3.2 Detailed Mathematical Modelling: FLIC Code

The CEA equilibrium models can be used to predict the gas composition based on the equilibrium temperature and solid composition but is not suitable for reactor design purposes. Therefore, a one-dimensional, unsteady mathematical model which includes the heat and mass transport for gas and solid and reaction rate kinetics for the combustion and gasification of char and gaseous species was used to model the gasification behaviour of the laboratory-scale plant as the air-to-steam ratio was varied. In the FLIC calculations, it is assumed that the major bed properties, i.e. temperatures of gas and solid phases inside the bed, gas compositions and solid compositions can be described one dimensionally as functions of bed height. The surface-volume averaged diameter is used as the shape of the particle is assumed to be spherical. The individual bed processes are viewed to take place layer by layer, from the bed top to the bottom. This model is suitable for small particle sizes as it assumes a uniform temperature profile inside a particle.

The FLIC code was previously designed and used to simulated packed bed combustion of solid fuels (Yang et al, 2003; Yang et al, 2005). The purpose of this work is to investigate the application of the FLIC code in the modelling of gasification processes. Several alterations were made to the code to allow the simulation to attain similar conditions to the experimental setup. The code was also modified to allow for partial combustion and gasification reactions.

The study of chemical reaction kinetics has been investigated by researchers such as Goetz (1983) and Johnson (1979). A wide range of kinetic rates for gasification reactions exist from different sources. The differences arise due to the different material employed, different heating rates, different experimental conditions and particle size. Therefore, part of this modelling work involves applying the various reaction kinetics and analyzing the differences in the gasification rates and composition compared to the experimental results.

The whole bed is divided into 60 sections along the bed height and time-dependent solutions are sought. The relaxation factor was set to 0.5 and the convergence criteria at 0.005. The calculated space height was set to 500mm. The model was used to simulate a laboratory-scale plant, which is cylindrical in shape with a 0.1m internal diameter and 1.5m length. The bed properties for the charcoal samples are those of experiments and are as listed in *Table 6.3*. The particle size is taken as 30mm and the bed porosity Φ is taken as 0.69. The wall temperature is set and maintained at 800°C assuming no heat losses to the surroundings as the equipment was well-insulated in the laboratory experiment. The heated wall is present for the whole combustion process. No over-bed radiation was used as the bed material was heated by the wall heaters. The steam and air flow rates are selected in accordance with the experimental conditions and at a temperature of 150°C. To compare predictions and measurements, simulations were made with three tests as indicated in *Table 6.4*.

Weight of samples	4kg
Bed Height	34.8cm
Bed Porosity, Φ	0.69
Bed diameter, D	0.1m
Particle diameter, d	3mm
	(wt% dry and ash free basis)
Carbon	94.76
Hydrogen	0.74
Oxygen	4.49

Table 6.3: Bed properties for charcoal samples as input condition in the FLIC calculations.

Case	Total feed flow rate	Air flow rate	Steam flow rate	Mass percentage of steam
	(kg/m²hr)	(kg/m²hr)	(kg/m²hr)	(%)
Case A110-S30	385.10	269.55	115.55	30
Case A110-S35	414.70	269.55	145.15	35
Case A110-S40	449.40	269.55	179.85	40

Table 6.4: Air feed rate, steam feed rate and the percentage of air to steam ratio.

6.3.2.1 Kinetic Rates

Table 6.5 summarises the kinetic rates obtained from different sources. *Figure 6.21*, *Figure 6.22* and *Figure 6.23* show the carbon oxidation, boudouard and water gas reaction rates obtained from different reference sources.

The obtained char oxidation rates varies from the very fast rate of Kashiwagi (1992) to the slowest rate from Hobbs (1992). The values obtained from Bryden, (1996); Cooper and Hallett (2000) showed similar modest reaction rates. The heterogeneous reaction of char/oxygen reaction is known to produce both CO and CO_2. The production of CO and CO_2 can be modelled in several ways. The molar ratio of CO to CO_2 can be modelled as a function of temperature for temperatures between 730 and 1170K:

$$CO/CO_2 = 2500\exp(-6420/T) \qquad \text{(Arthur, 1951)}$$

The CO/CO_2 ratio has also been correlated by Laurendeau (1978) as :

$$\lambda C + O_2 \rightarrow 2(\lambda - 1)CO + (2 - \lambda)CO_2$$

$$\frac{CO}{CO_2} = A\exp\left(-\frac{E}{RT}\right) = \frac{2(\lambda - 1)}{(2 - \lambda)}$$

where $A \approx 10^{2.5}$ and E≈25-38 kJ/mol for low pressures, and $A \approx 10^{3.5}$ and E≈50-80 kJ/mol for high pressures.

In many cases, the product of char/oxygen reaction is assumed to be exclusively CO especially at high temperatures. The product CO leaves the particle surface and is further oxidized to CO_2 in the gas phase. In this case, the oxidation of CO is limited not only by the reaction kinetics but also by the diffusion rate. For simplicity in calculations, many researchers have adopted this approach.

The kinetic rates used by Bryden (1996) for the char/CO_2 and char/steam reactions was very fast compared to the rates applied by Hobbs (1992). In the data given by Hobbs, the steam-char reaction is taken as the same as the carbon dioxide gasification rate due to the lack of reliable reaction data. The hydrogen gasification rate is taken to be three orders of magnitude smaller than the carbon dioxide rate. This assumption has been adopted by Di Blasi (2004) in his model of wood gasification in a counter-current gasification. The rates used by Groeneveld (1980) and Liliedahl (1997) in their model for wood char and lignite char lies in the mid-range in comparison to the former researchers.

Reference	*Reaction Constant (k_i,)/ Reaction Rate, (r_i) i = h1, h2, h3*	*Reaction*
Hobbs, (1992)	$k_{h1} = 2.3T_s \exp(-11100/T_s), m/s$	$C + 0.5O_2 \rightarrow CO$
	$k_{h2} = 589T_s \exp(-26800/T_s), m/s$	$C + CO_2 \rightarrow 2CO$
	$k_{h3} = 589T_s \exp(-26800/T_s), m/s$	$C + H_2O \rightarrow CO + H_2$
	$k_{h4} = 0.589T_s \exp(-26800/T_s), m/s$	$C + 2H_2 \rightarrow CH_4$
Groeneveld and van Swaaij, (1980)	$k_{g1} = 10^3 - 10^4 \exp(-26095/T_s), mls$	$C + CO_2 \rightarrow 2CO$
	$k_{g2} = 10^3 - 10^4 \exp(-26095/T_s) m/s$	$C + H_2O \rightarrow CO + H_2$
Cooper and Hallett, (2000)	$r_{c1} = 1.3x10^{11}[CO][O_2]^{1/2}[H_2O]^{1/2} \exp(-15105/T_s) kgm^{-3}s^{-1}$	$C + O_2 \rightarrow CO_2$
	$r_{c2} = 10400 p_{CO_2} \exp(-178/RT_s) kgm^{-2}s^{-1}$	$C + s_2CO_2 \rightarrow 2(1+s_2)CO$
	$r_{c3} = 860 \rho_{O_2} \exp(-18000/RT_s) kgm^{-2}s^{-1}$	$C + s_1O_2 \rightarrow (1+s_1)[\chi CO_2 + (1-\gamma)CO]$
Bryden, (1996)	$r_{b1} = M_{HC}\left(9.2x10^6\right)\exp(-9650/T_g)[HC]^{0.5}[O_2] kgm^{-3}s^{-1}$	$CH_4 + 1.5O_2 \rightarrow CO + 2H_2O$
	$r_{b2} = M_{CO_2} 10^{17.6} \exp(-2x10^4/T_e)[CO][O_2]^{0.25}[H_2O]^{0.5} kgm^{-3}s^{-1}$	$2CO + O_2 \rightarrow 2CO_2$
	$k_{b1} = 1.74T_s \exp\left(-9x10^3/T_s\right) m/s$	$C + 0.5O_2 \rightarrow CO$
	$k_{g2} = 3.42T_s \exp(-1.56x10^4/T_s) m/s$	$C + CO_2 \rightarrow 2CO$
	$k_{g4} = (1.67)3.42T_s \exp(1.56x10^4/T_s) m/s$	$C + H_2O \rightarrow CO + H_2$
Kashiwagi (1992)	$r_{B1} = 10^{11} \exp(-10000/T_g) C_H C_{O_2} kmolm^{-3}s^{-1}$	$H_2 + O_2 \rightarrow H_2O$
	$k_{B1} = 5.67x10^7 \exp(-19294/T_g) ms^{-1}K^{-1}$	$C + s_1O_2 \rightarrow (1+s_1)[\chi CO_2 + (1-\gamma)CO]$
Biba, (1978)	$k_{B'1} = 1.667 \exp(-26689/T_s) m/s$	$C + O_2 \rightarrow CO_2$
	$k_{B'2} = 5555 \exp(-43308/T_s) m/s$	$C + CO_2 \rightarrow 2CO$
	$k_{B'3} = 1.39x10^{-3} \exp(-14604/T_s) m/s$	$C + H_2O \rightarrow CO + H_2$
	$k_{B'4} = 2083 \exp(-27697/T_s) m/s$	$C + 2H_2 \rightarrow CH_4$
	$k_{B'5} = 2778 \exp(-1510/T_s) m/s$	$CO + H_2O \rightarrow CO_2 + H_2$
Mann *et al*, (2004)	$k_{m1} = 3.51x10^6 \exp(-10970/T_s)$	$xC + yO_2 \rightarrow zCO_2 + dCO$
	$k_{m2} = 8.10x10^2 \exp(-17664/T_s)$	$C + H_2O \rightarrow CO + H_2$
	$k_{m3} = 5.25x10^2 \exp(-59100/T_s)$	$C + CO_2 \rightarrow 2CO$
	$k_{m4} = 6.11x10^3 \exp(-9662/T_s)$	$C + 2H_2 \rightarrow CH_4$
	$k_{m5} = 3.23x10^7 \exp(-5938/T_g)$	$CO + H_2O \rightarrow CO_2 + H_2$
Liliedahl and Sjostrom, (1997)	$k_{L1} = 4.2x10^3 \exp(155/RT_s) s^{-1}MPa^{-1}$	$C + CO_2 \rightarrow 2CO$
	$k_{L2} = 0.29x10^3 \exp(121/RT_s) s^{-1}MPa^{-1}$	$C + H_2O \rightarrow CO + H_2$

Table 6.5: Reaction kinetics from different sources for coal and wood gasification.

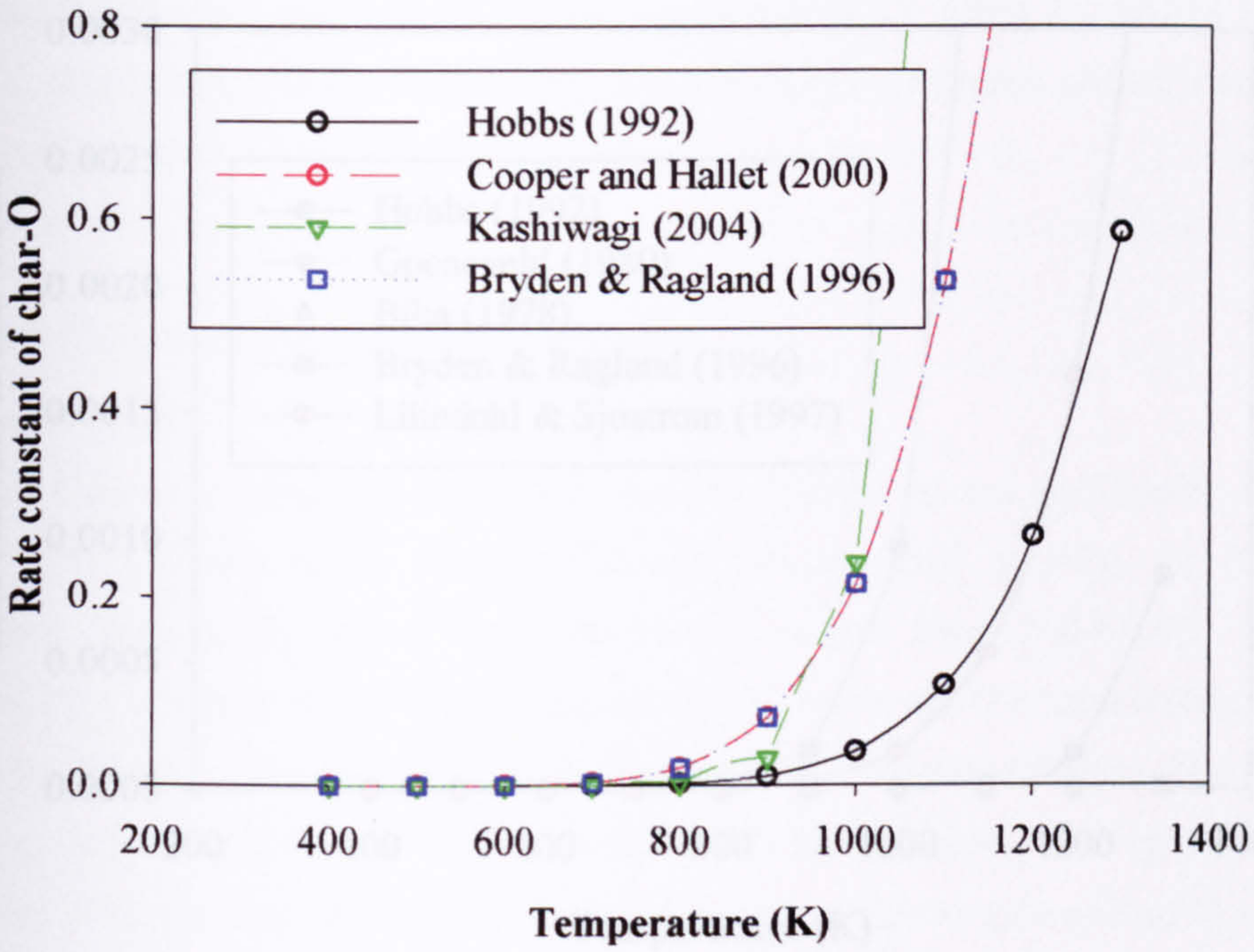

Figure 6.21: Char oxidation rates of coal, wood and cellulosic paper from different sources for particle sizes of up to 30mm as function of temperature.

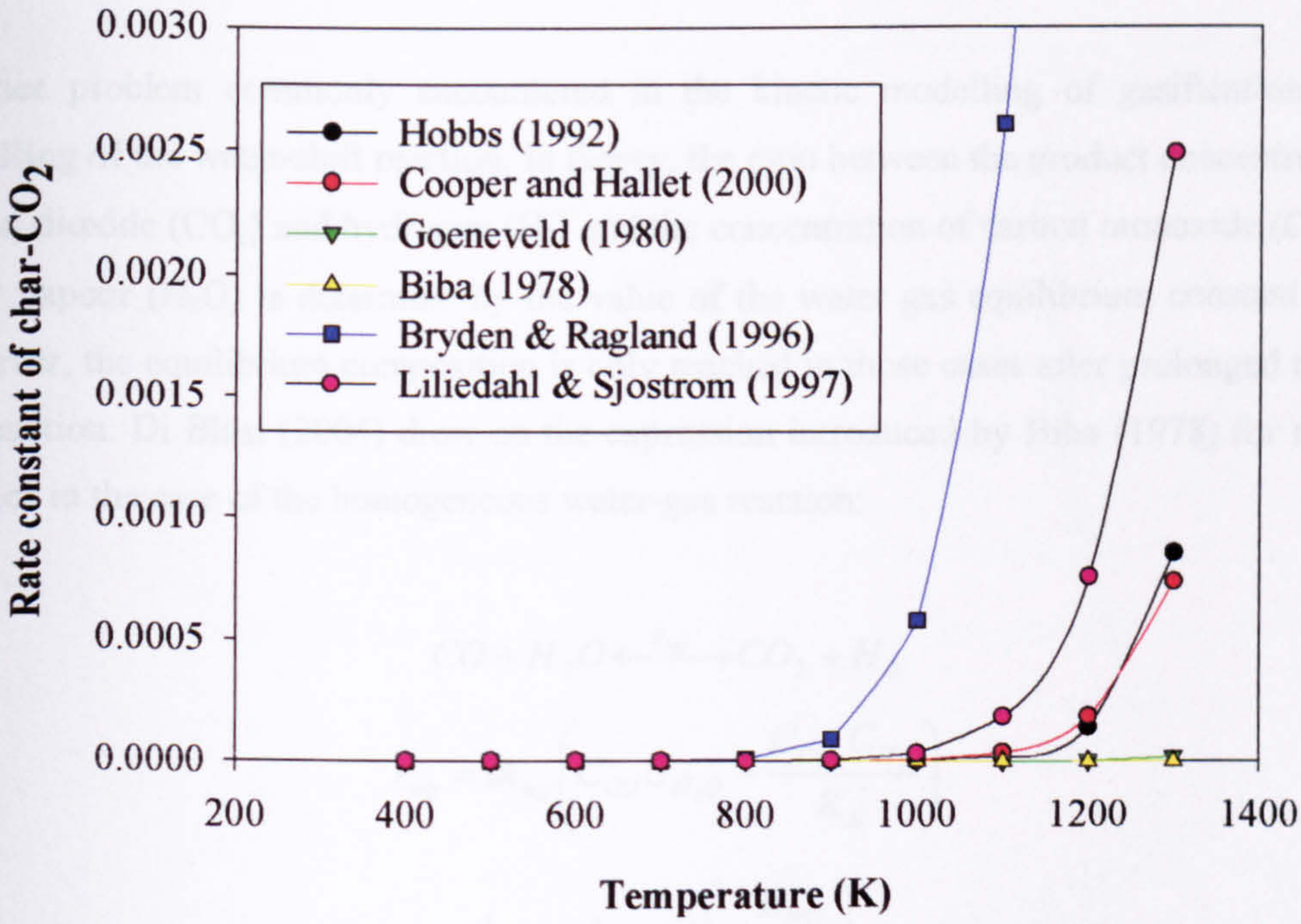

Figure 6.22: Char-CO_2 rates of coal and wood from different sources for particle sizes of up to 30mm as function of temperature.

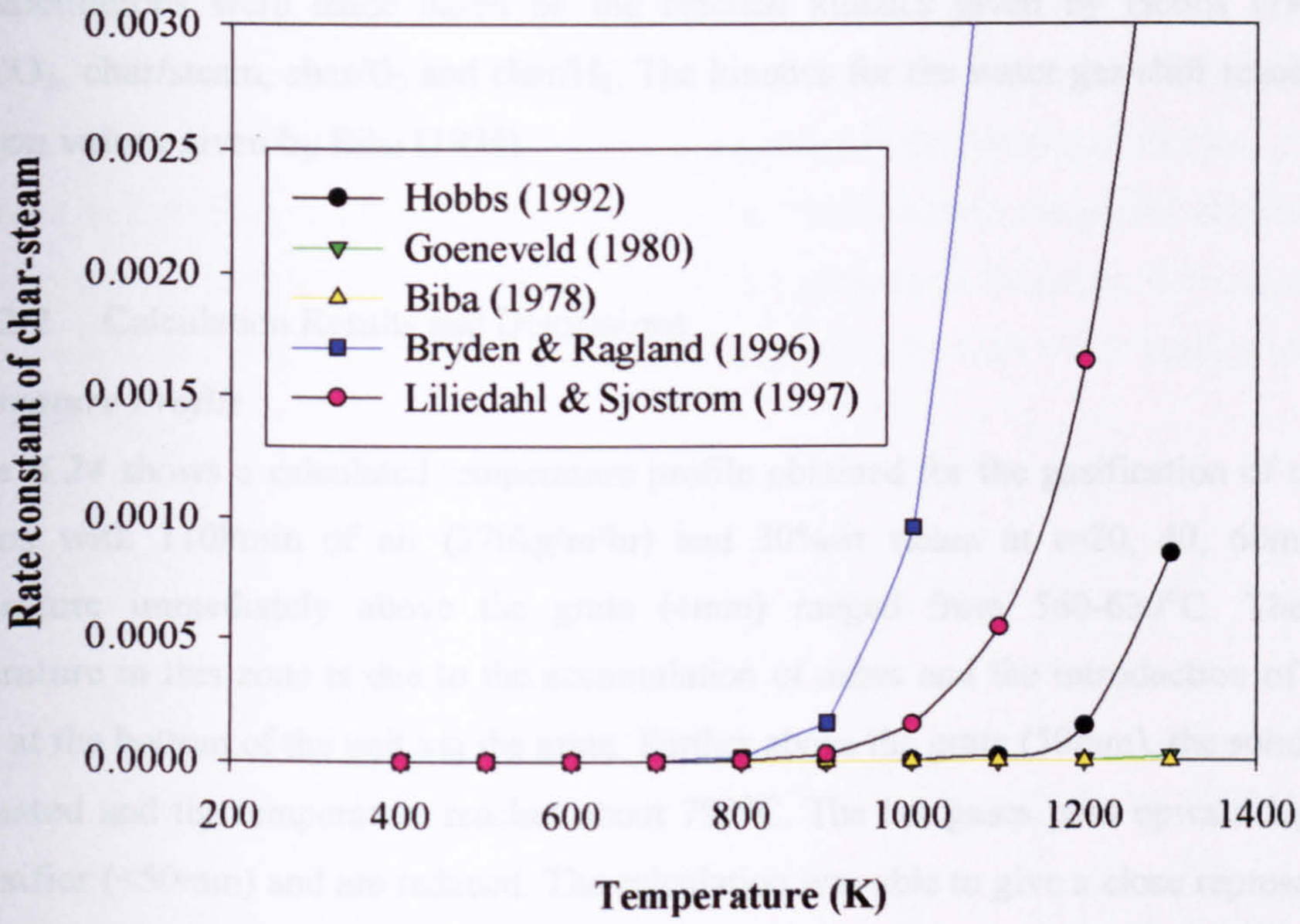

Figure 6.23: Char-H_2O rates of coal and wood from different sources for particle sizes of up to 30mm as function of temperature.

Another problem commonly encountered in the kinetic modelling of gasification is the modelling of the water-shift reaction. In theory, the ratio between the product concentration of carbon dioxide (CO_2) and hydrogen (H_2) and the concentration of carbon monoxide (CO) and water vapour (H_2O) is determine by the value of the water gas equilibrium constant (K_{WE}). However, the equilibrium composition is only reached in those cases after prolonged time for the reaction. Di Blasi (2004) drew on the expression introduced by Biba (1978) for reaction kinetics in the case of the homogeneous water-gas reaction:

$$CO + H_2O \xleftrightarrow{k_{wg}} CO_2 + H_2$$

$$r_{wg} = \varepsilon k_{wg}\left(C_{CO}C_{H_2O} - \frac{C_{CO_2}C_{H_2}}{K_E}\right)$$

$$k_{wg} = A_{wg}\exp\left(-\frac{E_{WG}}{RT_S}\right)$$

$$K_E = 0.0265\exp\left(\frac{3966}{T_S}\right)$$

The calculations were made based on the reaction kinetics given by Hobbs (1992) for char/CO_2, char/steam, char/O_2 and char/H_2. The kinetics for the water gas-shift reaction was based on values given by Biba (1978).

6.3.2.2 Calculation Results and Discussions

Temperature Profile

Figure 6.24 shows a calculated temperature profile obtained for the gasification of charcoal samples with 110l/min of air (270kg/m²hr) and 30%wt steam at t=20, 40, 60min. The temperature immediately above the grate (4mm) ranged from 560-630°C. The lower temperature in this zone is due to the accumulation of ashes and the introduction of air and steam at the bottom of the unit via the grate. Further above the grate (50mm), the solid char is combusted and the temperature reaches about 790°C. The hot gases pass upward higher up the gasifier (<50mm) and are reduced. The calculation was able to give a close representation of the dynamic change in temperature along the stratified gasifier.

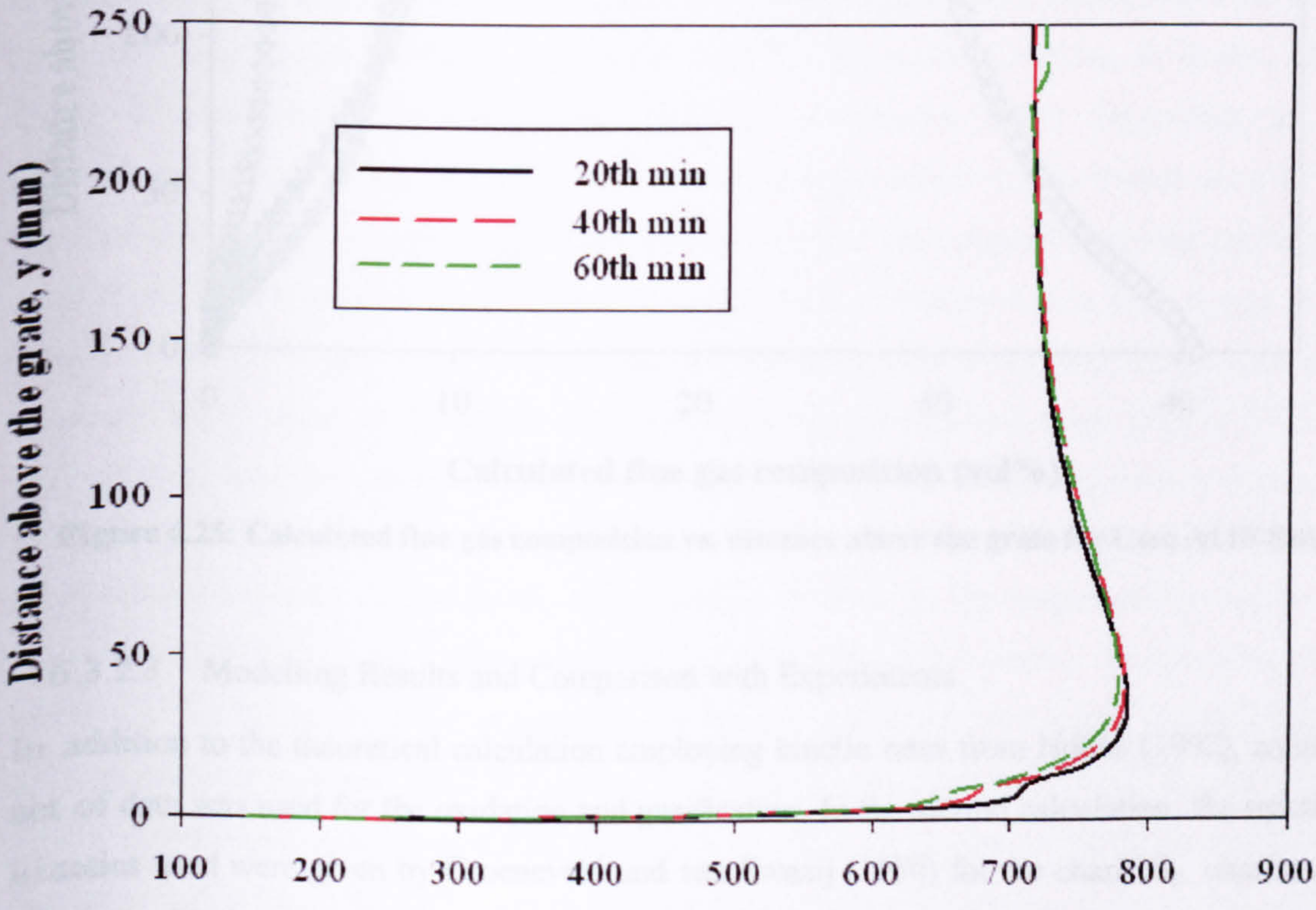

Figure 6.24: Calculated solid bed temperature vs. distance above the grate for Case A110-S30.

Gas Composition in the Flue Gases

Figure 6.25 shows the formation of CO, H_2, CO_2 and H_2O along the bed of the gasifier. The calculation indicates that CO is the dominant component at the bottom of the bed (<50mm) compared to the other two components, H_2 and CO_2. This is due to the partial combustion of the carbonaceous char material producing a higher temperature in this zone. Subsequently, H_2 is formed further along the bed due to the gasification reaction with water leading to release of CO and CO_2.

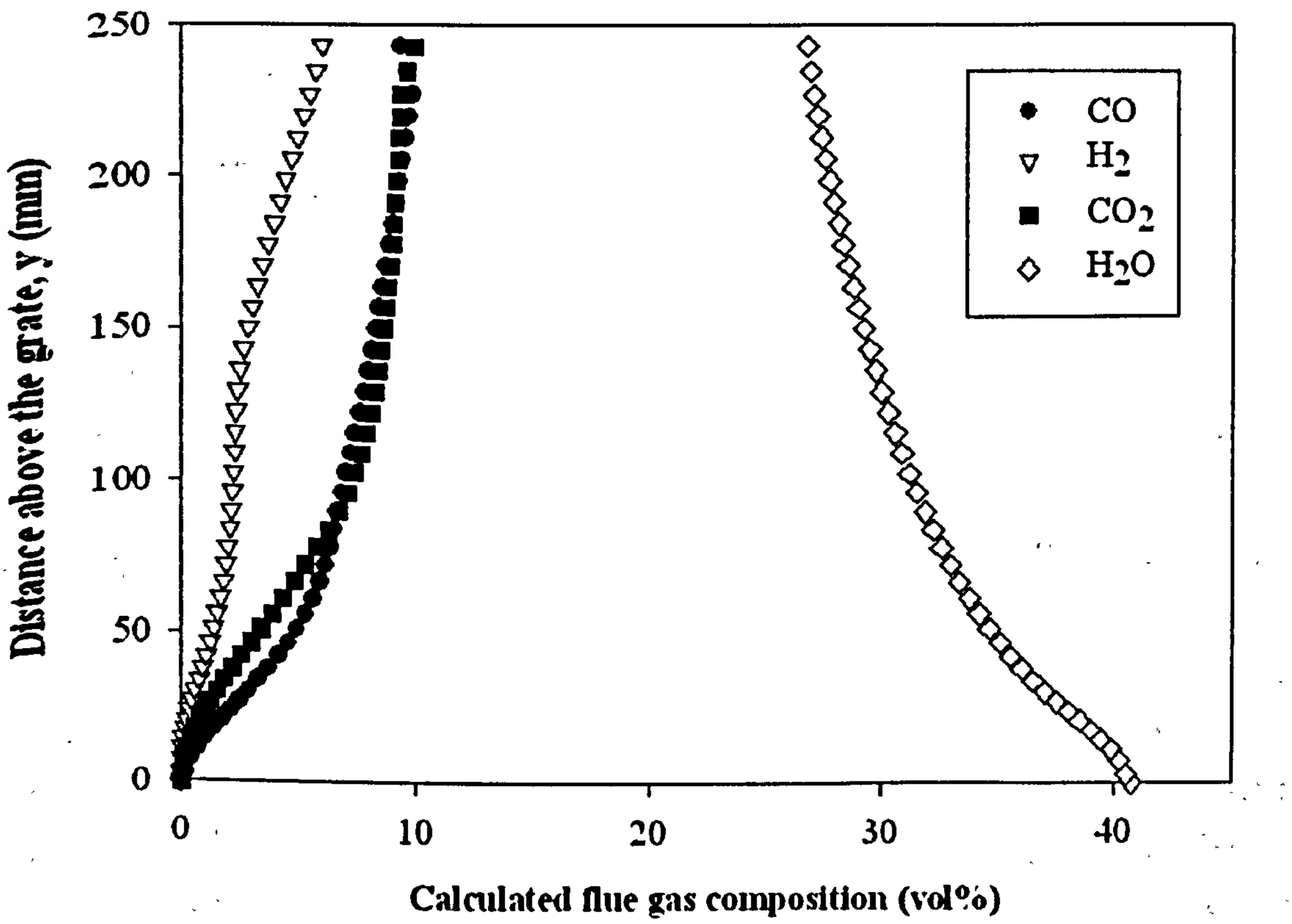

Figure 6.25: Calculated flue gas composition vs. distance above the grate for Case A110-S30.

6.3.2.3 Modelling Results and Comparison with Experiments

In addition to the theoretical calculation employing kinetic rates from Hobbs (1992), another set of data was used for the oxidation and gasification. In the second calculation, the reaction kinetics used were given by Groeneveld and van Swaaij (1980) for the char/CO_2, char/steam and char/H_2 and Kashiwagi (1992) for the char/O_2. The kinetics for the water gas-shift reaction was based on values given by Biba (1978). *Table 6.6* summarises the two set of kinetic rates used.

Oxidation/Gasification	Case A	Case B
References	Hobbs, 1992	Groeneveld and van Swaaij (1980) & Kashiwagi (1992)
A_{CO2}, m/s.K	589.0	1000
R_{CO2}, K	26,800	26095
A_{H2}, m/s.K	0.589	1
R_{H2}, K	26800	26095
A_{H2O}, m/s.K	589.0	1000
R_{H2O}, K	15700	26095
A_{O2}, m/s.K	2.3	5.67×10^7
R_{O2}, K	11,100	19294

Table 6.6: Oxidation and Gasification Kinetic Rate Constants.

Temperature Profile

Figure 6.26(a) and *(b)* illustrate the steam feed effect on the bed temperature. The experimental and calculated bed temperature was plotted against the distance above the grate. The calculated results employed the kinetics from the two references (Case A: Hobbs, 1992, Case B: Groeneveld and van Swaaij, 1980 and Kashiwagi, 1992). Depending on the percentage of steam feed, the maximum measured temperature at the hottest zone at the bottom of the bed (<50mm) ranged from 890-930°C. The bed temperature in the calculation was found to be somewhat lower. The maximum calculated temperature in Case A was in the range of 770-780°C and 780-790°C in Case B. The introduction of additional steam showed a more profound effect on the experimental bed temperature with an average drop of 23-26°C with higher steam percentage. However, the model predicts the correct trend as an increasing percentage of steam in the feed produces a lower bed temperature. The lower calculated bed temperature could be caused by the accumulation of ashes at the bottom of the bed in the simulation leading to a layer of inactive material. The wall temperature in the calculation was set to 725°C. However, in the experiment, the reactor was electrically heated and maintained at temperatures between 700-750°C using temperature controllers operating on a PID loop. The thermocouple accuracy and PID response will affect the heating of the furnace. Another factor contributing to the difference in the measurements and calculation is the slower carbon conversion rate obtained in the simulation as shown in *Figure 6.27*.

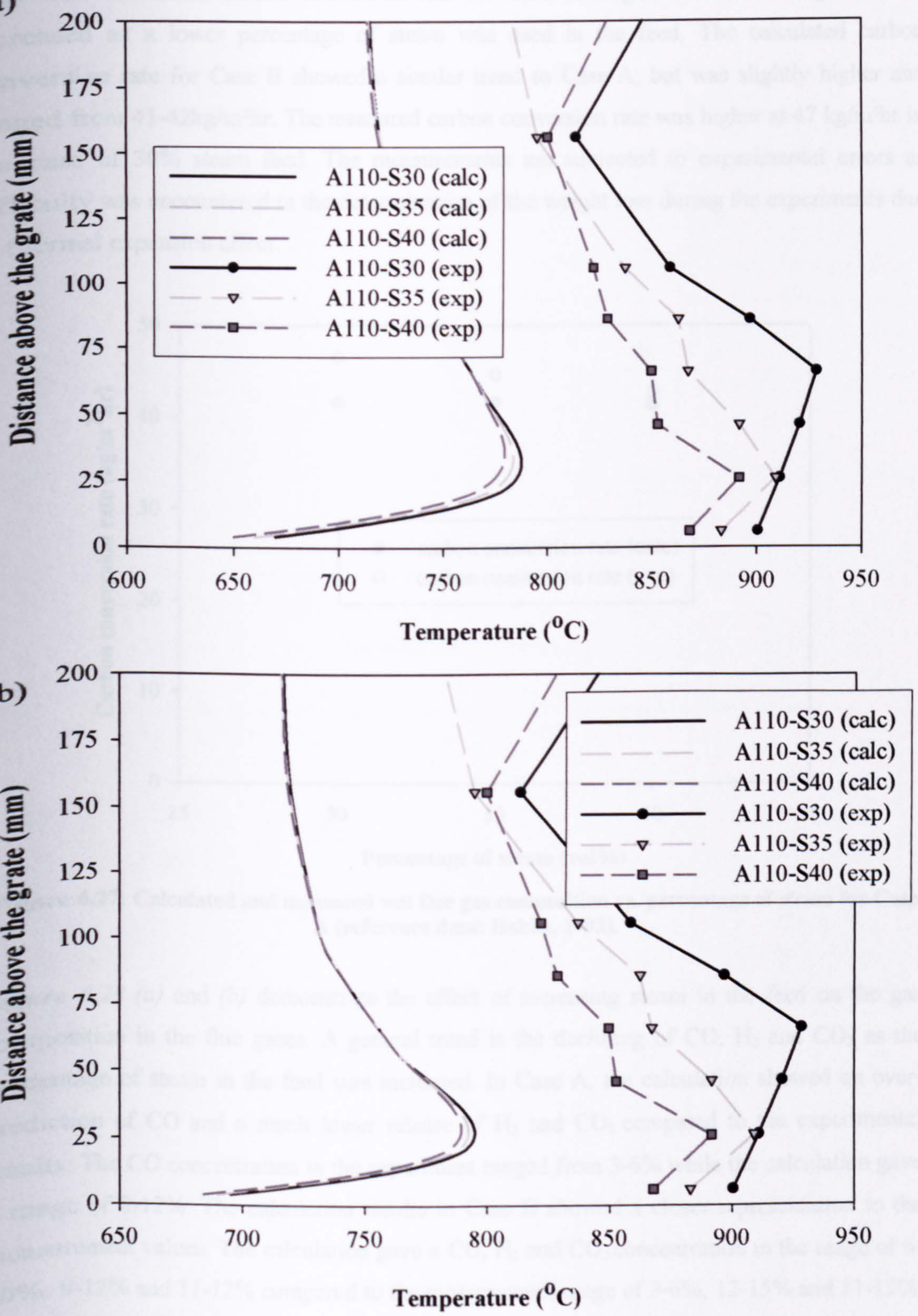

Figure 6.26: Calculated and measured temperature along the bed. (a) Case A (reference data: Hobbs, 1992); (b) Case B (reference data: Groeneveld,1980 and Kashiwagi, 1992).

Figure 6.27 shows the effect of the percentage of steam in the feed on the carbon conversion rate. The calculated carbon conversion rate for Case A ranged from 41-41.6kg/m²hr and increased as a lower percentage of steam was used in the feed. The calculated carbon conversion rate for Case B showed a similar trend to Case A, but was slightly higher and ranged from 41-42kg/m²hr. The measured carbon conversion rate was higher at 47 kg/m²hr in the case of 30% steam feed. The measurements are subjected to experimental errors as difficulty was encountered in the determination of the weight loss during the experiments due to thermal expansion effect.

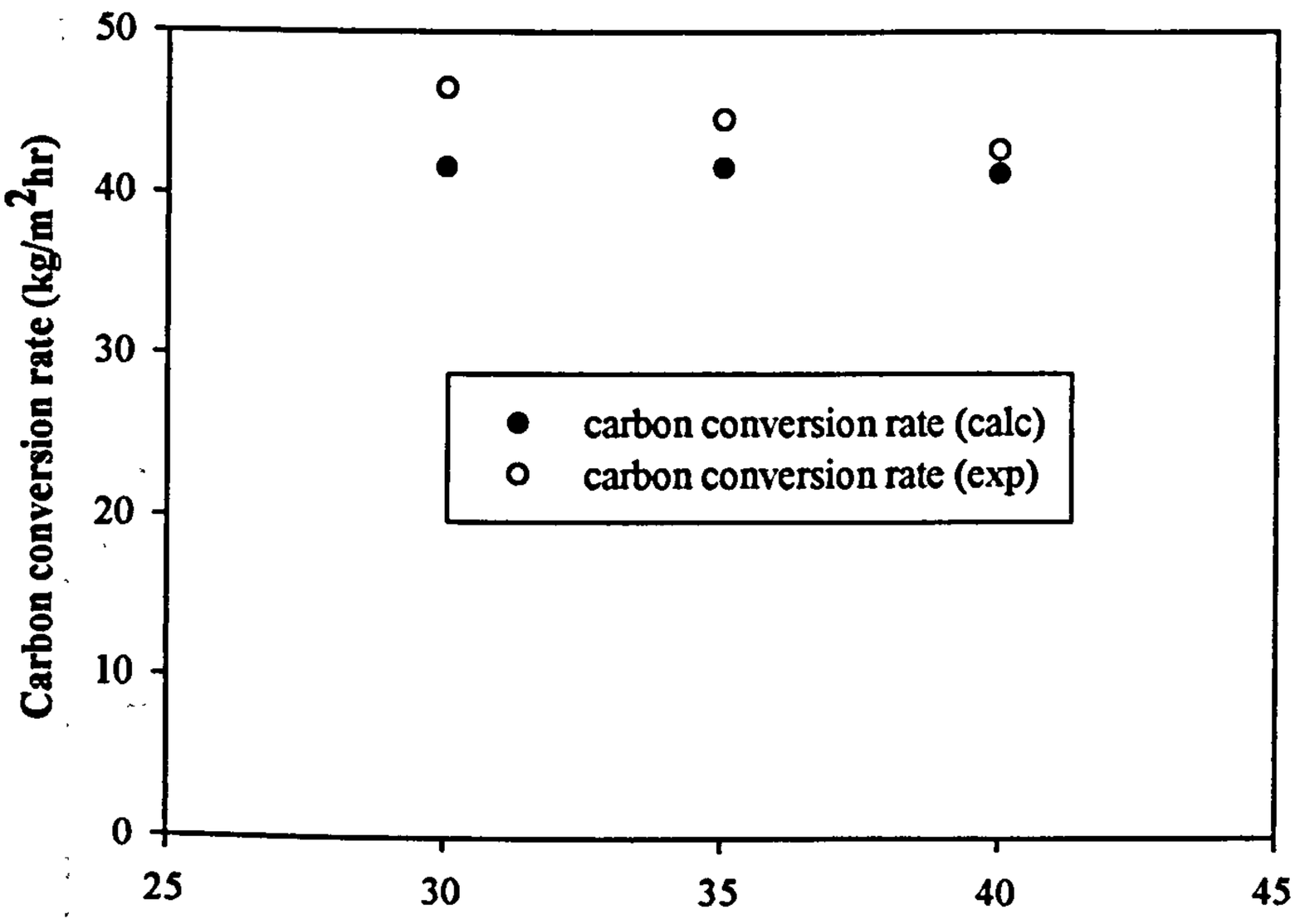

Figure 6.27: Calculated and measured wet flue gas composition vs. percentage of steam for Case A (reference data: Hobbs, 1992).

Figure 6.28 (a) and *(b)* demonstrate the effect of increasing steam in the feed on the gas composition in the flue gases. A general trend is the declining of CO, H_2 and CO_2 as the percentage of steam in the feed was increased. In Case A, the calculation showed an over-prediction of CO and a much lower release of H_2 and CO_2 compared to the experimental results. The CO concentration in the experiment ranged from 3-6% while the calculation gave a range of 8-12%. The calculation results in Case B showed a closer representation to the measurement values. The calculation gave a CO, H_2 and CO_2 concentration in the range of 6-10%, 9-12% and 11-12% compared to the measurement range of 3-6%, 12-15% and 11-13%. The intense char-O_2 reaction in Case B compared to Case A as shown in the previous *Figure 6.21* whereby kinetic rates were given by Kashiwagi (1992) and Hobbs (1992) respectively provides a larger amount of CO in the gases to be further reacted in the water-gas shift

reaction. The model predictions correctly reflect the measured trend but gave a slightly lower CO, H_2 and CO_2 across the whole percentage of steam range.

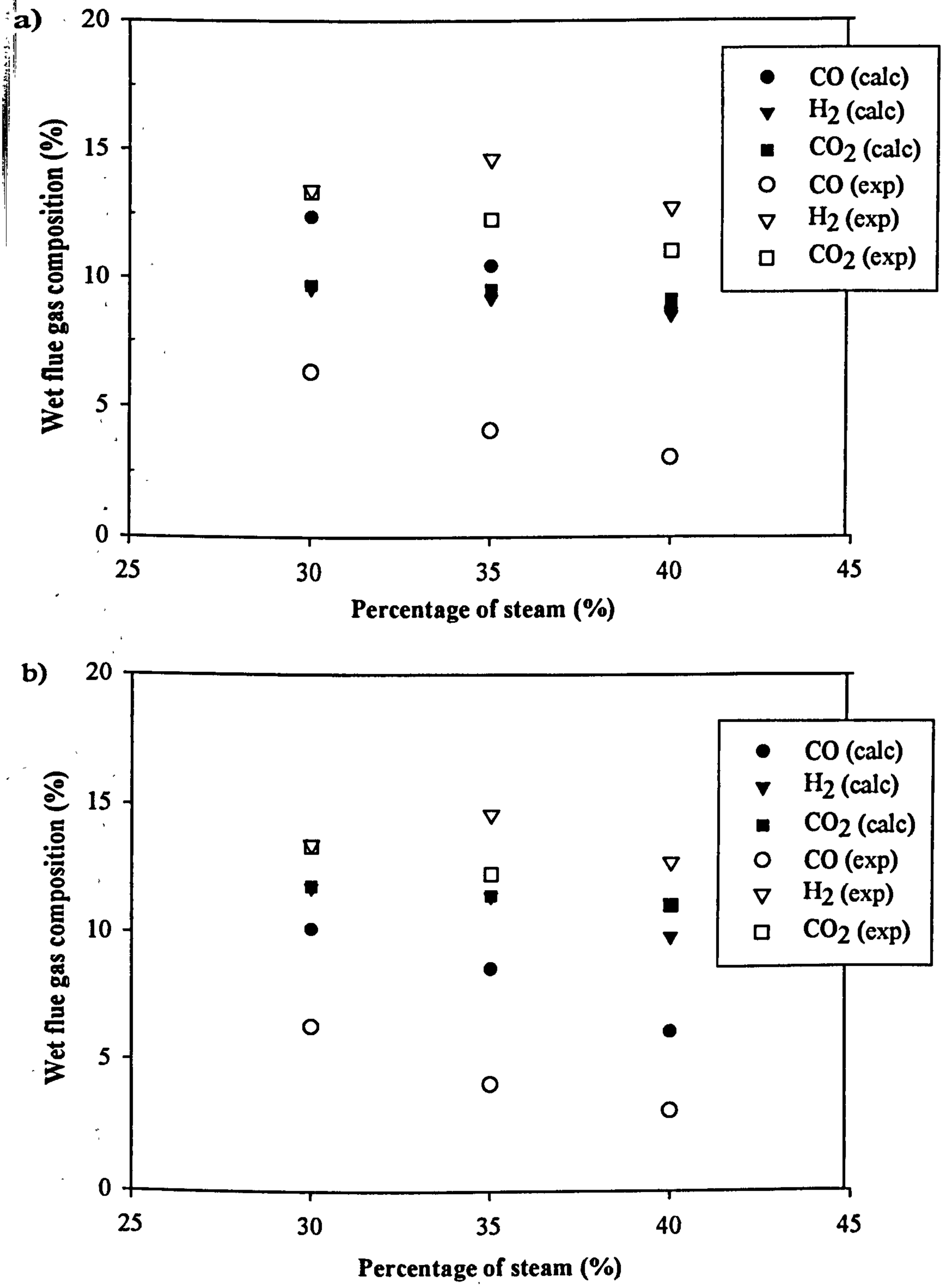

Figure 6.28: Calculated and measured wet flue gas composition vs. percentage of steam. (a) Case A (reference data: Hobbs, 1992); (b) Case B (reference data: Groeneveld,1980 and Kashiwagi, 1992).

6.4 SUMMARY

Fixed Bed Combustion

In the investigation concerning the bed modelling of the effect of fuel size on pinewood combustion in a packed bed, the following conclusions can be drawn from the current study:

1. Large fuel particles produced a higher burning temperature in the bed.
2. The moisture evaporation is rapid due to the low moisture content of the wood. The release of volatiles dominates the combustion process due to the large amount of volatile material in the wood.
3. The individual processes; drying, devolatilisation and char combustion for larger fuel overlapped, unlike smaller fuel particles where these processes occurred in series.
4. Burning rate decreases with increase in fuel particle size.
5. Ignition velocity is shorter with a bed of smaller particles than with larger particles at the same operating conditions.
6. The rapid combustion of smaller size fuel resulted in a fuel-richer combustion and a higher CO concentration in the flue gases.
7. The calculated temperature profile was lower compared to the measurement. The difference could be attributed to measurement methods, or combustion phenomena like the channelling effect.

Fixed Bed Gasification

1. The production of hydrogen gas is influenced by the air to steam ratio and the total feed flow rate.
2. The CEA results indicated that the increase in steam input would cause a drop in CO and H_2 for cases carried out with 110l/min (270kg/m^{2}hr) of air. However, the addition of steam to cases with 100l/min (245kg/m^{2}hr) encourages the production of H_2.
3. The calculated flue gas composition based on the carbon conversion rate of the gasification experiments using the CEA matched the measurements. This implied that the measurements were conducted when the bed was at equilibrium.
4. Although the equilibrium model is useful in predicting what is thermodynamically attainable, the equilibrium model has its limitation. Therefore, the carbon conversion is considered by a detailed mathematical calculation, FLIC.
5. In the FLIC calculations, the effect of increasing steam in the feed led to a lower bed temperature and carbon conversion rate. The flue gas composition varied as the calculation was carried out with kinetic data from different sources.
6. The predicted carbon conversion rate ranged from 40-42 kg/m^{2}hr.

7. The FLIC calculation was able to give a close representation of the dynamic change in temperature along the stratified gasifier.
8. The calculation agreed qualitatively with the experiments and showed similar trends in the performance of the gasifier with varying flow rates of the reactant feed.
9. Future work is required on determination of the kinetic rates of the gasification reactions.

CHAPTER 7
OVERALL DISCUSSION ON 'ENERGY FROM BIOFUEL'

There is a growing interest in 'Energy from Biofuel' as it is one of the key areas in the global clean energy strategy. This thesis presents a detailed study on energy from biofuel through two thermal-conversion processes; combustion and gasification. Energy crops with a high dry matter content are suited to four main thermal-conversion processes; pyrolysis, gasification, liquefraction and combustion.

The introduction of biofuel has been fast in a few countries in Europe but there is still a lot of research on biological and technical development needed for further improvement. In this study, the performances of wood and woody material, herbaceous and refuse-derived fuels (RDF) were tested in a fixed- bed combustor. Experimental investigation on a laboratory-scale plant provided detailed information on the structure, burning characteristics and gas composition. The smaller-scale pot burner provided the flexibility required for assessing the influence of parameters such as particle size and air flow rate, over wide ranges of the combustion process. Complementary to this, research into using biomass materials such as char from wood chips or fuel pellets derived from agricultural waste as a source of fuel in a counter-current gasification reactor was also carried out. Product gas with higher heating value of 4.52MJ/kg and 27% hydrogen content was successfully produced using a high temperature steam-air gasification unit. This technology produces a more transportable and valuable commodity; synthesis gas (syn gas). Another added advantage is the potential of hydrogen production as interest in hydrogen generation has grown dramatically. One of the impediments that the gasification technology has been facing is the ability to produce low tar content producer gas. Tar removal is much more difficult compared to particle removal hence; one of the key issues for the successful application of biomass derived producer gas is the reduction of tar content. In the tests carried out, the production of methane was negligible and no higher hydrogen carbons were detected. Therefore, if combined with a first stage pyrolyser unit, the high temperature char will act as a catalyst to crack the complex organic compounds to carbon and gas. Investigation to improve the gasification process also includes the influence of various parameters such as steam/air ratio, reactor temperature and particle sizes on the gasification process. Mathematical models were applied to both the combustion

and gasification process and this provided a deeper understanding of the biomass process in the bed.

The high temperature product gas formed from the gasification process if combined with hot gas clean-up (HGCU) to reduce the thermal efficiency losses associated with gas quenching could result in a higher efficiency energy recovery system such as the integrated gasification combined cycle (IGCC). The gasification process offers the opportunity for integration with combined cycle turbines or reciprocating engines, converting fuel energy to electricity more efficiently (+40%). For greater improvement, fuel cells can be added to Integrated Gasification Combined Cycle (IGCC) system, making it the Integrated Gasification Fuel Cell system (IGFC). The lower volume of product gas from the gasification system requires a smaller and less expensive gas cleaning equipment compared to the flue gas clean-up technology. The higher partial pressure of contaminants in the lower gas volume also increases the adsorption and particulate capture level. In terms of emission, the reducing conditions in the gasification process minimize the formation of dioxins and large quantities of SOx and NOx. As for the combustor, the energy is recovered through a steam cycle influenced by the contaminants and tar content in the fuel. Limitation is placed on the steam temperature to avoid excessive corrosion while economic reasons restrict the use of high temperature alloys. Therefore, combustion boilers have very low efficiency (~30%) from the point of view of thermal energy conversion to electricity.

Nevertheless, combustion is a well-established technology with historical operating experience to provide 'real' data and the control system of a conventional combustor is relatively simpler compared to gasification. Gasification technology on the other hand, is in its early stage of large-scale commercialisation as no suitable commercial biomass gasification plant exists to date. Long-term operating results from industrial plants are needed for gasification to become an attractive alternative to combustion. The success of these energy recovery systems depends on the production of clean producer gas from the gasification system and the development of ancillary systems for gas cleaning. The acceptable particle content for an IC engine operation is <50mg/Nm^3 and a tar content <100mg/Nm^3. Similarly, IGCC turbine's lifetime can be limited due to erosion and high temperature corrosion caused by the impaction of particles and deposition of impurities.

The current hot gas clean-up method centres on the use of metal oxide sorbents for sulphur removal and the utilization of a ceramic barrier filter for particulate cleaning. Innovative investigation using a molten tin irrigated packed bed scrubber as a multi-component cleanup device is currently underway. The cleaning up for the gasification process is different from

combustion in which, the gasification impurities are removed prior to the combustion of the gas. In a conventional combustion plant, the cleanup is carried out after the combustion, requiring a much larger volume of stack gases to be cleaned. There are several technologies related to synthesis gas cleaning. These technologies are known as cold gas clean-up (CGCU) and hot gas clean-up (HGCU) according to the fuel gas temperatures. Gasification plants can be configured to reach very low levels of emission by integration with an advanced clean up system. The study of the gasification process and the associated clean-up system is vital to increase the environmental performance without compromising the efficiency, making the process competitive to energy generation from conventional fuels.

The research carried out in this PhD also showed that the high content of alkali in crops could pose significant problems in the plant operation. Sintering of ashes was observed during the combustion of Miscanthus pellets. Conventional combustion equipment is not designed for the burning of energy crops and agricultural residues and some method for controlling alkali emissions is required. The two common processes used to attain the desired alkali levels in the producer gas are through adsorption and leaching. On the contrary, it was also reported in the literature that the alkali metal salts, especially those containing potassium enhances the gasification process. Thus, the high potassium found in herbaceous fuels could provide an inexpensive gasification catalyst. Therefore, further work on this topic is required.

Summing up, this PhD examines the conversion of biofuels through two processes; combustion and gasification. The two mechanisms and end-use of the products differ considerably; hence this critical evaluation of these two processes in the terms of the relevant technologies and environmental issues has been carried out and the conclusions presented.

CHAPTER 8

CONCLUSIONS AND SUGGESTIONS FOR FUTURE WORK

This chapter highlights the conclusions of the research work. It also outlines a number of suggestions for future work.

8.1 CONCLUSIONS

The main conclusions that can be drawn from this work are summarised below:

1. The experimental investigation on the fixed bed reactor successfully produced detailed measurements of temperature, burning rates, ignition front velocity and gas composition for solid biomass fuel bed combustion.
2. The ignition front speed and burning rate increased with increasing air flow, while leaving a smaller amount of char above the ignition front. The burning rate during the char oxidation period was much smaller than that for the ignition propagation period.
3. Two woody samples had faster ignition propagation than pellet samples, where the ignition front speed was inversely proportional to the bulk density.
4. The burning rate decreased linearly with the bulk density and difference between the samples was relatively small.
5. Large particles have a lower ignition front speed and burning rate, while a larger amount of char was left above the ignition front and the char oxidation period lasted longer. The temperature gradient at the ignition front also decreased with increasing particle sizes. The thickness of the ignition front from 200°C to 800°C was about the order of the particle size.
6. Channelling was observed around the side wall of the reactor for the small miscanthus pellets and at several locations in the bed for larger pinewood particles (35mm cubes).
7. The alkali index based on the elemental composition of bottom ash explained the sintered agglomerates of miscanthus ashes.

8. The experimental investigation of the high temperature counter-current biomass char gasification process gave measurement details of temperature, flue gas composition and char conversion rates.
9. The temperature profile showed that the bottom of the bed was the hottest due to the different chemical processes stratified along the reactor height.
10. Hydrogen yield was sensitive to the steam/air ratio, feed flow rates, reactor temperature and particle size.
11. Although hydrogen production generally increased with higher steam/air ratio, a too high steam/air ratio and a too low reactant flow will lower the reaction temperature, and cause the hydrogen yield to decrease.
12. The char conversion rate obtained in this experimental work ranged in the region of 26-42 kg/m^{2}hr depending on the reactant input.
13. The optimum condition to produce the highest calorific value dry gases (4.52MJ/kg) is with 220kg/m^{2}hr air and 147kg/m^{2}hr steam at a reactor temperature of 850°C.
14. The maximum hydrogen production ratio obtained was 15kg of hydrogen from 100kg of char.
15. A computational code developed by SUWIC was used to successfully predict the combustion and gasification process.
16. The fixed bed combustion model showed that the residual char burnout is the only process occurring in a bed of small particles during the final stage of combustion. However, both the char burnout and fuel devolatilisation occurred at the same time in a bed of large particles.
17. Chemical equilibrium calculations were carried out using version 2 of NASA Glenn's computer program Chemical Equilibrium with Application (CEA). The calculated gas phase composition was consistent with the experimental values.
18. The calculated char conversion rate from (FLIC) for the gasification model showed good qualitative agreement with the experimental results.

8.2 Suggestions for Future Work

The research work described in this thesis forms a useful basis and reference for future model development and investigation into the combustion and gasification behaviour of biomass energy conversion systems.

Gasification has a benefit over direct combustion as the biomass is upgraded from a solid fuel into a more viable source of energy - fuel gas. This increases the operating efficiencies and allows possible process system de-coupling for the development of a sustainable future. Based on the understanding gained in this PhD, the next step would be to combine the char gasifier with a first stage pyrolyser unit. The gasifier differs from conventional systems as it produces practically tar-free gas. The high operating temperature (about 800°C) acts as a catalyst for the cracking of tar to carbon and gas. The proposed gasifier is part of a two stage integrated unit that aims ultimately at utilising biomass fuel such wood chips or fuel pellets derived from agricultural waste. The high temperature of the exit gas opens up the opportunity to combine thermal gasification with a Stirling engine for use in a small combined heat and power plant which has very high overall energy efficiency (>85%). An advantage of the close-coupled arrangement is that an inefficiency in the gasifier, whereby the gas contains a greater proportion of carbon dioxide (and hence a higher exit gas temperature) does not affect the efficiency of the engine as all the gases will be burned to carbon dioxide in the engine combustor. *Figure 8.1* illustrates the schematic of the gasification rig constructed as part of the two stage unit.

Other future work in the gasification should also include investigation into alternative gasification processes with different main reactants; indirect gasification (steam only) and oxygen gasification. This would result in product gases with different calorific values and composition. This should also include investigations into other contributing factors such as pressure, temperature of the main reactants and variation in the solid fuel content.

Further improvements to FLIC should include the different expression used for the reaction kinetics in the case of the water-gas reaction. Additional data on the steam-char reaction rate should also be sourced. FLIC should also incorporate the continuous or discontinuous removal of ash during the gasification process to allow a simulation condition closer to the experimental situation. Improvement to FLIC should be carried out in parallel with experimental work so that any development or improvement to the model can be simultaneously validated.

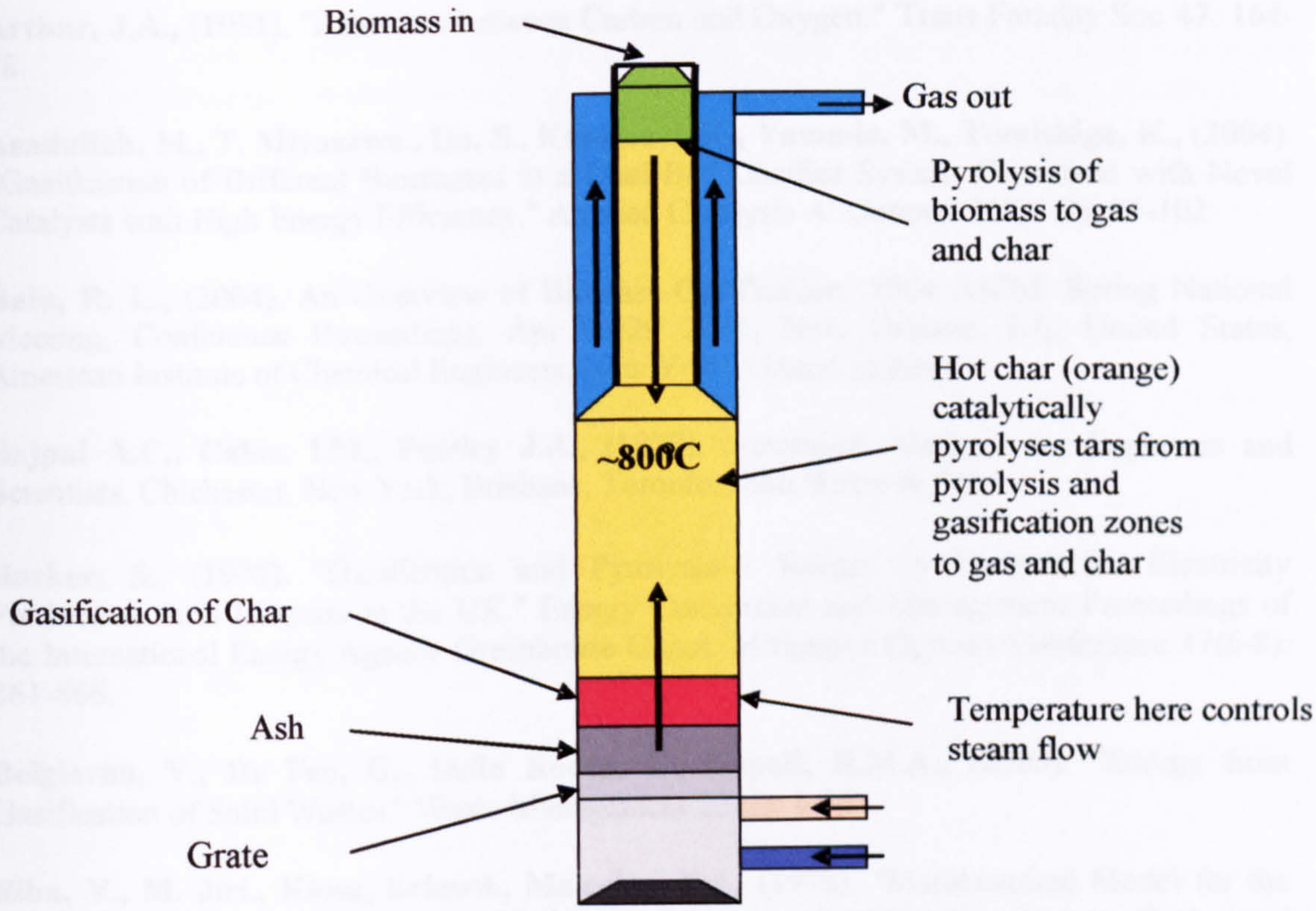

Figure 8.1: Proposed two stage gasifier unit.

REFERENCES

Aebiom (European Biomass Association)., **(1999)**. The European Heat Market & The Kyoto Protocol, available from, http://www.ecop.ucl.ac.be/aebiom/publications/Paper8.htm

Arthur, J.A., (1951). "Reactions between Carbon and Oxygen." Trans Faraday Soc 47: 164-78.

Asadullah, M., T. Miyazawa., Ito, S., Kunimori, K., Yamada. M., Tomishige, K., (2004). "Gasification of Different Biomasses in a Dual-Bed Gasifier System Combined with Novel Catalysts with High Energy Efficiency." Applied Catalysis A: General 267(1-2): 95-102.

Bain, R. L., (2004). An Overview of Biomass Gasification. 2004 AIChE Spring National Meeting, Conference Proceedings, Apr 25-29 2004, New Orleans, LA, United States, American Institute of Chemical Engineers, New York, United States.

Bajpai A.C., Calus. I.M., Fairley J.A., (1977). Numerical Methods for Engineers and Scientists. Chichester, New York, Brisbane, Toronto, John Wiley & Sons.

Barker, S., (1996). "Gasification and Pyrolysis - Routes to Competitive Electricity Production from Biomass in the UK." Energy Conversion and Management Proceedings of the International Energy Agency Greenhouse Gases: Mitigation Options Conference 37(6-8): 861-866.

Belgiorno, V., De Feo, G., Della Rocca, C., Napoli, R.M.A., (2003). "Energy from Gasification of Solid Wastes." Waste Management 23(1): 1-15.

Biba, V., M. Jiri., Klose, Erhard., Malecha, Jiri., (1978). "Mathematical Model for the Gasification of Coal under Pressure." Industrial & Engineering Chemistry Process Design and Development 17(1): 92-98.

Bruch, C., B. Peters., Nussbaumer, T., (2003). "Modelling Wood Combustion under Fixed Bed Conditions." Fuel 82(6): 729-738.

Brunner, C. R., (1993). Hazardous Waste Incineration. London, New York, McGraw-Hill.

Bryden, K. M., Ragland, K.W., (1996). "Numerical Modelling of a Deep, Fixed Bed Combustor." Energy and Fuels 10(2): 269-275.

Higman, C., Burgt M., (2003). Gasification, Boston : Elsevier/Gulf Professional Pub.

Carlsson K. B., (1999). Reliable and Cost Effective Pollution Control Systems for Waste-to Energy Plants. Second International Symposium on Incineration and Flue Gas Treatment Technologies, Sheffield.

Chen, G., Q. Yu., K. Sjostrom., (1997). "Reactivity of Char from Pyrolysis of Birch Wood." Journal of Analytical and Applied Pyrolysis'96. 40-41: 491-499.

Clayton, P., Coleman, P., Leonard, A., Loader, A., Marlower, I., Micheal, D., Richardson, S., Scott, D., and Woodfield, M., (1991). Review of Solid Waste Incineration in the UK. London, Warren Spring Laboratory (national Environmental Technology Centre), HMSO, Department of Trade and Industry.

Clift R., (1999). Public Sector Decisions on the Limits to Technological Assessment. Second International Symposium on Incineration and Flue Gas Treatment Technologies, Sheffield.

Coggins C., (2003). Alternatives to Incineration for Dealing with Residual Municipal Waste in the UK: Opportunities and Barriers. Proceedings of the 4th International Symposium on Waste Treatment Technologies, Sheffield.

Coggins. C., (1999). It's Role within an Integrated Waste Management Strategy. Second International Symposium on Incineration and Flue Gas Treatment Technologies, Sheffield.

Coombs., (1996). "Biomass Energy: Progress in the European Union." Renewable Energy 8(1-5): 17-21.

Cooper, J., and W. L. H. Hallett., (2000). "A Numerical Model for Packed-Bed Combustion of Char Particles." Chemical Engineering Science 55(20): 4451-4460.

Coulson, J. M., (1996). Coulson & Richardson's Chemical Engineering. - Vol.6 : Chemical Engineering Design, Oxford : Butterworth-Heinemann.

De Feo, G., Belgiorno, V., Napoli, R.M.A., Papale, U., (2000). Solid Wastes Gasification. SIDISA International Symposium on Sanitary and Environmental Engineering.

de Jong, W., A. Pirone., M. A. Wojtowicz., (2003). "Pyrolysis of Miscanthus Giganteus and Wood Pellets: TG-FTIR Analysis and Reaction Kinetics*." Fuel 82(9): 1139-1147.

Defra, Department of Environment, Food and Rural Affair., (2003). Energy crop scheme: Establishment Grants, available from http://www.defra.gov.uk/corporate/regulat/forms/erdp/ecs/ecs-estabgrant-explain.pdf

Defra, Department of Environment, Food and Rural Affair., (2004). Assessment Criteria Available for £32M New Technologies Funding, available from http://www.defra.gov.uk/news/2004/040202d.htm

Defra, Department of Environment, Food and Rural Affair., (2005). Climate Change: Kyoto Protocol Force at the WWW http://www.defra.gov.uk/news/latest/2005/climate-0216.htm

DeGroot, W. F., and G. N. Richards., (1988). "Effects of Ion-Exchanged Cobalt Catalysts on the Gasification of Wood Chars in Carbon Dioxide." Fuel 67(3): 345-351.

Di Blasi, C., (1993). "Modelling and Simulation of Combustion Processes of Charring and Non-Charring Solid Fuels." Progress in Energy and Combustion Science 19(1): 71-104.

Di Blasi, C., (2004). "Modelling Wood Gasification in a Counter-current Fixed-Bed Reactor." AIChE Journal 50(9): 2306-2319.

Di Blasi, C., B, Carmen., A, Santoro., Hernandez, E., (2001). "Pyrolytic Behaviour and Products of Some Wood Varieties." Combustion and Flame 124(1-2): 165-177.

Di Blasi, C., G. Signorelli., G. Portoricco., (1999). "Countercurrent Fixed-Bed Gasification of Biomass at Laboratory Scale." Ind. Eng. Chem. Res. 38(7): 2571-2581.

DTI (Department of Trade and Industry)., (1999). Digest of UK Energy Statistics.

DTI (Department of Trade and Industry)., (2001). Digest of UK Energy Statistics.

DTI (Department of Trade and Industry)., (1987) Straw as a Fuel in the UK. Energy from Biomass;5:27.

DTI (Department of Trade and Industry)., (1992) The Development of Compacted Straw Fuel. Energy from Biomass;5: 34.

Eduljee, G., (2003). A Technical Perspective on Urban Waste Stress. Proceedings of the 4th International Symposium on Waste Treatment Technologies, Sheffield.

EECI (European Energy Crops Internetwork)., (1999). Legislation Relating to Energy Crops in Ireland, available from http://www.eeci.net/archive/biobase/B10130.html

EECO (European Energy Crops Overview)., Biobase: Main findings of the European Energy Crops Overview (EECO) Project, European Energy Crops InterNetwork, available from http://www.eeci.net/archive/biobase/B10054.html

EIA, (European Information Administration). (2003). United Kingdom: Environmental Issues, available from http://www.eia.doe.gov/emeu/cabs/ukenv.html

Encinar, J. M., Gonzalez, Juan F., Rodriguez, Juan J., Ramiro, Maria J., (2001). "Catalysed and Uncatalysed Steam Gasification of Eucalyptus Char: Influence of Variables and Kinetic Study." Fuel 80(14): 2025-2036.

Energex (2002) - Environmental Control and Waste Recycling - Topic V 75(3-4): 275-285.

Eurostat (2002). Recovery and Disposal of Municipal Waste. Environment and Energy Datasets.

Faaij, A., R. van Ree., L, Waldheim., E. Olsson., A. Oudhuism., van Wijk, C., Daey-Ouwens., W. Turkenburg., (1997). "Gasification of Biomass Wastes and Residues for Electricity Production." Biomass and Bioenergy 12(6): 387-407.

Fristrom, R. M., (1995). Flame Structure and Processes. New York, Oxford University Press.

Fujita., (1999). Bioenergy at the WWW http://www.fujitaresearch.com/reports/biomass.html.

Fushimi, C., K. Araki., Y. Yamaguchi., A. Tsutsumi., (2003). "Effect of Heating Rate on Steam Gasification of Biomass. 1. Reactivity of Char." Industrial and Engineering Chemistry Research 42(17): 3922-3928.

Godavarty, A. and A. Agarwal., (2000). "Distribution and Catalytic Activity of Eutectic Salts in Steam Gasification of Coal." Energy Fuels 14(3): 558-565.

Goetz, G. J., (1983). Combustion and Gasification Kinetics of Chars from Four Commercially Significant Coals of Varying Rank. Proceedings - 1983 International Conference on Coal Science, Pittsburgh, PA, USA.

Goh Y. R., Lim C. N., Zakaria R, Chan K. H., Reynolds H., Yang Y. B., Siddall R. G., Nasserzadeh V., Swithenbank J., (1999). Mixing, Modelling and Measurements of Incinerator Bed Combustion. Second International Symposium on Incineration and Flue Gas Treatment Technologies, Sheffield.

Goh, Y. R., R. G. Siddall., V. Nasserzadeh., R. Zakaria., J. Swithenbank., D. Lawrence., N. Garrod and B. Jones., (1998). "Mathematical Modelling of the Burning Bed of a Waste Incinerator." Journal of the Institute of Energy 71(487): 110-118.

Gomez-Moreno, F. J., D. Sanz-Rivera., M. Martin-Espigares., D. Papameletiou., G. De Santi and G. Kasper., (2003). "Characterization of Particulate Emissions During Pyrolysis and Incineration of Refuse Derived Fuel." Journal of Aerosol Science 34(9): 1267-1275.

Gordon, S., and McBride, B. J., (1994). Computer Program for Calculation of Complex Chemical Equilibrium Compositions and Applications, Part 1: Analysis, Nasa RP-1331., National Aeronautics and Space Administration (NASA), Cleveland, OH.

Gort R., (1995). On the Propagation of a Reaction Front in a Packed Bed: Thermal Conversion of Municipal Solid Waste and Biomass. Netherlands, Universitieit Twente Enchede.

Groeneveld, M. J., and W. P. M. van Swaaij., (1980). "Gasification of Char Particles with CO_2 AND H_2O." Chemical Engineering Science 35(1-2): 307-313.

Hasler, P., and T. Nussbaumer., (1999). "Gas Cleaning for IC Engine Applications from Fixed Bed Biomass Gasification." Biomass and Bioenergy 16(6): 385-395.

Hautman, A.N., Dryer. F., Schlug KP., Glassman I., (1981). "A Multiple-Step Overall Kinetic Mechanism for the Oxidation of Hydrocarbons." Combust Sci Technology 25: 219.

Hendriks, C., and K. Blok., (1996). "Regulation for Combined Heat and Power in the European union." Energy Conversion and Management Proceedings of the International Energy Agency Greenhouse Gases: Mitigation Options Conference 37(6-8): 729-734.

Hernandez Allica, J., A. J. Mitre., J. r. e. A. Gonzalez Bustamante., C. Itoiz., F. Blanco., I. Alkorta and C. Garbisu., (2001). "Straw Quality for its Combustion in a Straw-Fired Power Plant." Biomass and Bioenergy 21(4): 249-258.

Hisaki, Y., (2003). Mathematical Modelling of a Japanese Incinerator. PhD Thesis. Department of Chemical and Process Engineering. Sheffield, University of Sheffield.

HMSO., (2000). The Energy Crops Regulation, statutory Instrument 2000 No. 3042, available from http://www.opsi.gov.uk/si/si2000/20003042.htm

Hobbs, M. L. R., Predrag T., Smoot, Douglas L., (1992). "Modelling fixed-bed coal gasifiers." AIChE Journal 38(5): 681-702.

Hoffman, E. J., (1978). Coal Conversion, Laramie, Wyo : Energon Co.

Howard, J. B., William, G. C., Fine, D.H., (1973). "Kinetics of Carbon Monoxide Oxidation in Post-Flame Gases." 14th Symposium (International) on Combustion, Pittsburgh: The Combustion Institute: 975-86.

Hunt, M.L., Tien, C. L., (1988). "Non-Darcian Convection in Cylindrical Beds." J. Heat Transfer 110: 378-84.

International Scientific Committee., (2005). International Symposium on the Stabilisation of greenhouse gas concentrations, available from http://www.stabilisation2005.com/Steering_Commitee_Report.pdf

Jenkins, B. M., L. L. Baxter., T. R. Miles Jr. and T. R. Miles., (1998). "Combustion Properties of Biomass." Fuel Processing Technology 54(1-3): 17-46.

Johnson J. L., (1979). Kinetics of Coal Gasification. Canada, John Wiley & Sons.

Jorgensen K, M. H., (1999). Modern Control Systems for MSW Plants. Second International Symposium on Incineration and Flue Gas Treatment Technologies, Sheffield.

Jurado, F., A. Cano., J. Carpio., (2003). "Modelling of Combined Cycle Power Plants using Biomass." Renewable Energy 28(5): 743-753.

Kashiwagi , T. N., Hidesaburo., (1992). "Global Kinetic Constants for Thermal Oxidative Degradation of a Cellulosic Paper." Combustion and Flame 88: 345-368.

Klasen T, G. K., (1999). Numerical Calculation and Optimization of a Large Municipal Solid Waste Incinerator Plant. Second International Symposium on Incineration and Flue Gas Treatment Technologies, Sheffield.

Kuo J. T., Hsu. W. S., Yo T. C., (1997). "Effect of Air Distribution on Solid Fuel Bed Combustion." American Society of Mechanical Engineering (ASME) 119: 120-128.

Kuo, T. J., Kuwata, M., Shieh, W.S., Essenhigh R. H., (1970). Combustion and Emission Phenomena in Incinerators. National Waste Incineration Conference, ASME: 327-330

Laurendeau, N. M., (1978). "Heterogeneous Kinetics of Coal Char Gasification and Combustion." Progress in Energy and Combustion Science 4(4): 221-270.

Ledin, S., (1996). "Willow wood properties, production and economy." Biomass and Bioenergy Modelling Short Rotation Forestry Growth 11(2-3): 75-83

Lewandowski, I., J. C. Clifton-Brown., J. M. O. Scurlock and W. Huisman., (2000). "Miscanthus: European Experience with a Novel Energy Crop." Biomass and Biocnergy 19(4): 209-227.

Li, S. and Y. Cheng., (1995). "Catalytic Gasification of Gas-Coal Char in CO_2." Fuel 74(3): 456-458.

Liliedahl, T. and K. Sjostrom., (1997). "Modelling of char-gas reaction kinetics." Fuel 76(1): 29-37.

Mann, M. D., R. Z. Knutson., J. Erjavec and J. P. Jacobsen., (2004). "Modelling Reaction Kinetics of Steam Gasification for a Transport Gasifier." Fuel Fundamental Mechanisms of Biomass, Pyrolysis and Oxidation 83(11-12): 1643-1650.

Martindale, L., (1985) The Potential for Straw as a Fuel in the UK. IMech E Conference Publications: 125.

McKendry, P., (2002). "Energy Production from Biomass (part 1): Overview of biomass." Bioresource Technology 83(1): 37-46.

McKendry, P., (2002). "Energy Production from Biomass (part 2): Conversion Technologies." Bioresource Technology 83(1): 47-54.

McKendry, P., (2002). "Energy Production from Biomass (part 3): Gasification Technologies." Bioresource Technology 83(1): 55-63.

Merrick, D., (1984). Coal Combustion and Conversion Technology. London, Macmillan.

Morris, M. and L. Waldheim., (1998). "Energy Recovery from Solid Waste Fuels using Advanced Gasification Technology." Waste Management 18(6-8): 557-564.

Mudge L.K., Sealock. L. J., Weber S. L., (1979). "Catalyzed Steam Gasification of Biomass." Journal of Analytical and Applied Pyrolysis: 165-175.

Na, J. I., Park S. J., Y. K. Kim., J. G. Lee and J. H. Kim., (2003). "Characteristics of Oxygen-Blown Gasification for Combustible Waste in a Fixed-Bed Gasifier." Applied Energy

Nasserzadeh, V. N., (1990). Optimisation study of Incineration in a Municipal Solid Waste Incinerator with a Vertical Radiation Shaft. PhD. Department of Chemical and Process Engineering, University of Sheffield.

Nieminen. J., Palonen. J., Kivela. M., (1999). "Circulating Fluidized Bed Gasifier for Biomass." VGB PowerTech 79(10/99): 69–74.

Oman, J., M. Tacer and M. Tume., (1999). "Overfeed Fixed-Bed Combustion of Wood." Bioresource Technology 67(2): 139-147.

Ower, E., (1984). The Measurement of air flow / by E. Ower and R.C. Pankhurst. - 5th ed. (in SI units).

Patankar SV., (1980). Numerical Heat Transfer and Fluid Flow. New York: Hemisphere.

Peters B., (1995). A Detailed Model for Devolatilisation and Combustion of Waste Material in Packed Beds. Third European Conference on Industrial Furnaces and Boilers (INFUB), Lisbon, Portugal; 18-21 April 1995.

Peters, B., (2002). "Measurements and Application of a Discrete Particle Model (DPM) to Simulate Combustion of a Packed Bed of Individual Fel Particles." Combustion and Flame 131(1-2): 132-146.

Phillips, P. S., R. M. Pratt., K. Pike., (2001). "An Analysis of UK Waste Minimization Clubs: Key Requirements for Future Cost Effective Developments." Waste Management 21(4): 389-404.

Ponder, G. R. and G. N. Richard., (1994). "Oxygen and CO_2 Gasification of Chars from Wood Treated with Iron (II) and Iron (III) Sulphates." Energy & Fuels 8(3): 705-713.

Pyle, D. L. and C. A. Zaror., (1984). "Heat Transfer and Kinetics in the Low Temperature Pyrolysis of Solids." Chemical Engineering Science 39(1): 147-158.

RCEP (Royal Commission on Environmental Pollution)., The alternatives to fossil fuels, available from http://www.rcep.org.uk/pdf/chp7.pdf

Rogaume, T., M. Auzanneau., F. Jabouille., J. C. Goudeau and J. L. Torero., (2002). "The Effects of Different Airflows on the Formation of Pollutants during Waste Incineration." Fuel 81(17): 2277-2288.

Rogers, J. E. L., Sarofim, A. F and Howard, J. B., (1972). Effect of Underfire Air Rate on a Burning Simulated Refuse Bed. Proceedings of the National Incinerator Conference, New York.

Ronnback, M., Axell, M., Gustavsson, L., (2000). "Combustion Processes in a Biomass Fuel Bed-Experimental Results." Progress in Thermochemical Biomass Conversion: 17-22.

Saastamoinen, J. J., R. Taipale., M. Horttanainen and P. Sarkomaa., (2000). "Propagation of the Ignition Front in Beds of Wood Particles." Combustion and Flame 123(1-2): 214-226.

Sarkar S., (1990). Fuels and Combustion, London ; Hyderabad, India : Sangam : Orient Longman.

Schilling, H.-D., (1979). Coal Gasification. London, Graham & Trotman.

Schmidt U., Nasserzadeh. V., Swithenbank J, Lawrence D., Garrod N. P., Mildenstein P., (1999). Implications of the Draft Commission Proposal for a Directive on the Incineration of Waste for the UK's. Second International Symposium on Incineration and Flue Gas Treatment Technologies.

Scurlock, J. M. O., (1998). Miscanthus: A Review of European Experience with a Novel Energy Crop, Oak Ridge National Laboratory Oak Ridge Tennessee.

Shafizadeh, F., (1982). "Introduction to Pyrolysis of Biomass." Journal of Analytical and Applied Pyrolysis 3(4): 283-305.

Shafizadeh, F., Overend., R.P., Milne, T.A., Mudge, L. K., Eds., (1985). "Pyrolytic Reactions and Products of Biomass in Fundamentals of Biomass Thermochemical Conversion." Elsevier: 183-217.

Shin, D. and S. Choi., (2000). "The Combustion of Simulated Waste Particles in a Fixed Bed." Combustion and Flame 121(1-2): 167-180.

Simell, P. A., J. K. Leppalahti., and J. B.-s. Bredenberg., (1992). "Catalytic Purification of Tarry Fuel Gas with Carbonate Rocks and Ferrous Materials." Fuel 71(2): 211-218.

Siminski, V., Wright FJ., Edelman RB., Economos C., Fortune OF., (1972). "Research on Methods of Improving the Combustion Characteristics of Liquid Hydrocarbon Fuels." AFAPL TR 72-74, Vols I and II, OH: Air Force Aeropropulsion Laboratory. Wright Patterson Air Force Base.

Smooth, L.D., Pratt, D.T., (1979). Pulverized-Coal Combustion and Gasification. New York, Plenum Press.

Smoot, L. D., Smith, P.J., (1985). Coal Combustion and Gasification. New York, Plenum Press.

Swithenbank, J., Nasserzadeh. V., Wasantakoran. A., Lee. P. H and Swithenbank. C., (1999). Future Intergrated Waste, Energy and Pollution Management (WEP). Second International Symposium on Incineration and Flue Gas Treatment Technologies, Sheffield.

Swithenbank, J., Yang. Y. B., Ryu. C., Goodfellow. J., Anderson. S and Nasserzadeh. V. Sharifi., (2003). Waste Treatment: Strategic Research Achievement. Proceedings of the 4th International Symposium on Incineration and Flue Gas Treatment Technologies, Sheffield.

Swithenbank. J., Nasserzadeh. V., Wasantakoran. A., Lee. PH and Swithenbank. C., (2003). Waste treatment: Strategic research achievement. Proceedings of the 4th International Symposium on Incineration and Flue Gas Treatment Technologies, Sheffield.

Tagashira, K., I. Torii., K. Myouyou., K. Takeda., T. Mizuko and Y. Tokushita., (1999). "Combustion Characteristics and Dioxin Behaviour of Waste Fired CFB." Chemical Engineering Science 54(22): 5599-5607.

Tancredi, N., T. Cordero., J. Rodriguez-Mirasol and J. J. Rodriguez., (1996). "CO_2 Gasification of Eucalyptus Wood Chars." Fuel 75(13): 1505-1508.

Taylor H. S., Neville. H. A., (1921). "Catalysis in the Interaction of Carbon with Steam and with Carbon Dioxide." J. Am. Chem. Soc 43: 2055-71.

Thunman, H. and B. Leckner., (2001). "Ignition and Propagation of a Reaction Front in Cross-Current Bed Combustion of Wet Biofuels." Fuel 80(4): 473-481.

Thunman, H. and B. Leckner., (2003). "Co-current and Counter-Current Fixed Bed Combustion of Biofuel--a Comparison*." Fuel 82(3): 275-283.

Thurner, F., Mann, U., (1981). "Kinetic Investigation of Wood Pyrolysis." Ind. Eng. Chem. Proc. Des. Dev 20: 482.

Tillman, D. A., (1991). The Combustion of Solid Fuels and Wastes, San Diego : Academic Press.

Umwelttechnick, W. E., (1995). W+E Umwelttechnick news 1/95 (1995) Information Newsletter , Zurich.

Vafai K., Sozen. M., (1990). "Analysis of Energy and Momentum Transport for Fluid Flow Through a Porous Bed." J. Heat Transfer 112(690-9).

van der Lans, R. P., L. T. Pedersen., A. Jensen, P. Glarborg and K. Dam-Johansen.,(2000). "Modelling and Experiments of Straw Combustion in a Grate Furnace." Biomass and Bioenergy 19(3): 199-208.

Venendaal, R., U. Jorgensen and C. A. Foster., (1997). "European Energy Crops: A Synthesis." Biomass and Bioenergy 13(3): 147-185.

Venturi, P. and G. Venturi., (2003). "Analysis of Energy Comparison for Crops in European Agricultural Systems." Biomass and Bioenergy 25(3): 235-255.

von Fredersdorff, G. C., and Elliott, M. A., (1963). Coal Gasification, Chemistry of Coal Utilization: Supplementary Volume. New York, John Wiley and Sons.

Wageningen, U., (2003). Switchgrass as an Alternative Energy Crop, (Chapt. 10: Management Guide for Panting and Production of Switchgrass as a Biomass Crop in Europe), available from http://www.switchgrass.nl/pdf/Sw-FinalRep-chapter10.pdf

Wakao N., Kaguei. S., (1982). Heat and Mass Transfer in Packed Beds. New York, Gordon and Breach.

Whiting, K. J., (2001). Large Scale MSW Incineration Technologies. Short Course on Incineration on Municipal Waste with Energy Recovery. Leeds, Department of Fuel and Energy, University of Leeds.

Wikipedia., The Free Encyclopedia, available from http://en.wikipedia.org/wiki/Biofuel

Wilen., (Technical Research Cent of Finland, Espoo, Finl)., Pekka S., Kai S., Jukka A., (1987). "Pelletization and Combustion of Straw." Symposium Papers - Energy from Biomass and Wastes: 469-484.

Williams, P. T., (1998). Waste Treatment and Disposal, Chichester : Wiley.

Yang Y. B., V. Nasserzadeh., Goodfellow J., Swithenbank J., (2003). "Simulation of Channel Growth in a Burning Bed of Solids." Chemical Engineering Research and Design 81(2): 221-232.

Yang, Y. B., C. Ryu, Khor, A., Yates, NE., Sharifi, VN., Swithenbank, J., (2005). "Effect of Fuel Properties on Biomass Combustion. Part II. Modelling Approach--Identification of the Controlling Factors." Fuel 84(16): 2116-2130.

Yang, Y. B., C. Ryu, Khor, A., Sharifi, V. N., Swithenbank, J., (2005). "Fuel Size Effect on Pinewood Combustion in a Packed Bed." Fuel 84(16): 2026-2038.

Yang, Y. B., H. Yamauchi., V. Nasserzadeh and J. Swithenbank., (2003). "Effects of Fuel Devolatilisation on the Combustion of Wood Chips and Incineration of Simulated Municipal Solid Wastes in a Packed Bed." Fuel 82(18): 2205-2221.

Yang, Y. B., V. Nasserzadeh., J. Goodfellow., Y. R. Goh and J. Swithenbank., (2002). "Parameter Study on the Incineration of Municipal Solid Waste Fuels in Packed Beds." Journal of the Institute of Energy 75(504): 66-80.

Yang, Y. B., V. Nasserzadeh., J. Goodfellow and J. Swithenbank., (2003). "Simulation of Channel Growth in a Burning Bed of Solids." Chemical Engineering Research and Design 81(2): 221-232.

Yang, Y. B., Y. R. Goh., V. Nasserzadeh and J. Swithenbank., (2002). "Mathematical Modelling of MSW Incineration on a Travelling Bed." Waste Management 22(4): 369-380.

Zakaria, R., (2000). Static Incineration Bed Combustion. PhD Thesis. Department of Chemical and Process Engineering. Sheffield, University of Sheffield.

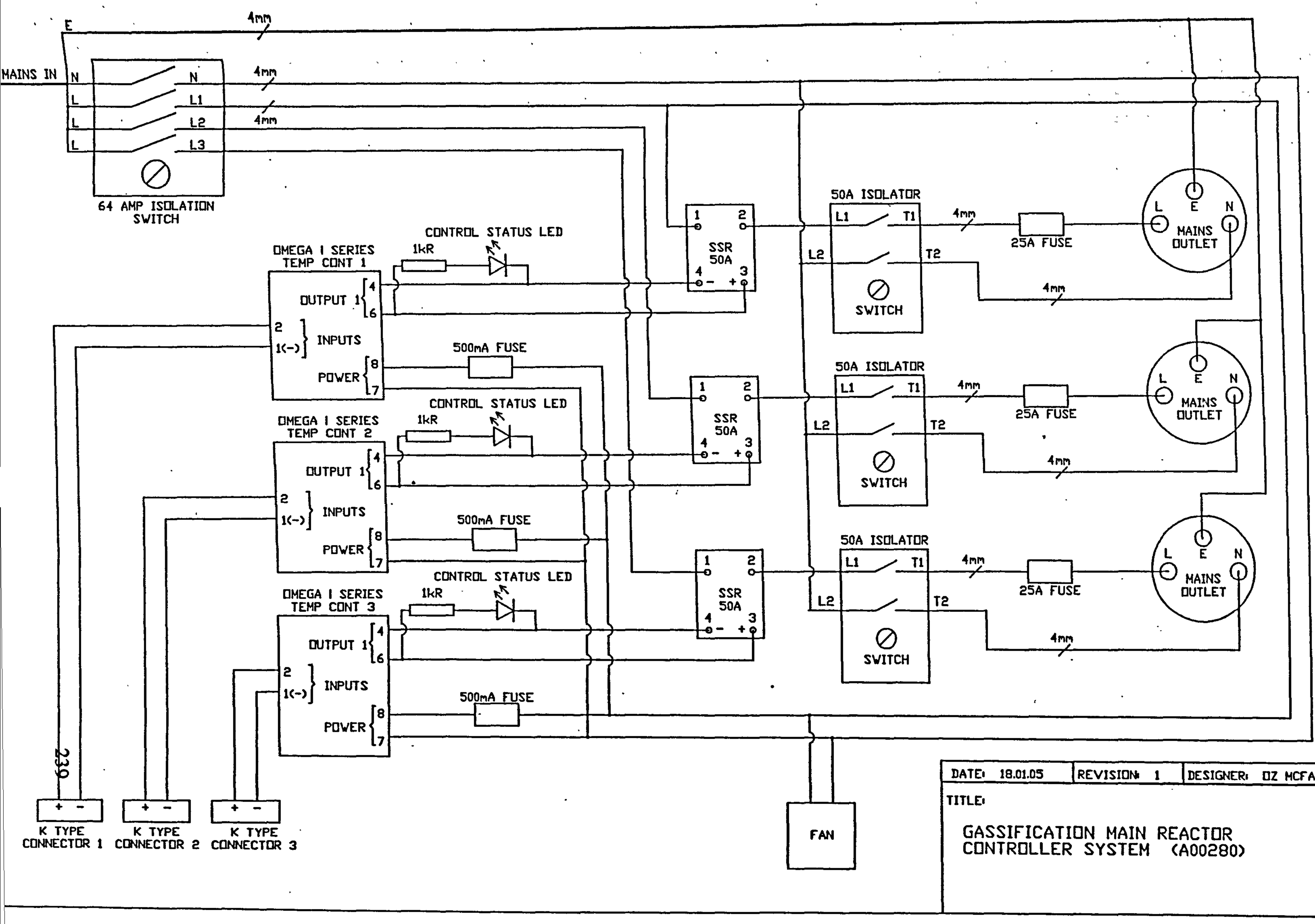
E
4mm
MAINS IN
N
L
L
L
N
L1
L2
L3
4mm
4mm
64 AMP ISOLATION SWITCH
CONTROL STATUS LED
OMEGA I SERIES TEMP CONT 1
1kR
OUTPUT 1
4
6
2
1(-)
INPUTS
POWER
8
7
500mA FUSE
SSR 50A
1
2
4
3
50A ISOLATOR
L1
T1
L2
T2
SWITCH
4mm
25A FUSE
L
E
N
MAINS OUTLET
4mm
CONTROL STATUS LED
OMEGA I SERIES TEMP CONT 2
1kR
OUTPUT 1
INPUTS
POWER
500mA FUSE
SSR 50A
50A ISOLATOR
SWITCH
25A FUSE
MAINS OUTLET
4mm
CONTROL STATUS LED
OMEGA I SERIES TEMP CONT 3
1kR
OUTPUT 1
INPUTS
POWER
500mA FUSE
SSR 50A
50A ISOLATOR
SWITCH
25A FUSE
MAINS OUTLET
4mm
239
K TYPE CONNECTOR 1
K TYPE CONNECTOR 2
K TYPE CONNECTOR 3
FAN
DATE: 18.01.05
REVISION: 1
DESIGNER: OZ MCFARLANE
TITLE:
GASSIFICATION MAIN REACTOR CONTROLLER SYSTEM (A00280)

Appendix A.2

Elemental Analysis Service for CHN and S

The samples are determined using the Perkin Elmer 2400 CHNS/O Series II Elemental Analyzer, which uses a combustion method in pure oxygen environment to convert the accurately weighted sample into the simple gases; CO_2, H_2O, N_2, SO_2. After reduction through pure copper the resulting C, H, N and S gases are then controlled to exact conditions of pressure, temperature and volume where upon the system uses a steady state wave front approach to separate the controlled gases. This approach involves separating a continuous homogenised mixture of gases through a chromatographic column. The gases eluting from the column are measured as a function of their thermal conductivity.

Appendix A.3

Figure 5B(i) shows the temperature profile obtained during the heating up of an empty furnace. As the temperature increased to 800°C, the weight dropped to -0.54kg as the pipeline restricted the thermal expansion of the furnace.

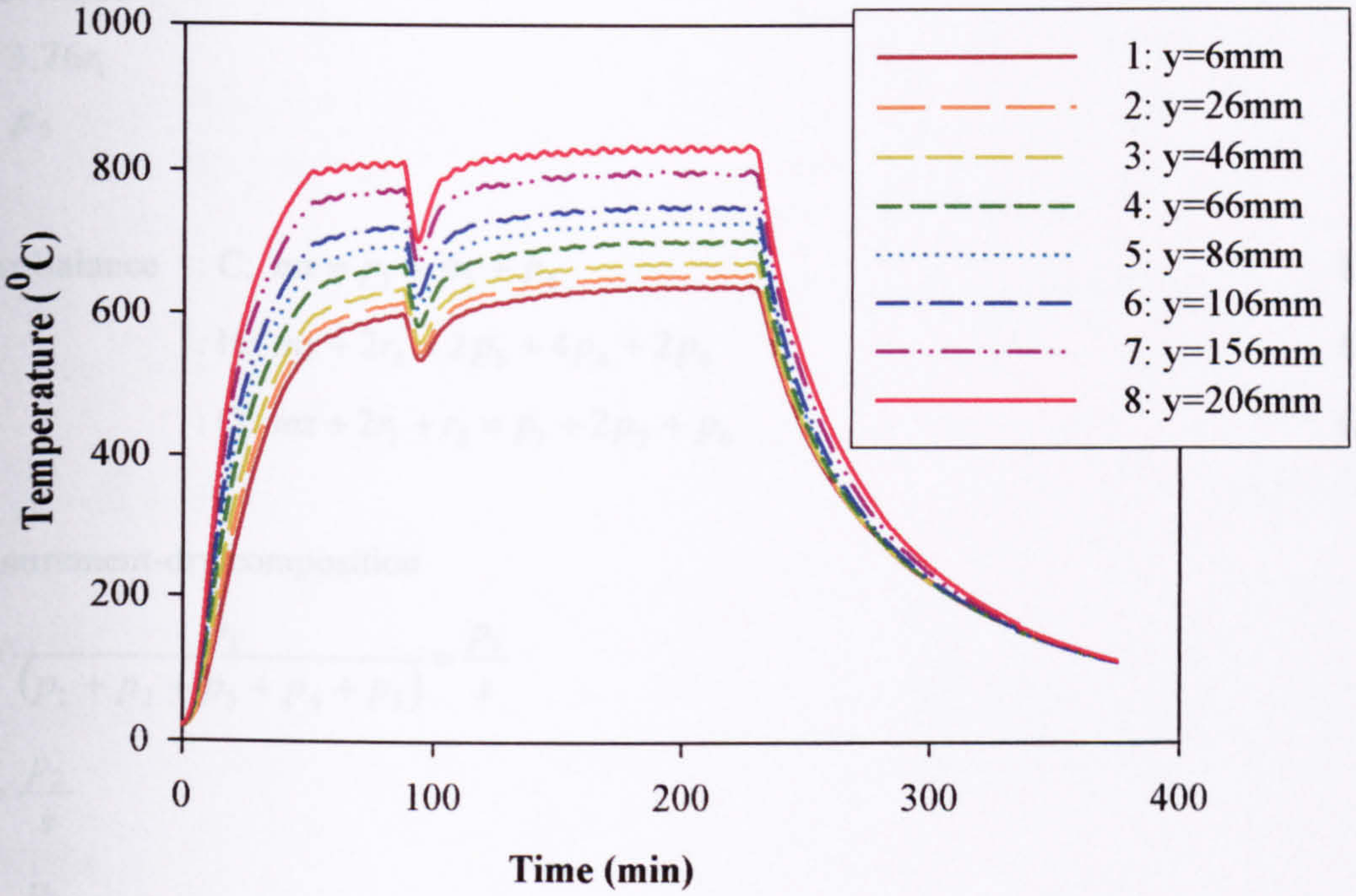

Figure 5B (i): Temperature vs time.

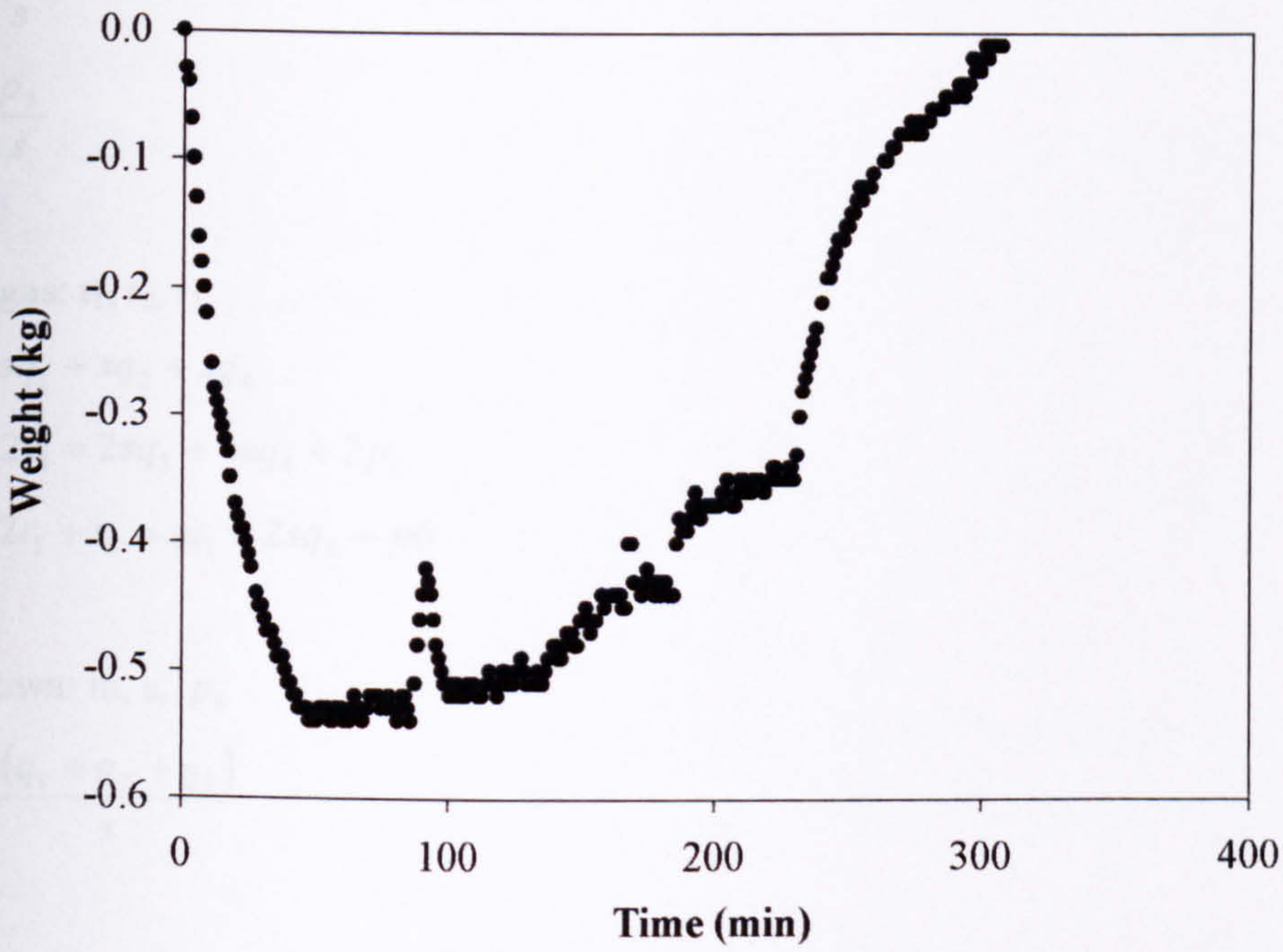

Figure 5B (ii): Weight vs. time.

Appendix A.4

Taking a mass balance over the entire reactor:

$$mC_xH_yO_z + r_1O_2 + r_2N_2 + r_3H_2O \rightarrow p_1CO + p_2CO_2 + p_3H_2 + p_4CH_4 + p_5N_2 + p_6H_2O$$

Basis: mol/s

$r_2 = 3.76r_1$

$r_2 = p_5$

Atom balance : C: $mx = p_1 + p_2 + p_4$ (1)

: H: $my + 2r_3 = 2p_3 + 4p_4 + 2p_6$ (2)

: O: $mz + 2r_1 + r_3 = p_1 + 2p_2 + p_6$ (3)

Measurement-dry composition

$$q_1 = \frac{p_1}{(p_1 + p_2 + p_3 + p_4 + p_5)} = \frac{p_1}{s}$$

$$q_2 = \frac{p_2}{s}$$

$$q_3 = \frac{p_3}{s}$$

$$q_4 = \frac{p_4}{s}$$

$$q_5 = \frac{p_5}{s}$$

Input gas: r_1, r_2, r_3

$mx = sq_1 + sq_2 + sq_4$ (1)'

$my + 2r_3 = 2sq_3 + 4sq_4 + 2p_6$ (2)'

$mz + 2r_1 + r_3 = sq_1 + 2sq_2 + p6$ (3)'

Unknown: m, s, p_6

$$m = \frac{s(q_1 + q_2 + q_5)}{x} \quad (4)$$

or $s = \frac{mx}{(q_1 + q_2 + q_4)}$ (4)'

(2)' – 2 x (3)' becomes

$$\textbf{LHS}: my + 2r_3 - (2mz + 4r_1 + 2r_3) = my - 2mz - 4r_1$$

$$\textbf{RHS}: 2sq_3 + 4sq_4 + 2p_6 - 2sq_1 - 4sq_2 - sp_6 = 2s(q_3 + 2q_4 - q_1 - 2q_2) \quad (5)$$

(4)' → (5)

$$my - 2mz - 4r_1 = \frac{2mx}{q_1 + q_2 + q_5}(q_3 + 2q_4 - q_1 - 2q_2) \quad (5)$$

$$\textbf{Let} \quad a = 2x\frac{(q_3 + 2q_4 - q_1 - 2q_2)}{(q_1 + q_2 + q_5)} \quad (6)$$

Therefore,

$$my - 2mz - ma = 4r_1$$

$$m = \frac{4r_1}{(y - 2z - a)} \quad (7)$$

s from (4)'

p_6 **from (3)'**

Input data

1) x, y, z from elemental composition

e.g. 44%wt C → $\frac{44}{12}$

2) $q_1 \Rightarrow 30\%CO$

3) r_1, r_2, r_3

100l/min air = 0.1m³/min

= 0.1 m³/60s

$$= \frac{0.1}{23.83} \times 1.23 \text{ mol/s}$$

Appendix B.1

Chemical Equilibrium

This section outlines the equations describing the chemical equilibrium and the mathematical solutions used in the equilibrium calculation carried out by the CEA2 programme. The equations are based on the minimisation of Gibbs' energy. The information given here is from the user's manual (Gordon, 1994).

Equations Describing Chemical Equilibrium

Equation of State

The gases are assumed to be ideal and the interaction among phases is neglected. The equation of state for the mixture is:

$$PV = nRT \qquad \textit{Equation 1a}$$

$$\frac{P}{\rho} = nRT \qquad \textit{Equation 1b}$$

where P is pressure (in newtons per square meter), V specific volume (in cubic metres per kilogram), n moles per unit mass of mixture (in kilograms-mole per kilogram), T temperature (in Kelvin), and ρ density (in kilograms per cubic meter).

Equation 1 is assumed to apply even when small amounts of condensed species (up to several percent by weight) are present. The condensed species are assumed to occupy a negligible volume relative to the gaseous species. The variables V, n, and ρ the volume and mole number refer to gases only, but the mass is for the entire mixture including condensed species. The word "mixture" is used to refer to mixtures of reaction products while the mixtures of reactants are referred to as "total reactants".

On the basis of this definition, n can be written as

$$n = \sum_{j=1}^{NG} n_j \qquad \textit{Equation 2}$$

where, n_j is the number of kilogram-moles of species j per kilogram of mixture and the index NG refers to the number of gases in the mixture. The molecular weight of the mixture M is defined as

$$M = \frac{1}{n} \qquad \textit{Equation 3a}$$

or equivalently as:

$$M = \frac{\sum_{j=1}^{NG} n_j M_j}{\sum_{j=1}^{NG} n_j} \qquad \textit{Equation 3b}$$

where M_j is the molecular weight of species j and the index NS refers to the number of species in the mixture. In the CEA program, among the NS species, gases are indexed from 1 to NG and condensed species from NG+1 to NS. The molecular weight is more conventionally defined as:

$$MW = \frac{\sum_{j=1}^{NS} n_j M_j}{\sum_{j=1}^{NS} n_j} \qquad \textit{Equation 4a}$$

Molecular weight is given the symbol MW in *Equation 5* to differentiate it from M. The two definitions of molecular weight, M and MW, give different results only in mixtures containing both gaseous and condensed species. MW may be obtained from M by means of:

$$MW = M\left(1 - \sum_{j=NG+1}^{NS} \chi_j\right) \qquad \textit{Equation 5}$$

where, χ_j is the mole fraction of species *j* relative to all species in the mixture

Minimisation of Gibbs Energy

For a mixture of NS species Gibbs energy per kg of mixture, g is given by:

$$g = \sum_{j=1}^{NS} \mu_j n_j \qquad \textit{Equation 6}$$

where the chemical potential per kmol of species *j* is defined by:

$$\mu_j = \left(\frac{\partial g}{\partial n_j}\right)_{T,P,n_{i \neq j}} \qquad \textit{Equation 7}$$

The condition of chemical equilibrium is the minimisation of free energy. This minimisation is usually subject to certain constraints, such as the mass-balance constraints.

$$\sum_{j=1}^{NS} a_{ij} n_j - b_i^0 = 0 \qquad (i = 1,\ldots,\ell) \qquad \textit{Equation 8}$$

where the stoichiometric coefficients a_{ij} are the number of atoms of element i per kmol of species j, the index ℓ is the number of chemical elements (if ions are considered, the number of chemical elements plus one), b_i^0 is the assigned number of atoms of element i per kg of total reactants, defining a term G to be:

$$G = g + \sum_{i=1}^{\ell} \lambda_i \left(b_i - b_i^0\right) \qquad \textit{Equation 9}$$

where λ_i are Lagrangian multipliers, and the condition for equilibrium becomes:

$$\partial G = \sum_{j=1}^{NS} \left(\mu_j + \sum_{i=1}^{\ell} \lambda_i a_{ij} \right) \partial n_j + \sum_{i=1}^{\ell} \left(b_i - b_i^0\right) \partial \lambda_i = 0 \qquad \textit{Equation 10}$$

Treating the variation ∂n_j and $\partial \lambda_i$ as independent gives:

$$\mu_j = \sum_{i=1}^{\ell} \lambda_i a_{ij} = 0 \qquad (j = 1,\ldots,NS) \qquad \textit{Equation 11}$$

as well as the mass balance equation (Equation 8). The chemical potential can be written as:

$$\mu_j = \mu_j^0 + RT \ln \frac{n_n}{n} + RT \ln P \quad (j = 1,\ldots, NG) \qquad \textit{Equation 12}$$

$$\mu_j = \mu_j^0 \qquad (j = NG+1,\ldots, NS)$$

where μ_j^0 for gases (j =1 to NG) and for condensed phases (j>NG) is the chemical potential in the standard state, which for gases it is the hypothetical ideal gas at standard state pressure and for a pure solid of liquid is the substance in the condensed phase at the standard-state pressure.

The thermodynamic state corresponding to oxidation at constant pressure is specified by enthalpy and pressure. The expression for enthalpy, h is:

$$h = \sum_{j=1}^{NS} n_j H_j^0 \qquad \textit{Equation 13}$$

where, H_j^0 is the standard-state molar enthalpy for species j at temperature T.

Gibbs Iteration Equations

The equation required to obtain composition are not all linear in the composition variables and therefore an iteration procedure is usually required. The CEA2 iteration procedure treats n as an independent variable and a Newton-Raphson method is used to solve for corrections to initial estimates of composition n_j, Lagrangian multipliers λ_j, and (when required) temperature T. This method involves a Taylor series expansion of the appropriate equations with all terms truncated that contain derivatives higher than the first. The correction variables used are $\Delta \ln n_j (j = 1,...,NG), \Delta n_j (NG+1,...,NS), \Delta \ln n, \pi_i = {}^{-\lambda_i}/_{RT}$ and $\Delta \ln T$. After making dimensionless those equations containing thermodynamic functions, the Newton-Raphson equations are:

$$\Delta \ln n_j - \sum_{i=1}^{\ell} a_{ij}\pi_i - \Delta \ln n_j - \frac{H_j^0}{RT}\Delta \ln nT = \frac{\mu_j}{RT} \qquad (j = 1,...,NG) \quad \textit{Equation 14}$$

$$-\sum_{i=1}^{\ell} a_{ij}\pi_i - \frac{H_j^0}{RT}\Delta \ln nT = \frac{\mu_j}{RT} \qquad (\text{j = NG+1,...,NS}) \quad \textit{Equation 15}$$

$$\sum_{j=1}^{NS} a_{kj} n_i \Delta \ln n_j + \sum_{j=NG+1}^{NS} a_{kj} n_i \Delta n_j = b_k^0 - b_k \qquad (\text{k = 1,...,}\ell) \quad \textit{Equation 16}$$

$$\sum_{j=1}^{NG} n_j \Delta \ln n_j - n\,\Delta \ln n = n - \sum_{j=1}^{NG} n_j \qquad \textit{Equation 17}$$

$$\sum_{j=1}^{NG} \frac{n_j H_j^0}{RT}\Delta \ln n_j + \sum_{j=NG+1}^{NS} \frac{H_j^0}{RT}\Delta n_j + \left(\sum_{j=1}^{NS} \frac{n_j c_{p,j}^0}{R}\right)\Delta \ln T = -\frac{h_0 - h}{RT} \qquad \textit{Equation 18}$$

$$\sum_{j=1}^{NG} \frac{n_j S_j}{RT}\Delta \ln n_j + \sum_{j=NG+1}^{NS} \frac{S_j^0}{R}\Delta n_j + \left(\sum_{j=1}^{NS} \frac{n_j c_{p,j}^0}{R}\right)\Delta \ln T = -\frac{s_0 - s}{RT} + n - \sum_{j=1}^{NG} n_j \qquad \textit{Equation 19}$$

Appendix B.2

Calculation of adiabatic temperature

$$C_{7.555}H_{0.71}O_{0.268} + \left(\frac{15.197}{2}\right)(O_2 + N_2) \rightarrow 7.555CO_2 + \frac{0.71}{2}H_2O + 15.197N_2$$

$$\sum_R n_i(H_1 - H_{298}) + \sum n_i CV_i = \sum_P n_i(H_2 - H_{298})$$

*Reactant are assumed to be at room temperature

Enthalpy is in Kj/mol

CV = 30.32 MJ/kg
= 2900 MJ/kmol
= 2.9x 10^6 kJ/kmol

M_w = 95.67 kg/kmol

RHS:

Molecule	n_1	(H_2-H_{298})
CO_2	7.555	$0.00458(\Delta T^2) + 45.59\ \Delta T$
H_2O	0.355	$0.00502(\Delta T^2) + 34.03\ \Delta T$
N_2	15.197	$0.00190(\Delta T^2) + 29.66\ \Delta T$

RHS = $0.0653(\Delta T^2) + 807\ \Delta T$

LHS = RHS

$2.9x\ 10^6 = 0.0653(\Delta T^2) + 807\ \Delta T$

$0.0653(\Delta T^2) + 807\ \Delta T - 2.9x\ 10^6 = 0$

T = 2908K

PUBLICATIONS

Yang, Y. B., Ryu, C., Khor, A., Sharifi, V. N., Swithenbank, J., 2005. Fuel size effect on pinewood combustion in a packed bed. *Fuel* 84 (2005) 2026-2038.

Yang, Y. B., Ryu, C., Khor, A., Yates, NE., Sharifi, VN., Swithenbank, J., 2005. Effect of fuel properties on biomass combustion. Part II. Modelling approach-identification of the controlling factors. *Fuel* 84 (2005) 2116-2130.

Ryu, C., Yang, Y.B., Khor, A., Sharifi, V. N., Swithenbank, J., 2004. Effect of Fuel Properties on Biomass Combustion: Part I Experiments- Fuel Type, Equivalent Ratio and Particle Size. *Fuel* 85(2006) 1039-1046.

Khor, A., Ryu, C., Yang, Y.B., Sharifi, V. N., Swithenbank, J., 2006. Straw Combustion in a Fixed Bed Combustor. Accepted for publication in *Fuel.*

Khor, A., Ryu, C., Yang, Y.B., Sharifi, V. N., Swithenbank, J., 2006. Clean Hydrogen Production via Novel Air-Steam Gasification of Biomass. *World Hydrogen Energy Conference (WHEC) 2006.* GVIII-716

CONFERENCE PRESENTATIONS (POSTER)

Khor, A., Ryu, C., Yang, Y.B., Sharifi, V. N., Swithenbank, J., 2005. Biomass Combustion in a Fixed Bed Combustor. *Tackling Waste 2005 Conference* (University of Nottingham).

Khor, A., Ryu, C., Yang, Y.B., Sharifi, V. N., Swithenbank, J., 2005. Biomass Combustion in a Fixed Bed Combustor. *Institute of Physics Young Combustion Meeting* (University of Loughborough).

Khor, A., Ryu, C., Yang, Y.B., Sharifi, V. N., Swithenbank, J., 2005. Biomass Combustion in a Fixed Bed Combustor. *24th Month Poster Presentation* (University of Sheffield).

Khor, A., Ryu, C., Yang, Y.B., Sharifi, V. N., Swithenbank, J., 2006. Clean Hydrogen Production via Novel Air-Steam Gasification of Biomass. *World Hydrogen Energy Conference (WHEC) 2006.* GVIII-716

Available online at www.sciencedirect.com
SCIENCE DIRECT®
Fuel 84 (2005) 2026–2038
FUEL
www.fuelfirst.com

Fuel size effect on pinewood combustion in a packed bed

Yao Bin Yang*, Changkook Ryu, Adela Khor, Vida N. Sharifi, Jim Swithenbank

Department of Chemical and Process Engineering, Sheffield University Waste Incineration Centre (SUWIC), Sheffield University, Mappin Street, Sheffield S1 3JD, UK

Received 15 September 2004; received in revised form 22 April 2005; accepted 26 April 2005
Available online 6 June 2005

Abstract

In this paper, particle size effect on pinewood combustion in a stationary packed bed was investigated. Mass loss rate, temperature profile at different bed locations and gas compositions in the out-of-bed flue gases were measured at a fixed primary air flow rate. Pinewood cubes was fired with size ranging from 5 to 35 mm. A unique numerical model applicable to thermally thick particles was proposed and relevant equations were solved to simulate the non-homogeneous characteristics of the burning process. It is found that at the operating conditions of the current study, smaller particles are quicker to ignite than larger particles and have distinctive combustion stages; burning rate is also higher with smaller fuel size; and smaller fuels have a thinner reaction zone and result in both higher CO and CH_4 concentrations in the out-of-bed flue gases; on the other hand, larger particles produced a higher flame temperature and result in higher H_2 concentration in the flue gases. Larger particles also cause the combustion process becoming more transient where the burning rate varies for most part of the combustion process.

Keywords: Combustion; Fuel size; Pinewood; Mathematical modelling

1. Introduction

Biomass is playing an important role for domestic heating and power generation, especially in some European countries. With the increasing concerns over global warming from fossil fuel combustion in recent years, some organisations have proposed energy crops to cut down the net CO_2 emission to the atmosphere [1,2]. In a broad sense, biomass fuels range from pruning waste, industrial and agrarian residuals, waste wood, cultivated crops to sewage sludge from domestic and industrial water treatment plants and paper industry. Although biomass burning is as old as humankind's history, the modern large-scale production of heat and electricity from biomass need sophisticated technology to control the process to minimise its environmental effects and promote efficiency. In most cases, raw biomass fuels cannot be burned as they are. Instead they need some pre-treatment. Pelletisation is now an accepted practice before biomass fuels are burned in furnaces or on beds. One of the key questions arises from this is what are the effects of the particle size on the combustion behaviour and how to assess the optimum pellet size from economic and technical points of view.

In this paper the size effect of pinewood cubes is investigated both theoretically and experimentally for packed bed combustion. Pinewood fuel is easy to prepare and can be cut into different sizes and shapes and is a good simulation of pelletised biomass fuels. The latter are normally difficult and expensive to prepare in terms of size variation. General combustion behaviours of biomass fuels on packed beds have been studied by a number of researchers. Gort [3] had conducted a series of tests on combustion of wood chips under different operating conditions. Friberg and Blasiak [4] measured the mass flux and stoichiometry of conversion gas from three different wood fuels as function of volume flux of primary air. Rönnbäck et al. [5] studied the influence of primary airflow and particle properties on the ignition front, its temperature and on the composition of the exiting gases in a biomass fuel bed. Saastamoinen et al. [6] investigated the propagation of ignition front in beds of wood particles where the effect of air flow, moisture, particle size, density and wood species were considered. Van der Lans et al. [7] performed experiments on straw combustion in a 15 cm diameter and 137 cm long vertical reactor where both air flow rate and inlet air temperature were varied. Channelling phenomena in packed beds have been studied by Yang et al. [8,9]. Other important works were summarised by Thunman [10], Thunman et al. [11] and Peters [12].

Though those studies provide important information on biomass combustion in packed beds, the obtained data were still very limited and in most cases only ignition speed and maximum flame-front temperature were reported. Results concerning particle size effect were also inconsistent. For example, Gort [3] and Rönnbäck [5] have reported increased ignition speed for larger particles in the size range of 10–30 mm while Peters [12] reported the maximum ignition rate was obtained at 15 mm in the size range of 5–25 mm. On the other hand, Friberg et al. [4] demonstrated decreasing burning rate as particles size increased.

Current work focuses on both experimental and theoretical studies for packed bed combustion and particle sizes from 5–35 mm were used. For the experimental work, a pot reactor of 0.2 m in diameter and 1.5 m in height was used. Some researchers [13] have used Thermogravimetric System (TGS) to study biomass combustion which gives a strictly controlled environment. The benefit of employing a pot reactor, however, is that it provides more realistic results for practical furnaces.

For mathematical modelling, a unique numerical model was proposed and detailed equations governing the fluid flow, heat and mass transfer between solid and gaseous phases were employed and solved. The advantage of theoretical study lies in its ability to reveal the detailed structure of the burning process inside a solid bed, such as reaction zone thickness, combustion staging, gas emission and char burning characteristics, thus contributing to better understanding and controlling of the process. These

* Corresponding author. Tel.: +44 114 2227500; fax: +44 114 2227501.
E-mail address: y.b.yang@sheffield.ac.uk (Y.B. Yang).

0016-2361/$ - see front matter © 2005 Elsevier Ltd. All rights reserved.
doi:10.1016/j.fuel.2005.04.022

Nomenclature

C	constant; molar fractions of species (fuel, oxygen)
C_{fuel}	fuel concentration, kg/m^3
C_{pg}	specific heat capacity of the gas mixture, J/(kg K)
C_{mix}	mixing-rate constant
D_{ax}	in-flow dispersion coefficient in bed, m^2/s
D_g	molecular diffusion coefficient of volatile hydrocarbons in air, m^2/s
D_{ig}	dispersion coefficients of the species Y_{ig}, m^2/s
d_p	particle diameter, m
d_{pore}	pore diameter in particle, m
D_r	cross-flow dispersion coefficient in bed, m^2/s
I	radiation heat flux, W/m^2
H_g	gas enthalpy, J/kg
H_s	solid-phase enthalpy, J/kg
h_s'	convective heat transfer coefficient between solid and gas, W/m^{2}K
k_a	absorption coefficient of radiation, 1/m
k_d	rate constants of char burning due to diffusion, kg/atm m^2 s
k_r	rate constants of char burning due to chemical kinetics, kg/atm m^2 s
k_s	scattering coefficient of radiation, 1/m
k_v	rate constant of devolatilisation, s^{-1}
M	moisture fraction in solid
M_0	initial moisture fraction in solid
p_g	gas pressure, Pa
Q_h	heat loss/gain of the gases, W/m^3
Q_{sh}	thermal source term for solid phase, W/m^3
q_r	radiative heat flux, W/m^2
R_{mix}	mixing-rate of gaseous phase in the bed, kg/m^3 s
S	stoichiometric coefficients in reactions
S_a	particle surface area, m^2
S_{sg}	conversion rate from solid to gases due to evaporation, devolatilisation and char burning, kg/m^3 s
Sy_{ig}	mass sources due to evaporation, devolatilisation and combustion, kg/m^3 s
Sy_{is}	source term, kg/m^3 s
t	time instant, s
T_g	gas temperature, K
T_s	solid temperature, K
T_{s0}	solid temperature at the particle surface, K
V_B	velocity of a moving boundary, m/s
V_g	superficial gas velocity (vector), m/s
VM	volatile matter in solid
VM_0	initial volatile matter in solid
Y_{ig}	mass fractions of gaseous compositions (CO, CO_2, O_2, CH_4, H_2, etc.)
Y_{is}	mass fractions of particle compositions (moisture, volatile, fixed carbon and ash)
y^+	distance above the bed-top surface, m;
ε_p	solid emissivity
σ_b	Boltzmann radiation constant, 5.86×10^{-8} W/m^{2}K^4
	void fraction in the bed
ρ_g	gas density, kg/m^3
ρ_s	solid material density in the bed, kg/m^3
λ_{ax}	in-flow diffusion coefficient in bed, W/m K
λ_c	thermal conductivity of char, W/m K
λ_g	thermal dispersion coefficient, W/m K
λ_r	cross-flow diffusion coefficient in bed, W/m K
λ_s	solid-phase thermal conductivity in bed, W/m K
λ_{wood}	effective thermal conductivity of the wood material, W/m K

Table 1
Proximate and ultimate analysis of willow wood fuel

Moisture (wt%)	Volatile (wt%)	Fixed carbon (wt%)	Ash (wt%)	C (wt%)	H (wt%)	O (wt%)	LCV (MJ/kg)
7.5	79.7	12.7	0.1	47.9	6.2	38.3	17.6

parameters are otherwise hard to obtain by conventional experimental techniques.

2. Experimental facilities

A fixed-bed reactor was employed to burn the pinewood fuel. This reactor has been used in previous studies [14–16]. It was a vertical cylindrical combustion chamber suspended from a weighing scale. The height of the chamber was 1.5 m with an inner diameter of 200 mm. It consisted of an interior tube surrounded by a thick layer of insulating material and an external casing. The grate was located at the bottom of the chamber and consisted of a perforated plate made from stainless steel, with approximately 700 holes of 2 mm diameter, representing 7% open area. Thermocouples were used to monitor the temperature of primary airflow, temperature inside the bed at different height levels and temperature of the flue gases. There was a gas-sampling probe inside the chamber at 430 mm above the grate. The main components of the gas measurements of interest were O_2, CO, CO_2.

A gas burner was placed at a 45° angle toward the waste at 750 mm above the grate. The gas burner was used to initiate the burning process of the fuel sample and switched off after a steady combustion was observed. Primary air was fed from the bottom of the fixed bed reactor through the grate without pre-heating.

The pinewood fuel was cut into four different sizes: 5×5×5, 10×10×10, 20×20×20 and 35×35×35 mm. Proximate and ultimate analysis of the fuel are shown in Table 1. Density of the fuel material was measured being 820 kg/m^3 and the bulk density in packed state is around 290 kg/m^3, giving a bed porosity of 0.65. For each run 3.8 kg of fuel was used and the initial bed height was around 410 mm. The primary air employed was 0.1 kg/m^2 s at room temperature for all the cases.

Fig. 1 illustrates the packed bed dimensions and operating conditions.

3. Mathematical model for biomass combustion in a packed bed

Peters [12] summarized the previous mathematical models on packed bed combustion. Those models can be generally classified into four categories: continuous-medium models [17–19] where the solid bed was treated as a continuous medium; neighbouring-layers models [20,21] where the packed bed above the grate was divided into four layers representing fuel, drying, pyrolysis and ash; well-stirred reactor models [22,23] where the bed was simulated by a cascade of well-stirred reactors; and the 1d+1d model [24] where a one-dimensional and transient single-particle model in spherical coordinates was implemented in a transient one-dimensional fuel-bed model.

The model used in current work is based on the governing equations proposed by Peters [25] for both the gas and solid phases in a moving bed and the previous modelling works of the authors [8–16]. The major difference of the current model from all the previous models is that it calculates both outside and inside the particles and thus fully accounts for the inhomogeneous nature of the bed and the effect of thermally thick particles. Compared to the 1d+1d model [24] the proposed mathematical method provides a more realistic simulation to the real combustion bed.

Illustration of the model concept is shown in Fig. 2. A packed bed consists of particles and the voids between them (Fig. 2a). By discretising the bed, three types of cells emerge: void cells, boundary cells and inner cells (Fig. 2b). The void cells are where the gas-flow passes and the inner cells are inside-particle cells. Boundary cells are solid-phase cells neighbouring the gas-flow around the particle outer surfaces. Thus, a particle is represented by a set of inner and boundary cells and the bed an assembly of inner, boundary and void cells.

For each cell, the law of conservation in momentum, energy and chemical species is applied and different schemes are employed, depending on the cell type. For example, for an inner cell heat conduction is the only heat transfer mode. But for a boundary cell, heat conduction, convection and radiation all play a part in the heat transfer

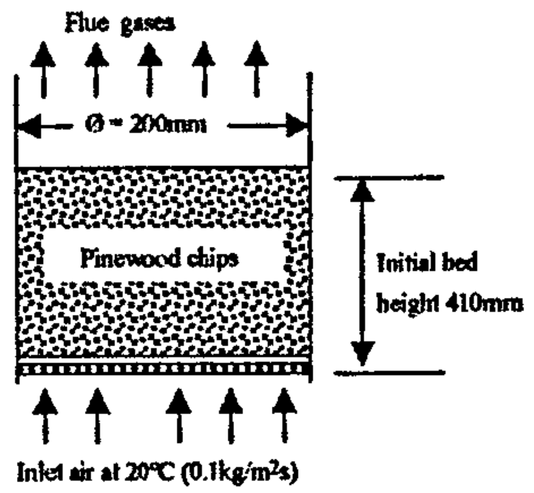

Fig. 1. The employed packed bed dimensions and operating conditions.

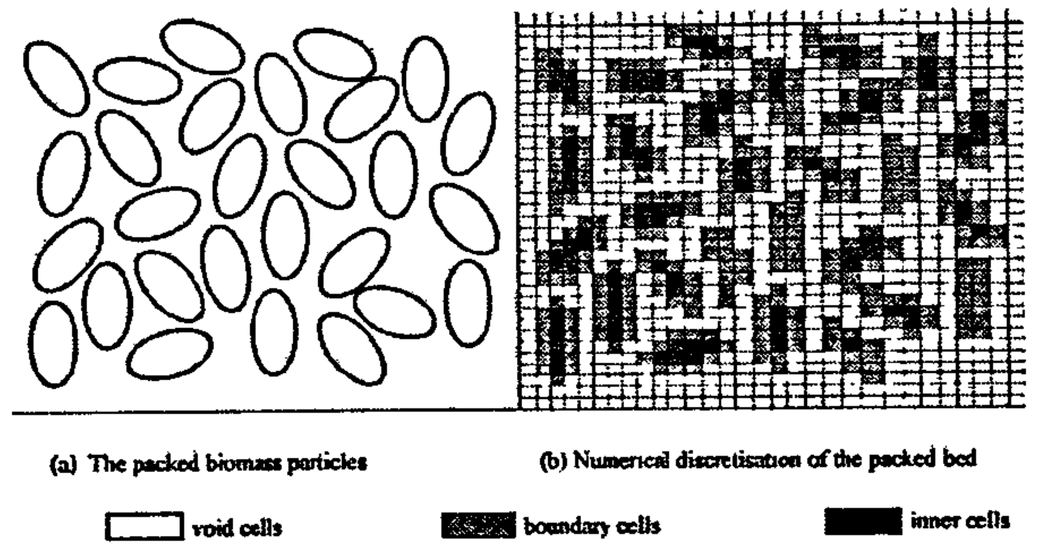

Fig. 2. Illustration of the model concept for thermally-thick particles.

process. For the void cells, apart from all these three heat transfer modes, turbulence effect is also included.

3.1. Transport equations for the gas phase in the void cells

The equations include mass continuity, momentum conservation, heat transfer and species transport.

$$\text{Continuity}: \quad \frac{\partial(\phi\rho_g)}{\partial t} + \nabla(\phi\rho_g(\mathbf{V}_g - \mathbf{V}_B)) = S_{xg} \tag{1}$$

where $\mathbf{V}_g$ is the gas velocity and $\mathbf{V}_B$ the velocity of a moving boundary. The source term S_{xg} is the conversion rate from solid to gas due to moisture evaporation, devolatilisation and char combustion.

$$\text{Momentum}: \quad \frac{\partial(\phi\rho_g\mathbf{V}_g)}{\partial t} + \nabla(\phi\rho_g(\mathbf{V}_g - \mathbf{V}_B)\mathbf{V}_g) = -\nabla p_g + F(\mathbf{v}) \tag{2}$$

where $F(\mathbf{v})$ represents resistance of solids to fluid flow in a porous medium and is calculated by Ergon's equations [26,27].

$$\text{Species transport}: \frac{\partial(\phi\rho_g Y_{ig})}{\partial t} + \nabla(\phi\rho_g(\mathbf{V}_g - \mathbf{V}_B)Y_{ig}) = \nabla(D_{ig}\nabla(\rho_g Y_{ig})) + S_{yig} \tag{3}$$

where Y_{ig} is mass fractions of individual species (e.g. H_2, H_2O, CO, CO2, C_mH_n, ...). The source term S_{yig} accounts for mass sources of the individual species during evaporation, devolatilization and the combustion of volatile gases and char.

The fluid dispersion coefficient D_{ig} consists of diffusion and turbulent contributions. For Re>5, the corresponding cross-flow and in-flow dispersion coefficients are given by the following Eqs. [28]:

$$D_r = E^0 + 0.1d_p|\mathbf{V}_g| \tag{4a}$$

$$D_{ax} = E^0 + 0.5d_p|\mathbf{V}_g| \tag{4b}$$

where E^0 is the effective diffusion coefficient.

$$\text{Energy}: \quad \frac{\partial(\phi\rho_g H_g)}{\partial t} + \nabla\cdot(\phi\rho_g(\mathbf{V}_g - \mathbf{V}_B)H_g) = \nabla\cdot(\lambda_g\nabla T_g) + S_a h_s'(T_w - T_g) + Q_h \tag{5}$$

where H_g represents gas enthalpy, λ_g the thermal dispersion coefficient and Q_h, the heat gain of the gas phase due to heat release during combustion. The thermal dispersion coefficient λ_g consists of diffusion and turbulent contributions in a similar way as species dispersion, and can be expressed as [28]:

$$\lambda_r = \lambda_g^0 + 0.1d_p|\mathbf{V}_g|\rho_g C_{pg} \tag{6a}$$

$$\lambda_{ax} = \lambda_g^0 + 0.5d_p|\mathbf{V}_g|\rho_g C_{pg} \tag{6b}$$

Where λ_g^0 is the effective thermal diffusion coefficient.

3.2. Governing equations for solid phase cells

Volume shrinkage of biomass particles during combustion is calculated by the following equation:

$$\frac{V}{V_0} = 1 - a_1(M_0 - M) - a_2(VM_0 - VM) - a_3(C_0 - C) \tag{7}$$

where V and V_0 represent the current and initial volumes of a particle and a_1, a_2, a_3 are shrinkage factors during moisture evaporation, volatile release and char burnout respectively. Their values are chosen such that $a_1=1$ represents the volume of the particle shrinking linearly with moisture loss and $a_1=0$ means no volume shrinkage occurring during evaporation. The same principle applies to a_2 and a_3.

Energy conservation for the boundary cells is described by

$$\frac{\partial(\rho_s H_s)}{\partial t} = \nabla(\lambda_s\nabla T_s) - S_a h_s'(T_w - T_g) + \nabla q_r + Q_{ch} \tag{8}$$

where H_s presents the solid-phase enthalpy, λ_s is the effective thermal conductivity of the solid bed and q_r the radiative heat flux. The source term Q_{sh} summarises heat effects due to moisture evaporation and heterogeneous combustion.

For inner cells the above equation is reduced to

$$\frac{\partial(\rho_s H_s)}{\partial t} = \nabla(\lambda_s \nabla T_s) + Q_{sh} \tag{8a}$$

by dropping out the radiation and convection terms.

The effective thermal conductivity of the solid material consists of a conductive and a radiative contribution [29]:

$$\lambda_s = \varepsilon_p \lambda_g^0 + \eta\lambda_{\text{wood}} + (1-\eta)\lambda_C + \lambda_{\text{rad}} \tag{9}$$

where ε_p is the local porosity of the solid cell and λ_{wood}, λ_C are thermal conductivity of the wood and char. The radiative part is calculated as following [30],

$$\lambda_{\text{rad}} = 4 \times \varepsilon_{\text{rad}} \sigma_b T_s^3 d_{\text{pore}} \tag{10}$$

where ε_{rad} is the emissivity of the pores inside a particle and d_{pore} the diameter of the pores.

The solid fuel is assumed to consist of four components: moisture, volatile matter, fixed carbon and ash. The incineration process of solid wastes can be divided into four successive sub-processes: evaporation of moisture from the solids, volatile release/char formation, burning of the hydrocarbon volatiles in the gaseous space, and the combustion of char particles. Calculation of the rates for moisture evaporation, devolatilisation and char burning can be found in the works of Yang et al. [14,15].

3.3. Mixing of volatile gases with under-grate air

Gaseous fuels released from the devolatilization process have first to mix with the surrounding air before any combustion of them can take place. Obviously the burning of the volatile hydrocarbon gases is limited not only by the reaction kinetics (temperature dependent) but also by the mixing-rate of the gaseous fuel with the under-grate air flow. The mixing rate inside the bed is assumed to be proportional to energy loss (pressure drop) through the bed and can be expressed as [31]:

$$R_{\text{mix}} = C_{\text{mix}}\rho_g \left\{ 150\frac{D_g(1-\phi)^{2/3}}{d_p^2\phi} + 175\frac{V_g(1-\phi)^{1/3}}{d_p\phi} \right\} \times \min\left\{ \frac{C_{fuel}}{S_{fuel}}, \frac{C_{O2}}{S_{O2}} \right\} \tag{11}$$

Where C_{mix} is an empirical constant, D_g the molecular diffusivity of the combustion air, V_g the air velocity, d_p the particle diameter, ϕ the local void fraction of the bed, C the molar fractions of the gaseous reactants and S their stoichiometric coefficients in the reaction.

In the free-board area immediately next to the bed surface, 'flame tongues' shoot out of the bed surface and the mixing rate of the volatile gases with surrounding air decreases with increasing distance from the bed surface. Detailed CFD calculations with simulated particle beds were conducted and have produced the following correlation between mixing rate and the distance from the bed-top [14]:

$$R_{\text{mix}} = R'_{\text{mix0}}(2.8e^{-0.2y++} - 1.8e^{-2y++})\min\left\{ \frac{C_{fuel}}{S_{fuel}}, \frac{CO2}{SO2} \right\} \tag{12}$$

and

$$y^{++} = y^{+}/d_p \tag{13}$$

where R'_{mix0} is calculated from Eq. (11) without the species concentration terms at the bed surface. y^+ denotes the physical distance from the bed top.

The actual combustion rate of the volatile gases is taken as the minimum between the mixing rate calculated by the above equations and the kinetic rate. Calculation of the latter can be found in Ref. [15].

3.4. Radiation heat transfer in the bed

Radiation is the major mechanism of heat transfer between solid particles in a packed bed. The widely used flux model [32] is employed:

$$\frac{dI_{xi}^{+}}{dx_i} = -(k_a + k_s)I_{xi}^{+} + \frac{1}{2N}k_a E_b + \frac{1}{2N}k_s\sum_{i=1}^{N}(I_{xi}^{+} + I_{xi}^{-}) \tag{14a}$$

$$-\frac{dI_{xi}^{-}}{dx_i} = -(k_a + k_s)I_{xi}^{-} + \frac{1}{2N}k_a E_b + \frac{1}{2N}k_s\sum_{i=1}^{N}(I_{xi}^{+} + I_{xi}^{-}) \tag{14b}$$

where N is the total number of space discretisation and I_{xi}^{+} and I_{xi}^{-} $(i=1,N)$ are the radiation fluxes in the positive and negative directions respectively of each discretisation. E_b represents the black-body radiation. k_a and k_s denote the absorption and scattering coefficients. In this work k_s is assumed to be zero and k_a is approximated by the following equation [19]:

$$k_a = -\frac{1}{d_p}\ln(\phi) \tag{15}$$

3.5. Particle size effects

According to the governing equations described above, particle size affects the combustion in five different ways. First is the two-phase heat and mass transfer (between the gas and solid), as indicated by the second RHS term in Eq. (8). These convective processes occur at the particle external surfaces and the rates are approximately inversely proportional to the particle diameter. Therefore, particles of a smaller size can enhance the moisture evaporation and char burning rates in the bed. Temperature difference between the solid and gas is also smaller for small particles.

The second effect is on the radiation heat transfer, as indicated in Eq. (15) where the bed absorption coefficient to radiation flux is inversely proportional to particle diameter. This means that a bed of smaller particles absorbs radiation more quickly. But the radiation flux, on the other hand, is less absorbed by a packing of larger particles and hence penetrates a longer distance in the bed. This can produce a thicker flame front in the bed and affects the temperature and gas concentration profiles as a consequence.

The third effect is on the turbulent dispersion of energy and gas species in the packed bed. As indicated in Eqs. (4) and (6), both the effective thermal and fluid dispersion coefficients are proportional to particle diameter. Larger particles produce larger-scale turbulence in the local bed structure and facilitate the cross-flow and inflow mixing in the gas phase. As a result, the reaction zone in the bed can be thicker for larger particles and thinner for smaller particles.

The fourth effect is on the burning rate of volatile gaseous fuel both in the voids of the bed and in the immediate area above the bed. The process is basically diffusion-controlled. As indicated in Eqs. (11)–(13), the mixing rate of the fuel gases with air flow from under the grate is a function of particle size and small particles produce higher rate the other conditions being the same and hence intensity the combustion in the gas phase.

The fifth effect lies in the non-uniform temperature distribution inside a particle. A large particle tends to be thermally thick and large temperature gradient exists inside the particle, especially during the period of ignition or around the flame front. This affects the moisture evaporation rate and devolatilisation rate of the particle, which are strong functions of local solid temperature.

4. Solving technique and boundary conditions

The solving technique is based on the SIMPLE algorithm [33] for the governing equations of both gas and solid phases. The whole bed is discretised into around 300 cells along the bed height and time-dependant numerical solution is sought for a set of parameters, including gas and solid temperatures, concentration of gaseous species (CH_4, CO, H_2, O_2, CO_2, H_2O and N_2), gas velocity and the four components of the solid phase (water, volatile matter, fixed carbon and ash). The calculation also gives detailed process-rate profiles such as hydrocarbon-gas production and consumption, char burning rate, radiation absorption, etc. The radiation equations are solved by the fourth-order Runge-Kutta method [34]. The total number of space discretisation in Eq. (14) is taken as two.

The composition of the volatile gases released during devolatilisation process is assumed to be 36% CH_4, 34% CO, 9.5% H_2, 13% CO_2 and 7.5% H_2O by volume. This is based on both elemental and heat balances so that the total masses of C, H and O in the product molecules equal to the those from the ultimate analysis and the total heat from the burning of the combustible gases equals to the calorific value of the volatiles, which can be deduced from the LCV of the fuel.

Particle shrinkage factors a_1, a_2 and a_3 in Eq. (7) are taken as being 0.8. Other fuel properties employed in the model are: the porosity of the wood particle $\varepsilon_p = 0.6$; wood conductivity $\lambda_{\text{wood}} = 0.2$ W/m K; char conductivity $\lambda_C = 0.1$ W/m K; particle pore size $d_{\text{pore}} = 50 \times 10^{-6}$ m; and pore cell emissivity $\varepsilon_{rad} = 0.9$. These data are based on reference [12].

The empirical mixing coefficient, C_{mix}, in Eq. (11) is taken as 0.5 [14,15]; The gas-to-solid heat transfer coefficient, h'_s in Eqs. (5) and (8) is calculated from $\text{Nu}\,(=d_p h'_s/\lambda_g) = 2 + 1.1\text{Pr}^{1/3}\text{Re}^{0.6}$ [28]. The fuel devolatilisation rate parameters are those of Alves and Figueiredo [15, 35] where $k_v = 7.0 \times 10^4 \exp(9977/T_s)$ and the kinetic rate of char combustion, $k_r = 2.3\,T_s \exp(-11100/T_s)$ [15].

The fuel is assumed to be ignited by over-board radiation at a temperature of 1173 K with emissivity of 0.8. This radiation source is present for the whole combustion processes. Primary air at 20 °C enters the bed from under the grate. Initial bed height is taken at 410 mm. The combustion starts at the bed top and the bed height falls as the flame front travels down towards the grate.

Boundary conditions: at the upper boundary, gradients of the gaseous temperature, concentrations and velocity are assumed to be zero (the second-type boundary). For the solid phase, the third-type boundary is assumed at both the bottom of the bed and the top surface for temperature (conduction and radiation heat exchange with the grate and over-bed radiation source are considered).

5. Experimental results

5.1. Mass loss history

Fig. 3 shows the mass loss history of fuel expressed as percentage of remaining mass on the bed as a function of reaction time. After switching on the over-bed gas-burner for initiating the reactions ($t=0$ min), there was an initial ignition period before a steady stage was reached. For the 5 mm pinewood fuel, the initial mass loss was quick, reaching a steady state at $t=2$ min. For the 10 mm pine wood cubes, the initial mass loss rate was slightly slower, reaching a steady state at $t=3.5$ min; For the 20 mm particle size, it was only after $t=7$ min that the mass loss rate reached a steady state. The 35 mm pinewood produced the longest ignition period (15 min) before a fully steady combustion stage was reached.

After the initial ignition period, a linear decrease in the total mass of the bed fuel was observed. Depending on the particle size, the length of this constant burning period

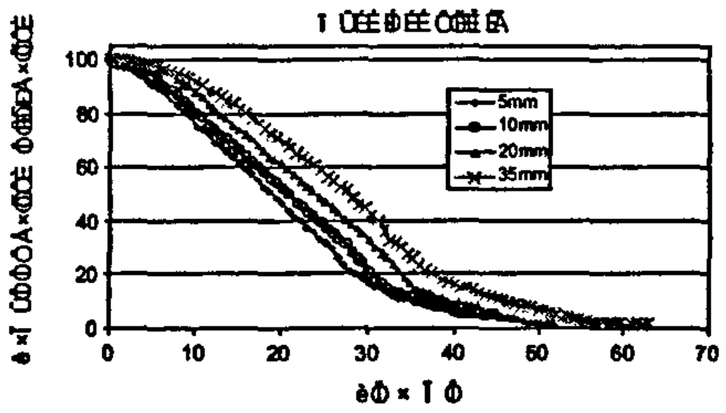

Fig. 3. Mass loss history as a function of reaction time.

ranged from 23 to 15 min, with the largest particles having the shortest period of constant burning.

Further on as the reaction time increased, the rate of the bed mass loss slowed down. For the small pinewood cubes of 5 mm, this final period of combustion was about 13 min before the whole combustion completed. For the 10 mm fuels, it increased to 15 min and for 20 mm, the final burning period further increased to 18 min. The largest fuel size, 35 mm, featured the longest final burning period of 25 min.

It was clear that the total burning time increased with increase in the fuel particle size. The obtained value was 42, 45, 50 and 57 min respectively for the pinewood of 5, 10, 20 and 35 mm.

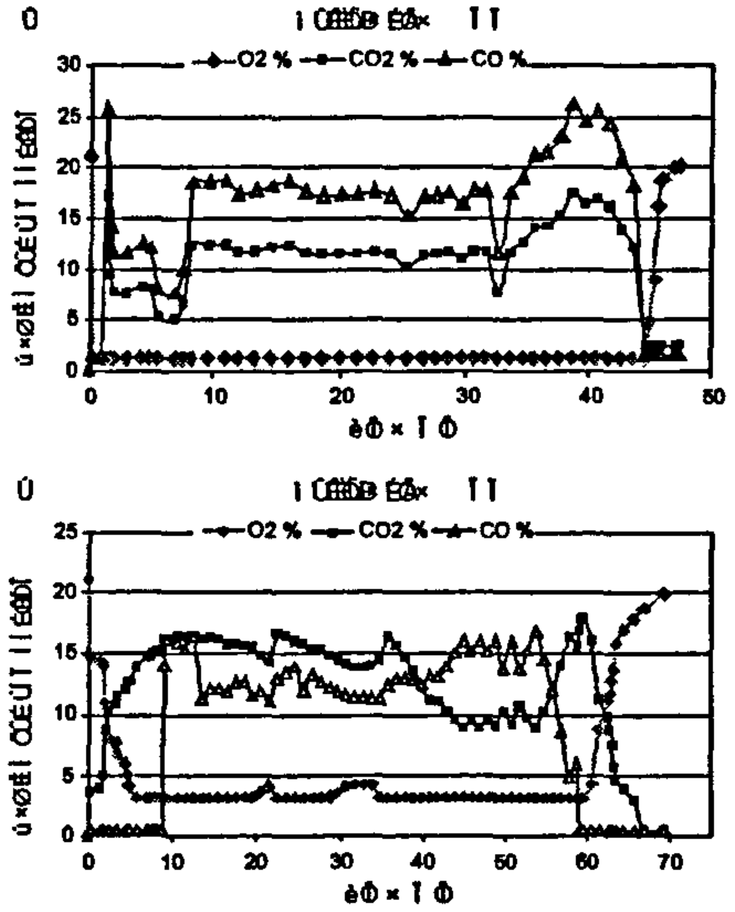

Fig. 4. Gas composition in the flue gases out of the bed top vs. reaction time. (a) Fuel size 10 mm; (b) fuel size 35 mm.

5.2. Gas composition in the out-of-bed flue gases

Fig. 4 shows the gas composition in the flue gases out of the bed top as a function of time for 10 and 35 mm pinewood chips. For the smaller size (Fig. 4a), the O_2 concentration in the flue gases quickly dropped from the ambient level of 21% to a minimum level (~1.0%) as soon as the gas-burner for ignition was switched on. There was an initial sharp spike for both CO and CO_2 concentrations, followed by a relatively steady and short period of low levels of CO and CO_2. Further on at about 8 min, the measured CO and CO_2 rose to an elevated steady state of 18 and 12%, respectively, while the O_2 remained unchanged (1.0%). At about 34 min, both CO and CO_2 began to rise again and peaked at 40 min with a value of 25 and 17%, respectively before quickly reducing to 0% at 44 min to complete the combustion.

For the 35 mm pinewood chips, the gas composition profile against the time (Fig. 4b) was different from the case of 10 mm chips in two ways: firstly the variation with time in the flue gas O_2 and CO_2 concentrations was less intensive during both the initial ignition stage and the final burnout stage; secondly, the levels of O_2 and CO_2 concentrations were higher while the CO concentration was lower during the major stead-state burning period. The CO_2 level was 14% on average compared to 12% and CO 13.5% on average compared to 18% for the 10 mm fuel.

5.3. Temperature profile in the bed

Fig. 5 shows the measured bed temperature against time at different bed heights above the grate for chip sizes of 10

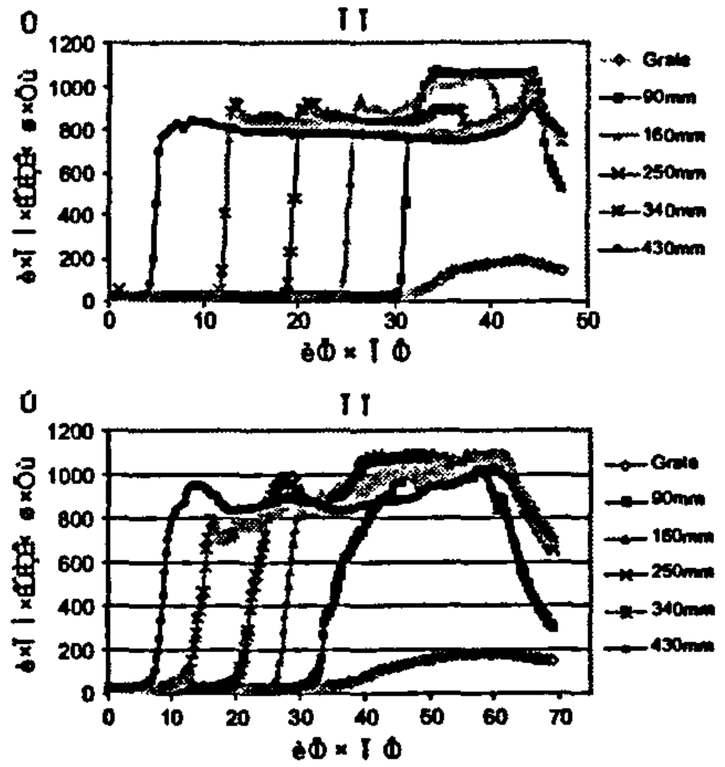

Fig. 5. Bed temperature vs. reaction time at different bed heights above the grate. (a) Fuel size 10 mm; (b) fuel size 35 mm.

and 35 mm. For the smaller pinewood (Fig. 5a), local bed temperature rose sharply from room level to a peak value as high as 910 °C as the flame front passed, then dropped slightly to a lower but stable level around 800 °C. It can be deduced that the flame downward propagation speed was 14.5 mm/min and the average time span for the local temperature rising from the ambient level to the peak level was 2.5 min, giving the flame front thickness of 36 mm (3.6 times the particle size). As the combustion approached the final stage (after $t=30$ min), the bed temperature rose to an even higher level of around 1100 °C, presumably as a result of char burning.

For the largest size of 35 mm (Fig. 5b), two differences can be noticed in the temperature profile from the case of 10 mm size. The first is the longer time span for the rising of local temperature from ambient level to the maximum point as the flame front passes. An average of 6 min was recorded (compared to 2.5 min for the 10 mm particles). The flame downward propagation speed is calculated being 13 mm/min, thus the flame front thickness is deduced to be 78 mm, or 2.2 times the original particle size.

The second difference is the measured maximum temperature level. The 35 mm pinewood produced a higher flame temperature than that for the 10 mm pinewood, reaching 980 °C at the flame front compared to 910 °C with 10 mm (excepting the final char burning stage).

6. Modelling results and comparison with experiments

6.1. Calculated process rates

Fig. 6(a) and (b) demonstrate the moisture evaporation rate distribution inside the bed as a function of time for the 10 and 35 mm fuels. For the 10 mm fuel (Fig. 6a), the upper boundary of the major moisture evaporation zone lies about 50 mm below the bed top and the zone extends 70 mm downward. The maximum local evaporation rate in the

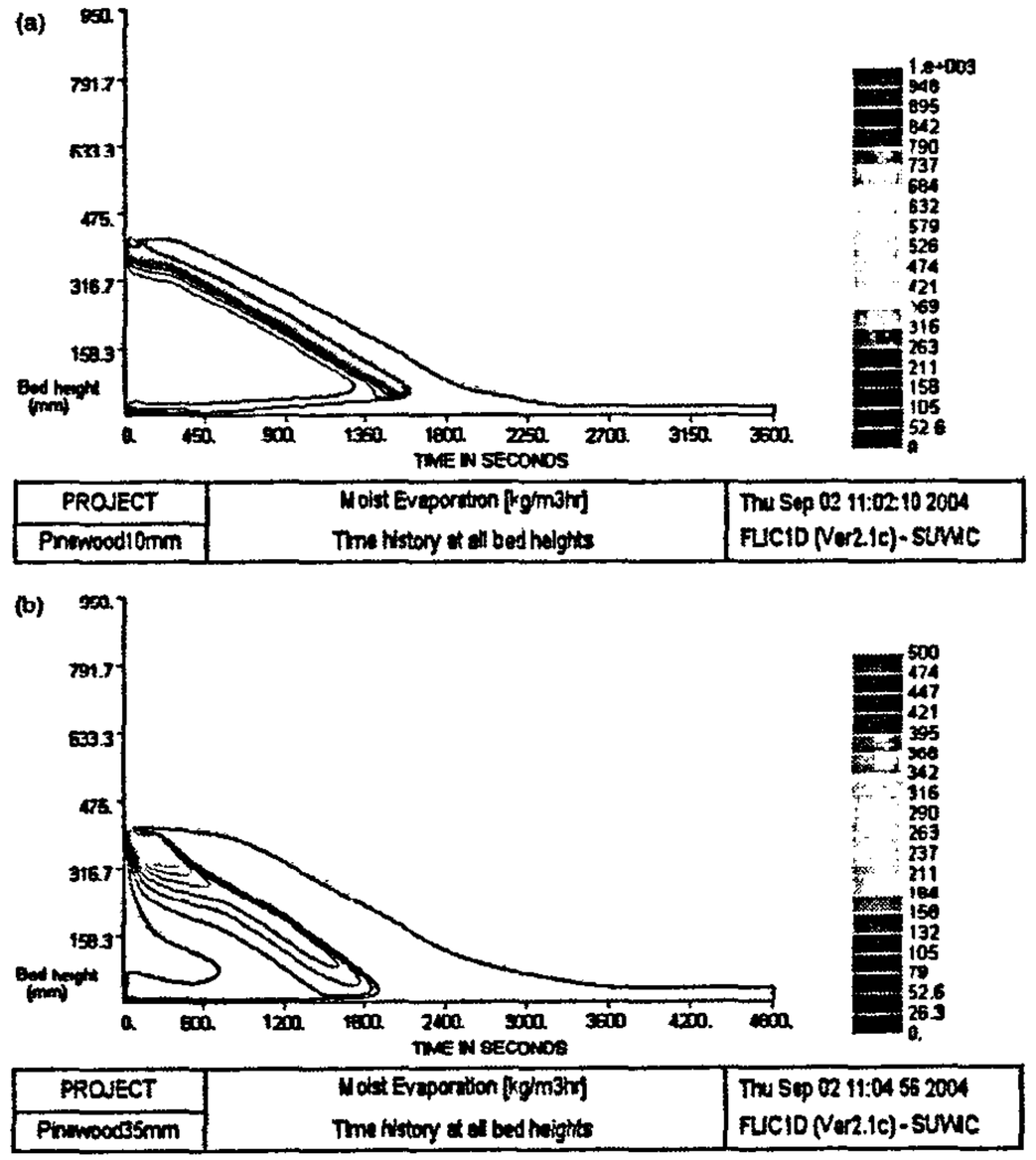

Fig. 6. Calculated process rate profiles in the bed vs. reaction time. (a) Moisture evaporation rate (10 mm); (b) moisture evaporating rate (35 mm); (c) Devolatilisation rate (10 mm); (d) devolatilisation rate (35 mm); (e) char burning rate (10 mm); (f) char burning rate (35 mm).

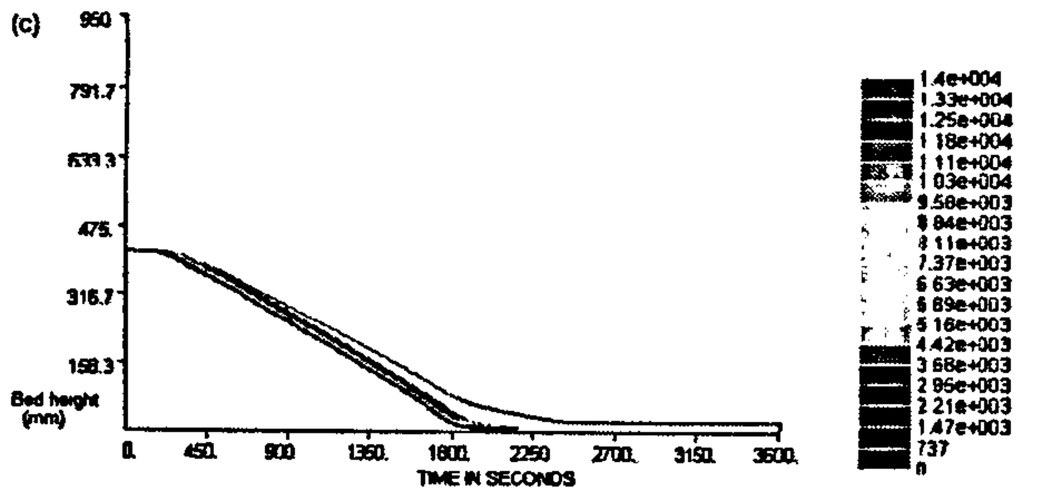

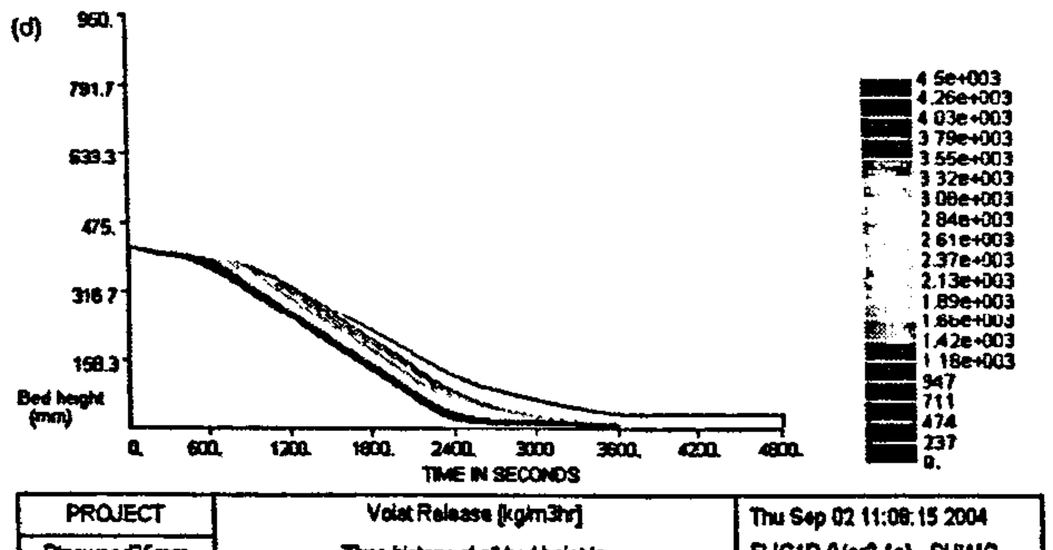

Fig. 6 (*continued*).

constant stage is around 550 kg/m^{3}h; for the 35 mm fuel (Fig. 6b), the upper boundary of the evaporation zone lies around 140 mm below the bed top and the zone extends 125 mm downwards. The maximum local rate in the constant stage is around 100 kg/m^{3}h, only a fifth of that with the 10 mm fuel.

Fig. 6(c) and (d) demonstrate the devolatilisation rate distribution inside the bed as a function of time for the two particle sizes. For the 10 mm fuel, the upper boundary of the major devolatilisation zone moves away from the bed top as the combustion proceeds and reaches a maximum 40 mm below the bed top line. The devolatilisation zone extends 28 mm along the bed height. The maximum local devolatilisation rate in the constant stage is around 1.2×10^4 kg/m^{3}h; For the 35 mm fuel, the thickness of the devolatilisation zone increases to around 75 mm and the maximum local rate in the constant stage reduces to around 3.5×10^3 kg/m^{3}h, only a third of the level for the 10 mm fuel.

Fig. 6(e) and (f) illustrate the char burning rate distribution along the bed height as a function of time. The char combustion and gasification zone extends about 20 and 30 mm in the bed for the 10 and 35 mm fuels, respectively.

Fig. 7 shows the bed-height integrated process rates vs. reaction time for the two fuel sizes of 10 and 35 mm. The moisture evaporation rate rises to a peak value shortly after the over-bed ignition source is switched on and the other two sub-processes, i.e. volatile release and char burning follow consecutively. For the smaller fuel (Fig. 7(a), devolatilisation starts at $t=2.5$ min and the volatile release rate reaches an elevated and constant level at $t=6$ min. For the 35 mm fuel, devolatilisation starts at 3 min but the volatile release rate takes a much longer time (at $t=18$ min) to reach a stabilized level of around 165 kg/m^{2}h, which is compared to the average level of 185 kg/m^{2}h for the 10 mm fuel. As devolatilisation approaches completion, the two particle sizes demonstrate different behavior: the 10 mm particles illustrates a surge in volatile release while the 35 mm particles show a smooth decline in the devolatilisation rate. The smaller fuel also has an earlier start in char

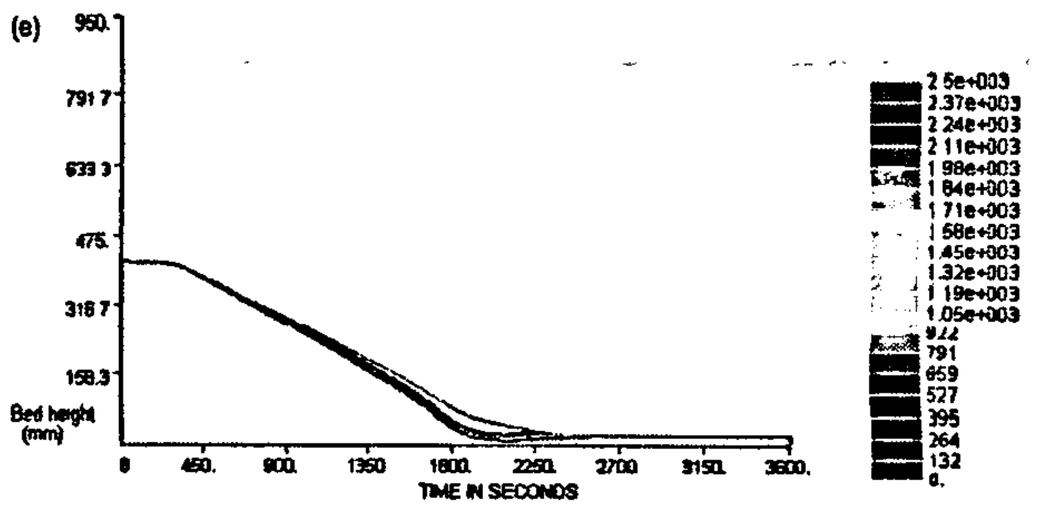

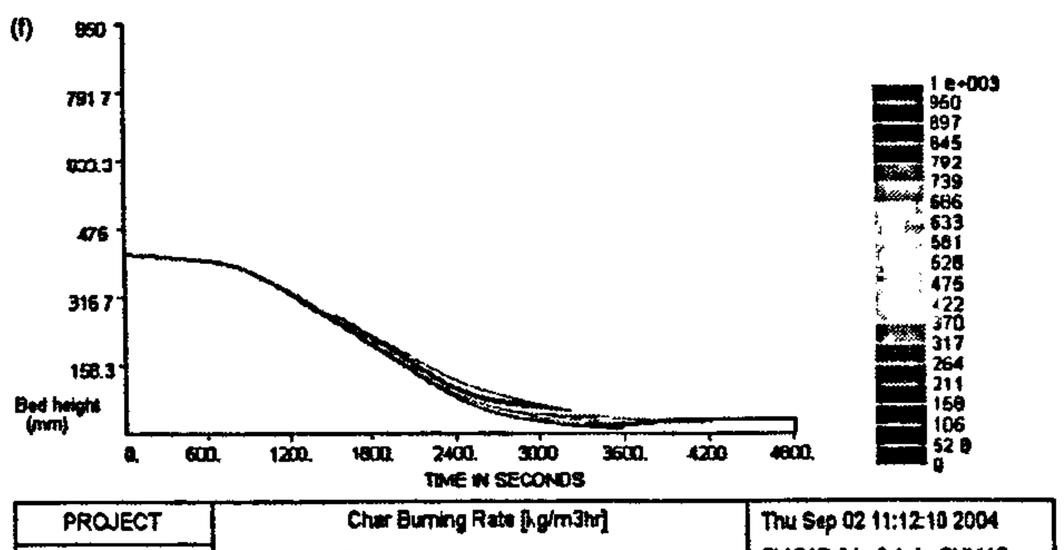

Fig. 6 (*continued*).

ignition and an overall higher char combustion/gasification rate than the bigger particles.

Fig. 7 also shows the calculated mass loss rate (including all the rates for the three sub-processes) compared to experimental measurements. The 10 mm particles feature a more constant and steady burning process during their major combustion stage while the 35 mm particles have most part of their combustion period undergoing gradual changes. Comparison between the modeling results and the measured ones are satisfactory for both the particle sizes.

6.2. *Fuel size effect on major combustion parameters*

Fig. 8 shows the fuel size effect on the average flame propagation speed during the major combustion stage (excluding the ignition and final burn-out periods). Experiments indicate a decreasing flame propagation speed with increasing particle size and the 35 mm fuel produced the lowest flame propagation speed of 150 kg/m^{2}h, compared to 205 kg/m^{2}h for the 5 mm fuel. The modeling prediction, however, shows the highest flame propagation speed is obtained at the fuel size of 10 mm. Consistency between experiments and predictions for the other three particle groups is fairly good, however.

Fig. 9 illustrates the fuel size effect on the average flame temperature during the major combustion stage (excluding the ignition and the final burn-out periods). Depending on the particle size, the measured level of flame temperature ranged from 810 to 900 °C and it is seen that fuel with a bigger size produced a higher combustion temperature. The model predicts the correct trend with variation in the particle size, but the calculated temperature level is 20~30 °C higher than the measured ones, in general. This could be caused by the measurement error where the tips of the thermocouples were exposed to the cooler walls of the test rig and possibly gave a lower temperature reading.

Fig. 10 demonstrates the fuel size effect on the gas composition in the out-of-bed flue gases during the major combustion stage. A general trend is the declining CO concentration as particle size increased. The model

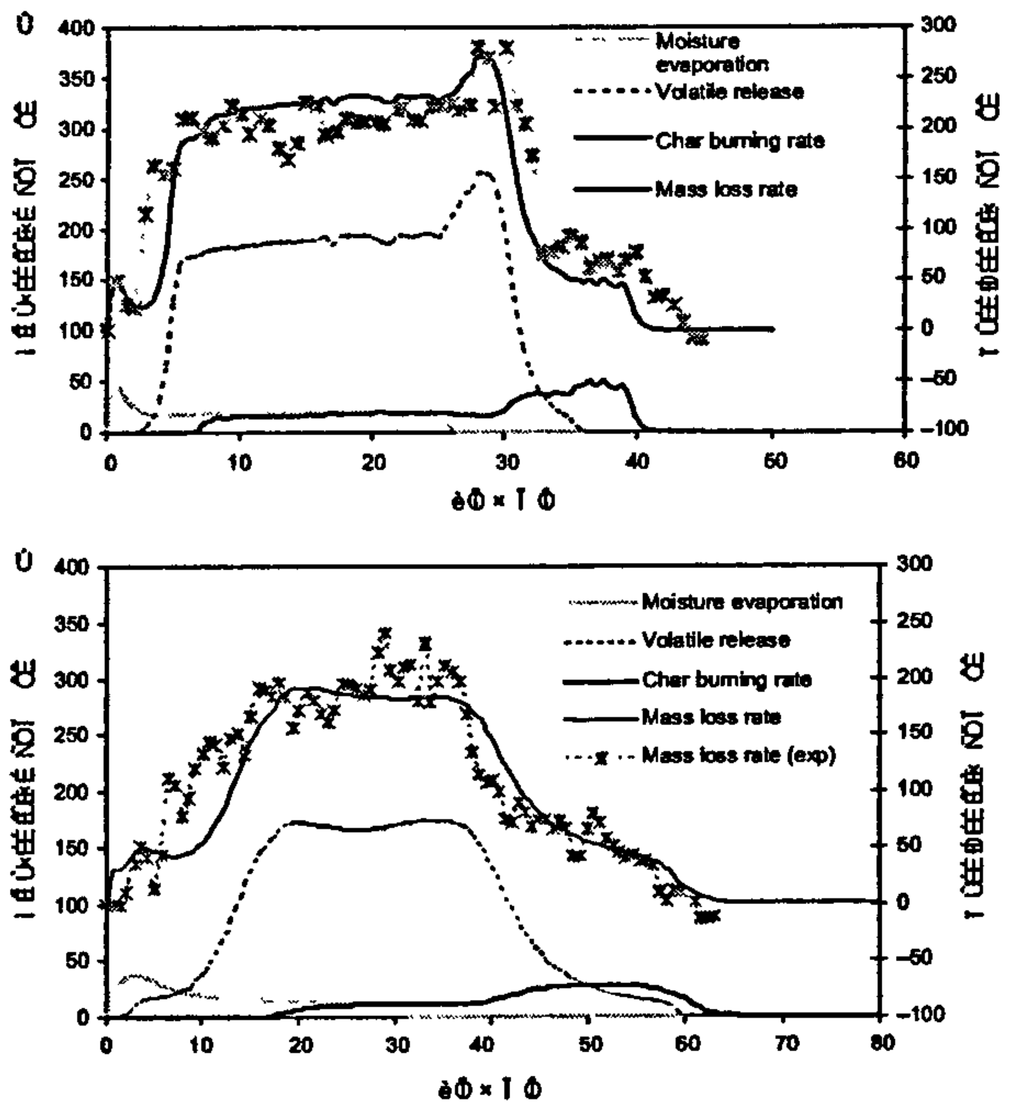

Fig. 7. Bed-height integrated process rates vs. reaction time. (a) 10 mm fuel; (b) 35 mm fuel.

predictions correctly reflect the measured trend but gives a slightly higher CO level across the whole size range.

Fig. 11 shows the predicted CH_4 and H_2 percentages in the out-of-bed flue gases as a function of fuel size. It is seen that the CH_4 concentration decreases with increasing fuel size, from 11% at 5 to 7.5% at 35 mm. The H_2 concentration, however, increases as fuel size increase, from 2.6% at 5 mm to 6.8% at 35 mm. Increasing in H_2 is due to slower mixing rate inside the bed of bigger size fuel between the H_2 and under-grate air. H_2 is both one of the primary devolatilisation products and the intermediate burning product of CH_4.

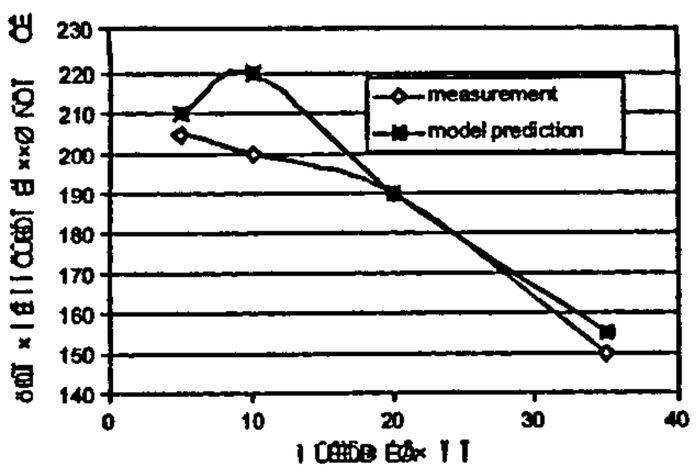

Fig. 8. Flame propagation speed vs. fuel size.

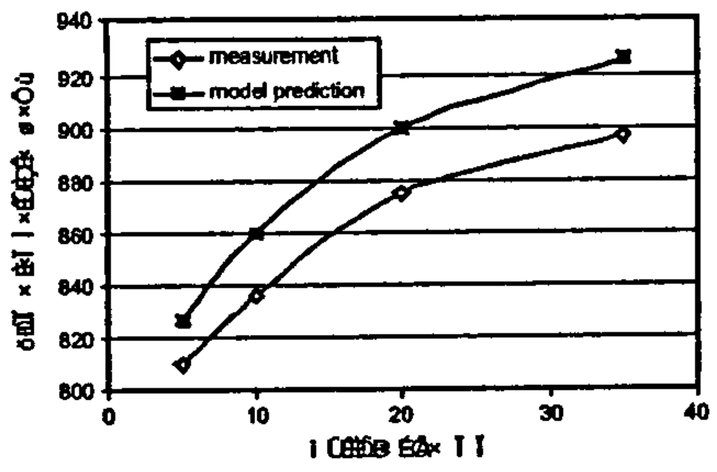

Fig. 9. Flame temperature vs. fuel size.

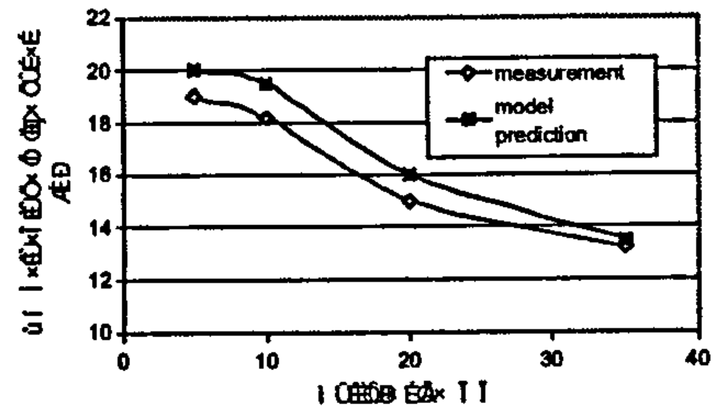

Fig. 10. CO percentage in the out-of-bed flue gases vs. fuel size.

7. Discussion and conclusions

The experiments demonstrated that a smaller size fuel tends to produce an earlier ignition of the bed than does a bigger size fuel, as indicated in Fig. 3. This is consistent with the experimental results of Friberg and Blasiak [4] where three different size fuels of wood were used. Mathematical modeling (Fig. 7) revealed that the smaller particle bed has a faster initial moisture evaporation rate when the over-bed ignition source is switched on so that the top surface of the bed is quicker to get dry and subsequently ignited. Similarly, dry-out of the whole bed is responsible for the temporally surge in the mass loss rate towards the end of the constant burning stage, as indicated by both the experiments and modeling prediction in Fig. 7 (more clearly for the case of 10 mm fuel).

Another obvious feature of the fuel size effect is that a bigger particle-size bed tends to burn transiently while a smaller particle-size bed can quickly build up a constant and steady burning pattern (Fig. 7). This finding is consistent with the results of Friberg and Blasiak [4]. This suggests that the control of a practical furnace firing bigger size fuels needs to be more carefully planned because of the constant variation of the burning pattern either with time if the bed is stationary or with bed length if the bed is moving. This can be explained by the ratio of the initial bed height to the reaction zone thickness. In the current experiments, this ratio is around 11.4 (410/36 mm) for the 10 mm fuel and 5.2 (410/78 mm) for the 35 mm fuel.

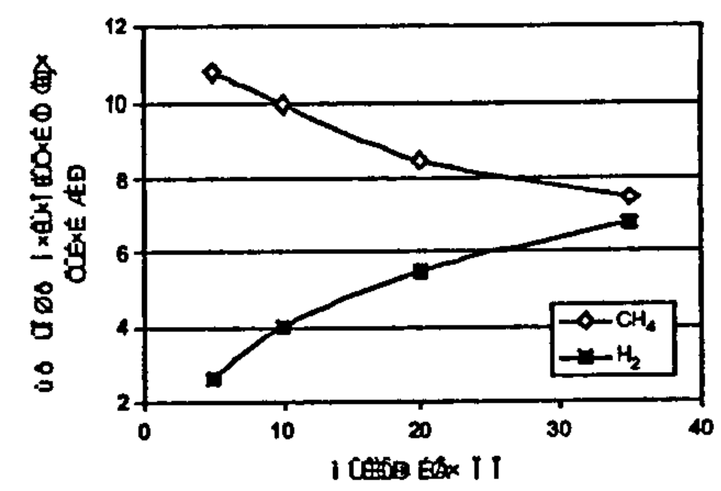

Fig. 11. Predicted CH_4 and H_2 concentrations in the out-of-bed flue gases vs. fuel size.

The measured flame propagation speed vs. particle size (Fig. 8) is consistent with the findings of Friberg et al. [4] who demonstrated decreasing burning rate as particles size increased. But the modelled trend is similar to the findings of Peters [12] who reported the maximum ignition rate obtained at 15 mm in the size range of 5–25 mm. However, the current results are contrary to the findings of Gort [3] and Rönnbäck et al. [5] who reported increased ignition speed for larger particles in the size range of 10–30 mm.

At the operating conditions of the current investigation, all fuels of the four sizes were burnt under sub-stoichiometric (fuel-rich) conditions. Understandably, a larger particle size produced a higher flame temperature (Fig. 9) as the burning rate slows down and the combustion shifts to less fuel-rich state.

Mathematical modeling results (Fig. 7) also reveal that a bed of small-particles has a distinctive final burning stage where all the moisture and volatile matter have been released but there is still a noticeable quantity of char remaining. The remaining char continues to burn until the total completion of the combustion process. For a bed of large-particles, however, the final burning stage features both the char burn-out and solid devolatilisation at the same time to a large extent. The knowledge of this difference is important because the operator of a real furnace has to plan the primary air distribution as correctly as possible for the emission control and optimization of the combustion efficiency.

In general, the following conclusions can be drawn from the current study in terms of the fuel size effect:

1. Ignition time is shorter with a bed of smaller particles than with larger particles at the same operating conditions;
2. Reaction zone is thicker with a larger-particle bed than with a smaller-particle bed;
3. Burning rate decreases with increase in fuel particle size;
4. Smaller fuel particles resulted in fuel-richer combustion and both higher CO and CH_4 concentrations in the out-of-bed flue gases; but the H_2 concentration decreases with decreasing in fuel size, according to model predictions;
5. Larger fuel particles produced higher burning temperature in the bed;
6. Small particles presented a uniform flame propagation speed during most part of the combustion process while large particles showed a more transient feature where the burning rate changes for most part of the combustion process;
7. In the final stage of the combustion, residual char burn-out is the only process occurring in a bed of small

particles. But in a bed of large particles, both char burnout and fuel devolatilisation occur at the same time.

Acknowledgements

This study was funded by EPSRC (UK) SuperGen Biomass Grant.

References

[1] Supergen web site: http://www.supergen-bioenergy.net/
[2] European Energy Crops InterNetwork: http://www.eeci.net/
[3] Gort R. On the propagation of a reaction front in a packed bed: thermal conversion of municipal waste and biomass. Academic Dissertation, University of Twente; 1995.
[4] Friberg R, Blasiak W. Measurements of mass flux and stoichiometry of conversion gas from three different wood fuels as function of volume flux of primary air in packed bed combustion. Biomass Bioenergy 2002,23:189–208.
[5] Rönnbäck M, Axell M, Gustavsson L. Combustion processes in a biomass fuel bed-experimental results. Progree in thermochemical conversion, Tyrol, Austria 2000 p. 17–22.
[6] Saastamoinen JJ, Taipale R, Horttanainen M, Sarkomaa P. Propagation of the ignition front in beds of wood particles. Combust Flame 2000;123 214–26.
[7] Van der Lans RP, Pedersen LT, Jensen A, Glarborg P, Dam-Johansen K. Modelling and experiments of straw combustion in a grate system. Biomass Bioenergy 2000;19:199–208.
[8] Yang Y, Goodfellow J, Goh Y, Nasserzadeh V, Swithenbank J. Investigation of channel formation due to random packing in a burning waste bed. Trans IChemE, Part B 2001;79:267–77.
[9] Yang YB, Nasserzadeh V, Goodfellow J, Swithenbank J. Simulation of channel growth in a burning bed of solids. Trans IChemE, Part A 2003;81:221–32.
[10] Thunman H, editor. Principles and models of solid fuel combustion. Göteborg, Sweden: Chalmers University of Technology; 2001.
[11] Thunman H, Leckner B. Ignition and propagation of a reaction front in cross-current bed combustion of wet biofuels. Fuel 2001,80:473–81.
[12] Peters B. Thermal conversion of solid fuels.: WIT Press; 2003.
[13] Liang XH, Kozinski JA. Numerical modelling of combustion and pyrolysis of cellulosic biomass in thermogravimetric systems. Fuel 2000;79:1477–86.
[14] Yang YB, Nasserzadeh V, Goodfellow J, Goh YR, Swithenbank J. Parameter study on the incineration of municipal solid waste fuels in packed beds. J Inst Energy 2002;66–80.
[15] Yang YB, Yamauchi H, Nasserzadeh V, Swithenbank J. Effects of fuel devolatilisation on the combustion of wood chips and incineration of simulated municipal solid wastes in a packed bed. Fuel 2003;82: 2205–21.
[16] Yang YB, Sharifi VN, Swithenbank J. Effect of air flow rate and fuel moisture on the burning behaviours of biomass and simulated municipal solid wastes in packed beds. Fuel 2004;83:1553–62.
[17] Behrendt Th. Thermodynamische modellierung des betriebsverhaltens einer hausmüllverbrennungsanlage am beispiel TAMARA. Fortschrittberichte reihe 15. Düsseldorf: VDI Verlag; 1992.
[18] Krüll F, Kremer H, Wirtz S. Feuerraumsimulation einer müllverbrennungsanlage bei gleichzeitiger simulation der verbrennung auf dem rost. VDI Bericht 1390, modellierung und simulation von dampferzeugern und feuerungen 1998 p. 199–212.
[19] Shin D, Choi S. The combustion of simulated waste particles in a bed. Combust Flame 2000;121:167–80.
[20] Goh YR, Siddall RG, Nasserzadeh V, Zakaria R, Swithenbank J, Lawrence D, et al. Mathematical modelling of the waste incinerator burning bed. J Inst Energy 1998.
[21] Adams T. A simple fuel bed model for predicting particulate emissions from a wood waste boiler. Combust Flame 1980;39: 225–39.
[22] Stapf M, Kircherer A, Kolb Th, Wölfert A, Seifert H. Verbrennung im Drehrohrofen: modellierung, betriebs-und technikumsversuche. Volume 15 of VDI-Berichte 1313. Düsseldorf: VDI Verlag; 1997.
[23] Beckmann M, Scholz R. Simplified mathematical model of combustion in stoker systems. The third European conference on industrial furnaces and boilers. Porto, Portugal; 1995, p. 61–70.
[24] Wurzenberger JC. A combined packed bed and single particle model applied to biomass combustion. PhD thesis, Graz University of Technology; 2001.
[25] Peters B. A detailed model for devolatilization and combustion of waste material in packed beds. The third European conference on industrial furnaces and boilers (INFUB). Lisbon, Portugal; 18–21 April, 1995, p. 86–104.
[26] Hunt ML, Tien CL. Non-Darcian convection in cylindrical beds. J Heat Trans 1988;110:378–84.
[27] Vafai K, Sozen M. Analysis of energy and momentum transport for fluid flow through a porous bed. J Heat Trans 1990,112:690–9.
[28] Wakao N, Kaguei S. Heat and mass transfer in packed beds. London: Gordon & Breach; 1982.
[29] Blasi CD. Heat, momentum and mass transport through a shrinking biomass particle exposed to thermal radiation. Chem Eng Sci 1996; 51:1121–32.
[30] Hottel HC, Sarofim AF. Radiative transfer. New York: McGraw-Hill Book Company; 1967.
[31] Yang YB, Goh YR, Zakaria R, Nasserzadeh V, Swithenbank J. Mathematical modelling of MSW incineration on a travelling bed. Waste Manage 2002;22:369–80.
[32] Smoot LD, Pratt DT. Pulverized-coal combustion and gasification. London: Plenum Press; 1979.
[33] Patankar SV. Numerical heat transfer and fluid flow. London, Washington: Hemisphere; 1980.
[34] Hornbeck RW. Numerical methods.: Quantum Publishers; 1975.
[35] Alves SS, Figueiredo JL. Pyrolysis kinetics of lignocellulosic materials by multistage isothermal thermo-gravimetry. J Analyt Appl Pyrol 1988;13:123–34.

Available online at www.sciencedirect.com
SCIENCE DIRECT®
Fuel 84 (2005) 2116–2130
FUEL
www.fuelfirst.com

Effect of fuel properties on biomass combustion. Part II. Modelling approach—identification of the controlling factors

Yao Bin Yang[a,*], Changkook Ryu[a], Adela Khor[a], Nicola E. Yates[b], Vida N. Sharifi[a], Jim Swithenbank[a]

[a]Sheffield University Waste Incineration Centre (SUWIC), Department of Chemical and Process Engineering, Sheffield University, Mappin Street, Sheffield S1 3JD, UK
[b]Rothamsted Research, Harpenden, Herts AL5 2JQ, UK

Received 8 March 2005; received in revised form 22 April 2005; accepted 26 April 2005
Available online 13 June 2005

Abstract

Biomass fuels come from many varieties of sources resulting in a wide range of physical and chemical properties. In this work, mathematical models of a packed bed system were employed to simulate the effects of four fuel properties on the burning characteristics in terms of burning rate, combustion stoichiometry, flue gas composition and solid-phase temperature. Numerical calculations were carried out and results were compared with measurements wherever possible. It was found that burning rate is mostly influenced by fuel size and smaller fuels result in higher combustion rate due to increased reacting surface area and enhanced gas-phase mixing in the bed; combustion stoichiometry is equally influenced by fuel LCV and size as a consequence of variation in burning rate as well as the mass ratio of combustible elements to the oxygen in the fuel; for the solid-phase temperature, material density has the strongest influence and a denser material has a higher maximum bed temperature as it results in a less fuel-rich combustion condition; while CO concentration in the flue gases is mostly affected by both fuel calorific value and size, CH_4 in the exiting flow is greatly affected by material density due to change in reaction zone thickness.

Keywords: Biomass; Combustion; Mathematical modelling

1. Introduction

Biomass constitutes 14% of the global primary energy, the fourth largest following coal, oil and natural gas. It is renewable and produces no net CO_2 emission in combustion. Fuel biomass comes from both primary and secondary sources. Primary sources are energy crops that have the sole purpose of energy production. Willow, miscanthus, reed canary grass and sorghum are a few examples of this category. Secondary sources are mainly from agriculture activities and wastes, including straw, forest residues, sugar cane fibre, rice husks, waste vegetables, cardboard and paper, etc.

The wide variety of biomass sources result in a wide range of biomass fuel properties, both physically and chemically. Table 1 illustrates the estimated variations of conventional properties of biomass which can be measured by standard methods. Moisture, for instance, can only be a few percent with pre-dried biomass or as high as 50% with freshly harvested crops. Volatile matter in biomass is much higher than in coals, ranging from 65 to 85%, while fixed carbon is much lower, ranging from 7 to 20%. Ash is generally under 5%, but can be as high as 20% with some specific mass, for example, rice hulls. For elemental analysis, a noticeable feature is the high oxygen content (32–45%).

Depending on the type of species and specific cultivation conditions, levels of other minor components, such as N, S, Cl and K can also vary widely.

The lower calorific value (LCV) ranges from 15 to 22 MJ kg^{-1} and the size can be from that of pulverized particles (~1 mm) to that of whole wood logs (~100 mm).

* Corresponding author. Tel.: +44 114 2227500; fax: +44 114 2227501.
E-mail address: y.b.yang@shef.ac.uk (Y.B. Yang).

0016-2361/$ - see front matter © 2005 Elsevier Ltd. All rights reserved.
doi:10.1016/j.fuel.2005.04.023

Nomenclature

A	flow cross-section area, m^2; particle surface area, $m^2\,m^{-3}$
A_r	pre-exponent factor in char burning rate, $kg\,m^{-2}\,s^{-1}$
A_v	pre-exponent factor in devolatilisation rate, s^{-1}
Bi	Biot number
Bi′	modified Biot number
C	constant; molar fractions of species
C_{fuel}	fuel concentration, $kg\,m^{-3}$
C_{pg}	specific heat capacity of the gas mixture, $J\,kg^{-1}\,K^{-1}$
C_{mix}	mixing-rate constant, 0.5
$C_{w,g}$	moisture mass fraction in the gas phase
$C_{w,s}$	moisture mass fraction at the solid surface
D_g	molecular diffusion coefficient of volatile hydrocarbons in air, $m^2\,s^{-1}$
D_{ig}	dispersion coefficients of the species Y_i, $m^2\,s^{-1}$
d_p	particle diameter, m
E_b	black body emission, Wm^{-2}
E_r	activation energy in char burning rate, $J\,kmol^{-1}$
E_v	activation energy in devolatilization rate, $J\,kmol^{-1}$
E^0	effective diffusion coefficient
F_2	fraction of the volume occupied by water replaced by pores during drying
F_3	fraction of the volume occupied by volatile matter replaced by pores during pyrolysis
FC	fixed carbon in fuel, wt%
H_{evp}	evaporation heat of the solid material, $J\,kg^{-1}$
H_g	gas enthalpy, $J\,kg^{-1}$
H_s	solid-phase enthalpy, $J\,kg^{-1}$
h_m	convective mass transfer coefficient between solid and gas, $kg\,m^{-2}\,s^{-1}$
h_s'	convective heat transfer coefficient between solid and gas, $W\,m^{-2}\,K^{-1}$
I_x^+	radiation flux in positive x-direction, $W\,m^{-2}$
I_x^-	radiation flux in negative x-direction, $W\,m^{-2}$
k	thermal conductivity of particle material, $W\,m^{-1}\,K^{-1}$
k_a	radiation absorption coefficient, m^{-1}
k_d	rate constants of char burning due to diffusion, $kg\,m^{-2}\,s^{-1}$
k_r	rate constants of char burning due to chemical kinetics, $kg\,m^{-2}\,s^{-1}$
k_v	rate constant of devolatilization, s^{-1}
k_s	radiation scattering coefficient, m^{-1}
K	permeability
L_b	bed top height, m
M	moisture in fuel, wt%
PA_i	primary air velocity levels ($i=1,4$)
P_g	gas pressure, Pa
Q_{ch}	heat loss/gain of the gases, $W\,m^{-3}$
Q_{sh}	thermal source term for solid phase, $W\,m^{-3}$
q_r	radiative heat flux, $W\,m^{-2}$
R_i	process rate ($i=2,3,4$), $kg\,m^{-3}\,s^{-1}$
R	Universal gas constant; reaction rate
R_{mix}	mixing-rate of gaseous phase in the bed, $kg\,m^{-3}\,s^{-1}$
S	stoichiometric coefficients in reactions
S_{sg}	conversion rate from solid to gases due to evaporation, devolatilisation and char burning, $kg\,m^{-3}\,s^{-1}$
Sy_{ig}	mass sources due to evaporation, devolatilisation and combustion, $kg\,m^{-3}\,s^{-1}$
Sy_{is}	source term, $kg\,m^{-3}\,s^{-1}$
t	time instant, s
T	temperature, K
V	velocity, ms^{-1}; volume of the bed, m^3
V_0	volume of the initial bed, m^3
VM	volatile matter in fuel, wt%
x	co-ordinate in bed height direction, m
Y_{ig}	mass fractions of individual species (e.g. H_2, H_2O, CO, CO2, C_mH_n,...).
Y_{is}	mass fractions of particle compositions (moisture, volatile, fixed carbon and ash)
$Y_{is,0}$	mass fraction of particles components at fresh feed state;
ε_s	system emissivity
σ_b	Stefan–Boltzmann constant, $5.86\times10^{-8}\,W\,m^{-2}\,K^{-4}$
v	remaining volatile in solid at time t
v_∞	ultimate yield of volatile
ϕ	void fraction in the bed
ρ	density, $kg\,m^{-3}$
ρ_{sb}	solid bulk density in the bed, $kg\,m^{-3}$
λ_g	thermal dispersion coefficient, $W\,m^{-1}\,K^{-1}$
λ_g^0	effective thermal diffusion coefficient, $W\,m^{-1}\,K^{-1}$
λ_s	effective thermal conductivity of the solid bed, $W\,m^{-1}\,K^{-1}$
μ	viscosity of gases, $kg\,m^{-1}\,s^{-1}$
$\omega_{i,k}$	volume fraction of component i in biomass k

Subscripts

env	environmental
g	gas phase
i	identifier for a component in the solid
p	particle
s	solid phase
2	moisture or moisture evaporation
3	volatile matter or devolatilisation
4	fixed carbon or char gasification
A	material in its initial state
B	dried material
C	dried and pyrolysed material
D	dried, pyrolysed and gasified material

Table 1
Variations in biomass fuel properties

M	VM	FC	Ash	C	H	O	N	S
5–50	65–85	7–20	0.5–20	38–53	4.5–7.0	32–45	0.15–2.7	0.02–0.35
Cl	LCV, MJ kg^{-1}	d_p, mm	Maximum dimension ratio		Thermal conductivity, k_s		Bulk density, ρ_{ab}	
0–0.5	15–22	1–100	1–15		0.07–0.5 W m^{-1} K^{-1}		20–710 kg m^{-3}	

The unit of the properties is in wt% unless indicated otherwise; elemental composition is on a dry basis.

The shape is non-spherical, normally with high dimension ratios and some biomass is pelletised to form a single shape and size. Bulk density of biomass fuels vary significantly, from the very light dry straw (20 kg m^{-3}) to the very heavy pellets ($\sim$700 kg m^{-3}).

This wide variation in biomass properties can greatly affect the burning characteristics of the biomass fuels. The effect of moisture level in fuel for packed bed systems was investigated by Yang et al. [1,2] in conjunction with primary air velocity in a packed bed. It was found that the maximum burning rate with a very dry fuel can be several times higher than with a very wet fuel and the reaction zone thickness becomes thinner as the moisture level in fuel increases. Flame extinction also occurs at high moisture levels, which was related to the minimum amount of combustible material (both volatile in solids and char) above the moisture evaporation layer. Thunman & Leckner [3] presented a calculated maximum propagation rate of the reaction front for 10 mm wood particles with different moisture contents. They also quoted the experimental results of Gort [4] with moisture level in fuel ranging from 10 to 56.6% on a wet basis.

Yang et al. [5] studied the effect of devolatilisation rate on biomass combustion characteristics in a packed bed which shows that the devolatilisation rate has an increasing influence as the moisture content in fuel decreases.

Some effects of the physical properties of biomass were also investigated though the conclusions were inconsistent. For example, Gort [4] and Rönnbäck et al. [6] reported increased ignition speed for larger particles in the size range of 10–30 mm while Peters [7] reported the maximum ignition rate was obtained at 15 mm in the size range of 5–25 mm. On the other hand, Friberg and Blasiak [8] demonstrated decreasing burning rate as particles size increased.

The effect of biomass fuel properties also depends on the type of reacting systems. There are three major types of reactor for biomass combustion: packed-bed, fluidized bed and entrained flow reactors. The packed-bed system is the mostly widely used, from small-scale home application to large-scale industrial facilities. The advantages of the system are minimum fuel pre-treatment, relatively well-known technology and low construction and running costs.

Overall, detailed and systemic studies on the effect of fuel properties on biomass combustion are still lacking, while demand for more information is increasing as more and more efforts are being made to utilize effectively and environmentally friendly the global biomass resources. Experimental approaches, though, provide invaluable practical data, however isolating one parameter from the rest with experimental methods is difficult to implement. The bulk density of the materials, for example, is very difficult to change unless the fuel is pelletised. Often the fuel sample comes with a specific particle size (or size distribution), bulk density and fixed contents of volatile matter, fixed carbon and ash. The sample may be pretreated by drying or wetting to vary moisture content, but nothing more can be done with the sample. This put a limitation to the experimental approach when the effect of individual parameters needs to be addressed.

Mathematical modeling, on the other hand, provides a flexible approach to evaluate the effects of individual fuel properties. The volatile content, for example, can be varied artificially, so can the particle size and its distribution, provided that the mathematical models incorporate those physical and chemical parameters. Mathematical modeling also provides such detailed information as temperature profile, gas compositions, bed height decrease, pollutant formation and combustion stoichiometry, etc.

In this paper, the mathematical approach is adopted to identify the controlling factors during biomass combustion in packed bed systems. The effects of fuel LCV, material density, particle size and packed bed porosity are investigated. The results from mathematical calculations are compared to experimental measurements where it is possible. Extensive numerical calculations are carried out in wide ranges of fuel parameters, and the results are presented in terms of average burning rate, combustion stoichiometry, bed temperature and gas compositions at the bed top. Experimental work is introduced in Part I of this paper.

2. Mathematical description of packed-bed biomass combustion

Peters [7] proposed the governing equations for packed-bed solid combustion. Yang et al. [9] first applied the proposed equations to waste incineration in a moving grate, followed by a series of theoretical studies on the effect of fuel moisture, devolatilisation rate and primary air velocity [1,2,5].

A packed bed consists of a number of solid particles which are piled up upon a support grate with a characteristic porosity. Primary air is supplied from underneath the grate and flows upward. For ordinary packed bed combustion, ignition starts at the bed top layer heated up by over-bed radiation from the over-bed flame and hot walls. Once the bed is ignited, the flame front travels downwards at a speed depending on fuel type and operating parameters, until it arrives at the bed bottom or the support grate. In ideal conditions, three reacting waves travel down the bed successively: moisture evaporation, devolatilisation and char combustion (Fig. 1). They may overlap each other, depending upon particle size or the Biot number. The Biot number is a measure of uniformity of temperature distribution inside a particle and for a single particle heated uniformly at the external surface, it is defined as

$$\mathrm{Bi} = h_s' d_p / k \tag{1}$$

When Bi $\gg$ 1.0 particles are considered thermally thick and there exists a significant temperature gradient inside the particles under an external heating source. Otherwise, the particles can be viewed as thermally thin, and the temperature gradient inside the particle is small.

The above definition of Biot number for a single particle, however, has to be modified to account for the changed heating conditions for the situation of a packed bed. Radiation from the flame front can only penetrate the bed through voids; therefore the actual external heated area of a particle in a packed bed is proportional to the local bed voidage. So we add an extra parameter, the void fraction to the original Biot number and the modified Biot Number is thus as follows:

$$\mathrm{Bi}' = \phi h_s' d_p / k \tag{1a}$$

Assuming an external radiation source of 1100 K, a bed porosity of 0.5 and the thermal conductivity of the particles

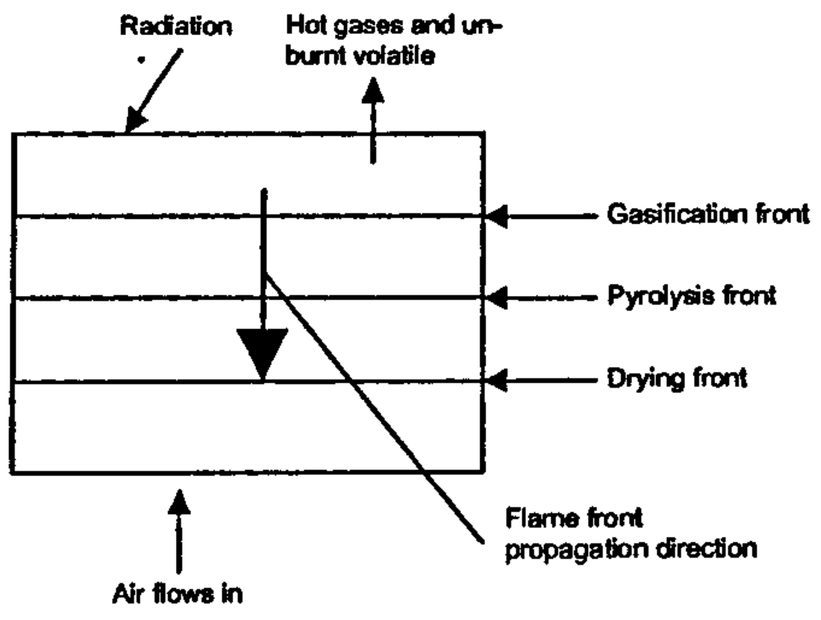

Fig. 1. Propagation of flame front in a packed bed.

being k=0.4 W m^{-1} K^{-1} [10], the modified Biot number Bi$'$<1 when d_p<15 mm and Bi$'$<2 when d_p<30 mm. So, generally speaking, particles smaller than 30 mm can be roughly regarded as thermally thin in the situation of packed bed combustion.

The assumption of thermally thin particles eliminates the need for a separate solution for temperature profile inside the particles. Instead, the whole bed can be viewed as a continuous porous medium with two phases (solid and gases), and continuous conservation or transport equations can be applied to both phases in a much simpler way. Table 2 summarises the equations employed for packed-bed biomass combustion in this work.

The whole set of equations consists of bed volume change, individual process rates, gaseous phase and solid phase conservation equations and radiation heat transfer in the bed. Biomass particles shrink as they lose mass through moisture evaporation, volatile release and char burnout and so the bed volume decreases as a result. Change in the bed volume is related to each individual process rates, R_2 for moisture evaporation, R_3 for devolatilisation and R_4 for char burnout. Moisture in the fuel evaporates via two mechanisms, convective drying by primary air and radiative drying by radiation from the flame front. For biomass devolatilisation, a single step global reaction proposed by Badzioch et al. [11] is adopted for simplicity. The pre-exponential factor A_v and activation energy E_v are fixed at 7.0×10^4 s^{-1} and 83 kJ mol^{-1}, respectively [12].

The gaseous products of devolatilisation are C_mH_m, CO, CO_2, H_2O and H_2 (C_mH_n is taken as CH_4 in this study). The two-step reaction mechanism is assumed for the oxidation of C_mH_n with CO and H_2 as the intermediate products. The gas-phase burning of C_mH_m, CO and H_2 is not only controlled by the kinetic rate but also by the mixing rate of the released volatile gases with primary air flow coming from underneath the grate. The gas-phase mixing rate is modeled by an equation proposed by Yang et al. [9] which relates the mixing rate to particle size, bed voidage and gas velocity. The actual burning rate of the combustible volatile gases is taken as the minimum of the kinetic rate and mixing rate.

The char formed from the devolatilisation process reacts with oxygen in the primary air flow to form both CO and CO_2, with the ratio of CO to CO_2 determined by the temperature level. The gasification rate of char is controlled by both the kinetic rate and the diffusion rate. The parameters in the kinetic rate, k_r, are taken as A_r= 290 kg m^{-2} s^{-1} and E_r=86 kJ mol^{-1} [13].

The conservation equations for the gas-phase in the packed bed include continuity, momentum, species and energy conservation equations. The gas species include O_2, CO_2, CO, H_2, CH_4, H_2O balanced by N_2. The conservation equations for the solid-phase take forms similar to the gas-phase, and the radiation heat transfer in the bed is modeled by the two-flux model proposed initially by Gosman & Lockwood [14].

Table 2
Summary of the equations employed for packed-bed biomass combustion

			Reference
Bed volume change		$\frac{dV}{V_0\,dt}=\frac{R_2}{\rho_{sb}\rho_{wb}}\left[\frac{(\phi_0-\phi_a)-(1-\phi_a)(1-F_c)\omega_{ch}}{(1-\phi_0)(1-\phi_a)}\right]+\frac{R_3}{\rho_{sb}\rho_{vb}}\left[\frac{(\phi_0-\phi_a)-(1-\phi_a)(1-F_c)\omega_{ch}}{(1-\phi_c)(1-\phi_a)}\right]+\frac{R_4}{\rho_{sb}\rho_{ch}C}\left[\frac{(\phi_c-\phi_a)}{(1-\phi_c)(1-\phi_a)}\right]$	Goh et al. [15]
Process rate equations	Moisture evaporation	$R_2=A_p h_s(C_{w,s}-C_{w,g})$ when $T_s<100$ °C	Goh et al. [15]
		$R_2=\frac{A_p h_s'(T_s-T_s')+\varepsilon_s\sigma_s(T_{sur}^4-T_s^4)}{H_{vap}}$ when $T_s=100$ °C	Goh et al. [15]
	Devolatilisation	$R_3(1-\phi)\rho_s k_v(\nu_m-\nu)\quad k_v=A_v\exp\left(-\frac{E_v}{RT_s}\right)$	Badzioch [11]
		$C_mH_n+\frac{m}{2}O_2\rightarrow mCO+\frac{n}{2}H_2\quad R_{C_mH_n}=59\,87T_g^{0.3}\exp(-12200/T_g)C_{C_mH_n}^{0.5}C_{O_2}$	Siminski et al. [16]
	Combustion of volatiles	$CO+\frac{1}{2}O_2\rightarrow CO_2\quad R_{CO}=1.3\times10^{11}\exp(-62700/T_g)C_{CO}C_{H_2O}^{0.5}C_{O_2}^{0.5}$	Howard et al. [17]
		$H_2+\frac{1}{2}O_2\rightarrow H_2O\quad R_{H_2}=3.9\times10^{17}\exp(-20500/T_g)C_{H_2}^{0.85}C_{O_2}^{1.42}$	Hautman et al. [18]
		$R_{min}=C_{mix}\rho_g\left[150\frac{\rho_s(1-\phi)^{20}}{d_p^2\phi}+1.75\frac{\rho_s(1-\phi)^{\omega_{ch}}}{d_p\phi}\right]\min\left[\frac{C_{fuel}}{\nu_{fuel}},\frac{C_{O_2}}{\nu_{O_2}}\right]\quad R=\min[R_{kinetic},R_{min}]$	Yang et al [9]
		$C(s)+\alpha O_2\rightarrow 2(1-\alpha)CO+(2\alpha-1)CO_2\quad\frac{CO}{CO_2}2500\exp\left(-\frac{6420}{T}\right)$	Arthur [19]
	Char gasification	$R_4=A_p C_{O_2}\left(\frac{1}{k_r}+\frac{1}{k_d}\right)\quad k_r=A_r\exp\left(-\frac{E_r}{RT_s}\right)$	Gray et al. [20], Field [21]
Gas phase conservation equations	Continuity	$\frac{\partial(\rho_g\phi)}{\partial t}+\frac{\partial(\rho_g V_g\phi)}{\partial x}=S_{vg}$	Peters [22]
	Momentum	$\frac{\partial(\rho_g V_g\phi)}{\partial t}+\frac{\partial(\rho_g V_g V_g\phi)}{\partial x}=-\frac{\partial p_g}{\partial x}+F(V_g)\quad F(V_g)=$	Peters [22]
		$\begin{cases}-\frac{\alpha}{K}V_g, & \text{if } Re<10\\ -\frac{\alpha}{K}V_g-\beta_g C V_g V_g, & \text{if } Re\geq 10\end{cases}$	
	Species	$\frac{\partial(\rho_g Y_{i,g}\phi)}{\partial t}+\frac{\partial(\rho_g V_g Y_{i,g}\phi)}{\partial x}=\frac{\partial}{\partial x}\left(D_{ig}\frac{\partial(\rho_g Y_{i,g}\phi)}{\partial x}\right)+S_{Y_{i,g}}$	Peters [22]
		$D_{ig}=E^0+0.5d_pV_g$	Wakao and Kaguei [23]
	Energy	$\frac{\partial(\rho_g H_g\phi)}{\partial t}+\frac{\partial(\rho_g V_g H_g\phi)}{\partial x}=\frac{\partial}{\partial x}\left(\lambda_g\frac{\partial T_g}{\partial x}\right)+Q_{sh}$	Peters [22]
		$\lambda_g=\lambda^0+0.5d_pV_g\rho_g C_{pg}$	Wakao and Kaguei [23]
Solid phase conservation equations	Continuity	$\frac{\partial((1-\phi)\rho_s)}{\partial t}+\frac{\partial((1-\phi)\rho_s V_s)}{\partial x}=-S_{vg}$	Yang et al. [5]
		$V_s=\frac{dV}{A_0\,dt}$	Goh et al. [15]
	Species	$\frac{\partial((1-\phi)\rho_s Y_{i,s})}{\partial t}+\frac{\partial((1-\phi)\rho_s V_s Y_{i,s})}{\partial x}=-S_{Y_{i,s}}$	Yang et al. [5]
	Energy	$\frac{\partial((1-\phi)\rho_s H_s)}{\partial t}+\frac{\partial((1-\phi)\rho_s V_s H_s)}{\partial x}=\frac{\partial}{\partial x}\left(\lambda_s\frac{\partial T_s}{\partial x}\right)+\frac{\partial q_r}{\partial x}Q_{sh}$	Yang et al. [1]
Radiation heat transfer		$\frac{dI_x^+}{dx}=-(k_a+k_s)I_x^++\frac{1}{2}k_aE_b+\frac{1}{2}k_s(I_x^++I_x^-)\quad-\frac{dI_x^-}{dx}=-(k_a+k_s)I_x^-+\frac{1}{2}k_aE_b+\frac{1}{2}k_s(I_x^++I_x^-)$	Gosman & Lockwood [14]
		$k_s=0\quad k_a=-\frac{1}{x}\ln(\phi)$	Shin & Choi [24]

Boundary conditions:
at the bed bottom ($x=0$),

$T_g=300$ K; $O_2=21$ vol%; $N_2=79$ vol%; $V_g=0.1, 0.14, 0.19, 0.23$ kg m^{-2} s^{-1}; $\partial T_g/\partial x=0$; $V_s=0$; $\partial Y_m/\partial x=0$;

at the bed top ($x=L_b$),

$\partial T_g/\partial x=0$; $\partial Y_g/\partial x=0$; $\partial V_g/\partial x=0$; $\partial T_s/\partial x=0$; $\partial Y_m/\partial x=0$; $\partial V_s/\partial x=0$;

at $t=0$,

$T_g=300$ K; $O_2=21$ vol%; $N2=79$ vol%; $V_g=0.1, 0.14, 0.19, 0.23$ kg m^{-2} s^{-1}; $T_s=300$ K; $V_s=0$; $Y_m=Y_{m,0}$; $f=0.35, 0.45, 0.55, 0.65, 0.75$;

The over-bed radiation source is set at 1123 K with an emissivity of 0.8. The primary air velocity and initial bed porosity take multiple values to cover the range of designated variation of operating parameters in this study.

The basic parameters used for the base or reference case are M=7.5%, VM=78%, FC=12.5, ASH=2%, C=46.9%, H=6.2%, O=37.4%, LCV=17.5 MJ kg^{-1}, d_p=10 mm, $\phi=0.65$, $\rho_{sb}=290$ kg m^{-3} and $L_b=410$ mm. For the variation cases, one of these parameters is varied while keeping the others the same. The four primary air levels of 0.1, 0.14, 0.19 and 0.23 kg m^{-2} s^{-1} are designated as PA1, PA2, PA3 and PA4, respectively.

The mathematical equations are solved by FLIC code developed by Yang et al. [9].

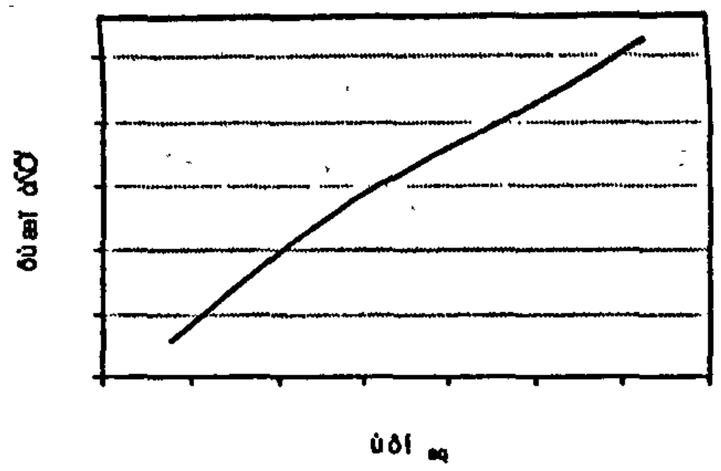

Fig. 2. Relationship between LCV and equivalence ratio of C and H to O in biomass fuel.

3. Results

3.1. Effect of fuel LCV

The LCV of biomass depends on the contents of moisture and ash as well as ratios of the three major elemental components, C, H and O. High moisture and high ash levels reduce the biomass LCV. Here moisture and ash in biomass are fixed at the level of the base case but the relative proportions of the three major elemental components are changed to obtain a variation in the biomass LCV. A parameter, CHO_{eq}, is used to reflect the equivalent (or stoichiometric) ratio of the combustible elements, C and H, to the non-combustible element O, based on the complete reactions of $C+O_2=CO_2$ and $H_2+\frac{1}{2}O_2=H_2O$:

$$CHO_{eq}=(0.5\times C/12+2.0\times H/1.0)/(O/16) \quad (2)$$

To obtain a variation in CHO_{eq}, the ratio of C to H is fixed at the value of base case while O is varied in a certain range. The LCV of fuel is estimated as

$$LCV=33.9\,C+10.3\,H-10.9\,O-2.5 \quad (MJ\,kg^{-1}) \quad (3)$$

where the units of C, H, O and M are mass fractions.

Fig. 2 shows the relationship between LCV and the equivalence ratio of combined C and H to O in biomass fuel.

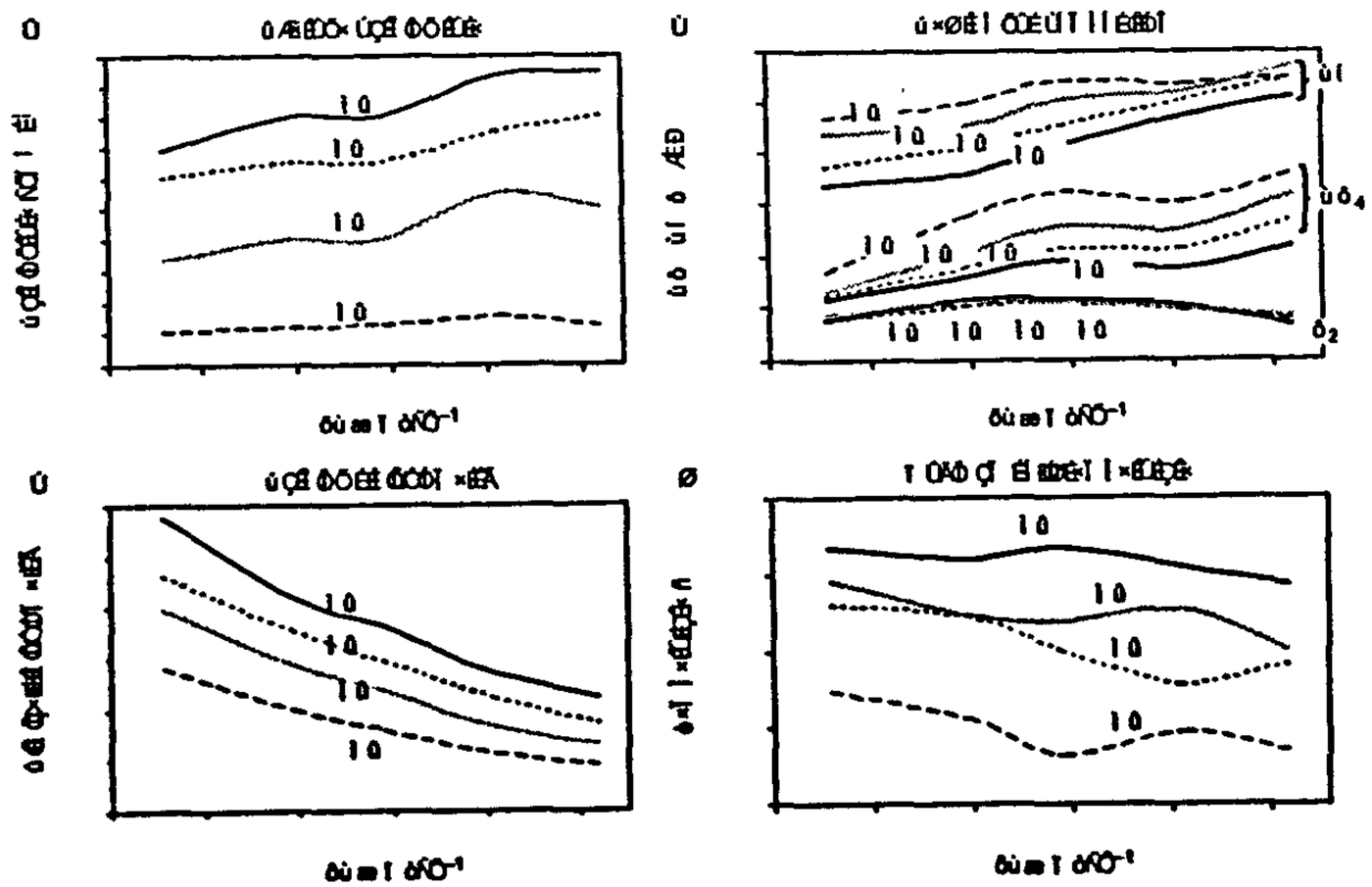

Fig. 3. Effect of fuel LCV at different primary air velocity levels: (a) average burning rate; (b) combustion stoichiometry; (c) gas composition at the bed top; (d) maximum solid temperature.

It is seen that the fuel LCV varies from 15 to 24.5 MJ kg^{-1} as CHO_{eq} covers a range from 4.8 to 10.5 and the LCV is roughly linearly proportional to the level of CHO_{eq} in fuel.

Fig. 3(a) demonstrates the calculated average burning rate vs. the fuel LCV. The average burning rate is obtained by dividing the total mass loss with the total time-span of combustion. It is seen that at a low primary air flow rate (PA1), the effect of LCV on the burning rate is quite insignificant, although the maximum is obtained around 22 MJ kg^{-1}. For a higher level of primary air flow (PA2), however, there is a slight increase in the average burning rate as LCV increases from 15 to 18 MJ kg^{-1}. The burning rate maintains virtually the same for LCV from 18 to 20 MJ kg^{-1} and then increases again for LCV from 20 to 23 MJ kg^{-1}. But for further higher LCVs, the burning rate displays a falling trend.

For the other two primary air flow levels (PA3 and PA4), the trend is similar to the situation of PA2, except that there is a continuous increase in the burning rate as the LCV rises beyond 20 MJ kg^{-1}.

Fig. 3(b) demonstrates the average air-to-fuel stoichiometric ratio as a function of LCV at the four primary airflow levels. The average value is taken over the whole time-span of combustion. The air-to-fuel stoichiometric ratio is the actual primary air supply to the packed bed compared to the theoretical air required to burn completely the combustible materials released during basically the pyrolysis process. The trend is clear: as the fuel LCV increases, the air-to-fuel stoichiometric ratio decreases and the burning process becomes more fuel-rich. At the primary air velocity level of PA1, for instance, the combustion stoichiometry drops from 0.48 to 0.28 as the LCV rises from 15 to 24.3 MJ kg^{-1}.

The burning process in a packed bed typically consists of three stages: the initial stage of ignition, the primary stage of stable combustion and the final stage of char burn-out [1,5]. Fig. 3(c) shows the volumetric fractions of CH_4, CO and H_2 in the flue gases exiting the bed top during the primary stage of stable combustion, which reflects the main characteristics of biomass combustion. For CO, the general trend is increasing volume fraction as the LCV increases, especially at high levels of primary air velocity. However, at low primary air velocity (PA1), there is no noticeable change of bed-top CO level when the LCV is increased beyond 20 MJ kg^{-1}. For CH_4, the volume fraction increases initially as the LCV increases until 20 MJ kg^{-1}. Then the CH_4 level in the bed-top flue gases either remains constant at high primary air velocity (PA3 and PA4) or slightly drops at low primary air velocity (PA1 and PA2) in the range of 20–22 MJ kg^{-1}. Further increase in the LCV level, however, results in modest rise in the bed-top CH_4 level.

A quite different trend is obtained for H_2 which shows a slight variation in H_2 over the whole range of the change in LCV. The maximum is obtained at 19 MJ kg^{-1}. The primary air velocity is also found having very little influence on the H_2 level.

Fig. 3(d) presents the maximum solid temperature as a function of the fuel LCV at different primary air velocities. When the value of LCV is below 18 MJ kg^{-1}, an increase in LCV causes a fall in the maximum solid temperature (slight fall at high primary air velocity of PA4). When the LCV is greater than 18 MJ kg^{-1}, different trends are observed for different primary air velocity levels. For a low primary air velocity of PA1, as the LCV increases beyond 18 MJ kg^{-1}, a further fall in the maximum solid temperature is observed until LCV is around 20 MJ kg^{-1}, followed then by a rise and fall in the flame temperature. For the primary air velocity level of PA2, the maximum solid temperature further drops to a minimum point around 22 MJ kg^{-1}, and then rises again as the LCV increases from 18 to 24 MJ kg^{-1}. For the primary air velocity of PA3, there is not much change in the maximum solid temperature over the LCV range of 18–22 MJ kg^{-1}. But, when the LCV is increased further beyond 22 MJ kg^{-1}, the solid temperature falls; for the high primary air velocity of PA4, there is a slight fall in the maximum solid temperature as the LCV increases from 19 to 24 MJ kg^{-1}.

3.2. Effect of particle size

The particle size covered in the calculations ranges from 2 to 35 mm. Fig. 4(a) shows the burning rate as a function of particle size at different primary air velocities. Generally, larger particle size results in lower burning rate. For instance, 5 mm particles have a burning rate of 0.06 kg m^{-2} s^{-1} at a primary air velocity of PA3, which is 1.5 times of the burning rate with 30 mm particles at the same primary air velocity. One exception is for the particle sizes of 4 and 5 mm at the primary air velocity PA2 where the 5 mm particles demonstrate a higher burning rate than the 4 mm particles.

Fig. 4(b) shows the combustion stoichiometry as a function of particle size. Generally, larger-size particles result in a higher air-to-fuel stoichiometric ratio or less fuel-rich combustion. For instance, 5 mm particles have an air-to-fuel stoichiometric ratio of 0.49 at PA3 compared to the ratio being 0.74 with 30 mm particles at the same conditions. One exception is for particle sizes of 4 and 5 mm at the primary air velocities PA2 and PA3 where the 5 mm particles produce a slightly fuel-richer condition than the 4 mm particles.

Fig. 4(c) shows the bed-top gas composition as a function of particle size. For CO, the volumetric percentage ranges from around 12 to 17% and larger particles have lower CO levels at the bed top; for CH_4, the volumetric percentage ranges from 5 to 9% and a noticeable change in the relationship with the particle size is only obtained for particles smaller than 5 mm at PA1, for particles smaller than 10 mm at PA2 and for particles smaller than 15 mm at PA3. Generally, increasing particle size reduces the methane concentration at the bed top.

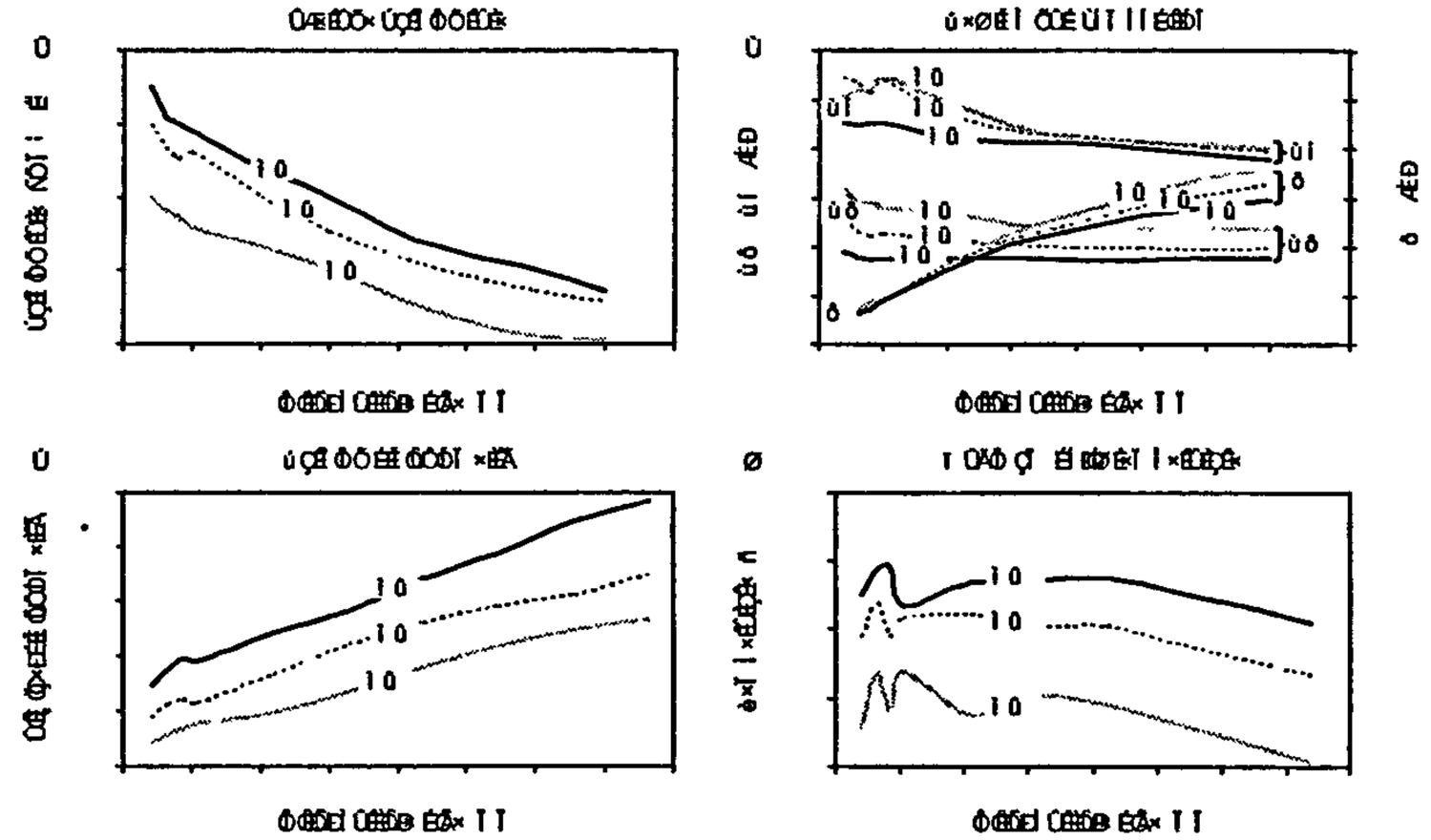

Fig. 4. Effect of particle size: (a) average burning rate, (b) combustion stoichiometry, (c) gas composition at the bed top; (d) maximum solid temperature.

For H_2, the volumetric percentage ranges from 1.5 to 7% and generally an increase in particle size results in higher hydrogen concentration at the bed top.

The primary air velocity has negligible effect on H_2 when particles are smaller than 10 mm. It also has negligible effect on CO when particle size is greater than 20 mm.

Fig. 4(d) shows the maximum solid temperature inside the bed as a function of particle size. It is seen that at PA1 the maximum solid temperature increases as particle size increases from 2 to 3 mm, then drops down 30 K at 4 mm, rises again at 5 mm to the maximum level of 1270 K. Beyond 5 mm, the general trend is decreasing solid temperature as particle size increases. At 35 mm, the maximum solid temperature is 70 K lower than the peak value obtained at 5 mm.

At PA2, the maximum solid temperature pattern in relation to the particle size is similar to the case of PA1, except that the absolute temperature level is about 50 K higher on the whole.

At PA3, the maximum solid temperature is obtained at 4 mm (1350 K) but falls to 1320 K at 5 mm. Over the range of 10–20 mm, the maximum solid temperature maintains a constant level of 1335 K.

3.3. Effect of material density

The material density covers a range from <100 to 2300 kg m^{-3}, with the light end being possibly dry straw and the heavy end, biomass pellets. Fig. 5(a) shows average burning rate as a function of biomass material density at three primary air velocity levels. At low primary air velocity (PA1), the burning rate maintains a more or less constant level between the material densities 400–800 kg m^{-3}, and then falls roughly linearly as material density rises from 800 to 1400 kg m^{-3}. The burning rate keeps constant again between densities 1400 and 1700 kg m^{-3} then falls as the material density increases further.

The situations with primary air velocities of PA1 and PA2 follow a similar pattern, with a drop in burning rate as the material density rises in the density ranges of 800–1400 kg m^{-3} and beyond 1800 kg m^{-3}. The burning rate, otherwise, remains roughly constant in relation to the material density variation.

It is also noted that material with a density of 100 kg m^{-3} produces a lower burning rate than material with a density of 200 kg m^{-3}.

Fig. 5(b) demonstrates the combustion stoichiometry as a function of material density. At low primary air velocity (PA1), the obtained air-to-fuel stoichiometric ratio ranges from 0.4 to 0.5, with a positively linear relationship between the combustion stoichiometry and the material density over the density range from 800 to 1400 kg m^{-3} and beyond 1800 kg m^{-3}. At primary air velocity levels PA2 and PA3, the pattern of change in combustion stoichiometry with increasing material density follows a similar trend to the situation of PA1, except that the whole air-to-fuel stoichiometric ratio be raised roughly 0.08 and 0.16 higher, respectively.

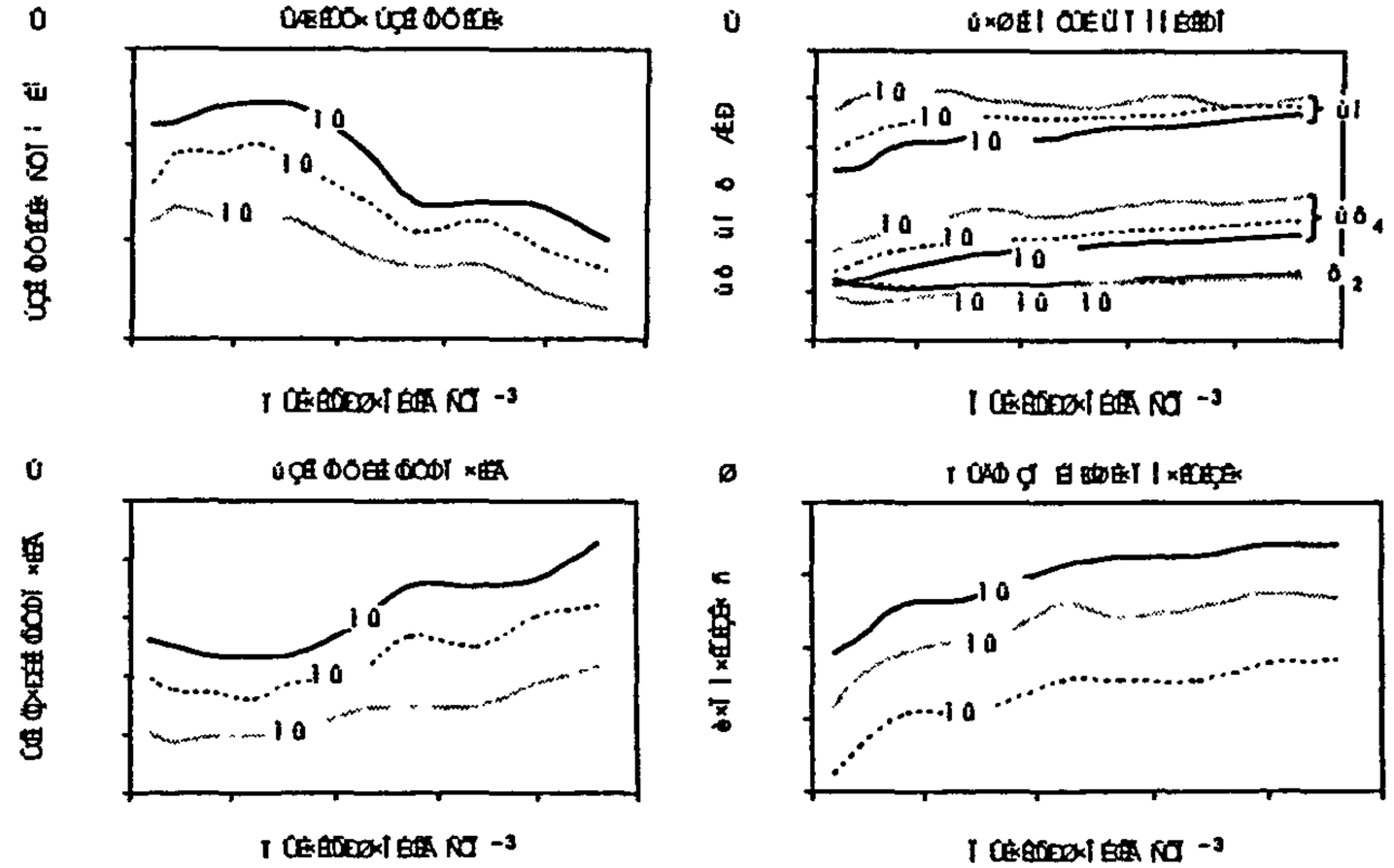

Fig. 5. Effect of material density: (a) average burning rate; (b) combustion stoichiometry; (c) gas composition at the bed top; (d) maximum solid temperature.

Fig. 5(c) shows the bed-top gas composition as a function of material density in the packed bed. For CO at PA1, the volumetric percentage varies in a narrow range of 14.5–15.5% as the material density rises from 100 to 2300 kg m^{-3}; for CO at PA2, the volumetric percentage rises from 12 to 14% as the material density increases from 100 to 600 kg m^{-3}, but only small change follows when the density is further increased; for CO at PA3, the trend of change is similar to the situation at PA2, except that the level is around 1.2% lower on the whole.

In general, the CH_4 concentration in the flue gases exiting the bed top increases with increase in the fuel material density, especially when the density is below 800 kg m^{-3}.

H_2 concentration at the bed top only shows a minor rise as the material density increases from the minimum to the maximum.

Fig. 5(d) presents the maximum solid temperature inside the bed as the fuel material density increases. Generally, the maximum solid temperature increases when the fuel material has a higher density. The temperature with the heaviest fuel is around 80 K higher than that with the lightest fuel at the same primary air velocity.

3.4. Effect of bed porosity

Bed porosity depends on a number of factors, including particle size distribution, particle shape, shaking or pressing of the bed, etc. A bed with a low porosity is called a compact bed and a bed with a high porosity is called a loose bed. In this section, the initial bed porosity is artificially changed while keeping all the other bed parameters the same. The porosity covers a range of 0.35–0.75.

Fig. 6(a) demonstrates the effect of bed porosity on the burning rate of the bed. It is seen that the effect of bed porosity depends on the level of primary air velocity. At low primary air velocities (PA1 and PA2), the general trend is decreasing burning rate as the bed porosity increases, though in some ranges the burning rate may maintain a more or less constant level (porosity 0.5–0.65 for PA1 and 0.65 onwards for PA2). At increased primary air velocity (PA3), the maximum burning rate is obtained between bed porosity of 0.45–0.55 and either a looser or denser bed would results in a lower burning rate. However, similar to the situation of PA2, the burning rate keeps constant as the bed porosity increases beyond 0.65.

Fig. 6(b) demonstrates the combustion stoichiometry against the initial bed porosity. Generally, the air-to-fuel stoichiometric ratio increases as the bed porosity increases. But the air-to-fuel ratio keeps constant in some part along the range, i.e. bed porosity from 0.5 to 0.65 for PA1 and from 0.65 onwards for PA2 and PA3.

Fig. 6(c) shows the bed-top gas composition as a function of bed porosity. For CO at PA1, very little change in its level is shown for the whole range of porosity variation; for CO at PA2, the volumetric level in the flue gases exiting the bed top falls in the range of 0.45–0.6 of the bed porosity, otherwise, it keeps a constant value; for CO at PA3,

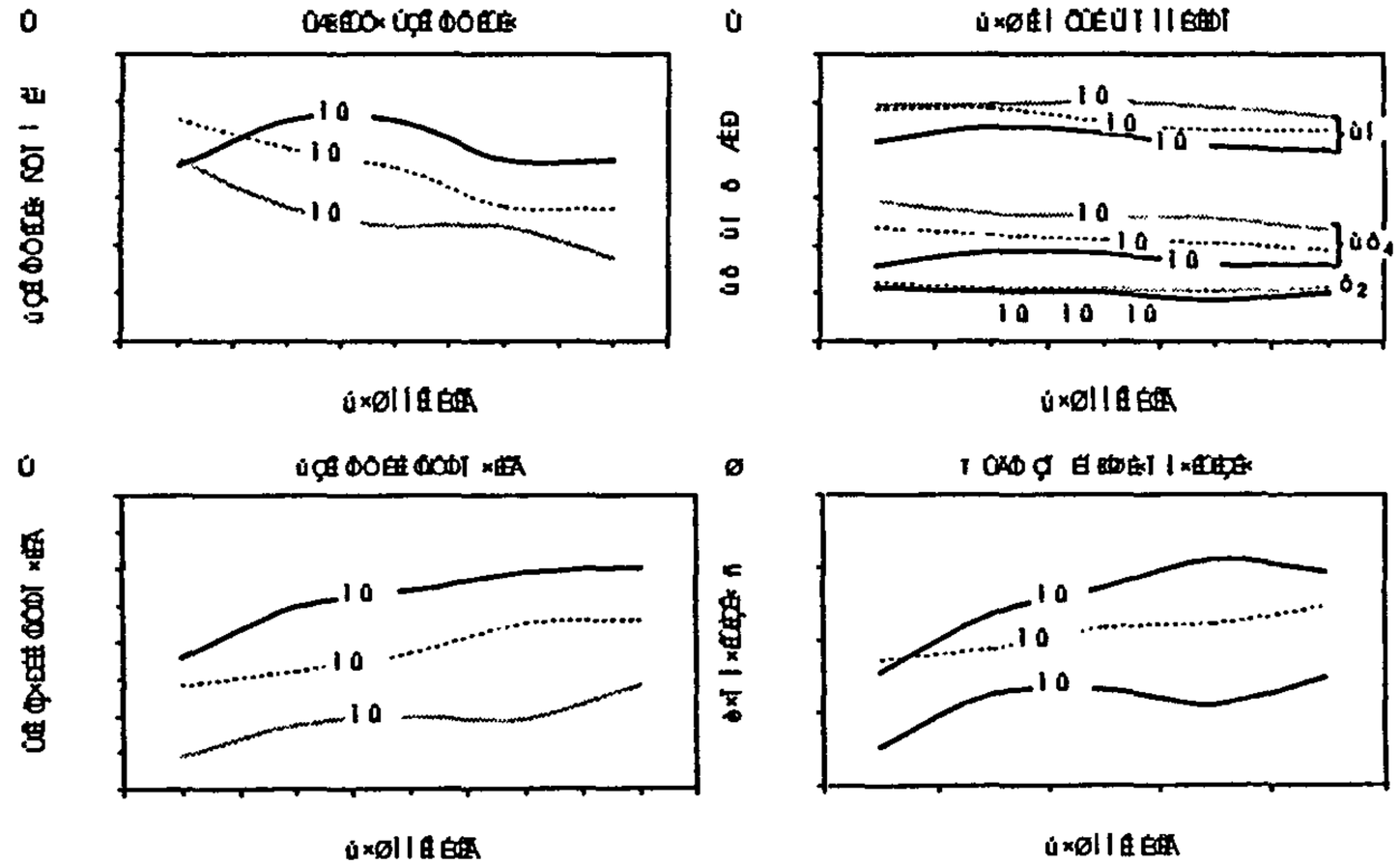

Fig. 6. Effect of bed porosity: (a) average burning rate; (b) combustion stoichiometry; (c) gas composition at the bed top; (d) maximum solid temperature.

the maximum level is obtained around a bed porosity of 0.45 and either a looser or denser bed results in a lower CO concentration at the bed top.

For CH_4 at PA1 and PA2, the general trend is reducing concentration level as the bed porosity increases; for CH_4 at PA3, the maximum level is obtained around the bed porosity of 0.5.

It is also seen that the H_2 concentration is not affected by either the bed porosity or the primary air velocity.

Fig. 6(d) demonstrates the maximum solid temperature against porosity variation. The pattern of variation depends on the primary air velocity. At the low air velocity of PA1, the maximum solid temperature rises as the bed porosity rises from 0.35 to 0.45, but keeps constant from 0.45 to 0.55, falls from 0.55 to 0.65 and then rises again from 0.65 onwards. At PA2, however, a continuous increase in the solid temperature is obtained as the bed porosity increases from the minimum to the maximum. For the situation of PA3, the solid temperature increases with increasing bed porosity until the porosity reaches 0.65, followed then by a fall in the maximum solid temperature as the bed porosity further increases.

4. Discussion and validation against experiments

The effect of moisture content in fuel and the fuel devolatilisation rate on packed-bed solid combustion has been studied earlier by Yang et al. [1,5]. The previous studies have shown that moisture content in fuel has a significant effect on the fuel burning and a very dry fuel can burn up to four times faster than does a very wet fuel. These experimental studies also showed that the kinetic rate of fuel devolatilisation affects the ignition time at high fuel-moisture levels but the effect was less noticeable for dry fuels. For the mass loss rate after the fuel ignition, the kinetic rate of fuel devolatilisation had the opposite effect, i.e. the mass loss rate is only significantly affected by fuel devolatilisation for dry fuels.

The current investigation contributes to the expansion of those previous studies by including more parameters. There are also two aspects different from previous studies: (1) the burning rate presented in this work is the averaged value over the whole combustion period, including ignition, volatile release and final char burnout, while most of the previous works [1–6] presented the burning rate as the gradient of an assumed linear section on the mass-loss curve, which excludes the initial ignition and final char burnout stages and does not reflect the whole combustion process; (2) the maximum solid temperature in the bed is now presented which differs from the traditionally measured maximum flame temperature. The latter cannot distinguish between the gas phase and the solid phase and the solid temperature was rarely addressed before. The mathematical model adopted in this work solves both the gaseous and solid temperature.

The following sections present an interpretation of the results obtained in the current work, and experimental data are presented for comparison wherever this is possible.

4.1. The effect of biomass LCV

The variation in LCV was achieved by varying the mass ratio of combustible elements (C and H) to the oxygen (O) in the fuel, so the effect of LCV is mainly through the change in air-to-fuel stoichiometry as illustrated in Fig. 3(b). In the range of primary air velocity of interest (0.1–0.23 kg $m^{-2} s^{-1}$), all the combustion of the investigated fuels occurs at the fuel-rich side and an increase in LCV makes the combustion more fuel-rich and hence the solid temperature in the flame front would decrease (Fig. 3(d)) and the CO and H_2 concentrations in the bed increase (Fig. 3(c)). This explains the insensitivity of the burning rate to the increase in LCV at low primary air velocity (0.1 kg $m^{-2} s^{-1}$). On the other hand, an increase in LCV results in locally stoichiometric combustion of the released volatile fuels occurring earlier in the flame front and nearer to the moisture evaporation front. The local solid temperature would be enhanced in the region of moisture evaporation and early devolatilisation and the rates of these two processes subsequently increase. This factor becomes dominant at higher primary air velocities where a positive relationship between LCV and the burning rate is more obvious (Fig. 3(a)).

The H_2 concentration in the flue gases exiting the bed top depends on the balance of H_2 production and consumption. The H_2 concentration is rather insensitive to the variation in primary air velocity because the production and consumption of H_2 keep more or less in balance as the primary air flow rate varies. The decrease in H_2 concentration at high LCV can be explained by incomplete oxidisation of CH_4 producing CO and H_2 as the burning goes fuel-richer on the whole.

4.2. The effect of particle size

Particle size affects the combustion processes in the bed in four different aspects. First is the two-phase heat and mass transfer between the gas and solid. These convective processes occur at the particle external surfaces and the rates are approximately inversely proportional to the particle diameter. Therefore, particles of a smaller size can enhance the moisture evaporation and char burning rates in the bed. On the other hand, the hot solids may be cooled down by the fresh primary air flow which enters the bed at room temperature.

The second effect is on the radiation heat transfer where the bed absorption of radiation flux is inversely proportional to particle diameter. This means that a bed of smaller particles absorbs radiation more quickly. But the radiation flux, on the other hand, is less absorbed by a packing of larger particles and hence penetrates a longer distance in the bed. This can produce a thicker flame front in the bed and affects the temperature and gas concentration profiles as a consequence.

The third effect is on the turbulent dispersion of energy and gas species in the packed bed. Both thermal and fluid dispersion coefficients are proportional to particle diameter. Larger particles produce larger-scale turbulence in the local bed structure and facilitate the cross-flow and inflow mixing in the gas phase. As a result, the reaction zone in the bed can be thicker for larger particles and thinner for smaller particles.

The fourth effect is on the burning rate of volatile gaseous fuel both in the voids of the bed and in the immediate area above the bed. The process is basically diffusion-controlled. As indicated in the equation summary (Table 2), the mixing rate of the fuel gases with air flow from under the grate is a function of particle size and small particles produce a higher rate (the other conditions being the same) and hence higher combustion intensity in the gas phase.

The obtained results shown in Fig. 4 are just the balanced results of the above factors. Generally, larger particles produce a slower burning rate and lower concentration of CO and CH_4 at the bed top. But H_2 concentration has the opposite trend, i.e. increasing particle size producing a higher H_2 level in the flue gases exiting the bed. This is because the oxidization rate of H_2 decreases with larger particle sizes.

The numerical results for the effect of particle size have been validated against experiments as shown in Fig. 7 for the mass-loss history. Four sizes of pinewood cubes were fired in a stationary packed-bed with an initial height of around 400 mm and primary air velocity of 0.1 kg $m^{-2} s^{-1}$ at an inlet temperature of 300 K (Part I). The bed was ignited at the top by an over-fire pilot gas burner and the primary air was supplied to the bed through the grate at the bottom of the bed. The model calculations generally match the measurements and accurately predict the trend as particle size increases. Both the predictions and

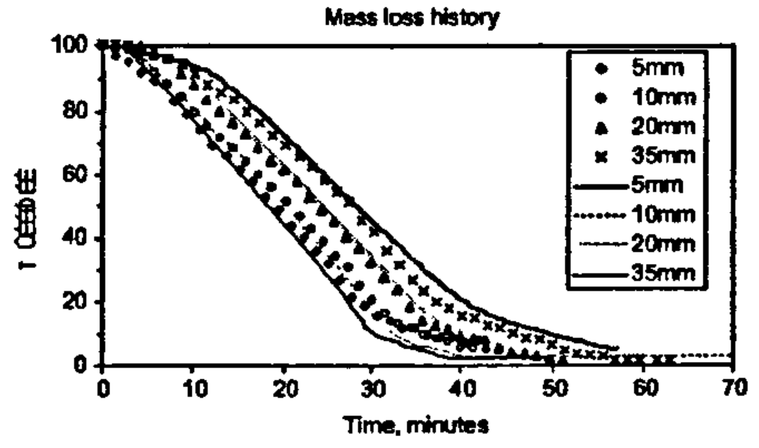

Fig. 7. Particle size effect—mass loss history in a stationary packed bed. Line: model prediction; symbols: measurements of this work (fuel: pinewood; primary air velocity: 0.1 kg $m^{-2} s^{-1}$ at 20 °C)

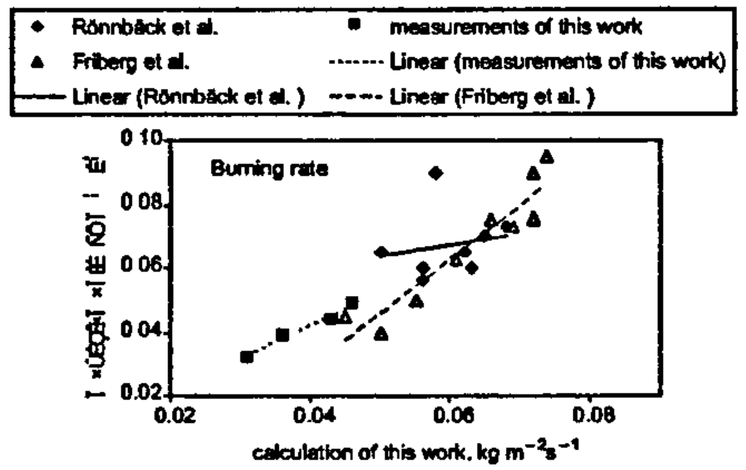

Fig. 8. Particle size effect—comparison of the model calculations of the burning rate to measurements from different sources. Symbols represent the measurements and lines represent the correlation between model calculations and the measurements.

measurements show the three periods in the pinewood combustion, the initial ignition stage followed by the constant combustion stage and the final char-burnout. The rate of the latter slows down as the combustion approaches completion.

The results obtained in this work are consistent with the measurements of Friberg and Blasiak [8] which demonstrated decreasing average burning rate as particles size increased. As mentioned above, Peters [7] reported the maximum ignition rate was obtained at 15 mm in the size range of 5–25 mm where the 5 mm particles produced no flame because the bed could not be ignited at the tested air velocity. Contrary to other researchers' finding, Rönnbäck et al. [6] reported increased ignition speed for larger particles in the size range of 8–34 mm.

Fig. 8 makes a comparison between the model calculations and the measurements of the burning rate from both the current work and other researchers. When compared to the measurements of this work, the average burning rate is used and when compared to the measurements from literature, the burning rate in the constant stage or the maximum rate is used. The correlation lines between the calculations and measurements are also drawn. The R^2 value of those correlations is 0.98 between the calculations and the measurements of this work, 0.88 between the calculations and the measurements of Friberg and Blasiak [8] and 0.05 for between the calculations and the measurements of Rönnbäck et al. [6]. The poor agreement between the calculations and the results of Rönnbäck et al. is possibly due to the particle shape effect (wood cylinders were used) which has not been included into this study and needs to be investigated further. The measurements reported by Peters [7] cannot be directly compared with the calculations because the fuels used in the measurements might have much higher moisture content, but the general trend is in line with the current calculations if the moisture effect is taken into account.

4.3. The effect of material density

For fuels of heavy material, more combustible mass is packed in a smaller volume and the fuel material density mainly affects the reaction zone thickness. Denser material tends to produce a thinner reaction zone, which reduces the residence time of the reacting gases. More heat is also required to heat up a specific volume of bed to the ignition temperature. Light material, on the other hand, tends to lose temperature easily by radiation as it has a smaller heat capacity per unit of volume. The combustion stoichiometry determines the bed temperature and a denser material has a higher maximum bed temperature as it has a less fuel-rich combustion condition. The concentrations of CO, CH_4 and H_2 in the flue gases exiting from the bed top increase as the material density increases due to the shorter residence time of the gases.

4.4. The effect of bed porosity

Bigger voids in the bed facilitate radiation penetration in the bed, but reduce mixing between the released volatile gases and the under-grate air flow and hence the gas-phase burning intensity. Void fraction also changes the gas-phase

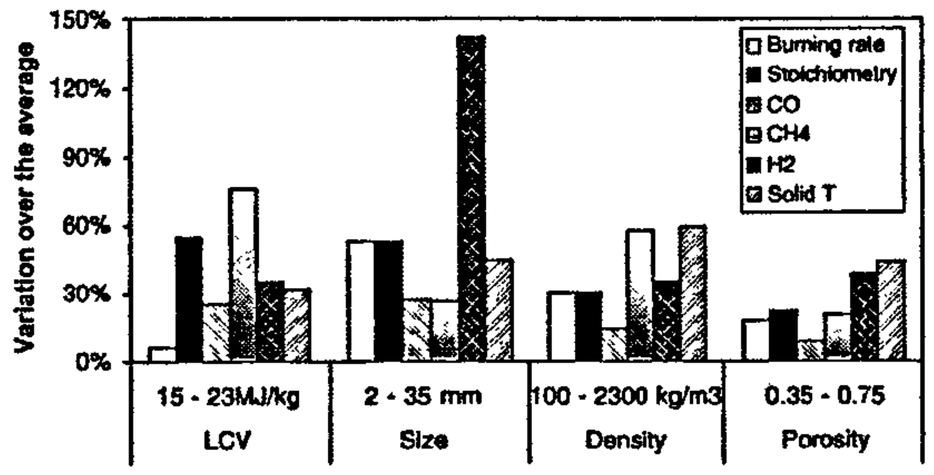

Fig. 9. Summary of the effects of different fuel properties.

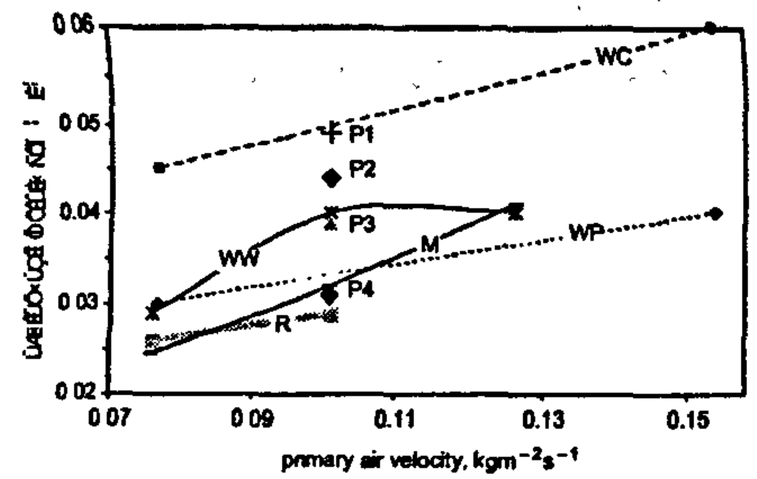

Fig. 10. Experimental measurements of burning rate for different type of fuels. Friberg and Blasiak [8]: WP: wood pellets (L=30 mm, $\varnothing$=6 mm); WW: wood chips (L=4–30 mm, $\varnothing$=2–5 mm). This work: R: residual deduced fuel (L=30–50 mm, $\varnothing$=7 mm); M. miscanthus pellets (L=5–8 mm, $\varnothing$=3 mm); WW: willow chips (L=10–40 mm, $\varnothing$=4–8 mm); P1: pinewood cubes (5 mm); P2: pinewood cubes (10 mm); P3: pinewood cubes (20 mm); P4 pinewood cubes (35 mm).

residence time in the bed as the bed becomes loose and bulky. At low air velocity, gas-phase mixing is the controlling factor, and the higher the bed porosity, the lower the gas-phase combustion rate; at high air velocity, radiation penetration as well as residence time of gases become important and the best results are around 0.45–0.55. But for a very compact bed and a very light material, local fluidisation or channelling can occur which will alter the trend. A slight decrease in bed-top CO and CH_4 at high bed porosity is the balanced result between reduced mass-loss rate and the slower reaction (mixing) rate of those combustible gases with primary air.

A summary of the effects of different fuel properties is illustrated in Fig. 9. It shows the relative variations in percentage of the six burning parameters (average burning rate, combustion stoichiometry, CO, CH_4 and H_2 in the flue gases exiting the bed top and the maximum solid temperature) around their average values as the four investigated fuel properties are varied over their designated ranges, respectively. It is seen that for average burning rate, the particle size has the greatest effect followed by fuel density, while LCV has the smallest effect; the combustion stoichiometry is most affected by both LCV and fuel size, while bed porosity has the smallest influence and a similar conclusion is obtained for CO; for CH_4, fuel LCV and material density are found to have the greatest effect and bed porosity has the least; for H_2, fuel size has a remarkably strong effect compared to the other three fuel properties; for the solid temperature, all the four properties have a noticeable effect with material density having the greatest.

4.5. Application to practical systems

The above results obtained in this work can be used to explain or understand the performance of real systems under similar conditions. Fig. 10 shows the experimental measurements of the burning rate with nine different fuels from both this work and Friberg and Blasiak [8]. The fuels included chips and pellets of a mixture of pine and spruce, pinewood cubes, willow chips, miscanthus pellets and refuse derived fuel (RDF) pellets. For pinewood cubes, the size ranged from 5 to 35 mm and a fixed primary air velocity was employed. For fuel LCV, the order from the lowest to highest is miscathus (16 MJ kg^{-1}), wood mixture (17 MJ kg^{-1}), willow wood (18 MJ kg^{-1}), pinewood (19 MJ kg^{-1}) and RDF (21 MJ kg^{-1}). For bed porosity, all the fuels are estimated to be the same around 0.55–0.6. For particle size and material density, the orders are shown in Table 3.

The general trend obtained from calculations show that higher LCV, smaller particle sizes and lower material density all favour a higher burning rate (see Figs. 3(a), 4(a) and 5(a)) and lower bed porosity favours a higher burning rate at low primary air velocity but the optimum is reached around 0.5 when primary air flow rate is high (see Fig. 6(a)). The calculations also show that among the above four fuel properties, particle size has the strongest effect, followed by material density. Porosity is the second least significant and LCV has the least effect. So roughly, the burning rate is

Table 3
Burning rate order of nine different fuels deduced from calculation results

Fuel type	Size	Size order	Density (est.) (kg m^{-3})	Density order	Deduced burning rate order
Miscanthus pellets	$\varnothing$ = 3 mm, L = 5–8 mm	1	1650	2	5
Wood mixture chips	$\varnothing$ = 2–5 mm, L = 4–30 mm	2	700	1	1
Pinewood cubes	5 mm × 5 mm × 5 mm	2	700	1	1
Pinewood cubes	10 mm × 10 mm × 10 mm	3	700	1	2
Willow chips	$\varnothing$ = 4–8 mm, L = 10–40 mm	4	450	1	3
Wood mixture pellets	$\varnothing$ = 6 mm, L = 30 mm	5	1650	2	6
RDF	$\varnothing$ = 7 mm, L = 30–50 mm	6	1800	3	8
Pinewood cubes	20 mm × 20 mm × 20 mm	7	700	1	4
Pinewood cubes	35 mm × 35 mm × 35 mm	8	700	1	7

Note that (1) the order is from small to large for size and density and high to low for burning rate, (2) densities of 450 and 700 kg m^{-3} are considered at the same level from the results shown in Fig. 5(a).

determined firstly by the fuel size and secondly by the material density.

Based on the above theoretical conclusion, Table 3 shows the deduced burning rate order of the nine different fuels. Wood mixture chips (symbol WC) and the pinewood cubes of 5 mm (symbol P1) come to the top because these two fuels have the smallest sizes (apart from miscanthus pellets) and the lowest material density. Miscanthus pellets are the smallest but have a very high density and the obtained burning rate is listed number 5 of the nine fuels. The RDF pellets come to the bottom of the list due to their highest material density and a relatively large size. For other fuels, the level of the burning rate depends on the combination of particle size and material density.

The deduced results in Table 3 match the experimental results shown in Fig. 10 and demonstrate the validity of the theoretical calculations. This provides great help in understanding and explaining the performance of practical systems. It also helps designers as well researchers predict the rough burning characteristics of a new fuel. Nevertheless, the conclusions in this study are still qualitative and care must be taken when using them in very different situations. The current work also did not carry out a multi-variable study where all the concerned parameters are varied at the same time. This would result in huge computation tasks that are beyond the ability of current human and machine resources.

5. Conclusions

A numerical method has been employed to simulate the effects of the four fuel properties on the burning characteristics of biomass in packed bed systems. The major conclusions are summarised in the following:

(1) average burning rate is mostly influenced by fuel size and smaller fuels result in higher combustion rate due to increased reacting surface area and enhanced gas-phase mixing in the bed;
(2) combustion stoichiometry is equally influenced by fuel LCV and size as a consequence of variation in burning rate as well as the mass ratio of combustible elements (C and H) to the oxygen (O) in the fuel; higher LCV, smaller particle size, lower material density and a more compact bed all favour a more fuel-rich combustion as a general trend;
(3) for the solid-phase temperature, material density has the strongest influence and a denser material has a higher maximum bed temperature as it results in a less fuel-rich combustion condition;
(4) for CO concentration in the flue gases exiting the bed top, both LCV and particle size have the strongest effect due to change in combustion stoichiometry; higher LCV and smaller particle size result in high CO;
(5) for CH_4 concentration in the flue gases exiting the bed top, both LCV and material density have the dominant influence; denser material tends to produce a thinner reaction region and reduce the residence time of the reacting gases so that less CH_4 is burnt;
(6) particle size has the greatest effect on the H_2 concentration in the bed; bsigger particles produce a higher H_2 level in the flue gases exiting the bed top; this is because the oxidization rate of H_2 deceases with larger particle sizes.
(7) calculated results agreed qualitatively with experiments and explain satisfactorily the observed performance of nine different fuels.

Acknowledgements

The authors thank the UK Engineering and Physical Sciences Research Council (EPSRC) for the financial support of this project.

References

[1] Yang YB, Yamauchi H, Shanfi VN, Swithenbank J. Effect of moisture on the combustion of biomass and simulated solid waste in a packed bed. J Inst Energy 2003;76:105–15.
[2] Yang YB, Swithenbank J, Shanfi VN. Effect of air flow rate and fuel moisture on the burning behaviours of biomass and simulated solid waste in a packed bed. Fuel 2004;83:1553–62.
[3] Thunman H, Leckner B. Ignition and propagation of a reaction front in cross-current bed combustion of wet biofuels. Fuel 2001;80:473–81.
[4] Gort, R. On the propagation of a reaction front in a packed bed: thermal conversion of municipal waste and biomass. Academic Dissertation, University of Twente; 1995.
[5] Yang YB, Sharifi VN, Swithenbank J. Effects of fuel devolatilisation on the combustion of wood chips and incineration of simulated municipal solid wastes in a packed bed. Fuel 2003;82:2205–21.
[6] Rönnbäck M, Axell M, Gustavsson L, Thunman H, Leckner Bo. Combustion processes in a biomass fuel bed-experimental results. Progress in Thermochemical Biomass Conversion, Tyrol, Austria; 17–22 September, 2000.
[7] Peters B. Thermal conversion of solid fuels. Southampton: WIT Press; 2003.
[8] Friberg R, Blasiak W. Measurements of mass flux and stoichiometry of conversion gas from three different wood fuels as function of volume flux of primary air in packed bed combustion. Biomass Bioenergy 2002;23:189–208.
[9] Yang YB, Goh YR, Zakaria R, Nasserzadeh V, Swithenbank J. Mathematical modeling of MSW incineration on a travelling bed. Waste Mgmt 2002;22:369–80.
[10] Thunman H. Principles and models of solid fuel combustion. PhD Thesis. Chalmers University of Technology, Göteborg, Sweeden; 2001.
[11] Badzioch S, Hawksley PGW, Peter CW. Kinetics of thermal decomposition of pulverized coal particles. Ind Eng Chem Process Des Develop 1970;9:521–30.
[12] Alves SS, Figueiredo JL. Pyrolysis kinetics of lignocellulosic materials by multistage isothermal thermo-gravimetry. J Analyt Appl Pyrolysis 1988;13:123–34.

[13] Smoot LD, Pratt DT. Pulverised-coal combustion and gasification: theory and applications for continuous flow processes. London: Plenum Press; 1979.
[14] Gosman AD, Lockwood FC. Incorporation of a flux model for radiation into a finite-difference procedure for surface calculations. Proceedings of the 14th Symposium (International) on Combustion. Pittsburgh, PA: The Combustion Institute; 1972 p. 661–71.
[15] Goh YG, Yang YB, Zakaria R, Siddall RG, Nasserzadeh V, Swithenbank J. Development of an incinerator bed model for municipal solid waste incineration. Combust Sci Technol 2001;162: 37–58.
[16] Siminski VJ, Wright FJ, Edelman RB, Economos C, Fortune OF. Research on methods of improving the combustion characteristics of liquid hydrocarbon fuels, AFAPL TR 72-74, vols. I and II, Air Force Aeropropulsion Laboratory, Wright Patterson Air Force Base, OH; 1972.
[17] Howard JB, William GC, Fine DH. Kinetics of carbon monoxide oxidation in postflame gases. Proceedings of the 14th Symposium (International) on Combustion. Pittsburgh, PA: The Combustion Institute; 1973 p. 975–86.
[18] Hautman AN, Dryer FL, Schlug KP, Glassman I. A multiple-step overall kinetic mechanism for the oxidation of hydrocarbons. Combust Sci Technol 1981;25:219.
[19] Arther JA. Reactions between carbon and oxygen. Trans Faraday Soc 1951;47:64–178.
[20] Gray D, Cogoli JG, Essenhigh RH. Problems in pulverised coal and char combustion. Adv Chem Ser 1974;131:72–91.
[21] Field MA. Rate of combustion of size-graded fractions of char from a low rank coal between 1200 and 2000 K. Combust Flame 1969;13: 237–52.
[22] Peters B. A detailed model for devolatilization and combustion of waste material in packed beds. Proceedings of the Third European Conference on Industrial Furnaces and Boilers (INFUB), Lisbon, Portugal; 18–21 April, 1995.
[23] Wakao N, Kaguei S. Heat and mass transfer in packed beds. London: Gordon & Breach; 1982.
[24] Shin D, Choi S. The combustion of simulated waste particles in a bed. Combust Flame 2000;121:167–80.

Available online at www.sciencedirect.com
SCIENCE DIRECT®
Fuel 85 (2006) 1039–1046
FUEL
www.fuelfirst.com

Effect of fuel properties on biomass combustion: Part I. Experiments—fuel type, equivalence ratio and particle size

Changkook Ryu [a], Yao Bin Yang [a,*], Adela Khor [a], Nicola E Yates [b], Vida N Sharifi [a], Jim Swithenbank [a]

[a] Department of Chemical and Process Engineering, Sheffield University Waste Incineration Centre (SUWIC), Sheffield University, Mappin Street, Sheffield S1 3JD, UK
[b] Rothamsted Research, Harpenden, Herts AL5 2JQ, UK

Received 8 March 2005; received in revised form 20 September 2005; accepted 27 September 2005
Available online 2 November 2005

Abstract

Moving bed combustion is commonly used for energy conversion of biomass. Conditions on the moving bed can be conveniently represented by a time dependent fixed bed. The present work experimentally investigates the combustion of four biomass materials having different fuel properties in a fixed bed under fuel-rich conditions Temperature, gas composition and mass loss curves identified two distinct periods as the combustion progresses in the bed: the ignition propagation and char oxidation. The effects of bulk density, particle size and air flow rate on the combustion characteristics during the two periods are interpreted by using the ignition front speed, burning rate, percentage of mass loss, equivalence ratio and temperature gradient. Different channelling of air was observed for small miscanthus pellets and large wood particles due to the fast propagation of the ignition front around a channel. The elemental ash composition was also analysed, which explained the sintered agglomerates of miscanthus ashes in terms of alkali index.

Keywords: Biomass combustion; Fuel type; Particle size; Fixed bed; Mathematical modelling

1. Introduction

Biomass refers to organic materials that stem from plants. It stores energy from sunlight by *photosynthesis* in bonds of carbon, hydrogen and oxygen molecules. It is characterised into four main types: woody plants, herbaceous plants/grasses, aquatic plants and manures [1]. Biomass is presently estimated to contribute of the order 10–14% of the world's energy supply. The sources of biomass are specially grown energy crops, agricultural wastes, forestry residues and the organic fraction of municipal wastes. Its energy is converted to heat, power or chemical feedstock mainly by *thermo-chemical conversion*.

Combustion is a widely used technology for energy conversion of biomass. Most biomass consumed at the present time is burned in fixed or moving beds. A fixed bed has two basic configurations depending on the flow direction of air and fuel: co-current and counter-current, while a moving bed on a grate is counter-current. However, the fixed bed has an analogy with the moving bed since the time elapsed in a fixed bed can be transformed into the location on the grate in the moving bed corresponding to the fuel residence time. Thus, the combustion characteristics and process rates in the fixed bed can be applied to the moving bed. This study is for a counter-current bed which is more commonly applied.

Combustion of solid fuel in a fixed bed involves complicated heat and mass transfer along with various chemical reactions. Conductive, convective and radiative heat transfer takes place (a) between solid phases and (b) between solid and gas within the bed, and (c) between the bed, the walls and the flame above the bed. The composition changes include drying, pyrolysis and char gasification of the solid fuel, and the reactions of volatile gases with air. Once the fuel is ignited by an external heat source (usually by radiation from above the bed), the ignition front propagates into the bed. The heat generated by gaseous reactions and char oxidation at the ignition front transfers downwards to dry and heat up the fresh particles below. Since the heterogeneous char oxidation is relatively slow and oxygen is consumed first by the volatile gases from the particles, carbonised particles remain above the ignition front. Therefore, the drying, pyrolysis, char oxidation

* Corresponding author. Tel.: +44 114 2227500; fax: +44 114 2227501.
E-mail address: y.b.yang@shef.ac.uk (Y.B. Yang).

0016-2361/$ - see front matter © 2005 Elsevier Ltd. All rights reserved.
doi:10.1016/j.fuel.2005.09.019

and ash zones appear sequentially from the bottom to the top of the bed during the ignition propagation, although these processes occur simultaneously for large fuel particles. Once the ignition front reaches the bed bottom, only the oxidation of the remaining char takes place.

Two process rates are often used to quantify the progress of combustion in fixed beds. The ignition front speed, which is also referred as flame front speed or reaction front velocity, is based on the temperature history within the bed. The burning rate is a mass loss rate of the bed per unit area and unit time.

The fuel properties and process conditions affect the combustion characteristics, altering the heat generation, heat transfer and reaction rates in a complicated manner [2–8]. The air flow rate is the key process parameter that determines the amount of oxygen available and convective heat transfer. The process rates are classified into three successive regimes depending on the air flow rate: Oxygen-limited, reaction-limited and extinction by convection regimes [2]. When the air flow rate is small, the propagation of the ignition front is controlled by the amount of oxygen and the process rates are linearly proportional to the air flow rate. In the reaction-limited regime, the process rates are limited by the reaction rate of the fuel. As the air supply increases further, the convective cooling of particles around the ignition front slows down the process and finally causes extinction of the flame. Gort [3] also presented similar classification: partial gasification, complete gasification and combustion regimes.

Biomass has a wide range of variety in physical properties, which significantly change the process rates and detailed phenomena. More fundamental studies are required to understand the combustion characteristics of different biomass materials. One important aspect in the fuel properties is pelletisation that is used because many raw biomass materials, especially grass, straw and sawdust, have a very low bulk density (usually less than 150 kg/m^3), which require high cost for storage, transportation and handling. Pelletisation significantly densifies biomass to over 600 kg/m^3, which is essential for biomass to compete with other sources of energy.

The ash composition is a major concern in biomass combustion. The high presence of alkali metals in biomass may cause slagging, fouling and ash agglomeration. The primary sources of these problems are: the reaction of alkali with silica to form alkali silicates that melt or soften at low temperatures (can be lower than 700 °C, depending on the composition), and the reaction of alkali with sulphur to form alkali sulphates on heat transfer surfaces [9]. Investigating the elemental composition of ash is important in order to identify possible operational problems in the actual application.

This paper is the first part of work that presents the combustion characteristics of biomass samples observed by experiments. The second part investigates the effect of various biomass properties by mathematical modelling in order to identify the controlling factors [10].

Combustion tests of two woody chips, one herbaceous and one refuse-derived pellets in a batch type fixed bed reactor are presented for different air flow rates and particle sizes. The ignition propagation and char oxidation periods are described using the measurements of temperature, gas concentration and mass loss histories, and quantified into key process rates and parameters. Then, the effects of bulk density, particle size and channelling on the combustion characteristics are discussed. Elemental ash compositions are also analysed to elucidate the behaviour of different bottom ashes.

2. Experimental

2.1. Biomass samples

The materials selected for the tests are three pure biomass samples (willow, miscanthus and pine) and one sample from a segregated waste having a large fraction of cellulosic materials. Table 1 lists the results of standard analyses and particle types of these samples. All the samples are fairly dry with less than 8% moisture content. The combustible components in the three pure biomass samples have similar elemental composition and ratio of volatile matter to fixed carbon content. The main differences between the samples lie in the ash content, particle size and density. The two woody samples have a low ash content, while the values for the other samples are over 10%. Willow samples were chopped to a length of about 35 mm. Miscanthus samples were pelletised with a diameter of 4 mm. Pine samples were cut into cubes with four different sizes (5, 10, 20 and 35 cm) in order to investigate the effect of particle size. Refuse-derived fuel (RDF) was prepared by pelletising municipal solid waste after pre-processing (shredding, digestion, segregation and screening). The non-organic combustible fraction in RDF is mainly plastic materials which represents one third by weight. This increases the volatile matter and

Table 1
Properties of biomass samples

Samples		Willow	Miscanthus	Pine	RDF
Proximate analysis (%-wt)	Moisture	7.2	6.1	5.5	1.9
	Volatile matter	78.1	67.9	81.2	69.9
	Fixed carbon	13.7	13.1	12.1	9.8
	Ash	1.0	12.9	1.2	18.7
Ultimate analysis (%-wt)	C	45.9	39.9	49.8	44.3
	H	6.6	6.3	8.1	6.3
	O (by difference)	39.3	34.8	38.3	28.8
Gross calorific value (MJ/kg)		17.8	15.4	18.3	22.3
Particle type		Length: 35 mm	Pellet: ϕ4 mm	Cube: 5, 10, 20 and 35 mm	Pellet: ϕ7 mm

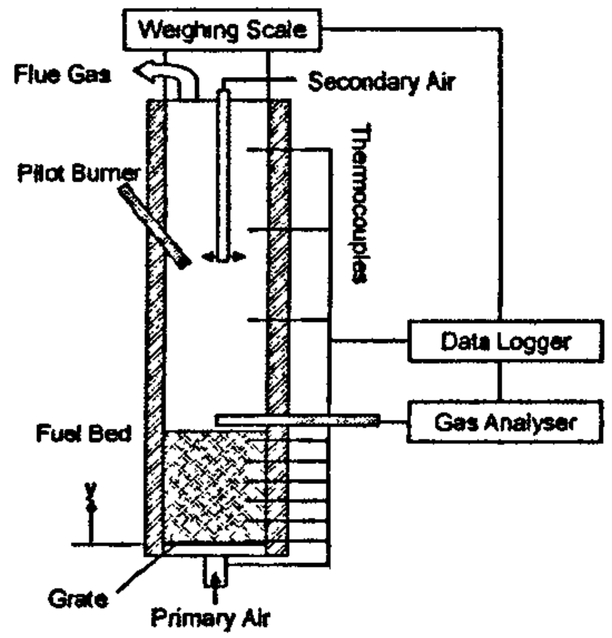

Fig. 1 Schematic of fixed bed reactor.

calorific value of RDF while reducing the oxygen content. Although the original materials are shredded and mixed during pre-processing, RDF pellets are not as homogeneous as the other samples, for example, there is up to 5% variation in ash content between pellets.

2.2. Packed bed reactor

The fixed bed reactor consists of a vertical cylindrical combustion chamber, pilot burner, grate, air supply system and weighing scale, as shown in Fig. 1. The chamber is made from inconell 600 nickel alloy having an inner diameter of 20 cm and a height 1.5 m with 8 cm-thick insulating material around the side wall. It has 11 measuring ports installed on the wall for access of K-type thermocouples and sampling probes, and seven of them are located within 43 cm from the level of the grate. The junctions of the thermocouples are aligned along the core of the reactor. A gas analyser (MGA 3000, Analytical Development) measures the O_2, CO and CO_2 concentrations continuously. The reactor is suspended from two weighing beams having four load cells in order to monitor the mass loss of the fuel bed. The weighing scale has a resolution of ± 20 g, while the initial sample feed is 2–7 kg depending on the density and bed height. However, the reactor is partially restricted by the flexible air supply line at the bottom end, and is stretched by thermal expansion during the combustion test. It results in a negative reading of the weighing scale near the end of the test. Thus, the mass loss needs to be normalised, based on the weights of the initial sample and the bottom ash collected after each test. The data logger records the measured temperatures, gas concentrations and mass loss every 15 or 30 s.

2.3. Experimental conditions

Table 2 lists the bulk density, bed height and operating conditions for the test cases. For the willow, miscanthus and RDF samples, the air flow rate varied from 120 to 200 l/min (270–451 kg/m^{2}h) at room temperature, while it was fixed at 160 l/min (360 kg/m^{2}h) for pine wood samples of different particle sizes. Each case is named according to the air flow rate or the particle size as shown in the table. The flow rate of secondary air was fixed at 100 l/min. The initial bed height was 35–40 cm for most cases. The bulk density of the fuel bed for the woody samples were 181 kg/m^3 and about 280 kg/m^3, respectively, while the values for the miscanthus and RDF samples were much higher (660 and 715 kg/m^3, respectively). Particle size of the pinewood did not affect the bulk density, which indicates that the fuel bed with larger particles have similar void fraction but bigger voids than with smaller particles.

3. Results and discussion

3.1. Temperature, gas composition and mass loss

Once the bed is ignited by the pilot burner, the combustion propagates continuously into the bed by transfer of the heat released from the gaseous reactions and char oxidation. Fig. 2 shows the temperatures within the bed and gas concentration at the bed top ($y=43$ cm) for Case P-20 (pine wood, particle size:

Table 2
Test cases and process conditions for each sample

Sample	Bulk density (kg/m3)	Bed height (mm)	Air flow rate		Case name
			(l/min)	(kg/m^{2}h)	
Willow	181	520	120	270	W120
		410	160	361	W160
		400	200	451	W200
Miscanthus	660	400	120	270	M120
		350	160	361	M160
		400	200	451	M200
RDF	715	360	120	270	R120
		350	160	361	R160
Pine, 5 mm	285	350	160	361	P-5
Pine, 10 mm	272	375	160	361	P-10
Pine, 20 mm	285	360	160	361	P-20
Pine, 35 mm	295	360	160	361	P-35

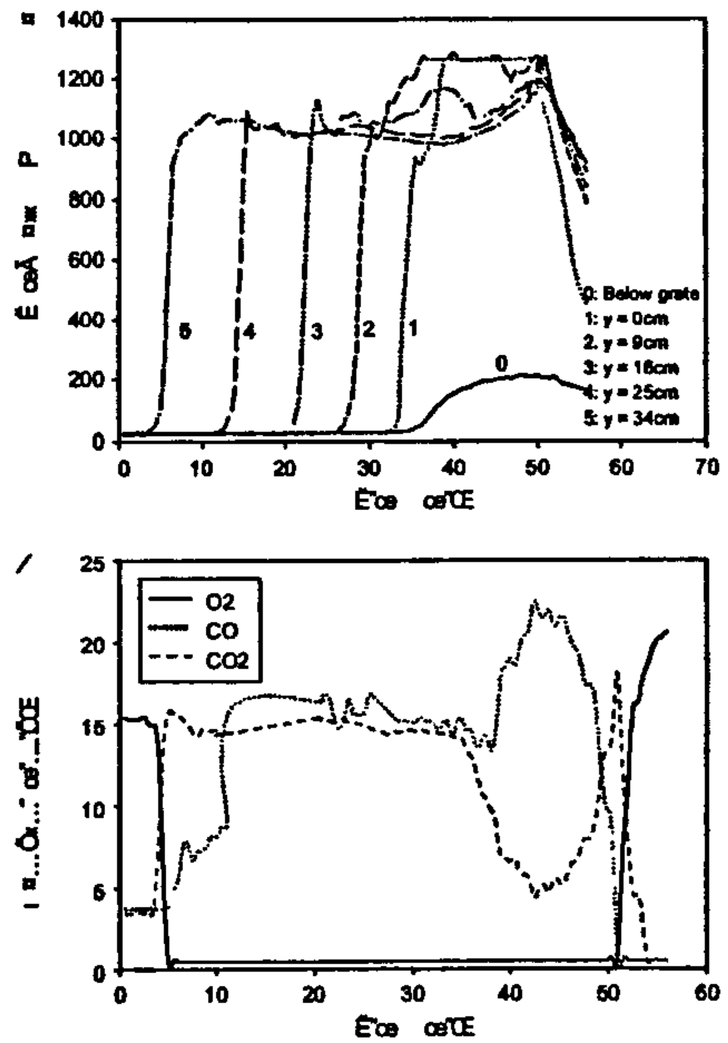

Fig. 2. Temperature history (a) and gas composition at the bed top (b) for Case P-20.

20 mm). The temperature at each thermocouple soars up to 1100 °C when the ignition front passes, and then become stable at around 1000 °C. At around $t=35$ min, the ignition front reaches the bed bottom. During this period, the gas at the bed top has about 15% of CO_2, a few percent higher CO and zero O_2, and luminous flames are observed between particles above the ignition front and above the bed.

From $t=35$ to 50 min, the bed shows very different behaviour by gasification of the remaining char layer. During this period, a sharp rise in CO concentration is observed, which is the major product of char gasification with CO_2 under insufficient air. CO_2 concentration decreases correspondingly. The thermocouple at $y=0$ cm and $y=9$ cm are saturated at about 1280 °C during this period. Hot char particles glow without forming a flame above the bed, and the whole bed collapses continuously due to the volume reduction of particles. When most char is consumed, CO decreases rapidly and then CO_2 shows a sharp peak (at 50 min) by the change in reaction stoichiometry.

Fig. 3 shows the mass left on the bed for the miscanthus samples. During the ignition propagation period, the mass left on the bed decreases with a uniform slope. Then, the mass loss slows down as the char oxidation period commences. The mass loss accelerates as the air flow rate increases.

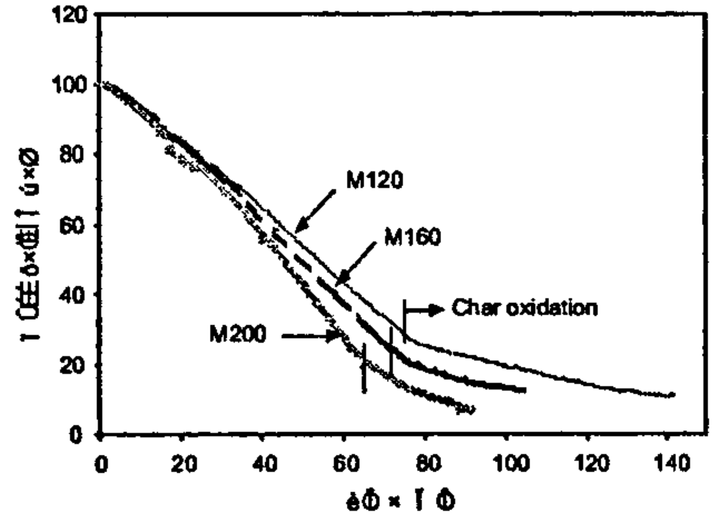

Fig. 3. Mass loss curves for miscanthus samples.

3.2. Burning rate and ignition front speed

Fig. 4 shows the effect of air flow rate on the burning rates during the ignition propagation period and char oxidation period. Willow wood samples have the highest values during the ignition propagation period, while RDF has the lowest. The increase in the burning rates is linearly proportional to the air flow rate, which suggests that all the cases are in the oxygen-limited regime.

The mass loss during the char oxidation period is much slower-in the order of one third. Miscanthus has a lower burning rate than RDF during this period. The reason is that the miscanthus ash is agglomerated during char oxidation and blocks the diffusion of oxygen into the particles. The ash properties are discussed later.

Table 3 lists some key results of the combustion characteristics for the test cases. The average burning rate and equivalence ratio are based on the mass loss during the whole period. As can be expected from the gas composition in

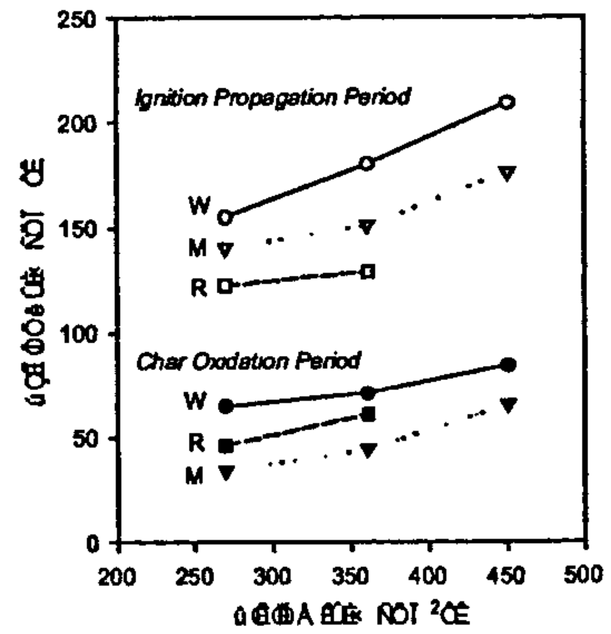

Fig. 4 Effect of air flow rates on the burning rate (W, Willow; M, Miscanthus; R, RDF).

Table 3
Key parameters of combustion characteristics for the biomass samples

Sample	Case	Percentage of mass loss during ignition propagation (%)	Ignition front speed (m/h)	Average burning rates (kg/m²h)	Average equivalence ratio
Willow	W120	68	1.08	104 4	4.13
	W160	80	1.22	137.2	3.52
	W200	82	1.19	141.5	2.90
Miscanthus	M120	75	N/A	93 6	2.33
	M160	79	N/A	118 8	2.26
	M200	81	0.36	148 0	2.07
RDF	R120	75	0.22	97.1	2.40
	R160	73	0 33	111.8	2.15
Pine, 10 mm	P-10	86	0 79	134	2.27
Pine, 20 mm	P-20	84	0 71	123	2 08

Fig. 2(b), all the test cases are in fuel-rich conditions with average equivalence ratios of 1.9–4.1. The ignition front speed increases with greater air supply in the test cases. The value for Cases M120 and M160 are not given, since the thermocouples were damaged or erratic when the temperature became high for these cases. The reason is probably the agglomeration of the ash.

The proportion of mass loss during the ignition propagation period increases for willow and miscanthus samples with increasing air flow rates. This means that the remaining char layer becomes thicker as the ignition front propagates faster.

Fig. 5 compares the burning rates for the ignition propagation period and ignition front speeds based on temperature for the air flow rate of 360 kg/m²h in order to show the effect of bulk density. The ignition front speed is inversely proportional to the bulk density, while the burning rate tends to decrease linearly. The speed for willow wood (bulk density: 181 kg/m³) has about four times higher that that for RDF (bulk density: 715 kg/m³). However, the willow wood burning rate is just 22% higher than that for RDF. The ignition front speed multiplied by the bulk density gives the ignition rate which is the rate of mass per unit area swept by the ignition front. The ignition rate is 202–236 kg/m²h for the test cases which is higher than the burning rate due to the char layer accumulated above the ignition front.

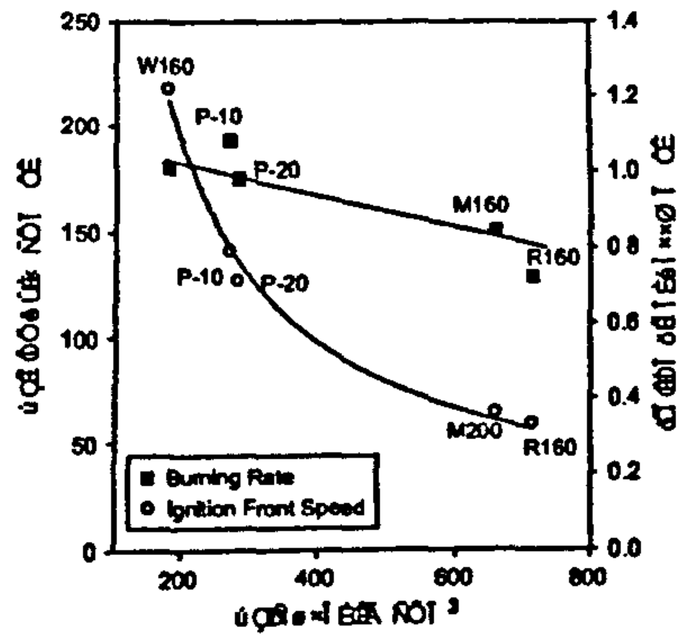

Fig. 5. Effect of bulk density on ignition front speed and burning rate during ignition propagation.

3.3. Effect of particle size

Fig. 6 compares the ignition front speed, burning rate and mass loss during the ignition propagation period for different particle sizes of pine wood. Small particles have higher burning rates and ignition front speeds. The mass loss during the ignition propagation period suggests that the amount of char left above the ignition front also decreases for smaller particles. In Case P-35, however, the ignition front speed is higher than P-20, while the mass loss and the burning rate are lower. This can be explained by the channelling effect becoming significant for this case due to larger voids within the bed, which is described later.

Large particles are thermally thick having slow devolatilisation rate and more distributed heat transfer to the nearby particles. The temperature history provides additional information for the effect of particle size on the ignition front. When the ignition front passes each thermocouple, it results in a sharp rise of temperature. The transient temperature gradient ($\Delta T/\Delta t$) between 200 and 800 °C at each thermocouple is shown in

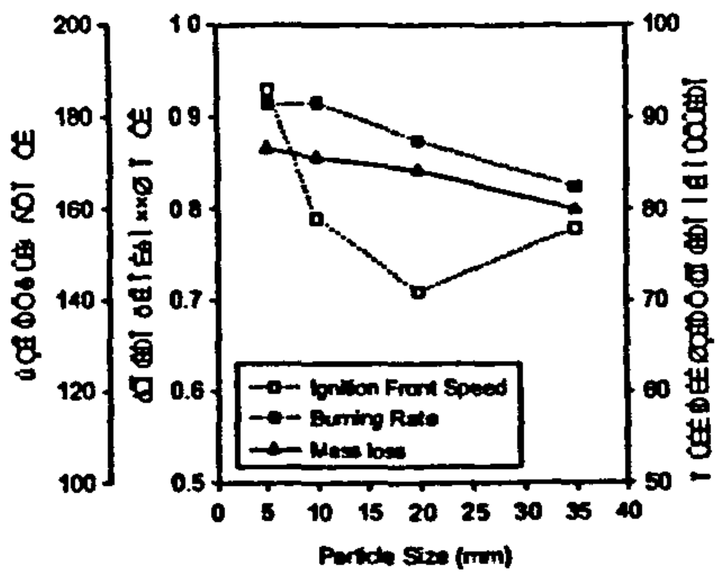

Fig. 6. Effect of particle size on ignition front speed and burning rate and mass loss during the ignition propagation period.

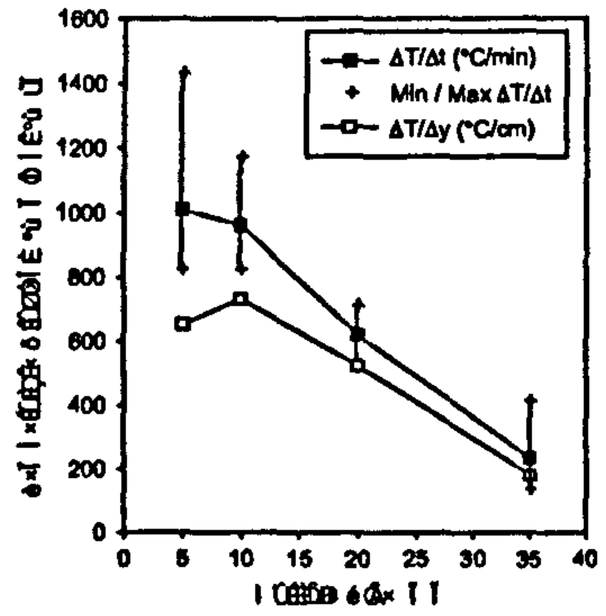

Fig. 7. Transient and spatial temperature gradients at the ignition front.

Fig. 7. When multiplied by the ignition front speed, it gives the spatial temperature gradient ($\Delta T/\Delta y$). This can be used as indicator of overall downward heat flux at the ignition front. The two gradients decrease with increasing particle sizes which suggests that the heat influx to the cold particles below the hot particles is more intense for smaller particles. It takes less than 1 min for the small particles to reach a temperature of 800 °C from 200 °C and about 3 min for 35 mm size particles. This corresponds to about 10 and 33 mm, respectively, in terms of height—about the order of the particle size for the selected air flow rate. Further study is required to investigate the effect of air flow rate on the temperature gradient at the ignition front.

The particle size also affects the char oxidation period. The temperature greater than 1250 °C or the temperature plateau in Fig. 2(a) characterises this period. Table 4 lists the key experimental results for the char oxidation period. As the particle size increases, the temperature plateau is prolonged and the height of the thermocouples where it appears increases. For Case P-35, it was observed by the thermocouples at $y=9$ cm and $y=16$ cm and lasts 23 min. Thus, the thickness of the char layer in this case is higher than 16 cm, which corresponds well to the increased proportion of mass loss for this period. The burning rate during this period decreases linearly as the particle size increases.

Fig. 8 compares CO_2 concentration for the test cases. Large particles have a higher level of CO_2 due to the slow burning rates. CO_2 decreases during the char oxidation period, but the difference between the cases becomes larger. The sharp peaks of CO_2 at the end of the test matches exactly with the ending points of the temperature plateaus.

3.4. Channelling and hot spots

Void spaces between particles in the bed are interconnected. Channelling causes most of the air or gas flow to pass through passages with higher local void fraction or 'short-cuts' inside the bed. The ignition front propagates much faster around the channel. It also causes large transient or spatial fluctuations of temperature and chaotic burning patterns [11].

During the tests, channelling was observed in the test cases for the miscanthus and Case P-35. In the bed of the miscanthus pellets, the channels appear around the side wall as indicated by the arrows in Fig. 9(a). Since the dense fuel bed of small miscanthus pellets gives large resistance or pressure drop to the gas phase, the gas passes preferentially through the spaces around the sidewall which results in the hot spots. This is also observed temporarily in the tests for other samples, but not as severe as with the miscanthus pellets. In Case P-35 shown in Fig. 9(b), large voids between particles create several short-cuts of air. Once the channels collapse by volumetric shrinkage of the nearby particles, new channels appear with different number and location.

3.5. Ash characterisation

The bottom ashes from RDF, willow and pinewood consists of fine grey particles being darker in that order. However, the ash from miscanthus forms hard agglomerates. Herbaceous fuel is known to contain a high level of silicon and potassium as their principal ash-forming constituents. Fig. 10 shows the elemental composition of the bottom ash for each sample. Si is dominant in the miscanthus ash (74%) with high composition of Ca, Fe and K in the remainder. The two wood materials have similar composition with high presence of Ca, Fe, P and K and significantly low Si. RDF ash has a high level of Al with Si, mainly due to the kitchen foils which is also identifiable in the original pellets.

The alkali index has been used in recent years as a threshold indicator for fouling and slagging [9]. All biomass fuels show fouling behaviour but at different rates depending on the composition and ash content. The alkali index expresses the quantity of alkali oxides (K_2O and Na_2O) in the fuel per unit of fuel energy (kg-alkali/GJ). Slagging and fouling are probable above 0.17 kg-alkali/GJ, and certainly occur above 0.34 kg-alkali/GJ. The alkali indices for the two wood samples are less

Table 4
Char oxidation period for different particle sizes of pinewood

Particle size	Proportion of mass loss (%)	Temperature plateau			Burning rate (kg/m²h)
		Starting time (min)	Duration (min)	At thermocouple (cm)	
Case P-5 (5 mm)	13 4	31.3	8.7	y=0	91.4
Case P-10 (10 mm)	14.4	34.0	10.3	y=0	84.6
Case P-20 (20 mm)	15.8	36.0	15.0	y=9	64.1
Case P-35 (35 mm)	20.0	39.5	22.5	y=9, 16	56.1

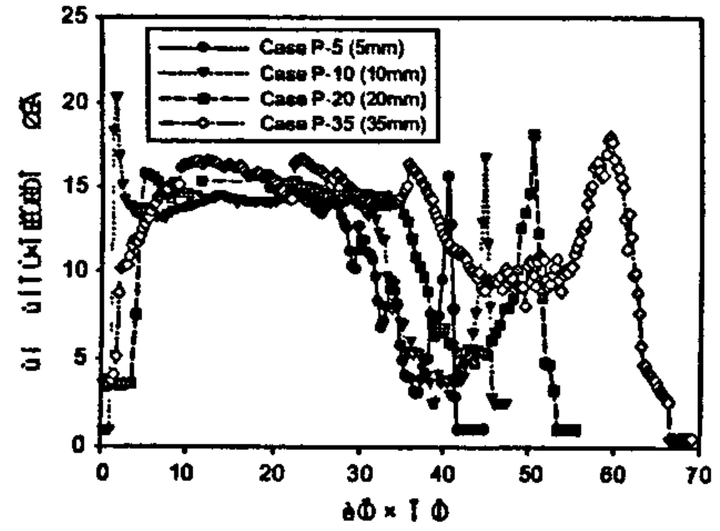

Fig. 8. CO_2 concentrations for the pinewood samples with different particle sizes.

than 0.1 kg-alkali/GJ. The values for the miscanthus samples are near or higher than 0.34 kg-alkali/GJ. Thus, agglomeration, slagging and fouling are bound to occur in the combustion of this herbaceous fuel. RDF also has a potential for fouling since the indices are over 0.2 kg-alkali/GJ.

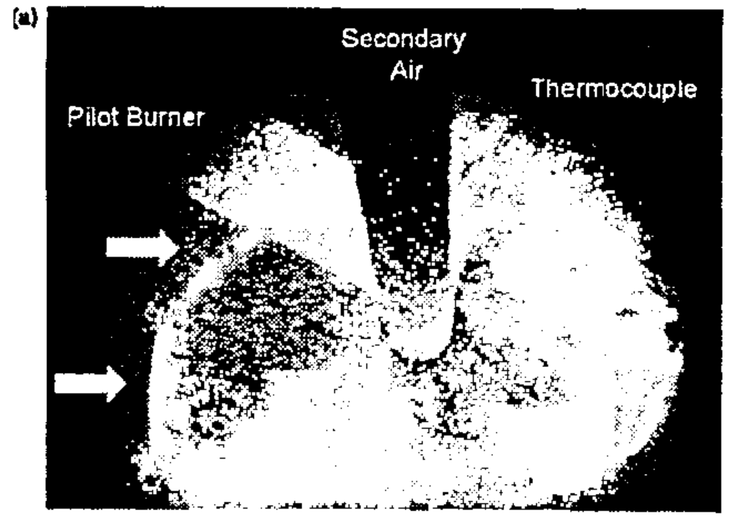

Case M200 during ignition propagation period

Case P-35 during char oxidation period

Fig. 9. Photos of fuel bed for Case M200 (a) and Case P-35 (b).

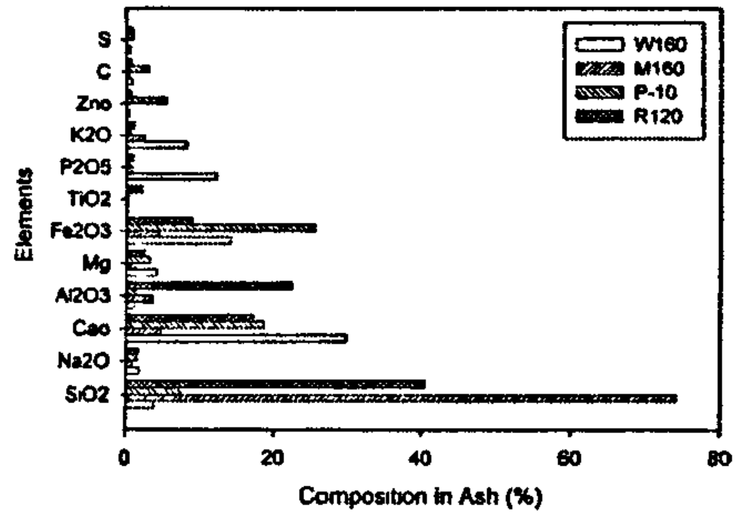

Fig 10. Elemental composition of the bottom ashes.

4. Conclusions

The fixed bed combustion of biomass samples with different particle types and properties was investigated. For the tested range of the air flow rate (270–451 kg/m^{2}h), all the samples were burned in fuel rich conditions (equivalence ratios of 1.8–4.1). The progress of combustion in the bed has two distinct periods: the steady propagation of the ignition front into the bed and the slow char oxidation periods.

The ignition front speed and the burning rate increased with increasing the air flow, while leaving a smaller amount of char above the ignition front. The burning rate during the char oxidation period was much smaller than that for the ignition propagation period. Two woody samples had faster ignition propagation than the pellet samples, where the ignition front speed was inversely proportional to the bulk density. The burning rate decreased linearly with the bulk density, and its difference between the samples was relatively small.

Larger particles had a lower ignition front speed and burning rate, while a larger amount of char was left above the ignition front and the char oxidation period lasted longer. The temperature gradient at the ignition front also decreased with increasing particle sizes, and the thickness of the ignition front from 200 to 800 °C was about the order of the particle size.

Channelling was observed around the side wall of the reactor for the small miscanthus pellets and at several locations in the bed for larger pinewood particles (35 mm cubes). The latter case resulted in a faster propagation of the ignition front to the bed bottom than the case with 20 mm cubes, but the effect of channelling on the burning rate was not significant.

Alkali index based on the elemental composition of bottom ash was useful to explain the sintered agglomerates of miscanthus ashes.

Acknowledgements

The authors would like to thank the UK Engineering and Physical Sciences Research Council (EPSRC) and Supergen Biomass and Bioenergy Consortium for the financial support and help for this study.

References

[1] McKendry P. Energy production from biomass (part 1): overview of biomass. Bioresour Technol 2002;83:37.
[2] Shin D, Choi S. The combustion of simulated waste particles in a fixed bed. Combust Flame 2000;121:167.
[3] Gort R. On the propagation of a reaction front in a packed bed: thermal conversion of municipal solid waste and biomass. PhD Thesis. Universiteit Twente, Enchede, The Netherlands; 1995.
[4] Saastamoinen JJ, Taipale R, Horttanainen M, Sarkomaa P. Propagation of the ignition front in beds of wood particles. Combust Flame 2000;123:214.
[5] Rönnbäck M, Axell M, Gustavsson L. Combustion processes in a biomass fuel bed- experimental results. Progress in thermochemical biomass conversion, 17–22 September, Tyrol, Austria; 2000.
[6] Yang YB, Yamauchi H, Nasserzadeh V, Swithenbank J. Effects of fuel devolatilisation on the combustion of wood chips and incineration of simulated municipal solid wastes in a packed bed. Fuel 2003;82:2205.
[7] Zakaria R. Static incineration bed combustion. PhD Thesis. Department of Chemical and Process Engineering, University of Sheffield, UK, 2000.
[8] van der Lans RP, Pedersen LT, Jensen A, Glarborg P, Dam-Johansen K. Modelling and experiments of straw combustion in a grate furnace. Biomass Bioenergy 2000;19:199.
[9] Jenkins BM, Baxter LL, Miles Jr TR, Miles TR. Combustion properties of biomass. Fuel processing technology. Fuel Process Technol 1998;54:17.
[10] Yang YB, Ryu C, Khor A, Yates NE, Sharifi VN, Swithenbank J. Effect of fuel properties on biomass combustion. Part II. modelling approach-identification of the controlling factors. Fuel 2005;84:2116.
[11] Yang YB, Nasserzadeh V, Goodfellow J, Swithenbank J. Simulation of channel growth in a burning bed of solids. Trans IChemE 2003;81(A):221.

Available online at www.sciencedirect.com
ScienceDirect
Fuel 86 (2007) 152–160
FUEL
www.fuelfirst.com

Straw combustion in a fixed bed combustor

Adela Khor, Changkook Ryu *, Yao-bin Yang, Vida N. Sharifi, Jim Swithenbank

Department of Chemical and Process Engineering, Sheffield University, Mappin Street, Sheffield S1 3JD, UK

Received 1 February 2006; received in revised form 29 June 2006; accepted 4 July 2006
Available online 14 August 2006

Abstract

Straw and herbaceous energy crops are key biomass materials for greenhouse gas neutral energy production. Combustion of straw and two herbaceous crops was investigated in a fixed-bed reactor for a range of air flow-rates (234–1170 kg/m² h). The fixed bed tests simulate the moving bed combustion where the distance along a grate corresponds to the time on the fixed bed. Measured temperatures, gas composition and mass loss were used to evaluate the combustion characteristics in terms of ignition front speed, burning rate, percentage of mass loss and the equivalence ratio. The average burning rates of herbaceous fuels reached a peak of 220–250 kg/m² h at air flow rates of 700–900 kg/m² h. An overlap of the two distinct periods of combustion was observed at high air flow rates, as the air supply was sufficient to simultaneously burn the char above the ignition front. When uncut straw was burned, less uniform packing of the long fibres increased the effect of air channelling and led to irregular propagation of the ignition front.

Keywords: Biomass; Herbaceous crops; Fixed bed combustion

1. Introduction

Coal energized the 19th century while oil worked for the 20th century. The question that remains pending is our future energy source. With the expanding population and growing demands from industrialization of countries such as India and China, total reliance on fossil fuel is not sustainable. The rapid dwindling of the North Sea reserves has increased UK dependence on import gases. The increase in wholesale electricity prices has pushed UK energy suppliers such as British Gas, Powergen, Npower to hike up retail prices accordingly, forcing thousands of people into fuel poverty. Meanwhile, greenhouse gas (GHG) emissions are soaring towards a crucial level leading to serious calls both nationally and locally for the highest possible reduction. The Kyoto Protocol imposes emission targets under which the UK agreed to keep annual greenhouse emission during the period of 2008–2012 to 12.5% below 1990 levels [1]. However, recent reports by the BBC show that the UK is at risk of missing its Kyoto target as carbon emissions increase.

The urgent need for green and sustainable fuel prompted research into energy crops as an alternative to fossil fuels. Some of the energy crops investigated in this research work are miscanthus, switchgrass, reed canary grass and straw. Miscanthus and switchgrass are C-4 perennial plants that reduce the atmospheric CO_2 by using a supplementary method of CO_2 uptake which forms a 4-carbon molecule instead of two 3-carbon molecules. The method of burning these fuels is one of the key questions that arise from the use of these energy crops. Straws are currently either burned in bales without pre-treatment or more commonly, they are scarified in short strands. Although pelletisation is a widely acceptable practise pre-treatment for crops, it brings in the question of economic viability and environmental cost.

The use of energy crops in the combustion industry is fairly novel in the UK compared to other European countries. Willow chips are used for co-firing, district heating stations and CHP (Combined Heat and Power) plants in Denmark. Willow and reed canary grass (RCG/Phalaris) are considered to be the two most promising energy crops in Sweden. Straw combustion is popular in Denmark as proven by the numerous straw burning plants; Haslev (CHP), Slagelse (CHP), Rudkoebing (CHP) and Hvidebaek (District Heating). Ely is the UK's first straw burning power station and also one of the worlds' largest straw burning plants. However, work on the combustion of energy crops are still at a premature stage compared to wood, coal and waste.

The UK produces an estimated 14 million ton of straw annually from Eastern England and parts of Central and Southern England [2]. Half of the produced straw is used for animal feed and bedding while in-field burning to dispose of the rest is now forbidden. The alternative method of straw removal leads to increased transportation and baling costs as well as a penalty in reduction of subsequent crop yield due to the removal of nutrients.

Straw has a significant calorific value (16 MJ/kg) approximately the same as seasoned wood, half that of coal, and one-third that of oil [3]. Loose straw has a bulk density of 30 kg/m³, which can be increased to 100–150 kg/m³ by baling. However, this would incur an additional cost of £18/ton to the farmer for the baling, handling, storage and transportation if straw was to be used in power stations. Delivery over 10 km would increase the cost to £22/ton [4]. Further fuel processing such as compression to briquettes or pellets increases the bulk density 5–10-fold to 450–650 kg/m³ [5]. Compacted straw can be delivered at £29–52/ton depending on the capacity of the equipment and the cost of raw material [2]. This makes the burning of bales straw only feasible in situations where the supplies of raw material and electricity consumers are in close proximity to avoid high transportation cost. The low energy density of straw puts it at a further disadvantage compared to fossil fuel such as oil and coal. However, the increasing prices of fossil fuel such as gas, oil and coal as well as climate tax and government subsidy for biofuels now puts biofuels at an equal level with conventional fuels. The substitution for straw would be an easier option for implementation compared to other biofuels such as miscanthus and switchgrass as a commercial supply system already exists.

This paper presents an experimental investigation into the combustion behaviour of straw in a fixed bed combustor. The effects of primary air flow rate on three herbaceous biofuels; straw, switchgrass and reed canary grass are analysed. This work focuses on improving the understanding of these fuels to obtain data on the reaction front propagation rate, temperature distribution inside the bed and composition of the gases in the bed. The crucial combustion parameter, primary air flow rate, has been widely studied by researchers such as Rogaume et al. [6], Swithenbank et al. [7], Jorgensen and Madsen [8], Yang et al. [9], Rönnbäck et al. [10]. van der Lans [11] developed a two-dimensional steady model for straw combustion in a cross-current moving bed and verified the model with experimental data for the effects of the inlet air flow rate and air temperature on the combustion process. His work was extended by Zhou et al. [12] who developed a one-dimensional transient model of fixed-bed straw combustion and validated the results with experimental measurements of temperature, gas emissions, ignition front propagation rate and flame temperature. Kaer [13] investigated a straw-fired grate boiler using the computation fluid dynamics (CFD), in which the model predictions were compared with measurements obtained from a full-scale boiler plant at Masnedø (Denmark). Wornat et al. [14] investigated the physical and chemical transformation of biomass chars (pine and switchgrass) during combustion. A major problem associated with the utilization of straw is the low ash melting temperature, producing cakes of sintered ash. Orlanders and Steenari [15] carried out the characterization of ashes from wood and straw.

2. Materials and method

The materials selected for combustion tests are three herbaceous crops: straw, switchgrass and reed canary grass. Table 1 lists the results of standard fuel analyses and fibre length of these samples. The elemental compositions of the three samples are fairly similar, varying in a narrow range of 1–2%. Reed canary grass has a slightly lower fixed carbon and higher moisture content compared to the other two fuels. Switchgrass has the highest calorific value due to the lower moisture and ash content. The calorific values of these herbaceous fuels are in the typical range for biomass.

2.1. Fixed-bed reactor

The experimental rig consists of a vertical cylindrical combustion chamber, suspended from two weighing beams, which incorporated four load cells. This reactor has been used in previous studies [16,17]. The height of the chamber was 1.5 m with an internal diameter of 200 mm made of 8 mm thick Inconel 600 nickel alloy. It is insulated by 80 mm thick Kaowool Blanket and a casing made of 30 mm thick 303 stainless steel. The grate located

Table 1
Fuel properties of herbaceous samples

Samples		Straw	Switchgrass	Reed canary grass
Proximate analysis (wt%)	Moisture	7.88	6.43	8.05
	Volatile matter	80.08	82.84	83.87
	Fixed carbon	6.76	7.24	3.75
	Ash	5.28	3.49	4.33
Ultimate analysis (wt%)	C	43.58	43.54	44.20
	H	5.48	5.47	5.71
	N	0.60	0.43	0.70
	S	0.38	0.51	–
	O*	36.80	40.13	37.01
Gross calorific value (MJ/kg)		16.36	17.26	16.41

* By difference.

* Corresponding author. Tel.: +44 114 222 7523; fax: +44 114 222 7501.
E-mail address: c.ryu@sheffield.ac.uk (C. Ryu).

0016-2361/$ - see front matter © 2006 Elsevier Ltd. All rights reserved.
doi:10.1016/j.fuel.2006.07.006

at the bottom of the combustor was a stainless steel perforated plate, with approximately 700 holes of 2 mm diameter, representing 7% open area. Ni/Cr-thermocouples (type K) were used to measure the bed temperature at different height levels, temperature of the flue gas and primary airflow. A gas sampling probe was connected from the centre of the reactor at 430 mm above the grate to a gas analyser (MGA3000, Analytical Development) for O_2, CO and CO_2. A gas burner was used to initiate the burning process at the bed surface.

A glass tube reactor made of quartz with an internal diameter of 100 mm was also used to visually observe the progress of combustion. In order to protect the tube, the test was carried out at a low air flow rate (280 kg/m^2 h). No measurement was taken during this test.

2.2. Experimental conditions

The bulk density, bed height and operating conditions are tabulated in Table 2. The experiments were carried out with primary air flow rates over a range of 230–1170 kg/m^2 h for cut straw and switchgrass. Uncut straw and reed canary grass were also tested with two air flow rates. The measured bulk densities for the bed of herbaceous crops were quite inconsistent due to the uneven distribution of material and large voids in the bed. The structure of herbaceous plants such as switchgrass and straw could generally be divided into three fractions: a micro-size dust, a large fraction of thin, flat and long sections (leafy section) and a small fraction with round dense nodes (stalk). The different density in the three fractions could result in a concentrated micro-size dust fraction gathering at the bottom of the furnace. Although the bed was stirred numerous times during the loading process to avoid materials gathering in the centre of the furnace, the bulk density of the straw bed varied over a wide range from 40 kg/m^3 to 65 kg/m^3 because the plant fibres tend to entwine and cause difficulty in spreading the material across the bed. This was more severe if longer straw is used (12 cm) as in Cases STU1 and STU3. The bed density would then vary depending on the local position that the bed height was taken and also the compactness of that particular situation. The bulk density of reed canary grass was almost double the density of straw as the former was shorter and more evenly cut.

3. Results and discussion

3.1. Mass loss history

Fig. 1 shows the mass loss history of straw expressed as a percentage of the remaining mass on the bed. For all the cases, a linear decrease in the mass was seen after the bed was ignited by the start-up burner. The gradient of the curves increased as the air flow rate increased from the air flow rate of 234 kg/m^2 h for Case ST1 to 702 kg/m^2 h for Case ST3 and then decreased at higher air flow rates. At the end of the steady mass loss period (ignition propagation stage), the mass loss slowed down gradually which indicates the second stage of combustion (char gasification stage). This stage was very short at high air flow rates (Cases ST4 and ST5). The key features of these two combustion stages are discussed below in terms of temperature profiles and gas composition, and then quantified into ignition rate, burning rate and equivalence ratio.

3.2. Case ST1

Fig. 2 shows the measure bed temperatures against reaction time at different bed heights above the grate for Case ST1. The two stages of combustion can be clearly identified in the temperature curves. In the ignition propagation stage, the local bed temperature rose sharply from room level to a peak value of about 550 °C as the ignition front passed, and then dropped as the ignition front propagated down the bed. The average time span required for each temperature jump was 1.5 min. The ignition front reached the grate ($y = 0$ cm) at $t = 11$ min.

At the end of the ignition propagation stage, the mass remaining in the bed was still very high (about 60%) as shown in Fig. 1. Considering that the amount of char left after pyrolysis of lignocellulosic materials above 500 °C is typically less than 30%, such a high percentage of mass implies that the bed contained a significant amount of material yet to be pyrolysed. After the propagation of the ignition front, the bed temperatures began to rise simultaneously and reached a peak at around $t = 13.5$ min. The maximum temperature appeared at $y = 9$ cm indicating active combustion at the bottom of the bed. Such a temperature increase can be explained as follows. First, the main oxidation zone in this stage stays the lower part of the bed near the grate where the oxygen is consumed by char or unburned material. The heat from the char oxidation near the grate is transferred upward by convection with gas, radiation and conduction between particles. Secondly, char is carbon-rich and thus has a higher calorific value that can increase the bed temperature to a much higher level than in the ignition propagation stage. Fig. 1 shows that the mass left at the peak of the bed temperatures point was 22% and the mass loss slowed down significantly after this point. As the combustible mass in the bed decreased, the bed temperatures dropped gradually.

It was visually observed during the experiment that the herbaceous fuel bed largely maintains its original structure and the collapse of the bed as seen in the combustion of other biomass materials did not occur [17]. The entanglement of the long, fibrous straws formed a 'nest-like' bed within the small laboratory furnace and the light weight of the straw enables it to maintain its structure. After the ignition front propagation stage, a bright yellow glow was seen at the bottom of the bed beneath the layer of pyrolysed char. The bed height gradually decreased as the char was combusted at the bottom.

Fig. 3 shows the gas emission profile as a function of reaction time obtained for Case ST1. The O_2 concentration in the gas dropped quickly in a space of 3 min at $t = 4$ min from ambient level (21%) to a minimum level (<1%). This was followed by a sharp increase in CO and CO_2 to 17% and over 20% respectively. Note that the upper measurement limit of the gas analyser for CO_2 was 20%. The level of CO_2 was mostly above 20% for 11 min from $t = 9$ min to $t = 20$ min. As the rate of mass loss gradually decreased (Fig. 1), CO concentration declined steadily from 17% to about 10% in that period of time. O_2 concentration began to rise at $t = 26$ min marking the final combustion stage.

3.3. Case ST5

Fig. 4 shows the measured bed temperature profiles for Case ST5. The temperature just below the bed top increased sharply at $t = 2.5$ min to 1064 °C in less than a minute. Such high temperatures and their gradients

Table 2
Test cases and process conditions for combustion tests in the fixed-bed reactor

Samples	Fibre length (mm)	Bed height (m)	Air flow rate		Bulk density (kg/m^3)	Case
			m/s	kg/m^2 h		
Straw (cut)	30–40	0.445	0.053	234	52	ST1
		0.471	0.106	468	60	ST2
		0.550	0.159	702	41	ST3
		0.550	0.212	936	41	ST4
		0.450	0.265	1170	65	ST5
Straw (uncut)	120–130	0.550	0.053	234	27	STU1
		0.550	0.159	702	39	STU3
Switchgrass	20	0.500	0.053	234	55	SW1
		0.450	0.106	468	68	SW2
		0.540	0.159	702	58	SW3
		0.560	0.212	936	57	SW4
		0.460	0.265	1170	66	SW5
Reed canary grass	10	0.540	0.053	234	99	RCG1
		0.600	0.106	468	90	RCG2

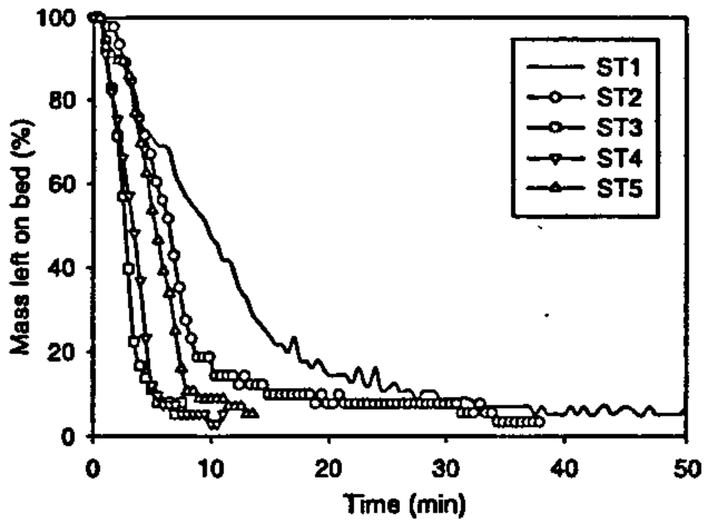

Fig. 1. Mass loss history as a function of reaction time.

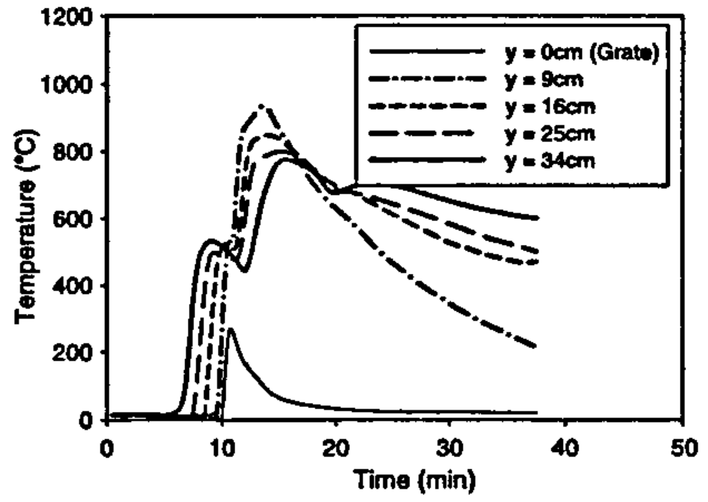

Fig. 2. Bed temperature profile for Case ST1.

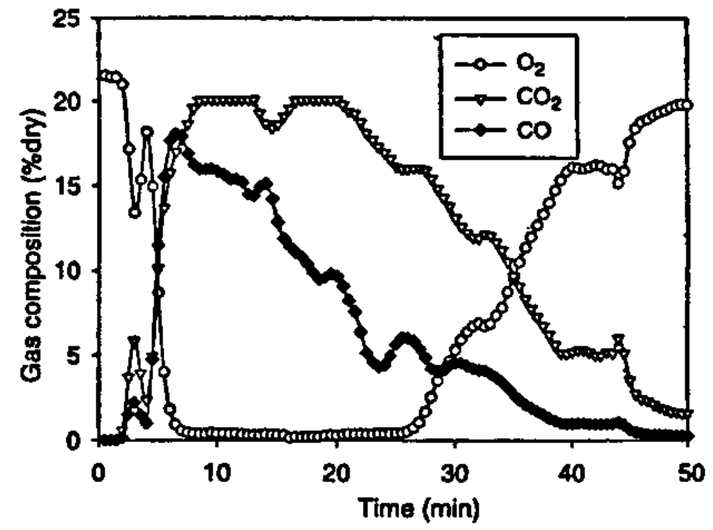

Fig. 3. Gas composition measured at the bed top for Case ST1.

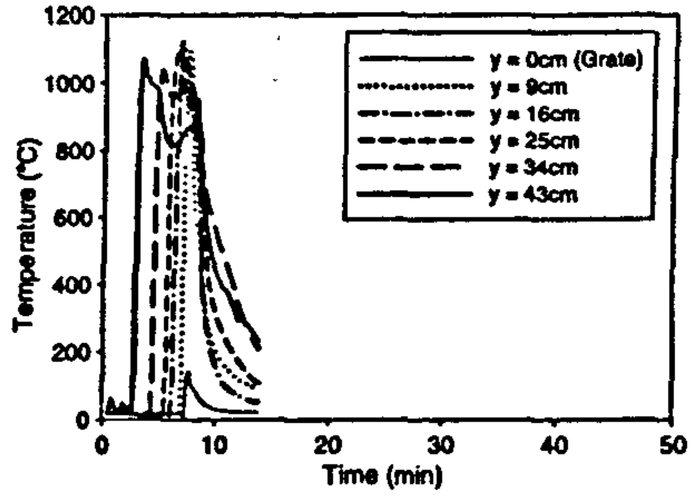

Fig. 4. Bed temperature profile for Case ST5.

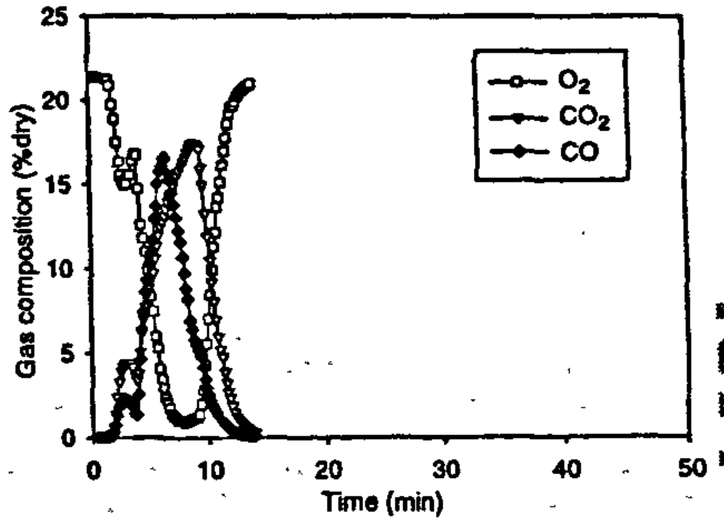

Fig. 5. Gas composition measured at the bed top for Case ST5.

indicate that the heat release at the ignition front and its transfer to fresh particles were more intensive than in Case ST1. In contrast to Case ST1, no further increase of temperature was observed after the ignition propagation stage. The whole combustion occurred mostly in a single stage, as the fuel has a large surface area per unit volume and the air supply was sufficient to oxidise char simultaneously with the reactions of volatiles.

Fig. 5 shows the gas composition in the flue gases for Case ST5. The CO and CO_2 level increased sharply at $t = 4$ min while O_2 concentration showed the opposite pattern. When the ignition front passed the gas sampling point ($y = 43$ cm), CO concentration peaked. Note that the gas residence time in the sampling line was about 1.6 min for this test. As the ignition front propagated further down, the CO concentration decreased and a peak CO_2 followed.

3.4. Ignition rate and burning rate

Fig. 6 compares the ignition rate and burning rate in the ignition propagation stage for cut straw and switchgrass. The burning rate represents the rate of mass loss per unit cross-sectional area, which was measured directly from the bed weight. The ignition rate is the rate of mass per unit cross-sectional area through which the ignition front passed. It was calculated by multiplying the ignition front speed by the bulk density of the bed. As the material should be pyrolysed before combustion, the ignition rate is always higher than the burning rate. The difference between the ignition rate and burning rate is the rate of mass accumulating above the ignition front, which is char and, if any, fresh material. As the remaining material after the ignition propagation stage burns at a much lower burning rate (20–80 kg/m² h for both herbaceous fuels), it is desirable to minimise the duration of the char gasification stage by increasing the mass loss in the ignition propagation stage.

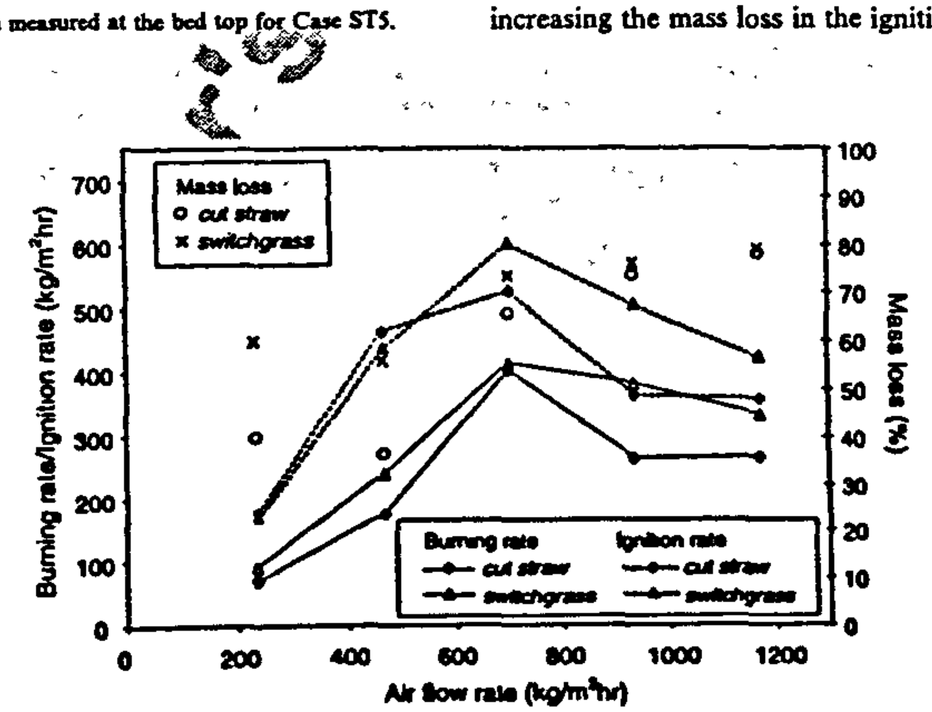

Fig. 6. Ignition rate, burning rate and mass loss in the ignition propagation stage for cut straw and switchgrass.

Table 3
Key parameters of combustion for the biomass samples

Sample	Case name	Mass loss in ignition propagation stage (%)	Ignition front speed (m/h)	Equivalence ratio in ignition propagation stage	Average burning rates (kg/m² h)
Straw	ST1	40	3.4	2.68	46
	ST2	36	7.7	3.37	109
	ST3	66	12.9	5.13	223
	ST4	74	8.9	2.55	169
	ST5	78	5.5	2.05	175
Switchgrass	SW1	60	3.0	3.54	60
	SW2	56	6.5	4.59	135
	SW3	73	10.4	5.23	168
	SW4	76	8.9	3.65	253
	SW5	79	6.5	2.55	186
Reed canary grass	RCG1	50	1.4	2.19	60
	RCG2	47	5.3	3.38	164

For the cases of straw at low air flow rates (ST1 and ST2) in Fig. 6, the ignition rate was much faster than the burning rate. The mass remaining after the ignition propagation stage was less than 60%. Such high level of mass indicates that the bed contained a large amount of fuel yet to be ignited. Two possible scenarios to explain this are (a) the ignition front propagates faster through larger voids between straw fibres, i.e., air channels and (b) some burning straw drop through the loosely packed bed and ignite the fresh straw below. This will be discussed later with the observation in the glass tube test for uncut straw. In Case ST5, however, the mass loss in the ignition propagation stage increased to about 80%. It suggests that all the fuel was pyrolysed and some of the char produced was oxidised during the ignition propagation stage.

Table 3 lists the key parameters for the combustion characteristics of tested biomass. The burning rate in the table is the averaged value for the whole duration of combustion. The end point of combustion was determined by the increase in oxygen concentration. The ideal air flow rate for straw and switchgrass combustion was in the range of 700–900 kg/m² h which provided a maximum burning rate and a short char gasification stage. The equivalence ratio was calculated for the ignition propagation stage from the burning rate, fuel elemental composition and air flow rate. As the grass fibres are very thin, they are quickly heated up and pyrolyse to release the volatiles which will then consume oxygen to provide heat required for the fresh material below the ignition front. The rapid ignition rate resulted in a fuel-rich condition in the bed as indicated by the equivalence ratios that were in the range of 2.0–5.2. The fuel-rich conditions were extreme when the burning rate in the ignition propagation stage peaked (Cases SW3 and ST3 in Fig. 6). High CO emission up to 28% and 21.5% respectively was measured in these two cases. The thin fibres are also less resistant to convective cooling by primary air which acts against the propagation of the ignition front. The reaction stoichiometry at the ignition front under higher air flow rates such as Cases ST4 and ST5 remained fuel-rich, although the burning rate decreased. Therefore, the effect of increased convection at the ignition front was stronger than the effect of increased temperature at high flow rates.

Fig. 7 shows the maximum bed temperatures measured in each stage of combustion for straw. Due to the high fuel-rich conditions, the maximum temperatures recorded in the ignition propagation stage were 550–720 °C for the air flow rates up to 702 kg/m² h. The peak values in the char gasification stage were about 910–990 °C in these cases. At high air flow rates, the char gasification stage

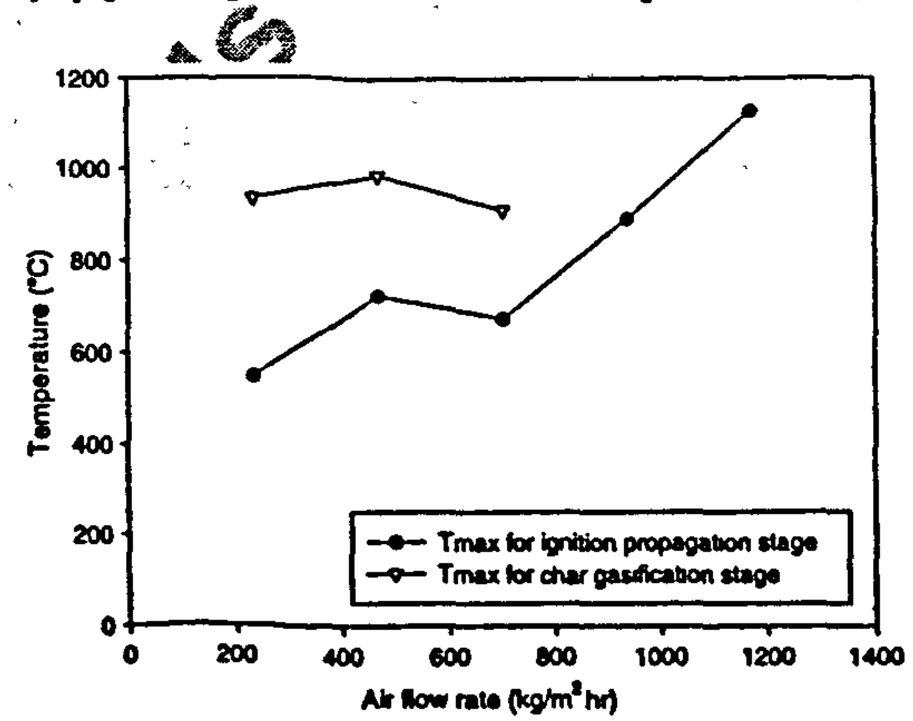

Fig. 7. Maximum temperatures measured in each stage of combustion for cut straw.

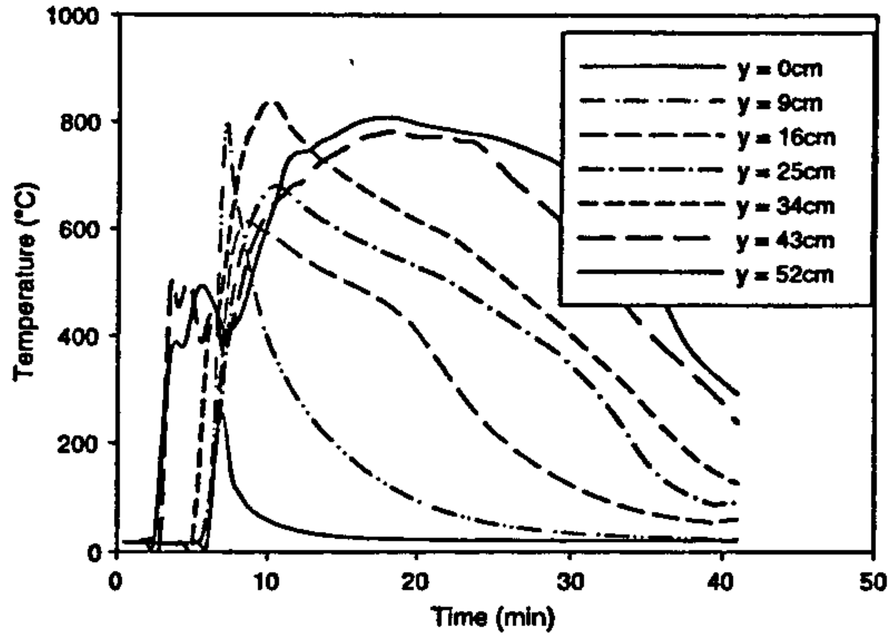

Fig. 8. Bed temperature profile for Case STU1.

was very short without a temperature peak, while the maximum temperature in the ignition propagation stage increased sharply to over 1100 °C for Case ST5.

3.5. Combustion of uncut straw

The combustion experiment was repeated for uncut straw (12 cm) in order to investigate the effect of fibre length on combustion. Fig. 8 shows the measured temperature history at different bed heights for Case STU1. Although the overall trend was similar to the cases of cut straw, the temperature jumps had irregular gaps between the thermocouples. After the ignition front reached the grate ($y = 0$ cm) in STU1, the temperatures at $y = 9$ cm and then $y = 34$ cm peaked. This means that the middle part of the bed was undergoing active combustion rather than the near the grate. This is caused by the non-uniform packing in which air penetrates through the easier path in the straw bed, igniting and burning the fuel as it propagates whilst by-passing sections of denser packed fuel.

The observation in the glass tube explained how the ignition front propagated in the bed at low air flow rates. Fig. 9 shows four photos taken during the glass tube test for uncut straw at an air flow rate of 280 kg/m^2 h. In Fig. 9a, another ignition front appeared 20 cm below the existing one on the right hand side. This happened several times and the lowest ignition front continued to develop consuming the air from below and leaving a large amount of partially unburned and carbonised material, as shown in Fig. 9b. Fig. 9c shows that the ignition front was not flat due to randomly developed air channels. After the ignition front reached the grate in Fig. 9d, the purple flame can be seen through the air channels across the bed. Therefore, both the two scenarios of air channels and falling down of burning particles mentioned previously were active during the ignition propagation stage. This resulted in a significant amount of unburned fuel above the ignition front. Fig. 9a also shows that the glass tube above the bed was filled with white smoke (aerosols of heavy-molecular-weight volatile matter condensed), and the flame was formed on top of the tube as the gas met the ambient air.

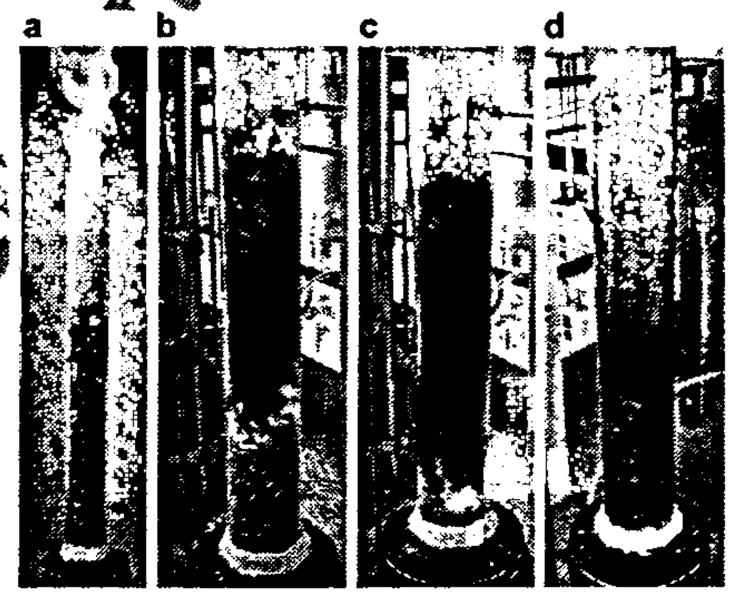

Fig. 9. Burning of uncut straw in a glass tube at an air flow rate of 280 kg/m^2 h: (a) $t = 20$ s; (b) $t = 106$ s; (c) $t = 194$ s; (d) $t = 207$ s.

Fig. 10 shows the gas composition in the flue gases for Case STU1. The behaviour of the flue gas composition in Case STU1 showed close qualitative similarity to Case ST1 (Fig. 3). However, a few percents of oxygen were available for a significant part of the combustion period. This indicates less efficient consumption of oxygen in the bed than in the Case ST1.

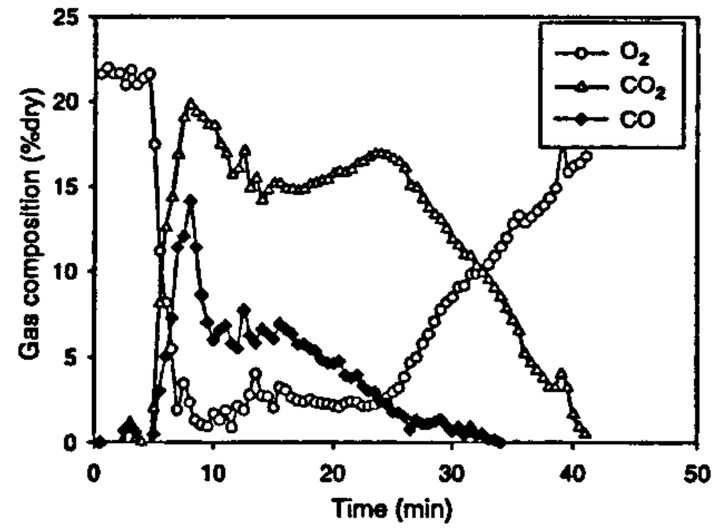

Fig. 10. Gas composition measured at the bed top for Case STU1.

Table 4 shows the key parameters for combustion of uncut straw. The length of straw clearly influenced the combustion behaviour by causing air channelling and irregular propagation of the ignition front. However, the high ignition rate did not accelerate the burning rate or mass conversion. The average burning rates in Table 4 are slightly lower than the corresponding cases of cut straw (ST1 and ST3) given in Table 3.

3.6. Characterization of bottom ash

The combustion of herbaceous fuels is hampered by high ash content and the ash fusion at low temperature leading to difficulty in grate operation and ash handling. Although the actual mechanism is still under investigation, it is well known that the reactions between K^+ and silicon (in the form of silica) with Cl^- as a facilitator leads to the formation of sintered and fused glassy deposits and slag. Allica et al. [18] suggested that the extraction of K^+ and Cl^- from straw by washing (leaching) the fuel with water as a means to reduce slagging and fouling in furnaces and other thermal conversion systems. In the study conducted by Allica et al. [18], the Cl^- content was captured in a closed straw cycle and the Cl^- content in the fertilizer also affected the content in the straw. The K^+ content was not influenced by the applied amount of K^+ fertilizer. Therefore, improved fuel quality can be achieved by washing the straw or application of a Cl^- free fertilizer. An alternative option suggested by Wilen et al. [5] was to raise the fusion temperature by powdery additives such as kaolin, talc and ceramic felspar. The addition of additive was estimated to increase the cost of pellets by 5% and increase the ash content leading to a reduction of heating value but it leads to cheaper combustion and ash handling equipment.

Table 5 shows the elemental composition of the bottom ash for three herbaceous crops compared to miscanthus pellets and willow wood chips from previous study [17]. The three herbaceous crops in this study had higher unburned carbon content as the combustion of thin fibres closer to the grate can be easily extinguished by convective cooling of primary air. Si, Ca, and K were dominant in the ashes of the herbaceous fuel. The fusion temperature of the ashes is increased by the presence of Si and reduced by K and Ca. The alkali index is the quantity of alkali oxide in the fuel per unit of fuel energy (kg alkali/GJ), which has been used as a threshold indicator for fouling and slagging. The problem of fouling and slagging is found to be likely for an alkali index above 0.17 kg/GJ and certain for an alkali index above 0.34 kg/GJ [19]. The highest alkali index was in straw (0.45 kg/GJ), followed by Miscanthus at 0.3 kg/GJ. However, the bottom ash of straw was not agglomerated due to the loose packing, unlike the Miscanthus pellets which sintered to form hard agglomerates of bottom ash [17].

Table 5
Elemental composition of bottom ash

Elements (%)	Switchgrass	Reed canary grass	Straw	Miscanthus[a]	Willow[a]
Si	22.40	22.20	11.45	34 90	2.73
Na	0.84	0.26	0 19	0.56	0.71
Ca	8.89	3.25	3 90	4.69	18.80
Al	1.45	0 29	0.29	1.97	0 82
Mg	1.14	0.58	0 62	1 03	2.28
Fe	1.19	0.43	0.63	5.40	13.20
Ti	0 23	0 03	0.04	0 19	0.20
P	0.92	0 84	0.24	0.33	4 65
Zn	0 05	0 02	0 02	0 05	0.22
K	1.88	1.33	7.55	2.24	5.24
C	14.20	24 40	10.60	0 43	0.67
S	0.43	0.24	0.79	0 15	0 48
Alkali index	0.07	0.05	0 45	0.30	0 04

[a] Data for miscanthus pellets and Willow wood chips in Ref. [17].

4. Conclusions

The combustion characteristics of three herbaceous crops were investigated in a fixed-bed reactor at various air flow rates. At low air flow rates, the progress of combustion had two distinctive stages: the ignition propagation

Table 4
Key parameters of combustion for uncut straw

Case name	Mass loss during ignition propagation (%)	Ignition front speed (m/h)	Ignition rate (kg/m^2 h)	Average burning rates (kg/m^2 h)	Equivalence ratio during ignition propagation
STU1	52	8 9	240	33	4.04
STU3	37	20 8	811	186	3 85

stage and the slow oxidation stage of char and unburned material. Single-stage combustion occurred at higher air flow rate because increased air supply oxidised most of the char remaining above the ignition front together with the volatile matter.

The ignition front speed and the average burning rate for straw peaked at 223 kg/m^2 h for an air flow rate of 702 kg/m^2 h and then decreased due to the convective cooling by primary air. At high air flow rates (936–1170 kg/m^2 h), less amount of char and unburned materials was left after the ignition propagation stage, which reduced the duration of the char gasification stage. The average burning rate of switchgrass had a maximum value of 253 kg/m^2 h at an air flow rate of 936 kg/m^2 h. As the grass fibres are less resistant to convective cooling by primary air, the air flow rates higher than the above value lowered the ignition and burning rates although the reaction was still highly fuel-rich. In the combustion of uncut straw, the severe channelling effect by the long fibres caused irregular propagation of the ignition front and lowered burning rates compared to the cases of cut straw.

The alkali index based on the elemental composition of bottom ash indicated that straw had a higher potential for slagging. However, it did not lead to the agglomeration of bottom ash due to the loose packing of the fibres.

Acknowledgements

The authors would like to thank the UK Engineering and Physical Sciences Research Council (EPSRC) and Supergen Biofuel and Bioenergy Consortium for financial support for this study. Thanks are also due to Nicola Yates (Rothamsted Research, UK) for the supply of straw and grass samples.

References

[1] Department of Environment, Food and Rural Affair (DEFRA). Climate change: Kyoto Protocol in force. Available from: http://www.defra.gov.uk/news/latest/2005/climate-0216.htm.

[2] Sir W Halcrow and Partners Ltd. The development of compacted straw fuel. In: Energy from biomass. Straw, poultry litter and energy crops as energy sources, vol. 5. London, UK: Department of Trade and Industry; 1999. p. 34.

[3] Martindale LP. The potential for straw as a fuel in the UK. IMech E Conference Publications, 1985. p. 125.

[4] Hare PM. Straw as a fuel in the UK. In: Energy from biomass. Straw, poultry litter and energy crops as energy sources, vol. 5. London, UK: Department of Trade and Industry; 1999. p. 27.

[5] Wilen C, Ståhlberg P, Sipilä K, Ahokas J. Pelletization and combustion of straw. Symposium papers – energy from biomass and waste, 1987. p 469.

[6] Rogaume T, Auzanneau M, Jabouille F, Goudeau JC, Torero JL. The effects of different airflows on the formation of pollutants during waste incineration. Fuel 2002;81:2277.

[7] Swithenbank J, Nasserzadeh V, Wasantakoran A, Lee PH, Swithenbank C. Future integrated waste, energy and pollution management (WEP). In: 2nd int symp incineration & flue gas treatment technologies, Sheffield, UK, 1999.

[8] Jorgensen K, Madsen H. Modern control systems for MSW plants. In: 2nd int symp incineration & flue gas treatment technologies, Sheffield, UK, 1999.

[9] Yang YB, Nasserzadeh V, Goodfellow J, Goh YR, Swithenbank J. Parameter study on the incineration of municipal solid waste fuels in packed beds. J Inst Energy 2002;75:66.

[10] Rönnbäck M, Axell M, Gustavsson L, Thunman H, Leckner B. Combustion processes in a biomass fuel bed – experimental results. Progress in thermochemical biomass conversion 17–22 September, Tyrol, Austria, 2000.

[11] van der Lans RP, Pedersen LT, Jensen A, Glarborg P, Dam-Johansen K. Modelling and experiments of straw combustion in a grate furnace. Biomass Bioenergy 2000;19:199.

[12] Zhou H, Jensen AD, Glarborg P, Jensen PA, Kavaliauskas A. Numerical modelling of straw combustion in a fixed bed. Fuel 2005;84:389.

[13] Kaer SK. Numerical modelling of straw-fired grate boiler. Fuel 2004;83 1183.

[14] Wornat MJ, Hurt RH, Yang NYC, Headley TJ. Structural and compositional transformations of biomass chars during combustion. Combust Flame 1995;100:131.

[15] Orlanders B, Steenari BM. Characterization of ashes from wood and straw. Biomass Bioenergy 1995;8:105.

[16] Yang YB, Ryu C, Khor A, Sharifi VN, Swithenbank J. Fuel size effect on pinewood combustion in a packed bed. Fuel 2005;84:2026.

[17] Ryu C, Yang YB, Khor A, Nasserzadeh V, Swithenbank J. Effect of fuel properties on biomass combustion: Part 1 experiments – fuel type, equivalence ratio and particle size. Fuel 2006;85:1039.

[18] Allica H, Mitre AJ, Gonzalez BJA, Itoiz C, Blanco F, Alkorta I, et al. Straw quality for its combustion in a straw-fired power plant. Biomass Bioenergy 2001;21:249.

[19] Jenkins BM, Baxter LL, Miles Jr TR, Miles TR. Combustion properties of biomass. Fuel Process Technol 1998;54:17.

Clean Hydrogen Production via Novel Steam-Air Gasification of Biomass

Adela Khor[a], Changkook Ryu[a], Yao-bin Yang[a], Vida N Sharifi[a] and Jim Swithenbank[a]

[a] *Department of Chemical and Process Engineering, Sheffield University*
Mappin Street, Sheffield S13JD, UK.
E-mail: cpp03ak@sheffield.ac.uk

ABSTRACT:

Gasification converts biomass into H_2 and CO rich product gas by using air, oxygen and/or steam as reaction agent. An experimental and modelling study of hydrogen production was conducted using a laboratory scale counter-current fixed bed gasifier with preheated air and steam as the gasifying agents. Commercial charcoal was used as the fuel and the reactor bed was maintained at temperatures of 750-960°C by external heaters H_2 (17-28vol%), CO (5-11vol%) and CO_2 (18-21vol%) forms a large portion of the synthesis gas produced depending on the ratio of the gasifying agent. The experimental work was coupled with both equilibrium and kinetic modelling to predict the equilibrium composition, conversion rates and temperature profile.

KEYWORDS : *gasification, hydrogen, synthesis gas, kinetic modelling, equilibrium modelling.*

1. INTRODUCTION

The demand for hydrogen is increasing due to the amount of hydrogen needed in refineries and the urgent need for a sustainable and renewable green energy. The Kyoto Protocol imposes emission targets under which the UK has agreed to the reduction of carbon emission by 12.5% on the 1990 level, by 2010 [1]. The shift towards a low CO_2 emission would mitigate the method of hydrogen and synthesis gas production from the common catalytic reforming of natural gas towards the production of hydrogen from water electrolysis or thermal conversion processes. The use of gasification to provide fuel for motor vehicles is an old art developed during the World War 2 where the shortage of petroleum products in Europe led to the use of a fixed bed gasifier unit attached to the front of a vehicle [2]. Similarly, the current energy and environmental situation led to many major companies such as Toyota, Daimler-Benz and General Motors investing in hydrogen-powered vehicle.

There are many types of gasification processes with a broad range of reactor types and operating conditions. The end-use of the gasification product and the economic factor are the primary factors that govern the selection of a particular type of gasification process. The gas turbine application is very sensitive to the quality of the gas and only extreme low levels of contaminants, principally tar, can be tolerated. This has traditionally rule out the application of counter-current gasification although the overall efficiency of the process is higher compared to the co-current gasification.

The three main parameters in the operation of a gasifier are the pressure, reactant and temperature. Gasification at high pressure increases the overall reaction rates at the expense of added complexity and lower formation of carbon monoxide and hydrogen. The gasification process comprises of both endothermic and exothermic reactions. The changes in temperature were found to influence the product gas composition [3]. Operation at high temperature increases the reaction rate especially for chemical reaction rate controlled processes. The presence of methane, steam and carbon dioxide in the product gas is favoured by low temperatures and high pressures whereas the presence of hydrogen and carbon monoxide is favoured by high temperatures and low pressures. Equilibrium consideration points to a high temperature, low pressure operating regime unless methane is the desired product [4].

The positive effect of an increase in reaction temperature on the tar content have been reported by several authors [5-8]. It is found that homogeneous secondary tar reactions become important at temperatures

higher than 650°C, indicated by the increasing concentrations of pyrolysis gases. In the investigation carried out by Morf [5], the gravimetric tar yield was found to decrease with increasing reactor temperatures during

homogeneous tar conversion. Therefore, in view of the positive effect of higher bed temperature on thermal tar cracking, work on high temperature gasification is underway. High bed temperatures in an air/steam gasifier can be achieved by either raising the feed temperature or by means of external heating. The latter is applied in this research to maintain the bed temperature at about 750-960°C.

The design of this gasifier is part of a two stage integrated unit that aims ultimately at utilizing biomass fuel such as wood chips or fuel pellets derived from agricultural waste. The gasifier differs from conventional system as it produces practically tar-free gases. The high operating temperature acts as a catalyst for the pyrolysis of tar to carbon and gas. Proposal is underway to combine this unit with a first stage pyrolysis chamber. The high exit gas temperature opens up opportunity to combine thermal gasification with Stirling engines for use in small combined heat and power plant due to increase in electricity generation efficiency (>15%). Another important feature of this gasifier is the rotating grate at the bottom of the system that allows ash particles to be removed from below the bed for a more efficient operation.

Mathematical modelling has always been a useful tool to provide detailed information on the temperature profile, gas compositions, bed height, pollutant formation and combustion stoichiometry. The three main types of models typically used for gasification system are the equilibrium, kinetic and Computational Fluid Dynamic (CFD). The type of model chosen depends on the objective and experimental information available. The gasification experiment was modelled using two different mathematical approaches in this study. The chemical equilibrium calculations were carried out using version 2 of NASA Glenn's computer program *Chemical Equilibrium with Application* (CEA) [2002]. The Fluid Dynamic of Incineration Combustion Code (FLIC) developed at the Sheffield University Waste Incineration Centre (SUWIC) to model packed bed combustion of solid fuel was adopted to model the gasification process [9-11].

2. EXPERIMENTAL SETUP

2.1 Gasification System

The experimental work was carried out using a batch type counter-current and updraft fixed-bed reactor at atmospheric pressure as presented in Fig 1. The reactor is a vertical cylindrical chamber suspended from a weighing scale. The height of the reactor is 1.5m with an inner diameter of 200mm and an interior tube of 4mm thick constructed with 316-stainless steel. The gasifier was heated electrically by ultra-high temperature, helically wound ceramic ribbon heaters. The grate at the bottom of the furnace was a perforated cone made with Inconel, with the centre slightly higher than the sides. A gear was fastened to the grate so that it can be rotated manually from the outside of the furnace to discharge ash if required.

The reactants (preheated steam and air) were fed into the gasifier through an L-shaped stainless steel tube located 100mm below the grate. Several outlet holes were located at the side of the tube to allow a uniform air flow across the cross-sectional area. The air was preheated electrically to 150°C. Saturated steam at temperature of 100°C was supplied from a steam generator. The temperature profiles were measured by a set of thermocouples located in the centre of the gasifier. The first thermocouple was placed just above the grate with the other 5 thermocouples placed 20mm apart from each other. This was followed by another 2 thermocouples placed 50mm apart.

The flue gas exits from the top of the furnace into two shell and tube condenser units to cool the gases down before gas measurements were taken. The condensed liquid which captures solid particles entrained by the gas flows down the tubes into collection bottles. The outlet gases are then flowed through a demister consisting of a glass cylinder filled with glass wool. This ensures that the outlet gases are sufficiently clean for online gas-chromatographic analysis (PCG2000) equipped with thermal conductivity detector (TCD)) with a span time of 570s. The CO, CO_2 and O_2 were also measured using an MGA 3000 gas analyser. The GC and the gas analyser were connected to a data logger together with the thermocouples.

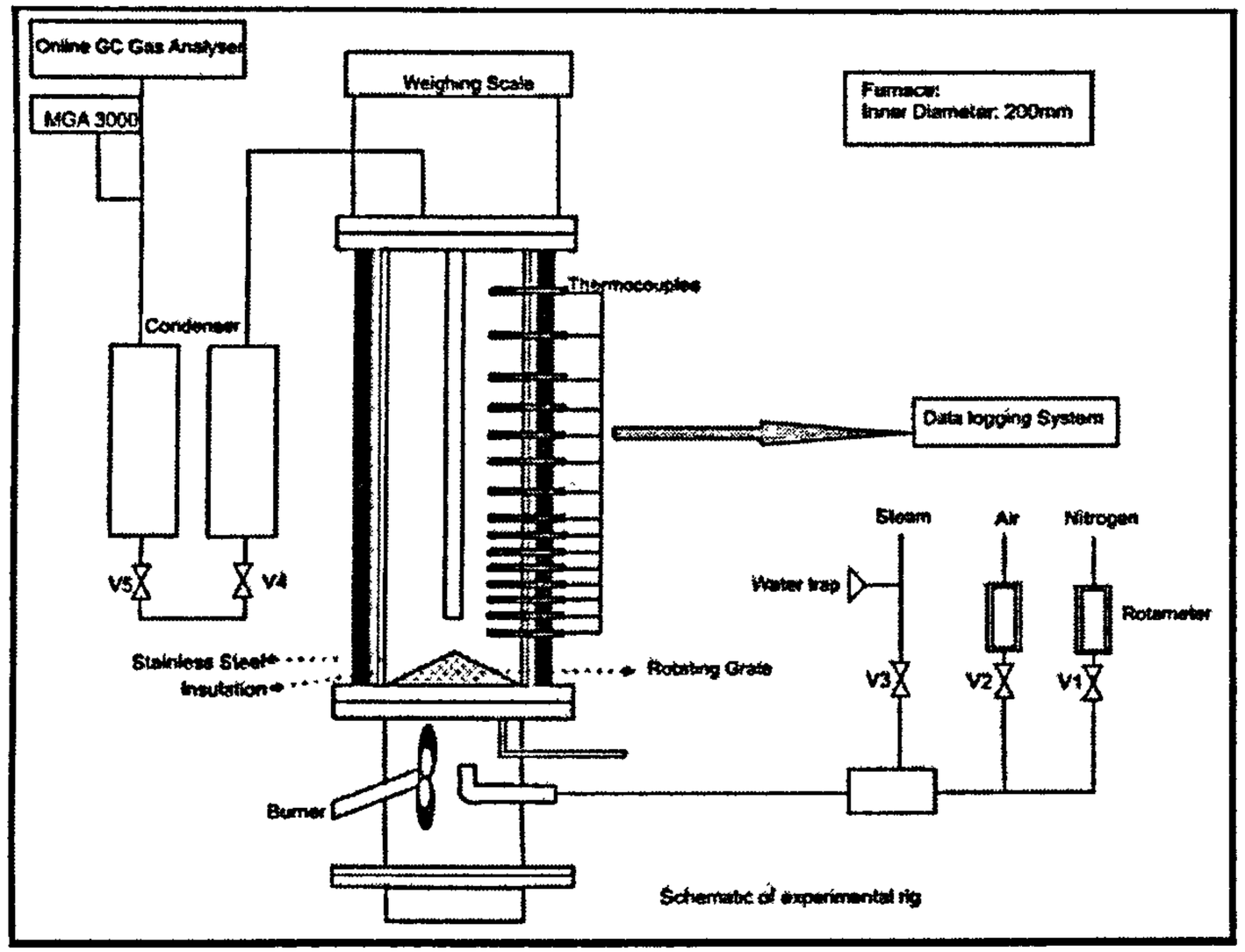

Fig. 1: Schematic diagram of the fixed-bed gasifier installation.

2.2 Test Conditions

The fuel used for the gasification tests was commercial lumpwood charcoal, sized manually to about 3mm in diameter. The furnace was initially filled with 4kg of lumpwood charcoal giving a bed height of about 348mm and preheated to about 700°C under the influence of nitrogen to prevent any oxidation reaction. The mass loss during the heating up of the charcoal is about 20% wt as the initial material contains 2.5% wt moisture and 20%wt volatile. Table 1 lists the results of the standard fuel analyses for the materials before and after preheating

Samples		Before preheating	After preheating
Proximate analysis (%wt)	Moisture	2 59	0 86
	Volatile matter	20 46	3 86
	Fixed Carbon	74 15	91 81
	Ash	2 81	3.47
Ultimate analysis (%wt)	C	75 32	90 66
	H	3 39	0.71
	O*	15 91	4 30
Gross Calorific Value (MJ/kg)		28 45	30.32

Table 1: Lumpwood charcoal analysis.

The supply of gasifying agents started when the bed temperature of the gasifier reached the target temperature. The operating conditions are as listed in Table 2. The effect of air and steam were investigated for the air flow rate ranging from 220kg/m²hr to 294kg/m²hr and steam flows of 95-196kg/m²hr. The test runs are named according to the volume of each reactant supplied. For example, the "A90-S30" run refers to the

gasification using 90l/min of air (220kg/m²hr) and with steam making up 30%wt of the total input reactant (preheated air and steam).

Air flow rate		Steam flow rate	Mass percentage of steam	Case Name
(lit/min)	(kg/m²hr)	(kg/m²hr)	(%)	
90	220 60	94 54	30	A90-S30
90	220.60	118.73	35	A90-S35
90	220 60	147.06	40	A90-S40
100	245 04	81 68	25	A100-S25
100	245.04	105.05	30	A100-S30
100	245.04	131.78	35	A100-S35
100	245.04	163 30	40	A100-S40
110	269.55	115 55	30	A110-S30
110	269 55	145 15	35	A110-S35
110	269 55	179.85	40	A110-S40
120	293 94	195 96	40	A120-S40

Table 2: Process conditions for the test cases.

3.0 MATHEMATICAL MODELLING

3.1 Chemical Equilibrium

The chemical equilibrium calculations were carried out using version 2 of NASA Glenn's computer program Chemical Equilibrium with Application (CEA) [2002]. CEA is based on a non-stoichiometric formulation to calculate reaction equilibrium based on the minimisation of Gibbs free energy [12]. The program obtains chemical equilibrium composition for the assigned thermodynamic state such as temperature and pressure. The CEA programme was used to calculate the chemical equilibrium for three cases (A110-S30, A110-S35 and A110-S40) from the gasification test. The gas phase composition was assigned to take into account the main species in the outlet gas such as CH_4, CO, CO_2, H_2, H_2O and also minor species that might be present, C_2H_6, C_3H_8, HCN, O_2 and NH_3. The elemental composition of the solid fuel (commercial charcoal) was set according to the ultimate analysis and the enthalpy of formation of the commercial charcoal was calculated to be -254kJ/mol based on the higher heating value.

The main objective of this calculation is to give an insight into the chemical equilibrium based on the carbon conversion rate of the gasification experiments.

3.2 Comprehensive Mathematical Modelling

The FLIC code is a one-dimensional, unsteady mathematical model which includes heat and mass transfer for gas, solid and reaction rate kinetics for the combustion and gasification of char and gaseous species. In this calculation, major bed properties, i.e. temperatures of gas and solid phases inside the bed, gas compositions and solid compositions is described on dimensionally as a function of bed height. The surface-volume averaged diameter used is the shape of a particle assuming it to be spherical. The individual bed processes is viewed to take place layer by layer, from the bed top to the bottom. The FLIC code was previously designed and used to simulate packed bed combustion of solid fuels [9-11].

In the simulation, the whole bed is divided into 60 sections along the bed height and time-dependent solutions were sought. The relaxation factor was set to 0.5 and the convergence criteria at 0.005. The calculated space height was set to 500mm. The model was used to simulate a laboratory-scale plant, which is cylindrical in shape with a 0.1m internal diameter and 1.5m length. The bed properties for the charcoal samples were those of experiments, as listed in Table 1. The particle size was taken as 30mm and the bed porosity Φ was taken as 0 69. The wall temperature was set and maintained at 725°C assuming no heat losses to the surrounding as the equipment was well-insulated in the laboratory experiment. The steam and air flow rates were selected in accordance with the experimental conditions and at temperature of 150°C. The calculations were made based on the reaction kinetics given by Hobbs [13] for char/CO_2, char/steam , char/O_2 and char/H_2. The kinetics for the water-gas shift reaction was based on the values given by Biba [14].

4.0 RESULTS AND DISCUSSION

4.1 Dynamic behaviour

Figure 2 shows the temperatures measured at several positions along the centre of the gasifier for Case A110-S30. The temperature profile in the bed was fairly steady and reproducible as this case was repeated several times. The temperature profile for the rest of the test cases also showed similar behaviour with the bottom of the bed the hottest due to the different chemical processes stratified along the reactor height. The temperature measurement at the bottom of the bed reflects the removal of ashes. The temperature at y=46mm is the highest at the start of the experiment. The lower temperature at the bottom of the bed (y=6mm) could be due to the contact with steam and air cooling the bed. The bottom temperature starts to drop 20°C during t=442-449min. The temperature decrease corresponded to the time when the ashes were removed from the bottom of the bed. The temperature at y=6mm started escalating after the discharge of the ashes while the temperature at the upper section starts declining (y=46mm, y=86, y=106mm) due to the bed movement. It can also be seen from the dynamic temperature oscillations at the bottom section of the bed that the conversion processes were very active in this region. The maximum bed temperature observed for this case was about 980°C.

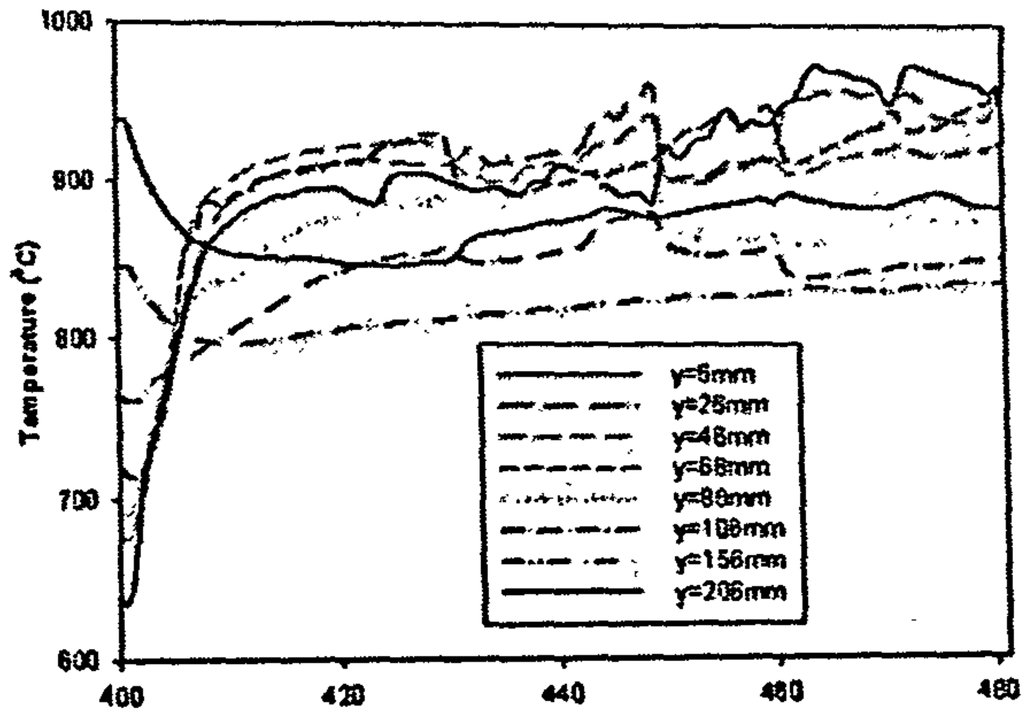

Figure 2: Temperature-time profile at several locations along the gasifier axis for Case A110-S30.

4.2 The Effect of Reactant Supply on the Production of Hydrogen Gas: Composition of Dry Product Gas and HHV

The product gas contains the combustible and non-combustible gases, moisture and soot. Figure 3 shows the dry product gas composition and higher heating values (HHV) of five representative gasification conditions operated with 40%wt of steam and air flow rates of 50l/min, 90l/min, 100l/min, 110l/min and 120l/min. The showed the effect of higher input reactant on the gasification reactions under a constant proportion of steam to air ratio. The synthesis of H_2 (28%) and CO (10%) was the highest for Case A90-S40 and declines as the total flow rate of reactant increases. The concentration of CO_2 was about 21% for all the cases except Case A90-S40. The evolution of H_2 and CO was considerably low for Case A50-S40 due to the limited amount of reactant supplied. CH_4 concentration was negligible with the highest concentration of only 0.32% shown in Case A100-S40. The average bed temperature for all the five cases increased with a higher input of reactant. Therefore, it can be said that the decrease in H_2 and CO arise from more air entering the reactor resulting in the exothermic burning of these two gases in the oxidation zone and thus, contributing to the increase in bed temperature. Therefore, it can also be postulated that the air flow rate have an exceeding influence over the production of H_2 compared to the steam flow rate as the higher mass flow rate in the input steam did not result in a higher production of H_2 in the test cases. The result obtained in this study agrees

with the observations made by Midili [15] in his experiment with an air-blown downdraft gasifier where the flow rate of hydrogen gas and temperatures at oxidation zone decreased arising from more air entering the reactor bed. Thus, combustion was said to occur in the reactor bed rather than the gasification. The dry product gas has around 19-38% of combustible gases with higher heating values of 2-4.4MJ/kg. The heating value of the flue gas decreases with increasing reactant feed because of the low amount of CO and H_2. The char conversion rates for the four cases (cases A90-S40, A100-S40, A110-S40 and A120-S40) with higher input reactants varied in the range of 40-50kg/m²hr.

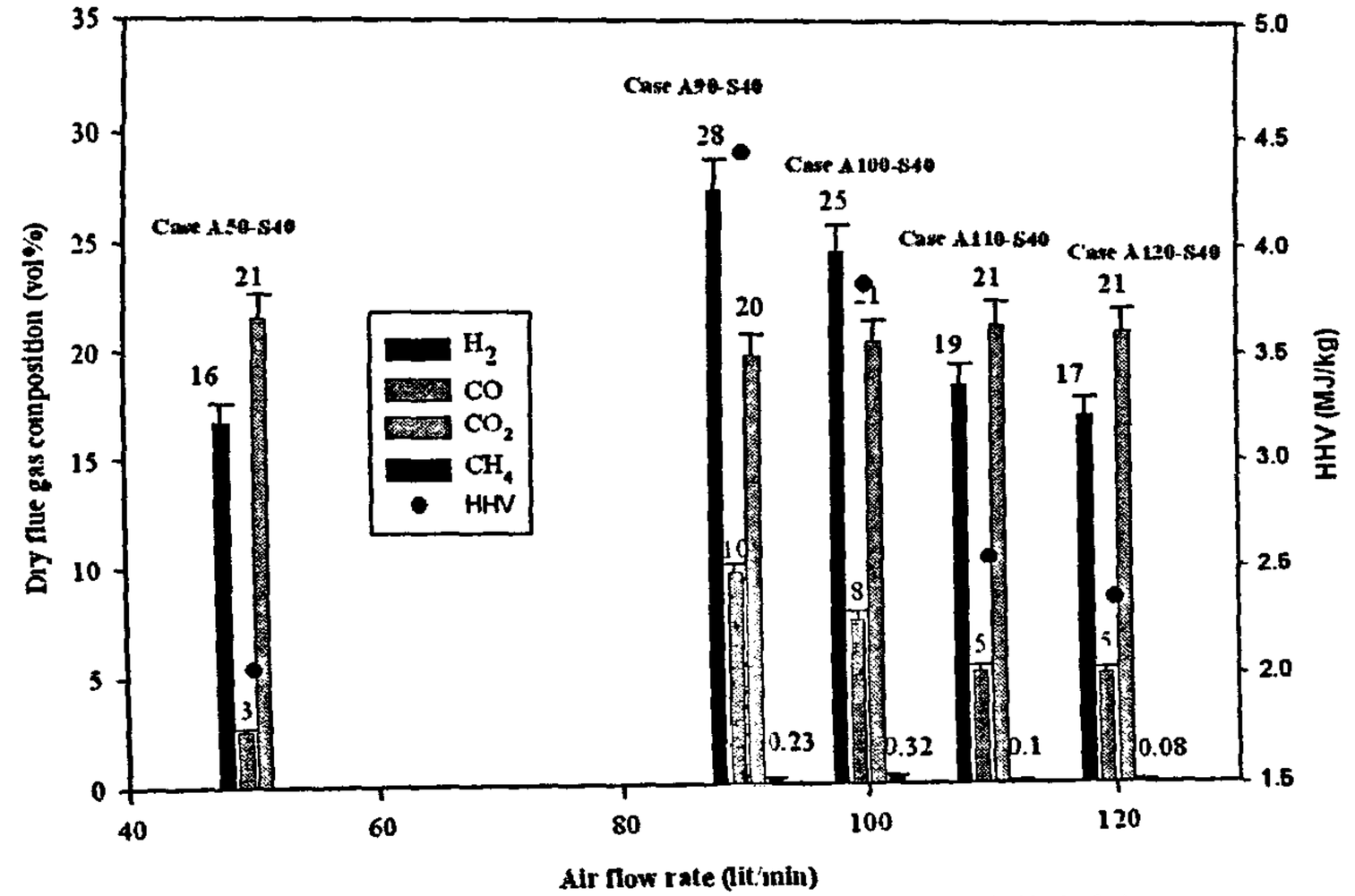

Figure 3: Dry flue gas composition and its HHV for all cases with 40%wt of steam.

Table 3 presents the conversion ratios of hydrogen gas from char gasification via steam-air blown downdraft gasification technique. The flow rate of hydrogen and combustible gas from char was calculated using the mass balance of the input reactants, conversion rate and flue gas concentration. The production ratio of the gases was calculated based on the mass of gases produced per mass of char converted.

Case	Hydrogen gas from char (kg/h)	Combustible gas from char (kg/h)	Hydrogen gas production ratio (%)	Combustible gas production ratio (%)
A50-S40	0.057	0.179	10.83	34
A90-S40	0.232	1.394	14.56	87.5
A100-S40	0.22	1.176	13.90	74.3
A110-S40	0.142	0.692	10.90	54
A120-S40	0 139	0 705	10 30	52

Table 3: The conversion ratios of char to hydrogen gas.

4.3 The Effect of Increasing Steam to Air Ratio on Hydrogen Production: Composition of Dry Flue Gas and HHV

The effect of steam flow rate on the gas composition was investigated in order to establish the role of the different reactions in the gasification process The air flow rate is kept constant at 110l/min while the steam composes of 30, 35 and 40%wt of the total reactant flow rate. A higher formation of H_2 was attained as the feed steam was increased from 30% in Case A110-S30 to 35% in Case A110-S35. The molar fraction of CO decreases at the expense of the production of CO_2. The bottom bed temperature was found to decrease from 900 to 880°C as the steam flow rate was increase from 30% to 40%. The char conversion rate was also found to be slower at a higher flow rate of steam feed. Two gasification reactions that have significant effects on the formation of H_2 are the water gas reaction ($C_{(s)} + H_2O_{(g)} \rightarrow H_{2(g)} + CO_{(g)}$) and the water-gas shift reaction ($CO_{(g)} + H_2O_{(g)} \leftrightarrow CO_{2(g)} + H_{2(g)}$) The increase of H_2 is favoured by the increase of the exothermal character of the water-gas shift reaction which begins and predominates between 500 to 600°C, and the water gas reaction which becomes significant at temperatures from 1000°C upward [15]. Assuming that the water-gas shift reaction and the water gas reaction are the main gasification reactions, the ratio of CO_2/CO would provide an indication of the main reaction governing the production of H_2, which in the case of this work is the water-gas shift reaction.

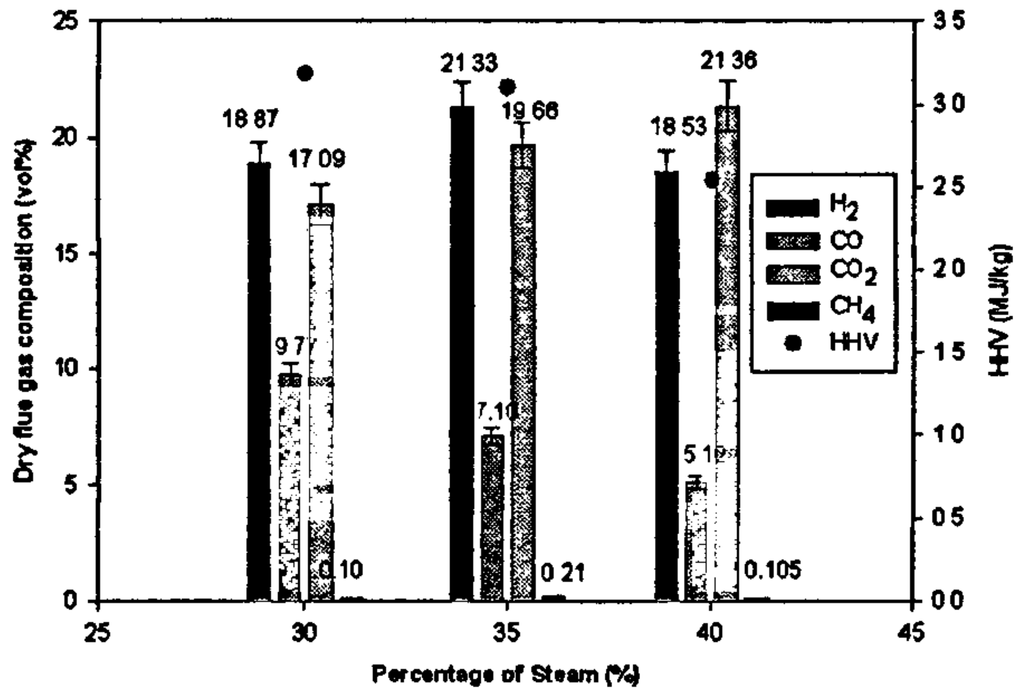

Figure 4: Dry flue gas composition and its HHV for all cases for 110l/min of air (preheated) and with steam at 30, 35 and 40% of the total reactant input.

The increase in H_2 evolution in Case A110-S35 may be due to the addition of steam in the reacting. This enhances the water-gas shift reaction and as consequence, result in a decrease of CO and an increase of CO_2 The higher formation of H_2 with increasing steam was also reported in work carried out by Lucas [16] where the steam-biomass reaction rates was enhanced relative to the competing reactions by increasing the reactive agent steam in the feed gas. A parallel increase in H_2 yield was seen with increasing steam/biomass was found in the gasification experimental investigation by Turn [17].

From Figure 4, the H_2 concentration declined to about 18% when the steam feed rate was further increased to 40%. The drop in H_2 evolution could be due to the influence of the lower bed temperature Both the reactor temperature and feed temperature was proven to have an effect on the H_2 yield [3, 17, 18]. The water-gas and Boudouard reactions are endothermic and thermodynamically favourable at high temperature. The lowering of bed temperature due to the addition of steam as in Case A110-S40 could have possibly reduce the influence of these two reactions resulting in both a slower char conversion rate, H_2 and CO_2 evolution. Similar trend was reported by Franco [18] whereby the H_2 formation reaches a maximum with increasing steam/biomass ratio and then declines as the ratio was further increased. In his work, the CO was found to decrease significantly while no significant changes was observed for CO_2.

The lack of existence of higher hydrocarbon, C_xH_y and negligible amount of CH_4 (0.1-0 2%) promises a tar free synthesis gas by utilizing a high temperature two-stage gasification process in which a large part of the higher hydrocarbons and contaminant were removed during the pyrolysis step. The result of which is a clean synthesis gas, without the necessity of excessive gas cleaning Work is currently underway to combine this high temperature gasifier with a first stage pyrolysis chamber using char for catalytic cracking of tar.

Figure 5 shows the effect of additional steam on the H_2/CO ratio at varying air flow rates. The H_2/CO molar ratio was quite high for steam and air gasification of the commercial char, ranging up to 3 6. The results show that as the steam feed increased, the ratio of H_2/CO increased sharply. The increase in H_2/CO ratio in the product gas was mainly due to the decrease in concentration of CO with increasing steam feed.

Therefore, the H_2/CO in the synthesis gas can be adjusted to suit different applications by manipulating the steam input.

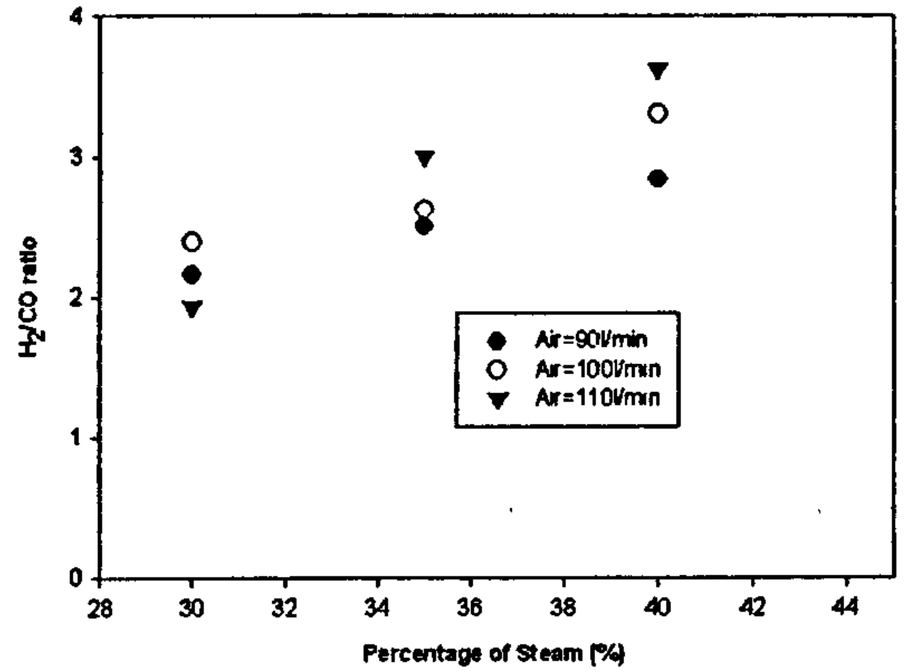

Figure 5: H_2/CO ratio obtained during steam and air gasification of commercial char at various feed flow rates.

4.4 Chemical Equilibrium Modelling

Figure 6 shows the results from the equilibrium calculation compared to the experimental measurements. Comparison was made based on the measured average temperature in the gasifier. The composition of the wet flue gas was calculated through mass balances as experimental measurements were made based on the dry flue gas composition.

On the overall, the calculation prediction of the influence of steam on the composition flue gas showed good agreement with the trend obtained from the experiment measurements. An increase of steam input causes a drop in the CO and H2 concentration and a step up in H2O concentration for cases carried out with 110l/min (A110).

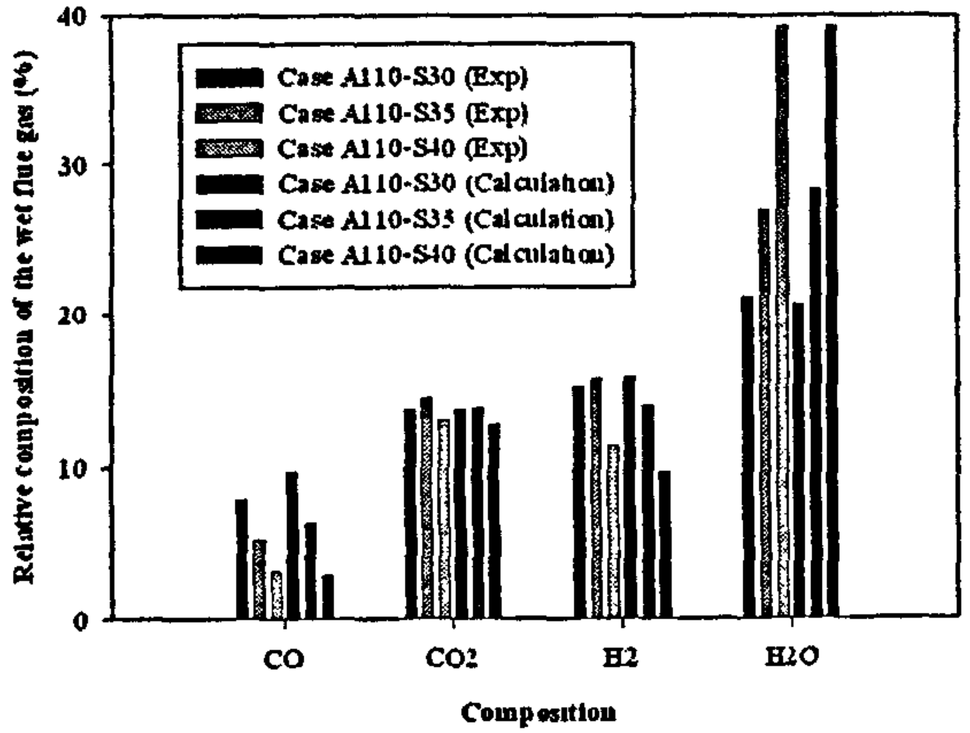

Figure 6: Comparison between the experimental and calculations showing the influence of steam cases with air feed of 110l/min (preheated).

4.5 Detailed Mathematical Modelling (FLIC)

a)

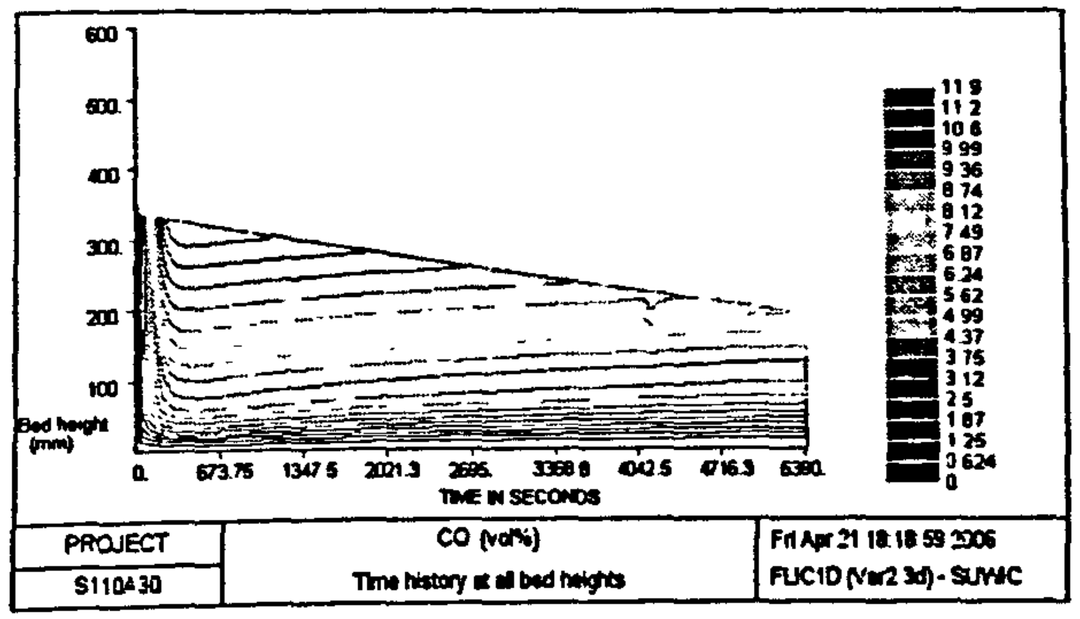

b)

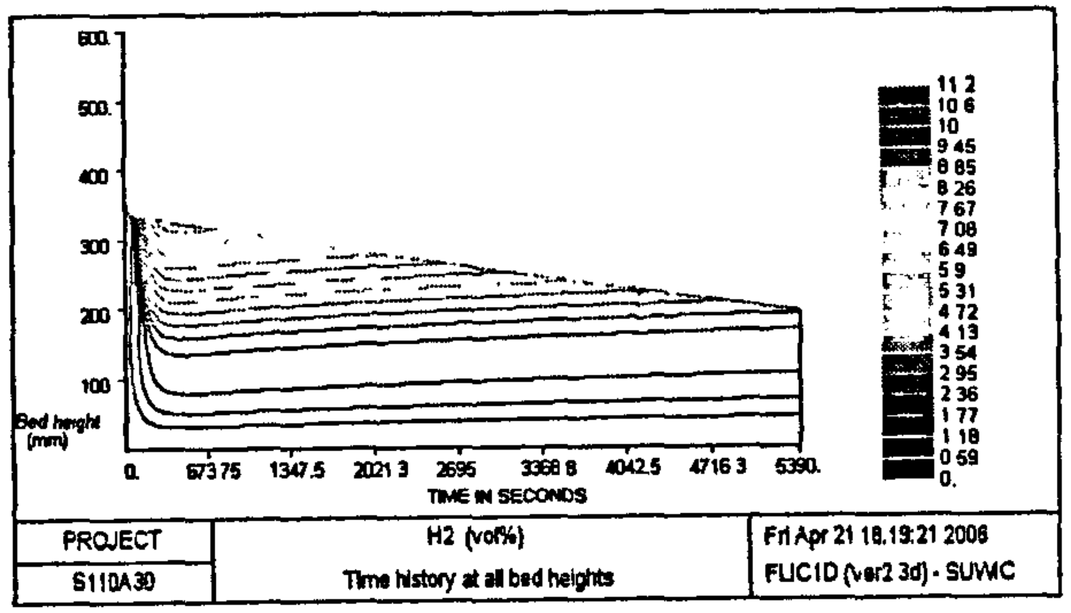

c)

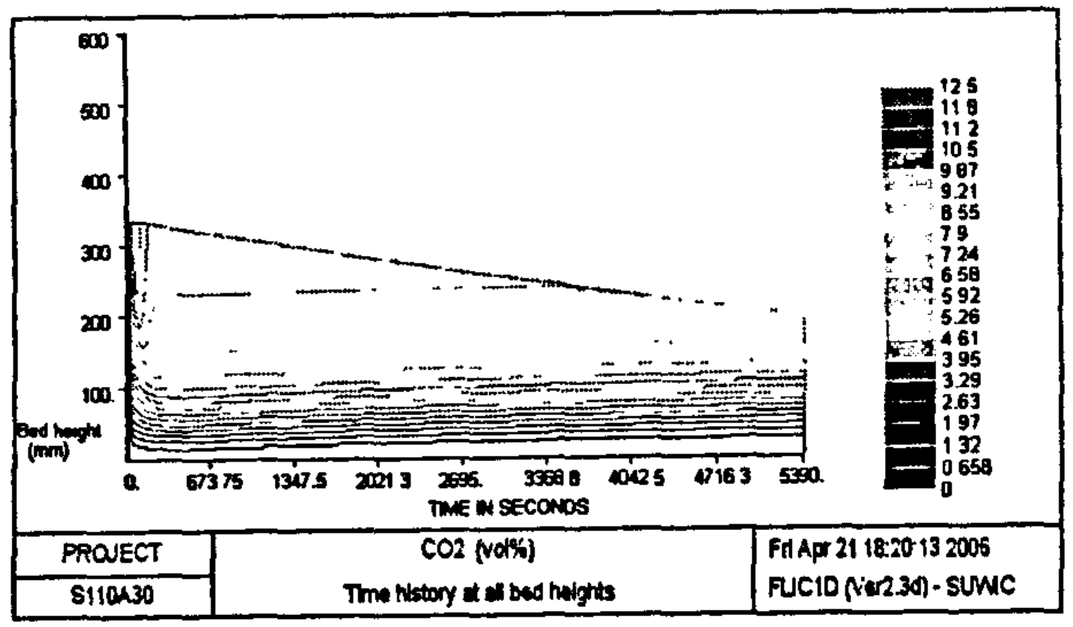

Figure 7: Calculated dry flue gas composition in the bed vs. reaction time. (a) CO; (b) H_2; (c) CO_2

The calculation demonstrates that CO is the dominant component at 100mm from the bottom of the bed compared to the other two components (H_2 and CO_2) due to the partial combustion of the carbonaceous char material (Figure 7). H_2 is formed further along the bed due to the gasification reactions with water leading to a release of CO and CO_2. The simulations showed layer of inactive material at the bottom of the bed due to the accumulation of ash. The accumulation of ashes at the bottom of the bed resulted in the loss of sensible heat in heating up the ashes in the calculation. Figure 8 below shows the calculated solid bed temperature for Case A110-S30. The temperature at the bottom of the bed (y=4mm, y=21mm) is decreases with time due to the loss in sensible heat in ashes. The temperature profile obtained from the calculation was about 150°C lower compared to the experimental measurements (Figure 2). However, the calculation was able give a close representation of the dynamic change in temperature along the stratified gasifier.

Figure 9 compares the calculated and measured wet flue gas composition for various steam feed. Both the calculation and measurements showed similar trend in the flue gas composition as flow rate of the feed steam was increased. The calculations showed a slight over-prediction of CO and a much lower release of CO_2 and H_2. This could be due to the under estimation of the CO combustion or water-gas shift reaction. The slow prediction of these exothermic reactions also explains the lower bed temperature in the calculations compared to the experiment. The calculated mass burning rate at 40kg/m²hr which is slower compared to the experimental mass burning rate of about 49kg/m²hr would in consequence result in a lower bed temperature.

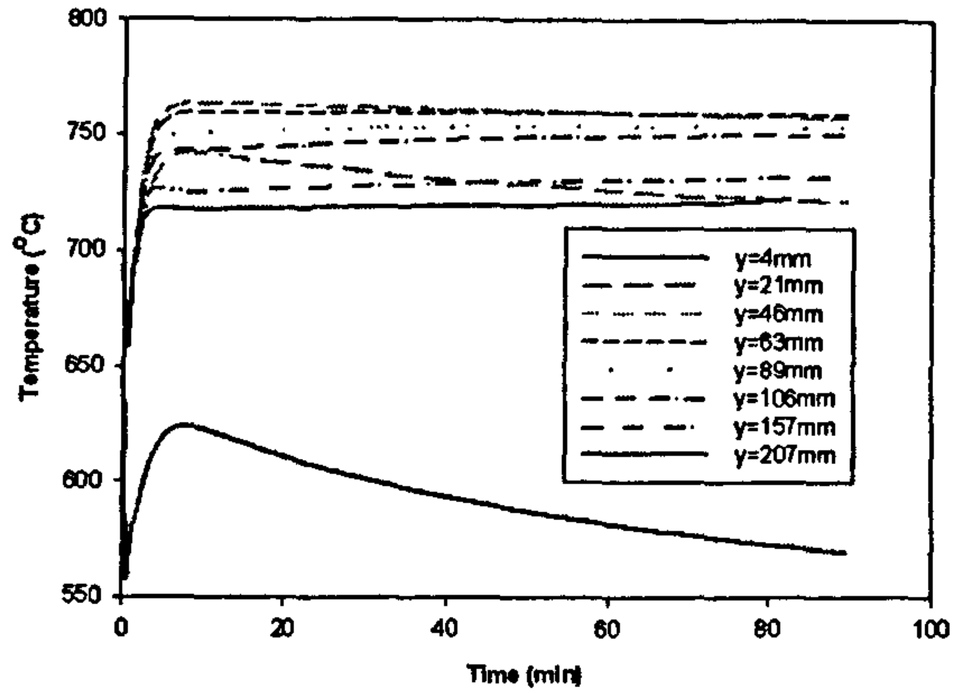

Figure 8: Calculated solid bed temperature vs. reaction time for Case A110-S30.

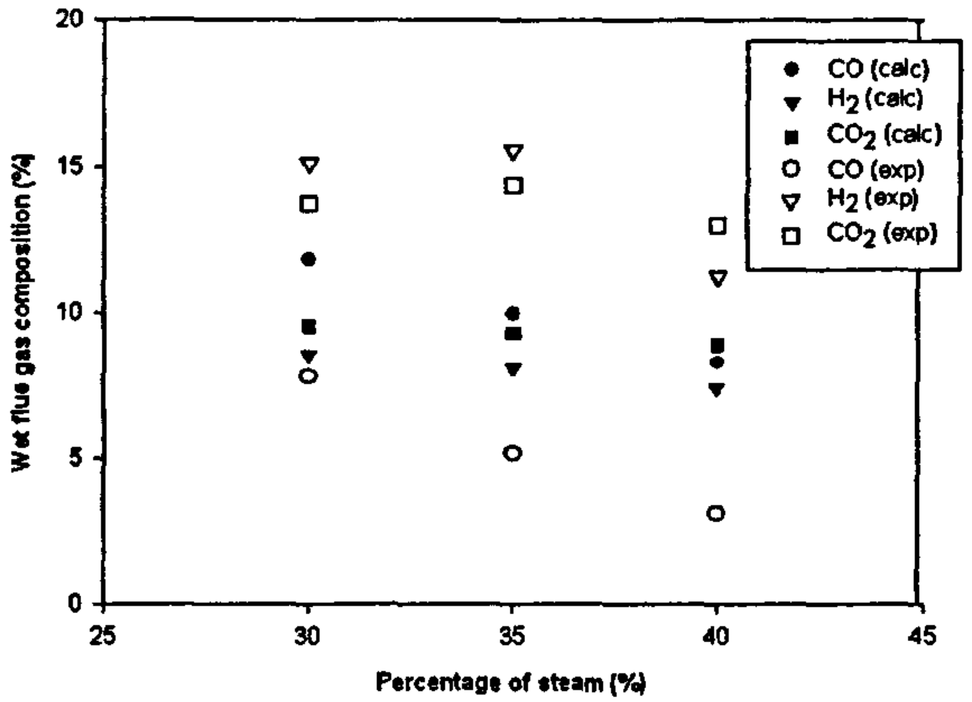

Figure 9: Measured and calculated wet flue gas composition showing the influence of steam for cases with air feed of 110l/min (preheated).

CONCLUSION

The following conclusion from the results of the high temperature air and steam gasification experiments and modelling can be summarised as follows:

(1) The percentage of hydrogen gas was the highest among all the combustible gases.
(2) The production of hydrogen gas was influenced by the air to steam ratio and the total feed flow rate. By entering more air in the oxidation zone, the production of hydrogen and carbon monoxide decreased as combustion occurred in the reactor bed. The addition of steam could lower the bed temperature resulting in a decrease of synthesis gas production. The ratio of H_2/CO could be manipulated by adjusting the steam feed.

(3) The conversion rate obtained in the experimental work ranged in the region of 40-50kg/m²hr depending on the reactant input.
(4) The hydrogen yield obtained in the counter-current reactor was about 10-14kg/hr of hydrogen from 100kg of biomass char.
(5) The rotating grate applied in the counter-current reactor successfully reduced the sensible heat losses in the ashes and helped maintain a high temperature and active region at the bottom of the bed.
(6) The production of methane was negligible and no higher hydrocarbons were detected. Therefore, proposed combination of this gasification chamber with a first stage tar-cracking pyrolyser would allow a low tar content in the synthesis gas.
(7) The calculated results agreed qualitatively with experiments and showed similar trends in the performance of the gasifier with varying flow rates of the reactant feed.

ACKNOWLEDGEMENTS

The authors would like to thank the UK Engineering and Physical Sciences Research Council (EPSRC) and Supergen Biofuel and Bioenergy Consortium for financial support for this study.

REFERENCES

1. Department of Trade and Industry, DTI. UK and Climate Change, available from http://www dti gov.uk/ccpo/uk.htm.
2. McKendry, P., Energy production from biomass (part 3). gasification technologies. Bioresource Technology. 83(1): p. 55-63 2002
3. Chaudhari, S.T., A.K. Dalai, and N.N. Bakhshi, Production of Hydrogen and/or Syngas (H2+ CO) via Steam Gasification of Biomass-Derived Chars. Energy Fuels. 17(4): p. 1062-1067. 2003.
4. Merrick, D., Coal combustion and conversion technology. Energy alternatives series.: London : Macmillan, 1984.
5. Morf, P., P. Hasler, and T. Nussbaumer, Mechanisms and kinetics of homogeneous secondary reactions of tar from continuous pyrolysis of wood chips. Fuel. 81(7): p 843-853. (2002)
6. Yu, Q., et al., Temperature impact on the formation of tar from biomass pyrolysis in a free-fall reactor. Journal of Analytical and Applied Pyrolysis PYROLYSIS '96. 40-41: p. 481-489. (1997).
7. Devi, L., K.J. Ptasinski, and F.J.J G. Janssen, A review of the primary measures for tar elimination in biomass gasification processes Biomass and Bioenergy. 24(2): p. 125-140. (2003).
8. Brandt, P., E. Larsen, and U. Henriksen, High Tar Reduction in a Two-Stage Gasifier. Energy Fuels. 14(4): p. 816-819.
9. Yang, Y.B., et al , Effects of fuel devolatilisation on the combustion of wood chips and incineration of simulated municipal solid wastes in a packed bed*. Fuel. 82(18): p. 2205-2221. 2003.
10. Yang, Y B., et al., Fuel size effect on pinewood combustion in a packed bed. Fuel. 84(16): p. 2026-2038 2005.
11. Yang, Y.B., et al , Effect of fuel properties on biomass combustion. Part II. Modelling approach–identification of the controlling factors. Fuel. 84(16): p. 2116-2130. 2005.
12. Gordon, S., and B. J. McBride:, Computer Program for the Calculation of Complex Chemical Equilibrium Compositions with Applications, I. Analysis. NASA Reference Publication 1311. 1994
13. Hobbs, M.L.B.Y.U.R., Predrag T.; Smoot, Douglas L., Modeling fixed-bed coal gasifiers. AIChE Journal. 38(5): p. 681-703. 1992.
14. Biba, V.M., Jiri; Klose, Erhard; Malecha, Jiri., Mathematical model for the gasification of coal under pressure. Industrial & Engineering Chemistry Process Design and Development. 17(1): p. 92-98. 1978.
15. Midilli, A., et al., Hydrogen production from hazelnut shell by applying air-blown downdraft gasification technique. International Journal of Hydrogen Energy. 26(1): p. 29-37. 2001.
16. Lucas, C., et al., High-temperature air and steam gasification of densified biofuels Biomass and Bioenergy Pellets 2002. The first world conference on pellets. 27(6): p. 563-575. 2004.
17. Turn, S., et al., An experimental investigation of hydrogen production from biomass gasification. International Journal of Hydrogen Energy. 23(8): p. 641-648. 1998.
18. Franco, C., et al., The study of reactions influencing the biomass steam gasification process*. Fuel. 82(7): p. 835-842. 2003.